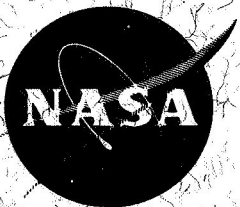


NASA TM X-63261

FINAL REPORT 1967 SESSION OF THE GODDARD SUMMER WORKSHOP

JUNE TO SEPTEMBER 1967



GODDARD SPACE FLIGHT CENTER
GREENBELT, MARYLAND

N 68-29123

(ACCESSION NUMBER)

(THRU)

407

(PAGES)

1

(CODE)

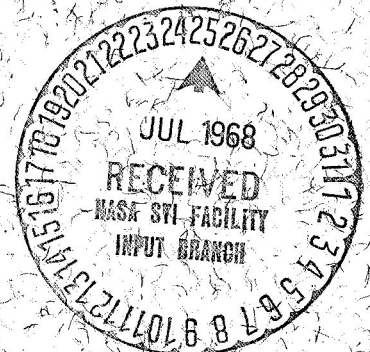
TMX-63261

(NASA CR OR TMX OR AD NUMBER)

10

(CATEGORY)

FACILITY



**FINAL REPORT
1967 SESSION OF THE
GODDARD SUMMER WORKSHOP**

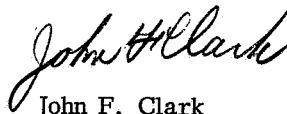
June to September 1967

**Goddard Space Flight Center
Greenbelt, Maryland**

FOREWORD

Initiated in 1962, the Goddard Summer Workshop has provided a valuable means of bringing together university faculty, graduate students, and Goddard staff members to investigate problems associated with the space program. As a result of this association, not only are many current problems solved but also new ideas and concepts emerge which often are of considerable value to the Center. At the same time the academic participants learn firsthand of the nature of the problems encountered on the frontiers of the space sciences. Also, ideas for course material, research projects and thesis topics are generated from these workshop investigations.

In addition to the reports written by the workshop participants and contained in this volume, several papers have been presented at appropriate technical meetings and published in the technical journals. This further serves the interests of the university as well as spreading awareness of space program problems in the academic community.



John F. Clark
Director

PREFACE

This document contains the collected papers written by participants in the 1967 Goddard Summer Workshop during the twelve-week session. The individual papers contained herein, while varied in subject matter, scope and format, represent the formal work product of the Workshop. There were also many valuable but less tangible benefits that accrued to the faculty members, graduate students, and NASA scientists and engineers who combined their talents and shared their experience throughout the Workshop session.

The Workshop program was initially divided into nine separate groups of subject matter, each group directing its attention to a particular technical area in which specific problems had been suggested for study and resolution. One of these groups was deferred to a future Workshop because of other more pressing problems areas, and another group resulted in a single study that was published separately from this report. The nine groups were:

Group A - Information Systems

Group B - Control Center Problems

Group C - Antennas

Group D - Electrophysics

Group E - Interdisciplinary Information Transfer (Biomedical)

Group F - Management Information Systems (Deferred to a future Workshop Session)

Group G - Technician Training (A separate study report entitled "Technician Training, Tracking Networks," was written by Mr. Arthur B. Rosenblatt and published in November 1967 as Document X-200-67-562.)

Group H - Atmospheric Studies

Group I - Computerized Guidance Counseling

The papers are presented in sections corresponding to the subject area groups, and a listing of participants precedes each section.



Fred B. Haynes
Director, Summer Workshop



PRECEDING PAGE BLANK NOT FILMED.

CONTENTS

GROUP A. INFORMATION SYSTEMS

	Page
A DIGITAL COMPUTER PROGRAM FOR CALCULATING THE RADIATION PATTERN OF AN ANTENNA OF ARBITRARY GEOMETRY WITH ARBITRARY PRIMARY FEED, by M. Javid	1
AUTOMATIC FREQUENCY SEARCH AND ACQUISITION TECHNIQUES FOR PHASE LOCK RECEIVERS, by B. Silverman	51
AN INTRODUCTION TO BOSE-CHAUDHURI-HOCQUENGHEM CODES, by S.A. Tretter	71
COHERENT DEMODULATION OF SPLIT-PHASE TELEMETRY SIGNALS, by F.M. Sobotkin	97
INFORMATION CAPACITY OF A HOLOGRAPHIC RECORDING SYSTEM, by G. Eichmann	115

GROUP B. CONTROL CENTER PROBLEMS

PRELIMINARY ANALYSIS FOR THE DESIGN OF AN AUTOMATED SPACE TRACKING NETWORK, by R.K. Golden and J.J. Fearnside	125
VISUAL CODING, by I.L. Goldstein	135

GROUP C. ANTENNAS

STRUCTURAL TRANSFER FUNCTIONS FOR THE ROSMAN-I ANTENNA, by Yu Chen and T.G. Toridis	141
RESPONSE OF THE ROSMAN-I 85-FOOT DISH ANTENNA TO IMPULSE EXCITATION, by J.M. Dalrymple	163

GROUP D. ELECTROPHYSICS

DIRECT AND INDIRECT TRANSITIONS IN GALLIUM ARSENIDE, by T.E. Leinhardt	177
AN ARC SOURCE OF LOW-ENERGY IONS, by J.H. Kinnier	185

CONTENTS (Continued)

	Page
INVESTIGATION AND DEVELOPMENT OF A FIELD EMISSION SOURCE FOR A QUADRUPOLE MASS SPECTROMETER, by P.O. Berrett and T.D. Hargreaves	203
SECONDARY TORQUES ON SPACECRAFT, by E.R. Sanford	227
MICROWAVE AMPLIFICATION AND GENERATION EMPLOYING SOLID STATE BULK EFFECT DEVICES, by S.V. Jaskolski	247
PSEUDOPOTENTIAL METHOD IN THE THEORY OF DEFECTS IN CRYSTALS - THE DIAMOND STRUCTURE, by M.M. Sokoloski	263
GROUP E. INTERDISCIPLINARY INFORMATION TRANSFER (BIOMEDICAL)	
PROCESS OF INFORMATION TRANSFER AND TECHNOLOGY UTILIZATION, by H.H. Sun, E. Fromm, and J.C. New	303
PHYSIOLOGIC SIGNALS FOR A PERSONAL-BORNE MONITORING SYSTEM, by E. Fromm and H.H. Sun	311
A SURVEY OF RECENT DEVELOPMENTS IN PHYSIOLOGICAL MONITORING SYSTEMS, by H.H. Sun, E. Fromm, and R. Zeskind	319
A MONITORING SYSTEM FOR PATIENT STUDIES, by H.H. Sun, E. Fromm, and R. Zeskind	327
GROUP H. ATMOSPHERIC STUDIES	
EQUIVALENT BLACKBODY TEMPERATURES OVER THE MOHAVE DESERT FROM 8.5 to 16 MICRONS, by W.R. Callahan	337
THE QUARTZ-IODINE LAMP AS A SECONDARY STANDARD FOR TOTAL RADIANT FLUX, by E.I. Mohr	343
CALIBRATION OF THE SIX-FOOT SPHERICAL INTEGRATOR, by E.I. Mohr	349
EFFECTS OF A HIGH-ENERGY PARTICLE ENVIRONMENT ON THE QUANTUM EFFICIENCY OF SPECTRALLY SELECTIVE PHOTOCATHODES FOR THE MIDDLE AND VACUUM ULTRAVIOLET, by J.H. McElaney and D.F. Heath	365

CONTENTS (Continued)

	Page
SOME MATHEMATICAL ASPECTS OF THE PROBLEM OF OBTAINING VERTICAL TEMPERATURE PROFILES FROM RADIOMETRIC DATA, by E.A. Franz	375
THE INFRARED EMISSIVITY AND REFLECTANCE OF LAVA, by R.R. Ross	385
GROUP I. COMPUTERIZED GUIDANCE COUNSELING	
ON PREDICTION AND DISCRIMINATION IN HIGH SCHOOL GUIDANCE COUNSELING, by R.M. Royall	389

GROUP A

INFORMATION SYSTEMS



Academic Personnel

Prin. Investigator : Dr. Mansour Javid (CUNY)

Faculty: Dr. Bernard Silverman (Syracuse)

Dr. Steven Tretter (Maryland)

Graduate Students: Mr. Fred Sobotkin (CUNY)

Mr. George Eichmann (CUNY)

Goddard Personnel

Staff Advisors: Dr. George Ludwig

Mr. Cyrus Creveling

A DIGITAL COMPUTER PROGRAM FOR CALCULATING THE RADIATION PATTERN OF AN ANTENNA OF ARBITRARY GEOMETRY WITH ARBITRARY PRIMARY FEED

Mansour Javid*

INTRODUCTION

There are many programs for calculating the radiation pattern of reflectors with specific geometry and specific illuminations placed at specific locations. Figure 1a shows one such reflector and its primary source. By design or accident the geometry of the reflector and pattern of the primary illumination source, as well as its location, may be perturbed. A requirement arose at Goddard for a computer program capable of taking account of these perturbations with the minimum of change to a master program. The program described in this paper achieves this purpose. Another feature of the program is its ability to compute the contribution of selected segments of the main reflector in the antenna system. This feature makes it possible to deduct from the field the contribution of those portions of the reflector which are obstructed by supports of the primary feed or are actual holes in the reflector not covered by metallic sheets.

The program consists of a driver and two subroutines. The driver program takes care of the input-output operations with certain amounts of computations, such as calculating, only once, transformation matrices for repeated use in the subroutines.

One subroutine, SETUP, computes the specification of the main reflector and illumination at its surface; and another subroutine, ADDUP, performs the integration required for computing the radiation pattern. Any change in the shape of the main reflector or its illumination will be taken care of by changing few instructions in the SETUP subroutine. The subroutines are written to minimize integration computations by taking advantage of any existing symmetry in the main reflector. If this symmetry is perturbed, few instructions in subroutines must be changed to branch to the portion of the program which does not assume symmetry.

BASIC THEORY

The basic theory used in calculating the radiation pattern of an antenna system is well understood. It shows that, in principle, if the sources of the field are known, the field itself may be computed from the specification of the source. In practice, there are many difficulties, and various techniques ranging from the simple optic-ray technique

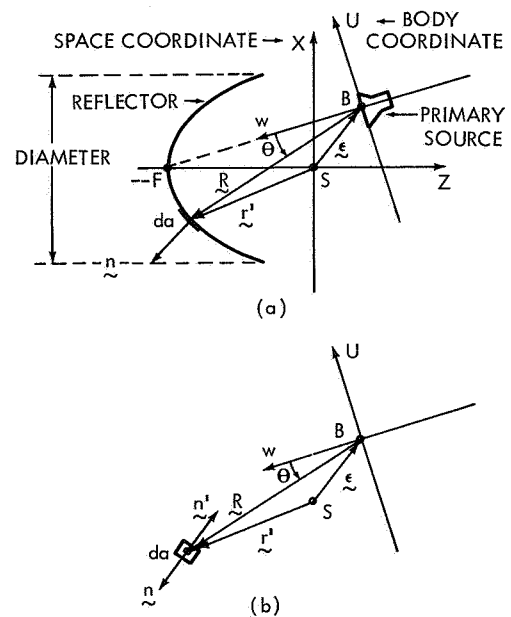


Figure 1-(a) The reflector and its primary source located off focus. (b) Vector quantities associated with (a).

*City University of New York.

to highly complex exact solutions in the form of boundary value problems are used. The shortcoming of the optic-ray technique is in the fact that it does not give detailed information about the characteristics of the beam, and the exact solutions are available for only a few problems with a high degree of symmetry.

Current Distribution Method

A standard technique for calculation of radiation pattern of an antenna system is the method of current distribution. In Figure 1b, the primary source (whose radiation field is assumed to be known) induces currents and charges on the surface of the main reflector. These currents and charges are then taken to be the sources for the field of the main reflector. It is known that, if the magnetic field on the surface of the reflector at an element of the area da located at the point \mathbf{r}' is $\mathbf{H}(\mathbf{r}')$ and the unit normal vector of da is $\mathbf{n}(\mathbf{r}')$, then the (far) field component of the electric field at a point with spherical coordinates (r, θ, ϕ) is proportional to the transverse (θ and ϕ) components of the vector quantity*

$$\mathbf{E}(r, \theta, \phi) = \frac{e^{-jk_r r}}{r} \iint \mathbf{n}(\mathbf{r}') \times \mathbf{H}(\mathbf{r}') e^{jka_r \cdot \mathbf{r}'} da(\mathbf{r}'), \quad (1)$$

where \mathbf{a}_r is the unit vector in the direction (θ, ϕ) , and

$$k = 2\pi/\lambda$$

with λ the wave length; and integration is carried out over the surface of the reflector. In the program to be described, the Cartesian components of the integral are calculated and from them the θ and ϕ components of the electric field are computed.

Systems of Coordinates

In an antenna system consisting of a primary source and a main reflector, it is convenient to deal with two independent systems of coordinates.

The first system, hereinafter referred to as the space coordinates, is fixed with respect to the main reflector. The coordinates of the field points, at which the power radiated per square meter (Poynting vector) is computed, are referred to this system of coordinates.

The second system, referred to as the body coordinates, is fixed with respect to the primary source of illumination. Its origin, B_s , is translated from the origin of the space coordinates, S , by the translation vector $\epsilon = \overline{SB}$ shown in Figure 1b.

Let the unit vectors of the space coordinates and body coordinates be $\mathbf{a}_x, \mathbf{a}_y, \mathbf{a}_z, \mathbf{a}_u, \mathbf{a}_v,$ and \mathbf{a}_w respectively, and be related by the transformation

$$\begin{vmatrix} \mathbf{a}_u \\ \mathbf{a}_v \\ \mathbf{a}_w \end{vmatrix} = \begin{vmatrix} e_{11} & e_{12} & e_{13} \\ e_{21} & e_{22} & e_{23} \\ e_{31} & e_{32} & e_{33} \end{vmatrix} \cdot \begin{vmatrix} \mathbf{a}_x \\ \mathbf{a}_y \\ \mathbf{a}_z \end{vmatrix} \quad (2)$$

where the e_{ij} matrix is assumed to be known.

*See Microwave Antenna Theory and Design, by Silver, McGraw-Hill Book Co., MIT Rad. Lab. Series No. 12, page 147.

Let the unit vector of the source polarization be

$$\mathbf{a}_p = \mathbf{a}_u D_1 + \mathbf{a}_v D_2 + \mathbf{a}_w D_3, \quad (3)$$

where D_1 , D_2 , and D_3 are specified. The center of the phase of the source is assumed to be at

$$\boldsymbol{\epsilon} = \mathbf{a}_x \epsilon_x + \mathbf{a}_y \epsilon_y + \mathbf{a}_z \epsilon_z, \quad (4)$$

and the element of the area da on the reflector has the position vector

$$\mathbf{r}' = \mathbf{a}_x x + \mathbf{a}_y y + \mathbf{a}_z z. \quad (5)$$

The distance of this element of area from the source (phase center) is then

$$\mathbf{R} = \mathbf{r}' - \boldsymbol{\epsilon} = \mathbf{a}_x (x - \epsilon_x) + \mathbf{a}_y (y - \epsilon_y) + \mathbf{a}_z (z - \epsilon_z) \quad (6)$$

Description of the Primary Source

As indicated above, for different types of primary sources, different SETUP subroutines must be written. However, it is possible to use a standard form given below, which, with the change of a parameter, designated as n , may describe many sources with good approximation. This form is

$$\mathbf{H}(\mathbf{r}') = \frac{\mathbf{R} \times \mathbf{a}_p}{|\mathbf{R} \times \mathbf{a}_p|} \cos^n \Theta \frac{e^{-jkR}}{R}, \quad (7)$$

where $R = |\mathbf{R}|$ and Θ is the spherical coordinate angle referred to the body coordinate (see Figure 1b). The value of n in Equation 7 determines the width of the cigar-shaped primary beam illuminating the reflector. For the sake of concreteness we will deal with the type of source described in Equations 7, 6, and 3.

From Figure 1b it is seen that

$$\cos \Theta = \frac{\mathbf{R} \cdot \mathbf{a}_w}{R} \quad (8)$$

From Equations 2 and 6 we have

$$\mathbf{R} \cdot \mathbf{a}_w = e_{31}(x - \epsilon_x) + e_{32}(y - \epsilon_y) + e_{33}(z - \epsilon_z)$$

and

$$\frac{1}{R} \cos^n \Theta = \frac{[e_{31}(x - \epsilon_x) + e_{32}(y - \epsilon_y) + e_{33}(z - \epsilon_z)]^n}{R^{n+1}}. \quad (9)$$

In Equation 3 the polarization vector is defined in terms of its components in the body system of coordinates. Its components in the space system of coordinates are found from the inverse of e_{ij} matrix. Since this matrix is unitary, its inverse is its transpose and

$$\mathbf{a}_p = \begin{vmatrix} \mathbf{a}_x & \mathbf{a}_y & \mathbf{a}_z \end{vmatrix} \cdot \begin{vmatrix} e_{11} & e_{21} & e_{31} \\ e_{12} & e_{22} & e_{32} \\ e_{13} & e_{23} & e_{33} \end{vmatrix} \cdot \begin{vmatrix} D_1 \\ D_2 \\ D_3 \end{vmatrix}. \quad (10)$$

It is convenient to assign symbols to the components of the polarization vector in space coordinates. Using p_x, p_y, p_z , we have

$$\mathbf{a}_p = \mathbf{a}_x P_x + \mathbf{a}_y P_y + \mathbf{a}_z P_z. \quad (11)$$

From Equations 10 and 11 we have

$$p_x = e_{11} D_1 + e_{21} D_2 + e_{31} D_3, \quad (12)$$

$$p_y = e_{12} D_1 + e_{22} D_2 + e_{32} D_3, \quad (13)$$

$$p_z = e_{13} D_1 + e_{23} D_2 + e_{33} D_3. \quad (14)$$

From the above and Equation 6 we have

$$\mathbf{R} \times \mathbf{a}_p = \begin{vmatrix} \mathbf{a}_x & \mathbf{a}_y & \mathbf{a}_z \\ x - \epsilon_x & y - \epsilon_y & z - \epsilon_z \\ P_x & P_y & P_z \end{vmatrix} \quad (15)$$

We denote the components of $\mathbf{R} \times \mathbf{a}_p$ by h_x, h_y, h_z such that

$$\mathbf{R} \times \mathbf{a}_p = \mathbf{a}_x h_x + \mathbf{a}_y h_y + \mathbf{a}_z h_z, \quad (15a)$$

and denote the magnitude of this vector by h such that

$$h = |\mathbf{R} \times \mathbf{a}_p| = [h_x^2 + h_y^2 + h_z^2]^{1/2}. \quad (16)$$

From the above we find that

$$h_x = (y - \epsilon_y) P_z - (z - \epsilon_z) P_y, \quad (17)$$

$$h_y = (z - \epsilon_z) P_x - (x - \epsilon_x) P_z, \quad (18)$$

$$h_z = (x - \epsilon_x) P_y - (y - \epsilon_y) P_x. \quad (19)$$

The vector $\mathbf{H}(\mathbf{r}')$ in the left side of Equation 7 is a complex quantity, that is,

$$\mathbf{H}(\mathbf{r}') = \mathbf{H}^r + j\mathbf{H}^i, \quad (20)$$

where the superscripts r and i refer to the real and imaginary parts and $j^2 = -1$. The x , y , and z components of the real and imaginary parts of $\mathbf{H}(\mathbf{r}')$ are then found from Equations 7, 11, 15, and 20 to be:

$$H_x^r = \frac{h_x \cos^n \theta}{h} \frac{\cos kR}{R}, \quad (21)$$

$$H_x^i = -\frac{h_x \cos^n \theta}{h} \frac{\sin kR}{R}, \quad (22)$$

$$H_y^r = \frac{h_y \cos^n \theta}{h} \frac{\cos kR}{R}, \quad (23)$$

$$H_y^i = -\frac{h_y \cos^n \theta}{h} \frac{\sin kR}{R}, \quad (24)$$

$$H_z^r = \frac{h_z \cos^n \theta}{h} \frac{\cos kR}{R}, \quad (25)$$

$$H_z^i = -\frac{h_z \cos^n \theta}{h} \frac{\sin kR}{R}. \quad (26)$$

If in Equation 1 we define the symbol \mathbf{I} to represent the integral,

$$\mathbf{I} = \iint \mathbf{n}(\mathbf{r}') \times \mathbf{H}(\mathbf{r}') e^{jk\mathbf{a}_r \cdot \mathbf{r}'} da, \quad (26a)$$

then the real and imaginary parts of the x , y , and z components of \mathbf{I} are obtained by noting that

$$\begin{aligned} \mathbf{n}(\mathbf{r}') \times \mathbf{H}(\mathbf{r}') &= \begin{vmatrix} \mathbf{a}_x & \mathbf{a}_y & \mathbf{a}_z \\ n_x & n_y & n_z \\ H_x & H_y & H_z \end{vmatrix} \\ &= \mathbf{a}_x (n_y H_z - n_z H_y) \\ &\quad + \mathbf{a}_y (n_z H_x - n_x H_z) \\ &\quad + \mathbf{a}_z (n_x H_y - n_y H_x), \end{aligned} \quad (27)$$

where n_x , n_y , and n_z are the components of \mathbf{n} .

Consider now the expression $\mathbf{n}(\mathbf{r}') \times \mathbf{H}(\mathbf{r}') da$ in the form

$$\begin{aligned} \mathbf{n}(\mathbf{r}') \times \mathbf{H}(\mathbf{r}') da &= \mathbf{a}_x \left(\frac{n_y}{n_z} H_z - H_y \right) n_z da \\ &+ \mathbf{a}_y \left(H_x - \frac{n_y}{n_z} H_z \right) n_z da \\ &+ \mathbf{a}_z \left(\frac{n_x}{n_z} H_y - \frac{n_y}{n_z} H_x \right) n_z da. \end{aligned} \quad (28)$$

In these expressions, for positive n_z , the term $n_z da = dx dy$, since n_z is the cosine of the angle between the vector area da and x - y plane.

In Equation 26a we define the distance

$$d = \mathbf{a}_r \cdot \mathbf{r}'. \quad (29)$$

The x , y , and z components of \mathbf{a}_r are given by

$$\mathbf{a}_r = \mathbf{a}_x \sin \theta \cos \phi + \mathbf{a}_y \sin \theta \sin \phi + \mathbf{a}_z \cos \theta, \quad (30)$$

and

$$d = x \sin \theta \cos \phi + y \sin \theta \sin \phi + z \cos \theta. \quad (31)$$

From Equations 21 to 31 we have

$$I_x^r = \iint \left[\frac{n_y}{n_z} (H_z^r + jH_z^i) - (H_y^r + jH_y^i) \right] [\cos kd + j \sin kd] dx dy \quad (32)$$

$$= \iint \left[\left(\frac{n_y}{n_z} H_z^r - H_y^r \right) + j \left(\frac{n_y}{n_z} H_z^i - H_y^i \right) \right] [\cos kd + j \sin kd] dx dy,$$

$$I_x^r = \iint \left[\left(\frac{n_y}{n_z} H_z^r - H_y^r \right) \cos kd - \left(\frac{n_y}{n_z} H_z^i - H_y^i \right) \sin kd \right] dx dy, \quad (33)$$

$$I_x^i = \iint \left[\left(\frac{n_y}{n_z} H_z^r - H_y^r \right) \sin kd + \left(\frac{n_y}{n_z} H_z^i - H_y^i \right) \cos kd \right] dx dy, \quad (34)$$

where I_x^r and I_x^i are the real and imaginary parts of I_x . Similarly,

$$I_y = \iint \left[(H_x^r + j H_x^i) - \frac{n_x}{n_z} (H_z^r + H_z^i) \right] [\cos kd + j \sin kd] dx dy, \quad (35)$$

$$= \iint \left[\left(H_x^r - \frac{n_x}{n_z} H_z^r \right) + j \left(H_x^i - \frac{n_x}{n_z} H_z^i \right) \right] [\cos kd + j \sin kd] dx dy, \quad (36)$$

$$I_y^r = \iint \left[\left(H_x^r - \frac{n_x}{n_z} H_z^r \right) \cos kd + \left(H_x^i - \frac{n_x}{n_z} H_z^i \right) \sin kd \right] dx dy, \quad (37)$$

$$I_y^i = \iint \left[\left(H_x^r - \frac{n_x}{n_z} H_z^r \right) \sin kd + \left(H_x^i - \frac{n_x}{n_z} H_z^i \right) \cos kd \right] dx dy, \quad (38)$$

$$I_z = \iint \left[\frac{n_x}{n_z} (H_y^r + j H_y^i) - \frac{n_y}{n_z} (H_x^r + j H_x^i) \right] [\cos kd + j \sin kd] dx dy, \quad (39)$$

$$= \iint \left[\left(\frac{n_x}{n_z} H_y^r - \frac{n_y}{n_z} H_x^r \right) + j \left(\frac{n_x}{n_z} H_y^i - \frac{n_y}{n_z} H_x^i \right) \right] [\cos kd + j \sin kd] dx dy,$$

$$I_z^r = \iint \left[\left(\frac{n_x}{n_z} H_y^r - \frac{n_y}{n_z} H_x^r \right) \cos kd - \left(\frac{n_x}{n_z} H_y^i - \frac{n_y}{n_z} H_x^i \right) \sin kd \right] dx dy, \quad (40)$$

$$I_z^i = \iint \left[\left(\frac{n_x}{n_z} H_y^r - \frac{n_y}{n_z} H_x^r \right) \sin kd + \left(\frac{n_x}{n_z} H_y^i - \frac{n_y}{n_z} H_x^i \right) \cos kd \right] dx dy. \quad (41)$$

All terms in Equations 32 to 41 have now been evaluated in terms of the description of the primary source and point of observation, except the two ratios n_x/n_z and n_y/n_z . These two terms will now be evaluated from the description of the geometry of the reflector.

Paraboloidal Reflector

Although the derivations which follow refer to a paraboloidal reflector, the main program and its subroutines can easily be amended (by changing few instructions, as seen from Equations 54 through 57 and Table 4) to apply to any reflector geometry. A single paraboloid (see Figure 1a) of focal length F is described by

$$Z = \frac{x^2 + y^2}{4F} - F = \frac{\rho^2}{4F} - F \quad (42)$$

where ρ is the cylindrical coordinate; $\rho = (x^2 + y^2)^{1/2}$. As a member of the family of confocal paraboloids, the paraboloid shown in Figure 1a is described by*

$$\sqrt{x^2 + y^2 + z^2} - z = \text{constant} = c = r - z, \quad (42a)$$

*See, for example, Electromagnetic Theory, by J. A. Stratton, McGraw-Hill Book Co., pages 54 and 57.

where the constant c is the square of the paraboloidal coordinate associated with the surface. The unit normal vector of this surface is

$$\mathbf{n} = \frac{\nabla c}{|\nabla c|}. \quad (43)$$

The ratio n_x/n_z is found from

$$\frac{n_x}{n_z} = \frac{\partial c/\partial x}{\partial c/\partial z} = \frac{x/r}{(z/r) - 1} = \frac{x}{z - r}. \quad (44)$$

Similarly

$$\frac{n_y}{n_z} = \frac{\partial c/\partial y}{\partial c/\partial z} = \frac{y/r}{(z/r) - 1} = \frac{y}{z - r}. \quad (45)$$

Although in Figure 1a the unit normal vector points outward and its z -component is negative, the ratio of components of

$$\mathbf{n}' = -\mathbf{n}$$

will still be given by Equations 44 and 45. It is recalled that in discussing

$$n_z da = dx dy \quad (46)$$

we assumed that n_z is positive. Since we are interested in the ratios of the components of the unit normal vector, the above results may be used for the case when \mathbf{n}' is this vector.

This concludes the evaluation of the value of the terms in Equations 32 through 41 in terms of the specification of the primary source, the geometry of the reflector, and the coordinates of the field point and elements of area on the reflector (da). The computer program evaluates the integrals given in Equations 33, 34, 37, 38, 40, and 41, and from the rectangular components given by these equations finds the spherical components of the radiated (far) field. In addition, it computes the Poynting vector as a function of θ and ϕ .

The results are reported in two forms. One form reports the detail of the contribution of the successive segments (annular rings) of the reflector to the electric field, and the other presents the radiated power in the form of db's below the maximum value, as a function of θ and ϕ of the field point (see Tables 5 and 6).

The formula used for the transformation from rectangular to spherical components is:

$$\begin{vmatrix} I_r^{r,i} \\ I_\theta^{r,i} \\ I_\phi^{r,i} \end{vmatrix} = \begin{vmatrix} \sin \theta \cos \phi & \sin \theta \sin \phi & \cos \theta \\ \cos \theta \cos \phi & \cos \theta \sin \phi & -\sin \theta \\ -\sin \phi & \cos \phi & 0 \end{vmatrix} \cdot \begin{vmatrix} I_x^{r,i} \\ I_y^{r,i} \\ I_z^{r,i} \end{vmatrix} \quad (47)$$

In the above, the superscripts r and i refer to the real and imaginary parts, and the subscripts r , θ , and ϕ refer to the r , θ , and ϕ components.

Euler Angles

In Equation 2 we have related the body coordinates to the space coordinates by means of the e_{ij} matrix. In practice, the rotation of the body system of coordinates with respect to the space coordinates is described in terms of the Euler angles* α , β , and γ . The elements of the e_{ij} matrix used in Equation 2 are found from the following formula:

$$\begin{aligned}
 e_{11} &= \cos \gamma \cos \alpha - \cos \beta \sin \alpha \sin \gamma \\
 e_{21} &= \sin \gamma \cos \alpha - \cos \beta \sin \alpha \cos \gamma \\
 e_{31} &= \sin \beta \sin \alpha \\
 e_{12} &= \cos \gamma \sin \alpha + \cos \beta \cos \alpha \sin \gamma \\
 e_{22} &= -\sin \gamma \sin \alpha + \cos \beta \cos \alpha \cos \gamma \\
 e_{32} &= \sin \beta \cos \alpha \\
 e_{13} &= \sin \gamma \sin \beta \\
 e_{23} &= \cos \gamma \sin \beta \\
 e_{33} &= \cos \beta
 \end{aligned} \tag{48}$$

Changes in the Primary Source and Geometry of the Reflector

If the description of the primary source or the geometry of the reflector is other than those assumed above, the subroutine SETUP must be changed accordingly.

Below we discuss reflection from a spheroid illuminated by a dipole located on the axis of the spheroid, as shown in Figure 2. This example should indicate the type of changes necessary in the subroutine.

To calculate the unit normal vector of the spheroid, we consider the family of confocal spheroids of major and minor diameter $2a$ and $2b$ with focal length

$$2c = 2(a^2 - b^2)^{1/2} \tag{49}$$

*The convention used here is after H. Goldstein's Classical Mechanics, Addison-Wesley, page 109. Equation 48 corresponds to this convention. For another convention see, for example, Field Analysis and Electromagnetics, by Javid and Brown, McGraw-Hill Book Co., Appendix I.

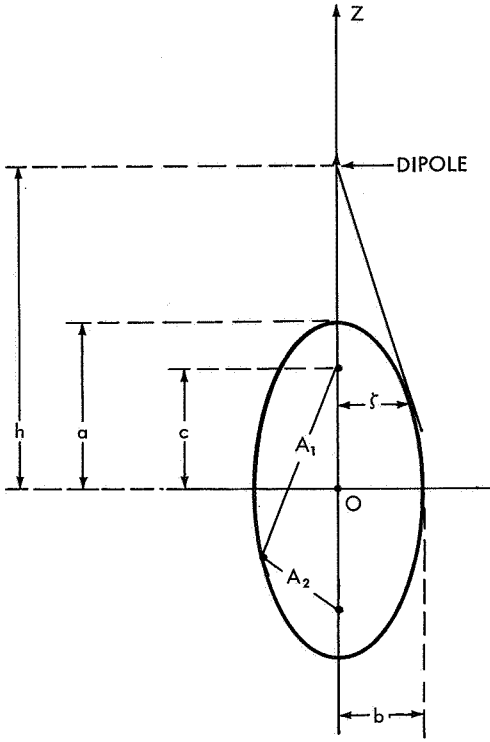


Figure 2—A spheroid illuminated by a dipole.

as shown in Figure 2. For fixed c and variable a , this family is described by

$$2a = [x^2 + y^2 + (z - c)^2]^{1/2} + [x^2 + y^2 + (z + c)^2]^{1/2}, \quad (50)$$

where

$$A_1 = [x^2 + y^2 + (z - c)^2]^{1/2} = [\rho^2 + (z - c)^2]^{1/2} \quad (51)$$

and

$$A_2 = [x^2 + y^2 + (z + c)^2]^{1/2} = [\rho^2 + (z + c)^2]^{1/2}. \quad (52)$$

are the distances of a point on the spheroid (corresponding to the value a) from the two foci respectively.

The unit normal vector of the spheroid is found from

$$\begin{aligned} \Delta(2a) = & \mathbf{a}_x \times \left(\frac{1}{A_1} + \frac{1}{A_2} \right) \\ & + \mathbf{a}_y \times \left(\frac{1}{A_1} + \frac{1}{A_2} \right) \\ & + \mathbf{a}_z \times \left(\frac{z - c}{A_1} + \frac{z + c}{A_2} \right) \end{aligned} \quad (53)$$

The ratio of the x and z components of this gradient gives the value of n_x/n_z , as discussed before. The ratio of the y and z components of the gradient gives n_y/n_z . Thus

$$\frac{n_x}{n_z} = \frac{x(A_1 + A_2)}{(z - c)A_2 + A_1(z + c)} \quad (54)$$

and

$$\frac{n_y}{n_z} = \frac{y(A_1 + A_2)}{(z - c)A_2 + A_1(z + c)}, \quad (55)$$

where z is obtained from

$$\frac{z^2}{a^2} + \frac{x^2 + y^2}{b^2} = 1 \quad (56)$$

$$z = a \left(1 - \frac{x^2 + y^2}{b^2} \right)^{1/2} = a \left(1 - \frac{\rho^2}{b^2} \right)^{1/2} \quad (57)$$

Equations 55, 56, and 57 for the spheroid are the counterpart of Equations 44, 45, and 42 for the paraboloid.

The dipole placed at $x = 0$, $y = 0$, and $z = h$ illuminates the spheroid up to a radius ρ (see Figure 2), which must satisfy the equation

$$\left| \frac{\partial z}{\partial \rho} \right| = \frac{h - z}{\rho} = \left| \frac{-a \rho}{b^2 \left(1 - \frac{\rho^2}{b^2} \right)^{1/2}} \right| = \frac{a \rho}{b(b^2 - \rho^2)^{1/2}} \quad (58)$$

Substituting for z from (57) into (58) and solving for ρ , we have

$$\rho = \left[b^2 - \frac{a^2 b^2}{h^2} \right]^{1/2} \quad (59)$$

As an example, for $a = 10$, $b = 5$, and $h = 20$, we have

$$\rho = 4.33, \quad (60)$$

which corresponds to a diameter of 8.66. These formulas and values are used in the SETUP subroutine shown in Table 4, written for a spheroid.

To compute the magnetic field at an elemental area on the spheroid, we note that if the source is taken as the origin of (body) spherical coordinates with the axis of the dipole as the axis of symmetry of the system (\mathbf{a}_w), then

$$\mathbf{H}(\mathbf{r}') = \mathbf{a}_\phi \frac{e^{-jkR}}{R}, \quad (61)$$

where the foregoing terms are defined in connection with Equation 7. Thus

$$\mathbf{H}(\mathbf{r}') = (-\mathbf{a}_x \sin \phi + \mathbf{a}_y \cos \phi) \frac{e^{-jkR}}{R}, \quad (62)$$

where

$$\sin \phi = \frac{y}{\rho} \text{ and } \cos \phi = \frac{x}{\rho}.$$

From these equations we find:

$$H_x^r = -\frac{y}{\rho R} \cos kR, \quad (63)$$

$$H_x^i = +\frac{y}{\rho R} \sin kR, \quad (64)$$

$$H_y^r = +\frac{x}{\rho R} \cos kR, \quad (65)$$

$$H_y^i = -\frac{x}{\rho R} \sin kR, \quad (66)$$

$$H_z^r = 0, \quad (67)$$

$$H_z^i = 0. \quad (68)$$

Equations 63 through 68 for the illumination due to a dipole are the counterparts of Equations 21 through 26 for the "standard" illumination described in Equation 7. The former (Equations 63-68) are used in the SETUP subroutine shown in Table 4, and the latter are used in the SETUP subroutine of Table 2. A comparison of these two subroutines shows that, in going from one geometry and source to another, very few instructions need be changed in the subroutines.

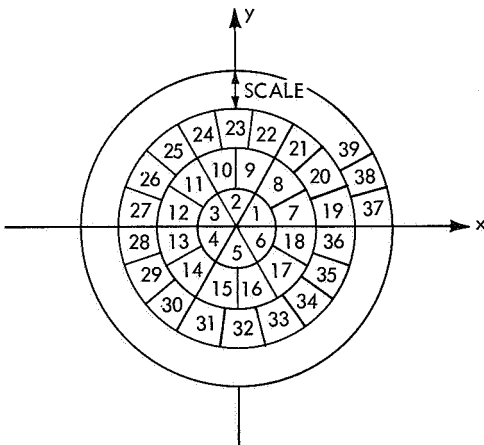


Figure 3—Division of the reflector into rings and elemental areas. First ring contains 6 elemental areas. Second ring has 12, and the nth ring 6n elemental areas.

DESCRIPTION OF THE COMPUTER PROGRAM

Table 1 (at end of paper) shows a simplified block diagram of the program. As indicated before, the program calculates the contribution of successive annular rings of the reflector (referred to as segments) to the radiated field.

Figure 3 shows the projection of the reflector on the x-y plane. This projection is divided into a number of rings of equal width, as shown in the figure. The width of these rings is a parameter of the program and is read in by means of data cards, as a fraction of the wavelength. This fraction of the wavelength is the scale of the program, and elements of area $dx dy$ referred to in Equation 32 are approximately the size of a square having the scale as its sides.

These elemental areas are formed as follows:

The first ring, which is a circle of radius equal to the scale, is divided into six equal sectors, as shown in Figure 3. The second ring, which is between the circles of radii equal respectively to one scale and two scales, is divided into 2×6 equal parts, as shown. The third ring is divided into 3×6 parts, and the nth

ring into $n \times 6$ parts. Thus, except for the first ring, every ring is divided into "squares" of size approximately equal to the squared scale. In the program the area of each of these elemental surfaces is taken as the value of $dx dy$ at the point of interest.

Another parameter read into the computer by means of the data cards is the upper limit of the number of elemental areas in a segment. This limit is denoted in the program by the letter M; and because of limitation of the computer memory locations it cannot be larger than 1,000, but can be chosen to be any number less than 1,000. A segment is then defined to be a number of rings each of width equal to scale, whose total elemental areas are less than or equal to M.

When the scale is chosen to be a very small fraction of the wavelength, it is possible that one ring contains more than M elemental areas. In this case the program takes the first M elemental areas in the ring, and counts that total area as one segment; and the remainder, if less than (or equal to) M, as another segment. If the remainder is more than M, the second M elemental areas form another segment, and the remainder another segment, and so on. In such cases, an appropriate message is printed in the preface of the report.

After completing the segmentation, the program prints the order number of the last ring in each segment, and the number of elementary areas in each segment. These information items are for the guidance of the user as to the way the reflector is divided into segments; and do not affect the final result, which is the power radiated in a given direction due to contributions of all elemental areas in the reflector.

After segmentation has been completed, the main program calls on the subroutine SETUP to compute and store in reserved arrays the following quantities for each of the elemental areas in the first segment:

- (a) The rectangular coordinates x , y , and z of the center of each elemental area in the segment.
- (b) The area of each "elemental area" of each ring in the segment. This quantity is computed only once for each ring.
- (c) The ratios n_x/n_z and n_y/n_z for each elemental area in the segment. For a paraboloidal reflector, these ratios are computed according to Equations 44 and 45. For other geometries of reflector, appropriate formulas are used. (See Equations 54 through 57.)
- (d) The real and imaginary parts of the x , y , and z components of the illumination at the center of every elementary area in the segment.

For the type of illumination assumed in Equation 7, these values are computed in accordance with Equations 21 through 26. The value of n in Equation 7, which determines the width of the illumination beam, is a parameter and is read into the computer by means of a data card. It is assigned the symbol NU in the program.

The above values are necessary for the evaluation of the integrals given in Equations 33, 34, 37, 38, 40, and 41. Once the subroutine SETUP has computed these values for all the elementary areas in the first segment, the main program calls upon the subroutine ADDUP to compute the real and imaginary parts of the x , y , and z components of the field at the first of the specified field points. These are the integrals given in Equations 33, 34, 37, 38, 40, and 41.

After evaluating these quantities, the ADDUP subroutine returns to the main program. This latter transforms the Cartesian components into spherical components, and calls again on ADDUP to compute the value of the above-mentioned integrals for the second of the specified field points. This process continues until the contribution of the (first) segment to all field points has been evaluated. At this time, the main program calls on SETUP to evaluate and store the value of the quantities referred to above in (a) through (d) for all the elementary areas in the second segment. When this operation has been done, the ADDUP subroutine is called upon to compute the contribution of the second segment to every one of the specified field points. This contribution is then transformed into spherical components and added to the contribution of the previous segment, and so on. The cumulative results are then printed as shown in Table 5 for every specified field point, indicating the segment number up to which the contributions have been computed. The power radiated is also printed. This is the power which would be radiated in the specified direction if the reflector diameter came only up to the end of the segment under consideration.

From the above description, it is seen that the values associated with each elemental area, as described in (a) to (d) above, are computed only once, no matter how many field points are to be considered. This rule insures maximum use of all computed data, with no repetition.

Every time the contribution of a segment to the field at a specified point is computed, and added to the contributions of preceding segments, the results are stored. At the end of these computations, the spherical components of the radiated field due to the "whole" reflector are in storage for every specified field point. From these components the corresponding radiated power in the specified directions is computed, the largest of these values is found, and all values normalized (in db's) with respect to the largest value and printed in the form of a separate report (see Table 6) with the direction of the maximum radiated power and its computed value printed in the preface to the report.

In addition to printing the reports discussed above, the program prepares a tape containing the data of the db level report. This tape is then used in conjunction with another program* to activate a Stromberg-Carlson 4020 plotter to plot the db levels as a function of θ for the various cuts (ϕ angles). Examples of these graphs are shown in Figures 4, 5, and 6 (at the end of paper).

THE FORMAT OF DATA CARDS

The number of data cards to be read in with each problem is not fixed, and depends on the number of field points at which the radiated power is to be computed. However, the first three cards of each set always carry the same type of information, regardless of the number of the field points.

First Data Card

This card contains five integers. Each of them can be as large as 10 digits, always right adjusted. Thus the first number MUST end in column 10, the second in column 20, and so on, with the last number ending in column 50. Following is an example:

1	2	3	4	5	6
1234567890	1234567890	1234567890	1234567890	1234567890	1234567890
27	8	999	4	0	

*This plotting program is written by Mr. Frank McGarry of GSFC.

The numbers 123 . . . indicate the columns of the data card here shown up to 60. The five integers end in columns 10, 20, 30, 40, and 50 respectively.

First Number: This is the number of thetas in each constant phi plane (to be specified) at which radiated power must be computed. In the above example there are to be 27 thetas. The value of these angles will be given in the following cards.

Second Number: This is the number of phis or the number of "cuts." In the above example there are to be 8 cuts. The angle of these cuts will be specified in the following cards.

Third Number: This is the upper limit of the number of elementary areas in each segment discussed in the previous section with program symbol M. Its value should not exceed 1,000. In the above example its value is 999.

Fourth Number: This is the value n in Equation 7. In this example it has the value 4, indicating a $\cos^4 \theta$ pattern for the primary source.

Fifth Number: The detailed report giving the contribution of the successive segments may be eliminated by placing a 1 in the 50th column of the first card. In the above example, the zero in the 50th column insures that this detailed report (see Table 5) will be printed. In the language of Fortran programming, the format of the first card is (5I10). (See statement number 40 in Table 1.)

Second Data Card

This card contains seven (floating point) numbers in the format (7F10.5). (See statement number 41 in Table 1.) Following is an example of this card:

1	2	3	4	5	6	7
1234567890	1234567890	1234567890	1234567890	1234567890	1234567890	1234567890
30.00000	0.00000	10.00000	180.00000	0.12500	0.49500	13.20000

It is seen that each number has five digits after the decimal point, the first number ending in column 10, the second in column 20, and so on. It is not necessary to key punch zeroes following a non-zero digit after the decimal point.

First Number: This is the diameter of the reflector in feet. In this example it is 30.0 feet (the decimal point must be there).

Second Number: In some problems, parts of the reflector are obstructed by supports for the primary source. The second number in this card is the diameter of the ring at which obstruction begins. It is given in feet. In this example the diameter is zero.

Third Number: This is the diameter in feet of the (second) ring to which the obstruction extends. In the above example it is 10 feet. Thus the part of the reflector extending from the center (zero diameter) to the ring with 10 feet diameter is, in this example, obstructed. With no obstruction, both the second and third numbers must be 0.0.

Fourth Number: Very often the phase of the primary source is not of the standard form e^{-jkR} given in Equation 7, and varies with θ . In the SETUP subroutine this is taken care of by assuming a phase angle of the form (see Table 2)

$$\text{Phase angle} = kR + A(1 - \cos \theta) \quad (69)$$

The fourth number in this card reads the value of A in Equation 69, in degrees. For no deviation from standard, its value is 0.0. In the preface this number is referred to as DEVIATION. Other formulas for the deviation of phase from the standard e^{-jkR} require changes in SETUP routine, and the fourth number in the second card may then be used to define an appropriate parameter.

Fifth Number: This is the scale, the fraction of the wavelength determining the width of successive rings, as discussed above. In this example its value is 0.125 (one eighth of wavelength).

Sixth Number: This is the wavelength in feet. In this example it is 0.495 foot.

Seventh Number: This is the focal length of the paraboloidal reflector. In this example it is 13.2 feet. If the shape of the reflector is other than paraboloid, some instructions in the program must be changed (see Table 4 for scattering from spheroid). In such cases the seventh number in the second card has no significance.

Third Data Card

This card contains nine (floating point) numbers in format (9F8.3), (see statement number 403, Table 1). It conveys the information about the translation and rotation of the body coordinates with respect to the space coordinates, as well as information about the polarization of the primary source. Following is an example of this card:

1	2	3	4	5	6	7
123456789012345678901234567890123456789012345678901234567890123456789012						
355.350	0.000	0.000	-0.144	0.144	0.000	1.000 0.000 0.000

First Number - Second Number - Third Number: These are the three Euler angles α , β , and γ discussed in Equation 48, given in degrees. In this example α is 355.35 degrees, β and γ are 0.0 and 0.0 respectively. If the body coordinate system is not rotated with respect to the space coordinate systems, all three numbers are 0.0.

Fourth Number - Fifth Number - Sixth Number: These are the x, y and z components of the translation of the origin of the body coordinates with respect to the space coordinates, as discussed in Equation 4. Their values are given in feet. In this example $\epsilon_x = -0.144$, $\epsilon_y = 0.144$ foot, and $\epsilon_z = 0.0$.

Seventh Number - Eighth Number - Ninth Number: These are the direction cosines of the primary source's polarization-vector with the body coordinates, referred to in Equation 3 as D_1 , D_2 , and D_3 . Their value is less than or equal to 1.0, and the sum of their squares must be 1. For this reason, the program computes the value of D_3 from the values given for D_1 and D_2 , regardless of the value indicated for D_3 on the card. In the above example, the polarization of the primary source is along a_u of the body coordinates, since $D_1 = 1.0$ and $D_2 = 0.0 = D_3$.

Theta Data Cards

Following the third data card, there will be enough cards to convey the information about the θ angles of the field points at which the radiated power is to be computed.

Each of these cards will be in (8(1X,F8.3)) format (see statement number 402 of Table 1). If the number of thetas is less than or equal to 8, only one card is needed. For

thetas (in this case 8). The program then goes to the next value of ϕ (in this case 90.0) and makes computations for all the values of θ . In our example, so far computations have been made for 16 field points, the ninth of which is ($\theta = 0.0$, $\phi = 90.0$). The program then proceeds with the next value of ϕ (in our example, $\phi = 270.0$) and computes for all thetas, thus making computations for 24 field points, the 17th of which is the point ($\theta = 0.0$, $\phi = 270.0$). If, in the card following the phi data card (or cards), we incorporate the format

```

          1         2         3         4         5         6         7
12345678901234567890123456789012345678901234567890123456789012
  9 17  0  0  0  0  0  0  0  0  0  0  0  0  0  0  0  0

```

then the computations for the ninth and 17th field points (0.0, 90.0) and (0.0, 270.0) will be skipped. In ordering the field points, the program will count the field point next to (0.0, 90.0), which is (0.1, 90.0), as the ninth field point. Similarly, (0.1, 270.0) will be counted as the 16th field point, instead of as the 18th field point.

The format of the field point elimination cards (three of them) is (18I4), (see statement number 877, Table 1). Each card may contain as many as 18 integers, four digits each, all of them right adjusted. That is, the first integer MUST end in column 4, the second integer in column 8, and so on. Thus $3 \times 18 = 54$ field points may be eliminated by punching their appropriate number in the three cards. All zeroes may be left as blanks, and the order in which the numbers are punched is immaterial. Thus instead of 9 17 above, we could have 17 9, with the same result. Three elimination cards must follow the phi data cards, regardless of the number of field points to be eliminated. If none of the field points are to be eliminated, these three cards are blank.

The Last Data Card

The set of cards described above may be repeated to compute different problems one after another. This procedure may be necessary for convenience (reducing the number of times the physical deck is presented to the computer), or it may be done in cases where the number of field points at which computations are required exceeds 250. (This is a limit set by available computer memory.) In the former case, each batch of data cards will differ in their description of the specifications of the problem, such as the diameter, wavelength, location of the source, etc. Data cards for one problem will follow those for the others. In the second case, the specification of the problem given in the first three cards may be the same, but the values on the phi and theta cards differ.

In all cases there must be an (additional) blank card at the end of the last set of data cards. Thus if one problem is run and no field points are eliminated, there will be four blank cards at the end of the data cards, three for elimination cards and the fourth the required blank card. If there are two problems to be computed one after the other, and no field points are to be eliminated, the first set will have three blank (elimination) cards, followed by the first card of the second problem. At the end of the data cards for the second problem, there must then be four blank cards (as contrasted with the three required for the data cards of the first problem).

This last card causes creation of a mark in the tape written for use with the 4020 plotter.

All data cards are followed (after the last blank card) by a 7-8 card.

PROGRAM LISTINGS

Table 1 gives the listing of the main program. This main program uses the unit 5 for reading the card, unit 6 for printing out reports, and unit 7 for writing the tape used in connection with the 4020 plotter. If the computer center at which the program is used utilizes other units for these purposes, appropriate control cards must precede the main program. An example of such cards is

	1
1	6
\$NAME	.UN 5. = .UN2.
\$NAME	.UN 6. = .UN3.
\$NAME	.UN 7. = .UN15.

The numbers 1 and 16 above refer to columns in the card.

The main program must be accompanied by the subroutines SETUP and ADDUP. The contents of these subroutines depend on the description of the primary source and the geometry of the reflector. All such subroutines are called by the main program as SETUP and ADDUP. (The subroutines have no arguments. They use common statements identical with those for the main program.) To distinguish one SETUP (or ADDUP) subroutine from another, they are given different names (or numbers) in their \$IBFTC card. For example, the SETUP subroutine shown in Table 2 has the name SET213 (it is for a paraboloid with standard illumination) and the SETUP subroutine shown in Table 4 has the name SETSFR (it is for scattering from a spheroid, the source being a dipole).

The main program of Table 1 and the ADDUP subroutine shown in Table 3 may be used with either one of the two SETUP subroutines shown in Tables 2 and 4 to compute, respectively, the radiated power from a paraboloid reflector or that from a spheroidal reflector.

RESULTS

In the time available, it was possible to run only a few test results. Some of them are presented in Tables 5 and 6, and Figures 4 through 9. The latter are in the form of computer-plotted graphs. The format in which the results are presented has not been finalized, and is due for improvement.

In the latest version, the program printout consists of three parts. The second part is not printed here because there is a 1 in column 50 of the first card. (See Tables 5 and 6). The first part prints an image of the data cards read, with column numbers 1 through 72 printed on top, for guidance in finding the location of data on the data card. The significance of the data is also printed over their values. The rest of this part consists of messages (see Table 5) which describe what values have been used in the problem. At the end of this part, the number of elementary areas in each segment is printed.

The third part of the report (see Table 6) gives the direction of the maximum radiated power, and the corresponding computed value. It must be understood that this is the largest of the values for power radiated in the directions specified in the problem. If the field point in whose direction the maximum power is actually radiated is not one of the specified field points for which the computation is made, the results must then be understood to be the largest of a set and not the actual maximum.

This part of the report also prints the values (in db's) of the power radiated in the direction of the specified field point, normalized with respect to the largest value. The computer-plotted graphs, examples of which are shown in Figures 4 through 8, are plotted from the results in the third part of the report.

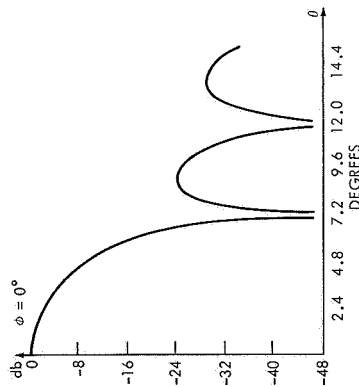


Figure 4—Radiation pattern of antenna with diameter = 85', focal length = 36', wavelength = 7.2', illuminated with a $\cos \theta$ primary source located at $x=0, y=0, z=0$, with polarization along x axis rotated by Euler angles $a=0, b=0, c=0$.

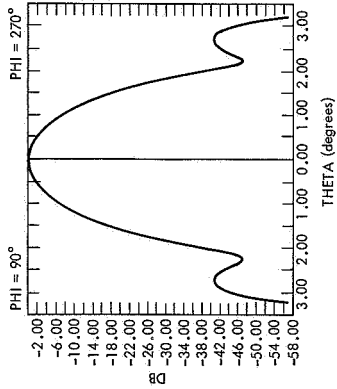


Figure 5—Radiation of pattern of ATS antenna with diameter = 30', focal length = 13.2', frequency = 2000 MHz, illuminated with a $\cos^4 \theta$ primary source located at $x=0, y=0, z=0$, with polarization along y axis rotated by Euler angles $a=0, b=0, c=0$.

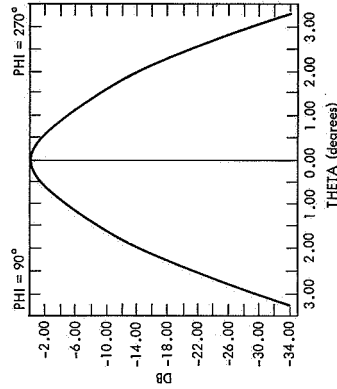


Figure 6—Graph illustrating the effect of primary source phase deviation on the radiation pattern of ATS antenna with diameter = 30', focal length = 13.2', frequency = 2000 MHz, illuminated with a $\cos \theta$ primary source located at $x=0, y=0, z=0$, with polarization along y axis rotated by Euler angles $a=0, b=0, c=0$.

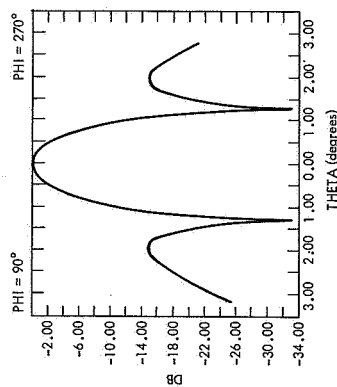


Figure 7—Graph illustrating the effect of obstructions on the radiation pattern of ATS antenna with diameter = 30', focal length = 13.2', frequency = 2000 MHz, illuminated with a $\cos^4 \theta$ primary source located at $x=0, y=0, z=0$, with polarization along y axis rotated by Euler angles $a=0, b=0, c=0$.

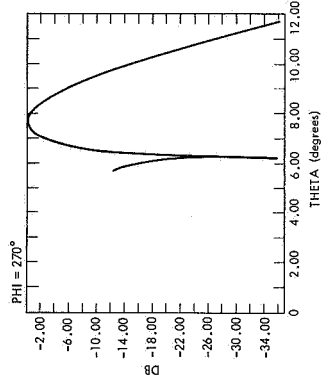


Figure 8—Graph illustrating the effect of source translation on the radiation pattern of ATS antenna with diameter = 30', focal length = 13.2', frequency = 2000 MHz, illuminated with a $\cos^4 \theta$ primary source located at $x=0, y=2', z=0$, with polarization along y axis rotated by Euler angles $a=0, b=0, c=0$.

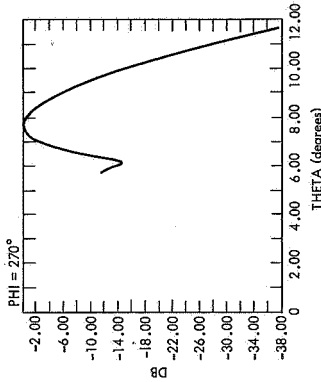
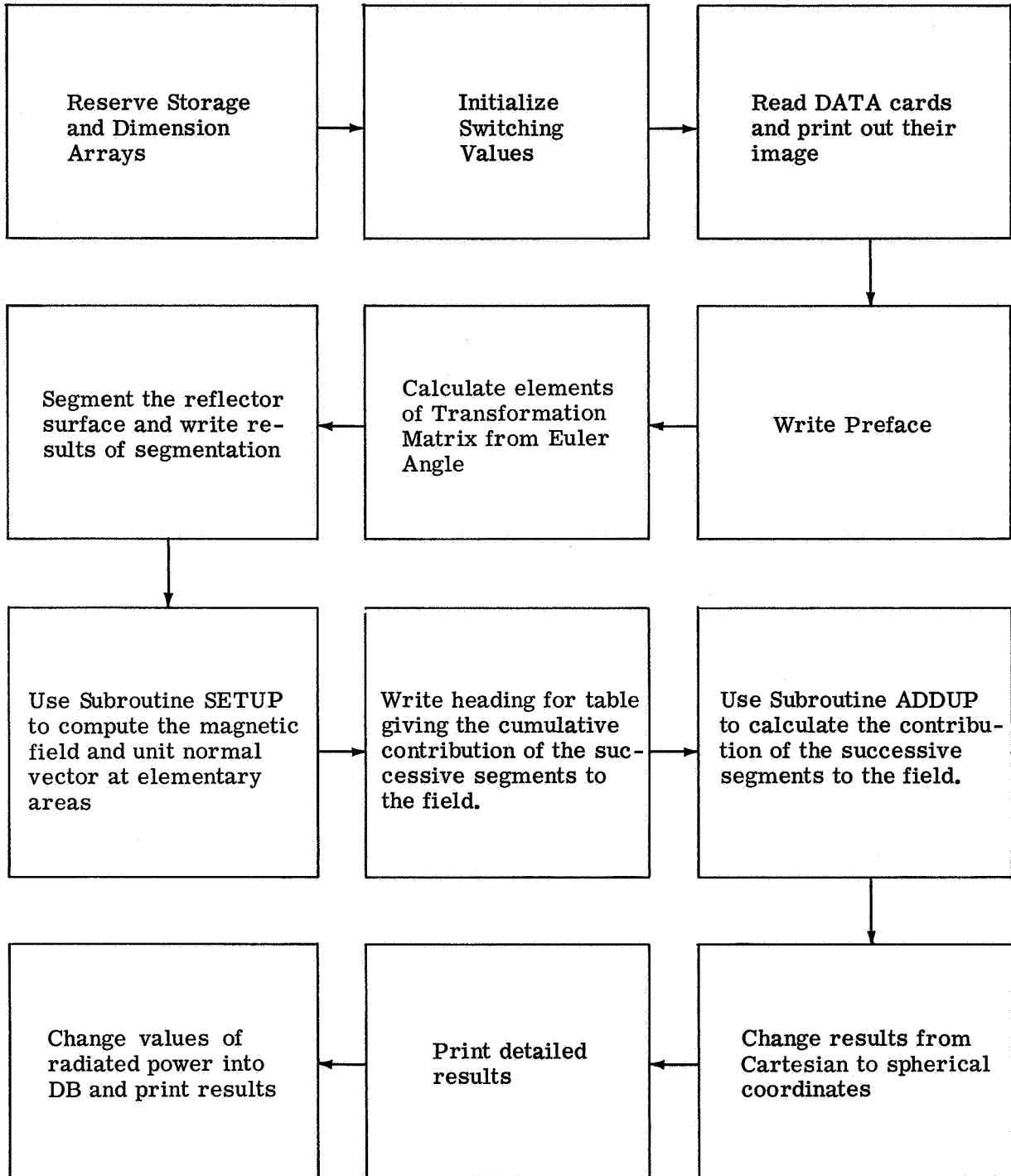


Figure 9—Graph illustrating the effect of primary source rotation and translation on the radiation pattern of ATS antenna with diameter = 30', focal length = 13.2', frequency = 2000 MHz, illuminated with a $\cos^4 \theta$ primary source located at $x=0, y=0, z=0$, with polarization along y axis rotated by Euler angles $a=351.30, b$ and c unspecified.

Table 1
Block Diagram
and
Listing of the Main Program (Version BIM 423)

Simplified Block Diagram of the Main Program



```

C
C *****DRIVER PROGRAM FOR COMPUTING RADIATION PATTERN*****
CJMMON A,AXI,AXR,AYI,AYR,AZI,AZR,A1,A2,A3,A4,A5,A6,A7, B,AR,BR
CJMMON CA,CB,CELNUM,CFI,CFR,CG,CKD,CKR,CRI,CRF,CTA,CTI,CELAST
CJMMON COSTA,CPHI,SINTA,SPHI
CJMMON D1,D2,D3,DIA,DPHI,DR,DRHC,DRR,CRI,CTR,DTI,DFR,DFI
CJMMON E11,E12,E13,E21,E22,E23,E31,E32,E33,EY,EZ
CJMMON F,FL,FLDA,FNUM,FRING,FR,FRC,FZ, GR,G,BIG
CJMMON H,HX,HY,HZ,HXF,HYF,HZF
CJMMON IS,IE,IT1,IT2,IT3,IT4,IT5,IT6,IT7,IT8,IF1,IF2,IF3,IF4,IF5
CJMMON IF6,IF7,IF8,N2,N3,N4,N5,N6,N7,IRP,LS,L6,L7,L8,L9,L10
CJMMON I,I1,I0,IOSUM,IEND,IENDC,IFI,IR,IFI,ISUP,ITI, IBI
CJMMON J,J1,J81,J8I,JR1NG, LIR,LIPI,LSM,L1,L2,L3,L4,M,TIST
CJMMON NFI,NFP,NPR,NR,NRING,NRINGI,ARSG,NSUMES,NT,NTA,NU,NULR,NUM
CJMMON PX,PY,PZ
CJMMON PHI,POWER, Q,QQ,CFI,QR,F,ASE, R1,R2,FF,RHC,RHO2
CJMMON SA,SB,SFI,SG,SKD,SKR,STA, T,TPI, VDSJ
CJMMON X,XI,XIUL,XR,XRUL,Y,YI,YIUL,YR,YRUL,Z,ZI,ZIUL,ZR,ZRUL
CJMMON NRI(400),NSUM(400),NUMSUP(400),NUMT(250),NUMF(250)
CJMMON OBSTD(250),OBSFD(250)
CJMMON VX(1000),VY(1000),VZ(1000),VDS(1000),VHXR(1000),VHXI(1000)
CJMMON VHYR(1000),VHYI(1000),VHZR(1000),VFZ(1000),VNXZ(1000)
CJMMON VNYZ(1000)
RCL NU
DIMENSION PWR(250)
DIMENSION FV(250,6)
DIMENSION JOK(54)
C
C *****BEGIN READING*****
29 READ(5,40)NTA,NFI,M,NU,L3 ,1 ,2 ,3 ,4 ,5 ,6
40 FJRMAT(3110,F10.3,11C)
I=INTA.EQ. 0) GO TO 8C60 ,7 ,8 ,9
READ(5,41)DIA,DIA1,DIA2,A1,FRC,FLDA,F ,10 ,11 ,12
FJRMAT(7F10.5)
41 READ(5,402)A,B,G,EX,EY,EZ,D1,D2,D3 ,13 ,14 ,15
FJRMAT(9F8.3)
403 READ(5,402)(OBSTD(I),I=1,NTA) ,16 ,17 ,18 ,19 ,20
READ(5,402)(OBSFD(I),I=1,NFI) ,21 ,22 ,23 ,24 ,25
FJRMAT(8(1X,F8.3))
402
C
C *****READ THE FIELD POINTS WHICH ARE ACTUALLY COMPUTED*****
877 READ(5,877)(JOK(J),J=1,54) ,26 ,27 ,28 ,29 ,30
FJRMAT(18I4)
C
C *****END OF READING*****
C
C *****INITIALISE*****
DJ 4321 I=1,250 ,31
DJ 4321 J=1,6 ,32
FV(I,J)=0. ,33

```

```

4321 CONTINUE DJ 205 ID=1,250 ,34 ,35 ,36
205 PWR(ID)=0.0 ,37
NJMSUM(1)=0 ,38 ,39
L>=0 ,40
L<=0 ,41
JIRNG=1000 ,42
I1ST=1000 ,43
DS=(1-D1**2-02**2)**.5 ,44
TPI=2.*3.141592654 ,45
DL=TPI/360. ,46
C
C *****BEGIN PREFACE WRITING*****
C
1006 WRITE(6,1006) ,47
FJRMAT(1H1) ,48 ,49
WRITE(6,5876) ,50 ,51
9876 FJRMAT(3X,66)THE DATA CARDS READ,THEIR CORRESPONDING PARAMETERS
IAND FORMAT ARE
WRITE(6,43) ,52 ,53
43 FJRMAT(73X,72H1234567E10123456782012345678301234567840123456785012
134567860123456787012)
WRITE(6,44) ,54 ,55
44 FJRMAT(73X,72HND. TETAS NO. FIS ARRAYS SIZE CCS**N DETAILS YES
I JR NO
WRITE(6,5874)NTA,NFI,M,NU,L3 ,56 ,57 ,58
9874 FJRMAT(3X,3110,F10.3,110)
WRITE(6,45) ,59 ,60
45 FJRMAT(73X,72HDIAMETER HOLE DIA1 HOLE DIA2 DEVIATION SCALE WAV
LE.ENGTH FOCAL DIST.)
WRITE(6,46)DIA,DIA1,DIA2,A1,FRC,FLDA,F ,61 ,62 ,63
FJRMAT(3X,7F10.5)
WRITE(6,9871) ,64 ,65
9871 FJRMAT(3X,4HALFA,4X,4HBETA,4X,4GAMA, 7X,1HX,7X,1HY,7X,1HZ,7X,2HD1
1, 6X,2HD2,6X,2HD3)
WRITE(6,9869)A,B,G,EX,EY,EZ,D1,D2,D3 ,66 ,67 ,68
9869 FJRMAT(3X,9F8.3)
WRITE(6,1003) ,69 ,70
1003 FJRMAT(1H1)
WRITE(6,9873) ,71 ,72
9873 FJRMAT(3X,28HTETA DEGREES OF FIELD POINTS)
WRITE(6,4021)(OBSTD(I),I=1,NTA) ,73 ,74 ,75 ,76 ,77
4021 FJRMAT(3X,8(1X,F8.3))
WRITE(6,1003) ,78 ,79
WRITE(6,9872) ,80 ,81
9872 FJRMAT(3X,26HFI DEGREES OF FIELD POINTS)
WRITE(6,4021)(OBSFD(I),I=1,NFI) ,82 ,83 ,84 ,85 ,86
WRITE(6,60) ,87 ,88
60 FJRMAT(73X,56)FOLLOWING POINTS IN THE TETA-FI MATRIX HAVE BEEN OMITTED
WRITE(6,61)(JOK(J),J=1,54) ,89 ,90 ,91 ,92 ,93
FJRMAT(3X,18I4)
C
C *****END OF PREFACE*****
C
C *****CALCULATE ELEMENTS OF EULER MATRIX*****

```

C	A1=A*DR	,94		
	CA=COS(AR)	,95		
	SA=SIN(AR)	,96		
	B1=B*DR	,97		
	CB=COS(BR)	,98		
	SB=SIN(BR)	,99		
	G1=G*DR	,100		
	CG=COS(GR)	,101		
	SG=SIN(GR)	,102		
	E11=CG*CA-CB*SA*SG	,103		
	E21=-SG*CA-CB*SA*CG	,104		
	E31=SB*SA	,105		
	E12=CG*SA+CB*CA*SG	,106		
	E22=-SG*SA+CB*CA*CG	,107		
	E32=-SB*CA	,108		
	E13=SG*SB	,109		
	E23=CG*SB	,110		
	E33=CB	,111		
	P4=D1*E11+D2*E21+D3*E31	,112		
	P7=D1*E12+D2*E22+D3*E32	,113		
	PZ=D1*E13+D2*E23+D3*E33			
C	*****BEGIN SEGMENTATION*****			
C	Q=TP1/FLDA	,114		
C	Q1MO=FLDA*FRC	,115		
	N1=(D1A/2.)/DRHO	,116		
	L7=(D1A1/2.)/DRHO	,117		
	L3=(D1A2/2.)/DRHO	,118		
	W1TE(6,102)NR	,119		
102	FJRMAT(//,3X,25HREFLECTOR IS DIVIDED INTO,14,7H RINGS.)	,120	,121	,122
	I=0	,123		
	J=0	,124		
13	I=I+1	,125		
	IF(I.GT.399) GO TO 7C1	,126	,127	,128
	ISUM=0	,129		
12	J=J+1	,130		
	IF(J.GT.NR) GO TO 10	,131	,132	,133
	ISUM=6*J	,134		
	IF(ISUM.GT.M) GO TO 14	,135	,136	,137
	ISUM=ISUM+ISUM	,138		
	IF(ISUM.GT.M) GO TO 11	,139	,140	,141
	GJ TO 12	,142		
11	I=I+1	,143		
	W1(I1)=J-1	,144		
	NSUM(I1)=ISUM-IDSUM	,145		
	J=J-1	,146		
	GJ TO 13	,147		
14	W1TE(6,103)J,M	,148	,149	,150
103	FJRMAT(/,2X,37H THE NUMBER OF ELEMENTAL AREAS IN THE,14,20H RING I IS LARGER THAN,15,42H .WILL CONSIDER PART OF RINGS AS SEGMENTS.)			
	IF(ISUM.EQ.0) GO TO 876	,151	,152	,153
	I=I+1	,154		
	NSUM(I1)=ISUM	,155		
	W1(I1)=J-1	,156		

	I=I1	,157		
	L5=1	,158		
876	L5=1	,159		
	J4ING=J	,160		
	I1ST=I1+1	,161		
51	NJIV=ISUM/M	,162		
	NREM=ISUM-NDIV*M	,163		
	DJ 511 ISK=1,NDIV	,164		
	I1=I1+1	,165		
	N1(I1)=J	,166		
	NSUM(I1)=M	,167		
511	CONTINUE	,168	,169	
	IF(NREM.EQ.0) GO TO 875	,170	,171	,172
	I1=I1+1	,173		
	W1(I1)=J	,174		
	NSUM(I1)=NREM	,175		
875	J=J+1	,176		
	IF(J.GT.NR) GO TO 10	,177	,178	,179
	ISUM=6*J	,180		
	GJ TO 51	,181		
10	W1TE(6,104)	,182	,183	
104	FJRMAT(/,2X,55H CONTRIBUTION OF ALL REFLECTOR RINGS WILL BE PROCES SED.)			
	IF(L5.EQ.1) GO TO 515	,184	,185	,186
	I=I+1	,187		
	W1(I1)=J-1	,188		
	NSUM(I1)=ISUM	,189		
515	I=I1	,190		
15	L1R=1	,191		
	L1R1=L1R-1	,192		
	W1(I1)=0	,193		
	NSUM(I1)=0	,194		
	NSUMDS=0	,195		
	DJ 201 IN=2,L1R	,196		
201	NSUMDS=NSUMDS+NSUM(I1)	,197	,198	
	W1TE(6,1009) NSUMDS,L1R1,M	,199	,200	,201
1009	FJRMAT(/,3X,35H THE TOTAL NO. OF AREAS IS NSUMDS = ,18, 123H, NO. OF SEGMENTS IS L1R1 = ,13,6H, P = ,14,2H .)			
	W1TE(6,1008)DIA,FLDA,FRC	,202	,203	,204
1008	FJRMAT(/,3X,37H RESULTS BASED ON INPUT DATA, CIA. = ,F8.4, 115H, WAVELENGTH = ,F8.4,31H, SIDE OF ELEMENTAL AREA FRC = ,F8.5, 215H OF WAVELENGTH.)			
	W1TE(6,1021)F,A,B,G,E,Y,EZ	,205	,206	,207
1021	FJRMAT(/,3X,21H F=,F8.3,6H,ALFA=,F8.3,6H,BETA=,F8.3,6H,GAMA=,F8.3, 123H, TRANSLATIONS ARE X=,F8.3,3H,Y=,F8.3,3H,Z=,F8.3,2H .)			
	W1TE(6,1031)D1,D2,D3	,208	,209	,210
1031	FJRMAT(/,3X,34H THE POLARIZATION COSINES ARE C1 = ,F8.5,6H,D2 = , 1F8.5,6H,D3 = ,F8.5,2H .)			
	W1TE(6,7113)	,211	,212	
7113	FJRMAT(/,3X,72H FOLLOWING ARE THE ORDER NUMBERS OF THE LAST RINGS I IN SUCCESSIVE SEGMENTS.)			
	W1TE(6,7114)(NR(I1),I=2,L1R)	,213	,214	,215 ,216 ,217
7114	FJRMAT(/ 21(3X,I2))			
	W1TE(6,7115)	,218	,219	
7115	FJRMAT(/,3X,67H FOLLOWING ARE THE NUMBER OF ELEMENTAL AREAS IN SUCC ESSIVE SEGMENTS.)			

BIM423
EXTERNAL FORMULA NUMBER - SOURCE STATEMENT - INTERNAL FORMULA NUMBER(S) 08/25/67 PAGE 5

```

WRITE(6,7114)(NSUM(I),I=2,LIR)
*****END OF SEGMENTATION*****
*****BEGIN PREPARATION FOR SETLF*****
      BLG=0. ,220 ,221 ,222 ,223 ,224
      LI=0 ,225
      L3=0 ,226
      LI=IR+1 ,227
*****ALL SEGMENTS DONE*****
      ,228
I=(IR.EQ.LIR) GO TO 30C ,229 ,230 ,231
WRITE(6,1003) ,232 ,233
NFP=0 ,234
LI=IR+1 ,235
I=(IR.LE.IR1ST) GO TO 5051 ,236 ,237 ,238
NJLR=NRI(IR) ,239
NPR=NRI(IR1) ,240
NSG=NPR-NULR ,241
IEND=0 ,242
I=1 ,243
J=-1 ,244
J=J+1 ,245
I=(J.EQ.NRSG) GO TO 3 ,246 ,247 ,248
NKN=NRI(IR)+J+1 ,249
L3W=0 ,250
NKN=NKN+1 ,251
FKNG=FLOAT(NRING) ,252
FKNG=FKNG-.5 ,253
R4D=FKNG*DRHO ,254
R4D2=R4D**2 ,255
I=I-1 ,256
IEND=IEND ,257
NJM=6*NRING ,258
FNUM=NUM ,259
DHI=TPI/FNUM ,260
IEND=IEND*FNUM ,261
NJSUM(NRING)=IEND ,262
I=(NRING.GT.L7.AND.NRING.LT.L8) GO TO 24
*****SETUP RING BY RING*****
      ,263 ,264 ,265
CALL SETUP
GJ TO 1 ,266
I=IEND+1 ,267
GJ TO 1 ,268
*****RING CONTAINS MORE THAN ONE SEGMENT*****
      ,269
5051 NPR=NRI(IR1) ,270
      NJLR=NPR-1 ,271
      NSG=1 ,272
      NKN=NRI(IR1) ,273
      L3W=0 ,274

```

BIM423
EXTERNAL FORMULA NUMBER - SOURCE STATEMENT - INTERNAL FORMULA NUMBER(S) 08/25/67 PAGE 6

```

NKN=NKN+1 ,275
FKNG=FLOAT(NRING) ,276
FKNG=FKNG-.5 ,277
R4D=FKNG*DRHO ,278
R4D2=R4D**2 ,279
NJM=6*NRING ,280
I=(NRI(IR1).EQ.NRI(IR)) GO TO 53 ,281 ,282 ,283
CELNUM=-.5 ,284
CELAST=FLOAT(NSUM(IR1)) ,285
I=0 ,286
FNUM=NUM ,287
DHI=TPI/FNUM ,288
NJSUM(NRING)=NSUM(IR1) ,289
IEND=1000000 ,290
I=(NRING.GT.L7.AND.NRING.LT.L8) GO TO 25
*****SETUP WHEN RING CONTAINS MORE THAN ONE SEGMENT*****
      ,291 ,292 ,293
CALL SETUP
      ,294
GJ TO 3 ,295
I=IEND+1 ,296
GJ TO 3 ,297
53 CELAST=CELAST+FLOAT(NSUM(IR1)) ,298
GJ TO 52
*****BEGIN WITH FIELD POINTS*****
      ,299
3 JAK=0 ,300
      D3 901 IFI=1,NFI ,301
      D3 901 ITI=1,NTA ,302
      JAK=JAK+1 ,303
      D3 903 JA=1,54 ,304
903 I=(JAK.EQ.JOK(JA)) GO TO 901 ,305 ,306 ,307 ,308
      NFP=NFP+1 ,309
      NJMF(NFP)=IFI ,310
      NJMT(NFP)=ITI
*****HEADING HAS BEEN WRITTEN*****
      ,311
I=(L4.EQ.1) GO TO 2222
*****PRINTING OF DETAILS NOT REQUIRED*****
      ,312 ,313 ,314
I=(L3.EQ.1) GO TO 2222
*****WRITE HEADING FOR DETAILED DATA TABLE*****
      ,315 ,316 ,317
WRITE(6,1006) ,318 ,319
WRITE(6,1003) ,320 ,321
WRITE(6,1003) ,322 ,323
WRITE(6,1034) ,324 ,325
1034 FFORMAT(3X,8HF)FOLLOWING TABLE GIVES WAFEL'S FIELD VALUES FOR INDICA
      IED FIELD POINTS AND SEGMENT NUMBERS
WRITE(6,1208)DIA,FLDA,FRC ,326 ,327 ,328
1208 FFORMAT(//3X,37H)THEY ARE BASED ON INPUT DATA, CIA. = ,F8.4,

```



```

N2=IS+1
N3=N2+1
N4=N3+1
N5=N4+1
N6=N5+1
N7=N6+1
M ITE(6,6660)IS,N2,N3,N4,N5,N6,N7,IE
FJRMAT(/3X,18FIELD POINT ,2X,6(I3,9X))
6666 I1=NUMT(I5)
I12=NUMT(N2)
I13=NUMT(N3)
I14=NUMT(N4)
I15=NUMT(N5)
I16=NUMT(N6)
I17=NUMT(N7)
I18=NUMT(IE)
I1=NUMF(I5)
I2=NUMF(N2)
I3=NUMF(N3)
I4=NUMF(N4)
I5=NUMF(N5)
I6=NUMF(N6)
I7=NUMF(N7)
I8=NUMF(IE)
M ITE(6,9222)OBSTD(I11),OBSTD(I12),CESTD(I13),CESTD(I14),OBSTD(I15
9222 I1),OBSTD(I16),OBSTD(I17),OBSTD(ITE)
FJRMAT(3X,12HETA DEGREES,6X,8F12.6)
M ITE(6,9333)OBSFD(IF1),OBSFD(IF2),OBSFC(IF3),OBSFC(IF4),OBSFD(IF5
9333 I1),OBSFD(IF6),OBSFD(IF7),OBSFD(IF8)
FJRMAT( 3X,10HFI DEGREES,8X,8F12.6)
M ITE(6,1003)
M ITE(6,1001)(PMR(J),J=IS,IE)
9672 M ITE(6,1001)(PMR(J),J=IS,IE)
1001 FJRMAT(3X,11HDB LEVEL ,4X,3X,8F12.6)
9673 I5=IS+8
I6=IE+8
208 CJNINUE
M ITE(15,8000)
8000 FJRMAT(5X,3HPHI,10X,5HTHETA,1CX,2HDB)
M ITE(15,8002) NFP
8002 FJRMAT(3X,I3)
DJ 8050 I=1,NFP
<I=NUMT(I)
<I=NUMF(I)
8050 M ITE(15,8001) OBSFD(KF),OBSTD(KT),PMR(I)
8001 FJRMAT(4X,F12.6,3X,F12.6,3X,F12.6)
GJ TO 29
8060 M ITE(15,8061)
8061 FJRMAT(5X,3HEND)
RETURN
701 M ITE(6,7111)
7111 FJRMAT(/3X,35HTHE RING DIMENSION IS INSUFFICIENT.)
EVD

```

```

,433
,434
,435
,436
,437
,438
,439 ,440 ,441
,442
,443
,444
,445
,446
,447
,448
,449
,450
,451
,452
,453
,454
,455
,456
,457
,458 ,459 ,460
,461 ,462 ,463
,464 ,465
,466 ,467
,468 ,469 ,470 ,471 ,472
,473
,474
,475 ,476
,477 ,478
,479 ,480 ,481
,482
,483
,484
,485 ,486 ,487 ,488
,489
,490 ,491
,492
,493 ,494
,495
,496

```

Table 2
Listing of subroutine SETUP (version SET 213)
Written for a paraboloidal reflector, illuminated
according to Eq. (7).

```

SJBROUTINE SETUP
CJMMON A,AXI,AXR,AYI,AYR,AZI,AZR,A1,A2,A3,A4,A5,A6,A7, B,AR,BR
CJMMON CA,CB,CELNUM,CFI,CFR,CG,CKD,CXR,CRI,CRR,CTA,CTI,CELAST
CJMMON COSTA,CPHI,SINTA,SPHI
CJMMON D1,D2,D3,DIA,DPHI,DR,DRHC,DRP,CRI,C1R,DTI,DFR,DFI
CJMMON E1,E12,E13,E21,E22,E23,E31,E32,E33,EX,EY,EZ
CJMMON F,FI,FLDA,FNUH,FRING,FR,FRC,FZ, GR,G,BIG
CJMMON H,HX,HY,HZ,HXF,HYF,HZF
CJMMON IS,IE,IT1,IT2,IT3,IT4,IT5,IT6,IT7,IT8,IF1,IF2,IF3,IF4,IF5
CJMMON IF6,IF7,IF8,N2,N3,N4,N5,N6,N7,IRP,L5,L6,L7,L8,L9,L10
CJMMON I,I1,ID,IDSUM,IEND,IENDC,IFI,IA,IR,IR1,ISUP,ITI, IBIG
CJMMON J,J1,JB1,JBIG,JRING, LIF,LIR1,LSW,L1,L2,L3,L4,M,I1ST
CJMMON NFI,NFP,NPR,NR,NRING,NRING1,NRSG,NSUMCS,NT,NTA,NU,NULR,NUM
CJMMON PX,PY,PZ
CJMMON PHI,POWER, Q,QD,QFI,QR,PHASE, R1,R2,RF,RFC,RHOZ
CJMMON SA,SB,SFI,SG,SKD,SKR,STA, TA,TPI, VDSJ
CJMMON X,XI,XIUL,XR,XRUL,Y,YI,YILL,YR,YRUL,Z,ZI,ZIUL,ZR,ZRUL
CJMMON NRI(400),NSUM(400),NUMSUM(400),NUMT(250),NUMF(250)
CJMMON OBSTD(250),OBSFD(250)
CJMMON VX(1000),VY(1000),VZ(1000),VDS(1000),VFXR(1000),VHXI(1000)
CJMMON VHYR(1000),VHYI(1000),VHZR(1000),VFZI(1000),VNXX(1000)
CJMMON VNYZ(1000)
REAL NU
2 I=I+1
IF (I.EQ.(IEND+1)) RETURN ,1
I=(IR1.GE.I1ST) GO TO 17 ,2 ,3 ,4
CELNUM=FLOAT(I-IEND) ,5 ,6 ,7
CELNUM=CELNUM-.5 ,8
18 C=DPHI*CELNUM ,9
C>HI=COS(PHI) ,10
S>HI=SIN(PHI) ,11
X=RHO*CPHI ,12
XE=X-EX ,13
VX(I)=X ,14
Y=RHO*SPHI ,15
YE=Y-EY ,16
VY(I)=Y ,17
IF (LSW.EQ.1) GO TO 31 ,18
VL(NRING)=RHO2/(F*4.)-F ,19 ,20 ,21
Z=VZ(NRING) ,22
ZE=Z-EZ ,23
R2=RHO2+Z**2 ,24
R1=R2**.5 ,25
Z1=Z-R1 ,26
VJ(NRING)=TP I*((RHO+.5*DRHO)**2-(RHO-.5*DRFC)**2)/(FNUM*2.) ,27
LSW=1 ,28
31 VXZ(I)=X/ZR1 ,29
VYZ(I)=Y/ZR1 ,30
C *****RP IS THE DISTANCE FROM THE PHASE CENTER TO ELEMENTAL AREA**
C R>=(XEX**2+YFY**2+ZYZ**2)**.5 ,31
CJ STA=(E31*XEX+E32*YFY+E33*ZYZ)/RP ,32
C *****FR IS = CCS TETA**NL/RP,THE PATTERN FACTOR OF SOURCE**

```

```

C CJ STA=ABS(COSTA) ,33
C FR=(COSTA**NU)/RP ,34
C QR=Q*RP-A1*DR*(1.-COSTA) ,35
C CR=COS(QR) ,36
C SR=SIN(QR) ,37
C *****HX,HY,HZ ARE THE COMPONENTS OF H IN DIRECTION OF H FIELD**
C HX=YFY*PZ-ZEZ*PY ,38
C HY=ZYZ*PX-XEX*PZ ,39
C HL=XEX*PY-YFY*PX ,40
C H=(HX**2+HY**2+HZ**2)**.5 ,41
C HF=HX*FR/H ,42
C HF=HY*FR/H ,43
C HF=HZ*FR/H ,44
22 V1XR(I)=HXF*CKR ,45
V1XI(I)=-HXF*SKR ,46
V1YR(I)=HYF*CKR ,47
V1YI(I)=-HYF*SKR ,48
V1ZR(I)=HZF*CKR ,49
V1ZI(I)=-HZF*SKR ,50
G) TO 2 ,51
17 CELNUM=CELNUM+1. ,52
I=(CELNUM.GT.CELAST) GO TO 19 ,53
G) TO 18 ,54 ,55 ,56
19 CELNUM=CELNUM-1. ,57
R=TURN ,58
END ,59
,60

```

Table 3
Listing of subroutine ADDUP (version ADD 193)

```

SJBROUTINE ADDUP
CJMMON A, AXI, AXR, AYI, AYR, AZI, AZR, A1, A2, A3, A4, A5, A6, A7, B, AR, BR
CJMMON CA, CB, CELNUM, CFI, CFR, CG, CKD, CKR, CRI, CRR, CTA, CTI, CELAST
CJMMON COSTA, CPHI, SINTA, SPHI
CJMMON D1, D2, D3, DIA, DPHI, DR, DRHC, DRP, CRI, CTF, CTI, CFR, DFI
CJMMON E1, E12, E13, E21, E22, E23, E31, E32, E33, EX, EY, EZ
CJMMON F, FI, FLDA, FNUM, FRING, FR, FRC, FZ, GR, G, BIG
CJMMON H, HX, HY, HZ, HXF, HYF, HZF
CJMMON IS, IE, IT1, IT2, IT3, IT4, IT5, IT6, IT7, IT8, IF1, IF2, IF3, IF4, IF5
CJMMON IF6, IF7, IF8, N2, N3, N4, N5, N6, N7, IRM, L5, L6, L7, L8, L9, L10
CJMMON I, I1, ID, IDSUM, IEND, IENDG, IFI, IA, IR, IR1, ISUM, ITI, IBIG
CJMMON J, J1, JB1, JBIG, JRING, LIR, LIR1, LSW, L1, L2, L3, L4, M, I1ST
CJMMON NF1, NFP, NPR, NR, NRING, NRIAG1, NRSG, NSUPCS, NT, ATA, NU, NULR, NUM
CJMMON PX, PY, PZ
CJMMON PHI, POWER, Q, QD, QFI, QR, PHASE, R1, R2, FF, FHC, RHO2
CJMMON SA, SB, SFI, SG, SKD, SKR, STA, TA, TFI, VDSJ
CJMMON X, XI, XIUL, XR, XRUL, Y, YI, YIUL, YR, YPUL, Z, ZI, ZIUL, ZR, ZRUL
CJMMON NRI(400), NSUM(400), NUMSUM(400), NUMT(250), NUFF(250)
CJMMON DBSTD(250), DBSFD(250)
CJMMON VX(1000), VY(1000), VZ(1000), VDS(1000), VHXR(1000), VHXI(1000)
CJMMON VHYR(1000), VHYZ(1000), VHZR(1000), VFZI(1000), VNXX(1000)
CJMMON VNYZ(1000)
REAL NU
I=0
J=NULR
J=J+1
J1=J+1
IF(J.GT.NPR) RETURN
VDSJ=VDS(J)
XIUL=0.
XIUL=0.
YIUL=0.
ZIUL=0.
ZIUL=0.
I=I+1
IF(I.GT.NUMSUM(J1)) GO TO 38
I=(J.GT.L7.AND.J.LT.L8) GO TO 37
QD=Q*(VX(I)*CFI*STA+VY(I)*SFI*STA+VZ(I)*CTA)
CD=COS(QD)
SD=SIN(QD)
AXR=VNYZ(I)*VHZR(I)-VHYR(I)
AYI=VNYZ(I)*VHZI(I)-VHYI(I)
XRUL=XRUL+(AXR*CKD-AXI*SKD)
XIUL=XIUL+(AXR*SKD+AXI*CKD)
AYR=VHXR(I)-VNXX(I)*VFZR(I)
AYI=VHXI(I)-VNXX(I)*VFZI(I)
YIUL=YIUL+(AYR*CKD+AYI*SKD)
YIUL=YIUL+(AYR*SKD+AYI*CKD)
AZR=VNXX(I)*VHYR(I)-VNYZ(I)*VHXR(I)
AZI=VNXX(I)*VHYI(I)-VNYZ(I)*VHXI(I)
ZIUL=ZIUL+(AZR*CKD-AZI*SKD)
ZIUL=ZIUL+(AZR*SKD+AZI*CKD)
GO TO 37
XI=XR+XRUL*VDSJ

```

```

,1
,2
,3
,4
,5 ,6 ,7
,8
,9
,10
,11
,12
,13
,14
,15
,16 ,17 ,18
,19 ,20 ,21
,22
,23
,24
,25
,26
,27
,28
,29
,30
,31
,32
,33
,34
,35
,36
,37
,38

```

```

XI=XI+XIUL*VDSJ
YI=YI+YIUL*VDSJ
ZI=ZI+ZIUL*VDSJ
I=I-1
GO TO 7
END

```

```

,39
,40
,41
,42
,43
,44
,45
,46

```

Table 4
Listing of the subroutine SETUP (version SET SFR)
Written for scattering from a spheroid illuminated
by an axial dipole. The subroutine implements
Eqs. 55 through 68.

```

SUBROUTINE SETUP
COMMON A,AXI,AXR,AYI,AYR,AZ,A3,A4,A5,A6,A7, B,AR,BR
COMMON CA,CB,CELNUM,CFI,CFR,CG,CKD,CKR,CRI,CRR,CTA,CTI,CELAST
COMMON COSTA,CPHI,SINTA,SPHI
COMMON D1,D2,D3,DIA,DPHI,DR,DRHO,DRR,DRI,DTR,DTI,DFR,DFI
COMMON E1,E12,E13,E21,E22,E23,E31,E32,E33,EX,EY,EZ GR,G,BIG
COMMON F,FI,FLDA,FNUM,FRING,FR,FRC,FZ,
COMMON H,HX,HY,HZ,HXF,HYF,HZF
COMMON IE,IT1,IT2,IT3,IT4,IT5,IT6,IT7,IT8,IF1,IF2,IF3,IF4,IF5
COMMON IF6,IF7,IF8,N2,N3,N4,N5,N6,N7,IRM,L5,L6,L7,L8,L9,L10
COMMON I,I1,ID,IDSUM,IEND,IENDD,IFI,IN,IR,IRI,ISUM,ITI, IBIG
COMMON J,J1,JB1,JBIG,JRING, LIR,LIRI,LSW,L1,L2,L3,L4,M,I1ST
COMMON NFI,NFP,NPR,NR,NRING,NRING1,NRSG,NSUMDS,NT,NTA,NU,NULR,NUM
COMMON PX,PY,PZ
COMMON PHI,POWER, Q,QD,QFI,QR,PHASE, R1,R2,RP,RHO,RHO2
COMMON SA,SB,SFI,SG,SKD,SKR,STA, TA,TPI, VDSJ
COMMON X,XI,XIUL,XR,XRUL,Y,YI,YIUL,YR,YRUL,Z,ZI,ZIUL,ZR,ZRUL
COMMON NRI(400),NSUM(400),NUMSUM(400),NUMT(250),NUMF(250)
COMMON OBSTD(250),OBSFD(250)
COMMON VX(1000),VY(1000),VZ(1000),VDS(1000),VHXR(1000),VHXI(1000)
COMMON VYR(1000),VHYI(1000),VHZR(1000),VHZI(1000),VNXZ(1000)
COMMON VNYZ(1000)
EA=10.
EB=5.
EC=(EA**2-EB**2)**.5
I=I+1
IF(I.EQ.(IEND+1)) RETURN
CELNUM=FLOAT(I-IENDD)
CELNUM=CELMUM-.5
PHI=DPHI*CELMUM
CPHI=(1.-CPHI)**.5
SPHI=(1.-CPHI)**.5
X=RHO*CPHI
Y=RHO*SPHI
VX(I)=X
VY(I)=Y
IF(LSW.EQ.1) GO TO 31
VZ(NRING)=EA*(1.-RHO2/EB**2)**.5
Z=VZ(NRING)
R2=RHO2+Z**2
R1=R2**2
VDSINRING=TPI*(RHO+.5*DRHO)**2-(RHO-.5*DRHO)**2/(FNUM*2.)
A1=(RHO2+(Z-EC)**2)**.5
A2=(RHO2+(Z+EC)**2)**.5
OPR=(A1+A2)/((Z-EC)*A2+(Z+EC)*A1)
LSW=1
VNXZ(I)=X*OPR
VNYZ(I)=Y*OPR
RP= ((X-EX)**2+(Y-EY)**2+(Z-EZ)**2)**.5
QR=Q*RP
CKR=COS(QR)
SKR=SIN(QR)
XRHOR=X/(RHO*RP)
YRHOR=Y/(RHO*RP)
VHXR(I)=-YRHOR*CKR
    
```

2

18

31

,1
 ,2
 ,3
 ,4
 ,5 ,6 ,7
 ,8
 ,9
 ,10
 ,11
 ,12
 ,13
 ,14
 ,15
 ,16
 ,17 ,18 ,19
 ,20
 ,21
 ,22
 ,23
 ,24
 ,25
 ,26
 ,27
 ,28
 ,29
 ,30
 ,31
 ,32
 ,33
 ,34
 ,35
 ,36
 ,37

SETSFR	EXTERNAL FORMULA NUMBER	SOURCE STATEMENT	INTERNAL FORMULA NUMBER(S)
			*38
		VHXI(I)= YRHOR*SKR	*39
		VHYR(I)= XRHOR*CKR	*40
		VHYI(I)=-YRHOR*SKR	*41
		VHZR(I)=0.	*42
		VHZI(I)=0.	*43
		GO TO 2	*44
		END	



PRECEDING PAGE BLANK NOT FILMED.

Table 5

Sample of the first part of report, produced by using main program BIM 423 (shown in Table 1), subroutines SET 213 (shown in Table 2) and ADD 193 (shown in Table 3).

The image of data cards used is given in this table. Calculations are for an antenna with Diameter = 85', Focal length = 36', Wavelength = 7.2 illuminated with a $\cos^4 \theta$ primary source located at $X = 0, Y = 0, Z = 0$ with polarization along X axis.

Sample 1

THE DATA CARDS READ, THEIR CORRESPONDING PARAMETERS AND FORMAT ARE

123456781012345678201234567830123456784012345678501234567860123456787012

ND. TETAS NO. FIS ARRAY SIZE COS**N DETAILS YES CF NO
 121 1 999 1.700 1

DIAMETER HOLE DIA1 HOLE DIA2 DEVIATION SCALE WAVELENGTH FOCAL DIST.
 15.0000 0. 0. 0. 0. C.50000 0.44700 6.00000
 ALFA BETA GAMMA X Y Z D1 D2 D3
 0. 0. 0. 0. 0. C.042 C. 0. 1.000 0.

TETA DEGREES OF FIELD POINTS

	0.	0.100	0.200	0.300	0.400	0.500	0.600	0.700
0.800	0.900	1.000	1.100	1.200	1.300	1.400	1.500	
1.600	1.700	1.800	1.900	2.000	2.100	2.200	2.300	
2.400	2.500	2.600	2.700	2.800	2.900	3.000	3.100	
3.200	3.300	3.400	3.500	3.600	3.700	3.800	3.900	
4.000	4.100	4.200	4.300	4.400	4.500	4.600	4.700	
4.800	4.900	5.000	5.100	5.200	5.300	5.400	5.500	
5.600	5.700	5.800	5.900	6.000	6.100	6.200	6.300	
6.400	6.500	6.600	6.700	6.800	6.900	7.000	7.100	
7.200	7.300	7.400	7.500	7.600	7.700	7.800	7.900	
8.000	8.100	8.200	8.300	8.400	8.500	8.600	8.700	
8.800	8.900	9.000	9.100	9.200	9.300	9.400	9.500	
9.600	9.700	9.800	9.900	10.000	10.100	10.200	10.300	
10.400	10.500	10.600	10.700	10.800	10.900	11.000	11.100	
11.200	11.300	11.400	11.500	11.600	11.700	11.800	11.900	
12.000								

FI DEGREES OF FIELD POINTS
 270.000

FOLLOWING POINTS IN THE TETA-FI MATRIX HAVE BEEN OMITTED

-0	-0	-0	-0	-0	-0	-0	-0	-0	-0	-0	-0	-0	-0	-0	-0	-0	-0
-0	-0	-0	-0	-0	-0	-0	-0	-0	-0	-0	-0	-0	-0	-0	-0	-0	-0
-0	-0	-0	-0	-0	-0	-0	-0	-0	-0	-0	-0	-0	-0	-0	-0	-0	-0

REFLECTOR IS DIVIDED INTO 33 RINGS.

CONTRIBUTION OF ALL REFLECTOR RINGS WILL BE PROCESSED.

THE TOTAL NO. OF AREAS IS NSUMDS = 2366, NO. OF SEGMENTS IS LIRI = 4, M = 999.

RESULTS BASED ON INPUT DATA, DIA. = 15.0000, WAVELENGTH = 0.4470, SIDE OF ELEMENTAL AREA FRC = 0.50000 OF WAVELENGTH.

F = 5.000, ALFA = 0., BETA = C., GAMMA = C., TRANSLATIONS ARE, X = 0., Y = 0.042, Z = 0.

THE POLARIZATION COSINES ARE D1 = C., D2 = 1.00000, D3 = 0.

FOLLOWING ARE THE ORDER NUMBERS OF THE LAST RINGS IN SUCCESSIVE SEGMENTS.

17 24 30 33

FOLLOWING ARE THE NUMBER OF ELEMENTAL AREAS IN SUCCESSIVE SEGMENTS.

918 882 990 576

Table 6

Sample of the 3rd. part of report, produced by the programs and data given in Table 5. Data from this table are transferred to a tape for plotting on a 4020 Stromberg Carlson plotter. Examples of these are shown in Figs. 5 through 9. Results of Table 5 are (hand) plotted in Fig. 4.

MAXIMUM POWER IS RADIATED IN DIRECTION TETA = C.300,FI= 270.000

RESULTS BASED ON INPUT DATA, DIA. = 15.0000, WAVELENGTH = 0.4470 ,SIDE OF ELEMENTAL AREA FRC = 0.5000 OF WAVELENGTH.

F# = 5.000,ALFA= 0. ,BETA= 0. ,GAMA= 0. ,TRANSLATIONS ARE,X= 0. ,Y= 0.042,Z= 0.

THE POLARIZATION COSINES ARE D1 = C. ,D2 = 1.00000,D3 = 0.

IN THE FOLLOWING TABLE EACH ROW GIVES THE POWER IN DB. THE ZERO DB REFERENCE IS THE POWER RADIATED IN THE DIRECTION

TETA = 0.300 AND FI = 270.000 AND HAS ABSOLUTE VALUE 191.180

FIELD POINT TETA DEGREES FI DEGREES	1 0. 270.000000	2 0.100000 270.000000	3 0.200000 270.000000	4 0.300000 270.000000	5 0.400000 270.000000	6 0.500000 270.000000	7 0.600000 270.000000	8 0.700000 270.000000
DB LE/EL	-C.2E2193	-0.13564C	-0.041734	0.	-0.010180	-0.072228	-0.186308	-0.352797
FIELD POINT TETA DEGREES FI DEGREES	9 0.800000 270.000000	10 C.900000 270.000000	11 1.000000 270.000000	12 1.100000 270.000000	13 1.200000 270.000000	14 1.300000 270.000000	15 1.400000 270.000000	16 1.500000 270.000000
DB LE/EL	-C.572293	-0.845623	-1.172866	-1.558376	-2.000807	-2.503166	-3.067854	-3.697744
FIELD POINT TETA DEGREES FI DEGREES	17 1.600000 270.000000	18 1.700000 270.000000	19 1.800000 270.000000	20 1.900000 270.000000	21 2.000000 270.000000	22 2.100000 270.000000	23 2.200000 270.000000	24 2.300000 270.000000
DB LE/EL	-4.356267	-5.167528	-6.016468	-6.949071	-7.972659	-9.096293	-10.331375	-11.692531
FIELD POINT TETA DEGREES FI DEGREES	25 2.400000 270.000000	26 2.500000 270.000000	27 2.600000 270.000000	28 2.700000 270.000000	29 2.800000 270.000000	30 2.900000 270.000000	31 3.000000 270.000000	32 3.100000 270.000000
DB LE/EL	-12.158923	-14.876527	-16.761730	-18.908216	-21.400405	-24.383733	-28.145513	-33.402418
FIELD POINT TETA DEGREES FI DEGREES	33 3.200000 270.000000	34 3.300000 270.000000	35 3.400000 270.000000	36 3.500000 270.000000	37 3.600000 270.000000	38 3.700000 270.000000	39 3.800000 270.000000	40 3.900000 270.000000
DB LE/EL	-43.154731	-46.574509	-37.805413	-34.596670	-33.151662	-32.658296	-32.843362	-33.621402
FIELD POINT TETA DEGREES FI DEGREES	41 4.000000 270.000000	42 4.100000 270.000000	43 4.200000 270.000000	44 4.300000 270.000000	45 4.400000 270.000000	46 4.500000 270.000000	47 4.600000 270.000000	48 4.700000 270.000000
DB LE/EL	-35.021311	-37.206675	-40.630488	-46.805271	-58.132679	-45.588230	-40.417949	-37.498684
FIELD POINT TETA DEGREES FI DEGREES	49 4.800000 270.000000	50 4.900000 270.000000	51 5.000000 270.000000	52 5.100000 270.000000	53 5.200000 270.000000	54 5.300000 270.000000	55 5.400000 270.000000	56 5.500000 270.000000
DB LE/EL	-35.634738	-34.417531	-33.662583	-33.275334	-33.206239	-33.433233	-33.955310	-34.792384
FIELD POINT TETA DEGREES FI DEGREES	57 5.600000 270.000000	58 5.700000 270.000000	59 5.800000 270.000000	60 5.900000 270.000000	61 6.000000 270.000000	62 6.100000 270.000000	63 6.200000 270.000000	64 6.300000 270.000000
DB LE/EL	-35.991630	-37.644647	-39.521818	-43.255361	-48.802133	-62.596784	-51.081481	-45.083494
FIELD POINT TETA DEGREES FI DEGREES	65 6.400000 270.000000	66 6.500000 270.000000	67 6.600000 270.000000	68 6.700000 270.000000	69 6.800000 270.000000	70 6.900000 270.000000	71 7.000000 270.000000	72 7.100000 270.000000
DB LE/EL	-41.887933	-39.882246	-38.572225	-37.745958	-37.297963	-37.173900	-37.349585	-37.823285
FIELD POINT TETA DEGREES FI DEGREES	73 7.200000 270.000000	74 7.300000 270.000000	75 7.400000 270.000000	76 7.500000 270.000000	77 7.600000 270.000000	78 7.700000 270.000000	79 7.800000 270.000000	80 7.900000 270.000000
DB LE/EL	-38.615215	-39.773774	-41.393481	-43.661133	-46.994269	-52.611845	-63.661200	-53.499735
FIELD POINT TETA DEGREES FI DEGREES	81 8.000000 270.000000	82 8.100000 270.000000	83 8.200000 270.000000	84 8.300000 270.000000	85 8.400000 270.000000	86 8.500000 270.000000	87 8.600000 270.000000	88 8.700000 270.000000
DB LE/EL	-47.525112	-44.801770	-42.785928	-41.442405	-40.560983	-40.044852	-39.840661	-39.923058
FIELD POINT TETA DEGREES FI DEGREES	89 8.800000 270.000000	90 8.900000 270.000000	91 9.000000 270.000000	92 9.100000 270.000000	93 9.200000 270.000000	94 9.300000 270.000000	95 9.400000 270.000000	96 9.500000 270.000000
DB LE/EL	-40.286964	-40.946275	-41.537728	-43.333023	-45.268432	-48.026191	-52.316046	-60.746084
FIELD POINT TETA DEGREES FI DEGREES	97 9.600000 270.000000	98 9.700000 270.000000	99 9.800000 270.000000	100 9.900000 270.000000	101 10.000000 270.000000	102 10.100000 270.000000	103 10.200000 270.000000	104 10.300000 270.000000
DB LE/EL	-60.530009	-52.783561	-48.750530	-46.332996	-44.699389	-43.607247	-42.920249	-42.567070
FIELD POINT TETA DEGREES	105 10.400000	106 10.500000	107 10.600000	108 10.700000	109 10.800000	110 10.900000	111 11.000000	112 11.100000

Sample 2.

THE DATA CARDS READ, THEIR CORRESPONDING PARAMETERS AND FORMAT ARE
 123456781012345678201234567830123456784012345678501234567860123456787012

NO. TETAS NO. FIS ARRAY SIZE COS**N DETAILS YES CF NO
 121 1 999 1.700 1

DIAMETER HOLE DIA1 HOLE DIA2 DEVIATION SCALE WAVELENGTH FOCAL DIST.
 15.0000 0. C. 0. 0.50000 0.44700 6.00000
 ALFA BETA GAMA X Y Z D1 D2 D3
 0. 0. 0. 0. -0.042 C. 0. 1.000 0.

TETA DEGREES OF FIELD POINTS

	0.	0.100	0.200	0.300	0.400	0.500	0.600	0.700
0.800	0.900	1.000	1.100	1.200	1.300	1.400	1.500	
1.600	1.700	1.800	1.900	2.000	2.100	2.200	2.300	
2.400	2.500	2.600	2.700	2.800	2.900	3.000	3.100	
3.200	3.300	3.400	3.500	3.600	3.700	3.800	3.900	
4.000	4.100	4.200	4.300	4.400	4.500	4.600	4.700	
4.800	4.900	5.000	5.100	5.200	5.300	5.400	5.500	
5.600	5.700	5.800	5.900	6.000	6.100	6.200	6.300	
6.400	6.500	6.600	6.700	6.800	6.900	7.000	7.100	
7.200	7.300	7.400	7.500	7.600	7.700	7.800	7.900	
8.000	8.100	8.200	8.300	8.400	8.500	8.600	8.700	
8.800	8.900	9.000	9.100	9.200	9.300	9.400	9.500	
9.600	9.700	9.800	9.900	10.000	10.100	10.200	10.300	
10.400	10.500	10.600	10.700	10.800	10.900	11.000	11.100	
11.200	11.300	11.400	11.500	11.600	11.700	11.800	11.900	
12.000								

FI DEGREES OF FIELD POINTS
 270.000

FOLLOWING POINTS IN THE TETA-FI MATRIX HAVE BEEN OMITTED
 -0 -0 -0 -0 -0 -0 -0 -0 -0 -0 -0 -0 -0 -0 -0 -0
 -0 -0 -0 -0 -0 -0 -0 -0 -0 -0 -0 -0 -0 -0 -0 -0
 -0 -0 -0 -0 -0 -0 -0 -0 -0 -0 -0 -0 -0 -0 -0 -0

REFLECTOR IS DIVIDED INTO 33 RINGS.

CONTRIBUTION OF ALL REFLECTOR RINGS WILL BE PROCESSED.

THE TOTAL NO. OF AREAS IS NSUMDS = 3366, NO. OF SEGMENTS IS LIRI = 4, M = 999.

RESULTS BASED ON INPUT DATA, DIA. = 15.0000, WAVELENGTH = 0.4470, SIDE OF ELEMENTAL AREA FRC = 0.50000 OF WAVELENGTH.

F = 5.000, ALFA = 0., BETA = 0., GAMA = C., TRANSLATIONS ARE, X = 0., Y = -0.042, Z = 0.

THE POLARIZATION COSINES ARE D1 = C., D2 = 1.00000, D3 = 0.

FOLLOWING ARE THE ORDER NUMBERS OF THE LAST RINGS IN SUCCESSIVE SEGMENTS.

17 24 30 33

FOLLOWING ARE THE NUMBER OF ELEMENTAL AREAS IN SUCCESSIVE SEGMENTS.

918 882 990 576

MAXIMUM POWER IS RADIATED IN DIRECTION TETA = 0. ,FI= 270.000

RESULTS BASED ON INPUT DATA, DIA. = 15.0000, WAVELENGTH = 0.4470, SIDE OF ELEMENTAL AREA FRC = 0.5000 OF WAVELENGTH.

F = 3.000, ALFA = 0. ,BETA = 0. ,GAMA = 0. ,TRANSLATIONS ARE, X = 0. ,Y = -0.042, Z = 0.

THE POLARIZATION COSINES ARE D1 = 0. ,D2 = 1.00000, D3 = 0.

IN THE FOLLOWING TABLE EACH ROW GIVES THE POWER IN DB. THE ZERO DB REFERENCE IS THE POWER RADIATED IN THE DIRECTION TETA = 0. AND FI = 270.000 AND HAS ABSOLUTE VALUE 179.152

FIELD POINT TETA JEGREES FI DEGREES	1 0. 270.000000	2 0.100000 270.000000	3 0.200000 270.000000	4 0.300000 270.000000	5 0.400000 270.000000	6 0.500000 270.000000	7 0.600000 270.000000	8 0.700000 270.000000
DB LE/EL	0.	-1.199906	-0.454116	-0.763847	-1.130621	-1.556296	-2.043122	-2.593809
FIELD POINT TETA JEGREES FI DEGREES	9 0.800000 270.000000	10 0.900000 270.000000	11 1.000000 270.000000	12 1.100000 270.000000	13 1.200000 270.000000	14 1.300000 270.000000	15 1.400000 270.000000	16 1.500000 270.000000
DB LE/EL	-3.211616	-3.900469	-4.665115	-5.511339	-6.446255	-7.478725	-8.619961	-9.884432
FIELD POINT TETA JEGREES FI DEGREES	17 1.600000 270.000000	18 1.700000 270.000000	19 1.800000 270.000000	20 1.900000 270.000000	21 2.000000 270.000000	22 2.100000 270.000000	23 2.200000 270.000000	24 2.300000 270.000000
DB LE/EL	-11.251265	-12.866535	-14.647184	-16.688233	-19.077319	-21.967777	-25.668930	-30.977407
FIELD POINT TETA JEGREES FI DEGREES	25 2.400000 270.000000	26 2.500000 270.000000	27 2.600000 270.000000	28 2.700000 270.000000	29 2.800000 270.000000	30 2.900000 270.000000	31 3.000000 270.000000	32 3.100000 270.000000
DB LE/EL	-41.478320	-41.220867	-33.402541	-30.194269	-28.531533	-27.699257	-27.426749	-27.593540
FIELD POINT TETA JEGREES FI DEGREES	33 3.200000 270.000000	34 3.300000 270.000000	35 3.400000 270.000000	36 3.500000 270.000000	37 3.600000 270.000000	38 3.700000 270.000000	39 3.800000 270.000000	40 3.900000 270.000000
DB LE/EL	-28.151843	-29.057705	-30.473148	-32.383270	-35.059991	-39.084095	-46.648369	-56.413739
FIELD POINT TETA JEGREES FI DEGREES	41 4.000000 270.000000	42 4.100000 270.000000	43 4.200000 270.000000	44 4.300000 270.000000	45 4.400000 270.000000	46 4.500000 270.000000	47 4.600000 270.000000	48 4.700000 270.000000
DB LE/EL	-42.526236	-38.338852	-35.764040	-34.160137	-33.164522	-32.612648	-32.421586	-32.550847
FIELD POINT TETA JEGREES FI DEGREES	49 4.800000 270.000000	50 4.900000 270.000000	51 5.000000 270.000000	52 5.100000 270.000000	53 5.200000 270.000000	54 5.300000 270.000000	55 5.400000 270.000000	56 5.500000 270.000000
DB LE/EL	-32.587578	-33.742545	-34.853508	-36.398892	-38.534076	-41.597378	-46.531765	-58.701677
FIELD POINT TETA JEGREES FI DEGREES	57 5.600000 270.000000	58 5.700000 270.000000	59 5.800000 270.000000	60 5.900000 270.000000	61 6.000000 270.000000	62 6.100000 270.000000	63 6.200000 270.000000	64 6.300000 270.000000
DB LE/EL	-52.775989	-45.272596	-41.660660	-39.455189	-38.023709	-37.112243	-36.557841	-36.417210
FIELD POINT TETA JEGREES FI DEGREES	65 6.400000 270.000000	66 6.500000 270.000000	67 6.600000 270.000000	68 6.700000 270.000000	69 6.800000 270.000000	70 6.900000 270.000000	71 7.000000 270.000000	72 7.100000 270.000000
DB LE/EL	-36.540578	-36.961874	-37.656827	-38.787927	-40.319637	-42.458180	-45.568555	-50.692566
FIELD POINT TETA JEGREES FI DEGREES	73 7.200000 270.000000	74 7.300000 270.000000	75 7.400000 270.000000	76 7.500000 270.000000	77 7.600000 270.000000	78 7.700000 270.000000	79 7.800000 270.000000	80 7.900000 270.000000
DB LE/EL	-63.825186	-54.535764	-48.136895	-44.649765	-42.460805	-41.005114	-40.047926	-39.473133
FIELD POINT TETA JEGREES FI DEGREES	81 8.000000 270.000000	82 8.100000 270.000000	83 8.200000 270.000000	84 8.300000 270.000000	85 8.400000 270.000000	86 8.500000 270.000000	87 8.600000 270.000000	88 8.700000 270.000000
DB LE/EL	-35.219672	-39.257481	-35.578065	-40.192115	-41.132444	-42.464735	-44.314054	-46.936958
FIELD POINT TETA JEGREES FI DEGREES	89 8.800000 270.000000	90 8.900000 270.000000	91 9.000000 270.000000	92 9.100000 270.000000	93 9.200000 270.000000	94 9.300000 270.000000	95 9.400000 270.000000	96 9.500000 270.000000
DB LE/EL	-50.569242	-58.858355	-64.004472	-53.177821	-48.716519	-46.066681	-44.325431	-43.161903
FIELD POINT TETA JEGREES FI DEGREES	97 9.600000 270.000000	98 9.700000 270.000000	99 9.800000 270.000000	100 9.900000 270.000000	101 10.000000 270.000000	102 10.100000 270.000000	103 10.200000 270.000000	104 10.300000 270.000000
DB LE/EL	-42.422028	-42.026165	-41.933564	-42.128221	-42.614222	-43.416989	-44.590464	-46.238556
FIELD POINT TETA JEGREES	105 10.400000	106 10.500000	107 10.600000	108 10.700000	109 10.800000	110 10.900000	111 11.000000	112 11.100000

Sample 3.

THE DATA CARDS READ, THEIR CORRESPONDING PARAMETERS AND FORMAT ARE

123456781012345678201234567830123456784012345678501234567860123456787012

NO. TETAS NO. FIS ARRAY SIZE COS**N DETAILS YES OF NO
 121 1 999 1.700 1

DIAMETER HOLE DIA1 HOLE DIA2 DEVIATION SCALE WAVELENGTH FOCAL DIST.
 15.0000 0. 0. 0. 0. C.50000 0.44700 6.00000
 ALFA BETA GAMA X Y Z D1 D2 D3
 0. 0. 0. 0. 0.083 0. 0. 0. 1.000 0.

TETA DEGREES OF FIELD POINTS
 0. 0.100 0.200 0.300 0.400 0.500 0.600 0.700
 0.800 0.900 1.000 1.100 1.200 1.300 1.400 1.500
 1.600 1.700 1.800 1.900 2.000 2.100 2.200 2.300
 2.400 2.500 2.600 2.700 2.800 2.900 3.000 3.100
 3.200 3.300 3.400 3.500 3.600 3.700 3.800 3.900
 4.000 4.100 4.200 4.300 4.400 4.500 4.600 4.700
 4.800 4.900 5.000 5.100 5.200 5.300 5.400 5.500
 5.600 5.700 5.800 5.900 6.000 6.100 6.200 6.300
 6.400 6.500 6.600 6.700 6.800 6.900 7.000 7.100
 7.200 7.300 7.400 7.500 7.600 7.700 7.800 7.900
 8.000 8.100 8.200 8.300 8.400 8.500 8.600 8.700
 8.800 8.900 9.000 9.100 9.200 9.300 9.400 9.500
 9.600 9.700 9.800 9.900 10.000 10.100 10.200 10.300
 10.400 10.500 10.600 10.700 10.800 10.900 11.000 11.100
 11.200 11.300 11.400 11.500 11.600 11.700 11.800 11.900
 12.000

FI DEGREES OF FIELD POINTS
 270.000

FOLLOWING POINTS IN THE TETA-FI MATRIX HAVE BEEN OMITTED
 -0 -0 -0 -0 -0 -0 -0 -0 -0 -0 -0 -0 -0 -0 -0 -0 -0 -0
 -0 -0 -0 -0 -0 -0 -0 -0 -0 -0 -0 -0 -0 -0 -0 -0 -0 -0
 -0 -0 -0 -0 -0 -0 -0 -0 -0 -0 -0 -0 -0 -0 -0 -0 -0 -0

REFLECTOR IS DIVIDED INTO 33 RINGS.

CONTRIBUTION OF ALL REFLECTOR RINGS WILL BE PROCESSED.

THE TOTAL NO. OF AREAS IS NSUMDS = 2364, NO. OF SEGMENTS IS LIRI = 4, M = 999.

RESULTS BASED ON INPUT DATA, DIA. = 15.0000, WAVELENGTH = 0.4470, SIDE OF ELEMENTAL AREA FRC = 0.50000 OF WAVELENGTH.

F = 0.000, ALFA = 0., BETA = 0., GAMA = 0., TRANSLATIONS ARE, X = 0., Y = 0.083, Z = 0.

THE POLARIZATION COSINES ARE D1 = 0., D2 = 1.00000, D3 = 0.

FOLLOWING ARE THE ORDER NUMBERS OF THE LAST RINGS IN SUCCESSIVE SEGMENTS.

17 24 30 33

FOLLOWING ARE THE NUMBER OF ELEMENTAL AREAS IN SUCCESSIVE SEGMENTS.

918 882 990 576

MAXIMUM POWER IS RADIATED IN DIRECTION TETA = C.700,FI= 270.000

RESULTS BASED ON INPUT DATA, DIA. = 15.0000, WAVELENGTH = 0.4470, SIDE OF ELEMENTAL AREA FRC = 0.50000 OF WAVELENGTH.

F= 0.000,ALFA= 0.,BETA= 0.,GAMA= 0.,TRANSLATIONS ARE,X= 0.,Y= 0.083,Z= 0.

THE POLARIZATION COSINES ARE D1 = C.,D2 = 1.00000,D3 = 0.

IN THE FOLLOWING TABLE EACH ROW GIVES THE POWER IN DB. THE ZERO DB REFERENCE IS THE POWER RADIATED IN THE DIRECTION

TETA = 0.700 AND FI = 270.000 AND HAS ABSOLUTE VALUE 190.850

FIELD POINT TETA DEGREES FI DEGREES	1 0. 270.000000	2 0.100000 270.000000	3 0.200000 270.000000	4 0.300000 270.000000	5 0.400000 270.000000	6 0.500000 270.000000	7 0.600000 270.000000	8 0.700000 270.000000
DB LEVEL	-1.153378	-0.824947	-0.552996	-0.336095	-0.173103	-0.063143	-0.005580	0.
FIELD POINT TETA DEGREES FI DEGREES	9 0.800000 270.000000	10 0.900000 270.000000	11 1.000000 270.000000	12 1.100000 270.000000	13 1.200000 270.000000	14 1.300000 270.000000	15 1.400000 270.000000	16 1.500000 270.000000
DB LEVEL	-0.046208	-0.144215	-0.294240	-0.496714	-0.752283	-1.061825	-1.426464	-1.847595
FIELD POINT TETA DEGREES FI DEGREES	17 1.600000 270.000000	18 1.700000 270.000000	19 1.800000 270.000000	20 1.900000 270.000000	21 2.000000 270.000000	22 2.100000 270.000000	23 2.200000 270.000000	24 2.300000 270.000000
DB LEVEL	-2.326915	-2.866461	-3.466664	-4.136413	-4.873141	-5.682934	-6.570681	-7.542269
FIELD POINT TETA DEGREES FI DEGREES	25 2.400000 270.000000	26 2.500000 270.000000	27 2.600000 270.000000	28 2.700000 270.000000	29 2.800000 270.000000	30 2.900000 270.000000	31 3.000000 270.000000	32 3.100000 270.000000
DB LEVEL	-8.604848	-9.767206	-11.044292	-12.437998	-13.978331	-15.685267	-17.591847	-19.745630
FIELD POINT TETA DEGREES FI DEGREES	33 3.200000 270.000000	34 3.300000 270.000000	35 3.400000 270.000000	36 3.500000 270.000000	37 3.600000 270.000000	38 3.700000 270.000000	39 3.800000 270.000000	40 3.900000 270.000000
DB LEVEL	-22.215165	-25.132343	-28.707795	-33.445112	-40.974355	-65.989950	-42.744058	-38.637311
FIELD POINT TETA DEGREES FI DEGREES	41 4.000000 270.000000	42 4.100000 270.000000	43 4.200000 270.000000	44 4.300000 270.000000	45 4.400000 270.000000	46 4.500000 270.000000	47 4.600000 270.000000	48 4.700000 270.000000
DB LEVEL	-37.070748	-36.755570	-37.357104	-38.858960	-41.537963	-46.360690	-55.867817	-48.169177
FIELD POINT TETA DEGREES FI DEGREES	49 4.800000 270.000000	50 4.900000 270.000000	51 5.000000 270.000000	52 5.100000 270.000000	53 5.200000 270.000000	54 5.300000 270.000000	55 5.400000 270.000000	56 5.500000 270.000000
DB LEVEL	-42.183019	-38.606747	-36.621212	-35.144192	-34.160873	-33.560441	-33.282296	-33.294718
FIELD POINT TETA DEGREES FI DEGREES	57 5.600000 270.000000	58 5.700000 270.000000	59 5.800000 270.000000	60 5.900000 270.000000	61 6.000000 270.000000	62 6.100000 270.000000	63 6.200000 270.000000	64 6.300000 270.000000
DB LEVEL	-33.586104	-34.162213	-35.048555	-36.295497	-38.002081	-40.358480	-43.791548	-49.567374
FIELD POINT TETA DEGREES FI DEGREES	65 6.400000 270.000000	66 6.500000 270.000000	67 6.600000 270.000000	68 6.700000 270.000000	69 6.800000 270.000000	70 6.900000 270.000000	71 7.000000 270.000000	72 7.100000 270.000000
DB LEVEL	-61.374949	-50.435534	-44.921647	-41.892921	-39.966744	-38.707028	-37.917301	-37.498701
FIELD POINT TETA DEGREES FI DEGREES	73 7.200000 270.000000	74 7.300000 270.000000	75 7.400000 270.000000	76 7.500000 270.000000	77 7.600000 270.000000	78 7.700000 270.000000	79 7.800000 270.000000	80 7.900000 270.000000
DB LEVEL	-37.400409	-37.600484	-38.055093	-38.918491	-40.109892	-41.772605	-44.102973	-47.541406
FIELD POINT TETA DEGREES FI DEGREES	81 8.000000 270.000000	82 8.100000 270.000000	83 8.200000 270.000000	84 8.300000 270.000000	85 8.400000 270.000000	86 8.500000 270.000000	87 8.600000 270.000000	88 8.700000 270.000000
DB LEVEL	-52.350859	-61.850050	-52.775543	-47.692865	-44.733951	-42.805203	-41.509208	-40.664189
FIELD POINT TETA DEGREES FI DEGREES	89 8.800000 270.000000	90 8.900000 270.000000	91 9.000000 270.000000	92 9.100000 270.000000	93 9.200000 270.000000	94 9.300000 270.000000	95 9.400000 270.000000	96 9.500000 270.000000
DB LEVEL	-40.176335	-39.995951	-40.059846	-40.484627	-41.165629	-42.181471	-43.606519	-45.582112
FIELD POINT TETA DEGREES FI DEGREES	97 9.600000 270.000000	98 9.700000 270.000000	99 9.800000 270.000000	100 9.900000 270.000000	101 10.000000 270.000000	102 10.100000 270.000000	103 10.200000 270.000000	104 10.300000 270.000000
DB LEVEL	-48.400927	-52.756293	-61.162040	-59.703238	-52.473783	-48.689395	-46.321192	-44.738265
FIELD POINT TETA DEGREES	105 10.400000	106 10.500000	107 10.600000	108 10.700000	109 10.800000	110 10.900000	111 11.000000	112 11.100000

FI DEGREES	270.00000	270.00000	270.00000	270.00000	270.00000	270.00000	270.00000	270.00000	270.00000	270.00000
DB LEVEL	-43.679811	-43.017768	-42.684696	-42.646480	-42.891542	-43.427409	-44.282831	-45.516351		
FIELD POINT	113	114	115	116	117	118	119	120		
TETA DEGREES	11.200000	11.300000	11.400000	11.500000	11.600000	11.700000	11.800000	11.900000		
FI DEGREES	270.00000	270.00000	270.00000	270.00000	270.00000	270.00000	270.00000	270.00000		
DB LEVEL	-47.237880	-49.662018	-53.258815	-59.132639	-62.569015	-55.839377	-51.585994	-48.907584		
FIELD POINT	121	122	123	124	125	126	127	128		
TETA DEGREES	12.000000	-0.000000	-0.000000	-0.000000	-0.000000	-0.000000	-0.000000	-0.000000		
FI DEGREES	270.00000	-0.000000	-0.000000	-0.000000	-0.000000	-0.000000	-0.000000	-0.000000		
DB LEVEL	-47.057257	0.	0.	0.	0.	0.	0.	0.		

Sample 4.

THE DATA CARDS READ, THEIR CORRESPONDING PARAMETERS AND FORMAT ARE
 123456781012345678201234567830123456784012345678501234567860123456787012

NO. TETAS NO. FIS ARRAY SIZE COS**A DETAILS YES OR NO
 121 1 999 1.700 1

DIAMETER HOLE DIA1 HOLE DIA2 DEVIATION SCALE WAVELENGTH FOCAL DIST.
 15.0000 0. 0. 0. 0. 0.5000 0.4470 6.0000
 ALFA BETA GAMA X Y Z D1 D2 D3
 0. 0. 0. 0. -0.083 0. 0. 0. 1.000 0.

TETA DEGREES OF FIELD POINTS
 0. 0.100 0.200 0.300 0.400 0.500 0.600 0.700
 0.800 0.900 1.000 1.100 1.200 1.300 1.400 1.500
 1.600 1.700 1.800 1.900 2.000 2.100 2.200 2.300
 2.400 2.500 2.600 2.700 2.800 2.900 3.000 3.100
 3.200 3.300 3.400 3.500 3.600 3.700 3.800 3.900
 4.000 4.100 4.200 4.300 4.400 4.500 4.600 4.700
 4.800 4.900 5.000 5.100 5.200 5.300 5.400 5.500
 5.600 5.700 5.800 5.900 6.000 6.100 6.200 6.300
 6.400 6.500 6.600 6.700 6.800 6.900 7.000 7.100
 7.200 7.300 7.400 7.500 7.600 7.700 7.800 7.900
 8.000 8.100 8.200 8.300 8.400 8.500 8.600 8.700
 8.800 8.900 9.000 9.100 9.200 9.300 9.400 9.500
 9.600 9.700 9.800 9.900 10.000 10.100 10.200 10.300
 10.400 10.500 10.600 10.700 10.800 10.900 11.000 11.100
 11.200 11.300 11.400 11.500 11.600 11.700 11.800 11.900
 12.000

FI DEGREES OF FIELD POINTS
 270.000

FOLLOWING POINTS IN THE TETA-FI MATRIX HAVE BEEN OMITTED
 -0 -0 -0 -0 -0 -0 -0 -0 -0 -0 -0 -0 -0 -0 -0 -0
 -0 -0 -0 -0 -0 -0 -0 -0 -0 -0 -0 -0 -0 -0 -0 -0
 -0 -0 -0 -0 -0 -0 -0 -0 -0 -0 -0 -0 -0 -0 -0 -0

REFLECTOR IS DIVIDED INTO 33 RINGS.

CONTRIBUTION OF ALL REFLECTOR RINGS WILL BE PROCESSED.

THE TOTAL NO. OF AREAS IS NSUMDS = 3366, NO. OF SEGMENTS IS LIRI = 4, M = 999.

RESULTS BASED ON INPUT DATA, DIA. = 15.0000, WAVELENGTH = 0.4470, SIDE OF ELEMENTAL AREA FRC = 0.50000 OF WAVELENGTH.

F = 5.000, ALFA = 0., BETA = 0., GAMA = 0., TRANSLATIONS ARE, X = 0., Y = -0.083, Z = 0.

THE POLARIZATION COSINES ARE D1 = 0., D2 = 1.00000, D3 = 0.

FOLLOWING ARE THE ORDER NUMBERS OF THE LAST RINGS IN SUCCESSIVE SEGMENTS.

17 24 30 33

FOLLOWING ARE THE NUMBER OF ELEMENTAL AREAS IN SUCCESSIVE SEGMENTS.

918 882 990 576

MAXIMUM POWER IS RADIATED IN DIRECTION TETA = C. PHI = 270.000

RESULTS BASED ON INPLT DATA, DIA. = 15.0000, WAVELENGTH = 0.4470, SIDE OF ELEMENTAL AREA FRC = 0.5000 OF WAVELENGTH.

F = 0.000, ALFA = 0. BETA = C. GAMMA = 0. TRANSLATIONS ARE, X = 0. Y = -0.083, Z = 0.

THE POLARIZATION COSINES ARE D1 = C. D2 = 1.00000, D3 = 0.

IN THE FOLLOWING TABLE EACH ROW GIVES THE POWER IN DB. THE ZERO DB REFERENCE IS THE POWER RADIATED IN THE DIRECTION TETA = 0. AND PHI = 270.000 AND HAS ABSCLUTE VALUE 146.337

FIELD POINT TETA DEGREES PHI DEGREES	1 0.000000 270.000000	2 C.100000 270.000000	3 0.200000 270.000000	4 0.300000 270.000000	5 0.400000 270.000000	6 0.500000 270.000000	7 0.600000 270.000000	8 0.700000 270.000000
DB LE/EL	0.	-0.386673	-0.833732	-1.343758	-1.919876	-2.565846	-3.286223	-4.086559
FIELD POINT TETA DEGREES PHI DEGREES	9 0.800000 270.000000	10 C.900000 270.000000	11 1.000000 270.000000	12 1.100000 270.000000	13 1.200000 270.000000	14 1.300000 270.000000	15 1.400000 270.000000	16 1.500000 270.000000
DB LE/EL	-4.913687	-5.956114	-7.044596	-8.252999	-9.595620	-11.109336	-12.817251	-14.775377
FIELD POINT TETA DEGREES PHI DEGREES	17 1.600000 270.000000	18 1.700000 270.000000	19 1.800000 270.000000	20 1.900000 270.000000	21 2.000000 270.000000	22 2.100000 270.000000	23 2.200000 270.000000	24 2.300000 270.000000
DB LE/EL	-17.065871	-19.830704	-23.350300	-28.317639	-37.482762	-40.776277	-31.829901	-28.267072
FIELD POINT TETA DEGREES PHI DEGREES	25 2.400000 270.000000	26 2.500000 270.000000	27 2.600000 270.000000	28 2.700000 270.000000	29 2.800000 270.000000	30 2.900000 270.000000	31 3.000000 270.000000	32 3.100000 270.000000
DB LE/EL	-26.380338	-25.357645	-24.656901	-24.860528	-25.183712	-25.843249	-26.848001	-28.241660
FIELD POINT TETA DEGREES PHI DEGREES	33 3.200000 270.000000	34 3.300000 270.000000	35 3.400000 270.000000	36 3.500000 270.000000	37 3.600000 270.000000	38 3.700000 270.000000	39 3.800000 270.000000	40 3.900000 270.000000
DB LE/EL	-30.120527	-32.685054	-36.407052	-42.839915	-66.057246	-42.925810	-37.619986	-34.793194
FIELD POINT TETA DEGREES PHI DEGREES	41 4.000000 270.000000	42 4.100000 270.000000	43 4.200000 270.000000	44 4.300000 270.000000	45 4.400000 270.000000	46 4.500000 270.000000	47 4.600000 270.000000	48 4.700000 270.000000
DB LE/EL	-33.063891	-31.993769	-31.351776	-31.163110	-31.260890	-31.668101	-32.391956	-33.466180
FIELD POINT TETA DEGREES PHI DEGREES	49 4.800000 270.000000	50 4.900000 270.000000	51 5.000000 270.000000	52 5.100000 270.000000	53 5.200000 270.000000	54 5.300000 270.000000	55 5.400000 270.000000	56 5.500000 270.000000
DB LE/EL	-34.562975	-37.025365	-39.955843	-44.588208	-54.993750	-53.273909	-44.689001	-40.825944
FIELD POINT TETA DEGREES PHI DEGREES	57 5.600000 270.000000	58 5.700000 270.000000	59 5.800000 270.000000	60 5.900000 270.000000	61 6.000000 270.000000	62 6.100000 270.000000	63 6.200000 270.000000	64 6.300000 270.000000
DB LE/EL	-38.506272	-37.007674	-36.050323	-35.500912	-35.290941	-35.387535	-35.782241	-36.488469
FIELD POINT TETA DEGREES PHI DEGREES	65 6.400000 270.000000	66 6.500000 270.000000	67 6.600000 270.000000	68 6.700000 270.000000	69 6.800000 270.000000	70 6.900000 270.000000	71 7.000000 270.000000	72 7.100000 270.000000
DB LE/EL	-37.545616	-39.033114	-41.106700	-44.104176	-48.963983	-60.957473	-55.115622	-47.530981
FIELD POINT TETA DEGREES PHI DEGREES	73 7.200000 270.000000	74 7.300000 270.000000	75 7.400000 270.000000	76 7.500000 270.000000	77 7.600000 270.000000	78 7.700000 270.000000	79 7.800000 270.000000	80 7.900000 270.000000
DB LE/EL	-43.842181	-41.558514	-40.045560	-39.049275	-38.444088	-38.165154	-38.179977	-38.478232
FIELD POINT TETA DEGREES PHI DEGREES	81 8.000000 270.000000	82 8.100000 270.000000	83 8.200000 270.000000	84 8.300000 270.000000	85 8.400000 270.000000	86 8.500000 270.000000	87 8.600000 270.000000	88 8.700000 270.000000
DB LE/EL	-39.068889	-39.982731	-41.282244	-43.086574	-45.638166	-49.529095	-56.973626	-65.593241
FIELD POINT TETA DEGREES PHI DEGREES	89 8.800000 270.000000	90 8.900000 270.000000	91 9.000000 270.000000	92 9.100000 270.000000	93 9.200000 270.000000	94 9.300000 270.000000	95 9.400000 270.000000	96 9.500000 270.000000
DB LE/EL	-52.676428	-47.953025	-45.155871	-43.401447	-42.200264	-41.432477	-41.014061	-40.901750
FIELD POINT TETA DEGREES PHI DEGREES	97 9.600000 270.000000	98 9.700000 270.000000	99 9.800000 270.000000	100 9.900000 270.000000	101 10.000000 270.000000	102 10.100000 270.000000	103 10.200000 270.000000	104 10.300000 270.000000
DB LE/EL	-41.077991	-41.545535	-42.328291	-43.478630	-45.097029	-47.382692	-50.789431	-56.717141
FIELD POINT TETA DEGREES	105 10.400000	106 10.500000	107 10.600000	108 10.700000	109 10.800000	110 10.900000	111 11.000000	112 11.100000

AUTOMATIC FREQUENCY SEARCH AND ACQUISITION TECHNIQUES FOR PHASE LOCK RECEIVERS*

Bernard Silverman**

ABSTRACT

In the acquisition and tracking of modulated telemetry signals using phase lock loops, the receiver may erroneously lock on a sideband rather than the carrier frequency. When this happens, it is almost impossible to demodulate and recover the information contained in the signal.

Three circuits are presented which overcome this shortcoming of sideband lock. However, no analysis is given of their performance in the presence of noise. From experience it is known that all three circuits exhibit a threshold due to the presence of noise.

Since these circuits are nonlinear and exact analytical results cannot be obtained, it is recommended that an experimental study be made along with further analysis to determine the limits of performance.

INTRODUCTION

In telemetry and communications with satellites or deep space probes, the problem exists of acquiring and tracking a radio signal that is masked by noise. In cases where the predetection signal-to-noise ratio (SNR) (in decibels) is negative, coherent communications receivers using phase lock loops (PLL) have been employed.

Two recent books (Reference 1 and 2) describe the general behavior of the PLL and analyze the performance of such receivers.

A particular problem arises when a receiver locks on a sideband frequency ($\omega_c \pm \omega_m$) of a signal while searching for the carrier, ω_c . Since the received signal normally is recorded on magnetic tape and not demodulated at the time of reception, this condition of sideband lock may not be apparent. When demodulation of the signal is attempted later, it is practically impossible if there has been false sideband lock.

In this paper, first a description of the noise-free behavior of the phase lock loop is presented. Then three different circuits are discussed which overcome the problem of sideband lock. They are: (1) the balanced discriminator, (2) the quadricorrelator, (3) the contiguous comb-type PLL's.

The first two of these circuits operate satisfactorily only with relatively high signal-to-noise ratios. However, the third circuit seems to offer the possibility of performance comparable to that of a narrow-band PLL. Gardner (Reference 1, page 23) gives the hold-in SNR threshold for narrow-band PLL as 0-1 db and the threshold for acquisition as 3-6 db.

*This problem was proposed by Mr. T.U. Saliga of GSFC.

**Syracuse University.

No noise analysis is given for these circuits; it is recommended that they be given further theoretical and experimental study.

THE NOISE-FREE PHASE LOCK LOOP (PLL)

The problem will be introduced by describing the operation of a phase lock loop (PLL). Several parameters of the system will be defined which will be useful in evaluating its performance under sideband lock conditions.

Consider the block diagram of the PLL shown in Figure 1. Let:

$$S = \sqrt{2} V_1 \sin \omega_1 t = \sqrt{2} V_1 \sin \theta_1, \quad (1)$$

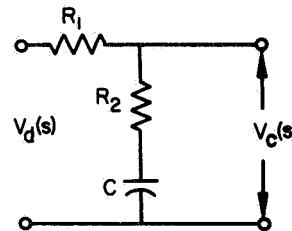
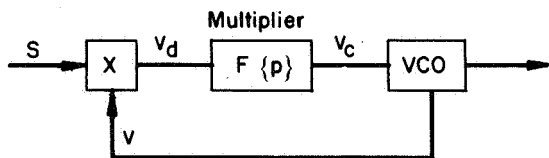
$$v = \sqrt{2} V_2 \cos (\omega_2 t + \theta (0)) = \sqrt{2} V_2 \cos \theta_2. \quad (2)$$

But:
$$\dot{\theta}_2 = \omega_2 = \omega_0 + h v_c = \omega_0 + h F \{v_d\} \quad (3)$$

where

$$\dot{\theta}_2 = \frac{d\theta_2}{dt},$$

ω_0 is the free-running frequency of the VCO, and h is the sensitivity constant of the voltage-sensitive reactance (or timing) element in the VCO. It also accounts for any linear amplification in the loop.



$$F_1(s) = \frac{V_c(s)}{V_d(s)} = \frac{sCR_2 + 1}{sC(R_1 + R_2) + 1} = \frac{s\tau_2 + 1}{s(\tau_1 + \tau_2) + 1}$$

S- Input signal

X- Multiplier or phase detector

F {p} : Linear network (filtering, gain)

VCO: Voltage controlled oscillator

Note: It is convenient to use F {p}, the Heaviside operator notation, in defining the differential equation which describes the PLL, because of the nonlinearity introduced by the multiplier, X. However, F is a linear network, and sometimes it is convenient to describe it by its transfer function, $\frac{V_d(s)}{V_c(s)} = F(s)$, which is a function of the complex variable, s.

Figure 1-Phase lock loop.

Furthermore: $v_d = S v$

$$= V_1 V_2 [\sin (\theta_1 + \theta_2) + \sin (\theta_1 - \theta_2)].$$

Here and throughout this paper, the high-frequency terms in the output of the multiplier are not retained because the response to these high-frequency signals is negligible as a result of the low-pass nature of $F\{p\}$. Also, in practice most detector outputs include only low-frequency components. Thus:

$$v_d = V_1 V_2 \sin (\theta_1 - \theta_2). \quad (4)$$

Substituting (4) into (3):

$$\begin{aligned} \dot{\theta}_2 &= \omega_0 + h V_1 V_2 F \{ \sin (\theta_1 - \theta_2) \} \\ &= \omega_0 + K F \{ \sin (\theta_1 - \theta_2) \}, \end{aligned} \quad (5)$$

where $K = h V_1 V_2$.

This equation may be rearranged as:

$$(\dot{\theta}_1 - \dot{\theta}_2) + K F \{ \sin (\theta_1 - \theta_2) \} = \dot{\theta}_1 - \omega_0 \quad (6)$$

or

$$\dot{\phi} + K F \{ \sin \phi \} = \Delta \omega, \quad (7)$$

where: $\phi = \theta_1 - \theta_2$, the phase error, and

$\Delta \omega = \dot{\theta}_1 - \omega_0$, the initial detuning or initial frequency error.

Equation 7 describes the noise-free behavior of the PLL. Note that $\phi(t)$ is a slowly varying quantity. Consequently, the synchronization of two high-frequency signals, S and v in Figure 1, has been reduced to the process of adjusting a slowly varying phase to a constant. This allows $F\{p\}$ to be a low-pass filter — a condition which results in a great enhancement of the signal-to-noise ratio in the PLL, which is the principal advantage of this type of circuit. It is implied in this discussion that the approximate value of the frequency of the signal is known.

In order to discuss the PLL further, an explicit expression for $F\{p\}$ must be given. Typically, this is a double-time constant network whose transfer function may be expressed as:

$$F(s) = \frac{s + a}{s + b}. \quad (8)$$

Equation (7) reduces to:

$$\ddot{\phi} + (b + K \cos \phi) \dot{\phi} + a K \sin \phi = b (\Delta \omega) \quad (9)$$

The behavior of this nonlinear equation has been studied extensively and the results are summarized in Chapter 3 of Viterbi (Reference 2). Observe that if lock or synchronization is achieved, $\phi = \text{constant}$ and $\dot{\phi} = \ddot{\phi} = 0$. Since $\sin \phi$ is always less than or equal to 1, the system achieves lock only if

$$\frac{b (\Delta \omega)}{a K} \leq 1. \quad (10)$$

Equation 10 gives a useful bound on the loop performance.

LINEAR DESIGN CRITERIA

When a high-gain PLL is synchronized, the phase error, $\phi = (\theta_1 - \theta_2)$ in Equation 5, is small and $\sin (\theta_1 - \theta_2)$ may be approximated by $(\theta_1 - \theta_2)$.

Furthermore, if the substitutions

$$\theta_{i_1} = \theta_1 - \omega_0 t$$

$$\theta_{L} = \theta_2 - \omega_0 t$$

$$\sin (\theta_1 - \theta_2) = (\theta_1 - \theta_2)$$

are made, Equation 5 reduces to:

$$\dot{\theta}_L + KF \{ \theta_L - \theta_{i_1} \} = 0. \quad (11)$$

This is a linear equation (if $F \{p\}$ is linear) whose solution is well known. While this equation does not apply during the acquisition of the signal (out-of-sync condition) or for large phase errors, useful design criteria can be obtained from its solution.

For instance, when the filter circuit of Figure 1 is used,

$$F_1 \{p\} = \frac{p \tau_2 + 1}{p (\tau_1 + \tau_2) + 1}$$

Substituting this in Equation 11 and taking the Laplace transform yields:

$$\frac{\theta_L(s)}{\theta_i(s)} = H_1(s) = \frac{s \omega_n (2\zeta - \omega_n/K) + \omega_n^2}{s^2 + 2\zeta \omega_n s + \omega_n^2}, \quad (12)$$

where

$$\omega_n^2 = \frac{K}{\tau_1 + \tau_2}$$

and

$$\zeta = \frac{\omega_n}{2} \left(\tau_2 + \frac{1}{K} \right).$$

The loop noise bandwidth is defined (Reference 1) as:

$$B_L = \int_0^{\infty} |H(j\omega)|^2 \frac{d\omega}{2\pi}. \quad (13)$$

when $H(j\omega) = H_1(j\omega)$ of Equation 12,

$$B_L = \frac{\omega_n}{2} \left(\zeta + \frac{1}{4\zeta} \right). \quad (14)$$

The mean-square or variance of the output phase jitter, $\bar{\theta}_L^2$, due to white input noise is directly proportional to B_L . Consequently, it is desirable to make this quantity as small as possible.

On the other hand, it can be shown (Reference 1) that for high-gain systems under high signal-to-noise ratio conditions:

(1) The holdin frequency range, the maximum value of $(\omega_1 - \omega_0)$ for which a synchronized PLL will remain synchronized, is:

$$\Delta\omega_H = K. \quad (15)$$

(2) The acquisition or pullin range, the maximum initial frequency difference $(\omega_1 - \omega_0)$ for which an unsynchronized system will achieve synchronization, can be approximated by:

$$\Delta\omega_p \approx 2\zeta \omega_n K. \quad (16)$$

(3) The acquisition or pullin time can be approximated by:

$$T_p \approx \frac{(\Delta\omega)^2}{2 \zeta \omega_n^3}, \quad (17)$$

where $\Delta\omega$ is the initial frequency detuning.

Usually it is desirable for B_L and T_p to be as small as possible and $\Delta\omega_H$ and $\Delta\omega_p$ to be as large as possible. Since these quantities are interrelated, some compromise must be made in any particular design.

RESPONSE TO A MODULATED SIGNAL

Consider now the case of a PLL tracking a narrow-band split-phase modulation signal. The power density spectrum for this signal is derived in the Appendix. For purposes of discussion, the case of a continuous "one" modulating the carrier will be considered. It may be represented as:*

$$\begin{aligned} S_1 &= \sqrt{2} V \sin (\omega_c t + \beta \sin \omega_m t) \\ &\approx \sqrt{2} V [J_0(\beta) \sin \omega_c t + J_1(\beta) \sin (\omega_c + \omega_m) t \\ &\quad - J_1(\beta) \sin (\omega_c - \omega_m) t] \end{aligned} \quad (18)$$

Proper operation of the anti-sideband-lock circuits discussed later requires only that the spectrum of the signal be symmetrical about the carrier. The exact signal spectrum will affect the carrier-to-noise ratio and consequently affect the range of signal power required for satisfactory operation. However, it will not affect the principle of operation.

For the circuit shown in Figure 1, when $S = S_1$ of Equation 18 and again $v = \sqrt{2} V_2 \cos (\omega_2 t + \theta(0)) = \sqrt{2} V_2 \cos \theta_2$:

$$\begin{aligned} \dot{\theta}_2 &= \omega_2 = \omega_0 + h F \{ (S_1) (v) \} \\ &= \omega_0 + K F \{ J_0(\beta) \sin [(\omega_c - \omega_2) t - \theta(0)] + J_1(\beta) \sin [(\omega_c + \omega_m) t - \theta(0)] \\ &\quad - J_1(\beta) \sin [(\omega_c - \omega_m) t - \theta(0)] \}, \end{aligned} \quad (19)$$

where only the low-frequency terms have been retained.

*For $\beta = \pi/3 \approx 1$, $J_0^2(1) + 2 J_1^2(1) = (.76)^2 + 2 (.44)^2 = 0.96$. In other words, the carrier and first sidebands containing about 96 percent of the energy, and 4 percent is in the higher sidebands.

This equation can be rearranged as

$$\begin{aligned} \dot{\theta}_2 = \omega_0 + K F \{ J_0(\beta) \sin [(\omega_c - \omega_2) t - \theta(0)] \\ + 2 J_1(\beta) \sin(\omega_m t) \cos [(\omega_c - \omega_2) t - \theta(0)] \} \end{aligned} \quad (20)$$

or

$$\begin{aligned} \dot{\theta}_2 = \omega_0 + K F \left\{ \sqrt{J_0^2(\beta) + 4 J_1^2(\beta) \sin^2 \omega_m t} \right. \\ \left. \sin [(\omega_c - \omega_m) t - \theta(0) + \theta_m(t)] \right\}, \end{aligned}$$

where

$$\theta_m(t) = \arctan \left(\frac{2 J_1(\beta) \sin \omega_m t}{J_0(\beta)} \right). \quad (21)$$

This last equation indicates that the effect of the modulating signal on the acquisition and tracking of the carrier is that of adding amplitude and phase modulation to the error voltage which is filtered and applied to the VCO.

Suppose $(\omega_c - \omega_2) t - \theta(0) = \phi$, $\omega_c - \omega_0 = \Delta\omega$, and

$$F(s) = \frac{s + a}{s + b}.$$

Then Equation 20 reduces to:

$$\begin{aligned} \ddot{\phi} + b \dot{\phi} + K [J_0(\beta) \cos \phi - 2 J_1(\beta) \sin \omega_m t \sin \phi] \dot{\phi} \\ + K [a J_0(\beta) \sin \phi + 2 J_1(\beta) (a \sin \omega_m t \\ + \omega_m \cos \omega_m t) \cos \phi] = b \Delta\omega. \end{aligned} \quad (22)$$

Usually in a tracking PLL

$$\omega_n^2 = a K J_0(\beta) \ll \omega_m^2. \quad (23)$$

Under this condition, the effect of the terms which include the modulating frequency ω_m in Equation 22 is negligible when the PLL is locked on and tracking ω_c . If the terms including the modulating frequency in Equation 22 are neglected, this equation reduces to Equation 9, which describes the PLL tracking a single frequency.

Unfortunately, the same condition obtains if the loop is tracking one of the sideband frequencies. For instance, if we return to Equation 19 and let $\omega_c + \omega_m = \omega_U$, the equation may be written as:

$$\begin{aligned} \dot{\theta}_2 = \omega_0 + KF \{ & J_0(\beta) \sin [(\omega_U - \omega_m - \omega_2)t - \theta(0)] \\ & + J_1(\beta) \sin [(\omega_U - \omega_2)t - \theta(0)] \\ & - J_1(\beta) \sin [(\omega_U - 2\omega_m - \omega_2)t - \theta(0)] \}. \end{aligned} \quad (24)$$

This reduces to

$$\begin{aligned} \dot{\theta}_2 = \omega_0 + KF \{ & [J_0(\beta) \cos \omega_m t + J_1(\beta) + J_1(\beta) \cos (2\omega_m t)] \\ & [\sin [(\omega_U - \omega_2)t - \theta(0)]] \\ & - [J_0(\beta) \sin \omega_m t - J_1(\beta) \sin 2\omega_m t] \\ & [\cos [(\omega_U - \omega_2)t - \theta(0)]] \}. \end{aligned} \quad (25)$$

This equation points out that if a narrow band loop, i.e., $\omega_n \ll \omega_m$, is tracking the upper (or lower) sideband (i.e., $\omega_U = \omega_2$), the loop response to the error signal due to the presence of the carrier will be negligible and the loop will remain in sideband lock. Consequently, a method is required that detects the difference between carrier and sideband lock and provides an error signal which facilitates the proper synchronization with the carrier.

In fact, the above discussion indicates that a telemetry receiver requires three modes of tuning:

1. First the receiver must be tuned to the approximate frequency of the desired signal.
2. Then, in the acquisition mode, the receiver should lock on or synchronize with the desired carrier.
3. Finally, in the tracking mode, the receiver should remain synchronized with the signal. It should follow any drift and slow change in the signal carrier frequency but be immune to noise.

THE BALANCED DISCRIMINATOR CIRCUIT

One method of detecting the sideband lock condition uses a balanced frequency discriminator as illustrated in Figure 2. (See Reference 3.)

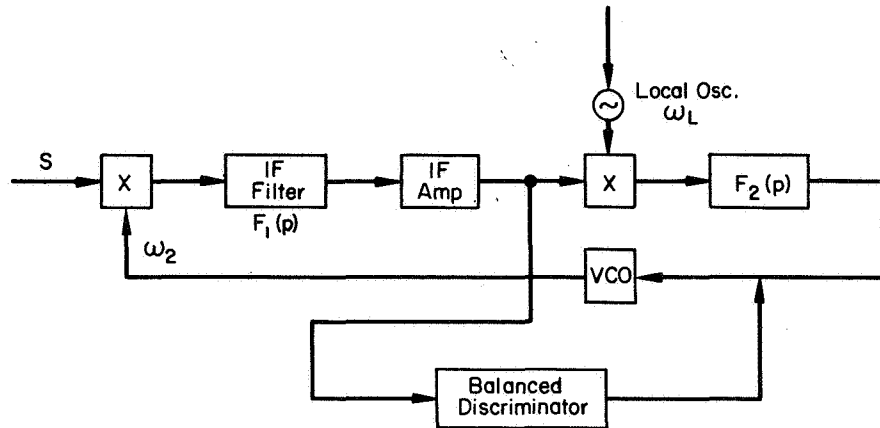


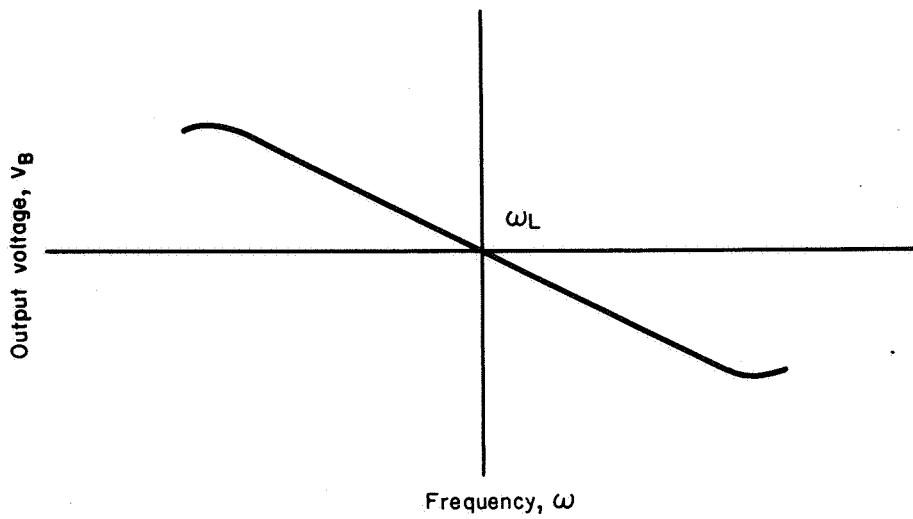
Figure 2-Balanced discriminator anti-sideband lock circuit.

In the PLL configuration shown here, an IF stage and a fixed-frequency local oscillator are included. If the bandpass characteristics of the IF filter are symmetrical about its center frequency, this circuit performs like the PLL previously described.

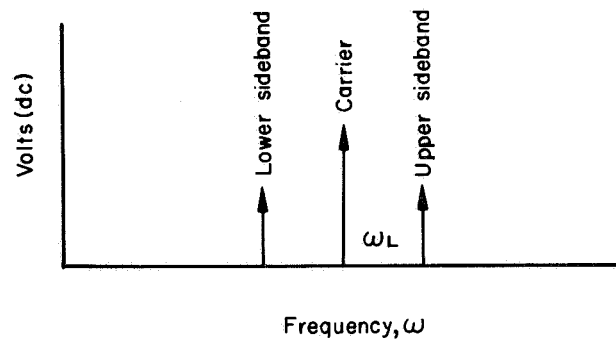
In figure 2 the center frequency of both the IF filter and the balanced discriminator is the same as the frequency of the local oscillator, ω_L . When synchronized, the frequency of the VCO, ω_1 , equals the difference between the carrier and local oscillator frequencies, $(\omega_c - \omega_L)$.

The principle of operation of this circuit is explained in Figure 3. When the VCO is locked on a carrier whose signal spectrum is symmetrical about that carrier, there is no output from the discriminator (except that due to noise) and the circuit operates as an ordinary PLL (see Figure 3b). On the other hand, if the input to the discriminator (output of the IF) is unsymmetrical about the center frequency, ω_L , there is a discriminator output voltage which is applied to the VCO to correct its frequency. Figure (3c) shows the condition of upper sideband lock.

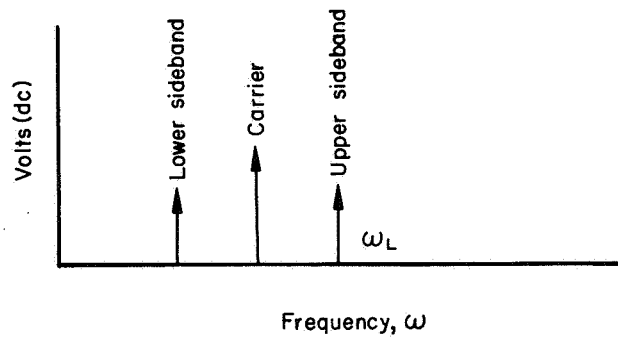
In the practice, when there is a discriminator output, the tuning of the receiver should be continued by changing the free-running frequency, ω_o , and not by applying the discriminator output voltage to the reactance element of the VCO. This is necessary because: (1) the discriminator voltage decreases as carrier lock is approached, and this decrease in voltage would cause a detuning of the VCO, resulting in unsatisfactory operation; (2) the voltage-sensitive reactance element has a limited range, and this range should be reserved for the tracking mode. Furthermore, if the tuning of the receiver is continued at a constant rate during this period, the total time to acquire carrier lock is shorter.



(a.) Balanced discriminator characteristic.



(b.) Discriminator input for carrier lock.



(c.) Discriminator input for upper sideband lock

Figure 3

As the frequency of the VCO approaches the frequency ($\omega_c - \omega_L$), the output of the discriminator decreases. When the frequency reaches some nominal value corresponding to the pullin range of the PLL, the discriminator circuit is disabled, automatic tuning of the free-running frequency, ω_0 , is discontinued, and the PLL takes over the final acquisition and tracking.

This type of circuit performs satisfactorily under conditions of moderate signal-to-noise ratios (SNR). (See Reference 3.) However, balanced detector circuits of this type exhibit a noise threshold (Reference 4). Gardner (Reference 1, page 61) states that for typical circuits currently available this threshold occurs around an SNR = -30 db.

At this point, the circuit in Figure 2 should be reexamined. The largest contribution to the noise power is white noise uniformly distributed throughout the frequency spectrum. Consequently, the SNR at any point in the circuit is inversely proportional to the bandwidth of that portion of the circuit. In order that the circuit in Figure 2 operate satisfactorily, the IF and discriminator bandwidth must be greater than twice the modulating frequency ($2\omega_m$); typically, it is three to five times this frequency. Modulating frequencies from a few hundred Hz to over 100,000 Hz have been used. The bandwidth of a tracking PLL may be as low as 10 Hz. Therefore, it is apparent that the balanced-discriminator anti-sideband lock circuit will fail to operate satisfactorily, as the SNR decreases, in a range where a narrow-band PLL continues to track satisfactorily. Of course, the PLL still needs help in acquiring the signal.

THE QUADRICORRELATOR CIRCUIT

The quadricorrelator (Reference 5) shown in Figure 4 is another circuit which detects sideband lock. If the input signal voltage, S , consists of a carrier plus upper and lower sidebands which are symmetrical about the carrier, the dc component of output, v_3 , of multiplier x_3 is zero when the frequency of the VCO equals the carrier frequency. When the frequency of the VCO is not equal to the signal carrier frequency, v_3 includes a dc component which is proportional to the difference between the VCO and carrier frequencies. As in the case of the balanced discriminator circuit, this dc can be used to tune the free-running frequency, ω_0 , of the VCO and facilitate carrier lock.

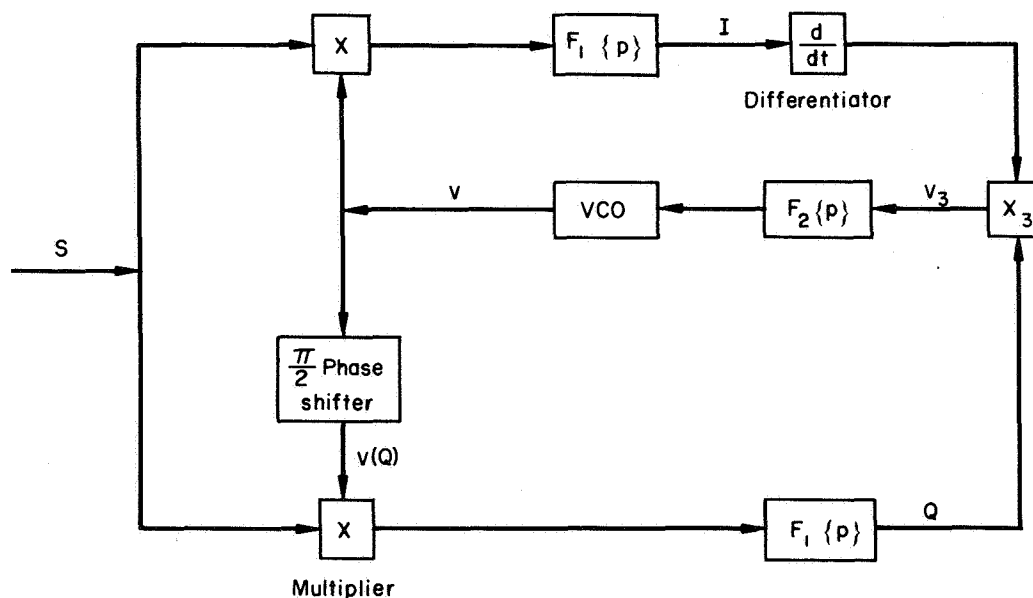


Figure 4—Quadricorrelator anti-sideband lock circuit

The expressions for v_3 are determined below for two cases: where the frequency of the VCO is the carrier frequency ω_c , and where it is not equal to ω_c .

Referring to Figure 4, let:

$$S = \sqrt{2} [J_0(\beta) \sin \omega_c t + J_1(\beta) \sin (\omega_c + \omega_m) t - J_1(\beta) \sin (\omega_c - \omega_m) t]$$

$$v = \sqrt{2} \sin [\omega_c t + \phi(t)]$$

$$v(Q) = \sqrt{2} \cos [\omega_c t + \phi(t)]$$

Retaining only the low-frequency terms because of the filtering of $F_1(p)$:

$$I = J_0(\beta) \cos \phi + J_1(\beta) \cos(\phi - \omega_m t) - J_1(\beta) \cos(\phi + \omega_m t)$$

$$\frac{dI}{dt} = -\dot{\phi} [J_0(\beta) \sin \phi - 2J_1(\beta) \sin \omega_m t \cos \phi] + 2J_1(\beta) \omega_m \sin \phi \cos \omega_m t$$

$$Q = - [J_0(\beta) \sin \phi - 2J_1(\beta) \sin \omega_m t \cos \phi]$$

Note that for proper operation of this circuit the bandwidth of networks $F_1(p)$ must be greater than $2 \omega_m$.

If the frequency of the VCO is ω_c , $\dot{\phi}$ is zero. Then v_3 , which consists of the low-frequency components of the output of x_3 , reduces to:

$$v_3 = Q \frac{dI}{dt}, \dot{\phi} = 0$$

or

$$v_3 = -2J_1(\beta) \omega_m \sin \phi \cos \omega_m t [J_0(\beta) \sin \phi - 2J_1(\beta) \sin \omega_m t \cos \phi].$$

Inspection of this equation reveals that the average value of v_3 , $\langle v_3 \rangle$, is zero when the VCO frequency equals ω_c .

Suppose, now, that the VCO frequency does not equal ω_c . Under this condition, $\dot{\phi}$ is not zero and the average value of v_3 is:

$$\langle v_3 \rangle = \frac{\dot{\phi}}{2} [J_0^2(\beta) + 2J_1^2(\beta)].$$

Thus an output voltage proportional to the frequency error is available when the VCO is not locked to the carrier.

Richman (Reference 5) gives a noise analysis of the quadricorrelator for high SNR. Apparently no information is available concerning an SNR threshold. However, since this is a balanced-type circuit, no doubt its performance for low SNR is not as good as that of the conventional PLL. Experimental data for this condition would be helpful.

CONTIGUOUS COMB-TYPE PHASE LOCK LOOPS (PLL's)

From the discussion so far, it is clear that to operate in a poor SNR environment it is desirable to utilize a narrow-band PLL. However, some method must be found to provide a reasonable range of pullin frequencies and pullin times. Such a circuit is shown in Figure 6.

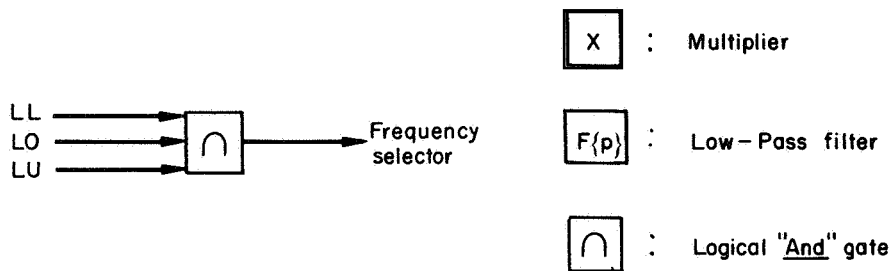
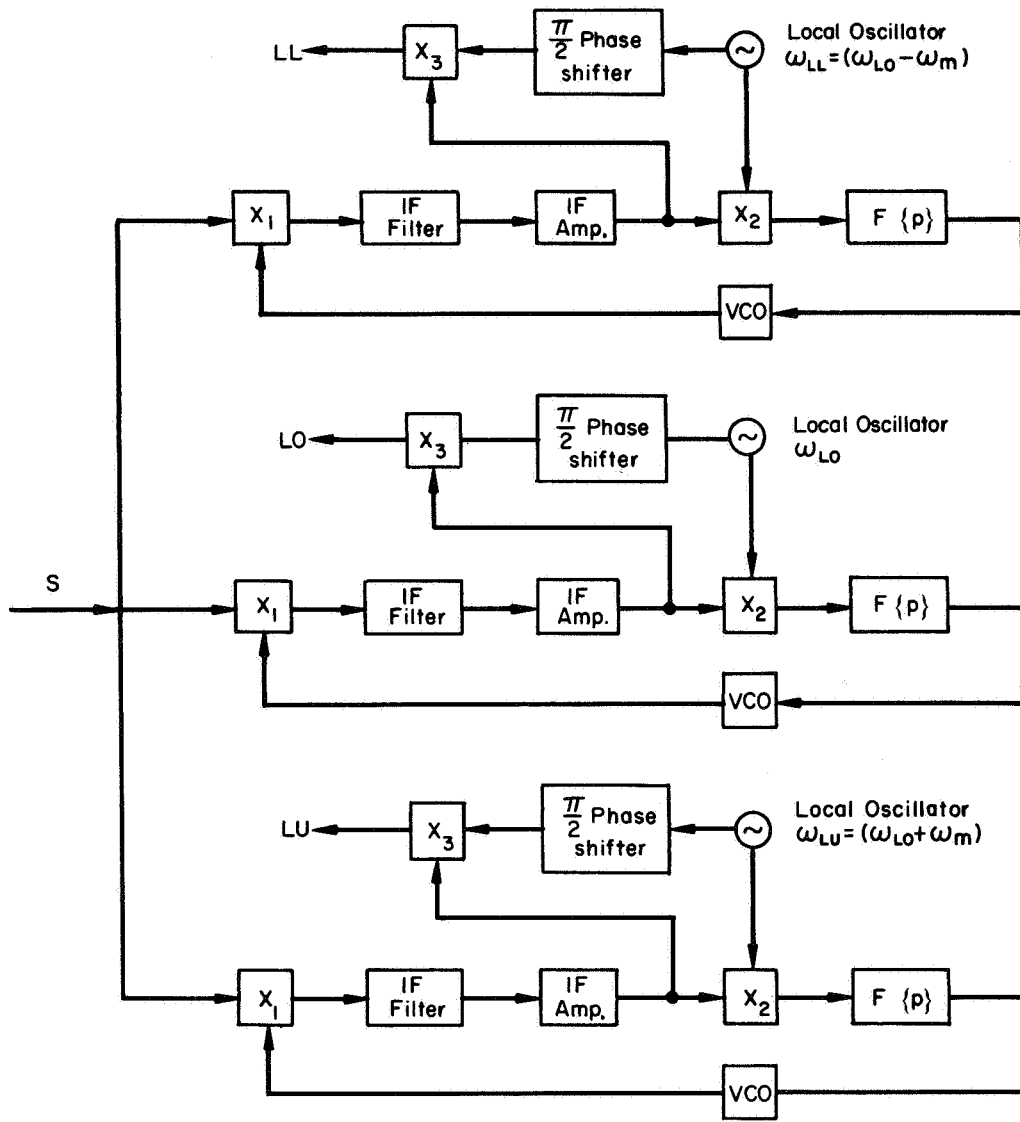
Before discussing the circuit of Figure 6, consider the simpler circuit of Figure 5. The only purpose served by Figure 5 is to introduce the more general case of Figure 6. The reason for the apparently arbitrary arrangement in Figure 5 will become clear when Figure 6 is discussed.

Three separate PLL's are shown in Figure 5. In each loop the center frequency of the IF filter equals the frequency of its corresponding local oscillator. The input signal is assumed to be a carrier plus upper and lower sideband. The bandwidth of each loop is made narrow enough so that each loop responds to – at most – one of the frequencies at a time. Suppose the center loop acquires the carrier frequency, ω_c . Then the upper loop acquires the upper sideband frequency, and the lower loop acquires the lower sideband frequency.

Under these conditions the outputs from the multipliers (or detectors), x_2 , are small (proportional to $\sin \theta$, where θ is the steady-state phase error). Therefore the outputs from the multipliers, x_3 , are large. The outputs from the x_3 's are applied to a logical "AND" gate. When the output of the "AND" gate is "one," this signal can be used to have the receiver choose the center PLL as the correct loop which is tracking the carrier frequency, ω_c . If the center PLL locks on one of the sidebands, the output of the "AND" gate is zero. This signal can be used to continue tuning of the free-running frequencies of the VCO's. Again, this scheme requires the presence of both upper and lower sidebands.

There is no particular advantage to using the circuit of Figure 5. However, if the bandwidth of the loops is decreased and the total number of loops is increased so that a frequency range of three to five times the subcarrier frequency, ω_m , is covered, then performance comparable to a single narrow-band PLL should be obtained. Such an arrangement is shown in Figure 6. In this case the logic circuitry for the proper frequency selection is more involved, but not complicated. It is assumed that the power density spectrum of the actual signal is symmetrical about the carrier frequency, that the spectrum peaks around frequencies corresponding to the sideband frequencies of the subcarrier frequency, ω_m , and that component frequencies far removed from these are too weak to cause a loop to lock. (See the Appendix.) In Figure 6 there is a "select-logic" circuit for each PLL except 1 and N. When the system is operating properly, there should be an output from – at most – one of the select circuits. Then the corresponding PLL is selected as tracking the carrier, ω_c . If the outputs of all the select circuits are "0's," the free-running frequencies of all the VCO's are tuned.

Thus this circuit seems to offer the possibility of performance comparable to that of the narrow-band PLL without the problem of false sideband lock.



$$S = J_0(\beta) \sin \omega_c t + J_1(\beta) \sin (\omega_c + \omega_m) t - J_1(\beta) \sin (\omega_c - \omega_m) t.$$

Figure 5—Modified comb-type filter

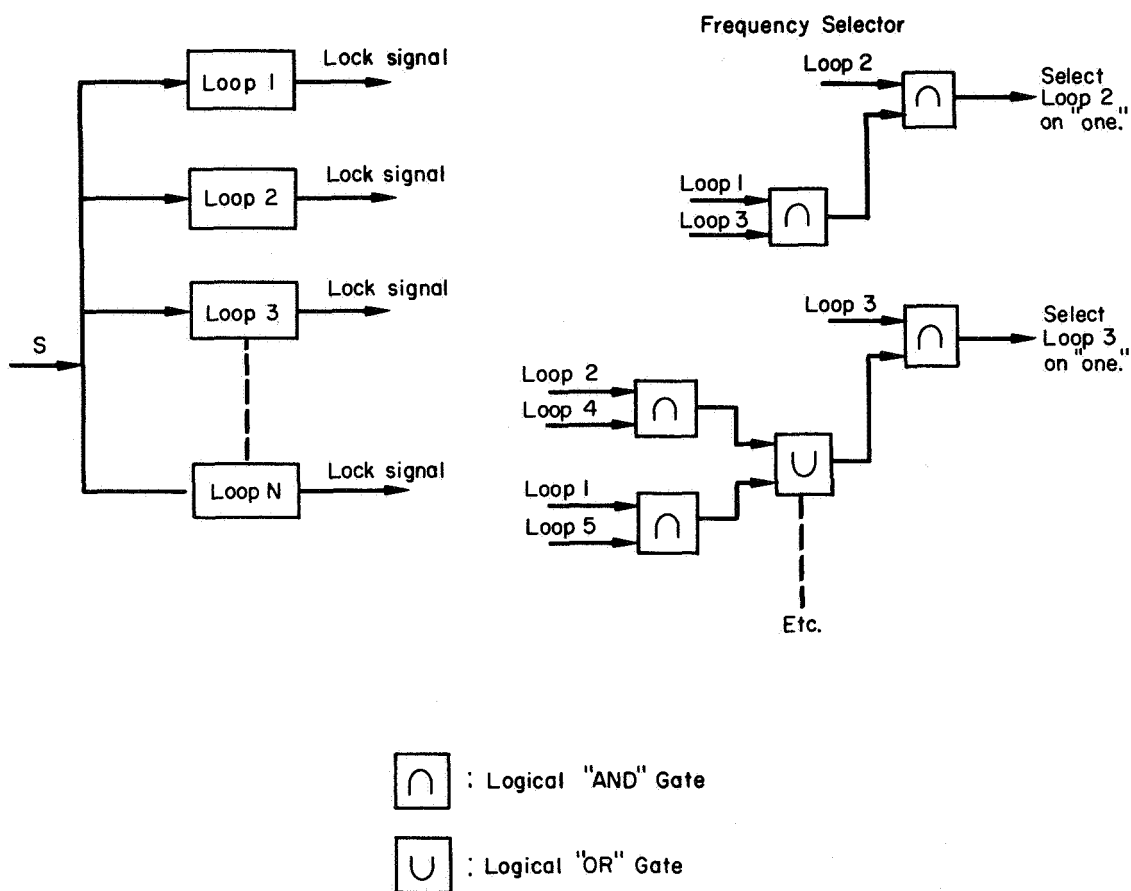


Figure 6—Comb-type PLL's

At least two objections can be raised concerning this system. First of all, it is data-dependent, i.e., proper operation of this scheme requires the presence of symmetrical sidebands and in any actual case only the statistical distribution or power density spectrum of the signal is known. Further, this system will not acquire an unmodulated carrier.

If one is searching for an unmodulated carrier, this whole system should be disabled and only one of the PLL's should be used in a conventional way.

CONCLUSIONS

Three circuits have been discussed which eliminate the condition of false sideband lock. However, two operate satisfactorily only for relatively large SNR.

The third, the comb-type PLL's, seems to offer the possibility of satisfactory performance for very low SNR. Further theoretical and experimental study of this circuit is recommended to obtain the limits on the range of its performance.

ACKNOWLEDGMENT

The author gratefully acknowledges the assistance received from T.V. Saliga of GSFC during this investigation.

REFERENCES

1. Gardner, F.M., Phaselock Techniques, New York: John Wiley and Sons, 1966.
2. Viterbi, A.J., Principles of Coherent Communications, New York: McGraw-Hill Book Co., 1966.
3. Casson, W.H., and Hall, C.C., "New Phase-Tracking Demodulator will not Lock on Sidebands," Electronics 36(6): 52-55, Feb. 8, 1963.
4. Richmond, D., "Color-Carrier Reference Phase Synchronization Accuracy in NTSC Color Television," Proc. IRE 42:106-133, January, 1954.
5. Stumpers, F.L.H.M., "Theory of Frequency Modulation Noise," Proc. I.R.E. 36, 1948.

APPENDIX
Power Density Spectrum of a Narrow-Band Split-Phase Modulated Signal

A narrow-band split-phase modulated signal may be represented as:

$$s = V \sin [\omega_c t + \beta f(t)]$$

where ω_c is the carrier frequency.

β is the phase deviation. In narrow-band modulation it is assumed that β is small enough for the signal to be adequately represented by the carrier and the first set of sidebands.

$f(t)$ is the modulating signal. In split-phase modulation it may be represented as:

$$f(t) = A(t) \sin \omega_m t; A(t) = \pm 1.$$

$A(t)$ is a random variable each of whose two values are equally probable. The value +1 may represent "one" and the -1 may represent "zero." The so-called bit rate of $f(t)$ is $T = 2\pi / \omega_m$. The random variable A may change values at times $t = nT$, where ω_m is an integer. The frequency ω_m is called the subcarrier. (See Figure A-1.)

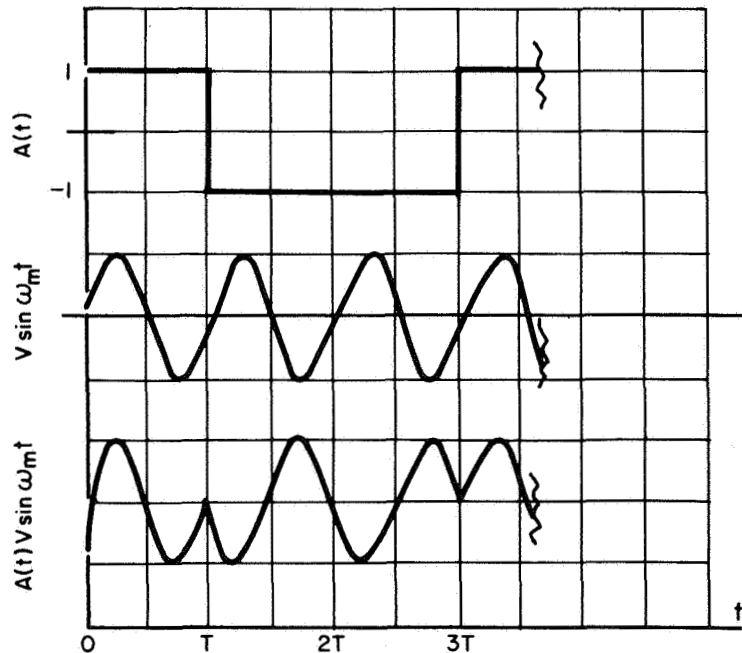


Figure A-1—Split-phase modulated signal ($T = 2\pi / \omega_m$)

The power density spectrum of s , $G(f)_s$, is defined as:

$$G(f)_s = \int_{-\infty}^{+\infty} R(\tau)_s e^{-j\omega\tau} d\tau$$

where

$$R(\tau)_s = \lim_{P \rightarrow \infty} \frac{1}{2P} \int_{-P}^{+P} s(t) s(t + \tau) dt.$$

In this case

$$\begin{aligned} s(t) &= V \sin(\omega_c t + \beta A(t) \sin \omega_m t) \\ &\approx V J_0[\beta A(t)] \sin \omega_c t + J_1[\beta A(t)] \sin(\omega_c + \omega_m) t \\ &\quad - J_1[\beta A(t)] \sin(\omega_c - \omega_m) t. \end{aligned}$$

where $J_0(\beta)$ and $J_1(\beta)$ are the zero and first-order Bessel functions, respectively. Recall that $J_0(\beta) = J_0(-\beta)$ and $J_1(\beta) = -J_1(-\beta)$. In what follows, let $v = 1$.

The calculation can be facilitated by finding the power density spectrum of $A(t)$, namely, $G(f)_A$.

$$\begin{aligned} G(f)_A &= \int_{-\infty}^{+\infty} R(\tau)_A e^{-j\omega\tau} d\tau, \\ R(\tau)_A &= \lim_{P \rightarrow \infty} \frac{1}{2P} \int_{-P}^{+P} A(t) A(t + \tau) dt \\ &= \left(1 + \frac{\tau}{T}\right); \quad -T \leq \tau \leq 0 \\ &= \left(1 - \frac{\tau}{T}\right); \quad 0 \leq \tau \leq T \\ &= 0 \quad ; \quad T < |\tau|. \end{aligned}$$

$$G(f)_A = \frac{T \sin^2\left(\frac{\omega T}{2}\right)}{\left(\frac{\omega T}{2}\right)^2} = \frac{T \sin^2(\pi f T)}{(\pi f T)^2}.$$

Now consider $r(t) = f(t) \cos at$.

Recall that:

$$\begin{aligned} R(\omega) &= \int_{-\infty}^{+\infty} r(t) \epsilon^{-j\omega t} dt \\ &= \int_{-\infty}^{+\infty} \frac{f(t) (\epsilon^{at} + \epsilon^{-at})}{2} \epsilon^{-j\omega t} dt \\ &= \frac{F(\omega + a) + F(\omega - a)}{2}. \end{aligned}$$

Furthermore:

$$\begin{aligned} R(\tau)_{J_0}[\beta A(t)] &= J_0^2(\beta), \\ R(\tau)_{J_1}[\beta A(t)] &= J_1^2(\beta) R(\tau)_{A(t)}. \end{aligned}$$

After some calculations, it follows that:

$$\begin{aligned} G(f)_s &= \frac{1}{4} \left[J_0^2(\beta) [\delta(f_c) + \delta(-f_c)] + T J_1^2(\beta) \left(\frac{\sin^2 [\pi(f + f_c + f_m)T]}{(\pi(f + f_c + f_m)T)^2} \right. \right. \\ &\quad + \frac{\sin^2 [\pi(f - f_c - f_m)T]}{(\pi(f - f_c - f_m)T)^2} \\ &\quad \left. \left. + \frac{\sin^2 [\pi(f + f_c - f_m)T]}{(\pi(f + f_c - f_m)T)^2} + \frac{\sin^2 [\pi(f - f_c + f_m)T]}{[\pi(f - f_c + f_m)T]^2} \right) \right] \end{aligned}$$

where

$$\begin{aligned} \delta(f_c) &= 1, f = f_c \\ &= 0, f \neq f_c. \end{aligned}$$



PRECEDING PAGE BLANK NOT FILMED.

AN INTRODUCTION TO BOSE-CHAUDHURI-HOCQUENGHEM CODES

S. A. Tretter

ABSTRACT

Reliable communication at low signal-to-noise ratios requires the use of error correction and detection codes. A class of codes known as the Bose-Chaudhuri-Hocquenghem codes is described in this report. The fundamental mathematics necessary for understanding the code structure is presented. Circuits for performing arithmetic in finite Galois fields are introduced. The mathematical structure of general cyclic, block codes is presented, and the Bose-Chaudhuri-Hocquenghem codes are described in detail. Several examples are given.

INTRODUCTION

Prospective deep-space probes have increased GSFIC interest in reliable methods of communication at low signal-to-noise ratios. The limited power and sensitivity of transmitters and receivers necessitate the use of error correction and detection codes for reliability assurance. Codes with a wide range of error correction capabilities and rates are needed. An erroneous satellite command signal could have disastrous effects; therefore, command codes must have a large error correction and detection capability. However, a moderate number of errors in a picture transmitted from a weather satellite would cause little information loss. In this case codes with a high percentage of information symbols and small error correction capabilities could be used. These codes must be simple, reliable, and inexpensive for practical implementation.

Bose-Chaudhuri-Hocquenghem (BCH) codes are the most efficient class of algebraic block codes known for random error correction. These codes possess a wide range of rate and error correction capabilities. They were devised by Hocquenghem (Reference 1) in 1959 and independently by Bose and Chaudhuri (References 2 and 3) in 1960 as a constructive proof of the existence of binary block codes of length $2^m - 1$ that correct errors using a maximum of mt parity check symbols. The Reed-Solomon, Golay, and Hamming codes also belong to this class. The first decoding procedure for binary codes was discovered by Peterson (Reference 4) in 1960. A generalized method of decoding both binary and non-binary codes was found soon afterwards by Gorenstein and Zieler (References 5 and 6). By taking advantage of the cyclic nature of BCH codes, Chien (Reference 7) in 1964 proposed a decoding procedure for binary codes that increased speed and decreased complexity for special purpose decoding computers. In 1965 Massey (Reference 8) devised a step-by-step procedure for decoding both binary and nonbinary codes. The hardware mechanization of Massey's method is slightly simpler than that of Chien's. Forney (Reference 9) expanded the decoding methods to include erasures in addition to errors, thus improving the algebraic code performance on the basis of the optimum probabilistic decoding procedures. The principal advantages of the algebraic block codes are the simplicity of the coding and decoding algorithms and the resulting efficiency of implementation.

FUNDAMENTAL MATHEMATICAL CONCEPTS

This report is designed to be a tutorial introduction to the BCH codes. These codes are based on the concepts of modern algebra. This section introduces the basic mathematical concepts and definitions necessary for understanding and using these codes. A

more complete and rigorous presentation is given in Peterson (Reference 10) and modern algebra texts.

Concept 1: Arithmetic Modulo p

Given two numbers, b and p , if b is divided by p , the result is a quotient q and a remainder $r < p$. That is,

$$b = qp + r.$$

The expression $c = b$ modulo p , usually written $c = b \bmod p$, is defined as the remainder r when b is divided by p .

Example 1:

$$21 \bmod 5 = 1,$$

since

$$21 = 4 \times 5 + 1.$$

Definition 1: Equivalence Classes—Any numbers having the same remainders with respect to p are said to be equivalent or in the same equivalence class. That is, $a = b$ if $a \bmod p = b \bmod p$.

Example 2: All even numbers modulo 2 are equivalent to 0, and all odd numbers modulo 2 are equivalent to 1.

Examples 1 and 2 illustrate the relationship of the binary number system to arithmetic modulo 2.

Example 3: Addition modulo 2 may be demonstrated as follows:

$$(0 + 0) \bmod 2 = 0,$$

$$(0 + 1) \bmod 2 = 1,$$

$$(1 + 1) \bmod 2 = 0.$$

Subtraction modulo 2 is equivalent to addition modulo 2 since $1 - 1 = 0$.

Concept 2: Polynomial Modulo $g(x)$

Definition 2: Polynomial of Order N —An algebraic expression of the form:

$$f(x) = a_n x^n + a_{n-1} x^{n-1} + \dots + a_1 x + a_0,$$

where

$$a_0, a_1, \dots, a_n$$

are fixed numbers, and x is an indeterminate. The result of dividing polynomial $f(x)$ by polynomial $g(x)$ is a quotient $q(x)$ and a remainder $r(x) < g(x)$. That is, $f(x)$ can be written as:

$$f(x) = q(x)g(x) + r(x).$$

Definition 3: $f(x) \text{ Mod } g(x)$ —The term $f(x) \text{ mod } g(x)$ is defined as the remainder $r(x)$.

Polynomials having the same remainder are said to be equivalent or in the same equivalence class.

Example 4: The value of $(x^3 + x^2 + 1) \text{ mod } (x + 1)$ may be obtained in the following manner:

$$\begin{array}{r}
 x^2 \\
 x + 1 \overline{) x^3 + x^2 + 1} \\
 \underline{x^3 + x^2} \\
 1
 \end{array}$$

therefore

$$q(x) = x^2, \quad r(x) = 1,$$

so that

$$x^3 + x^2 + 1 = x^2(x + 1) + 1,$$

and

$$(x^3 + x^2 + 1) \text{ mod } (x + 1) = 1.$$

Concept 3: Group

Definition 4: Group—A collection of elements a_1, a_2, a_3, \dots and an operation denoted by (\cdot) that satisfy the following axioms:

1. Closure—For any two elements a_1, a_2 in a group, $a_1 \cdot a_2$ is in the group.
2. Associative Law— $a_1 \cdot (a_2 \cdot a_3) = (a_1 \cdot a_2) \cdot a_3$
3. Identity Element—The group contains a unique element I such that $a \cdot I = I \cdot a = a$ for all a in the group.
4. Inverses—For each element a_1 , the group contains an inverse element a_1^{-1} such that $a_1 \cdot a_1^{-1} = a_1^{-1} \cdot a_1 = I$.

If for any two elements $a_1 \cdot a_2 = a_2 \cdot a_1$, the group is called commutative or Abelian. The groups used in describing algebraic codes are Abelian.

Example 5: An additive group of integers modulo 5 may be explained as follows: Let the elements of the group be the integers 0, 1, 2, 3, 4, and the operation (\cdot) be addition modulo 5, denoted by the symbol (+). Then the identity element $I = 0$ since $0 (+) a = a$. The addition table and the table of inverses are shown below.

Addition Table

	0	1	2	3	4
0	0	1	2	3	4
1	1	2	3	4	0
2	2	3	4	0	1
3	3	4	0	1	2
4	4	0	1	2	3

Table of Inverses

Element (a)	Inverse (-a)
0	0
1	4
2	3
3	2
4	1

Example 6: A multiplicative group of integers modulo 5 may be explained as follows. Let the group elements be 1, 2, 3, 4, and the operation (\cdot) be multiplication with the result reduced modulo 5. Then the identity $I = 1$.

Multiplication Table

	1	2	3	4
1	1	2	3	4
2	2	4	1	3
3	3	1	4	2
4	4	3	2	1

Table of Inverses

Element (a)	Inverse (a^{-1})
1	1
2	3
3	2
4	4

Note: It can be shown (Reference 10) that the integers $1, 2, \dots, p$, where p is a prime number, and the operation, multiplication modulo p , form a group.

Definition 5: Order of a Group—The number of elements in the group.

Definition 6: Powers of Elements—

$$a^0 = I,$$

$$a^2 = a \cdot a,$$

$$a^3 = a \cdot a \cdot a = a^2 \cdot a.$$

Definition 7: Order of an Element—The smallest nonzero integer e such that $a^e = I$. The order of an element always divides the order of the group.

Example 7: The order of the group in Example 6 is 4. The order of the various elements may be determined as follows:

$$1^1 = 1 \quad \text{so} \quad e_1 = 1,$$

$$2^2 = 4, \quad 2^3 = 8 = 3, \quad 2^4 = 16 = 1 \quad \text{so} \quad e_2 = 4,$$

$$3^2 = 9 = 4, \quad 3^3 = 12 = 2, \quad 3^4 = 6 = 1 \quad \text{so} \quad e_3 = 4,$$

$$4^2 = 16 = 1 \quad \text{so} \quad e_4 = 2.$$

Thus, the order of each element divides 4, the order of the group. Notice that the powers of the elements 2 and 3 generate all the other elements of the group.

Definition 8: Primitive Element—An element, a , whose powers generate all the group elements. Every group contains at least one primitive element.

Definition 9: Subgroup—A set of elements taken from a group satisfying all the group axioms (see Definition 4). The elements 1, 4 form a subgroup of the group in Example 6.

Concept 4: Field

Definition 10: Field—A set of elements closed under addition (+) and multiplication (\cdot) which satisfies the following axioms:

1. The set of elements is an Abelian group under addition.
2. The set of nonzero elements form an Abelian multiplicative group.
3. The distributive law applies: $a(b + c) = ab + ac$.

Example 8:

1. The real numbers form a field with ordinary arithmetic.
2. The numbers 0, 1 form a field under arithmetic modulo 2.
3. The numbers 0, 1, 2, 3, 4 form a field under arithmetic modulo 5.

4. The integers $0, 1, \dots, p$, where p is a prime number, form a field under arithmetic modulo p .

Definition 11: Galois Field—A field containing a finite number of elements p denoted as $GF(p)$.

Concept 5: Polynomials Over a Field

Definition 12: Polynomial of Order n over $GF(p)$ —An expression of the form:

$$f_n x^n + f_{n-1} x^{n-1} + \dots + f_0,$$

where the coefficients f_0, f_1, \dots, f_n are all elements of $GF(p)$, and $f_n \neq 0$. $GF(p)$ is called the ground field.

Addition and multiplication of polynomials are performed according to the ordinary rules except that the coefficients are found by using arithmetic modulo p . Therefore, if

$$f(x) = \sum_{i=0}^n f_i x^i$$

and

$$g(x) = \sum_{i=0}^n g_i x^i,$$

$$f(x) + g(x) = \sum_{i=0}^n [(f_i + g_i) \bmod p] x^i,$$

and

$$f(x) \cdot g(x) = \sum_{i=0}^{2n} \left[\left(\sum_{j=0}^i f_j g_{i-j} \right) \bmod p \right] x^i.$$

Example 9: Polynomials over $GF(2)$ may be explained as follows: Let the ground field be $GF(2)$ with elements 0 and 1. Let $f(x) = x^2 + 1$, and $g(x) = x^3 + x^2 + 1$. Then $f(x) + g(x) = x^3 + (1 + 1)x^2 + (1 + 1) = x^3$, and

$$\begin{array}{r} x^3 + x^2 + 1 \\ \underline{x^2 + 1} \\ x^5 + x^4 + x^2 \\ \underline{x^3 + x^2 + 1} \\ f(x) \cdot g(x) = x^5 + x^4 + x^3 + 1 \end{array}$$

Definition 13: Irreducible Polynomial—A polynomial $f(x)$ is irreducible over $GF(p)$ if it can not be expressed as the product of two polynomials $g(x)$ and $h(x)$ each of degree at least one, with coefficients in $GF(p)$.

Example 10: In $GF(2)$ $x^2 + 1 = (x + 1)^2$ is not irreducible while $x^2 + x + 1$ cannot be expressed as the product of two polynomials over $GF(2)$ and is therefore irreducible.

Given a polynomial $g(x)$ over $GF(p)$ of order n and a polynomial $f(x)$ over $GF(p)$ of arbitrary order, $f(x) \bmod g(x)$ was defined (see Concept 2) as the remainder when $f(x)$ is divided by $g(x)$. Therefore, $f(x) \bmod g(x)$ is the $n-1$ order polynomial, and

$$r(x) = r_{n-1} x^{n-1} + \dots + r_0.$$

For fixed $g(x)$ and arbitrary $f(x)$, $r(x)$ can be p^n different polynomials since each r_0, r_1, \dots, r_{n-1} can be any one of the p elements of $GF(p)$. (Note that these p^n polynomials form an additive group.) If $g(x)$ is irreducible, the $p^n - 1$ nonzero polynomials form a multiplicative group if multiplication modulo $g(x)$ is performed (Reference 10). Therefore, under the operations of polynomial addition and polynomial multiplication modulo $g(x)$ with all coefficients determined by using arithmetic modulo p , the p^n polynomials of order $n-1$ form a field when $g(x)$ is irreducible. Therefore, these p^n polynomials are the elements of a Galois field $GF(p^n)$. It is convenient for polynomial addition to represent the elements $r(x) = r_{n-1} x^{n-1} + \dots + r_0$ of $GF(p^n)$ by the n dimensional vector $r = [r_0, r_1, \dots, r_{n-1}]$. This notation will be used interchangeably with the polynomial form.

Example 11: Let the base field be $GF(2)$, and $g(x) = x^3 + x + 1$. It can be shown that $g(x)$ is an irreducible polynomial so that the field generated by polynomials modulo $g(x)$ has the order $2^3 = 8$. It is instructive to examine the elements $x^k \bmod g(x)$ for $k = 0, 1, \dots$. The table below was generated by dividing x^k by $g(x)$ to find the remainder $r(x)$.

$r(x)$	r_0	r_1	r_2
0	0	0	0
1	1	0	0
x	0	1	0
x^2	0	0	1
x^3	1	1	0
x^4	0	1	1
x^5	1	1	1
x^6	1	0	1
x^7	1	0	0

As stated previously, the nonzero elements of $GF(2^3)$ must form a multiplicative group of order 7. The preceding table shows that the powers of the element x generate all of the elements of this group; therefore, x is a primitive element. The polynomial $g(x)$ is called a primitive polynomial. Also observe that $x^7 = 1$. It can be shown that for any element, a , of a group of order e , $a^e = 1$. To find the inverse element of any member of the group observe that $x^i x^j = x^{i+j} = 1$ if $i + j = 7$ so that $[x^i]^{-1} = x^{-1} = x^j$. For example, from the

table it is observed that $x^3 = 1 + x$ and $x^4 = x + x^2$ so that $x^3 \cdot x^4$ should be 1. Multiplying gives:

$$x^3 \cdot x^4 = \frac{\begin{array}{r} 1 + x \\ x + x^2 \\ \hline x + x^2 \\ \hline x^2 + x^3 \end{array}}{x + x^3}$$

Reducing $x + x^3$ modulo $g(x)$ gives:

$$x^3 + x + 1 \overline{) x^3 + x} \begin{array}{r} 1 \\ \hline x^3 + x + 1 \\ \hline 1 \end{array}$$

which shows that the remainder is 1 as expected.

Concept 6: Roots and Extension Fields

Definition 14: Root of a Polynomial—Any element α of a polynomial $f(x)$ such that $f(\alpha) = 0$.

If α is a root of $f(x)$, then $x - \alpha$ must be a factor of $f(x)$, i.e., $f(x) = (x - \alpha)h(x)$.

The roots of a polynomial over $GF(p)$ may or may not belong to $GF(p)$. This is illustrated by the following two examples.

Example 12: Polynomial over $GF(2)$, with roots in $GF(2)$.

Let $f(x) = x^2 + 1 = (x + 1)^2$. Then, clearly, $f(1) = 0$, and 1 is a double root of $f(x)$ and belongs to $GF(2)$.

Example 13: Polynomial over real numbers with no real roots.

Let $f(x) = x^2 + 1$. Then there is no real number, α , such that $\alpha^2 + 1 = 0$. However, if our root field is extended to include complex numbers, then a root α of $f(x)$ is customarily denoted as $\alpha = i = \sqrt{-1}$. Since α is a root of $f(x)$,

$$\begin{aligned} f(\alpha) &= \alpha^2 + 1 = 0, \\ \text{or } \alpha^2 &= -1 \\ \text{and } \alpha^3 &= -\alpha \\ \text{and } \alpha^4 &= -\alpha^2 = 1. \end{aligned}$$

Any complex number $c = a + ib$ is a linear combination of the powers of the roots of $f(x)$; i.e., $c = a\alpha^0 + b\alpha$.

Example 14: Polynomial over $GF(2)$, without roots in $GF(2)$.

Let $f(x) = x^3 + x + 1$ as in Example 11. Since $f(1) = f(0) = 1$, $f(x)$ has no roots in $GF(2)$. Let a root of $f(x)$ in some extension field be abstractly designated as α . Therefore,

$$f(a) = a^3 + a + 1 = 0,$$

$$\text{or } a^2 = a + 1.$$

Using this relationship for a^3, a^k for $k = 0, 1, \dots$ can always be expressed as a linear combination of $a^0 = 1, a$ and a^2 . For example,

$$a^4 = a \cdot a^3 = a^2 + a,$$

$$a^5 = a \cdot a^4 = a^3 + a^2 = (a + 1) + a^2 = a^2 + a + 1, \text{ etc.}$$

It is convenient to represent $a^k = c_0 + c_1 a + c_2 a^2$ as a three-dimensional vector, $a^k = [c_0, c_1, c_2]$, in some cases. A table of the powers of the root a of $f(x)$ is shown below.

Table

	c_0	c_1	c_2
a^0	1	0	0
a^1	0	1	0
a^2	0	0	1
a^3	1	1	0
a^4	0	1	1
a^5	1	1	1
a^6	1	0	1
a^7	1	0	0

The elements $1, a, a^2, a^3, a^4, a^5, a^6$ form a group under multiplication. Since $a^7 = 1$, $a^i a^j = a^{i+j} = 1$ if $i + j = 7$. Therefore, $[a^{-i}]^{-1} = a^i$ so that each element has an inverse. For any integer k , $k = q \cdot 7 + k \text{ mod } 7$ so $a^k = a^{q \cdot 7} a^{k \text{ mod } 7} = a^{k \text{ mod } 7}$. Therefore the set of powers of a is closed. From the table it can be seen that the powers of the root a generate all the elements of the group so that a is a primitive element.

Definition 15: Primitive Polynomial—An irreducible polynomial with at least one primitive root a .

All linear combinations of $1, a$, and a^2 , i.e., elements of the form $c_0 + c_1 a + c_2 a^2$ with the coefficients c_0, c_1, c_2 taken from $\text{GF}(2)$, form an additive group with $2^3 = 8$ elements. Therefore, the roots generate an extension field $\text{GF}(2^3)$.

A comparison of Examples 11 and 14 illustrates that the field corresponding to polynomials modulo $x^3 + x + 1$ is identical to the extension field generated by the root a of $x^3 + x + 1$. This equivalence is generally true. Given an irreducible polynomial $g(x)$ of degree n over $\text{GF}(p)$ with a root a , an arbitrary polynomial $f(x)$ can be expressed by application of the Euclidean division algorithm as

$$f(x) = q(x) g(x) + r(x),$$

where the degree of $r(x)$ is less than n . Substituting α for x gives:

$$f(\alpha) = q(\alpha) g(\alpha) + r(\alpha).$$

But since α is a root of $g(x)$, $g(\alpha) = 0$ and $f(\alpha) = r(\alpha)$, which is exactly equivalent to $f(x) \bmod g(x) = r(x)$ (with x replaced by α). Therefore, either point of view generates the Galois field $GF(p^n)$.

The result stated in Theorem I is important because it determines the block length of the algebraic codes.

Theorem I: A primitive polynomial $g(x)$ of order n over $GF(p)$ divides $x^{p^n-1} - 1$.

Proof:

Any root α_i of $g(x)$ generates an extension field of $GF(p)$ with p^n elements. The set of $p^n - 1$ nonzero elements form a multiplicative group. Therefore, $\alpha_i^{p^n-1} = 1$ or $\alpha_i^{p^n-1} - 1 = 0$ for $i = 1, \dots, n$; since $p^n - 1$ is the order of the multiplicative group. Thus, each root of $g(x) = \prod_{i=1}^n (x - \alpha_i)$ is also a root of $x^{p^n-1} - 1$, so $g(x)$ must divide $x^{p^n-1} - 1$.

QED

If $g(x)$ is irreducible but not primitive, its roots will generate an extension field of order $e < p^n$ so that $g(x)$ will divide $x^{e-1} - 1$. These polynomials are useful for generating codes of length $e-1$. It should be observed that $g(x)$ will still divide $x^{p^n-1} - 1$ since its roots form a subfield of $GF(p^n)$.

The following theorem and corollary are important in finding the generator polynomials (defined later) for BCH codes.

Theorem II: Given a polynomial

$$f(x) = \sum_{i=0}^n f_i x^i$$

over $GF(p)$,

$$[f(x)]^p = f(x^p).$$

Proof:

First consider the case where $n = 1$. Then according to the binomial theorem

$$(f_0 + f_1 x)^p = \sum_{r=0}^p \binom{p}{r} f_0^r (f_1 x)^{p-r} = f_0^p + f_1^p x^p,$$

since

$$\binom{p}{r} = \frac{p!}{r! (p-r)!}$$

is divisible by p except when $r = 0$ or p . Since the coefficients f_i are elements of $GF(p)$, $f_i^p = f_i$ so that

$$(f_0 + f_1 x)^p = f_0 + f_1 x^p.$$

Now let $f(x)$ be an n^{th} order polynomial and assume that the theorem is true for $n - 1^{\text{th}}$ order polynomials. Then,

$$f(x) = \sum_{i=0}^n f_i x^i = \sum_{i=0}^{n-1} f_i x^i + f_n x^n,$$

and

$$\begin{aligned} [f(x)]^p &= \left[\sum_{i=0}^{n-1} f_i x^i + f_n x^n \right]^p \\ &= \left[\sum_{i=0}^{n-1} f_i x^i \right]^p + f_n^p x^{pn} \\ &= \sum_{i=0}^n f_i (x^p)^i = f(x^p). \end{aligned}$$

QED

Corollary 1: If α is a root of the polynomial $f(x)$ over $GF(p)$, then α^p is also a root.

Proof:

According to Theorem II,

$$[f(x)]^p = f(x^p),$$

so that

$$[f(\alpha)]^p = 0 = f(\alpha^p).$$

QED

Definition 16: Monic Polynomial—A polynomial with unity as the coefficient of its highest order term.

Definition 17: Minimum Polynomial—Let β be an element of an extension field $GF(p^n)$. The monic polynomial $m(x)$ of smallest degree over $GF(p)$ such that $m(\beta) = 0$ is called the minimum polynomial of β . It can be shown (Reference 10) that the degree of $m(x)$ is n or less.

Example 15: Consider the extension field $GF(2^3)$ discussed in Example 14. Since α is a root of $f(x) = x^3 + x + 1$, according to Corollary 1, α^2 and α^4 must also be roots of $f(x)$. Notice that $(\alpha^4)^2 = \alpha^8 = \alpha$. Therefore α , α^2 , and α^4 are the three roots of $f(x)$ so that $f(x) = (x-\alpha)(x-\alpha^2)(x-\alpha^4)$. Using the table of Example 14,

$$f(\alpha^2) = \alpha^6 + \alpha^2 + 1 = \begin{bmatrix} 1 \\ 0 \\ 1 \end{bmatrix} + \begin{bmatrix} 0 \\ 0 \\ 1 \end{bmatrix} + \begin{bmatrix} 1 \\ 0 \\ 0 \end{bmatrix} = \begin{bmatrix} 1 \\ 0 \\ 0 \end{bmatrix},$$

and

$$f(\alpha^4) = \alpha^{12} + \alpha^4 + 1 = \alpha^5 + \alpha^4 + 1 = \begin{bmatrix} 1 \\ 1 \\ 1 \end{bmatrix} + \begin{bmatrix} 0 \\ 1 \\ 1 \end{bmatrix} + \begin{bmatrix} 1 \\ 0 \\ 0 \end{bmatrix} = \begin{bmatrix} 0 \\ 0 \\ 0 \end{bmatrix}.$$

The minimum polynomial $m_3(x)$ for α^3 will now be calculated. According to Corollary 1, α^6 , $\alpha^{12} = \alpha^5$, $\alpha^{10} = \alpha^3$ must be roots of $m_3(x)$. Therefore,

$$m_3(x) = (x-\alpha^3)(x-\alpha^6)(x-\alpha^5) = [x^2 - (\alpha^3 + \alpha^6)x + \alpha^9](x - \alpha^5) = x^3 - (\alpha^3 + \alpha^5 + \alpha^6)x^2 + (\alpha^8 + \alpha^9 + \alpha^{11})x - \alpha^{14}.$$

According to the table in Example 14,

$$\alpha^3 + \alpha^5 + \alpha^6 = \begin{bmatrix} 1 \\ 1 \\ 0 \end{bmatrix} + \begin{bmatrix} 1 \\ 1 \\ 1 \end{bmatrix} + \begin{bmatrix} 1 \\ 0 \\ 1 \end{bmatrix} = \begin{bmatrix} 1 \\ 0 \\ 0 \end{bmatrix},$$

$$\alpha^8 + \alpha^9 + \alpha^{11} = \begin{bmatrix} 0 \\ 1 \\ 0 \end{bmatrix} + \begin{bmatrix} 0 \\ 0 \\ 1 \end{bmatrix} + \begin{bmatrix} 0 \\ 1 \\ 1 \end{bmatrix} = \begin{bmatrix} 0 \\ 0 \\ 0 \end{bmatrix},$$

and

$$\alpha^{14} = \begin{bmatrix} 1 \\ 0 \\ 0 \end{bmatrix},$$

so that

$$m_3(x) = x^3 + x^2 + 1.$$

It is instructive to find $m_3(x)$ by an alternate method. Assume that

$$m_3(x) = c_0 + c_1 x + c_2 x^2 + x^3.$$

Then

$$m_3(a^3) = c_0 + c_1 a^3 + c_2 a^6 + a^9 = 0 =$$

$$c_0 \begin{bmatrix} 1 \\ 0 \\ 0 \end{bmatrix} + c_1 \begin{bmatrix} 1 \\ 1 \\ 0 \end{bmatrix} + c_2 \begin{bmatrix} 1 \\ 0 \\ 1 \end{bmatrix} + \begin{bmatrix} 0 \\ 0 \\ 1 \end{bmatrix} = \begin{bmatrix} 0 \\ 0 \\ 0 \end{bmatrix}$$

From the last three equations, it is concluded that $c_2 = 1$. From the second equation, c_1 is found to be 0, and thus c_0 must be 1. Therefore, $m_3(x) = x^3 + x^2 + 1$ as before.

CIRCUITS FOR ARITHMETIC IN GF (p^m)

Algebraic block codes are attractive because of the simplicity of the digital equipment necessary for coding and decoding. This simplicity, in the case of binary codes, results from the fact that multiplication of elements in GF (2^m) can be performed instantaneously using logic gates while division is easily performed with shift registers. Some typical circuits used for GF (p^m) arithmetic are discussed in this section.

Multiplication of Elements of GF (p^m)

The preceding section shows that any element of GF (p^m) can be represented as a linear combination of the elements $1, a, a^2, \dots, a^{m-1}$, where a is the root of a primitive polynomial of order m . In decoding BCH codes, it is necessary to find powers and products of elements in GF (p^m). For binary codes decoding can be performed readily by using logic gates. The technique is illustrated for GF (2^3) in the following example.

Example 16: Let GF (2^3) be represented as shown in Example 14. Let two elements of GF (2^3) be:

$$c = c_0 + c_1 a + c_2 a^2,$$

$$d = d_0 + d_1 a + d_2 a^2.$$

Then cd can be found by using ordinary multiplication:

$$cd = d_0 c_0 + (d_0 + d_1 c_0) a + (d_0 c_2 + d_1 c_1 + d_2 c_0) a^2 + (d_1 c_2 + d_2 c_1) a^3 + d_2 c_2 a^4.$$

But, from the table in Example 14,

$$a^3 = 1 + a \text{ and } a^4 = a + a^2.$$

Therefore, after simplification,

$$cd = (d_0 c_0 + d_1 c_2 + d_2 c_1) + (d_0 c_1 + d_1 c_0 + d_1 c_2 + d_2 c_1 + d_2 c_2) \alpha + d_2 c_2 \alpha^2.$$

The GF (2) equations for the coefficients of cd can easily be translated into a set of Boolean equations. These equations can be minimized and the corresponding logic network synthesized.

Division of $f(x)$ by $g(x)$

The notation of Peterson (Reference 10) will be used here. The symbol (+) represents a modulo p adder, and the symbol \square represents a storage element of a shift register. The circuit shown in Figure 1 can be used to divide the polynomial $f(x) = f_0 + f_1 x + \dots + f_n x^n$ by the polynomial $g(x) = g_0 + g_1 x + \dots + x^m$. The coefficients of $f(x)$ are applied serially to the input from highest to lowest order. The coefficients of the quotient appear serially at the output from highest to lowest order also. After n shifts, the coefficients of the remainder are left in the shift register with the coefficient of highest order on the right. The circuit operation is analogous to ordinary long division and is explained in detail in Reference 10, pp. 111-113.

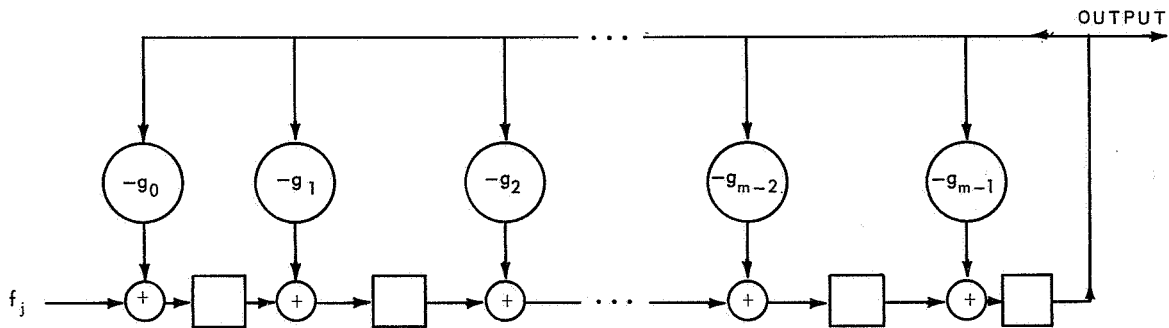


Figure 1—Circuit for division of polynomials.

For decoding it is necessary to evaluate $f(\alpha)$ where α is a root of $g(x)$. Since $f(x) = q(x)g(x) + r(x)$, $f(\alpha) = r(\alpha)$. Therefore, only the remainder $r(x)$ is needed. Examination of the division circuit operation is instructive in finding $f(\alpha)$. Consider the storage elements of the shift register containing, from left to right, the coefficients of $1, \alpha, \dots, \alpha^{m-1}$. The storage elements are first set to zero. The contents of the register are $f_n, f_{n-1} + \alpha f_n$, and $f_{n-m+1} + f_{n-m+2} \alpha + \dots + f_n \alpha^{m-1}$ after one, two and m shifts, respectively. This is true because feedback occurs only when the data reach the last stage of the shift register. At the $m+1$ shift feedback begins to occur. Suppose, for the time being, that the feedback link was broken and that the register contained additional storage elements. Then after the $m+1$ shift the contents of the register would correspond to

$$f_{n-m} + f_{n-m+1} \alpha + \dots + f_{n-1} \alpha^{m-1} + f_n \alpha^m.$$

However, since α is a root of $g(x)$,

$$\alpha^m = -g_0 - g_1 \alpha - \dots - g_{m-1} \alpha^{m-1}.$$

Example 18: Let $g(x) = x^3 + x + 1$ again and $k = 5$. The circuit for finding $a^5 f(a)$ is shown in Figure 4.

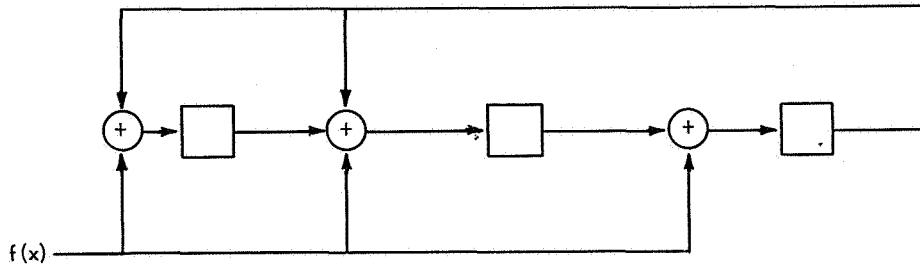


Figure 4—Circuit for finding $a^5 f(a)$.

CYCLIC BLOCK CODES

BCH codes belong to the class of algebraic codes known as cyclic codes. In this section cyclic codes are defined, and some of their properties are explained.

Definition 18: Least Common Multiple—The smallest number divisible by each of the set of given integers e_1, e_2, \dots, e_m .

Given a set of polynomials $e_1(x), \dots, e_m(x)$, their least common multiple is the polynomial of lowest order divisible by all of them.

Let $g(x)$ be a polynomial of order r over $GF(p)$ with roots $\alpha_1, \alpha_2, \dots, \alpha_r$ that are elements of $GF(p^m)$. Let the orders of the roots be e_1, \dots, e_r , and let n be the least common multiple of the orders. Then $n = q_1 e_1 = q_2 e_2 = \dots = q_r e_r$ and $\alpha_i^n = \alpha_2^n = \dots = \alpha_r^n = 1$, since $\alpha_i^n = \alpha_i^{q_i e_i} = (\alpha_i^{e_i})^{q_i} = 1^{q_i} = 1$. Therefore, each root of $g(x)$ is a root of $x^n - 1$ so that $g(x)$ divides $x^n - 1$ and n is the smallest integer such that $x^n - 1$ is divisible by $g(x)$.

Consider the set of all $n - 1$ order polynomials of the form

$$f(x) = q(x) g(x) \text{ mod } (x^n - 1),$$

where $g(x)$ is an arbitrary polynomial over $GF(p)$, and n is the smallest integer such that $x^n - 1$ is divisible by $g(x)$. The following two theorems show that each of these polynomials is divisible by $g(x)$ and that the set is closed under addition, thus forming a linear vector subspace.

Theorem III: Let n be the smallest integer such that $x^n - 1$ is divisible by $g(x)$. Then $q(x) g(x) \text{ mod } (x^n - 1)$ is also divisible by $g(x)$.

Proof:

According to the Euclidean division algorithm,

$$q(x) g(x) = h(x) (x^n - 1) + r(x),$$

where $h(x)$ is the quotient, and $q(x) g(x) \text{ mod } (x^n - 1) = r(x)$ by definition. Clearly $g(x)$ divides the left-hand side of this equation. The value $g(x)$ divides $x^n - 1$, and therefore it must also divide $r(x)$ if the right-hand side is to be divisible by $g(x)$.

QED

Theorem IV: Let $f_1(x) = q_1(x) g(x) \bmod (x^n - 1)$, and $f_2(x) = q_2(x) g(x) \bmod (x^n - 1)$. Then $f_1(x) + f_2(x)$ is divisible by $g(x)$.

Proof:

According to Theorem IV, both $f_1(x)$ and $f_2(x)$ are divisible by $g(x)$. Therefore, the sum is divisible by $g(x)$.

QED

The set of polynomials $q(x) g(x) \bmod (x^n - 1)$ will be taken as the code vectors. Theorems III and IV clearly show that these vectors form a subspace of an n dimension vector space and that each code vector is a multiple of $g(x)$. The polynomial $g(x)$ is the generator polynomial for the code, and n is the code length.

It can be shown (Reference 10) that the code vectors form an $n-r$ dimensional subspace. That is, $n-r$ components can be arbitrarily chosen as information symbols, and the remaining r symbols must be check symbols. Usually it is convenient to choose the first $n-r$ components, i.e., the coefficients of $x^{n-1}, x^{n-2}, \dots, x^r$, as information symbols. Codes of this type are called systematic codes. Encoding can be performed according to the following procedures:

Let the information correspond to the polynomial $I(x) = i_{n-1} x^{n-1} + \dots + i_r x^r$. Then according to the Euclidean division algorithm

$$I(x) = q(x) g(x) + c(x),$$

where $c(x) = c_{r-1} x^{r-1} + \dots + c_0$ is the remainder when $I(x)$ is divided by $g(x)$. Therefore, $q(x) g(x) = I(x) - c(x) = i_{n-1} x^{n-1} + \dots + i_r x^r - c_{r-1} x^{r-1} - \dots - c_0$ is a code word with the information symbols appearing first. Encoding can be performed by using the previously discussed circuits to divide $I(x)$ by $g(x)$ to find $c(x)$. A more complete discussion and alternate circuits are given by Peterson (Reference 10).

Given any code word

$$f(x) = f_{n-1} x^{n-1} + f_{n-2} x^{n-2} + \dots + f_0,$$

then

$$x f(x) = f_{n-1} x^n + f_{n-2} x^{n-1} + \dots + f_0 x$$

must also be a code word since it is still a multiple of $g(x)$. Since $x^n \bmod (x^n - 1) = 1$, $x f(x) \bmod (x^n - 1) = f_{n-2} x^{n-1} + \dots + f_0 x + f_{n-1}$. If $f(x)$ is represented in the vector form $f(x) = (f_0, f_1, \dots, f_{n-1})$, then $x f(x) = (f_{n-1}, f_0, f_1, \dots, f_{n-2})$ is just a cyclic shift of the vector $f(x)$. For this reason, these are called cyclic codes.

BOSE-CHAUDHURI-HOCQUENGHEM CODES

BCH codes are cyclic codes with symbols in $GF(p)$ and can be described most easily in terms of their generator polynomials. Let α be an element of an extension field $GF(p^m)$, for example, a root of a primitive polynomial of order m over $GF(p)$, and let m_0 be an arbitrary integer. Then the generator polynomial $g(x)$ is the polynomial of smallest degree that has the roots $\alpha^{m_0}, \alpha^{m_0+1}, \dots, \alpha^{m_0+d-2}$. Since each code vector $f(x)$ is a multiple of $g(x)$,

these must also be roots of $f(x)$. If $m_0 = 0$ then 1 is a root of $f(x)$ so that

$$f(1) = \sum_{i=0}^{n-1} f_i = 0,$$

which corresponds to a simple parity check. The code length n is the smallest integer such that $g(x)$ divides $x^n - 1$. Peterson (Reference 10) shows that n is the order of α for $d > 2$, for example, $n = p^m - 1$ if α is primitive. The code vectors are the set of all polynomials of the form $q(x)g(x) \bmod (x^n - 1)$.

Example 19: Let α be a root of the primitive polynomial $x^3 + x + 1$ as in Example 14. Then the code length is $n = 2^3 - 1 = 7$. Let $m_0 = 1$ and $d = 3$, then α and α^2 must be roots of $g(x)$. According to Corollary 1, if α is a root of a polynomial, then α^2 is also a root. Therefore, $g(x) = x^3 + x + 1$, and the code vectors contain four information symbols and three check symbols. For example, let the information symbols be $x^6 + x^3$, then

$$\begin{array}{r} x^3 + x \\ x^3 + x + 1 \overline{) x^6 + 0 + 0 + x^3} \\ \underline{x^6 + x^4 + } \\ + x^4 + \\ + x^4 + x^2 + x \\ \underline{ + x^4 + x^2 + x} \\ + + + \\ + + + x \end{array}$$

Therefore, the check symbols are $x^2 + x$, and the code vector becomes

$$f(x) = x + x^2 + x^3 + x^6 = (0, 1, 1, 1, 0, 0, 1).$$

As an exercise the reader might show that for $d > 3$ the code becomes degenerate and consists of only check symbols.

Stenbit (Reference 11) has calculated the generator polynomials for all non-trivial BCH codes up to length 255 with $m_0 = 1$ and α a primitive element. Peterson's book (Reference 10) contains a table of irreducible polynomials over $GF(2)$ and minimum polynomials for powers of primitive elements, which can be used for calculating the generator polynomials for additional codes.

Distance Structure

The minimum Hamming distance of the BCH codes is at least d (Reference 10). Therefore, to ensure that the codes are capable of correcting t errors d must be at least $2t + 1$. These codes will then detect $2t = d - 1$, or less, errors.

For binary codes where $m_0 = 1$ and $d = 2t + 1$; $\alpha, \dots, \alpha^{2t}$ must be roots of $g(x)$. Since every even power of α is a root of the minimum polynomial of some odd power of α , $g(x)$ is the least common multiple of $m_1(x), m_3(x), \dots, m_{2t-1}(x)$. If α is an element of $GF(2^m)$, then each minimum polynomial has order m or less, and $g(x)$ is the product of t polynomials of order m so that the order of $g(x)$ is at most mt . Therefore, if α is a primitive root, $g(x)$ generates a code of length $2^m - 1$ with a maximum of mt check digits. The generator polynomials for codes with various t and n are given in Stenbit (Reference 11).

If $g(x)$ has order $n - k$, where k is the number of information symbols, the BCH codes will also detect all bursts of length $n - k$ or less. A burst of length L is an error pattern of the form $x^r(b_0 + b_1x + \dots + b_{L-1}x^{L-1}) = x^r B(x)$ where b_i 's are elements of $GF(p)$ and

$b_0 \neq 0, b_{L-1} \neq 0$. Since x^r is not divisible by $g(x)$ because no root of $g(x)$ raised to the r^{th} power is zero, and $B(x)$ is not divisible by $g(x)$ if $L \leq n - k$; the burst cannot be a code vector.

If $m_0 = 1$, and $d = 3$ with α a primitive root, the BCH codes are equivalent to the well known Hamming codes. In this case α and α^2 must be roots of $g(x)$, so that $g(x)$ is just the primitive polynomial with α as its root (Example 19).

Error Detection

Since each transmitted code vector $f(x)$ is a multiple of $g(x)$, it is only necessary to divide the received vector by $g(x)$ to check for errors. If a detectable error has occurred, the remainder will not be zero. If no error or an undetectable error has occurred, the remainder will be zero. The division can be performed by shifting $f(x)$ into the division circuit (Figure 1).

Error Correction

All known error correction schemes are based on Newton's identities relating the elementary symmetric functions to the power sum symmetric functions. Since these relations are not clearly explained in the literature on BCH codes, they will be derived here by using the method of Bocher (Reference 12). With this background, the reader should be able to understand the literature (4, 5, 7, 8, 9, 10, 13), without serious difficulty, and therefore these decoding methods will not be discussed here.

Definition 19: Elementary Symmetric Functions—Given a set of numbers x_1, \dots, x_n , the polynomial

$$\begin{aligned} \sigma(x) &= (x - x_1)(x - x_2) \dots (x - x_n), \\ &= x^n - \sigma_1 x^{n-1} + \sigma_2 x^{n-2} + \dots + (-1)^n \sigma_n \end{aligned}$$

is formed. The coefficients $\sigma_1, \dots, \sigma_n$ are defined as the elementary symmetric functions of x_1, \dots, x_n .

If the σ_i 's are calculated, it is found that:

$$\sigma_1 = \sum_{i=1}^n x_i$$

$$\sigma_2 = \sum x_i x_j \text{ for all different combinations of } i \text{ and } j$$

$$\sigma_3 = \sum x_i x_j x_k \text{ for all different combinations of } i, j, k.$$

-
-
-

$$\sigma_n = x_1 x_2 \dots x_n,$$

If any two numbers x_i and x_j are interchanged, the values of the symmetric functions remain the same. Therefore, the functions $\sigma_1, \dots, \sigma_n$ are said to be symmetric with respect to the variables x_1, \dots, x_n .

Definition 20: Power Sum Symmetric Functions—Given the set of numbers x_1, \dots, x_n , the k^{th} power sum symmetric function of these numbers is

$$S_k = \sum_{i=1}^n x_i^k.$$

The elementary symmetric functions and power sum symmetric functions are related by a set of linear equations known as Newton's identities. Using the factored form of $\sigma(x)$,

$$\frac{d\sigma}{dx} = \frac{\sigma}{x - x_1} + \frac{\sigma}{x - x_2} + \dots + \frac{\sigma}{x - x_n}.$$

Since

$$\sigma(x_i) = 0,$$

$$\sigma(x) = (x^n - x_i^n) - \sigma_1 (x^{n-1} - x_i^{n-1}) + \dots,$$

and

$$\frac{\sigma(x)}{x - x_i} = x^{n-1} + (x_i - \sigma_1) x^{n-2} + (x_i^2 - \sigma_1 x_i + \sigma_2) x^{n-3} + \dots,$$

and

$$\frac{d\sigma}{dx} = nx^{n-1} + (S_1 - n\sigma_1) x^{n-2} + (S_2 - \sigma_1 S_1 + n\sigma_2) x^{n-3} + \dots.$$

From the unfactored form,

$$\frac{d\sigma}{dx} = nx^{n-1} - (n-1)\sigma_1 x^{n-2} + (n-2)\sigma_2 x^{n-3} + \dots.$$

Equating coefficients of like powers of x in these two expressions gives

$$S_1 - n\sigma_1 = -(n-1)\sigma_1$$

$$S_2 - \sigma_1 S_1 + n\sigma_2 = (n-2)\sigma_2$$

-
-
-

$$S_{n-1} - \sigma_1 S_{n-2} + \sigma_2 S_{n-3} - \dots + (-1)^{n-1} n\sigma_{n-1} = (-1)^{n-1} \sigma_{n-1},$$

or

$$S_1 - \sigma_1 = 0$$

$$S_2 - \sigma_1 S_1 + 2\sigma_2 = 0$$

•
•
•

$$S_{n-1} - \sigma_1 S_{n-2} + \sigma_2 S_{n-3} - + \dots + (-1)^{n-1} (n-1) \sigma_{n-1} = 0.$$

Shortened BCH Codes

Codes of different length than $p^m - 1$ may be desired because of equipment on format specifications. These are obtained easily by making some of the initial information symbols 0 in an unshortened BCH code and not transmitting these symbols. Since the shortened words are still code vectors, the minimum Hamming distance remains unchanged, and the error correction and detection capabilities are unchanged. Encoding and decoding procedures for the natural length codes also apply to the shortened codes.

An alternative method for obtaining codes of different length is to choose α as a non-primitive element of $GF(p^m)$. A table of some binary BCH codes, generated by nonprimitive elements, can be found in Peterson (Reference 10).

Appendix

Example of Triple-Error Correcting (15, 5) BCH Code

Let α be a root of the primitive polynomial $m_1(x) = x^4 + x + 1$. Then any element in $GF(2^4)$ can be represented in the form

$$c_0 + c_1 \alpha + c_2 \alpha^2 + c_3 \alpha^3.$$

The following table shows this representation of $GF(2^4)$:

	c_0	c_1	c_2	c_3
1	1	0	0	0
α	0	1	0	0
α^2	0	0	1	0
α^3	0	0	0	1
α^4	1	1	0	0
α^5	0	1	1	0
α^6	0	0	1	1
α^7	1	1	0	1
α^8	1	0	1	0
α^9	0	1	0	1
α^{10}	1	1	1	0
α^{11}	0	1	1	1
α^{12}	1	1	1	1
α^{13}	1	0	1	1
α^{14}	1	0	0	1
α^{15}	1	0	0	0

According to Theorem II, α , α^2 , α^4 , and α^8 are roots of the same polynomial. Therefore, the minimum polynomial for each of these elements is $m_1(x) = x^4 + x + 1$. If α^3 , α^6 , α^{12} , and $\alpha^{24} = \alpha^9$, all must be roots of the minimum polynomial $m_3(x)$ for α^3 . If

$$m_3(x) = c_0 + c_1 x + c_2 x^2 + c_3 x^3 + x^4,$$

then

$$m_3(\alpha^3) = c_0 + c_1 \alpha^3 + c_2 \alpha^6 + c_3 \alpha^9 + \alpha^{12} = 0.$$

A tabular representation is shown below:

$$c_0 \begin{bmatrix} 1 \\ 0 \\ 0 \\ 0 \end{bmatrix} + c_1 \begin{bmatrix} 0 \\ 0 \\ 0 \\ 1 \end{bmatrix} + c_2 \begin{bmatrix} 0 \\ 0 \\ 1 \\ 1 \end{bmatrix} + c_3 \begin{bmatrix} 0 \\ 1 \\ 0 \\ 1 \end{bmatrix} + \begin{bmatrix} 1 \\ 1 \\ 1 \\ 1 \end{bmatrix} = \begin{bmatrix} 0 \\ 0 \\ 0 \\ 0 \end{bmatrix}$$

The solution of this set of four equations is $c_0 = 1$, $c_1 = 1$, $c_2 = 1$, and $c_3 = 1$, so $m_3(x) = 1 + x + x^2 + x^3 + x^4$.

The elements α^5 and α^{10} are the roots of

$$\begin{aligned} m_5(x) &= (x - \alpha^5)(x - \alpha^{10}) = x^2 + (\alpha^5 + \alpha^{10})x + \alpha^{15} \\ &= x^2 + x + 1. \end{aligned}$$

Let $m_0 = 1$ and $d = 7$, then $\alpha, \alpha^2, \dots, \alpha^6$ must be roots of $g(x)$. Therefore,

$$\begin{aligned} g(x) &= m_1(x) m_3(x) m_5(x) \\ &= x^{10} + x^8 + x^5 + x^4 + x^2 + x + 1. \end{aligned}$$

The minimum polynomials could have been found directly from the tables in Peterson (Reference 10) and $g(x)$ from Stenbit (Reference 11).

The circuit shown in Figure 5 can be used for encoding. The five information digits are simultaneously shifted into the register and transmitted over the channel. Since this circuit automatically premultiplies its input by x^{10} , the check bits $I(x) \bmod g(x)$ remain in the register after the information bits have been shifted into it. The feedback is then disabled, and the check bits are transmitted over the channel.

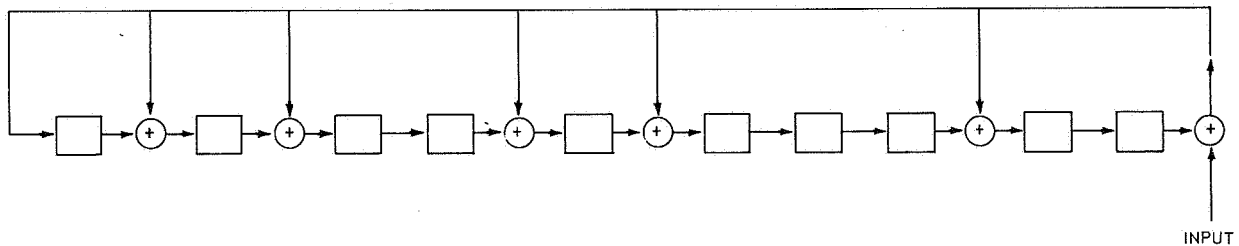


Figure 5—Encoding circuit for (15, 5) BCH code.

An identical circuit can be used for error detection except that the entire 15-bit received vector $r(x)$ is shifted into the register. The circuit calculates $x^{10} r(x) \bmod g(x)$. For error correction, the input must be added into the first stage of the register, rather than at the end, so that $r(x) \bmod g(x)$ is calculated.

REFERENCES

1. Hocquenghem, A., "Codes Correcteurs d'erreurs," *Chiffres* 2:147-156, September 1959.
2. Bose, R. C., and Ray Chaudhuri, P. K., "On a Class of Error Correcting Binary Group Codes," *Information and Control*, 3, pp. 68-79, 1960.
3. Bose, R. C., and Ray Chaudhuri, P. K., "Further Results on Error Correcting Binary Group Codes," *Information and Control* 3:279-290, 1960.
4. Peterson, W. W., "Encoding and Error-correction Procedures for BCH Codes," *IRE Transactions on Information Theory* IT-6:459-470, September 1960.
5. Zieler, N., "A Class of Cyclic Linear Error-Correcting Codes in p^m Symbols," MIT Lincoln Labs Group Report 55-19, Lexington, Mass., January 1960.
6. Zieler, N., and Gorenstein, D., "A Class of Error-Correcting Codes in p^m Symbols," *J. SIAM* 9(2):207-214, June 1961.
7. Chien, R. T., "Cyclic Decoding Procedures for Bose-Chaudhuri-Hocquenghem Codes," *IEEE Transactions on Information Theory* IT-10:357-363, October 1964.
8. Massey, J. L., "Step-by-Step Decoding of the Bose-Chaudhuri-Hocquenghem Codes," *IEEE Transactions on Information Theory* IT-11:580-585, October 1965.
9. Forney, G. D., "On Decoding BCH Codes," *IEEE Transactions on Information Theory* IT-11:549-557, October 1965.
10. Peterson, W. W., *Error Correcting Codes*, MIT Press and John Wiley & Sons, Inc., 1961.
11. Stenbit, J. P., "Table of Generators for Bose-Chaudhuri Codes," *IEEE Transactions on Information Theory*, IT-10(4):390-391, October 1964.
12. Bochner, M., *Introduction to Higher Algebra*, Chapter 18, Macmillan Co., New York, 1907.
13. Wozencraft, J. M., and Jacobs, I. M., *Principles of Communication Engineering*, New York: John Wiley and Sons, 1965, pp. 441-443.

BIBLIOGRAPHY

- Bartee, T. C., and Schneider, D. I., "An Electronic Decoder for Bose-Chaudhuri-Hocquenghem Error Correcting Codes," IEEE Transactions on Information Theory IT-8(5):517-24, September 1962.
- Berlekamp, E. R., "On Decoding Binary Bose-Chaudhuri-Hocquenghem Codes," IEEE Transactions on Information Theory IT-11(4):577-580, October 1965.
- Bose, R. C., and Kuebler, R. R., "On the Construction of a Class of Error Correcting Binary Signaling Codes," Technical Report, University of North Carolina, Chapel Hill, N.C., May 1958.
- Bose, R. C., and Shrikhande, S. S., "A Note on a Result in the Theory of Code Construction," Information and Control 2:183-184, 1959.
- Chien, R. T., and Tang, D. T., "On Detecting Errors After Correction," Proceedings of the IEEE 62:974, August 1964.
- Chien, R. T., and Lum, V., "On Golay's Perfect Codes and Step-by-Step Decoding," IEEE Transactions on Information Theory IT-2:403-404, July 1966.
- Forney, G. P., "Generalized Minimum Distance Decoding," IEEE Transactions on Information Theory IT-12:125-131, April 1966.
- Gross, A. J., "Augmented Bose-Chaudhuri Codes which Correct Single Bursts of Errors," IEEE Transactions on Information Theory IT-9(2):121, April 1963.
- Mattson, H. F., and Solomon, G., "A New Treatment of Bose-Chaudhuri Codes," J. SIAM 9:654-670, December 1961.
- Peterson, W. W., and Massey, J. L., "Coding Theory, URSI Report of Progress in Information Theory in the United States, 1960-1963," IEEE Transactions on Information Theory IT-9:223-229, 1963.
- Polinghorn, F., "Decoding of Double and Triple Error Correcting Bose-Chaudhuri Codes," IEEE Transactions on Information Theory, IT-2(4):480-482, October 1966.
- Reed, I. S., and Solomon, G., "Polynomial Codes Over Certain Finite Fields," J. SIAM 8:300-304, 1960.
- Szwaja, Z., "On Step-by-Step Decoding of BCH Binary Codes," IEEE Transactions on Information Theory IT-13(2):350-351, April 1967.



PRECEDING PAGE BLANK NOT FILMED.

COHERENT DEMODULATION OF SPLIT-PHASE TELEMETRY SIGNALS

Fred M. Sobotkin*

ABSTRACT

This paper considers the problem of coherent demodulation for a split-phase telemetry signal in the presence of additive white gaussian noise. The performance of a self-synchronized communication system which could be used to extract the digital information from the received signal is discussed. The system contains a square-law device to remove the data dependence of the signal to obtain a discrete frequency sinusoid which is then tracked by a phase-lock loop to generate the timing information. The system bit error probability is then calculated for signal-to-noise ratios in the phase-lock loop ranging from 0 to 10 db.

INTRODUCTION

Split-phase modulation is one type of binary-phase modulation used by Goddard in satellite and space-probe telemetry systems. The data, $m(t)$, to be transmitted is a binary sequence whose value during a particular baud length of T seconds is either 0 or 1. The modulator on board the satellite maps the message $m(t)$ into a split-phase signal $s(t)$ (Figure 1) which in turn is used to phase-modulate a carrier that is transmitted over the channel to a ground station.

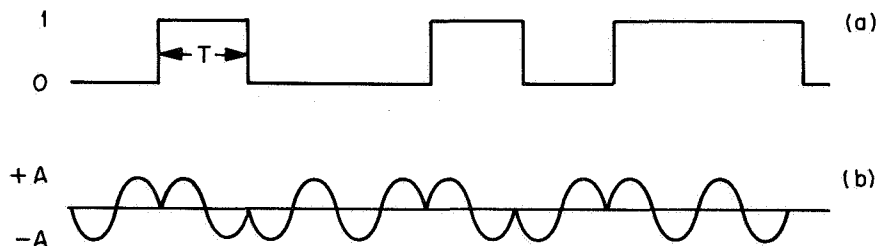


Figure 1—(a) Information sequence $m(t) = [01001011]$ and (b) split-phase signal $s(t)$.

The transmitted signal may therefore be written as

$$f(t) = \cos [\omega_c t + s(t)].$$

The split-phase signal $s(t)$ is constructed by multiplying a subcarrier

$$\sin \omega_m t, \quad (\omega_m = 2\pi/T),$$

*The City College of The City University of New York.

which is in phase with $m(t)$, by $+A$ when $m(t) = 1$ and by $-A$ when $m(t) = 0$. Therefore, the split-phase signal can be represented by

$$s(t) = P(t) \sin \omega_m t,$$

where $P(t)$ is either $\pm A$ in a particular baud.

When the telemetry signal is received at the ground station, it is phase-demodulated to obtain the split-phase signal $s(t)$, which is assumed to be degraded by additive noise $N(t)$, a stationary wideband gaussian process of zero mean with flat spectral density $N_0/2$ watts/Hz. The problem of interest to Goddard is the extraction of the message $m(t)$ from the waveform

$$x_1(t) = s(t) + N(t) = P(t) \sin \omega_m t + N(t).$$

when the signal-to-noise ratio is small.

For detection and processing of the split-phase signal, it is necessary to have a "clock" that is coherent with the bit rate. Phase-lock techniques are widely used to obtain the synchronizing information (clock) from the received waveform. But examination of the spectrum of the split-phase signal (Appendix A) indicates that there are no discrete frequency components present to be tracked and used for timing purposes. To obtain the synchronizing signal, we must first perform some non-linear operation on the signal to remove its dependence on the data and produce a discrete sinusoid.

A self-synchronized system that could be used for coherent detection and demodulation of the signal $s(t)$ is shown in Figure 2.

The following is a brief description of the system operation in the absence of noise. The received signal $s(t)$ is assumed to be unchanged after passing through the filter $H_1(\omega)$ because 94 percent (Appendix A) of the total power is concentrated in the passband. The input to the square-law device is

$$s(t) = P(t + \theta/\omega_m) \sin(\omega_m t + \theta),$$

where θ is an arbitrary phase caused by transmission. The output

$$y(t) = A^2 \sin^2(\omega_m t + \theta) = A^2/2 [1 - \cos(2\omega_m t + 2\theta)].$$

The discrete frequency component $\cos(2\omega_m t + 2\theta)$ is then tracked by the phase-lock loop and the output of the Voltage-Controlled Oscillator (VCO) is

$$v = \sin(\omega_m t + \theta + \phi/2),$$

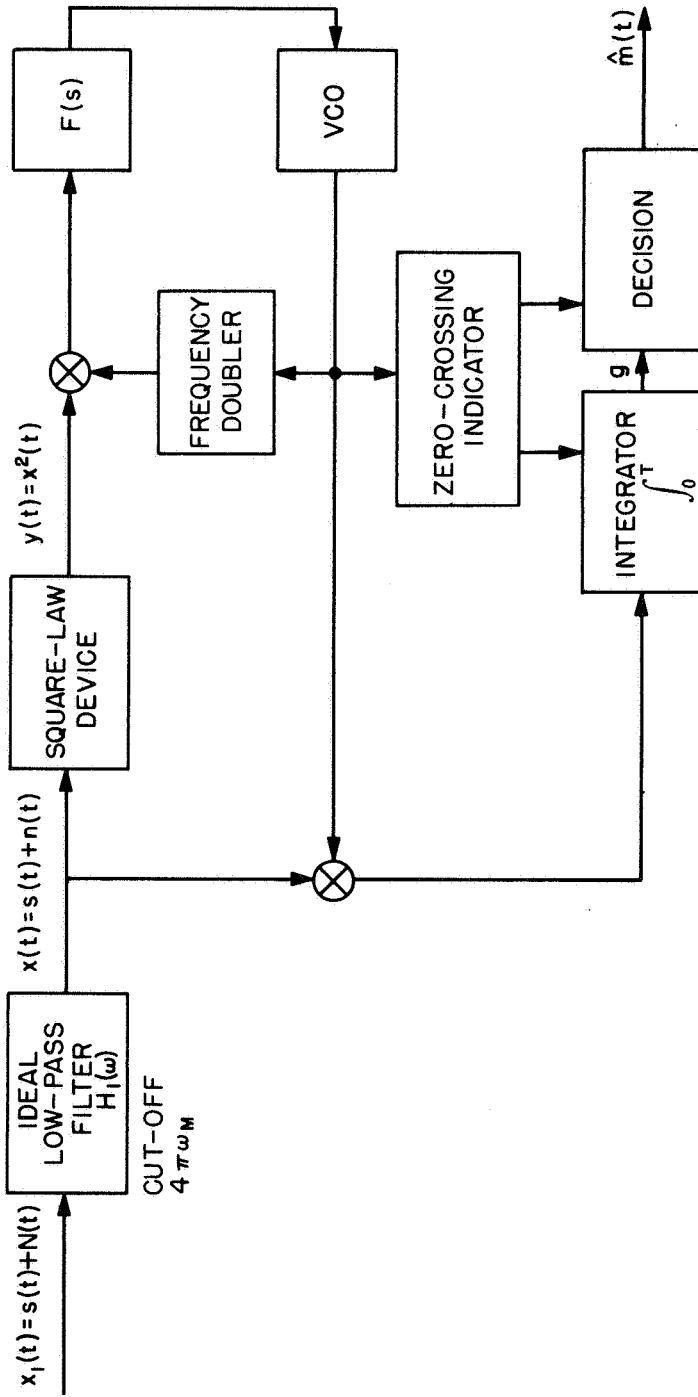


Figure 2-Self-synchronized communication system for split-phase signals.

where ϕ equals the phase error of the loop. This waveform is multiplied by $s(t)$ and applied to an integrator which obtains its timing information from the zero-crossings of v . Thus,

$$g = \int_0^T \pm A \sin(\omega_m t + \theta) [\sin(\omega_m t + \theta + \phi/2)] dt$$

$$= \int_0^T \pm A/2 [\cos(\phi/2) - \cos(2\omega_m t + 2\theta + \phi/2)] dt.$$

It is assumed that both θ and ϕ are varying very slowly ($d\theta/dt, d\phi/dt \ll \omega_m$) and may be considered constant over the interval $(0, T)$. Therefore

$$g = \pm \frac{AT}{2} \cos \frac{\phi}{2}.$$

If g is positive, we decide that $\hat{m}(t) = 1$; and if g is negative, then $\hat{m}(t) = 0$.

It should be pointed out, before continuing, that the timing of the system could be in error by $T/2$ seconds because of the frequency doubler in the loop. The frequency doubler output would have the same value if

$$v = \sin\left(\omega_m t + \theta + \frac{\phi}{2} \pm \pi\right) \quad \text{or} \quad v = \sin\left(\omega_m t + \theta + \frac{\phi}{2}\right)$$

However, if this timing error did occur, the integrator output would be zero for most of the decision times and a correction could be made to advance the timing.

OPERATION WITH NOISE PRESENT

The split-phase signal plus noise $N(t)$ is passed through the ideal low-pass filter $H_1(\omega)$ to eliminate the undesirable effects of the noise outside the frequency band of interest. The input to the square-law device is

$$x(t) = s(t) + n(t),$$

where $n(t)$ is a stationary gaussian process with flat spectral density $N_0/2$ watts/Hz over the band of $H_1(\omega)$ and zero outside. The input signal-to-noise ratio is

$$\text{SNR}_x = \frac{\pi A^2}{2N_0 \omega_m}.$$

After passing through the square-law device, we obtain

$$y(t) = [s(t) + n(t)]^2$$

with a spectral density as calculated in Appendix B, where it is also shown that the input to the phase-lock loop may be considered to be

$$y_1(t) = -\sqrt{2P} \cos 2\omega_m t + n'(t).$$

The value of $P=A^4/8$ watts, and $n'(t)$ is a zero mean gaussian process with flat spectral density

$$\frac{N'_0}{2} = \frac{1.53 N_0 A^2}{\pi} + \frac{N_0^2 \omega_m}{4\pi}$$

over the effective bandwidth of the phase-lock loop.

3. The phase-lock loop used to obtain the reference or timing signal is shown in Figure 3.

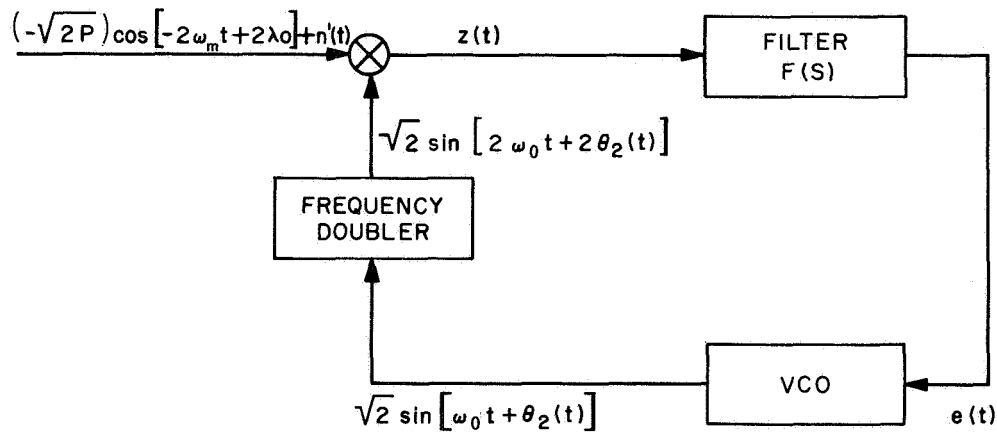


Figure 3-Phase-lock loop.

The VCO has a quiescent frequency ω_0 radians/sec and a VCO constant $K/2$ radians/sec/volt. Therefore

$$\frac{d\theta_2(t)}{dt} = \frac{K}{2} e(t).$$

The noise component $n'(t)$ can be expressed as

$$n'(t) = \sqrt{2} n_1(t) \sin(2\omega_m t + 2\lambda_0) + \sqrt{2} n_2(t) \cos(2\omega_m t + 2\lambda_0),$$

where $n_1(t)$ and $n_2(t)$ are both stationary, white gaussian processes with spectral density (double sided) $(N'_0/2)$ watts/Hz.

We now let

$$\omega t + \lambda_0 = \omega_0 t + \theta_1(t),$$

where λ_0 is an arbitrary phase caused by transmission. The multiplier output is

$$\begin{aligned} z(t) &= \left\{ -\sqrt{2P} \cos[2\omega_0 t + 2\theta_1(t)] + \sqrt{2} n_1(t) \sin[2\omega_0 t + 2\theta_1(t)] \right. \\ &\quad \left. + \sqrt{2} n_2(t) \cos[2\omega_0 t + 2\theta_1(t)] \right\} \left\{ \sqrt{2} \sin[2\omega_0 t + 2\theta_2(t)] \right\} \\ &= -\sqrt{P} \sin\{2[\theta_2(t) - \theta_1(t)]\} + 2n_1(t) \cos 2[\theta_2(t) - \theta_1(t)] \\ &\quad + n_2(t) \sin 2[\theta_2(t) - \theta_1(t)] + 4\omega_0 \text{ frequency terms.} \end{aligned}$$

The $4\omega_0$ frequency terms may be neglected since neither the filter $F(s)$ nor the VCO will respond significantly to them.

Letting $\phi(t) = 2[\theta_2(t) - \theta_1(t)]$ loop phase error,

$$\frac{d\phi(t)}{dt} = 2 \left(\frac{d\theta_2(t)}{dt} - \frac{d\theta_1(t)}{dt} \right) = Ke(t) - 2(\omega_m - \omega_0),$$

where

$$e(t) = F(s) [-\sqrt{P} \sin \phi(t) + n_1(t) \cos \phi(t) + n_2(t) \sin \phi(t)].$$

Therefore

$$\frac{d\phi(t)}{dt} = KF(s) [-\sqrt{P} \sin \phi(t) + n_1(t) \cos \phi(t) + n_2(t) \sin \phi(t)] - 2(\omega_m - \omega_0).$$

Since $n_1(t)$ and $n_2(t)$ have a correlation time much shorter than $\phi(t)$, the noise component can be represented by a gaussian process $n''(t)$ which has the same statistics and spectral density as $n_1(t)$ or $n_2(t)$. Therefore

$$\frac{d\phi(t)}{dt} = -KF(s) [\sqrt{P} \sin \phi(t) + n''(t)] - 2(\omega_m - \omega_0).$$

A second-order loop is the best compromise between acquisition of a signal in the presence of noise and the maintaining of lock on a weak signal. We therefore choose our loop filter to be $F(s) = 1 + a/s$, which consists of the parallel combination of an ideal integrator with gain "a" and a direct connection. The equation for $d\phi/dt$ becomes

$$\frac{d\phi}{dt} = -K [\sqrt{P} \sin \phi(t) + n''(t)] - aK \int_0^t [\sqrt{P} \sin \phi(\lambda) + n''(\lambda)] d\lambda - 2(\omega_m - \omega_0).$$

Statistical parameters for the phase-error behavior of a phase-lock loop tracking a constant frequency signal in the presence of additive stationary Gaussian noise have been obtained by Viterbi (Reference 1) by treating the problem as a continuous random walk with a sinusoidal restoring force. He shows that the second order differential equation representing the phase error $\phi(t)$, can be decomposed into two first order equations to constitute a two-dimensional vector Markov process for which he derives the Fokker-Planck equations. He then goes on to obtain an approximate solution for the steady-state phase-error distribution for the special case when $\omega_m = \omega_0$. Therefore the VCO quiescent frequency is exactly at the frequency of the incoming signal. In this report, we will assume that the baudlength T is known exactly and ω_0 will be set equal to ω_m so that we may use Vitterbi's result for the probability density function of the phase error

$$P_\phi(\phi) = \frac{e^{[R \cos \phi]}}{2\pi I_0(R)} \quad -\pi < \phi < \pi,$$

where I_0 is the zeroth-order modified Bessel function and

$$R = \frac{P}{N'_0(\sqrt{PK} + a)/4}.$$

The equivalent noise-bandwidth of this second order loop is $B_L = (\sqrt{PK} + a)/4$ Hz and therefore $R = P/(N'_0 B_L)$, which is the signal-to-noise ratio in the effective bandwidth of the loop.

Viterbi indicates that $P_\phi(\phi)$ is valid only for large values of SNR (R) because of a linear approximation he made in his solution of the Fokker-Planck equation. However, experimental results (Reference 7) substantiate that $P_\phi(\phi)$ is a good approximation for SNR $R > 0$ db.

As the phase error in the loop increases, there is a tendency for the loop VCO to gain or drop a cycle relative to the incoming signal. When this occurs, the phase-error

has changed by 2π radians and the loop has dropped out of lock. Viterbi obtained an expression for the mean time to loss of lock

$$T(2\pi) = \frac{\pi^2 R I_0^2 (R)}{2 B_L}$$

But this gives no indication of loop behavior after the first skipped cycle because we do not know whether the loop goes back to its locked state or keeps on skipping cycles at an ever-increasing rate. At low values of signal-to-noise ratio (R) it is expected that the latter is likely to occur, because of the system inertia. The system would therefore lose synchronization and a good deal of data bits would be lost.

It would be impossible to obtain analytically complete detailed information about the system operation with respect to cycle slippage and lock acquisition or pull-in. System simulation is the only means of obtaining these results, and should be done in future studies.

EXPECTED PROBABILITY OF BIT-ERROR

An estimate of the expected probability of bit errors (Table 1) can be obtained by use of the distribution of the phase-lock loop error $\phi(t)$. The output of the integrator g (Figure 2) is obtained by multiplying the VCO response by $x(t) = s(t) + n(t)$ and then integrating over the baud length T . Therefore

$$\begin{aligned} g &= \sqrt{2} \int_0^T x(t) \sin\left(\omega_m t + \frac{\phi}{2}\right) dt \\ &= \pm \sqrt{2} A \int_0^T \sin \omega_m t \sin\left(\omega_m t + \frac{\phi}{2}\right) dt + \sqrt{2} \int_0^T n(t) \sin\left(\omega_m t + \frac{\phi}{2}\right) dt \\ &= \frac{\sqrt{2}}{2} P(t) \int_0^T \cos \frac{\phi}{2} dt - \frac{\sqrt{2}}{2} P(t) \int_0^T \cos\left(2\omega_m t + \frac{\phi}{2}\right) dt + \sqrt{2} \int_0^T n(t) \sin\left(\omega_m t + \frac{\phi}{2}\right) dt. \end{aligned}$$

Since $d\phi(t)/dt \ll \omega_m$, the value of $\phi(t)$ is essentially constant over the baud T , and therefore

$$\begin{aligned} \int_0^T \cos \frac{\phi}{2} dt &= T \cos \frac{\phi}{2} \\ \int_0^T \cos\left(2\omega_m t + \frac{\phi}{2}\right) dt &= 0 \\ \int_0^T n(t) \sin\left(\omega_m t + \frac{\phi}{2}\right) dt &= \tilde{n}, \end{aligned}$$

where \tilde{n} is a gaussian random variable with zero-mean and variance σ^2 . Before proceeding further, we must calculate the value of σ^2 , the expected value of $\cos \phi(t)/2$, and a relationship between the signal-to-noise ratio in the loop (R) and the signal-to-noise ratio of $x(t)$ (SNR_x).

The transfer function of the integrator

$$H(j\omega) = \frac{1}{j\omega} [1 - e^{-j\omega T}]$$

and

$$|H(j\omega)|^2 = \frac{4 \sin^2 \omega T/2}{\omega^2}$$

Since the autocorrelation of the process $\sqrt{2} n(t) \sin(\omega_m t + \phi/2)$ equals $R_n(\tau) \cos \omega_m \tau$,

$$\begin{aligned} \sigma^2 &= \frac{N_0}{2\pi} \left(\int_{-3\omega_m}^{3\omega_m} \frac{\sin^2 \omega T/2}{\omega^2} d\omega + \int_{-\omega_m}^{\omega_m} \frac{\sin^2 \omega T/2}{\omega^2} d\omega \right) \\ &= \frac{N_0}{\omega_m} (2.936) = \frac{1.468 \pi A^2}{\omega_m^2 (\text{SNR}_x)} \end{aligned}$$

The probability density of \tilde{n} is

$$P_{\tilde{n}} = \frac{e^{-n^2/2\sigma^2}}{\sqrt{2\pi}\sigma}$$

The expected value of $\cos \phi(t)/2$ is

$$E \left\{ \cos \frac{\phi}{2} \right\} = \int_{-\pi}^{+\pi} \cos \frac{\phi}{2} P_{\phi}(\phi) d\phi,$$

where

$$P_{\phi}(\phi) = \frac{e^{R \cos \phi}}{2\pi I_0(R)} = \frac{1}{2\pi I_0(R)} \left[I_0(R) + 2 \sum_{n=1}^{\infty} I_n(R) \cos n\phi \right]$$

Therefore

$$\begin{aligned} E \left\{ \cos \frac{\phi}{2} \right\} &= \frac{1}{2\pi I_0(R)} \int_{-\pi}^{+\pi} \cos \frac{\phi}{2} \left[I_0(R) + 2 \sum_{n=1}^{\infty} I_n(R) \cos n\phi \right] d\phi \\ &= \frac{1}{2\pi I_0(R)} \left[4 I_0(R) - 2 \sum_{n=1}^{\infty} \frac{(-1)^n}{n^2 - 1/4} I_n(R) \right] \end{aligned}$$

which is a series that converges very rapidly.

The value of R can be expressed in terms of SNR_x .

$$\frac{1}{R} = \frac{B_L}{\omega_m (\text{SNR}_x)} \left[12.24 + \frac{\pi}{(\text{SNR}_x)} \right]$$

when

$$R < 10,$$

$$R \approx \frac{\omega_m}{\pi B_L} (\text{SNR}_x)^2$$

In practice, B_L is chosen to be 0.1 percent of $f_m = 2\pi\omega_m$, and therefore

$$R \approx 500 \left(\frac{\text{SNR}_x}{\pi} \right)^2$$

The decision as to whether the data bit is 0 or 1 in the baud interval will be based on the sign of g . If g is positive, then $\hat{m}(t) = 1$, and if g is negative $\hat{m}(t) = 0$. An error will occur if the value of the random variable n causes the sign of g to change from its value determined by $\sqrt{2}/2 P(t) E\{\cos \phi/2\}$. Therefore, the probability of a bit error

$$P_E = \text{Prob}\left(P(t) = +A \text{ and } n < -\frac{\sqrt{2}}{2} ATE \left\{ \cos \frac{\phi}{2} \right\}\right) \\ + \text{Prob}\left(P(t) = -A \text{ and } n > \frac{\sqrt{2}}{2} ATE \left\{ \cos \frac{\phi}{2} \right\}\right)$$

Since n has zero mean, is independent of $P(t)$, and $P(t) = \pm A$ with equal probability

$$P_E = \text{Prob}\left(n > \frac{\sqrt{2}}{2} ATE \left\{ \cos \frac{\phi}{2} \right\}\right) \\ = \frac{1}{\sqrt{2\pi}\sigma} \int_{\frac{\sqrt{2}}{2} ATE \left\{ \cos \frac{\phi}{2} \right\}}^{\infty} e^{-n^2/2\sigma^2} \\ P_E = \frac{1}{\sqrt{\pi}} \int_{\sqrt{\frac{\pi (\text{SNR}_x)}{1.468}} E \left\{ \cos \frac{\phi}{2} \right\}}^{\infty} e^{-n^2} dn$$

where

$$E \left\{ \cos \frac{\phi}{2} \right\} \sqrt{\frac{\pi(\text{SNR}_x)}{1.468}} = \sqrt{1/2 \text{ the signal-to-noise ratio at integrator output}}$$

Table 1
Expected probability of bit errors for phase-lock
loop SNR (R) ranging from 0-10 db.

R	R (db)	SNR _x db	P _E
1	0	-8.54	.306
2	3.01	-7.01	.202
3	4.77	-6.14	.170
4	6.02	-5.51	.147
5	7.00	-5.03	.135
6	7.80	-4.63	.124
7	8.50	-4.30	.112
8	9.03	-4.01	.104
9	9.80	-3.75	.097
10	10.00	-3.53	.091

R = signal-to-noise ratio in the phase-lock loop

SNR_x = signal-to-noise ratio of received split-phase
 signal after initial filtering

P_E = expected probability of bit-errors

APPENDIX A

CHARACTERISTICS OF A SPLIT-PHASE SIGNAL

The split-phase signal can be represented by

$$s(t) = P(t) \sin \omega_m t$$

where $P(t)$ is a Random Binary Signal whose value is $\pm A$ with equal probability in the interval

$$(n-1)T \leq t < T \quad \left(T = \frac{2\pi}{\omega_m} \right)$$

The value of $P(t)$ during any interval of baud length T is independent of the values in all other intervals.

To obtain the spectrum of $s(t)$, we consider the process

$$s\left(t + \frac{\theta}{\omega_m}\right) = P\left(t + \frac{\theta}{\omega_m}\right) \sin(\omega_m t + \theta),$$

where θ is a random variable uniformly distributed in the $(0, 2\pi)$ interval, and since $T = 2\pi/\omega_m$, θ/ω_m is uniformly distributed in the $(0, T)$ interval. The random phase θ would correspond to the uncertainty of the time origin of the received signal.

The autocorrelation function of the process $s(t + \theta/\omega_m)$ is

$$R_s(\tau) = E \left\{ P\left(t + \frac{\theta}{\omega_m}\right) P\left(t + \frac{\theta}{\omega_m} + \tau\right) \sin(\omega_m t + \theta) \sin[\omega_m(t + \tau) + \theta] \right\},$$

where $E\{\}$ denotes the expectation. Since $P(t + \theta/\omega_m)$ is statistically independent of θ

$$R_s(\tau) = E \left\{ P\left(t + \frac{\theta}{\omega_m}\right) P\left(t + \frac{\theta}{\omega_m} + \tau\right) \right\} E \left\{ \sin(\omega_m t + \theta) \sin[\omega_m(t + \tau) + \theta] \right\}$$

If the autocorrelation of $P(t + \theta/\omega_m) = R_p(\tau)$,

$$\begin{aligned}
R_s(\tau) &= R_p(\tau) E \left\{ \frac{1}{2} \cos \omega_m \tau + \frac{1}{2} \cos (2\omega_m t + \omega_m \tau + 2\tilde{\theta}) \right\} \\
&= \frac{1}{2} R_p(\tau) \cos \omega_m \tau + \frac{1}{4\pi} \int_0^{2\pi} \cos [2\omega_m t + \omega_m \tau + 2\tilde{\theta}] d\theta \\
&= \frac{1}{2} R_p(\tau) \cos \omega_m \tau.
\end{aligned}$$

To determine $R_p(\tau)$, we let $P_1(t) = P(t + \tilde{\theta}/\omega_m)$ and consider the process at two different instants of time, $P_1(t_1)$, $P_1(t_2)$. Since the process is independent in different baud intervals and $E\{P_1(t_1)\} = E\{P_1(t_2)\} = 0$, the $E\{P_1(t_1) P_1(t_2)\}$ will equal zero if t_1 and t_2 are located in different bauds and equal A^2 if they are in the same baud.

Suppose first that $|t_1 - t_2| > T$. Since $\tilde{\theta}/\omega_m < T$,

$$E\{P_1(t_1) P_1(t_2) | \tilde{\theta}/\omega_m\} = 0$$

and the

$$E\{E\{P_1(t_1) P_1(t_2) | \tilde{\theta}/\omega_m\}\} = 0.$$

If $|t_1 - t_2| < T$ and $t_1 = nT$, then only for $\tilde{\theta}/\omega_m < T - |t_1 - t_2|$ will t_1 and t_2 be located in the same interval

$$E\left\{P_1(t_1) P_1(t_2) \frac{\tilde{\theta}}{\omega_m}\right\} = \begin{cases} A^2 & \text{for } \frac{\tilde{\theta}}{\omega_m} < T - |t_1 - t_2| \\ 0 & \text{otherwise} \end{cases}$$

Therefore

$$\begin{aligned}
E\{P_1(t_1) P_1(t_2)\} &= A^2 \cdot \text{Probability} \left[\frac{\tilde{\theta}}{\omega_m} < T - |t_1 - t_2| \right] \\
&= A^2 \left(1 - \frac{|t_1 - t_2|}{T} \right) \quad \text{for } |t_1 - t_2| < T, \\
&= 0 \quad \text{for } |t_1 - t_2| > T.
\end{aligned}$$

Since the process is stationary, we can replace $t_1 - t_2$ by τ :

$$R_p(\tau) = A^2 \left(1 - \frac{|\tau|}{T}\right) \quad |\tau| < T$$

$$= 0 \quad \tau > T,$$

and

$$R_s(\tau) = \frac{1}{2} A^2 \left[1 - \frac{|\tau|}{T}\right] \cos \omega_m \tau \quad |\tau| < T$$

$$= 0 \quad |\tau| > T.$$

The spectral density of $s(t)$,

$$S_s(\omega) = \int_{-\infty}^{+\infty} \frac{1}{2} R_p(\tau) \cos \omega_m \tau e^{-j\omega\tau} d\tau$$

$$= \frac{1}{4} [S_p(\omega - \omega_m) + S_p(\omega + \omega_m)],$$

where

$$S_p(\omega) = A^2 \int_{-T}^{+T} \left(1 - \frac{|\tau|}{T}\right) e^{-j\omega\tau} d\tau$$

$$= \frac{A^2 T \sin^2(\omega T/2)}{(\omega T/2)^2}.$$

Inspection of $S_s(\omega)$ indicates that most of the signal power is concentrated in the frequency band

$$|2\pi\omega| < 4\pi\omega_m,$$

and

$$\frac{1}{2\pi R_s(0)} \int_{-2\omega_m}^{2\omega_m} S_s(\omega) d\omega = 0.94.$$

Since 94 percent of the total power is in this band, the signal may be considered to be band-limited to $|2\pi\omega| < 4\pi\omega_m$.

APPENDIX B

CHARACTERISTICS OF THE PHASE-LOCK LOOP INPUTS (EFFECTIVE SQUARE-LAW DEVICE OUTPUT)

Both components of the input to the square-law device, $s(t) = P(t) \sin mt$ and $n(t)$, are sample functions from statistically independent random processes with zero mean. The output $y(t) = [s(t) + n(t)]^2$.

If the autocorrelation function of $y(t) = R_y(t_1, t_2)$ and $y(t_n) = y_n$, then

$$\begin{aligned} R_y(t_1, t_2) &= E\{y_1 y_2\} = E\{(s_1 + n_1)^2 (s_2 + n_2)^2\} \\ &= E\{s_1^2 s_2^2\} + 4E\{s_1 s_2\} E\{n_1 n_2\} + \\ &\quad E\{s_1^2\} E\{n_2^2\} + E\{s_2^2\} E\{n_1^2\} + E\{n_1^2 n_2^2\} \\ &\quad + 2E\{n_2 s_1^2 s_2 + n_1 s_1 s_2^2 + s_1 n_1 n_2^2 + n_1^2 n_2 s_2\}. \end{aligned}$$

The last term equals zero because $n(t)$ and $s(t)$ have zero mean, and are independent.

$$R_y(t_1, t_2) = R_y(\tau), \text{ where } \tau = t_1 - t_2$$

because of stationarity. Therefore,

$$R_y(\tau) = R_{ss}(\tau) + 4R_s(\tau) R_n(\tau) + 2R_s(0) R_n(0)$$

with

$$R_{ss}(\tau) = E\{s_1^2 s_2^2\},$$

$$R_{nn}(\tau) = E\{n_1^2 n_2^2\}.$$

$R_y(\tau)$ contains three types of terms:

$$R_y(\tau) = R_{ss}(\tau) + R_{sn}(\tau) + R_{nn}(\tau).$$

The term $R_{ss}(\tau)$ is due to the interaction of the signal with itself; $R_{nn}(\tau)$ is due to the interaction of the noise with itself; and $R_{sn}(\tau) = 4R_s(\tau)R_n(\tau) + 2R_s(0)R_n(0)$ is due to the interaction of the signal with the noise.

The spectral density of $y(t)$ is given by

$$S_y(\omega) = S_{ss}(\omega) + S_{sn}(\omega) + S_{nn}(\omega)$$

$$S_{ss}(\omega) = \int_{-\infty}^{+\infty} R_{ss}(\tau) e^{-j\omega\tau} d\tau,$$

where

$$R_{ss}(\tau) = E\{s^2(t) s^2(t + \tau)\}$$

$$= E\{A^4 \sin^2 \omega_m t \sin^2 \omega_m (t + \tau)\}$$

$$= A^4 \left(\frac{1}{4} + \frac{1}{8} \cos 2\omega_m \tau \right);$$

therefore

$$S_{ss}(\omega) = \frac{A^4 \pi}{2} \delta(\omega) + \frac{A^4 \pi}{8} [\delta(\omega - 2\omega_m) + \delta(\omega + 2\omega_m)]$$

which contains the discrete frequency component at twice the data rate, with power $P = A^4 / 8$ watts.

$$S_{sn}(\omega) = \int_{-\infty}^{+\infty} R_{sn}(\tau) e^{-j\omega\tau} d\tau,$$

where

$$R_{sn}(\tau) = 4R_s(\tau)R_n(\tau) + 2R_s(0)R_n(0)$$

$$= 4R_s(\tau)R_n(\tau) + \frac{A^2 N_0 \omega_m}{\pi},$$

$$S_{sn}(\omega) = \frac{2}{\pi} \int_{-2\omega_m}^{2\omega_m} S_s(\omega - \lambda) \frac{N_0}{2} d\lambda + 2A^2 N_0 \omega_m \delta(\omega),$$

$$S_{nn}(\omega) = \int_{-\infty}^{+\infty} R_{nn}(\tau) e^{-j\omega\tau} d\tau,$$

where $R_{nn}(\tau) = E\{n_1 n_2 n_1 n_2\}$, but since the noise is gaussian,

$$\begin{aligned}
R_{nn}(\tau) &= E\{n_1 n_1\} E\{n_2 n_2\} + 2 E\{n_1 n_2\} E\{n_1 n_2\} \\
&= R_n^2(0) + 2 R_n^2(\tau);
\end{aligned}$$

$$S_{nn}(\omega) = \left(\frac{N_0 \omega_m}{\pi}\right)^2 2\pi \delta(\omega) + \frac{1}{2\pi} [S_n(\omega) * S_n(\omega)],$$

where * denotes convolution.

The phase-lock loop following the square-law device is used to track the discrete frequency component ($2\omega_m$) of $y(t)$. In general, the noise associated with $y(t)$ is not gaussian, however (Reference 3), if $y(t)$ is to be passed through a narrow band filter (in the steady state conditions, the phase-lock loops is in essence a very narrow band filter) having a bandwidth which is very much smaller than the bandwidth of the ideal filter preceding the square-law device, the effective noise term tends toward a gaussian process with zero mean and flat spectral density over the effective bandwidth. The value of the noise spectral density ($N'_0/2$ watts/Hz) may be approximated by its value at the center frequency of the narrow filter, $\omega = 2\omega_m$. Therefore,

$$\frac{N'_0}{2} = S_{sn}(2\omega_m) + S_{nn}(2\omega_m),$$

$$S_{sn}(2\omega_m) = \frac{N_0 A^2}{\pi} \quad (1.53),$$

$$S_{nn}(2\omega_m) = \frac{\omega_m}{\pi} \left(\frac{N_0}{2}\right)^2$$

so that

$$\frac{N'_0}{2} = \frac{1.53 N_0 A^2}{\pi} + \frac{N_0^2 \omega_m}{4\pi}.$$

CONCLUSION

The performance of a self-synchronized communication system which could be used for the demodulation of a split-phase telemetry signal has been discussed. Even with the many approximations that were made, complete detailed information about the system operation could not be obtained analytically. System simulation is the only means of obtaining complete and accurate results, and should be done in future studies. During simulation, the effects of cycle slippage and lock acquisition could be examined. Also the case where there is an uncertainty in the data frequency rate could be studied.

REFERENCES

1. Viterbi, A. J., Principles of Coherent Communication, New York: McGraw-Hill Book Co., 1966.
2. Gardner, F. M., Phaselock Techniques, New York: John Wiley and Sons, Inc., 1966.
3. Davenport, W. B., and Root, W. L., An Introduction to the Theory of Random Signals and Noise, New York: McGraw-Hill Book Co., 1958.
4. Papoulis, A., Probability, Random Variables and Stochastic Processes, New York: McGraw-Hill Book Co., 1965.
5. VanTrees, H. L., "Optimum Power Division in Coherent Communication Systems," Tech. Report 301, Lincoln Laboratory, Massachusetts Institute of Technology, Feb. 19, 1963.
6. Charles, F. J., and Lindsey, W. C., "Some Analytic and Experimental Phase-Locked Loop Results for Low Signal-to-Noise Ratios," Proc. IEEE 54 (9): 1152-1166, Sept. 1966.
7. Develet, J. A., "A Threshold Criterion for Phaselock Demodulation," Proc. IEEE 51(2): 349-356, Feb. 1963.
8. Develet, J. A., "A Note on Product Demodulation of Binary PCM/PM Signals," Space Technology Laboratories Inc., Feb. 12, 1961.

INFORMATION CAPACITY OF A HOLOGRAPHIC RECORDING SYSTEM

George Eichmann*

ABSTRACT

This report describes the capacity of a holographic recording system, based on a two-dimensional extension of the Shannon-Hartley fundamental channel capacity formula. The signal and noise power needed in this expression are determined for a photographic film recording medium. A linearized optical transmission characteristic is derived, and noise power is assumed to be caused by granularity. To calculate noise power, two stochastic grain models are given. The final result is an integral that is a function of the signal-to-noise ratio.

INTRODUCTION

Although the concept of channel capacity is well known in communication theory, its application in optical systems has been limited to incoherent optical systems (References 1, 2, and 3). However, the recent works of several authors (References 4 and 5), in considering the effect of noise on a coherent optical system, give the channel capacity of the system. The capacity serves as a figure of merit for such a system. In particular, the maximum amount of information available from a holographic recording is determined, providing results useful, for example, in optical telemetry applications.

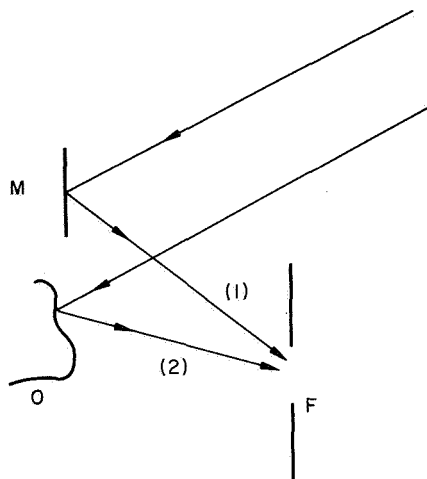
The method of calculation used in this paper is based on the use of a two-dimensional form of the Shannon-Hartley (Reference 6) fundamental channel capacity formula. By evaluating the signal and noise power of the holographic recording output, the aforementioned expression is used to derive the channel capacity of the holographic recording. The result is specialized to the case of a rotationally symmetric system. For such a system, it is shown that, for a given complex object amplitude, the desired signal and the specification of three parameters (the film cut-off line frequency, the optical bias level, and the radius of a typical grain) allow the numerical calculation of the channel capacity. These results are given in Equations 17 and 18.

DETERMINISTIC MODEL

In this section, a linear deterministic model is presented for the holographic recording process. First a qualitative, and then an analytical, description of the information storing mechanism is presented.

As shown in Figure 1, a light beam generated by a coherent source is allowed to reflect from a mirror M as well as an object O. The term "object" is used to denote the information that is to be recorded. The two scattered beams, the object and the reference beam shown are interfering constructively and destructively in front of a transparency. The transparency captures the magnitude square of the amplitude, defined as the intensity, of the incoming combined

*City College of the City University of New York.



M - MIRROR O - OBJECT F - TRANSPARENCY
 1 - REFERENCE BEAM
 2 - OBJECT BEAM

Figure 1 - Diagram of a holographic recording.

scattered beams. The useful information is contained in the interference term of the record intensity. In our mathematical model, a linearized transmission characteristic is used.

To derive a quantitative model for the storing mechanism, consider a complex object amplitude $O(x,y)$ and a complex reference amplitude $R(x,y)$; these amplitudes represent the scattered beams in front of the transparency. The transparency records the intensity, I , where

$$I(x,y) = |O(x,y) + R(x,y)|^2 \quad (1)$$

Performing the indicated operation, we have

$$I(x,y) = |O(x,y)|^2 + |R(x,y)|^2 + O^*(x,y)R(x,y) + O(x,y)R^*(x,y), \quad (2)$$

where the asterisk denotes complex conjugation. In the case of weak object field, and with only the real image considered, Equation 2 reduces to

$$I(x,y) = |R(x,y)|^2 + O^*(x,y)R(x,y), \quad (3)$$

the equation used to represent intensity in the subsequent discussion. The condition that the object beam be weak is satisfied in practice, and neglecting the virtual image in Equation (2) is justified if the process is linear. In this case, it can be accounted for by use of the principle of linear superposition. To insure the necessary linearity, a linear transparency model is next presented. In deriving the linearized model, we consider first a static, and then a dynamic, model. The linear static model is derived from the nonlinear characteristic by the introduction of a Taylor series expansion about an optical bias point. This model is then modified to include the direction-dependence of the transparency.

The static characteristic is expressed by the T vs E curve, the optical transmission plotted as function of the exposure (see Figure 2). The linearization of this nonlinear characteristic follows from the usual small-signal procedure. First, a bias — an optical bias — point is established with no signal present. Remembering that $E = I t$ (where t is the speed) and holding the speed constant gives, from Equation (3), the optical bias

$$E_0 = |R(x,y)|^2 t. \quad (4)$$

Corresponding to E_0 , and determined by the characteristic curve, T_0 may be obtained. By expanding in a Taylor series the characteristic curve, about $E = E_0$, the graph is linearized, giving (see Figure 2)

$$T = T_0 - \chi(E - E_0), \quad (5)$$

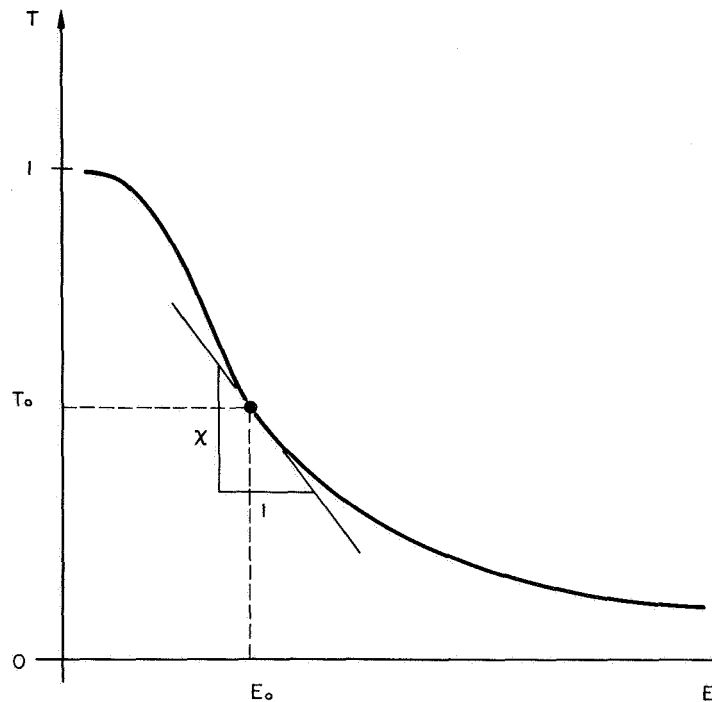


Figure 2—Static characteristic of the transparency.

where χ is the slope of the T vs E curve. This method, therefore, allows the separation of the static and the dynamic parts of the transmission function (Reference 7). The linearization thus presented stands in contradistinction to the two-step process, where the product of the γ 's is set equal to -2 , and γ is the slope of the T vs $\log E$ curve, or the small γ approximation. It represents, to a good degree of faithfulness, the holographic recording process (Reference 8).

Having discussed the static aspect of the transmission model, we next include the effect of the direction-dependence of the transparency (Reference 9). Let $S(x, y)$ represent the small signal, bias-dependent, optical spread function of the transparency. Let its spatial Fourier transform, the so-called complex modulation transfer function, of the small-signal spread function be denoted by $s(u, v)$, where u and v are direction cosines. The complete system model of the holographic recording process is

$$T(x, y) = T_0 - a s(x, y) \otimes R(x, y) O^*(x, y), \quad (6)$$

where a is a constant and \otimes denotes the two-dimensional spatial convolution. Letting the spatial Fourier transform of $T(x, y)$ be $t(u, v)$, and taking the spatial Fourier transform, denoted by $\mathfrak{F}\{ \}$, of Equation 6 yields

$$t(u, v) = T_0 \delta(u) \delta(v) - a s(u, v) \mathfrak{F}\{RO^*(x, y)\}, \quad (7)$$

where δ denotes the Dirac delta function. This equation is the desired deterministic system model of the recording process. It will be used in the subsequent channel capacity calculation. We here note that the optical spread function $S(x, y)$ and its corresponding complex modulation transfer function $s(u, v)$ were measured for various commercial films, using incoherent optical

systems. These results are available in the literature (Reference 10). Furthermore, measuring techniques using coherent optical systems are now available (Reference 11), allowing meaningful definition of $s(u, v)$ for holographic studies. Having developed a deterministic model, we turn our attention to the calculation of "noise" in the holographic recording process.

NOISE ANALYSIS

The sources of noise (Reference 12) in the recording process are:

- (a) Random thickness variation in the base and the emulsion,
- (b) Air bubbles in the base,
- (c) Surface roughness in the base,
- (d) Uneven distribution of the individual silver-halide grains.

The effects of (a) through (c) can be minimized, to some extent, by using optically flat surfaces and immersing the emulsion in a liquid whose index of refraction matches that of the gelation of the emulsion. In this report, however, only the effect of (d) is studied. For this purpose we present two models of the grain structure yielding the noise power spectrum necessary for the channel capacity calculation. They are the so-called checkerboard and overlapping circular grain (Reference 13) models.

The checkerboard model (see Figure 3) assumes that grains are square-shaped with sides of length ℓ on a square transparency having sides of length L . The unit cells are either completely transmitting or completely blocking the transmission; that is, the transmissivity is either 0 or 1. This is the reason for the "checkerboard" model name. By assuming that random variables x and y , the Cartesian coordinates of a point on the transparency, are independent and the "switching" distance ϵ (see Figure 4) is uniformly distributed on an

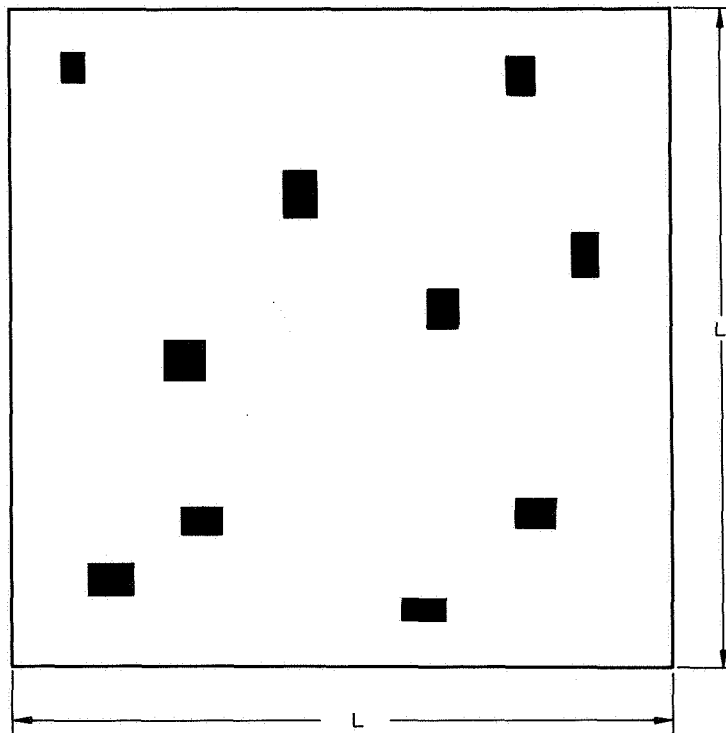


Figure 3—Checkerboard noise model.

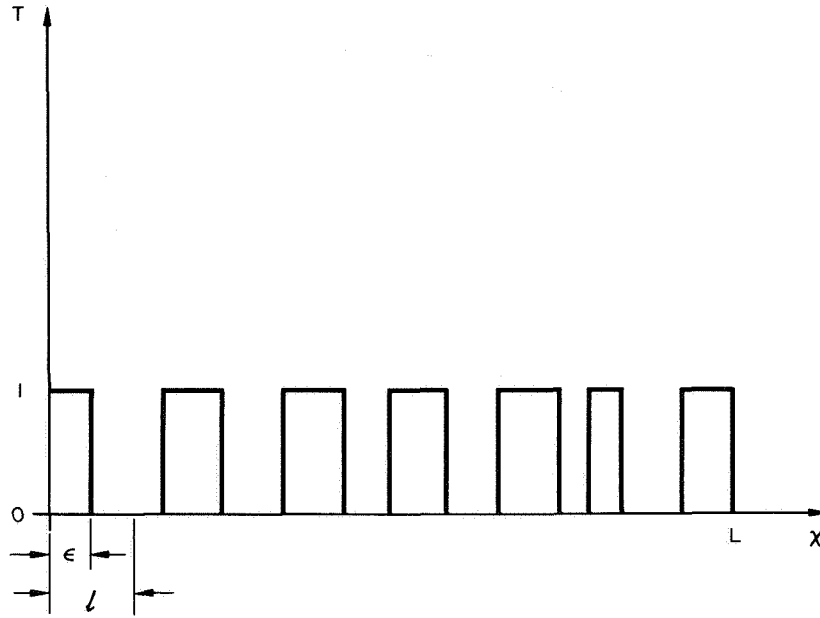


Figure 4—One-dimensional random binary signaling.

interval $(0, \ell)$ and it is independent of T , we have a random binary transmission type process. Let \bar{T} be the average transmission defined as

$$\bar{T} = \lim_{A \rightarrow \infty} \frac{1}{A} \iint_A T(x, y) dx dy,$$

where A is the area of the transparency. Let $t(x, y) = T(x, y) - \bar{T}$, with the autocorrelation function of $t(x, y)$ being defined as

$$\phi_{tt}(x, y) = t(\xi, \eta) t(\xi + x, \eta + y) \triangleq \lim_{A \rightarrow \infty} \frac{1}{A} \iint_A t(\xi, \eta) t(\xi + x, \eta + y) d\xi d\eta.$$

The autocorrelation function of the checkerboard model is (Reference 13)

$$\phi_{tt}(x, y) = \begin{cases} \bar{T}(1 - \bar{T}) \left(1 - \frac{|x|}{\ell}\right) \left(1 - \frac{|y|}{\ell}\right) & |x| \leq \ell \\ & |y| \leq \ell \\ 0 & |x|, |y| > \ell \end{cases} \quad (8)$$

The noise power spectrum, the two-dimensional spatial Fourier transform of the autocorrelation function (Equation 8), is

$$\Phi_{tt}(u, v) \triangleq \mathfrak{F}[\phi_{tt}(x, y)] = \bar{T}(1 - \bar{T})\ell^2 \frac{\sin^2\left(\frac{u\ell}{2}\right)}{\left(\frac{u\ell}{2}\right)^2} \frac{\sin^2\left(\frac{v\ell}{2}\right)}{\left(\frac{v\ell}{2}\right)^2}. \quad (9)$$

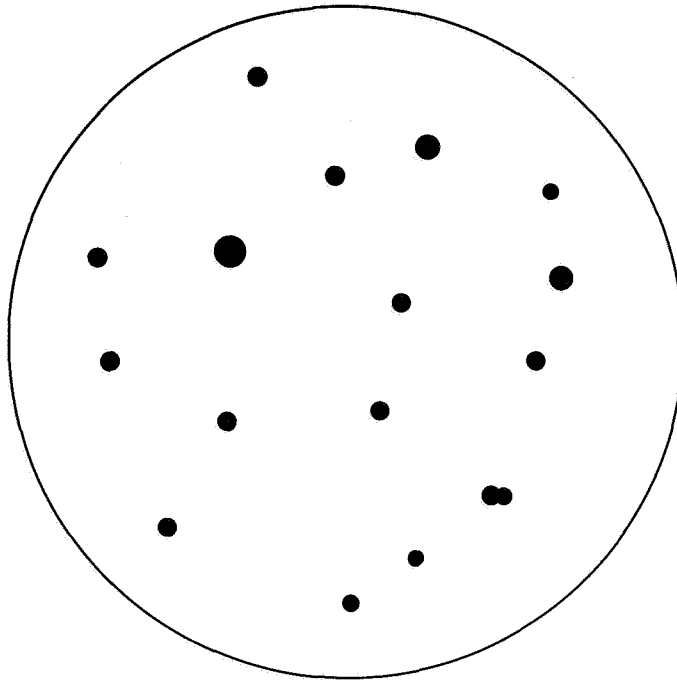


Figure 5—Overlapping circular grain model.

This is the required noise power for the channel capacity calculation.

A more realistic model of the grain structure is the overlapping circular grain model (see Figure 5). Here the following assumptions are made:

- (a) The grains are circular with radius R on a circular transparency whose total area is A .
- (b) The grain centers fall randomly on the plate as independent events with Poisson distribution on the interval $(0, \sqrt{A/2\pi})$, and are independent of T . That is, the probability of the grain center falling on radius α having made n switches is

$$P_n(\alpha) = \frac{(\lambda\alpha)^n e^{-\lambda\alpha}}{n!},$$

where λ is proportional to the average number of grains on the area A .

- (c) The grain radius follows the distribution law

$$P(r) = \begin{cases} 0 & r < R \\ 1 & r \geq R \end{cases}, \quad (10)$$

where R is the radius of a typical grain.

With these assumptions, the autocorrelation function of the overlapping circular grain model (Reference 13) is

$$\phi_{tt}(z) = \begin{cases} (\bar{T})^2 [(\bar{T})^{-F(z)} - 1] & 0 \leq z \leq 1 \\ 0 & z > 1 \end{cases}, \quad (11)$$

where

$$F(z) = \frac{2}{\pi} \arccos z - \sqrt{1 - z^2}$$

and

$$z = \frac{\sqrt{x^2 + y^2}}{2R} \triangleq \frac{\sigma}{2R}.$$

The normalized spectrum of the overlapping circular grain model is

$$\Phi_{tt}(\bar{s}, \bar{T}) = \frac{\mathfrak{F}[\phi_{tt}(z)]}{\bar{T}^2}, \quad (12a)$$

where

$$\mathfrak{F}[\phi_{tt}(z)] = \int_0^{\infty} J_0(4\pi\bar{s}Rz) \phi_{tt}(z) z dz, \quad (12b)$$

and J_0 is the Bessel function of zero order. We note here that, because of radial symmetry, the two-dimensional Fourier transform is replaced by a Hankel transform with

$$\bar{s} = Rs \quad (12c)$$

as its normalized line frequency. The spectrum, Equation 12a, is a function of two parameters R and \bar{T} and, as opposed to the previous case, it can not be evaluated in a closed form. Plots of $\phi_{tt}(z)$ and its noise spectrum $\phi_{tt}(\bar{s})$, with \bar{T} as their parameter, are available in the literature (Reference 14). These curves, by proper choice of \bar{T} and R , do match the measured noise characteristics of commercial films. Before leaving the subject, we point out that these models represent only a first-order approximation to physical grains. That is, they neglect the variable size, shape, and transmittance, both in amplitude and in phase, of grains in physical emulsions.

CHANNEL CAPACITY OF A HOLOGRAPHIC RECORDING

Now that we have the background for calculating the signal and the noise power spectrum, we turn our attention to the channel capacity of a holographic recording system. In information theory (Reference 6) it is shown that for band-limited gaussian time signals perturbed by independent, additive gaussian noise, the maximum rate of transmission of information, if the signal and noise power are limited to $S(w)$ and $N(w)$ respectively, is

$$C_t = \int_0^W \log_2 \left[1 + \frac{S(w)}{N(w)} \right] dw \quad \text{bits/second}, \quad (13)$$

where w is the circular frequency and W is the highest circular frequency present. This expression is called the Shannon-Hartley Fundamental Channel Capacity Formula. In our case, a two-dimensional analogue of Equation 13 is needed. Let $M(u, v)$ and $N(u, v)$ be the signal and noise power of the two-dimensional system with u and v as their direction cosines; then

$$C_{xy} = \int_0^{w_1} \int_0^{w_2} \log_2 \left[1 + \frac{M(u, v)}{N(u, v)} \right] dudv \quad \text{bits/mm}^2, \quad (14)$$

where C_{xy} is the channel capacity of the additive, gaussian two-dimensional channel and w_1 and w_2 are the maximum values of u and v . This is the formula used in the calculation of the channel capacity of the holographic recording.

The signal power, from Equation 7, is

$$M(u, v) = a^2 (\bar{T}) S^2(u, v) |\mathfrak{F}[RO^*(x, y)]|^2, \quad (15)$$

where $a(\bar{T})$ is a bias-dependent constant, $S(u, v)$ is the complex modulation transfer function of the transparency, $R(x, y)$ is the complex reference, and $O^*(x, y)$ is the conjugate complex object amplitude in front of the transparency. The noise power spectrum $\Phi_{tt}(\bar{T}, u, v)$ is given by Equations 9 and 12. Substituting Equations 15 and 9 in Equation 14 yields,

$$C_{xy} = \int_0^{w_1} \int_0^{w_2} \log_2 \left\{ 1 + \frac{a^2(\bar{T}) S^2(u, v) |\mathfrak{F}[RO^*(x, y)]|^2}{T(1-\bar{T})\ell \frac{2\sin^2(u\ell/2)}{(u\ell/2)^2} \frac{\sin^2(v\ell/2)}{(v\ell/2)^2}} \right\} dudv, \quad (16)$$

the desired channel capacity formula. We here note that for a given object and reference beam, a given biasing condition \bar{T} , a specified complex modulation transfer function $S(u, v)$, and grain size ℓ , the integral may be numerically evaluated. If there is circular symmetry, Equation 14 may be reduced by the use of Equation 12 to,

$$C = \frac{2\pi}{R} \int_0^{\bar{w}} \log_2 \left\{ 1 + \frac{a^2(\bar{T}) S^2(\bar{S}) |\mathfrak{F}[RO^*(x, y)]|^2}{\Phi_{tt}(\bar{T}, \bar{S})} \right\} ds, \quad (17)$$

where $\Phi_{tt}(\bar{T}, \bar{S})$ is defined by Equations 11 and 12. Let

$$S^2(\bar{S}) = \left(\frac{1}{1 + \left(\frac{\bar{S}}{\bar{S}_0}\right)^2} \right)^2, \quad (18)$$

$$R(\sigma) = e^{-jk\sigma}$$

where k is the wavenumber, and $S(\bar{S})$ is the complex modulation transfer function suggested by Paris (Reference 10) with a line "cut-off" frequency \bar{S}_0 and $R(\sigma)$ is the "cylindrical" reference beam, be given. By the used of Equation 18 in Equation 17 we have

$$C_{\sigma} = \frac{2\pi}{R} \int_0^{\bar{w}} \log_2 \left[1 + \frac{a^2(\bar{T})K^2(\bar{S})}{\left| 1 + \left(\frac{\bar{S}}{S} \right)^2 \Phi_{tt}(\bar{T}, \bar{S}) \right|} \right] d\bar{s}, \quad (19)$$

where

$$K(\bar{s}) = \int_0^{\infty} e^{-j\sigma k} J_0(4\pi R\sigma\bar{s}) O^*(\sigma) d\sigma. \quad (19a)$$

Thus, as indicated, by specifying three parameters \bar{S}_0 , \bar{T} , and R , the line "cut-off" frequency of the film, the average transmittance and the radius of a typical grain, and the complex signal $O^*(\sigma)$ C_{σ} may be numerically evaluated, resulting in a figure of merit for a coherent optical communication system.

CONCLUSIONS

In this study, a figure of merit—the channel capacity—of a holographic recording system is evaluated. The result is in the form of an integral that depends on the desired signal and the physical parameters of the system. For a given transparency, the parameters are obtainable from published data. The capacity integral may, therefore, be evaluated numerically.

ACKNOWLEDGMENT

The author wishes to express his appreciation to GSFC personnel for their advice and encouragement.

REFERENCES

1. Jones, R. Clark, "Information Capacity of Photographic Films," JOSA 51(1):1159-1171, 1961.
2. Linfoot, E. H., "Equivalent Quantum Efficiency and the Information Content of Photographic Images," J. of Photo Sci. 9:188-194, 1961.
3. Shaw, R., "The Application of Fourier Techniques and Information Theory to the Assessment of Photographic Image Quality," PSE 6(5):281-286, 1962.
4. Goodman, J. W., "Film-Grain Noise in Wavefront-Reconstruction Imaging," JOSA 57(4):493-502, 1967.
5. Frieden, B. Roy, "Band-Unlimited Reconstruction of Optical Objects and Spectra," JOSA 57(8):1013-1019, 1967.
6. Reza, F. M., "An Introduction to Information Theory," Chapter 9, New York: McGraw-Hill, 1961.
7. Kozma, A., "Photographic Recording of Spatially Modulated Coherent Light," JOSA 56(4):428-432, 1966.
8. Falconer, D. G., "Role of the Photographic Process in Holography," PSE 10(3):133-139, 1966.
9. Kelly, D. H., "System Analysis of the Photographic Process I, A Three Stage Model," JOSA 50(3):269-276, 1960.

10. Paris, D. P., "Approximation of the Sine-Wave Response of Photographic Emulsions," JOSA 51(9):988-991, 1961.
11. Vander Lugt, A., and Mitchel, R. H., "Technique for Measuring Modulation Transfer Functions of Recording Media," JOSA 57(3):372-379, 1967.
12. Falconer, D. G., (ibid) p. 139.
13. O'Neil, E. L., "Introduction to Statistical Optics," Chapter 7, Reading, Mass.: Addison-Wesley, 1963.
14. Savelli, M. M., "Résultats Pratiques d' étude d'un modèle," Comptes Rendus, 246:3605-3608, 1958.

GROUP B

CONTROL CENTER PROBLEMS

Academic Personnel

Prin. Investigator: Dr. Robert Golden (CUNY)

Faculty: Dr. Irwin Goldstein (Maryland)

Graduate Students: John Fearnside (Maryland)

Goddard Personnel

Staff Advisors: Dr. Robert Coates

Dr. Thomas Lynch

PRELIMINARY ANALYSIS FOR THE DESIGN OF AN AUTOMATED SPACE TRACKING NETWORK

R. K. Golden* and J. J. Fearnside[†]

ABSTRACT

Through a world-wide distribution of remote stations, tracking, monitoring and control, and telemetry reception are being performed for a large and growing number of satellites. These stations are divided into three independently operated networks: Space Tracking and Data Acquisition (STADAN), with control at Goddard Space Flight Center (GSFC) in Greenbelt, Maryland; Manned Flight Network (MFN), with control at the Manned Spacecraft Center in Houston; and Deep Space Network (DSN), with control at Jet Propulsion Laboratory in Pasadena, California.

The desire to introduce increased automation into the remote stations is the impetus for this study. Automation will be accomplished under computer control and will encompass all facets of station operation: station management and scheduling, equipment status-monitoring and setup, network calibration and communication, real-time command generation and verification, real-time receipt of data and preliminary analysis, and mission simulation and training.

The study, through conferences with many cognizant groups at GSFC and with GSFC contractors, adopted a preliminary model of an automated station. It was also decided that a dynamic, computer-generated event simulator of the station and network would offer the best return in determining how the station would actually perform and whether or not to apply automation to specific station functions. A simulation language, General Purpose Systems Simulator (GPSS), was obtained, made operational on GSFC computers, and was used to evaluate several initial models.

The station model will be used to determine the time-dependent inter-relationships among the various functions being simultaneously performed and the dynamic loadings of the equipment under actual conditions of use.

INTRODUCTION

Purpose of Study

The increasing numbers and complexity of satellites have been adding to the workload of the remote tracking stations of the networks. This trend and the difficulty in acquiring adequately trained personnel, have generated a need to increase the station throughput while reducing reliance upon numbers and skill of available personnel. To meet this need, a study of the feasibility and methods of automating a tracking station has been in progress at GSFC for some time. This investigation started from the viewpoint of examining the computer requirements to sustain the loadings that would be likely under future operation and to accomplish the multi-function operation that would be necessary.

* Adjunct Professor, City University of New York.

[†] Graduate Student, Department of Electrical Engineering, University of Maryland.

Sources of Information

Information was gathered by discussing the problems of individual areas with the responsible organizations at GSFC. In addition, a survey was made of the contractual studies performed for GSFC over the past few years. A bibliography of the literature, both contractor-provided and GSFC documents, is appended to this report. These sources led to a logical grouping of required activities, as to function and relative importance in time, that closely paralleled the thinking of GSFC groups and their contractors.

Decision to Use Simulation

It was also clear that the involved interrelationship of the various portions of the system made it impossible to determine the overall effects of merely specifying desired individual functions of the system. In addition, the scope of the activity was sufficiently broad to require the attention of many groups and organizations within GSFC. It was therefore decided that a simulation of the entire effort would provide the needed means of testing the entire system under individual variations, and would provide a central source of information about the system to all groups working with it. Most important, simulation would provide a definitive method by which firm design and specification decisions could be made and supported. Simulation would also permit potentially costly mistakes to be corrected before great expenditures of time and money.

A FUNCTIONAL DESCRIPTION OF THE STATION

Major Functions

Tracking Station Management and Control

Under tracking station management and control, bookkeeping, personnel, maintenance, and inventory functions are performed. The specific functions are as follows:

Inventory Control.—Maintain current stock and ordering records for all equipment and supplies needed at the station.

Scheduling.—Assign personnel and equipment to properly perform the servicing of satellites due to arrive above the station during a specified future time period.

Equipment Status and Maintenance.—Maintain records of the operating status of all station equipment and monitor required maintenance procedures. These records are also a source of failure probability statistics and station performance indices.

Generation of Data for Satellite Servicing.—Prepare the specific steps of the routines to be followed, the data to be transmitted to the satellite, tracking information, the manner of handling information received from the satellite, and post-pass calibration and data handling requirements.

These functions are free of time pressure and can be done under computer control in an off-line, time-independent manner.

Tracking Station Operation

In this area the equipment is exercised and kept operational for testing, calibration, pre-pass readiness, and simulation. The functions are:

Configuration Setup and Test.—The equipment requirements for a given pass are interconnected, tuned, and adjusted to meet the established needs for that pass.

Link Readiness Checks.—The items of equipment required to service upcoming satellite passes are continuously monitored for proper settings and alignment.

Communication Setup and Checks.—The required links to and from all points external to the tracking station are established and checked for proper operation.

These functions are relatively free of time pressure and can be performed under computer control on a non-real-time basis. However, there are limits on the total time to be used in completing them, both before and after a pass.

Satellite Pass Servicing

This group of functions relates to the actual performance while the satellite is in sight of the tracking station and information is being transmitted up and down link. The functions are:

Control of Tracking Station Equipment.—Proper operating levels of all equipment are continuously checked during the pass, and operating standby equipment is substituted when a deviation is detected.

Tracking Through Antenna Control.—On-line control of the tracking antenna is performed, using available orbit predictions or search patterns to locate the satellite, and tracking on the received signal when the satellite is found.

Processing Telemetry.—The telemetry signal is decommutated and processed into related groups. Possible data compression functions and quick-look extraction are also performed.

Command Generation and Verification.—Satellite commands are transmitted and proper receipt is verified.

These functions must be performed in real time as the satellite completes its pass. Both time and volume constraints must be met completely.

Though the described functions can be grouped as shown, they are not entirely independent of one another. The performance of many functions provides input or preliminary preparation for the performance of others. Those described as time-independent are sometimes required in a limited form during the time-dependent satellite pass period. Many of the functions are being performed simultaneously and are dependent upon having current data transferred between them. The overall result of this picture is a complicated series of operations for which requirements and resultant loadings can only be determined dynamically.

Required Information for a Proper Design

In order to specify and design a system of this sort, a series of questions must be answered in a rough progression. The effect of an answer to a later question can alter the answer to one asked previously. Thus the analysis is iterative and must be performed repetitively until the data or answer no longer varies. The questions are:

1. What functions are to be considered within the automatic system?
2. What is the overall philosophy of operation within the system (completely automatic, manned override, a combination, etc.)?
3. What are the main objectives in performance: speed, reliability, volume, etc.?
4. How are individual criteria to be met (equipment redundancy, parallel operation, manual standby, etc.)?
5. What is gained by a definitive answer to any of the previous questions over any other choice or over the present method?
6. What is the relative cost of proceeding in any given direction in money, manpower, time, etc.?

In such a complicated, interrelated system it is impossible to answer these questions theoretically without impossibly elaborate analysis. Under the circumstances, a simulation model becomes a practical and powerful method of determining answers to the questions posed and of gathering information to design the system and specify the operating entities within it.

SYSTEM SIMULATION

General Discussion

Simulation involves the construction of a mathematical or physical model which will simulate a selected set of working properties of the actual system being investigated. This approach can be equally applied to an existing system that is unavailable or too costly to use, or to a system that exists only in terms of a prospective design. The selected model can be tailored to meet the needs of the investigator, to the required degree of accuracy. In the case at hand, physical construction of the devices in the system is not necessary. What is needed is a description of the manner of operation and communication flow among a large number of known devices, interacting in time. In short, we may assume that we know how each individual device operates under specified input conditions, but we require an accurate tabulation of the flow of events from device to device when a large number of devices are tied together in a given way. Further, we wish to know how the flow of events will change when the devices are interconnected in a different way and required to perform the same total job. The time and event simulation of the system should serve as a working experiment to answer as many of the posed questions as possible. This concept requires that the model be relatively easy to build and generate, readily alterable, dynamic and self-interactive in operation, and capable of providing statistically reliable results.

The General Purpose Systems Simulator (GPSS)

GPSS is an existing programming language designed to permit the construction of time and event simulations of complex systems. The language used is English-oriented, and the program is obtained directly from a block diagram of the system to be operated. Using a special symbol language, the block diagram is constructed to show the flow of operations within the system and to outline the ground rules for system operation. Specific magnitudes of volume, rate, time to perform, etc., are added to the block diagram to complete the physical description of the individual devices being modeled. Each block in the diagram is now translated to a punched card and the resultant deck becomes the input to the GPSS program.

The GPSS program contains all of the information necessary to translate the input deck into a computer program. The required computer programs to operate the model, record the flow of events, generate statistics and tables, and provide the requested information in edited, readable form are also within the GPSS structure. The user is not required to have programming knowledge. Alterations in the system can be made as rapidly as the block diagram can be changed. Physical characteristics can be readily changed, as well as the extent of interaction among different devices in the system.

RESULTS OF PRELIMINARY APPLICATION

The Initial Model

Initially, it was decided to model a station containing four complete links and capable of serving four satellites simultaneously. The question of interest was the effect of a reduction in pre-pass and post-pass calibration and setup times, by means of automation, on successful servicing of a heavy satellite load.

The station was presented with a flow of satellites that were exponentially distributed, with a mean time between arrivals of 90 minutes. The station was operated so that link 1 was assigned to a satellite whenever that link was free. If link 1 was busy, link 2 was assigned next; link 3 next; link 4 next; and if all four were busy the satellite information was assumed to be lost. In this manner the number of satellites that would be lost by a station equipped with only one, or two, or three operational links could be immediately determined from the statistics.

Without automation, each link required 20 minutes of pre-pass setup and calibration, and 10 minutes of post-pass calibration. Under automation, the times were 2 minutes and 1 minute, respectively. In both cases, pass time was exponentially distributed around a mean of 20 minutes.

Figure 1 shows the above-described model using GPSS symbol language. The comments on the side describe the functions of each block. Figure 2 shows the program equivalent of the block diagram that became the input to the GPSS program.

Results of Initial Runs

Figures 3 to 7 show the output of the GPSS program for the two simulation runs. Note that the longer pre- and post-pass intervals resulted in a loss of four passes out of a thousand. Automating to shorten the length of these intervals achieved the ability to service the four passes that were previously lost.

Reducing the station to three links instead of four would mean the loss of 16 passes out of a thousand under manual operation and one pass out of a thousand under automated operation.

These simulations now offer a concrete means of evaluating the overall effect of simultaneously or individually automating certain activities at the station, and/or reducing the equipment capacity at the station. Estimating the costs and savings of the steps taken gives an immediate measure of the overall cost of achieving incremental performance standards at the extremes of their distributions.

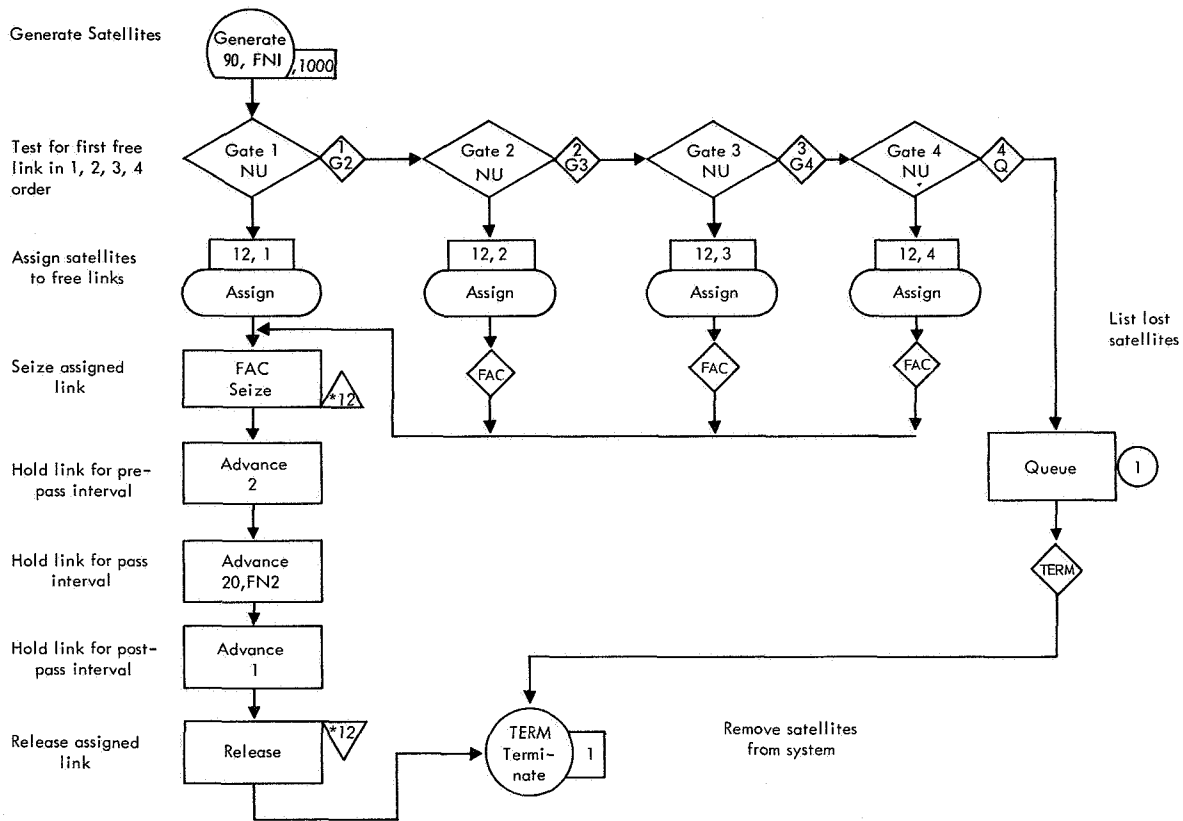


Figure 1-Model block diagram.

BLOCK NUMBER	*LOC	OPERATION	A,B,C,D,E,F,G	COMMENTS	CARD NUMBER
		SIMULATE			1
		1 FUNCTION	RN1,C24		2
0	0	.1	.104 .2 .222 .3 .355 .4 .509 .5 .69		3
.6	.915	.7	1.2 .75 1.38 .8 1.6 .84 1.83 .88 2.12		4
.9	2.3	.92	2.52 .94 2.81 .95 2.99 .96 3.2 .97 3.5		5
.98	3.9	.99	4.6 .995 5.3 .998 6.2 .999 7.0 .9997 8.0		6
		2 FUNCTION	RN2,C24		7
0	0	.1	.104 .2 .222 .3 .355 .4 .509 .5 .69		8
.6	.915	.7	1.2 .75 1.38 .8 1.6 .84 1.83 .88 2.12		9
.9	2.3	.92	2.52 .94 2.81 .95 2.99 .96 3.2 .97 3.5		10
.98	3.9	.99	4.6 .995 5.3 .998 6.2 .999 7.0 .9997 8.0		11
1		GENERATE	90, FN1, .1000		12
2		GATE NU	1, GATE2		13
3		ASSIGN	12, K1		14
4	FAC	SEIZE	*12		15
5		ADVANCE	2		16
6		ADVANCE	20, FN2		17
7		ADVANCE	1		18
8		RELEASE	*12		19
9	TERM	TERMINATE	1		20
10	GATE2	GATE NU	2, GATE3		21
11		ASSIGN	12, K2		22
12		TRANSFER	.FAC		23
13	GATE3	GATE NU	3, GATE4		24
14		ASSIGN	12, K3		25
15		TRANSFER	.FAC		26
16	GATE4	GATE NU	4, QUEUE		27
17		ASSIGN	12, K4		28
18		TRANSFER	.FAC		29
19	QUEUE	QUEUE	1		30
20		TRANSFER	.TERM		31
		START	1000		32
		END			33

Figure 2-Program equivalent of block diagram.

RELATIVE CLOCK			87035			ABSOLUTE CLOCK			87035		
BLOCK COUNTS											
BLOCK	CURRENT	TOTAL	BLOCK	CURRENT	TOTAL	BLOCK	CURRENT	TOTAL	BLOCK	CURRENT	TOTAL
1	0	1000	11	0	289						
2	0	1000	12	0	289						
3	0	628	13	0	83						
4	0	996	14	0	67						
5	0	996	15	0	67						
6	0	996	16	0	16						
7	0	996	17	0	12						
8	0	996	18	0	12						
9	0	1000	19	0	4						
10	0	372	20	0	4						

Figure 3-Long pre- and post-pass periods count of transaction flow through blocks.

FACILITY	AVERAGE UTILIZATION	NUMBER ENTRIES	AVERAGE TIME/TRAN	SEIZING TRANS. NO.	PREEMPTING TRANS. NO.
1	.354	628	49.140		
2	.159	289	47.927		
3	.037	67	48.582		
4	.007	12	55.083		

Figure 4-Long pre- and post-pass periods link utilization.

QUEUE	MAXIMUM CONTENTS	AVERAGE CONTENTS	TOTAL ENTRIES	ZERO ENTRIES	PERCENT ZEROS	AVERAGE TIME/TRANS	AVERAGE TIME/TRANS	TABLE NUMBER
1	4	1.796	4		.0	39082.000	39082.000	

AVERAGE TIME/TRANS = AVERAGE TIME/TRANS EXCLUDING ZERO ENTRIES

Figure 5-Long pre- and post-pass periods tabulation of lost satellites.

RELATIVE CLOCK			87014			ABSOLUTE CLOCK			87014		
BLOCK COUNTS											
BLOCK	CURRENT	TOTAL	BLOCK	CURRENT	TOTAL	BLOCK	CURRENT	TOTAL	BLOCK	CURRENT	TOTAL
1	0	1000	11	0	204						
2	0	1000	12	0	204						
3	0	771	13	0	25						
4	0	1000	14	0	24						
5	0	1000	15	0	24						
6	0	1000	16	0	1						
7	0	1000	17	0	1						
8	0	1000	18	0	1						
9	0	1000	19	0	0						
10	0	229	20	0	0						

Figure 6-Reduced pre- and post-pass periods count of transaction flow through blocks.

FACILITY	AVERAGE UTILIZATION	NUMBER ENTRIES	AVERAGE TIME/TRAN	SEIZING TRANS. NO.	PREEMPTING TRANS. NO.
1	.192	771	21.761		
2	.048	204	20.789		
3	.007	24	28.333		
4	.000	1	82.000		

Figure 7-Reduced pre- and post-pass periods link utilization.

Direction of Continuing Effort

The initial model represents the first trial effort. The model will be expanded to include increased detail in the internal structure. The links will be represented by the various types of equipment needed and will be assembled to meet the requirements of a particular pass. The effect of equipment failure rates and repair times will be included. The satellite passes will be made to occur in relation to actual orbit times, and attempts will be made to schedule satellites or other possible stations if the equipment at the primary station is not available. Limitations on communication equipment will be added as well. These characteristics will be built in until the model is as close an analog of the actual station and network as possible.

From that point, the effect of various modes of operation on performance and equipment capability can be rapidly measured, and design and specification judgments can be realistically made in advance of contractual or monetary commitments.

BIBLIOGRAPHY

- "Aerospace Data Systems Standards," Goddard Space Flight Center Document X-520-63-2, Jan. 7, 1963.
- "Development of Specifications for a Central Station, Real Time, Multi-Programming Computer System and a Tracking Station Real Time Computer System," CSA NAS5-3968, Vol. 1 (June 15, 1964), Vol. 2 (Jan. 31, 1965).
- Dickinson, W. B., Wilson, D. D., and Turner, V. E., "Implementation of a Worldwide High Speed Data Transmission System for NASA Mission Support," Goddard Space Flight Center Document X-500-66-402, Aug. 1966.
- Hahn, W., and Hendel, Z., "NASCOM On-Line Data Switching System," Goddard Space Flight Center Document X-500-66-403, Aug. 1966.
- "PCM/DHE for the Network Test and Training Facility," NASA-GSFC S-521-P-4, Jan. 3, 1967.
- "Phase I Report for Study of Data Transmission System," AD/COM NAS5-10503, Feb. 1967-Mar. 1967.
- "Preliminary Performance Analysis of High Speed Digital Data Circuits in NASCOM," Goddard Space Flight Center Document X-576-67-264, June 1967.
- "Programmable Command Generator," NASA-GSFC S-521-P-1, April 16, 1965.
- "Real Time Computing System," NASA-GSFC S-521-P-3, Nov. 4, 1966.
- "Real Time, Multi-Processing Computer System Study," CSA NAS5-9976, Dec. 10, 1965-May 1, 1966.
- Shawe, M. E., "Station Automation," Goddard Space Flight Center Document X-521-66-168, April 1966.
- "Space Tracking and Data Acquisition Network Facilities Report," Goddard Space Flight Center Document X-530-66-33, Dec. 1965.
- "STADAN Generation Breakdown," GB 1, 160, 000, Vol. 1 (Jan. 1967), Vol. 2 (June 1967).
- "STADAN Manual," Goddard Space Flight Center Document X-530-67-304, July 1967.
- "Station Technical Operations Control Equipments," NASA-GSFC S-534-P-7, May 17, 1967.
- "Station Technical Operations Control Project Working Group Study," Goddard Space Flight Center Document X-534-67-161, Dec. 1966.
- "A Study of Advanced Ground Station Development and Documentation of an Evaluation Model," Operations Research Inc., NAS5-9653, Mar. 7, 1967.
- "A Study of Station Performance Criteria," Operations Research Inc. NAS5-9910, Mar. 21, 1966.

"Technical Proposal for PCM/DHE for NTTF," Vector Engineering-United Aircraft
S521-23760-335, Mar. 7, 1967.

"Technical Proposal for STOC System," Scientific Systems Data S-534-P-7, July 28,
1967.

"Technical Proposal for PCM/DHE System," Scientific Systems Data S-521-P-4,
April 26, 1967.

VISUAL CODING

Irwin L. Goldstein*

Since the display is man's only contact with the data base of an information-processing system, attention is eventually focused on the display requirements. Unfortunately, the design of the display and the consideration of the capabilities and limitations of the human element is usually the last step in the design of the man-machine system. At this stage of the process, innovations are difficult to work into the system and the design of the display usually becomes a carryover from past display requirements. This procedure more often than not leads to a breakdown in man-machine communication with the standard solution being the development of better hardware. What is actually needed is more research on the qualitative and quantitative requirements of the man-machine system. When these types of analyses are performed, it is possible to learn the exact type of employee behavior necessary to perform the job well. At this point the information needed to perform the job becomes obvious, and the design of the display becomes tied to the information requirements rather than to preconceived notions about display surface characteristics.

This paper discusses some of the general data available in visual coding of information. It does not begin to approximate all of the considerations necessary for display analysis. Instead, it is intended to provide an overview of the type of data available on one process—visual coding. Which part of this paper is relevant will depend upon the particular job being considered. An illustration of this point is the use of color as a coding device. Colors may not provide a good coding scheme when the lighting is poor because the human visual system requires a certain level of illumination in order to discriminate colors.

In a situation where an observer was asked to judge a single stimulus of a particular dimension, the data indicated that the transmission rate varied between two and three bits. This was approximately equal to the correct identification of seven different stimuli. These data included investigations which varied the following stimuli: pointer positions on linear scales—3.1 bits transmitted; visual size—2.8 bits transmitted; hue—3.1 bit transmitted; brightness—2.3 bits transmitted (References 1 and 2). Interestingly, similar results have been obtained for investigations of audition, gustation, and olfaction (Reference 2). The transmission of two to three bits of information is not very impressive, and does not explain our ability to choose among several thousand words or objects. Part of the explanation lies in our ability to use more than one dimension when making judgments. Indeed, the clearly two-dimensional judgments of a dot in a square led to a channel capacity of 4.6 bits, meaning that people could judge accurately any one of 24 positions in a square (Reference 3). It was interesting to note that the use of extra dimensions did not result in an additive process in information transmitted. The one dimensional judgment of a position of a point in an interval resulted in 3.25 bits transmitted. Performing this judgment for a two dimension object like a square might be expected to result in 6.5 bits capacity. Thus, the addition of the second dimension did improve performance, with the added consequence that there was a law of diminishing returns in operation.

*Department of Psychology, University of Maryland, College Park, Maryland.

The human's ability to gain more information from multidimensional stimuli is related to the way that such stimuli are coded. When faced with large masses of unorganized data, an observer codes his information into categories or groups. The purpose of the coding scheme is to enable an observer to interpret a display quickly and easily. There are many different types of coding schemes, and their relative merits depend upon:

- a) The number of discriminable steps (such as the number of shapes that can be identified without confusion) in a given coding method.
- b) The amount by which the code interferes with other codes and/or produces fatigue and distraction.
- c) The space required to display the information.

A good summary of the various coding methods can be found in Table 1 (from Reference 4).

There are not many studies which have directly compared the coding schemes presented in Table 1. One excellent study, by Hitt (Reference 5), has compared five different coding methods (numeral, letter, geometric shape, configuration, and color) for five different tasks (identification, location, counting, comparison, and verification). The subjects were told that speed and accuracy were important, and the data were reported in terms of mean correct responses per minute, (Table 2).

In general, as can be seen from the data, the numerical and color codes were best for most tasks with the configuration code producing the poorest performance. Hitt pointed out that numerical coding was best for an identification task but that for the remaining tasks there were no significant differences between colors and numerals.

From Hitt's data and the summary table, it can be concluded that color and alpha-numerics provide two useful coding techniques. In many cases, color coding has been combined with previous associations to ease the learning process. For example, colors commonly used to describe physical hazards (e.g. red for fire, yellow for caution, green for safety, purple for radiation hazard) are often used for visual displays. The use of color is limited by the visual attributes of the individual's sensory system (many males are red-green color blind), the brightness of the color, the size of the display, and the color of the light illuminating the display. For these reasons, color coding should be used with extreme caution. In other words, there appears to be ample evidence for the use of color as a coding device, but many variables must be examined to determine the appropriateness of color for a given situation.

The number of combinations of letters and numerals for coding purposes is for all practical purposes virtually unlimited. Restrictions in using letter and number codes are imposed by the space required and by the operator's ability to learn what the numbers and letters stand for. Numerals and letters should be designed for maximum legibility. Space restrictions and illumination should also be considered. The preferred numerical style (Reference 6) has the numeral width $\frac{3}{5}$ of the height, except for the 4 which should be one stroke wider than other numerals and the 11 which should also be one stroke wider. A stroke should be $\frac{1}{6}$ to $\frac{1}{8}$ of numeral height. The letter style preferred is the capital case since it is more visible than the lower case. The letter style should have a width $\frac{3}{5}$ of the height, except for the 1 which should be one stroke wide, and the M and W which should be $\frac{1}{5}$ wider than other letters. A stroke should be $\frac{1}{6}$ to $\frac{1}{8}$ of the letter height.

Table 1
Summary Table of Coding Methods
(Baker & Grether, 1954)

Code Dimension	Number of Code Steps	Evaluation	Comments
Color	11	Good	Objects of a given color quickly and easily identified in a field of various colored objects. Little space required.
Numerals and Letters	Unlimited	Good	Number of coding steps unlimited. Requires little space if there is good contrast and resolution.
Geometric Figures	15 or more	Good	Certain geometric shapes are easily recognized. Little space required if resolution is good.
Areas	5	Fair	Requires considerable space on display.
Visual Number	6	Fair	Requires considerable space on display.
Length	4-5	Fair	Limited number of usable code steps. Will clutter a display with many signals.
Angular Orientation	12	Fair	95 percent of the estimates will be in error by less than 15°.
Brightness	3-4	Poor	Limited number of usable code steps. Poor contrast effects will reduce visibility of weaker signals. Fatiguing.
Flash Rates	5	Poor	Distracting and fatiguing. Interacts poorly with other codes.
Stereoscopic Depth	?	Fair	Realistic method of coding range or altitude. Requires complex electronic displays.

Table 2
Comparison of Five Coding Methods
for Five Tasks
(Hitt, 1961)

Task	Coding Method				
	Numeral	Letter	Shape	Color	Config.
Identification	13.64	13.02	12.53	12.34	11.77
Location	8.46	7.42	7.25	6.94	4.03
Counting	12.60	12.22	11.49	11.11	7.07
Comparison	6.85	6.72	6.56	6.33	4.76
Verification	10.01	9.95	9.50	9.05	6.60

The real advantage of geometric figures relates to the ease of learning correct associations. It is important to have the shapes compatible with and associated with the coded objects that they represent.

The other types of coding schemes presented in the summary chart have serious disadvantages and should be used with extreme caution. Under certain circumstances, they may prove to be quite valuable. A good illustration of this fact is found when the visual mode is overloaded with alpha-numerics and a warning signal must be given. In that case a flashing signal which distracts attention could be the perfect stimulus to use. It should be noted that there are other types of stimuli besides visual signals which have been investigated and proven efficient for certain situations. For example, the use of an auditory signal as a warning device has proven to be useful in situations where the visual mode is overloaded and the noise level is low.

There are certain general principles which should be considered independently of the type of stimulus used. These include the following:

- a. The operator should be able to see all of the display from his normal viewing position. The plane at which the display lies should be perpendicular to the line of sight. The distance of the display from the operator's eyes should be no less than 13 inches and no more than 29 1/2 inches (Reference 6). For greater distances, the display size must be increased.
- b. The arrangement of controls and displays must be standardized. If the controls and displays look alike, they should behave alike (Reference 7).
- c. When a number of displays appear on the same panel, each display should be located above its associated control with the display on the upper portion and the control on the lower portion of the panel. When rows of displays must be associated with columns of controls, the left should correspond with the top and the right with the bottom (Reference 6).
- d. Most visual codes are symbolic. In order to use them efficiently, an operator must be trained.

In conclusion, visual codes can provide a useful technique for presenting information. It is necessary to be extremely careful in the choice of the proper technique. There are many other sensory coding devices and interactions between them which must be examined carefully before a good choice can be made. This paper is not an attempt to discuss all of the relevant issues. The purpose is to indicate that there is information available to help the engineer choose the correct display.

REFERENCES

1. McCormick, E. J., Human Factors Engineering, New York:McGraw-Hill, 1964.
2. Miller, G. A., "The Magical Number Seven, Plus or Minus Two: Some Limits On Our Capacity for Processing Information," Psychol. Rev. 63:81-97, 1956.
3. Klemmer, E. T., and Frick, F. C., "Assimilation of Information from Dot and Matrix Patterns," J. Exp. Psychol. 45:15-19, 1953.
4. Baker, C. A., and Grether, W. F., "Visual Presentation of Information," USAF WADC Technical Report 54-160, 1954.
5. Hitt, W. D., "An Evaluation of Five Different Abstract Coding Methods," Human Factors 3:120-130, 1961.
6. Morgan, C. T., Cook, J. S., III, Chapanis, A., and Lund, M. W., Human Engineering Guide to Equipment Design, New York:McGraw-Hill, 1963.
7. Chapanis, A., Man-machine Engineering, Belmont, Calif.:Wadsworth, 1965.

GROUP C

ANTENNAS



Academic Personnel

Prin. Investigator:

Dr. Yu Chen (Rutgers)

Faculty:

Dr. Jean Dalrymple (Mich. T. U.)

Consultant:

Dr. Theodore Toridis (G. W.)

Goddard Personnel

Staff Advisors:

Dr. Robert Coates

Dr. Thomas Lynch

STRUCTURAL TRANSFER FUNCTIONS FOR THE ROSMAN-I ANTENNA

Yu Chen* and T. G. Toridis**

ABSTRACT

A dynamic model for the Rosman-I antenna structure is constructed by lumping masses to 13 appropriately selected points on the actual structure. When each mass is permitted 3 translational degrees of freedom, a model with 39 degrees of freedom is obtained. A computer program is developed to generate the natural frequencies and the modal shapes of the model and to calculate the response of the system due to inputs.

It is found that the structural model possesses a frequency range of 1.03 to 43.5 cps, which encompasses the experimentally observed frequency range. A transfer matrix is determined for the model with $(39)^3$ transfer coefficients. Some response calculations to inputs are made by using the computer program and generating the relevant transfer coefficients in the computer. Results show reasonable agreement with experimentally measured responses.

Knowledge of the antenna structure is essential in studies of future large antenna designs. Studies using the dynamic characteristics of the antenna structure are generally oriented around control system principles. The antenna control system consists of various subsystems – the power amplifier, hydraulic drive, and the structure – interconnected to form a servoloop. A simplified block diagram of a system is given in Figure 1. When each block in the loop is described by its transfer function, the loop can be analyzed to determine the characteristics of the control system. It is the objective of this investigation to determine such transfer functions for the structure of the antennas for use in the control system studies.

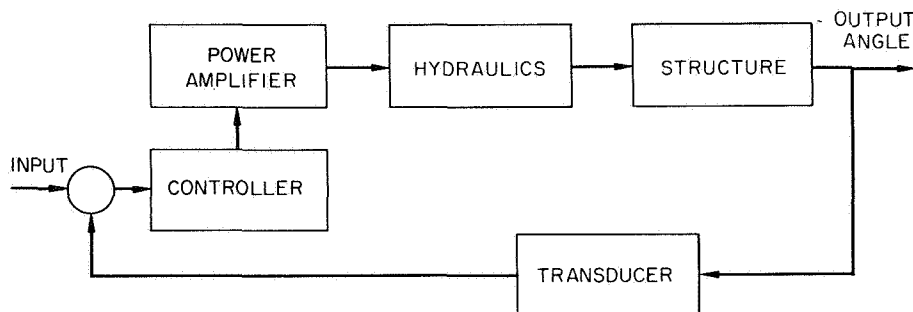


Figure 1—Antenna control system

*Rutgers University, New Brunswick, N. J.

**George Washington University, Washington, D.C.

The Rosman-I antenna is an X-Y mounted, ground-based antenna with an 85-foot-diameter paraboloidal reflector (Figure 2). A quadruped structure supports the radio-signal receiving elements at the paraboloid focus. A detailed examination of the antenna structure reveals several substructures: the foundation and the tower, the X-wheel, the Y-wheel, the reflector, and the feed support.

In constructing a simplified mathematical model, each substructure may be represented by one or more grid points or lumped masses. These points may be chosen to coincide with certain key locations on the antenna such as the drive system, the X- and the Y-bearings, the reflector dish, or the feedbox. After the model has been built, results can be compared with experimental measurements recorded in actual on-site tests.

The mass of the structure is lumped on 13 points. Since there is a translational degree of freedom along each of the x-, y-, and z-directions of a Cartesian coordinate system, a simplified model of 39 degrees of freedom is obtained (the x- and y-directions coincide with the directions of the X-wheel and the Y-wheel shafts, respectively, and z represents the vertical direction). Information regarding the selection of points and the mass associated with each point is given in Appendix A.

In order to simulate the actual behavior of the structure in the simplified model, the various masses would have to be interconnected by complicated springs. The determination of the proper connections is rather difficult if the simplified model is to closely simulate the actual structure at the higher frequency range. Since the static properties of the actual structure have previously been determined by the Martin Co. SB038 program, it is desirable to incorporate this information in the present investigation. This is possible by choosing key locations on the structure that coincide with the existing grid points used in the SB038 program. A small computer program is written to generate an influence coefficient matrix for the simplified model (39×39) used in this study from the tape that has the complete influence coefficient matrix of the structure (645×645). This is accomplished by applying successive unit loads at each degree of freedom and allowing the program to compute the resulting deflections at all 39 points.

The influence coefficient matrix obtained in this manner is found to be unsymmetrical. However, in order to use a simple eigenvalue routine presently available in the GSFC computer library, the influence coefficient matrix has been forced into a symmetrical form. In addition, because the diagonal terms of the matrix do not always dominate, in magnitude, the off-diagonal terms, it has been necessary to reestimate some of the diagonal terms to improve the conditioning of the matrix. The resulting matrix is given in Appendix B.

After the mass and the influence coefficient matrices of the simplified model have been determined, the differential equations governing the dynamics of structure may be written in matrix form as

$$M\ddot{X} + D^{-1}X = Q,$$

or

$$DM\ddot{X} + X = DQ, \quad (1)$$

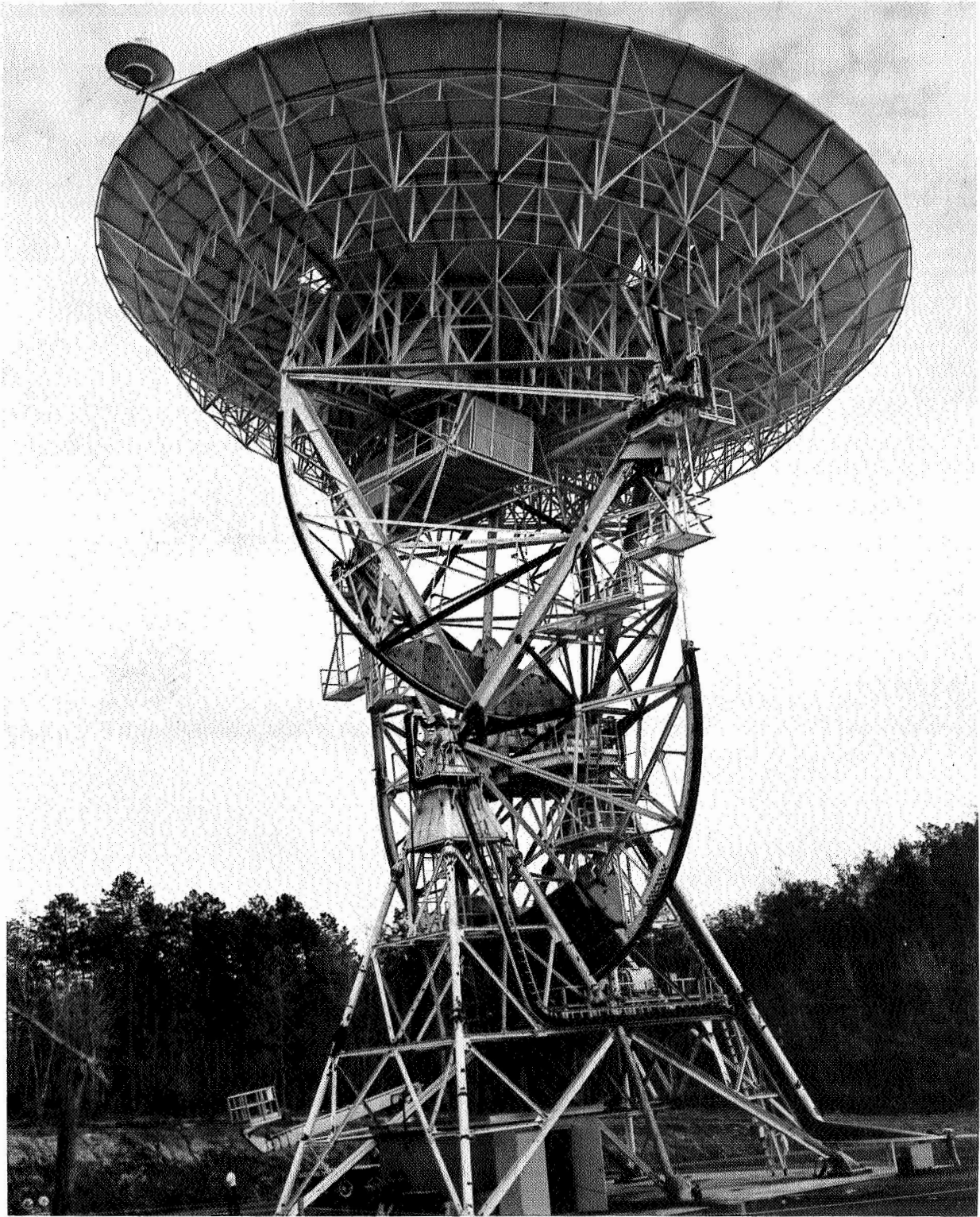


Figure 2—Rosman-1 antenna at zenith position

where M and D are the mass and influence coefficient matrices, respectively X and \ddot{X} represent the displacement and the acceleration vectors, respectively, and Q denotes the force vector.

Pre multiplying Equation 1 by the transpose M^T of M , and noting that $M^T = M$,

$$M^T DM\ddot{X} + M^T X = M^T DQ,$$

or

$$A\ddot{X} + MX = MDQ, \quad (2)$$

where $A = MDM$; A is a symmetrical matrix.

NATURAL FREQUENCIES AND MODES OF VIBRATIONS

The free vibrations of the system are governed by the homogeneous equation associated with Equation 2; namely,

$$A\ddot{X} + MX = 0. \quad (3)$$

Let

$$X = \phi^j \sin \omega_j t, \quad j = 1, 2, \dots, N, \quad (4)$$

where N is the number of degrees of freedom and ω_j and ϕ^j represent the j^{th} natural frequency and mode of vibration, respectively. When Equation 4 is substituted into Equation 3 and $\sin \omega_j t$ is canceled from both sides,

$$-\omega_j^2 A \phi^j + M \phi^j = 0. \quad (5)$$

Premultiplying Equation 5 by $(\phi^j)^T$ yields

$$-\omega_j^2 (\phi^j)^T A \phi^j + (\phi^j)^T M \phi^j = 0,$$

or

$$(\phi^j)^T M \phi^j = \omega_j^2 (\phi^j)^T A \phi^j. \quad (6)$$

It can be shown (see, e.g., Reference 1), that

$$(\phi^j)^T M \phi^k = 0 \quad \text{for } j \neq k, \quad (7)$$

which is the orthogonality relationship existing between any two of the different modal vectors.

If all the ϕ^j column vectors are assembled into an $N \times N$ matrix Φ ,

$$\Phi^T M \Phi = \omega^2 \Phi^T A \Phi, \quad (8)$$

where ω^2 is a diagonal matrix whose diagonal elements are successively $\omega_1^2, \omega_2^2, \dots, \omega_N^2$. Equation 8 defines the eigenvalue problem, which is later solved numerically by the computer routine previously mentioned.

FORCED VIBRATION

The solution to the equation governing the forced vibration (Equation 2) is given by

$$X = \sum_j \phi^j \xi_j = \Phi \xi, \quad (9)$$

in which ξ_j is a scalar time function associated with the j^{th} mode, and ξ represents a column vector whose elements are the ξ_j 's. Substituting Equation 9 into Equation 2 yields

$$A \Phi \ddot{\xi} + M \Phi \dot{\xi} = M D Q. \quad (10)$$

Premultiplying Equation 10 by Φ^T yields

$$\Phi^T A \Phi \ddot{\xi} + \Phi^T M \Phi \dot{\xi} = \Phi^T M D Q. \quad (11)$$

Let

$$B \equiv \Phi^T A \Phi. \quad (12)$$

It can be shown that B is a diagonal matrix [1]. Premultiplying Equation 11 by B^{-1} , yields

$$\ddot{\xi} + B^{-1} \Phi^T M \Phi \dot{\xi} = B^{-1} \Phi^T M D Q \quad (13)$$

This equation reduces, after some elementary calculations, to

$$\ddot{\xi} + \omega^2 \xi = \Phi^{-1} M^{-1} Q. \quad (14)$$

The solution to Equation 14 depends on the nature of the force vector Q .

TRANSFER FUNCTIONS

Taking the Laplace transforms of both sides of Equation 14 and denoting the transformed variables by the same symbols as the original variables but with a bar yields

$$\ddot{\bar{\xi}} + \omega^2 \bar{\xi} = \Phi^{-1} M^{-1} \bar{Q}, \quad (15)$$

and also

$$\bar{X} = \Phi \bar{\xi}. \quad (16)$$

Hence,

$$\bar{\xi} = \Phi^{-1} \bar{X} \quad (17)$$

and

$$\ddot{\bar{\xi}} = \Phi^{-1} \ddot{\bar{X}}.$$

Substituting Equations 17 into Equation 15 results in

$$\Phi^{-1} \ddot{\bar{X}} + \omega^2 \Phi^{-1} \bar{X} = \Phi^{-1} M^{-1} \bar{Q}. \quad (18)$$

When zero initial conditions are assumed and the properties of the Laplace transforms of the derivatives of a function are used, Equation 18 may be reduced to

$$\Phi^{-1} s^2 \bar{X} + \omega^2 \Phi^{-1} \bar{X} = \Phi^{-1} M^{-1} \bar{Q}. \quad (19)$$

Equation 19 can be rewritten, by noticing that s^2 is a scalar, as

$$s^2 I \Phi^{-1} \bar{X} + \omega^2 \Phi^{-1} \bar{X} = \Phi^{-1} M^{-1} \bar{Q},$$

or

$$(s^2 I + \omega^2) \Phi^{-1} \bar{X} = \Phi^{-1} M^{-1} \bar{Q}, \quad (20)$$

where I is the identity matrix. When a diagonal matrix Z defined by

$$Z = \begin{bmatrix} s^2 + \omega_1^2 & 0 & 0 & \cdots & 0 \\ 0 & s^2 + \omega_2^2 & 0 & \cdots & 0 \\ \vdots & \vdots & \vdots & \ddots & \vdots \\ \vdots & \vdots & \vdots & \vdots & \vdots \\ 0 & 0 & 0 & \cdots & s^2 + \omega_n^2 \end{bmatrix} \quad (21)$$

is introduced, Equation 20 can be expressed in the form

$$Z\Phi^{-1}\bar{X} = \Phi^{-1}M^{-1}\bar{Q}$$

or

$$\bar{X} = \Phi Z^{-1}\Phi^{-1}M^{-1}\bar{Q}. \quad (22)$$

For computer programming purposes it is desirable to avoid finding the inverse of the modal matrix Φ . Since from Equation 12

$$\Phi^{-1} = B^{-1}\Phi^T A = B^{-1}\Phi^T M D M,$$

consequently

$$\bar{X} = \Phi Z^{-1}B^{-1}\Phi^T M D \bar{Q}. \quad (23)$$

Since matrices Z and B are diagonal, their inverses can be found easily.

Let

$$\Psi = B^{-1}\Phi^T M D, \quad (24)$$

and

$$T = \Phi Z^{-1}\Psi. \quad (25)$$

Equation 23 reduces, after substituting Equations 24 and 25, to

$$\bar{X} = T\bar{Q}. \quad (26)$$

The structure of the T matrix can be developed by expanding the right-hand side of Equation 25; i.e.,

$$t_{ij} = \sum_{k=1}^N \phi_{ik} \psi_{kj} / (s^2 + \omega_k^2), \quad (27)$$

where t_{ij} , ϕ_{ik} , and ψ_{kj} are the elements of the respective matrices T , Φ , and Ψ .

Since the transfer function for a one-degree-of-freedom system is the function which, when multiplied by an input function, gives the output function, the matrix T (Equation 26) is obviously the transfer matrix of the structural model. To evaluate a particular pair of output-input relationships

$$\bar{x}_i = \sum_j t_{ij} \bar{q}_j = \sum_j \bar{q}_j \sum_{k=1}^N \phi_{ik} \psi_{kj} / (s^2 + \omega_k^2), \quad (28)$$

where the index j denotes all the input points. If \bar{x}_i is due to a single input at the j^{th} coordinate, the summation sign over j drops out.

Thus far the structural system has been assumed to be frictionless, and the analysis has been based on the undamped vibrations. An approximate analysis which includes damping may be made by assuming that the system damping is very light. For this condition the modal analysis remains valid. In this case the transfer matrix is obtained by modifying Z into Z_d as

$$\begin{bmatrix} s^2 + 2\zeta_1 \omega_1 s + \omega_1^2 & 0 & 0 \cdots \cdots \cdots 0 \\ 0 & s^2 + 2\zeta_2 \omega_2 s + \omega_2^2 & 0 \cdots \cdots \cdots 0 \\ \cdot & \cdot & \cdot \\ \cdot & \cdot & \cdot \\ \cdot & \cdot & \cdot \\ 0 & 0 & 0 \cdots \cdots s^2 + 2\zeta_N \omega_N s + \omega_N^2 \end{bmatrix} \quad (29)$$

where $\zeta_1, \zeta_2, \dots, \zeta_N$ are the modal damping coefficients for modes 1, 2, \dots , N respectively.

NUMERICAL RESULTS

On the basis of the above analysis, a computer program has been developed to calculate the natural frequencies, the modes of vibration, and the transfer matrix of the system. The natural frequencies and the modes of vibration obtained from the computer are listed in Figure 3. The eigenvalues represent the values of ω_j^2 or the squared value of the circular frequencies. The corresponding frequencies, in cycles per second, can be found from

$$f_j = \frac{\omega_j}{2\pi}$$

A simple computation shows that the eigenvalues correspond to frequencies of 1.03 to 43.5 cps. This range partially agrees with the experimentally measured frequency range. This may be evidence that the mathematical model constructed in this study has realistic dynamic behavior insofar as the frequency aspect is concerned. Generally speaking, the simulation of the modal shapes is not expected to give the same agreement as that in the frequencies. A response calculation will be made to compare with available results of the experimental measurements.

The transfer coefficients $t_{ij}^{(k)} = \varphi_{ik} \psi_{kj}$ obtained by using the computer program are shown in Figure 4. Since the total number of transfer coefficients is $N \times N \times N$, the values listed are those associated only with the fundamental frequency ω_1 . The complete listing of all the values of t_{ij} is available in computer printout form at the Antenna System Branch of Goddard Space Flight Center.

EIGENVALUE NO. 1 = 0.41606855E 02
EIGENVECTOR
0.47454407E-02 0.61378168E-02 0.75857676E-03 0.47156435E-02 0.51422128E-02 0.92711108E-03 0.18282567E-02 0.16255552E-02
-0.61708604E-03 0.87233666E-03 0.16228247E-02 0.14038168E-03 0.76204967E-02 0.28392918E-02 0.32052314E-04 -0.14515366E-02
0.89188892E-02 0.69380621E-05 0.72589798E-02 0.14703825E-01 -0.23524769E-03 0.14301590E-01 0.14919756E-01 0.11224742E-02
0.37639046E-01 0.17896407E-01 -0.49338460E-02 -0.33005985E-02 0.95339906E-02 0.22226173E-04 0.12445154E-01 0.15762818E-01
-0.60350998E-03 0.94899494E-02 0.15303484E-01 -0.15176263E-02 0.57311071E 00 0.31528994E-00 0.97208806E-02

EIGENVALUE NO. 2 = 0.75857990E 02
EIGENVECTOR
-0.98071045E-02 0.59558247E-01 -0.90543457E-03 -0.99149724E-02 0.61042193E-01 -0.17327492E-02 -0.38884884E-02 0.15614480E-01
0.37674259E-02 -0.13200055E-02 0.15622148E-01 0.17288411E-01 -0.17445996E-01 0.30232649E-01 0.14194981E-02 0.16239659E-02
0.74512286E-01 0.93310896E-04 -0.16090232E-01 0.11539984E-00 -0.12884589E-02 -0.34426912E-01 0.11627361E-01 0.88277671E-02
-0.57691523E-01 0.79659951E-01 0.10244548E-05 0.71043544E-02 0.88751132E-01 0.49265742E-03 -0.15294024E-01 0.12902788E-00
-0.44525883E-02 -0.72701591E-02 0.12685394E-00 -0.14865999E-01 -0.39374733E-00 0.66847448E 00 0.17215927E-01

EIGENVALUE NO. 3 = 0.11089526E 03
EIGENVECTOR
0.27064084E-01 0.16160738E-00 0.71429315E-03 0.27626527E-01 0.16165175E-00 0.43311813E-02 0.89633105E-02 0.38472214E-01
-0.22040464E-01 0.36658435E-02 0.38457571E-01 0.29661585E-01 0.58437605E-01 0.83646980E-01 0.30025408E-03 -0.86292308E-02
0.14815842E-00 0.33272803E-03 0.40915098E-01 0.19351684E-00 -0.30675647E-02 0.41137783E-01 0.18908759E-01 0.18932216E-01
0.89353466E-01 0.17864814E-00 0.84193633E-02 -0.16721807E-01 0.19609089E-00 0.14220540E-02 0.36412340E-01 0.22261412E-00
-0.99850146E-02 0.37711270E-01 0.22273488E-00 -0.32705064E-01 0.14950383E-00 -0.44824563E-00 0.35327446E-01

EIGENVALUE NO. 4 = 0.12252107E 03
EIGENVECTOR
0.11298352E-00 -0.44211185E-01 -0.20080002E-02 0.11271220E-00 -0.33227916E-01 0.16166644E-01 0.37476975E-01 -0.92578578E-02
-0.23451530E-02 0.10741047E-01 -0.92833313E-02 -0.15415648E-01 0.26060677E-00 -0.19884668E-01 0.19454926E-02 -0.25264166E-01
-0.28099295E-01 0.19858871E-03 0.11770802E-00 -0.32119857E-01 0.10194661E-02 0.14683228E-00 -0.32091606E-01 -0.50480848E-02
0.18038108E-00 -0.30619451E-02 -0.28682537E-01 -0.81608538E-01 -0.41210739E-01 -0.24479602E-04 0.15135086E-01 -0.4864866E-01
0.25759288E-02 0.13262576E-00 0.40913482E-01 0.78031110E-02 -0.16040707E-00 0.16733088E-00 -0.91132085E-02

EIGENVALUE NO. 5 = 0.22765797E 03
EIGENVECTOR
-0.13166660E-03 -0.23036680E-00 0.65801434E-02 -0.74368916E-04 -0.23111016E-00 0.33600497E-02 0.21614504E-02 -0.39725287E-01
0.10749691E-00 0.31909300E-03 -0.39800844E-01 -0.12757464E-01 -0.20514443E-01 -0.14970761E-00 0.28114638E-02 -0.67644231E-02
0.45215984E-01 0.20758864E-02 0.18118485E-01 0.34551685E-00 0.34477448E-03 0.17348665E-01 0.34398312E-00 -0.25708564E-02
0.14790940E-00 0.18950063E-00 -0.13885865E-00 0.25651259E-01 0.13329098E-00 0.46457299E-02 0.24351326E-01 0.55209066E 00
-0.77132415E-03 0.32698815E-01 0.52069471E 00 0.12938587E-01 0.24775402E-01 -0.12579525E-00 0.62550591E-01

EIGENVALUE NO. 6 = 0.27718224E 03
EIGENVECTOR
0.10722940E-00 0.55209408E-01 0.46322980E-01 0.11160429E-00 -0.64959148E-01 0.17111951E-01 0.12435015E-01 0.84115878E-02
-0.28720074E-01 0.23093347E-01 0.76203010E-02 -0.14926276E-01 -0.18258363E-00 0.47790086E-01 0.57161447E-02 -0.30661133E-01
0.16963511E-01 0.91052940E-03 0.13690977E-00 -0.18392757E-01 -0.30816160E-02 0.23413495E-00 -0.58436476E-01 -0.3758759E-02
0.14099269E 01 0.32862531E-00 -0.72199760E-01 -0.94147764E-01 -0.33780460E-01 -0.19259726E-02 0.23335212E-00 -0.11739858E-00
-0.97686479E-02 0.94846164E-01 -0.10561703E-00 0.17951897E-01 -0.12516949E-01 0.65687536E-01 0.10202640E-00

EIGENVALUE NO. 7 = 0.29869714E 03
EIGENVECTOR
0.79537502E-01 -0.46777108E-00 0.23982219E-01 0.80047772E-01 0.32310747E-00 0.97058296E-02 0.26682454E-01 0.21044051E-01
-0.11344025E-01 -0.34456351E-02 0.21176045E-01 -0.63465575E-02 0.84599814E-01 0.14824597E-00 0.14324504E-02 -0.52487950E-02
-0.46320433E-02 0.76687394E-03 -0.20292089E-00 -0.26452796E-02 0.28290304E-02 0.14268512E-00 -0.72714005E-02 -0.77536222E-02
-0.21557575E-00 0.38238578E-01 -0.63421067E-01 -0.66775706E-01 -0.11493647E-01 0.26405509E-02 0.24013648E-01 0.20897532E-01
0.10693986E-01 0.32191315E-00 0.16249925E-01 0.28135321E-01 0.54355606E-02 -0.10430059E-01 -0.17620302E-01

EIGENVALUE NO. 8 = 0.30124167E 03
EIGENVECTOR
-0.46046688E-01 -0.69345076E-01 -0.13637817E-01 -0.45981117E-01 -0.34258427E-00 -0.52685775E-02 -0.11428522E-01 0.60614166E-01
-0.19676154E-02 0.25999267E-02 0.60664015E-01 0.20501221E-01 0.48771838E-01 0.40864053E-00 -0.25330922E-02 0.36913233E-02
-0.8138005E-01 -0.33868057E-03 0.63698434E-01 0.34294913E-01 0.73086116E-02 -0.80096328E-01 0.44085766E-01 -0.3746322E-01
-0.49977965E-01 -0.49704286E-01 -0.93275202E-01 0.60932994E-01 -0.59001987E-01 -0.10318250E-02 -0.88565917E-01 0.88258361E-01
0.25595937E-01 -0.12471785E-00 0.75372007E-01 0.64524289E-01 0.10437043E-01 -0.83268788E-02 -0.67389723E-01

EIGENVALUE NO. 9 = 0.34074771E 03
EIGENVECTOR
-0.10605978E-00 -0.14497362E-00 -0.21318026E-01 -0.10607875E-00 -0.74529521E-01 -0.11479481E-01 -0.50062726E-02 -0.27146471E-02
-0.78606849E-01 -0.72642967E-02 -0.29275463E-02 -0.12681190E-01 0.48877160E-01 -0.12440248E-01 -0.70547654E-02 -0.38753171E-02
0.18624533E-00 -0.23378482E-02 -0.45151596E-01 -0.11035366E-00 -0.10514450E-02 0.89997501E-03 -0.14255668E-00 -0.41963720E-02
0.20402540E-00 0.96918544E-01 0.10244176E-00 -0.12683746E-01 0.89153658E 00 0.44566058E-02 0.11085656E-01 -0.45874452E-00
0.36099102E-02 0.58142265E-02 -0.30952916E-00 -0.14283347E-01 -0.13359457E-01 0.24434158E-01 -0.50141016E-01

EIGENVALUE NO. 10 = 0.34272581E 03
EIGENVECTOR
-0.33220951E-00 -0.91489074E-01 -0.48307372E-01 -0.33000084E-00 0.18249695E-00 -0.19848100E-01 -0.1508844E-01 0.33318630E-03
0.24142803E-01 -0.25500339E-01 -0.50167930E-03 0.71427840E-02 0.14563885E-00 -0.16969157E-02 -0.56604657E-02 0.52339692E-02
-0.49738417E-01 -0.12443611E-02 -0.16621660E-00 0.17838675E-01 -0.14005871E-02 0.36458073E-01 0.20597386E-02 -0.6159840E-02
0.81720769E 00 0.10928652E-00 0.59204025E-01 0.41348756E-00 -0.28887697E-00 -0.81192562E-02 0.40098643E-02 0.83480617E-01
0.32108288E-02 0.30723721E-01 0.15770640E-01 -0.15770640E-01 0.34177364E-01 0.13922574E-01 -0.27841806E-01

EIGENVALUE NO. 11 = 0.40941392E 03
EIGENVECTOR
-0.50975154E-02 -0.26725031E-02 -0.34338986E-02 -0.17939842E-02 -0.21925016E-02 -0.45563558E-02 -0.46070212E-02 0.26493415E-03
0.13396348E-01 -0.22327507E-02 0.27080198E-03 0.28515017E-02 0.71893407E-03 -0.14233872E-02 -0.73206217E-02 -0.21678535E-03
0.17704786E-00 0.81526191E-03 0.39496454E-02 0.72911354E-01 -0.13354152E-03 -0.16589904E-01 0.28544415E-01 -0.86392733E-03
-0.23584645E-01 0.32215374E-01 -0.30827234E-01 -0.30937193E-01 -0.92544266E-01 0.32940556E-02 0.21820505E-02 -0.11137486E 01
0.26441468E-03 -0.12658889E-02 0.11583665E 01 -0.15837436E-03 0.24949055E-02 -0.45809194E-02 0.54651921E-02

EIGENVALUE NO. 12 = 0.41398474E 03
EIGENVECTOR
0.22376062E-00 0.46050031E-01 0.93884882E-01 0.20821218E-00 -0.81168407E-02 0.96090878E-01 0.16421632E-01 -0.32924979E-02
-0.87625203E-01 0.81731964E-01 -0.25076789E-02 -0.72402666E-01 -0.40250877E-01 -0.57411023E-02 0.10465355E-01 -0.7780547E-01
-0.14968827E-01 0.38239178E-02 0.64952800E-01 -0.92474874E-01 0.33242125E-02 0.15315956E-00 -0.25653686E-01 0.29290821E-02
-0.12146842E-00 -0.2933537E-00 -0.15024813E-00 0.10090542E 01 0.23800521E-01 0.27480809E-02 0.43885976E-01 -0.48790617E-02
0.20081265E-01 0.17430697E-01 0.70877004E-01 -0.22518502E-01 -0.42134225E-02 0.14148816E-01 -0.17231324E-01

EIGENVALUE NO. 13 = 0.57339258E 03
EIGENVECTOR
-0.64511520E 00 0.69036329E-03 0.19943966E-01 0.65457990E 00 -0.61986747E-02 0.20800260E-01 0.38690872E-02 0.18945320E-02
0.24840482E-01 0.26860679E-02 0.20223965E-02 0.22995242E-01 0.41654270E-02 0.16964208E-03 0.21771406E-01 -0.88162497E-02
0.12752813E-01 0.49690511E-02 -0.7574465E-04 0.23284990E-01 -0.23026131E-02 -0.12456211E-01 -0.74490875E-01 -0.1164170E-01
-0.63870074E-01 0.14528473E-00 -0.24107211E-01 0.38068221E-01 -0.77244943E-02 0.56447900E-02 0.20983805E-01 -0.14245604E-01
-0.12149153E-01 0.31709515E-01 -0.25556699E-01 0.25214215E-01 0.17319100E-02 -0.31734388E-02 0.10264716E-01

Figure 3—Eigenvalues and eigenvectors

EIGENVALUE NO. 14 = 0.58270378E 03
EIGENVECTOR
-0.68476340E-01 0.10428378E-0C -0.18323985E-01 -0.12559033E-00 -0.94260582E-01 -0.29450447E-01 0.18794305E-C2 -C.1.151454E-01
-0.62654126E-01 0.31045674E-01 -0.88120509E-02 -0.74646220E-01 -0.29654085E-01 -0.10034365E-01 -0.60376464E-1 -C 30876249E-02
0.23213989E-01 -0.29010930E-01 0.38315625E-00 -0.29617275E-00 -0.56521595E-03 -0.11098777E-0C -G.1286199C -i -C.25762641E-01
-0.62332901E 00 0.12077256E 01 -0.17910319E-00 0.82770010E-01 -0.33665220E-01 -0.18148934E-02 0.10904897E 00 -C.19064994E-00
0.29797670E-01 0.25326823E-00 0.17337095E-00 -0.27260166E-01 -0.81642187E-03 -0.19556433E-02 -0.2394355E-0

EIGENVALUE NO. 15 = 0.59831614E 03
EIGENVECTOR
0.27527718E-01 -0.12879365E-01 -0.48061953E-01 0.68016139E-01 0.56601067E-01 -0.40586204E-01 -0.13329772E-01 -0.75060794E-02
-0.11704987E-00 -0.15036734E-01 -0.83964440E-02 -0.53732439E-01 0.98031776E-02 0.17011768E-01 -0.4645491E-1 0 62874954E-01
-0.40687575E-00 -0.17501754E-01 -0.28128463E-00 -0.14351878E-01 -0.28018097E-02 0.16163399E-00 -0.12545275E C1 -0.32593601E-01
0.40214472E-00 -0.49052738E-00 0.25299819E-00 -0.10868899E-00 0.18601492E-00 -0.37980621E-02 -0.66980264E 00 0.53482154E 00
0.22363387E-01 -0.14649840E-01 0.66018284E 00 -0.53288223E-01 -0.18474370E-01 0.53690951E-01 -0.5345375E-C3

EIGENVALUE NO. 16 = 0.62787373E 03
EIGENVECTOR
0.51823791E-01 -0.20289002E-01 0.29127289E-00 -0.58125079E-01 0.16031887E-01 0.29142606E-00 -0.3C247926E-01 0.28550960E-01
-0.43422838E-00 -0.16222731E-01 0.28320932E-01 0.42723911E-00 0.37455824E-01 0.82987510E-02 0.4723891E-00 C.30632178E-01
-0.94341591E-01 0.98331861E-01 -0.12465800E-00 0.58085433E-01 0.18817142E-01 -0.59458097E 0C -0.6008639E 00 -C.23279156E-00
0.73914588E-02 0.37788240E-03 0.26513124E-00 0.28709071E-01 0.25216639E-01 0.94286320E-01 -0.18517514E-01 -0.21437577E-01
-0.18010480E-00 0.53547093E-01 0.14166775E-01 0.41440292E-00 0.10582467E-01 -0.83294880E-02 0.4726842E-

EIGENVALUE NO. 17 = 0.66985094E 03
EIGENVECTOR
0.19623584E-00 -0.10550452E-00 -0.13828920E-00 0.13064979E-00 0.53613360E-01 -0.11128592E-0C 0.34590524E-01 0.25584140E-02
-0.56766603E-01 0.44095819E-02 0.21716823E-02 -0.10961993E-00 0.39108091E-01 0.15555444E-02 -0.1886865E-00 -C.77307445E-01
0.19910944E-00 -0.49271996E-01 -0.29336628E-00 0.83804530E 00 0.21594074E-02 -0.17490470E 01 -0.69839734E -C -C.12463722E-00
0.26671886E-00 0.78930827E 00 -0.88390116E-01 0.10681700E-00 -0.89543552E-01 -0.53931204E-01 -0.7225205E-01 -0.8094821E-01
0.78949036E-01 0.92655869E-01 -0.15376956E-00 -0.21790919E-00 0.29358322E-01 -0.24140797E-01 0.1525028CE-C

EIGENVALUE NO. 18 = 0.75459960E 03
EIGENVECTOR
0.43368915E-01 -0.12871977E-01 -0.23712101E-03 0.11445936E-01 -0.28400354E-02 0.51199408E-02 0.37578803E-02 0.55525609E-02
0.32579468E-01 0.69385080E-02 0.56459551E-02 0.26441219E-01 -0.11342134E-01 -0.14126923E-02 -0.11208375E-1 -C.20548428E-01
0.11745505E-00 -0.25429866E-01 -0.47602324E-01 -0.19664051E 01 0.60177352E-02 -0.13267663E 01 -0.15241799E 01 -C.21073324E-01
0.11967367E-01 0.61331252E 00 -0.67241964E-01 0.47362024E-01 -0.26552874E-01 0.33870325E-02 0.25148784E-0 -C.14794754E-01
0.21963295E-02 0.18521626E-00 0.33341179E-03 0.94256622E-02 0.15976457E-01 -0.22957528E-01 0.1224446CE-

EIGENVALUE NO. 19 = 0.10362227E 04
EIGENVECTOR
0.44585233E-01 -0.12323627E-00 -0.55855289E-01 0.93028909E-01 0.17753433E-00 -0.31703234E-01 0.2433882CE-01 0.40185889E-01
0.12213480E-00 -0.41125085E-01 0.37820406E-01 -0.13065866E-01 0.17705169E-01 0.12501232E-01 -0.63484517E-12 -0.5394894E-02
-0.17734984E 01 0.60891882E-02 0.48947428E-00 0.32373012E-00 -0.24919212E-03 -0.92374237E 00 0.73507562E-C1 -0.13389075E-01
0.36433931E-00 -0.32362305E-03 0.83984576E 00 -0.16659185E-01 0.14936303E-00 0.81258835E-01 0.78320075E -C -C.28102938E-01
-0.82635792E-01 -0.15237873E 01 0.19990189E-00 0.97991502E-01 0.10712949E-01 0.17599892E-01 -0.72319412E -C

EIGENVALUE NO. 20 = 0.10901555E 04
EIGENVECTOR
0.45712195E-01 -0.20010603E-01 -0.21606297E-01 0.67948480E-01 0.11201642E-00 -0.30954095E-01 -0.12201738E-01 0.12350552E-00
-0.12608736E-00 -0.47472796E-01 0.12156307E-00 0.93921814E-01 0.27803278E-01 -0.43446265E-01 0.6332665E-1 0.36327869E-01
0.25560451E 01 -0.1970344E-01 0.69990825E 00 -0.43924472E-00 -0.12109097E-01 0.67073174E-01 0.37993755E-C0 -C.36679120E-01
0.14602914E-00 0.22375752E-01 -0.23052610E-00 -0.36490995E-01 -0.17777456E-00 -0.12294300E-01 -0.990836CE-C2 -C.17772172E-00
-0.12758024E-00 -0.14474191E 01 -0.57245276E-01 0.28381734E-00 0.63844930E-02 0.69656391E-02 -C.39520121E-1C

EIGENVALUE NO. 21 = 0.12694551E 04
EIGENVECTOR
0.85397996E-02 0.63359088E-01 0.27661761E-02 -0.15068427E-01 0.11191279E-01 -0.10313454E-0C 0.18726132E-C1 0.75849152E 00
-0.10287574E-00 -0.16418953E-01 0.75785279E 00 -0.23369637E-01 0.40501031E-02 -0.83863880E-01 -C.2336056E-C0 -C.23117140E-01
-0.31919343E-00 -0.86744428E-02 -0.31045150E-00 0.86204678E-01 -0.62791910E-01 -0.17003118E-0C -C.70911656E-01 -C.13447353E-01
0.23368273E-02 -0.32528885E-03 -0.79638058E 00 0.14432445E-01 0.80686812E-01 -0.46229744E-02 0.96440241E-1 -C.26941645E-02
-0.11364304E-00 0.15301317E-00 0.16778383E-01 0.22377163E 01 -0.40073339E-02 -0.30498324E-02 0.4024571CE-00

EIGENVALUE NO. 22 = 0.14610061E 04
EIGENVECTOR
0.42316212E-01 -0.10721883E-00 0.62256780E-01 0.71145865E-02 0.10137434E-00 0.97568052E-01 0.98865397E-01 0.15811483E-00
0.89400104E 00 0.18309005E-01 0.16147958E-00 -0.45816220E-00 0.77244679E-02 0.47346123E-03 -0.32372316E-0 -C.35097247E-00
-0.84500776E 00 -0.9597529E-02 0.15202215E 01 -0.44354875E-00 -0.22826858E-01 0.13722017E 00 0.22150912E-C0 -C.84586711E-02
-0.38821166E-00 0.18473449E 01 -0.11319579E-00 0.13477536E-00 -0.56366079E-02 -0.30084053E-01 -0.1082105E-1 -0.24672967E-00
-0.81432720E-02 -0.50201127E 00 -0.20293009E-00 -0.45842884E-01 -0.68442903E-02 0.10048600E-01 0.42909829E-C0

EIGENVALUE NO. 23 = 0.15190768E 04
EIGENVECTOR
-0.53178111E-01 -0.20802853E-01 -0.18581553E-00 8.34312701E-01 -0.43206877E-01 -0.98995566E-01 0.19832534E-0C 0.7862983E 00
-0.48728306E-02 0.11452299E-01 0.79062343E 00 -0.93674939E 00 -0.23277117E-01 -0.60901366E-01 0.37136183E-C -0.68362355E-02
-0.40186038E-01 -0.21149509E-01 0.34537555E-00 0.16633641E-01 -0.46196580E-02 0.29349293E-0C 0.3173952E-C -C.13881873E-01
-0.14706162E-01 0.87908699E 00 0.10713939E 01 -0.33616347E-01 -0.11048291E-00 -0.47823790E-01 -0.6673495E -C -C.2890545E-01
-0.88974980E-01 0.57918436E 00 -0.18433996E-01 -0.53187110E-01 0.10205632E-01 0.14126042E-01 -0.2150875CE -C1

EIGENVALUE NO. 24 = 0.17554041E 04
EIGENVECTOR
0.48231948E-01 -0.23699046E-01 -0.43531954E-00 -0.43236759E-01 -0.55649333E-01 0.94415925E-01 0.63883642E CC 0.88390456E 00
0.42192069E-00 0.16515645E-00 0.89800198E 00 -0.61338355E 00 -0.15442780E-01 -0.21985603E-01 0.13879655E-C -C.49905086E-00
0.84405748E-01 0.32611571E-01 -0.45672809E-00 -0.13823121E-00 0.94746947E-02 0.11648259E-00 -0.21799421E-0 -C.4753875E-00
-0.15467716E-00 -0.42302085E-03 0.60898870E-02 0.16314693E-01 0.16141266E-01 -0.54248068E-02 0.56003177E CC -0.27369939E-01
-0.36386406E-01 -0.48541363E-00 -0.23888852E-01 -0.11520468E 01 -0.16630677E-01 -0.17357625E-01 0.2426825E C1

EIGENVALUE NO. 25 = 0.17901269E 04
EIGENVECTOR
0.88793630E-02 -0.54707353E-01 -0.39194085E-00 -0.35269670E-01 0.13573458E-01 -0.38292569E-00 0.23770934E-CC -0.52463006E 00
-0.10084926E 01 0.10637140E-00 -0.51399621E 00 -0.59597217E 00 -0.17857215E-01 0.26105557E-01 0.4981031CE -C.1433427E-00
-0.91425662E 00 -0.42064369E-01 0.17071027E 01 -0.13566630E-01 -0.20472825E-01 0.73824407E-01 0.16792254E-0 -0.9152372E-01
-0.20604111E-00 0.46500491E-00 -0.15947712E 01 0.24832413E-03 0.63633659E-01 -0.81701764E-01 -0.4963259E-C -C.57471149E-01
0.69407132E-01 -0.21007445E-00 0.30762319E-01 0.52243575E 00 -0.22167850E-01 0.20244694E-01 0.103269CE C1

EIGENVALUE NO. 26 = 0.18662229E 04
EIGENVECTOR
0.16392160E-01 -0.47141325E-01 0.92860581E 00 -0.12985255E-01 0.41903601E-01 -0.32125656E-00 -0.1394549E C1 0.4.6769C1E-0C
-0.89253422E-01 -0.75030444E 00 0.33923535E-00 -0.98024429E 00 0.67602818E-01 -0.34590391E-02 -0.1785631E-1 -C.7843341E 00
-0.23907604E-00 -0.12938615E-00 0.40455986E-00 -0.51152001E-02 -0.11985794E-01 -0.51553655E-00 -0.276799CE-1 -0.7820810E-01
-0.58783078E-01 -0.85280401E-01 -0.58250968E 00 0.80728804E-01 0.25899158E-01 -0.14530648E-01 -0.4940202E-01 -0.23340614E-01
-0.28647533E-00 -0.16317404E-00 -0.36290935E-02 -0.69031180E-01 -0.11649328E-01 0.35357731E-02 0.68875507E

Figure 3—Eigenvalue and eigenvectors (Continued)

EIGENVALUE NO. 27 = 0.20625701E 04
EIGENVECTOR
-0.16124329E-00 -0.68323216E-01 0.13964832E-00 -0.16326976E-00 0.74958660E-01 0.12257165E 01 0.29625203E-00 0.66357423E-01
0.58796771E 00 0.52355419E 00 0.13064533E-00 -0.54390184E 00 -0.16501444E-01 -0.14428018E-01 -0.21976764E-01 0.18593029E -1
-0.22955496E-01 0.7288405E-01 0.15250273E 01 0.15654920E-00 -0.18048210E-01 -0.62073447E 00 -0.92935058E-03 -0.47825151E-00
0.65448523E-01 -0.45078459E-00 -0.22659338E-00 -0.27678746E-00 -0.11663300E-01 0.12196789E-00 -0.22300455E-03 0.7397759E-01
0.61800298E 00 0.16965146E-00 0.71913539E-01 -0.72513739E-01 -0.12243196E-01 0.17788056E-01 0.27425583E-C1

EIGENVALUE NO. 28 = 0.28413404E 04
EIGENVECTOR
-0.30127999E-01 0.17632927E-01 -0.76802229E-01 0.31835366E-01 0.11033963E-01 0.17498145E-02 -0.30658226E-00 -0.23762873E 01
0.19672693E-00 0.28614633E-00 0.22749359E 01 -0.14712806E-00 0.12955147E-01 0.72787738E-02 0.24652439E-01 0.35797635E-00
-0.49615698E-01 -0.11849906E-01 -0.44264691E-00 -0.39129204E-01 0.91764983E-02 0.13267909E-00 0.59636144E-C2 0.87782980E-01
-0.38752162E-02 0.17008412E-00 -0.31520872E-00 0.19686567E-01 0.1714278E-01 -0.19317350E-01 0.80514078E-C2 -0.28962847E-01
-0.50896094E-02 -0.16812117E-00 -0.26765389E-01 0.31947003E-01 0.26127951E-02 -0.44534670E-02 -0.79702678E-C1

EIGENVALUE NO. 29 = 0.29499044E 04
EIGENVECTOR
-0.13990626E-00 -0.13179897E-00 0.54588502E 00 -0.14727010E-00 -0.70535390E-01 -0.32668936E-00 0.10424555E 01 0.56377241E-01
-0.12515747E 01 -0.63232025E 00 0.95076857E 00 0.12528184E 01 -0.48407676E-01 -0.67902008E-01 -0.94238472E-01 -0.15754137E 01
0.10314918E-00 -0.48289838E-01 0.22755451E 01 0.21286877E-00 -0.27618177E-01 -0.6895551E 00 -0.23763956E-01 -0.56138115E 00
0.48354388E-01 -0.91114099E 00 0.14702596E 01 -0.56706657E-01 -0.10363044E-00 0.21178371E-01 -0.31122274E-01 0.14189667E-00
-0.44035437E-00 0.85606109E 00 0.14143139E-00 -0.52651046E 00 -0.13276463E-01 0.23066368E-01 0.38888659E-01

EIGENVALUE NO. 30 = 0.31578216E 04
EIGENVECTOR
-0.52190883E-01 0.33163501E-01 0.30764341E-00 -0.96358743E-01 0.19978188E-01 0.41183361E-01 0.80427735E 00 -0.95895746E 00
0.61311773E 00 -0.50071023E 00 -0.71998511E 00 -0.18802164E 01 -0.54903788E-02 0.12703675E-00 -0.23046652E-C1 -0.12924871E 01
0.85821486E 00 0.11876317E-00 0.49174473E-00 0.39174584E-01 -0.14439276E-00 -0.30892396E-01 0.20075731E-01 0.11790712E 01
-0.86240495E-01 -0.35948008E-01 0.27286411E 01 0.17311183E-01 -0.53071496E-01 0.16429251E-00 0.29413965E-01 0.87715326E-01
-0.76665538E-01 0.13195580E-00 0.31155351E 01 0.12849359E 01 -0.14778733E-01 0.42903950E-02 0.12114674E 01

EIGENVALUE NO. 31 = 0.34575645E 04
EIGENVECTOR
-0.14938111E-00 -0.11816850E-00 -0.39783755E-00 0.95410430E-01 -0.13257760E-00 0.36721150E-00 -0.17765388E 01 0.16940206E-03
-0.16886548E 01 0.16597209E-00 0.11352583E-00 0.33851253E-00 0.31229531E-01 -0.52586431E-01 0.14551173E-01 -0.73466732E 00
-0.76515225E-01 0.22265902E-00 -0.83478444E 00 0.10565063E-00 -0.18020277E-00 0.97434989E 00 0.44247521E-01 -0.38634529E-00
-0.32167861E-00 0.14947321E 01 0.29686370E 01 0.31906059E-00 -0.26585685E-00 0.79148088E-01 -0.37910638E-01 0.16977365E-01
0.93833246E 00 -0.42301204E-00 0.31881044E-01 0.47374447E-00 -0.12332663E-01 0.79536488E-02 0.14009550E 01

EIGENVALUE NO. 32 = 0.42399381E 04
EIGENVECTOR
-0.24721623E-01 0.73946143E-01 -0.26299464E-00 0.13768614E-01 0.10995043E-00 0.25041814E-00 -0.68740404E 00 0.24742952E-02
0.86175537E 00 -0.13941194E 01 0.20977455E-00 -0.56432615E-01 -0.54341804E-01 -0.97803594E-02 0.13213222E-01 -0.27604657E 00
0.20074522E-00 0.75317784E 00 0.10539019E 01 -0.46505313E-01 -0.97943455E-01 -0.57145224E 00 -0.26320924E-01 -0.83662717E 00
0.26876298E-00 -0.10500076E 01 -0.12272781E 01 -0.48903687E-01 0.14865202E-00 0.66418459E 00 0.11956649E-01 0.41338890E-01
0.39152313E 01 0.38741327E-00 0.23771163E-01 0.63588096E-01 0.57109859E-02 0.39748390E-02 -0.80730406E-01

EIGENVALUE NO. 33 = 0.52757567E 04
EIGENVECTOR
-0.39726041E-01 -0.29183947E-01 -0.61822882E 00 -0.29828875E-01 0.11619955E-00 0.86547163E-01 -0.20837154E 01 0.31579510E-01
0.11018312E 01 0.19279772E 01 -0.16453223E-00 -0.57251517E-01 -0.91060022E-01 0.46550111E-01 -0.58656101E-01 -0.20801875E 01
0.60866959E 00 -0.85619280E-01 0.29509482E 01 0.67968261E-01 0.20005296E-00 -0.10427506E 01 -0.36641660E-01 -0.44945958E-00
0.26639301E-00 -0.20819822E 01 0.44624285E-00 0.16827021E-00 0.11972659E-00 -0.38257528E-00 0.20985557E-C1 0.11695434E-00
-0.19567601E 01 0.12945800E 01 0.84779639E-01 0.13672908E-00 -0.82609714E-03 0.65419172E-02 0.62827936E-01

EIGENVALUE NO. 34 = 0.64358766E 04
EIGENVECTOR
0.84359398E-02 -0.74775595E-01 0.36873600E-00 -0.92490918E-02 0.14792392E-01 -0.13093352E 01 0.13550812E-00 0.37636355E-00
0.48876010E-00 0.24683148E 01 0.16066068E-00 0.45751463E-00 0.10063138E-01 -0.99275736E-02 0.38119316E-01 0.26378515E 01
0.3871082E-00 0.61987006E 00 0.11989098E 01 0.48727868E-01 -0.97714666E-01 -0.28412642E-00 -0.71455276E-01 0.2394857E 01
0.83051851E-01 -0.59558733E 00 0.14343109E 01 0.16167398E-00 -0.42620602E-01 0.13437616E 01 0.14153328E-01 0.25723825E-01
0.28652896E 01 0.29255136E-00 -0.87494795E-02 -0.87313148E-01 -0.46317147E-02 -0.1523982E-02 0.89277641E 01

EIGENVALUE NO. 35 = 0.11979070E 05
EIGENVECTOR
-0.27899997E-01 -0.55898581E-01 -0.25798781E-00 -0.21892405E-01 -0.32928755E-01 0.56090084E 00 -0.28783544E-00 0.24195051E-00
-0.10489574E 01 -0.99424805E-01 0.24824361E-00 -0.25538261E-00 0.10935974E-01 -0.19391541E-01 -0.22625375E-01 0.24026332E 01
-0.61447199E 00 0.15999838E-01 -0.63630914E 00 -0.14108927E-01 -0.96491823E 00 -0.52874074E-02 0.47521121E-01 0.39567841E 01
0.10254008E-01 0.46043257E-00 -0.20014271E 01 -0.18802058E-00 -0.68001803E-01 0.49356924E 01 -0.3127328E-00 0.4137408E-01
-0.27238547E 01 -0.34854557E-00 -0.55091493E-01 -0.85841328E-00 -0.37385055E-02 0.11276936E-01 -0.71944202E 00

EIGENVALUE NO. 36 = 0.14104619E 05
EIGENVECTOR
0.12457131E-02 -0.11499470E-00 -0.53988293E 00 -0.37041239E-02 -0.77172880E-01 0.58970032E 00 -0.43927924E-01 0.62553924E 00
-0.62272319E 00 -0.10156088E 01 0.68679812E 00 0.44080709E-00 -0.46709928E-01 -0.36733067E-01 -0.95189367E-01 -0.55736743E 00
-0.39055571E-00 0.88603465E 00 0.93465241E 00 -0.34963798E-01 0.17701515E-00 -0.49621818E-00 -0.13803548E-00 0.1516914E 02
0.89316445E-01 -0.64588676E 00 -0.10021245E 01 -0.18188771E-01 0.48455099E-02 -0.29902326E 01 0.14555479E-01 0.40488369E-02
0.68908965E 00 0.2435326E-00 0.50068431E-01 -0.92668749E-00 -0.49507120E-02 -0.59471293E-01 0.17014053E-01

EIGENVALUE NO. 37 = 0.19881830E 05
EIGENVECTOR
-0.33118033E-00 0.22641435E-01 -0.22784526E 01 0.30553806E-00 -0.64427853E-01 -0.26224382E-00 -0.64622258E 01 -0.24642610E-01
0.13644983E 00 -0.44128617E 01 -0.63067704E-03 0.11048775E 01 -0.17728113E-00 0.56532901E-01 0.84863161E-01 0.7561130E 01
0.74373260E 00 -0.75120542E 00 0.31069461E 01 0.11912083E-00 -0.46241192E-01 -0.14057350E-00 -0.10914731E-01 0.16085161E-01
0.82353596E-01 -0.11845379E 01 0.25627243E 01 0.94906937E 00 -0.39557232E-01 0.11880146E 01 0.45421574E-01 0.11527587E-01
-0.15947602E 01 0.18115476E 01 -0.59467475E-01 0.48883405E-00 -0.8234690E-02 -0.12757156E-01 0.12240856E 01

EIGENVALUE NO. 38 = 0.34170587E 05
EIGENVECTOR
0.79005421E-01 0.13964687E-01 -0.28867170E-00 0.73567981E-01 -0.53129631E-02 -0.47739435E-00 0.17347647E-00 -0.1375577E-00
0.16597412E-00 -0.67381359E 00 -0.10290185E-00 0.44466201E-01 -0.18835088E-01 0.10576711E-01 -0.1085188E-01 0.2663633E 01
0.25252309E-00 0.18126112E 02 0.53723286E 00 -0.10915760E-00 0.62834854E 01 0.50009280E-01 0.20733938E-01 0.1922823E 01
-0.53099485E-01 0.14281195E-00 0.73039977E 00 0.22650141E-00 -0.20756654E-01 -0.61525411E 00 0.4246351E-01 0.15010627E-01
-0.12248979E 01 0.30914289E-00 -0.11254890E-01 0.18221640E-00 0.23620216E-02 -0.73471382E-03 0.27347921E-01

EIGENVALUE NO. 39 = 0.74040363E 05
EIGENVECTOR
0.16985650E-00 -0.12205906E-01 -0.12198363E 01 0.16032514E-00 -0.14853740E-01 -0.35667642E-00 -0.44232086E-00 0.12447178E-00
0.47700867E-00 -0.18784208E 01 0.21810809E-00 0.62068500E-00 -0.99322972E-01 -0.93787425E-02 -0.73684072E-02 0.40537840E 01
0.43646630E-00 -0.94259172E 01 0.20744830E 01 0.18980616E-00 0.25631459E 02 0.95019442E-01 0.73472492E-01 0.2580912E 01
0.10186975E-00 -0.618126674E 01 0.20604105E 01 0.54551234E 00 -0.66658618E-01 0.30813444E 01 0.19259553E-01 0.6785180E-02
0.74757759E 00 0.90602553E 00 -0.32091212E-01 0.54723641E 00 0.54723641E 00 0.14569248E-02 0.1243833E 01

Figure 3-Eigenvalues and eigenvectors (Continued)

DEGREE OF FREEDOM NO. 1								
0.54125E-06	0.70006E-06	0.86519E-07	0.53785E-06	0.58650E-06	0.10574E-06	0.20853E-06	0.18540E-06	
-0.70386E-07	0.10017E-06	0.18509E-06	0.16007E-07	0.86916E-06	0.32384E-06	0.36544E-08	-0.16318E-06	
0.10173E-05	0.78754E-09	0.82793E-06	0.16770E-05	-0.26814E-07	0.16312E-05	0.17017E-05	0.11776E-06	
0.42929E-05	0.20412E-05	-0.54345E-06	-0.32460E-06	0.10874E-05	0.25342E-08	0.14194E-05	0.17910E-05	
-0.67864E-07	0.10824E-05	0.17454E-05	-0.16514E-06	0.65366E-04	0.35961E-04	0.11087E-05		
DEGREE OF FREEDOM NO. 2								
0.70006E-06	0.90547E-06	0.11190E-06	0.69566E-06	0.75859E-06	0.13677E-06	0.26971E-06	0.23980E-06	
-0.91038E-07	0.12956E-06	0.23940E-06	0.20704E-07	0.11242E-05	0.41885E-06	0.47267E-08	-0.21105E-06	
0.13157E-05	0.10186E-08	0.10709E-05	0.21691E-05	-0.34682E-07	0.21098E-05	0.22010E-05	0.15231E-06	
0.55525E-05	0.26401E-05	-0.70291E-06	-0.41984E-06	0.14065E-05	0.32778E-08	0.18359E-05	0.23165E-05	
-0.87776E-07	0.14000E-05	0.22576E-05	-0.21360E-06	0.84546E-04	0.46512E-04	0.14340E-05		
DEGREE OF FREEDOM NO. 3								
0.86520E-07	0.11191E-06	0.13830E-07	0.85977E-07	0.93754E-07	0.16903E-07	0.33334E-07	0.29637E-07	
-0.11251E-07	0.16013E-07	0.29588E-07	0.25588E-08	0.13894E-06	0.51766E-07	0.58417E-09	-0.26084E-07	
0.16261E-06	0.12589E-09	0.13235E-06	0.26808E-06	-0.42863E-08	0.26075E-06	0.27202E-06	0.18824E-07	
0.68624E-06	0.32629E-06	-0.86873E-07	-0.51888E-07	0.17383E-06	0.40511E-09	0.22690E-06	0.28629E-06	
-0.10848E-07	0.17302E-06	0.27901E-06	-0.26399E-07	0.10449E-04	0.57484E-05	0.17723E-06		
DEGREE OF FREEDOM NO. 4								
0.53785E-06	0.69567E-06	0.85976E-07	0.53447E-06	0.58282E-06	0.10508E-06	0.20722E-06	0.18424E-06	
-0.69944E-07	0.99542E-07	0.18393E-06	0.15907E-07	0.86370E-06	0.32180E-06	0.36315E-08	-0.16215E-06	
0.10109E-05	0.78259E-09	0.82273E-06	0.16665E-05	-0.26646E-07	0.16209E-05	0.16910E-05	0.11702E-06	
0.42660E-05	0.20284E-05	-0.54004E-06	-0.32256E-06	0.10806E-05	0.25183E-08	0.14105E-05	0.17797E-05	
-0.67438E-07	0.10756E-05	0.17345E-05	-0.16411E-06	0.64956E-04	0.35735E-04	0.11018E-05		
DEGREE OF FREEDOM NO. 5								
0.58650E-06	0.75860E-06	0.93753E-07	0.58282E-06	0.63554E-06	0.11458E-06	0.22596E-06	0.20090E-06	
-0.76271E-07	0.10855E-06	0.20057E-06	0.17346E-07	0.94183E-06	0.35091E-06	0.39600E-08	-0.17682E-06	
0.11023E-05	0.85338E-09	0.89715E-06	0.18173E-05	-0.29056E-07	0.17676E-05	0.18439E-05	0.12760E-06	
0.46519E-05	0.22118E-05	-0.58889E-06	-0.35174E-06	0.11783E-05	0.27461E-08	0.15381E-05	0.19407E-05	
-0.73538E-07	0.11729E-05	0.18914E-05	-0.17895E-06	0.70832E-04	0.38967E-04	0.12014E-05		
DEGREE OF FREEDOM NO. 6								
0.10574E-06	0.13677E-06	0.16903E-07	0.10508E-06	0.11458E-06	0.20658E-07	0.40739E-07	0.36222E-07	
-0.13751E-07	0.19570E-07	0.36161E-07	0.31273E-08	0.16981E-06	0.63267E-07	0.71396E-07	-0.31880E-07	
0.19874E-06	0.15386E-09	0.16175E-06	0.32764E-06	-0.52386E-08	0.31868E-06	0.33245E-09	0.23006E-07	
0.83870E-06	0.39878E-06	-0.10617E-06	-0.63416E-07	0.21244E-06	0.49511E-09	0.27732E-06	0.34990E-06	
-0.13259E-07	0.21146E-06	0.34100E-06	-0.32264E-07	0.12771E-04	0.70256E-05	0.21661E-06		
DEGREE OF FREEDOM NO. 7								
0.20852E-06	0.26971E-06	0.33333E-07	0.20721E-06	0.22596E-06	0.40738E-07	0.80338E-07	0.71430E-07	
-0.27117E-07	0.38592E-07	0.71310E-07	0.61671E-08	0.33486E-06	0.12476E-06	0.14079E-08	-0.62866E-07	
0.39191E-06	0.30341E-09	0.31897E-06	0.64611E-06	-0.10330E-06	0.62844E-06	0.65560E-06	0.45367E-07	
0.16539E-05	0.78640E-06	-0.20937E-06	-0.12506E-06	0.41894E-06	0.97636E-09	0.54686E-06	0.69000E-06	
-0.26146E-07	0.41700E-06	0.67245E-06	-0.63624E-07	0.25183E-04	0.13854E-04	0.42715E-06		
DEGREE OF FREEDOM NO. 8								
0.18540E-06	0.23981E-06	0.29637E-07	0.18424E-06	0.20091E-06	0.36222E-07	0.71431E-07	0.63510E-07	
-0.24111E-07	0.34313E-07	0.63404E-07	0.54833E-08	0.29773E-06	0.11093E-06	0.12518E-08	-0.55896E-07	
0.34846E-06	0.26977E-09	0.28361E-06	0.57447E-06	-0.91851E-08	0.55876E-06	0.58291E-06	0.40337E-07	
0.14705E-05	0.69921E-06	-0.18616E-06	-0.11119E-06	0.37249E-06	0.86811E-09	0.48623E-06	0.61350E-06	
-0.23247E-07	0.37077E-06	0.59790E-06	-0.56570E-07	0.22391E-04	0.12318E-04	0.37979E-06		
DEGREE OF FREEDOM NO. 9								
-0.70383E-07	-0.91035E-07	-0.11251E-07	-0.69941E-07	-0.76267E-07	-0.13750E-07	-0.27116E-07	-0.24109E-07	
-0.91528E-08	-0.13026E-07	-0.24069E-07	-0.20816E-08	-0.11302E-06	-0.42111E-07	-0.47521E-09	0.21219E-07	
-0.13228E-06	-0.10241E-09	-0.10766E-06	-0.21808E-06	0.34868E-08	-0.21211E-06	-0.22128E-06	-0.15313E-07	
-0.55824E-06	-0.26543E-06	0.70670E-07	0.42210E-07	-0.14140E-06	-0.32955E-09	-0.18458E-06	-0.23289E-06	
0.88249E-08	-0.14075E-06	-0.22697E-06	0.21475E-07	-0.85001E-05	-0.46762E-05	-0.14418E-06		
DEGREE OF FREEDOM NO. 10								
0.10017E-06	0.12956E-06	0.16012E-07	0.99539E-07	0.10854E-06	0.19569E-07	0.38592E-07	0.34312E-07	
-0.13026E-07	0.18538E-07	0.34255E-07	0.29625E-08	0.16085E-06	0.59932E-07	0.67632E-09	-0.30199E-07	
0.18826E-06	0.14575E-09	0.15322E-06	0.31037E-06	-0.49624E-08	0.30188E-06	0.31493E-06	0.21793E-07	
0.79449E-06	0.37776E-06	-0.10058E-06	-0.60073E-07	0.20124E-06	0.46901E-09	0.26270E-06	0.33145E-06	
-0.12560E-07	0.20031E-06	0.32302E-06	-0.30563E-07	0.12097E-04	0.66552E-05	0.20519E-06		
DEGREE OF FREEDOM NO. 11								
0.18509E-06	0.23940E-06	0.29587E-07	0.18393E-06	0.20057E-06	0.36161E-07	0.71311E-07	0.63403E-07	
-0.24070E-07	0.34256E-07	0.63297E-07	0.54741E-08	0.29723E-06	0.11074E-06	0.12497E-08	-0.55802E-07	
0.34788E-06	0.26932E-09	0.28313E-06	0.57351E-06	-0.91697E-06	0.55782E-06	0.58193E-06	0.40270E-07	
0.14681E-05	0.69803E-06	-0.18585E-06	-0.11100E-06	0.37187E-06	0.86665E-09	0.48542E-06	0.61247E-06	
-0.23208E-07	0.37015E-06	0.59689E-06	-0.56475E-07	0.22354E-04	0.12298E-04	0.37915E-06		
DEGREE OF FREEDOM NO. 12								
0.16011E-07	0.20710E-07	0.25594E-08	0.15911E-07	0.17350E-07	0.31281E-08	0.61687E-08	0.54847E-08	
-0.20822E-08	0.29633E-08	0.54755E-08	0.47354E-09	0.25712E-07	0.95798E-08	0.10811E-09	-0.48272E-08	
0.30093E-07	0.23297E-10	0.24492E-07	0.49611E-07	-0.79322E-09	0.48254E-07	0.50340E-07	0.34835E-08	
0.12700E-06	0.60383E-07	-0.16077E-07	-0.96023E-08	0.32168E-07	0.74969E-10	0.41991E-07	0.52981E-07	
-0.20076E-08	0.32019E-07	0.51634E-07	-0.48853E-08	0.19337E-05	0.10638E-05	0.32799E-07		

Figure 4—Transfer coefficients

DEGREE OF FREEDOM NO. 13							
0.86917E-06	0.11242E-05	0.13894E-06	0.86371E-06	0.94183E-06	0.16980E-06	0.33486E-06	0.29773E-06
-0.11303E-06	0.16086E-06	0.29723E-06	0.25706E-07	0.13957E-05	0.52003E-06	0.58685E-08	-0.26204E-06
0.16336E-05	0.12647E-08	0.13295E-05	0.26931E-05	-0.43059E-07	0.26194E-05	0.27326E-05	0.18910E-06
0.68938E-05	0.32778E-05	-0.87271E-06	-0.52125E-06	0.17462E-05	0.40696E-08	0.22794E-05	0.28760E-05
-0.10898E-06	0.17381E-05	0.28029E-05	-0.26520E-06	0.10497E-03	0.57747E-04	0.17804E-05	
DEGREE OF FREEDOM NO.							
0.32384E-06	0.41886E-06	0.51766E-07	0.32181E-06	0.35091E-06	0.63267E-07	0.12477E-06	0.11093E-06
-0.42113E-07	0.59934E-07	0.11074E-06	0.95775E-08	0.52003E-06	0.19376E-06	0.21865E-08	-0.97632E-07
0.60864E-06	0.47120E-09	0.49537E-06	0.10034E-05	-0.16043E-07	0.97597E-06	0.10181E-05	0.70456E-07
0.25685E-05	0.12213E-05	-0.32516E-06	-0.19421E-06	0.65062E-06	0.15163E-08	0.84928E-06	0.10716E-05
-0.40604E-07	0.644761E-06	0.10443E-05	-0.98808E-07	0.39110E-04	0.21516E-04	0.66337E-06	
DEGREE OF FREEDOM NO. 15							
0.36558E-08	0.47285E-08	0.58438E-09	0.36328E-08	0.39614E-08	0.71421E-09	0.14085E-08	0.12523E-08
-0.47541E-09	0.67659E-09	0.12502E-08	0.10812E-09	0.58706E-08	0.21873E-08	0.24683E-10	-0.11022E-08
0.68709E-08	0.53193E-11	0.55921E-08	0.11327E-07	-0.18111E-09	0.11018E-07	0.11494E-07	0.79536E-09
0.28996E-07	0.13787E-07	-0.36707E-08	-0.21924E-08	0.73447E-08	0.17117E-10	0.95874E-08	0.12097E-07
-0.45838E-09	0.73107E-08	0.11789E-07	-0.11154E-08	0.44151E-06	0.24289E-06	0.74887E-08	
DEGREE OF FREEDOM NO. 16							
-0.16556E-06	-0.21414E-06	-0.26465E-07	-0.16452E-06	-0.17940E-06	-0.32344E-07	-0.63784E-07	-0.56711E-07
0.21530E-07	-0.30640E-07	-0.56616E-07	-0.48963E-08	-0.26586E-06	-0.99055E-07	-0.11178E-08	0.49913E-07
-0.31116E-06	-0.24089E-09	-0.25325E-06	-0.51297E-06	0.82019E-08	-0.49895E-06	-0.52051E-06	-0.36019E-07
-0.13131E-05	-0.62436E-06	0.16623E-06	0.99287E-07	-0.33262E-06	-0.77518E-09	-0.43418E-06	-0.54782E-06
0.20758E-07	-0.33108E-06	-0.53389E-06	0.50514E-07	-0.19994E-04	-0.11000E-04	-0.33914E-06	
DEGREE OF FREEDOM NO. 17							
0.10173E-05	0.13157E-05	0.16261E-06	0.10109E-05	0.11023E-05	0.19874E-06	0.39192E-06	0.34846E-06
-0.13229E-06	0.18827E-06	0.34788E-06	0.30085E-07	0.16336E-05	0.60864E-06	0.68683E-08	-0.30668E-06
0.19119E-05	0.14801E-08	0.15561E-05	0.31519E-05	-0.50396E-07	0.30657E-05	0.31982E-05	0.22132E-06
0.80684E-05	0.38363E-05	-0.10214E-05	-0.61107E-06	0.20437E-05	0.47630E-08	0.26678E-05	0.33661E-05
-0.12755E-06	0.20343E-05	0.32805E-05	-0.31038E-06	0.12285E-03	0.67587E-04	0.20838E-05	
DEGREE OF FREEDOM NO. 18							
0.79133E-09	0.10235E-08	0.12650E-09	0.78636E-09	0.85749E-09	0.15460E-09	0.30487E-09	0.27107E-09
-0.10291E-09	0.14645E-09	0.27061E-09	0.23404E-10	0.12708E-08	0.47346E-09	0.53429E-11	-0.23857E-09
0.14873E-08	0.11514E-11	0.12105E-08	0.24519E-08	-0.39203E-10	0.23849E-08	0.24879E-08	0.17217E-09
0.62765E-08	0.29843E-08	-0.79456E-09	-0.47457E-09	0.15898E-08	0.37052E-11	0.20753E-08	0.26185E-08
-0.99221E-10	0.15825E-08	0.25519E-08	-0.24145E-09	0.95569E-07	0.52576E-07	0.16210E-08	
DEGREE OF FREEDOM NO. 19							
0.82793E-06	0.10709E-05	0.13235E-06	0.82273E-06	0.89715E-06	0.16175E-06	0.31898E-06	0.28361E-06
-0.10767E-06	0.15323E-06	0.28313E-06	0.24486E-07	0.13295E-05	0.49536E-06	0.55901E-08	-0.24961E-06
0.15561E-05	0.12047E-08	0.12665E-05	0.25653E-05	-0.41017E-07	0.24952E-05	0.26030E-05	0.18013E-06
0.65668E-05	0.31223E-05	-0.83131E-06	-0.49653E-06	0.16634E-05	0.38766E-08	0.21713E-05	0.27396E-05
-0.10381E-06	0.16557E-05	0.26699E-05	-0.25261E-06	0.99989E-04	0.55008E-04	0.16960E-05	
DEGREE OF FREEDOM NO. 20							
0.15771E-05	0.21692E-05	0.26808E-06	0.16665E-05	0.18173E-05	0.32764E-06	0.64612E-06	0.57447E-06
-0.21809E-06	0.31038E-06	0.57351E-06	0.49599E-07	0.26931E-05	0.10034E-05	0.11323E-07	-0.50561E-06
0.31520E-05	0.24402E-08	0.25654E-05	0.51963E-05	-0.83083E-07	0.50542E-05	0.52726E-05	0.36487E-06
0.13302E-04	0.63246E-05	-0.16839E-05	-0.10058E-05	0.33693E-05	0.78524E-08	0.43982E-05	0.55494E-05
-0.21028E-06	0.33538E-05	0.54082E-05	-0.51170E-06	0.20254E-03	0.11142E-03	0.34354E-05	
DEGREE OF FREEDOM NO. 21							
-0.26857E-07	-0.34738E-07	-0.42931E-08	-0.26689E-07	-0.29103E-07	-0.52469E-08	-0.10347E-07	-0.51999E-08
0.34926E-08	-0.49705E-08	-0.91845E-08	-0.79430E-09	-0.43128E-07	-0.16069E-07	-0.18133E-09	0.80970E-08
-0.50477E-07	-0.39078E-10	-0.41083E-07	-0.83216E-07	0.13305E-08	-0.80940E-07	-0.84438E-07	-0.58432E-08
-0.21302E-06	-0.10128E-06	0.26967E-07	0.16107E-07	-0.53958E-07	-0.12575E-09	-0.70434E-07	-0.88870E-07
0.33675E-08	-0.53708E-07	-0.86610E-07	0.81945E-08	-0.32435E-05	-0.17844E-05	-0.55016E-07	
DEGREE OF FREEDOM NO. 22							
0.16312E-05	0.21098E-05	0.26075E-06	0.16209E-05	0.17676E-05	0.31868E-06	0.62845E-06	0.55876E-06
-0.21213E-06	0.30189E-06	0.55782E-06	0.48242E-07	0.26194E-05	0.97596E-06	0.11013E-07	-0.49177E-06
0.30657E-05	0.23734E-08	0.24952E-05	0.50542E-05	-0.80811E-07	0.49160E-05	0.51284E-05	0.35489E-06
0.12938E-04	0.61516E-05	-0.16378E-05	-0.97825E-06	0.32772E-05	0.76376E-08	0.42779E-05	0.53975E-05
-0.20453E-06	0.32620E-05	0.52603E-05	-0.49770E-06	0.19700E-03	0.10838E-03	0.33414E-05	
DEGREE OF FREEDOM NO. 23							
0.17017E-05	0.22010E-05	0.27202E-06	0.16910E-05	0.18440E-05	0.33245E-06	0.65561E-06	0.58291E-06
-0.22129E-06	0.31494E-06	0.58194E-06	0.50327E-07	0.27326E-05	0.10181E-05	0.11490E-07	-0.51303E-06
0.31983E-05	0.24760E-08	0.26030E-05	0.52726E-05	-0.84304E-07	0.51284E-05	0.53501E-05	0.37023E-06
0.13497E-04	0.64175E-05	-0.17086E-05	-0.10205E-05	0.34188E-05	0.79677E-08	0.44628E-05	0.56309E-05
-0.21337E-06	0.34030E-05	0.54877E-05	-0.51921E-06	0.20551E-03	0.11306E-03	0.34858E-05	
DEGREE OF FREEDOM NO. 24							
0.11775E-06	0.15230E-06	0.18823E-07	0.11701E-06	0.12760E-06	0.23005E-07	0.45366E-07	0.40336E-07
-0.15313E-07	0.21793E-07	0.40268E-07	0.34825E-08	0.18909E-06	0.70453E-07	0.79504E-09	-0.35500E-07
0.22131E-06	0.17133E-09	0.18012E-06	0.36485E-06	-0.58336E-08	0.35487E-06	0.37021E-06	0.25619E-07
0.93396E-06	0.44407E-06	-0.11823E-06	-0.70618E-07	0.23657E-06	0.55134E-09	0.30881E-06	0.38964E-06
-0.14764E-07	0.23548E-06	0.37973E-06	-0.35928E-07	0.14221E-04	0.78235E-05	0.24121E-06	

Figure 4—Transfer coefficients (Continued)

DEGREE OF FREEDOM NO. 25								
0.42930E-05	0.55526E-05	0.68624E-06	0.42660E-05	0.46519E-05	0.83869E-06	0.16539E-05	0.14705E-05	
-0.55827E-06	0.79451E-06	0.14681E-05	0.12696E-06	0.68938E-05	0.25685E-05	0.28985E-07	-0.12943E-05	
0.80685E-05	0.62464E-08	0.65668E-05	0.13302E-04	-0.21268E-06	0.12938E-04	0.13497E-04	0.53400E-06	
0.34050E-04	0.16190E-04	-0.43105E-05	-0.25746E-05	0.86249E-05	0.20101E-07	0.11258E-04	0.14205E-04	
-0.53827E-06	0.85850E-05	0.13844E-04	-0.13099E-05	0.51846E-03	0.28523E-03	0.87939E-05		
DEGREE OF FREEDOM NO. 26								
0.20412E-05	0.26401E-05	0.32629E-06	0.20284E-05	0.22119E-05	0.39878E-06	0.78641E-06	0.69921E-06	
-0.26544E-06	0.37777E-06	0.69804E-06	0.60368E-07	0.32778E-05	0.12213E-05	0.13782E-07	-0.61539E-06	
0.38363E-05	0.29700E-08	0.31224E-05	0.63246E-05	-0.10112E-06	0.61516E-05	0.64175E-05	0.44409E-06	
0.16190E-04	0.76978E-05	-0.20495E-05	-0.12241E-05	0.41009E-05	0.95574E-08	0.53531E-05	0.67543E-05	
-0.25594E-06	0.40819E-05	0.65825E-05	-0.62280E-06	0.24652E-03	0.13562E-03	0.41813E-05		
DEGREE OF FREEDOM NO. 27								
-0.56274E-06	0.72786E-06	-0.89954E-07	-0.55920E-06	-0.60979E-06	-0.10994E-06	-0.21680E-06	-0.19276E-06	
0.73180E-07	-0.10415E-06	-0.19244E-06	-0.16643E-07	-0.90367E-06	-0.33669E-06	-0.37995E-08	0.16966E-06	
-0.10576E-05	-0.81880E-09	-0.86080E-06	-0.17436E-05	0.27879E-07	-0.16959E-05	-0.17692E-05	-0.12243E-06	
-0.46634E-05	-0.21222E-05	0.56503E-06	0.33748E-06	-0.11306E-05	-0.26349E-08	-0.14758E-05	-0.18621E-05	
0.70559E-07	-0.11253E-05	-0.18147E-05	0.17170E-06	-0.67962E-04	-0.37388E-04	-0.11527E-05		
DEGREE OF FREEDOM NO. 28								
-0.37645E-06	-0.48692E-06	-0.60177E-07	-0.37409E-06	-0.40793E-06	-0.73546E-07	-0.14504E-06	-0.12895E-06	
0.48955E-07	-0.69672E-07	-0.12874E-06	-0.11134E-07	-0.60453E-06	-0.22524E-06	-0.25418E-08	0.11349E-06	
-0.70753E-06	-0.54775E-09	-0.57585E-06	-0.11664E-05	0.18650E-07	-0.11345E-05	-0.11836E-05	-0.19033E-07	
-0.29859E-05	-0.14197E-05	0.37799E-06	0.22577E-06	-0.75632E-06	-0.17626E-08	-0.98727E-06	-0.12457E-05	
0.47202E-07	-0.75282E-06	-0.12140E-05	0.11486E-06	-0.45464E-04	-0.25012E-04	-0.77115E-06		
DEGREE OF FREEDOM NO. 29								
0.10874E-05	0.14065E-05	0.17382E-06	0.10806E-05	0.11783E-05	0.21244E-06	0.41895E-06	0.37249E-06	
-0.14141E-06	0.20125E-06	0.37187E-06	0.32160E-07	0.17462E-05	0.65061E-06	0.73420E-08	-0.32784E-06	
0.20437E-05	0.15822E-08	0.16634E-05	0.33693E-05	-0.53871E-07	0.32772E-05	0.34188E-05	0.23658E-06	
-0.86249E-05	0.41009E-05	-0.10918E-05	-0.65214E-06	0.21847E-05	0.50915E-08	0.28518E-05	0.35982E-05	
-0.13634E-06	0.21746E-05	0.35067E-05	-0.33179E-06	0.13133E-03	0.72248E-04	0.22275E-05		
DEGREE OF FREEDOM NO. 30								
0.25350E-08	0.32789E-08	0.40523E-09	0.25191E-08	0.27470E-08	0.49526E-09	0.97667E-09	0.86837E-09	
-0.32966E-09	0.46917E-09	0.86692E-09	0.74973E-10	0.40709E-08	0.15167E-08	0.17116E-10	-0.76427E-09	
0.47645E-08	0.36886E-11	0.38778E-08	0.78547E-08	-0.12559E-09	0.76399E-08	0.79701E-08	0.55153E-09	
0.20107E-07	0.95602E-08	-0.25454E-08	-0.15203E-08	0.50931E-08	0.11870E-10	0.66482E-08	0.63884E-08	
-0.31785E-09	0.50695E-08	0.81750E-08	-0.77348E-09	0.30616E-06	0.16843E-06	0.51929E-08		
DEGREE OF FREEDOM NO. 31								
0.14195E-05	0.18360E-05	0.22690E-06	0.14105E-05	0.15381E-05	0.27731E-06	0.54687E-06	0.48623E-06	
-0.18459E-06	0.26270E-06	0.48542E-06	0.41980E-07	0.22794E-05	0.84928E-06	0.95839E-08	-0.42794E-06	
0.26678E-05	0.20654E-08	0.21713E-05	0.43981E-05	-0.70321E-07	0.42779E-05	0.44627E-05	0.30882E-06	
0.11258E-04	0.53531E-05	-0.14252E-05	-0.85127E-06	0.28518E-05	0.66462E-08	0.37226E-05	0.46969E-05	
-0.17798E-06	0.28386E-05	0.45775E-05	-0.43310E-06	0.17143E-03	0.94309E-04	0.29077E-05		
DEGREE OF FREEDOM NO. 32								
-0.17910E-05	0.23165E-05	0.28629E-06	0.17798E-05	0.19407E-05	0.34990E-06	0.69002E-06	0.61351E-06	
-0.23291E-06	0.33147E-06	0.61248E-06	0.52969E-07	0.28761E-05	0.10716E-05	0.12093E-07	-0.53996E-06	
0.33661E-05	0.26060E-08	0.27396E-05	0.55494E-05	-0.88728E-07	0.53976E-05	0.56309E-05	0.38966E-06	
0.14205E-04	0.67543E-05	-0.17983E-05	-0.10741E-05	0.35983E-05	0.83859E-08	0.46970E-05	0.59264E-05	
-0.22456E-06	0.35816E-05	0.57757E-05	-0.54646E-06	0.21630E-03	0.11899E-03	0.36688E-05		
DEGREE OF FREEDOM NO. 33								
-0.68834E-07	-0.89032E-07	-0.11003E-07	-0.68402E-07	-0.74589E-07	-0.13448E-07	-0.26520E-07	-0.23579E-07	
0.89514E-08	-0.12739E-07	-0.23540E-07	-0.20358E-08	-0.11054E-06	-0.41184E-07	-0.46476E-09	0.20752E-07	
-0.12937E-06	-0.10016E-09	-0.10529E-06	-0.21328E-06	0.34101E-08	-0.20745E-06	-0.21641E-06	-0.14976E-07	
-0.54596E-06	-0.25959E-06	0.69115E-07	0.41281E-07	-0.13829E-06	-0.32230E-09	-0.18052E-06	-0.22777E-06	
0.86307E-08	-0.13765E-06	-0.22198E-06	0.21002E-07	-0.83131E-05	-0.45733E-05	-0.14100E-06		
DEGREE OF FREEDOM NO. 34								
0.10824E-05	0.14000E-05	0.17302E-06	0.10756E-05	0.11729E-05	0.21146E-06	0.41701E-06	0.37077E-06	
-0.14076E-06	0.20032E-06	0.37015E-06	0.32012E-07	0.17381E-05	0.64761E-06	0.73081E-08	-0.32632E-06	
0.20343E-05	0.15749E-08	0.16557E-05	0.33537E-05	-0.53623E-07	0.32620E-05	0.34030E-05	0.23549E-06	
0.85850E-05	0.40819E-05	-0.10868E-05	-0.64913E-06	0.21746E-05	0.50680E-08	0.28386E-05	0.35816E-05	
-0.13571E-06	0.21645E-05	0.34905E-05	-0.33025E-06	0.13072E-03	0.71914E-04	0.22172E-05		
DEGREE OF FREEDOM NO. 35								
0.17455E-05	0.22576E-05	0.27901E-06	0.17345E-05	0.18914E-05	0.34100E-06	0.67247E-06	0.59790E-06	
-0.22699E-06	0.32304E-06	0.59690E-06	0.51622E-07	0.28029E-05	0.10443E-05	0.11785E-07	-0.52623E-06	
0.32805E-05	0.25397E-08	0.26700E-05	0.54083E-05	-0.86472E-07	0.52603E-05	0.54877E-05	0.37975E-06	
0.13844E-04	0.65825E-05	-0.17526E-05	-0.10468E-05	0.35067E-05	0.81726E-08	0.45775E-05	0.57757E-05	
-0.21885E-06	0.34905E-05	0.56288E-05	-0.53257E-06	0.21080E-03	0.11597E-03	0.35755E-05		
DEGREE OF FREEDOM NO. 36								
-0.17309E-06	-0.22389E-06	-0.27669E-07	-0.17201E-06	-0.18757E-06	-0.33817E-07	-0.66688E-07	-0.59293E-07	
0.42510E-07	-0.32035E-07	-0.59194E-07	-0.51193E-08	-0.27796E-06	-0.10356E-06	-0.11687E-08	0.52185E-07	
-0.32532E-06	-0.25186E-09	-0.26478E-06	-0.53633E-06	0.85753E-08	-0.52166E-06	-0.54421E-06	-0.37659E-07	
-0.13729E-05	-0.65278E-06	0.17380E-06	0.10381E-06	-0.34776E-06	-0.81047E-09	-0.45395E-06	-0.57277E-06	
0.21703E-07	-0.34615E-06	-0.55820E-06	0.52814E-07	-0.20905E-04	-0.11500E-04	-0.35458E-06		

Figure 4—Transfer coefficients (Continued)

DEGREE OF FREEDOM NO. 37							
0.65367E-04	0.84547E-04	0.10449E-04	0.64956E-04	0.70832E-04	0.12770E-04	0.25184E-04	0.22391E-04
-0.85005E-05	0.12098E-04	0.22354E-04	0.19332E-05	0.10497E-03	0.39110E-04	0.44135E-06	-0.19707E-04
0.12285E-03	0.95111E-07	0.99990E-04	0.20254E-03	-0.32383E-05	0.19700E-03	0.20551E-03	0.14221E-04
0.51846E-03	0.24651E-03	-0.65633E-04	-0.39202E-04	0.13133E-03	0.30606E-06	0.17143E-03	0.21630E-03
-0.81960E-05	0.13072E-03	0.21080E-03	-0.19944E-04	0.78944E-02	0.43430E-02	0.13390E-03	
DEGREE OF FREEDOM NO. 38							
0.35961E-04	0.46513E-04	0.57484E-05	0.35735E-04	0.38967E-04	0.70255E-05	0.13855E-04	0.12318E-04
-0.46765E-05	0.66554E-05	0.12298E-04	0.10635E-05	0.57747E-04	0.21516E-04	0.24280E-06	-0.10842E-04
0.67587E-04	0.52324E-07	0.55008E-04	0.11142E-03	-0.17815E-05	0.10838E-03	0.11306E-03	0.78238E-05
0.28522E-03	0.13562E-03	-0.36107E-04	-0.21566E-04	0.72248E-04	0.16838E-06	0.94309E-04	0.11899E-03
-0.45089E-05	0.71914E-04	0.11597E-03	-0.10972E-04	0.43430E-02	0.23892E-02	0.73664E-04	
DEGREE OF FREEDOM NO. 39							
0.11087E-05	0.14341E-05	0.17723E-06	0.11018E-05	0.12014E-05	0.21661E-06	0.42716E-06	0.37979E-06
-0.14418E-06	0.20520E-06	0.37916E-06	0.32791E-07	0.17804E-05	0.66337E-06	0.74859E-08	-0.33426E-06
0.20838E-05	0.16132E-08	0.16960E-05	0.34354E-05	-0.54927E-07	0.33414E-05	0.34858E-05	0.24122E-06
0.87939E-05	0.41813E-05	-0.11132E-05	-0.66492E-06	0.22275E-05	0.51913E-08	0.29077E-05	0.36687E-05
-0.13902E-06	0.22172E-05	0.35755E-05	-0.33829E-06	0.13390E-03	0.73664E-04	0.22712E-05	

Figure 4-Transfer coefficients (Continued)

As expected, the transfer coefficients $\varphi_{ik} \psi_{kj}$ possess symmetry properties since the transfer matrix of a linear conservative system is symmetrical according to Maxwell's Principle of Reciprocity.

In order to illustrate the use of the transfer function in calculating the response to a given input, a sample problem is solved. An exponentially decaying unit load with a time constant of 0.230258 is applied at each of the four grid points representing the reflector, and the Z-component of the feedbox response due to the applied load is computed. The response to the load

$$f(t) = e^{-0.230258 t}$$

can be obtained by determining \bar{x} and finding its inverse transform; i.e.,

$$x_i(t) = \mathcal{L}^{-1} \left[\sum_j \sum_{k=1}^{15} \frac{\varphi_{ik} \psi_{kj}}{(s + 0.230258)(s^2 + \omega_k^2)} \right],$$

where the j-summation is taken over the four grid points depicting the reflector. An elementary calculation yields

$$x_i(t) = \sum_j \sum_{k=1}^{15} \varphi_{ik} \psi_{kj} \left[\frac{(e^{-0.230258t} - \cos \omega_k t) + (0.230258 \sin \omega_k t) / \omega_k}{(0.230258)^2 + \omega_k^2} \right].$$

Since the load decays to 10 percent of its initial strength in 10 seconds, the computer results corresponding to only a 15-second time response are given in Figure 5. A graphical representation of the results is given in Figure 6.

```

-0.95480996E-05 -0.10462610E-04 0.39789322E-06 -0.77416304E-05 -0.10945956E-04 0.25699070E-06 -0.65265290E-05 -0.11069904E-04
0.63516897E-06 -0.50058944E-05 -0.11475364E-04 0.17123598E-06 -0.33884340E-05 -0.11412334E-04 -0.57450923E-06 -0.18032273E-05
-0.11038788E-04 -0.14415824E-05 -0.56042932E-06 -0.10592290E-04 -0.19464616E-05 0.66285486E-06 -0.10449530E-04 -0.28928706E-05
0.17830962E-05 -0.95981105E-05 -0.36149517E-05 0.24923598E-05 -0.88112189E-05 -0.45400576E-05 0.31312405E-05 -0.77153595E-05
-0.55120091E-05 0.37703136E-05 -0.65021659E-05 -0.69363455E-05 0.39257941E-05 -0.47042643E-05 -0.74722736E-05 0.36305489E-05
-0.36258258E-05 -0.78197392E-05 0.33565124E-05 -0.26881713E-05 -0.80945891E-05 0.32540064E-05 -0.13661001E-05 -0.86675536E-05
0.25096848E-05 0.33570529E-06 -0.87183011E-05 0.14004511E-05 0.15523641E-05 -0.85839756E-05 0.54206166E-06 0.26536269E-05
-0.83017974E-05 -0.29644979E-06 0.35399593E-05 -0.78862119E-05 -0.13582798E-05 0.42551874E-05 -0.69647276E-05 -0.23974045E-05
0.45522825E-05 -0.62209982E-05 -0.33660075E-05 0.52858977E-05 -0.51900274E-05 -0.46487924E-05 0.56093107E-05 -0.40657406E-05
-0.59018865E-05 0.54743644E-05 -0.25182056E-05 -0.62952303E-05 0.48893676E-05 -0.16227200E-05 -0.66458680E-05 0.45294947E-05
-0.43100978E-06 -0.71561691E-05 0.38480391E-05 0.93922558E-06 -0.75840492E-05 0.29142816E-05 0.23782495E-05 -0.74703727E-05
0.19418018E-05 0.31261559E-05 -0.74220997E-05 0.12717453E-05 0.41000828E-05 -0.72745601E-05 0.51021817E-07 0.49527771E-05
-0.65125390E-05 -0.12013988E-05 0.56225642E-05 -0.55123924E-05 -0.26035712E-05 0.57166432E-05 -0.46487425E-05 -0.34509932E-05
0.62680834E-05 -0.37016960E-05 -0.46656745E-05 0.61202043E-05 -0.25530627E-05 -0.52927034E-05 0.58143161E-05 -0.14326610E-05
-0.59025844E-05 0.51919621E-05 -0.33823471E-06 -0.63885795E-05 0.48642731E-05 0.11330814E-05 -0.71924061E-05 0.37529179E-05
0.25960590E-05 -0.71385577E-05 0.26860590E-05 0.33981808E-05 -0.69048215E-05 0.18796186E-05 0.40529968E-05 -0.66048599E-05
0.11186226E-05 0.48216856E-05 -0.65504164E-05 -0.35419553E-06 0.58677997E-05 -0.55174134E-05 -0.17363251E-05 0.62667356E-05
-0.47205617E-05 -0.29873489E-05 0.65538025E-05 -0.36753034E-05 -0.38960098E-05 0.64946694E-05 -0.27526732E-05 -0.48457990E-05
0.61610412E-05 -0.13349514E-05 -0.52613753E-05 0.55143967E-05 -0.44851553E-06 -0.59071692E-05

```

Figure 5—Feedbox response

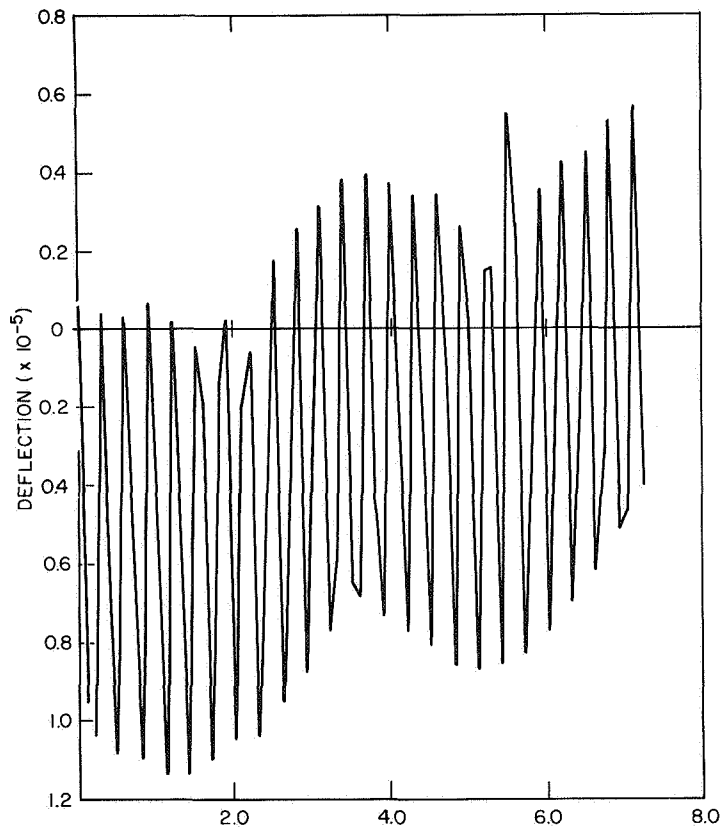


Figure 6—Feedbox Z—movement: reflector excited by decaying exponential unit load

A second calculation is made to subject the reflector to a unit impulse and to evaluate the response in the Z-direction at the feedbox. In this case damping is introduced in each mode as mentioned before. An elementary calculation yields

$$X_i(t) = \sum_j \sum_{k=1}^{15} \frac{\phi_{ik} \psi_{kj}}{\omega_k} e^{-\zeta_k t} \sin \omega_k t.$$

The damping coefficients used are as follows:

$$\zeta_1 = 0.27$$

$$\zeta_2 = 0.16$$

$$\zeta_3 \text{ to } \zeta_{15} = 0.03$$

Again only the first 15 modes are used. Computer results of the response for the first 15 seconds are given in Figure 7, and a graphical representation of the results is given in Figure 8. It can be observed that the response is damped out in 4 seconds. This is in general agreement with some of the experimental results.

```

-0.11481063E-03  0.95020248E-04  0.24107242E-04  -0.10351011E-03  0.64893853E-04  0.34389099E-04  -0.87603598E-04  0.46919283E-04
0.39332536E-04  -0.76225489E-04  0.28255833E-04  0.43349678E-04  -0.60263617E-04  0.12217317E-04  0.42665851E-04  -0.45562367E-04
0.34377806E-07  0.39073902E-04  -0.33002862E-04  -0.57641957E-05  0.35293675E-04  -0.25442768E-04  -0.10950186E-04  0.31769156E-04
-0.16778825E-04  -0.13226732E-04  0.26132813E-04  -0.10853491E-04  -0.14149141E-04  0.21403852E-04  -0.54682706E-05  -0.14210884E-04
0.17184868E-04  -0.14707997E-05  -0.14749496E-04  0.12942486E-04  0.27653086E-05  -0.13003606E-04  0.83957715E-05  0.38254269E-05
-0.10691167E-04  0.59352098E-05  0.42357514E-05  -0.88785630E-05  0.41775821E-05  0.44601901E-05  -0.78806458E-05  0.23008901E-05
0.53030784E-05  -0.60510731E-05  0.34963525E-06  -0.48355011E-05  -0.44839813E-05  -0.50738965E-06  0.44542818E-05  -0.32507543E-05
-0.10948739E-05  0.38293318E-05  -0.24068249E-05  -0.14982466E-05  0.33869030E-05  -0.13506166E-05  -0.16844673E-05  0.25276887E-05
-0.84571350E-06  -0.15900926E-05  0.22133271E-05  -0.34053151E-06  -0.17018058E-05  0.17156699E-05  0.62107351E-07  -0.16702534E-05
0.12843738E-05  0.51012409E-06  -0.13991723E-05  0.69734526E-06  0.46301724E-06  -0.10711274E-05  0.59035467E-06  0.54145698E-06
-0.96730465E-06  0.30122488E-06  0.56373230E-06  -0.78963166E-06  0.14613808E-06  0.64587051E-06  -0.58137538E-06  -0.87571613E-07
0.48108184E-06  -0.40654681E-06  -0.31570186E-07  0.48788195E-06  -0.35734571E-06  -0.18085786E-06  0.41314601E-06  -0.20729889E-06
-0.17627143E-06  0.37661338E-06  -0.11258950E-06  -0.24802505E-06  0.23961921E-06  -0.30598591E-07  -0.15706673E-06  0.23176488E-06
-0.26003613E-07  -0.22389447E-06  0.15431426E-06  0.53944549E-07  -0.14775388E-06  0.11726622E-06  0.43627223E-07  -0.15964077E-06
0.60360906E-07  0.66940908E-07  -0.93391006E-07  0.65282235E-07  0.52225927E-07  -0.13168500E-06  0.16767952E-07  0.95763021E-07
-0.60578513E-07  -0.40274342E-08  0.55078068E-07  -0.63370997E-07  -0.14892898E-07  0.60358804E-07  -0.24957746E-07  -0.46528271E-08
0.37950461E-07  -0.49057447E-07  -0.21640366E-07  0.59464690E-07  -0.70259080E-08  -0.27090892E-07  0.26603746E-07  -0.15401088E-07
-0.25044736E-07  0.34602129E-07  0.61672452E-08  -0.21850265E-07  0.14643293E-07  -0.51617868E-08  -0.22685607E-07  0.21843218E-07
0.14478779E-07  -0.17643096E-07  0.13579335E-08  0.89809648E-09  -0.12007864E-07  0.12536705E-07

```

Figure 7—Damped feedbox response

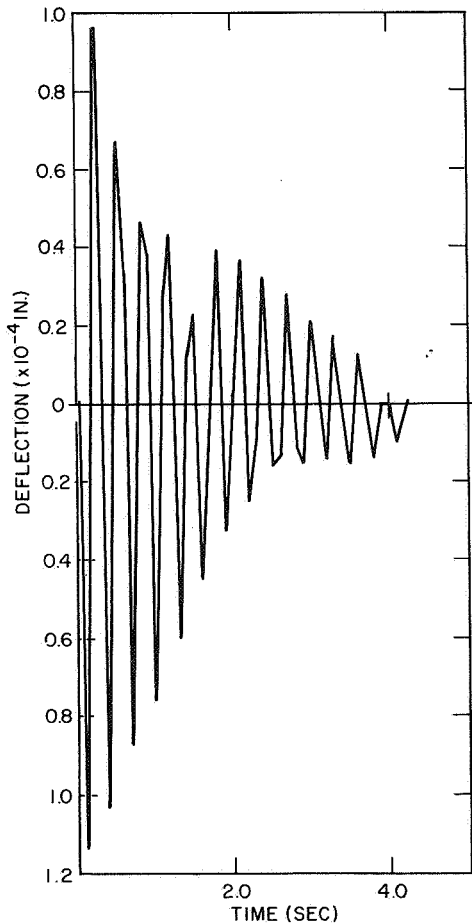


Figure 8—Damped feedbox Z—movement: reflector excited by unit impulse

In order to calculate the response to other forced inputs, a rather simple computer program can be added to the main routine which generates the transfer coefficients of the model system, as was done in the previous two calculations.

CONCLUSION

A dynamic model of the Rosman-I antenna structure, having 39 degrees of freedom, has been derived. This model yields natural frequencies encompassing the experimentally observed frequency range. The transfer functions obtained for the model are used in response calculations and are found to give realistic results.

REFERENCE

1. Chen, Yu, Vibrations: Theoretical Methods, Reading, Mass., Addison-Wesley, 1966.

APPENDIX A
SELECTION OF MASS POINTS AND VALUES OF MASSES

LUMPED MASS POINTS

The lumped mass points are given in Table A-1.

Table A-1
Lumped Mass Points

Grid Point	Lumped Mass
1, 2	X-wheel bearings
3, 4	Hydraulic drive
5	X-wheel counterweight
6 to 9	Reflector dish
10	Y-wheel counterweight
11, 12	Y-wheel bearings
13	Feedbox

NUMERICAL VALUES OF LUMPED MASS

The numerical values of the lumped masses are given in Table A-2.

Table A-2
Values of Lumped Masses

Mass	Value (lb-sec ² /in.)
$M_{1,1} = M_{2,2} = M_{3,3}$	666
$M_{4,4} = M_{5,5} = M_{6,6}$	666
$M_{7,7} = M_{8,8} = M_{9,9}$	252
$M_{10,10} = M_{11,11} = M_{12,12}$	252
$M_{13,13} = M_{14,14} = M_{15,15}$	1200
$M_{16,16} = M_{17,17} = M_{18,18}$	88
$M_{19,19} = M_{20,20} = M_{21,21}$	88
$M_{22,22} = M_{23,23} = M_{24,24}$	88
$M_{25,25} = M_{26,26} = M_{27,27}$	88
$M_{28,28} = M_{29,29} = M_{30,30}$	300
$M_{31,31} = M_{32,32} = M_{33,33}$	156
$M_{34,34} = M_{35,35} = M_{36,36}$	156
$M_{37,37} = M_{38,38} = M_{39,39}$	96

APPENDIX B
INFLUENCE COEFFICIENT MATRIX

The complete printout of the rows of the influence coefficient matrix is given in Figure B-1.

1	0.39104459E-05	-0.41383299E-10	0.28515480E-06	0.13021597E-05	0.85830159E-09	0.28568593E-06	0.56091559E-06	-0.19348300E-08
	-0.20064399E-06	0.28032123E-06	-0.19348300E-08	-0.20004699E-06	0.13034819E-05	-0.39807699E-08	0.62066825E-08	0.41222665E-06
	0.46243779E-08	0.21707530E-09	0.13034819E-05	0.15678310E-07	0.10749699E-07	0.13034819E-05	0.10274699E-07	-0.59543999E-08
	0.13034819E-05	-0.45139100E-07	-0.34283199E-06	-0.87783330E-06	0.46246190E-08	0.21709830E-09	0.13034815E-05	0.15678730E-07
	0.10749889E-07	0.13034819E-05	0.10275120E-07	-0.59545499E-08	0.13034819E-05	0.38598579E-07	-0.24000255E-06	
2	-0.41383299E-10	0.68470969E-05	0.17926960E-09	0.52564839E-09	0.22805686E-05	-0.20103800E-09	-0.10353299E-06	0.69626159E-06
	0.62757299E-06	0.10208949E-06	0.69626231E-06	0.62832950E-06	0.33806950E-09	0.11069536E-05	-0.14093400E-09	-0.11221999E-09
	0.22823656E-05	0.17685989E-09	0.11401699E-05	0.22823656E-05	-0.75605665E-07	0.70030999E-06	0.22823656E-05	0.46966666E-06
	0.47081940E-06	0.22823656E-05	0.86550630E-06	-0.10124600E-09	0.22823656E-05	0.17683220E-05	-0.70030999E-06	0.22823656E-05
	-0.23907566E-06	-0.11405899E-05	0.22823656E-05	-0.87783330E-06	0.19101020E-06	0.22823656E-05	0.59792120E-06	
3	0.28515480E-06	0.17926960E-09	0.85546440E-06	0.28515480E-06	0.13669290E-09	0.28515480E-06	-0.20243400E-06	-0.21297999E-09
	0.28515480E-06	-0.20256200E-06	-0.21152499E-09	0.28515480E-06	-0.22069699E-06	-0.36447499E-09	0.28515480E-06	0.28515480E-06
	-0.63902499E-09	0.28515480E-06	0.28515480E-06	-0.26351500E-08	0.19599789E-07	0.28515480E-06	0.13791705E-06	0.13791705E-06
	0.28515480E-06	-0.14046900E-07	0.52569189E-07	0.28515480E-06	-0.63907399E-09	0.11170846E-06	0.28515480E-06	-0.53468759E-09
	-0.23907566E-06	0.28515480E-06	0.13790870E-08	0.28515480E-06	0.13790870E-08	-0.92514499E-05	0.28515480E-06	
4	0.13021597E-05	0.52564839E-09	0.28515480E-06	0.39064790E-05	0.14696699E-08	0.28568593E-06	0.56091559E-06	0.96038020E-10
	-0.21554630E-06	0.28032123E-06	0.93748690E-10	-0.21227499E-06	0.13021597E-05	0.40808939E-08	-0.49203699E-08	-0.41222665E-06
	0.22823656E-05	0.10851619E-08	0.13021597E-05	-0.10920799E-08	-0.26351500E-08	0.13021597E-05	0.37388115E-08	0.51622459E-09
	0.13021597E-05	0.52741289E-07	-0.35071699E-06	0.87783330E-06	0.25951319E-08	0.10851800E-08	0.13021597E-05	-0.16898400E-08
	-0.23907566E-06	0.13021597E-05	0.37392440E-08	0.56959900E-09	0.13021597E-05	0.22249410E-08	0.22249410E-08	
5	0.85830159E-09	0.22805686E-05	0.13669290E-09	0.14696699E-08	0.68417059E-05	0.23749089E-09	0.88911315E-07	0.69626159E-06
	-0.60620999E-06	0.86394999E-07	0.69626231E-06	0.60721429E-06	0.26755559E-08	0.11069536E-05	-0.13497800E-05	0.28332230E-09
	0.22805686E-05	0.18810649E-09	-0.11320200E-05	0.22805686E-05	-0.75605665E-07	0.46633209E-06	0.22805686E-05	0.46966666E-06
	-0.69829599E-06	0.22805686E-05	0.86568479E-06	0.28330179E-09	0.22805686E-05	0.18809489E-05	0.46633270E-06	0.22805686E-05
	-0.23907566E-06	0.22805686E-05	-0.23907566E-06	-0.75599900E-06	-0.22065400E-06	0.22805686E-05	0.59792158E-06	
6	0.28568593E-06	-0.20103800E-09	0.28515480E-06	0.28568593E-06	0.23749089E-09	0.85705779E-06	0.20406960E-06	0.49847219E-09
	0.28568593E-06	0.20442639E-06	0.49917959E-09	0.28568593E-06	0.21628340E-06	-0.48273599E-09	0.28568593E-06	0.28568593E-06
	-0.26766230E-08	0.13675240E-06	0.28568593E-06	-0.43699599E-08	0.38131789E-07	0.28568593E-06	-0.24731900E-08	0.51471379E-07
	0.28568593E-06	-0.42145199E-07	0.19555140E-06	0.28568593E-06	-0.26765499E-08	0.11170846E-06	0.28568593E-06	0.43545169E-08
	0.51471419E-07	0.28568593E-06	-0.24730799E-08	0.19555140E-06	0.28568593E-06	-0.67133299E-06	0.28568593E-06	
7	0.56091599E-06	-0.10353299E-06	-0.20243400E-06	0.56091599E-06	0.88911319E-07	0.20406960E-06	0.16827480E-05	0.50854759E-07
	-0.60711499E-07	0.28032123E-06	0.50854759E-07	-0.62788300E-07	0.56091599E-06	0.18893799E-07	0.22479059E-08	-0.41222665E-06
	-0.67760099E-08	0.21094269E-08	0.56091599E-06	0.47278269E-08	0.91318018E-08	0.56091599E-06	0.66878059E-08	0.92909159E-08
	0.56091599E-06	-0.11169100E-06	-0.89350899E-07	0.56091599E-06	-0.67759299E-08	0.21094350E-08	0.56091599E-06	0.47289629E-08
	0.13677800E-07	0.56091599E-06	0.46878190E-08	-0.92909599E-08	0.56091599E-06	-0.15266000E-07	-0.63728859E-06	
8	-0.19348300E-08	0.69626199E-06	-0.21297999E-09	0.96058020E-10	0.69626199E-06	0.49847219E-09	0.50854759E-07	0.28878599E-05
	-0.16353030E-07	-0.47316900E-07	0.69626231E-06	-0.48963699E-07	0.69626199E-06	-0.69626199E-06	-0.17806155E-10	-0.86386459E-09
	0.69626199E-06	0.24024360E-10	-0.43870799E-07	0.69626199E-06	-0.35664400E-07	-0.45539899E-07	0.69626199E-06	0.14545759E-06
	0.14545759E-06	0.69626199E-06	0.14550620E-06	-0.86387299E-09	0.69626199E-06	0.24015250E-10	-0.45539899E-07	0.69626199E-06
	-0.14545759E-06	-0.54935399E-07	0.69626199E-06	0.35669090E-06	0.13523550E-07	0.69626199E-06	0.99243379E-07	
9	-0.20064399E-06	-0.62757299E-06	0.28515480E-06	-0.21554600E-06	-0.60620999E-06	0.28568593E-06	-0.60711459E-07	0.16353130E-07
	-0.22901060E-05	0.60957700E-07	0.16354869E-07	0.51919840E-06	-0.67989500E-07	-0.43921999E-06	0.30513943E-06	0.26182659E-06
	-0.63071799E-06	0.13675240E-06	-0.38722999E-06	0.76336866E-06	0.37237049E-07	-0.33325699E-06	0.76336866E-06	0.38152640E-06
	-0.43127299E-06	0.76336866E-06	0.16290080E-06	-0.26181699E-06	-0.63071799E-06	0.11170846E-06	-0.33423255E-06	0.76336866E-06
	-0.23907566E-06	-0.33325699E-06	0.76336866E-06	0.19024180E-06	-0.58131399E-06	0.76336866E-06	0.60828000E-06	
10	0.28032123E-06	0.10208949E-06	-0.20256200E-06	0.28032123E-06	-0.86394999E-07	0.20442639E-06	0.28032123E-06	-0.47316900E-07
	-0.60957700E-07	0.84096370E-06	0.18971869E-07	0.87964489E-08	0.88181248E-07	0.20759860E-07	0.21980730E-06	0.28032123E-06
	-0.67327779E-08	0.20603419E-08	0.28032123E-06	0.71004799E-08	0.10752379E-07	0.28032123E-06	-0.71401455E-08	0.15695340E-07
	0.28032123E-06	0.13099810E-06	-0.10556400E-06	0.28032123E-06	0.64328569E-08	0.20603459E-08	0.28032123E-06	-0.71003259E-08
	-0.11410899E-07	0.28032123E-06	-0.71399899E-08	0.15695290E-07	0.28032123E-06	0.10563870E-07	-0.68342800E-07	
11	-0.19348300E-08	0.69626231E-06	-0.21152499E-09	0.93748690E-10	0.69626231E-06	0.49917959E-09	0.50854759E-07	0.69626231E-06
	0.16354869E-07	0.18971869E-07	0.20887870E-05	-0.41553800E-07	-0.48963699E-08	0.69626231E-06	-0.17806959E-10	-0.86386459E-09
	0.69626231E-06	0.24023610E-10	-0.43870799E-07	0.69626231E-06	-0.35664400E-07	-0.45539899E-07	0.69626231E-06	0.14545759E-06
	-0.11939030E-07	0.69626231E-06	0.14550620E-06	-0.86387199E-09	0.69626231E-06	0.24015090E-10	-0.45539899E-07	0.69626231E-06
	-0.14545759E-06	-0.54935300E-07	0.69626231E-06	0.35669090E-06	0.13523550E-07	0.69626231E-06	0.99243379E-07	
12	-0.20004699E-06	0.62832950E-06	0.28515480E-06	-0.21227499E-06	0.60721429E-06	0.28568593E-06	-0.62798300E-07	0.41554800E-07
	-0.51919840E-06	0.87964489E-08	-0.41553800E-07	0.23220009E-05	-0.66411999E-07	0.42382079E-06	0.30513943E-06	0.26156199E-06
	-0.63313019E-06	0.13675240E-06	-0.32879299E-06	0.77400032E-06	0.12721670E-07	-0.37822099E-06	0.77400032E-06	0.28305930E-06
	-0.34314299E-06	0.77400032E-06	0.261456099E-06	-0.63313019E-06	0.11170846E-06	-0.32879299E-06	0.32879299E-06	0.77400032E-06
	-0.23907566E-06	-0.34314299E-06	0.77400032E-06	0.43333589E-06	-0.57414299E-06	0.77400032E-06	0.67673310E-06	
13	0.13034819E-05	0.33806950E-09	-0.22069699E-06	0.13021597E-05	0.26755559E-08	0.21628340E-06	0.56091559E-06	-0.48963699E-08
	-0.67989500E-07	0.88181248E-07	-0.48963699E-08	-0.66411999E-07	0.56612439E-05	-0.63171299E-08	0.51495060E-09	-0.41222665E-06
	-0.78231259E-08	0.21782110E-09	0.18870813E-05	0.21097480E-07	0.13498429E-07	0.18870813E-05	0.18705485E-07	-0.13446599E-07
	0.18870813E-05	-0.29084900E-07	-0.20711499E-06	0.88778333E-06	0.78232099E-08	0.21782309E-08	0.18870813E-05	0.18705485E-07
	-0.13498519E-07	0.18870813E-05	0.21092220E-07	-0.13044800E-07	0.18870813E-05	0.57944289E-07	-0.14743959E-06	
14	-0.39807699E-08	0.11069536E-05	-0.36447499E-09	0.40808939E-08	0.11069536E-05	-0.48273599E-05	-0.18893759E-07	0.69626159E-06
	-0.43921999E-06	0.20759860E-07	0.69626231E-06	0.42382079E-06	-0.63171299E-08	0.33208609E-05	-0.18784959E-05	-0.10182859E-08
	0.11069536E-05	-0.64383599E-06	0.41590159E-08	0.11069536E-05	0.85331899E-08	-0.80194399E-05	0.11069536E-05	0.32448830E-07
	0.90347379E-09	0.11069536E-05	-0.32517900E-07	0.10182859E-08	0.11069536E-05	-0.64383599E-06	0.41588770E-08	0.11069536E-05
	0.32448729E-07	-0.80205399E-09	0.11069536E-05	-0.85422099E-07	0.85639188E-08	0.11069536E-05	-0.24170600E-07	

Figure B-1—Computer printout of rows of D matrix

15	0.62066829E-08	0.14093400E-09	0.28515480E-06	0.49206399E-08	0.13497800E-09	0.28568593E-06	0.22459095E-08	0.17806199E-10
	0.30513943E-06	0.21980730E-08	0.17806999E-10	0.30513943E-06	0.51495060E-09	0.18784999E-09	0.91541830E-06	0.15087820E-08
	0.16567790E-08	0.13675240E-06	0.10212299E-08	0.29327469E-07	0.32351279E-07	0.43611539E-08	0.21036100E-07	0.30513943E-06
	0.34341149E-07	0.22800900E-07	0.30513943E-06	0.15087450E-08	0.16567790E-08	0.11170846E-06	0.10210759E-08	0.29327469E-07
	0.23907566E-06	0.43608119E-07	0.21036000E-07	0.30513943E-06	0.37138499E-09	0.69026009E-08	0.30513943E-06	
16	0.41222665E-06	0.10122199E-09	0.28515480E-06	0.41222665E-06	0.28322230E-09	0.28568593E-06	0.41222665E-06	0.86386459E-09
	0.26181699E-06	0.28032123E-06	0.86386399E-09	0.26156199E-06	0.41222665E-06	0.10182899E-08	0.15087820E-08	0.12366759E-05
	0.12585200E-06	0.86697899E-07	0.41222665E-06	0.27573599E-06	0.75605665E-07	0.41222665E-06	0.26433200E-06	0.69014749E-07
	0.41222665E-06	0.41222665E-06	0.41222665E-06	0.41222665E-06	0.34402629E-06	0.24139709E-08	0.41222665E-06	0.76306669E-08
	0.66758389E-08	0.41222665E-06	0.75325818E-08	0.16081200E-08	0.41222665E-06	0.31826700E-07	0.41222665E-06	
17	0.46243779E-08	0.22823656E-05	0.63902499E-09	0.25948809E-08	0.22805686E-05	0.26766200E-08	0.67760059E-08	0.69626159E-06
	0.63071999E-06	0.64327709E-08	0.69626231E-06	0.63313019E-06	0.78231269E-08	0.11069536E-05	0.16567790E-08	0.12585200E-06
	0.13207839E-04	0.40284099E-07	0.15081820E-06	0.44026133E-05	0.75605665E-07	0.12636899E-06	0.44026133E-05	0.46966666E-06
	0.15934270E-06	0.44026133E-05	0.11746600E-05	0.34402359E-06	0.42858366E-05	0.98021299E-08	0.53092375E-08	0.28337319E-05
	0.23907566E-06	0.21336900E-08	0.44026133E-05	0.75077332E-06	0.17144299E-07	0.44026133E-05	0.67106859E-06	
18	0.21707530E-09	0.17685989E-09	0.52569089E-07	0.10851619E-08	0.18810649E-09	0.13675240E-06	0.21094265E-08	0.24024360E-10
	0.13675240E-06	0.20603419E-08	0.24023610E-10	0.13675240E-06	0.21782110E-09	0.64338599E-10	0.13675240E-06	0.86697899E-07
	0.40284099E-07	0.410287799E-07	0.20827799E-07	0.13630400E-06	0.33512529E-07	0.83828978E-07	0.46604025E-07	0.13675240E-06
	0.23455790E-07	0.12708800E-06	0.13675240E-06	0.24139819E-06	0.98021899E-08	0.11170846E-06	0.32817059E-09	0.41787300E-08
	0.13675240E-06	0.13675240E-06	0.17125669E-07	0.13675240E-06	0.23657200E-08	0.34926499E-08	0.13675240E-06	
19	0.13034819E-05	0.11401699E-05	0.28515480E-06	0.13021597E-05	0.11320200E-05	0.28568593E-06	0.56091555E-06	0.43873759E-07
	0.38722299E-06	0.28032123E-06	0.43870799E-07	0.32872999E-06	0.18870813E-05	0.41590159E-08	0.10212299E-08	0.41222665E-06
	0.15081820E-06	0.13675240E-06	0.76592088E-05	0.31146210E-06	0.13630400E-06	0.25530696E-05	0.32634760E-05	0.20727500E-06
	0.25530696E-05	0.25530696E-05	0.93198999E-06	0.88778333E-06	0.53097809E-08	0.32816399E-05	0.25530696E-05	0.50902169E-08
	0.56854999E-09	0.64846400E-06	0.50014640E-08	0.37354000E-10	0.25530696E-05	0.63437199E-06	0.64824199E-06	
20	0.57657831E-07	0.22823656E-05	0.53460499E-09	0.16902699E-08	0.22805686E-05	0.43699599E-08	0.47288265E-08	0.69626159E-06
	0.76336866E-06	0.71004799E-08	0.69626231E-06	0.77400032E-06	0.21097480E-07	0.11069536E-05	0.29327469E-07	0.27573599E-06
	0.44026133E-05	0.13630400E-06	0.31146210E-06	0.21782110E-06	0.75605665E-07	0.26447699E-06	0.76057666E-05	0.46966666E-06
	0.33446790E-06	0.56504766E-05	0.11746600E-05	0.76306009E-08	0.42858366E-05	0.41787499E-08	0.50893475E-08	0.76057666E-05
	0.23907566E-06	0.33920799E-08	0.76057332E-06	0.75077332E-06	0.46464200E-07	0.76057666E-05	0.14380434E-05	
21	0.10749699E-07	0.75605665E-07	0.19599789E-07	0.26351500E-08	0.75605665E-07	0.38131789E-07	0.91318018E-08	0.35664400E-07
	0.37237049E-07	0.10752379E-07	0.35664400E-07	0.12721670E-07	0.13498429E-07	0.85331899E-06	0.32351279E-07	0.75605665E-07
	0.75605665E-07	0.35664400E-07	0.75605665E-07	0.75605665E-07	0.26881700E-06	0.65645599E-07	0.75605665E-07	0.75605665E-07
	0.75605665E-07	0.75605665E-07	0.75605665E-07	0.66758040E-08	0.75605665E-07	0.75605665E-07	0.56893055E-07	0.75605665E-07
	0.75605665E-07	0.30195549E-08	0.75605665E-07	0.75605665E-07	0.29648000E-07	0.75605665E-07	0.75605665E-07	
22	0.13034819E-05	0.70030999E-06	0.28515480E-06	0.13021597E-05	0.46633209E-06	0.28568593E-06	0.56091555E-06	0.45539859E-07
	0.33256999E-06	0.28032123E-06	0.45539899E-07	0.32822099E-06	0.18870813E-05	0.80194399E-05	0.43611535E-08	0.41222665E-06
	0.12636899E-06	0.88937878E-07	0.25530696E-05	0.27647699E-06	0.65645599E-07	0.16352150E-04	0.27643400E-06	0.22236349E-06
	0.54507166E-05	0.25461199E-05	0.93643799E-06	0.88778333E-06	0.21332899E-08	0.41507319E-08	0.36206033E-05	0.33912300E-08
	0.30199990E-08	0.25336959E-05	0.34497899E-08	0.55912649E-08	0.54507166E-05	0.92379399E-06	0.64818655E-06	
23	0.10749699E-07	0.22823656E-05	0.13791709E-08	0.37388119E-08	0.22805686E-05	0.24731900E-08	0.46876805E-08	0.69626159E-06
	0.76336866E-06	0.71004799E-08	0.69626231E-06	0.77400032E-06	0.18705489E-07	0.11069536E-05	0.21036100E-07	0.26433200E-06
	0.44026133E-05	0.46604029E-07	0.32634740E-06	0.76057666E-05	0.75605665E-07	0.27643400E-06	0.23601310E-04	0.46966666E-06
	0.32011150E-06	0.28337289E-05	0.11746600E-05	0.75325509E-06	0.42858366E-05	0.17125639E-07	0.50004459E-08	0.78603866E-05
	0.23907566E-06	0.34497699E-08	0.76108632E-05	0.75077332E-06	0.46388400E-07	0.78671032E-05	0.13671820E-05	
24	0.59543999E-08	0.46966666E-06	0.28515480E-06	0.50612459E-09	0.46966666E-06	0.51471379E-07	0.92909055E-06	0.14545759E-06
	0.38151640E-06	0.15695360E-07	0.14545799E-06	0.28305930E-06	0.13044699E-07	0.32448830E-07	0.30513943E-06	0.69014749E-07
	0.46966666E-06	0.13675240E-06	0.46966666E-06	0.46966666E-06	0.75605665E-07	0.22236349E-06	0.46966666E-06	0.14089999E-05
	0.12613700E-06	0.46966666E-06	0.46966666E-06	0.16081200E-08	0.46966666E-06	0.11170846E-06	0.37315459E-10	0.46966666E-06
	0.23907566E-06	0.55914239E-08	0.46966666E-06	0.46966666E-06	0.2717579E-07	0.46966666E-06	0.71044520E-07	
25	0.13034819E-05	0.47081940E-06	0.28515480E-06	0.13021597E-05	0.69829599E-06	0.28568593E-06	0.56091555E-06	0.11939050E-07
	0.43127299E-06	0.28032123E-06	0.11939000E-07	0.34314299E-06	0.18870813E-05	0.90347379E-05	0.34341145E-07	0.41222665E-06
	0.15934270E-06	0.23455790E-07	0.25530696E-05	0.33446790E-06	0.75605665E-07	0.54507166E-05	0.32011150E-06	0.12613700E-06
	0.39210239E-04	0.56504766E-05	0.11746600E-05	0.64843799E-06	0.12585100E-06	0.86697800E-07	0.36206033E-05	0.27573499E-06
	0.21952400E-06	0.25336959E-05	0.26432999E-06	0.69014049E-07	0.13070800E-04	0.31823200E-07	0.24036845E-05	
26	0.45139100E-07	0.22823656E-05	0.14046900E-07	0.52741289E-07	0.22805686E-05	0.42145199E-07	0.11169100E-06	0.69626159E-06
	0.76336866E-06	0.13099810E-06	0.69626231E-06	0.77400032E-06	0.29084900E-07	0.11069536E-05	0.22800900E-07	0.41222665E-06
	0.44026133E-05	0.12708800E-06	0.25530696E-05	0.56504766E-05	0.75605665E-07	0.25461199E-05	0.28337289E-05	0.46966666E-06
	0.56504766E-05	0.16951430E-04	0.11746600E-05	0.88778333E-06	0.42858366E-05	0.40284000E-07	0.36206033E-05	0.56504766E-05
	0.23907566E-06	0.25336959E-05	0.56504766E-05	0.75077332E-06	0.22933610E-05	0.56504766E-05	0.15531815E-05	
27	0.34283199E-06	0.86550630E-06	0.52569189E-07	0.35071699E-06	0.86568479E-06	0.19555140E-06	0.89350895E-07	0.14556200E-06
	0.16290080E-06	0.10556400E-06	0.14550620E-06	0.26140340E-06	0.20711499E-06	0.32517900E-07	0.30513943E-06	0.41222665E-06
	0.11746600E-05	0.13675240E-06	0.93198999E-06	0.11746600E-05	0.75605665E-07	0.93643799E-06	0.11746600E-05	0.46966666E-06
	0.11746600E-05	0.11746600E-05	0.35239799E-06	0.88778333E-06	0.96109680E-06	0.11170846E-06	0.11746600E-05	0.11746600E-05
	0.23907566E-06	0.11746600E-05	0.11746600E-05	0.71848699E-06	0.11746600E-05	0.11746600E-05	0.11746600E-05	
28	0.88778333E-06	0.10124600E-09	0.28515480E-06	0.88778333E-06	0.28330179E-09	0.28568593E-06	0.56091555E-06	0.86387259E-09
	0.26181699E-06	0.28032123E-06	0.86387199E-09	0.26156099E-06	0.88778333E-06	0.10182899E-08	0.15087820E-08	0.41222665E-06
	0.34402359E-08	0.24139819E-08	0.88778333E-06	0.76306009E-08	0.66758040E-08	0.88778333E-06	0.75325509E-06	0.16081200E-08
	0.64843799E-06	0.88778333E-06	0.88778333E-06	0.26633500E-05	0.15081850E-06	0.20827600E-07	0.88778333E-06	0.31146200E-06
	0.12931140E-06	0.88778333E-06	0.32634780E-06	0.20727500E-06	0.88778333E-06	0.83369499E-07	0.88778333E-06	
29	0.46246190E-08	0.22823656E-05	0.63907399E-09	0.25951319E-08	0.22805686E-05	0.26765499E-08	0.67759299E-08	0.69626159E-06
	0.63071999E-06	0.64328599E-08	0.69626231E-06	0.63313019E-06	0.78232309E-08	0.11069536E-05	0.16567790E-08	0.12585200E-06
	0.42858366E-05	0.98021899E-08	0.53097809E-08	0.42858366E-05	0.75605665E-07	0.21332899E-08	0.42858366E-05	0.46966666E-06
	0.12585100E-06	0.42858366E-05	0.96109680E-06	0.15081850E-06	0.12585099E-04	0.11170846E-06	0.12636799E-06	0.42858366E-05
	0.23907566E-06	0.15934420E-06	0.42858366E-05	0.75077332E-06	0.17142700E-07	0.42858366E-05	0.67106859E-06	
30	0.21709830E-09	0.17683220E-09	0.11170846E-06	0.10851800E-08	0.18809489E-09	0.11170846E-06	0.21094350E-08	0.24024360E-10
	0.11170846E-06	0.20603459E-08	0.24015090E-10	0.11170846E-06	0.21783289E-09	0.64348698E-10	0.11170846E-06	0.86697899E-07
	0.98021729E-08	0.11170846E-06	0.32816399E-09	0.41787499E-08	0.75605665E-07	0.41507319E-08	0.1	

```

32
0.15678730E-07 0.22823656E-05 -0.53468799E-09 -0.16898400E-08 0.22805686E-05 0.43541569E-08 0.47289629E-08 0.69626159E-06
0.76336866E-06 -0.71003299E-08 0.69626231E-06 0.77400032E-06 0.18705180E-07 0.11069536E-05 0.29327480E-07 0.76206669E-08
0.28337319E-05 -0.41787300E-08 0.50902169E-08 0.76057666E-05 -0.75605665E-07 -0.33912300E-08 0.78603866E-05 0.46966666E-06
-0.27573499E-06 0.56504766E-05 -0.11746600E-05 0.31146280E-06 0.42858366E-05 0.48603950E-07 -0.26447555E-06 0.23581160E-04
-0.23907566E-06 0.33447040E-06 0.76108632E-05 -0.75507332E-06 -0.44643300E-07 0.78603866E-05 0.14380415E-05
33
0.10749889E-07 -0.23907566E-06 -0.23907566E-06 -0.26349499E-08 -0.23907566E-06 0.51471419E-07 0.13677800E-07 -0.14545759E-06
-0.23907566E-06 -0.11410899E-07 -0.14545799E-06 -0.23907566E-06 0.13498519E-07 0.32448729E-07 -0.23907566E-06 0.66758389E-08
-0.23907566E-06 0.13675240E-06 -0.56854999E-09 -0.23907566E-06 -0.75605665E-07 0.30199990E-08 -0.23907566E-06 -0.23907566E-06
0.25336959E-05 -0.23907566E-06 -0.23907566E-06 0.12931140E-06 -0.23907566E-06 0.11170846E-06 -0.23907566E-06 -0.23907566E-06
-0.71722699E-06 0.20936080E-06 -0.23907566E-06 -0.23907566E-06 -0.29646600E-07 -0.23907566E-06 -0.23907566E-06
34
0.13034819E-05 -0.11405899E-05 0.28515480E-06 0.13021597E-05 0.11303770E-05 0.28568593E-06 0.56091595E-06 -0.54935399E-07
-0.33325699E-06 0.28032123E-06 -0.54935300E-07 -0.34314299E-06 0.18870813E-05 -0.80205399E-05 0.43608115E-08 -0.41222665E-06
-0.21336900E-08 0.41506549E-08 -0.64844099E-06 -0.33920799E-08 0.30195549E-08 0.25336959E-05 -0.34497695E-08 0.55914239E-08
0.25336959E-05 0.25336959E-05 -0.11746600E-05 -0.88778333E-06 0.15934420E-06 0.23455829E-07 0.25336959E-05 -0.33447.40E-06
0.20936080E-06 0.76010879E-05 0.32011410E-06 -0.12613799E-06 0.25336959E-05 0.92379580E-06 0.64818715E-06
35
0.10275120E-07 0.22823656E-05 0.13790870E-08 0.37392440E-08 0.22805686E-05 -0.24730799E-08 0.46878150E-08 0.69626159E-06
0.76336866E-06 -0.71399899E-08 0.69626231E-06 0.77400032E-06 0.21092220E-07 0.11069536E-05 -0.21036600E-07 0.75325189E-08
-0.44026133E-05 0.17125669E-07 0.50014640E-08 0.76057666E-05 -0.75605665E-07 -0.34491999E-08 0.76108632E-05 0.46966666E-06
-0.26432999E-06 0.56504766E-05 -0.11746600E-05 0.32634780E-06 0.42858366E-05 0.11170846E-06 -0.27643259E-06 0.76108632E-05
-0.23907566E-06 0.32011410E-06 0.22823656E-05 -0.75507332E-06 -0.46385600E-07 0.76108632E-05 0.13671820E-05
36
-0.59545499E-08 -0.75507332E-06 0.28515480E-06 0.50595900E-09 -0.75507332E-06 0.19555150E-06 -0.92909598E-08 0.35669050E-06
0.19024180E-06 0.15695290E-07 0.35669090E-06 0.43333589E-06 -0.13044800E-07 -0.85422099E-07 0.30513943E-06 -0.16081200E-08
-0.75507332E-06 0.13675240E-06 -0.37735400E-10 -0.75507332E-06 -0.75605665E-07 0.55912649E-08 -0.75507332E-06 0.46966666E-06
0.69014049E-07 -0.75507332E-06 -0.71848699E-06 -0.20727500E-06 -0.75507332E-06 0.11170846E-06 0.22236320E-06 -0.75507332E-06
-0.23907566E-06 -0.12613799E-06 -0.75507332E-06 -0.22652200E-05 0.27174439E-07 -0.75507332E-06 0.71044578E-07
37
0.13034819E-05 0.19101020E-06 0.28515480E-06 0.13021597E-05 -0.22065400E-06 0.28568593E-06 0.56091595E-06 0.13523550E-07
-0.58131399E-06 0.28032123E-06 0.13523550E-07 -0.57414299E-06 0.18870813E-05 0.85639188E-08 -0.37138495E-05 -0.41222665E-06
-0.17144299E-07 -0.23657200E-08 0.25530696E-05 -0.44646200E-07 -0.29648000E-07 0.54507166E-05 -0.46388400E-07 0.27175479E-07
0.13070080E-04 0.22933610E-05 -0.11746600E-05 -0.88778333E-06 -0.17142700E-07 -0.23655299E-08 0.36206033E-05 -0.446433.0E-07
-0.29646600E-07 0.25336959E-05 -0.46385600E-07 0.27174439E-07 0.22044060E-03 0.51221232E-04 0.24036845E-05
38
0.38598579E-07 0.22823656E-05 -0.92514499E-09 0.22249410E-08 0.22805686E-05 -0.67133299E-08 -0.15266000E-07 0.69626159E-06
0.76336866E-06 0.10563870E-07 0.69626231E-06 0.77400032E-06 0.57944289E-07 0.11069536E-05 0.69026000E-08 -0.31826700E-07
-0.44026133E-05 -0.34926499E-08 -0.63437199E-06 0.76057666E-05 -0.75605665E-07 -0.92379399E-08 0.78671032E-05 0.46966666E-06
-0.31823200E-07 0.56504766E-05 -0.11746600E-05 -0.83369499E-07 0.42858366E-05 -0.34927499E-08 0.89848600E-06 0.78603866E-05
-0.23907566E-06 0.92379580E-06 0.76108632E-05 -0.75507332E-06 0.51221232E-04 0.15366369E-03 0.22490945E-05
39
-0.24000299E-06 0.59792120E-06 0.28515480E-06 0.24084199E-06 0.59871589E-06 0.28568593E-06 -0.63728855E-07 0.99243379E-07
0.60828000E-06 -0.68342800E-07 0.99243379E-07 0.67673310E-06 -0.14743999E-06 -0.24170600E-07 0.30513943E-06 -0.41222665E-06
0.67106859E-06 0.13675240E-06 -0.64824199E-06 0.14380430E-05 -0.75605665E-07 -0.64818699E-06 0.13671820E-05 0.71044520E-07
0.24036849E-05 0.15531819E-05 -0.11746600E-05 -0.88778333E-06 0.67106859E-06 0.11170846E-06 -0.64824155E-06 0.143804.19E-05
-0.23907566E-06 0.64818719E-06 0.13671820E-05 0.71044578E-07 0.24036849E-05 0.22490969E-05 0.72110549E-05

```

Figure B-1-Computer printout of rows of D matrix (Continued)

RESPONSE OF THE ROSMAN I 85-FOOT DISH ANTENNA TO IMPULSE EXCITATION

Jean M. Dalrymple

ABSTRACT

This report presents a continuation of work done during the summers of 1965 and 1966 on vibrational analysis of the Rosman I 85-foot dish antenna. The work this summer consisted of cross-checking antenna natural frequencies to compare consistency from sensor to sensor and to check accuracy, developing spectrum analyzer calibration charts for analysis of single-degree-of-freedom, damped sine waves, and developing a procedure for simulating a multi-degree-of-freedom system by the addition of several single-degree-of-freedom systems. The approach recommended is the simulation of a frequency spectrum chart, rather than simulation of a time response directly. Procedure and results are given for the simulation of three- and four-degree-of-freedom systems, with recommendations for further generalization.

INTRODUCTION

The work described in this report is a continuation of a project started 2 years ago. During the summer of 1965, experiments were made on the Rosman I 85-foot dish antenna. The vibrational response of the antenna to various types of input signals was measured by means of as many as 24 sensors and recorded on magnetic tape. The ultimate goals of the project were:

1. To determine the effect of antenna vibration on boresight movement (basic information required for any redesign to increase antenna tracking accuracy),
2. To develop a realistic mathematical model of the antenna structure to aid in more rational design of future antennas.

The first summer allowed only a brief examination of some of the experimental results and the formulation of some tentative ideas concerning the most productive methods of analysis.

The determination of natural frequencies and associated damping factors was the primary objective during the second summer (1966). Different methods were considered and sampled, with the spectrum analyzer being selected as the most feasible approach. An instrumentation setup was designed to convert the magnetic tape data to a recognizable spectrum analysis. Frequencies, damping factors, and amplitudes were obtained from some of the sensor responses to impulse excitation of the antenna. These were tabulated in the 1966 Summer Workshop Report. The spectrum analysis work was continued during the winter by GSFC personnel so that a complete record from all sensors in all antenna attitudes was obtained.

When the results were tabulated, an almost continuous spectrum of natural frequencies was obtained. The work of this summer consisted of three parts:

1. Compare in detail the natural frequencies obtained from different sensors to evaluate consistency from sensor to sensor and to determine whether or not the continuous frequency spectrum representation is necessary.

2. Determine a calibration procedure to obtain amplitude, in millivolts or g's, of the time response of a damped sine wave corresponding to amplitude in decibels read from a spectrum analyzer chart.
3. Determine a method of obtaining the transfer function for a given point on the antenna, using the observed sensor data.

FREQUENCY SPECTRUM

Once a satisfactory procedure for obtaining a spectrum analysis from the data tape was developed, the spectra for all sensors caused by impulse excitation of the antenna, in three antenna attitudes and two excitation modes, were obtained more or less routinely. Inspection of the spectra obtained raised this question: Do all the frequency maxima observed actually represent distinct natural frequencies of the antenna or is some of the frequency spread caused by the following factors?

1. Noise response,
2. Variations in reading the spectrum chart,
3. Variations in spectrum analyzer frequency calibration.

In connection with item 1, frequency spectra were obtained from background noise data. The results showed no predominant noise frequencies, but, rather, a pattern of random noise frequencies. This reinforced the notion that none of the observed frequency maxima could be attributed to a predominant noise signal. Instead, the noise signals caused the minor irregularities observed in the spectrum curves.

Items 2 and 3 were investigated by a detailed cross-check among all the sensor spectra for X-angle excitation with the antenna in the zenith position. The initial observations gave 160 frequencies below 20.8 Hz and 62 below 6.3 Hz, with considerable scatter among 12 sensors, in the vicinity of any one frequency. By comparing one spectrum with another and by correcting frequency calibration discrepancies, the number of frequencies below 6.3 Hz was reduced to 54, with much less scatter among the sensors. A listing of these 54 frequencies is given in Table 1. Since the spectrum analysis chart can be read accurately to 0.1 Hz (0.1 Hz corresponds approximately to 0.16 in. on the chart), the number of frequencies shown could be reduced from 54 to 43 by arbitrarily selecting frequencies to the nearest 0.1 Hz. As an example, however, the frequency 0.65 Hz appearing in the table was retained because, by direct superposition of the two spectra involved, the 0.6-Hz frequency was not the same as the 0.65-Hz frequency. Further, reduction of frequencies in this tabulation, as well as further cross-checking of higher frequencies and of other excitations, might well be postponed until a particular application of the data is called for, because of the amount of time required. In simulating the displacement transfer function of a sensor, for example, it is probable that the frequency range will be restricted to approximately 10 Hz and, at least for a first approximation, less than 20 frequencies used in this range. This restricted number of frequencies, then, could be cross-checked for consistency and accuracy.

AMPLITUDE CALIBRATION

One of the major goals of this project is to obtain transfer functions for the various sensors and thus be able to simulate the time response of a sensor – by means of an analog computer, for instance. To do this, it is necessary to know the relationship between amplitude as read from a frequency spectrum chart and the amplitude of the time response

Table 1
NATURAL FREQUENCIES BELOW 6.3 Hz

(Antenna is in zenith position and the x-axis drive system is excited with an impulse function; tabulation is made after cross-checking all sensors.)

Feedbox		Y Bearing		X Bearing			Yoke Position	Tach.	Diff. press	Drive amp.	Seis-ometer
X dir.	Y dir.	Y dir.	Z dir.	X dir.	Y dir.	Z dir.					
H	H	H	H	H	H	H	0.15	H	H	0.15	H
H	0.25	0.25	H	H	0.25	S	H	0.25	0.25	H	S
0.35	0.4	H	vs	0.4	0.55	0.3 0.45	H	H	H	0.4	VS
VS	0.7	0.65 0.8	0.7	VS	0.9	0.95	0.7	VS	0.6	0.8 0.95	VS
VS	1.1	1.1	1.1	VS	VS	VS	1.1	VS	1.1	H	VS
S	H	H	1.25	VS	1.25	VS	H	H	H	H	VS
1.3	1.3	1.3	H	VS	VS	VS	H	1.3	H	H	VS
VS	1.5	1.5	H	1.5	1.5	VS	1.5	1.5	H	1.5	VS
1.8	1.8	1.8	1.8	1.6 VS	VS	1.9	H 2.0	VS 2.0	1.8	1.8	H 2.0
H	H	H	H	2.35	2.35		H	2.3	H	2.2 2.45	2.3
2.45	2.5	2.5	2.5	2.6	H	S	2.5	H	2.5		N
N	2.7	2.7	2.7		2.7	2.7	H	2.7	N	H 2.9	2.7
VS	H	3.0	3.0	3.1	3.0	VS	H	3.0	N		H
VS	3.2	3.35	H	VS	VS	3.2	3.2 3.35	H	H	3.2	3.2
VS	3.5		H	3.55	3.5	N	3.5	3.5	H	H	3.5
VS	3.9	3.9	3.9	3.9	VS	N	3.9	3.95	VS	3.9	H
VS	H	H	4.0	H	VS	VS	H	H	VS	4.1	4.0
VS	4.25	4.25	H	H 4.4	VS 4.4	VS	4.25	H 4.4	4.25	H	N
VS	4.6	H	vs	4.75	H	4.7	H	H 4.7	S 4.7	4.6	4.6
VS	4.9	H	H	H	H	VS	4.9	5.0		5.0	4.9
S	H	5.2	H	VS	H	VS	5.2	H			H
VS	5.4	5.5	H	5.4	H	S	H	5.4	N 5.5	5.5	5.4
VS	S		5.55	5.55	5.55	5.55	5.55	H			H
5.8	5.85			5.85				5.7	H	H	5.7
		6.15	6.15	H	6.15	S	H	6.25	6.15	H	6.15

LEGEND: H—frequency may be present, but hidden in the skirts of adjacent frequency response; N—no frequency present; S—frequency present, but of small amplitude (35 to 40 db down); VS—frequency observable, but of very small amplitude (> 40 db down).

of the corresponding signal. It is assumed that a frequency spectrum chart for a multi-degree-of-freedom system with light damping (such as the antenna) can be simulated by adding the outputs of an appropriate number of single-degree-of-freedom systems. Thus amplitude, frequency, and damping factor, as read from a spectrum chart, should be correlated with the time response of the damped single-degree-of-freedom system. Amplitude calibration is provided with the spectrum analyzer, however, to analyze undamped sine waves. When a damped sine wave is analyzed, the shape and frequency of the spectrum is as expected. The correspondence of damping factor (ζ) as obtained from the spectrum is as expected, namely $\zeta = \Delta f / 2f_0$, except at low values of $\zeta\omega$; the amplitude calibration is not that for a sine wave. An analytical expression for damped amplitude calibration was developed, but did not agree with the experiment - presumably because all of the significant characteristics of the spectrum analyzer were not included. Consequently, two calibration charts were constructed experimentally for $\zeta\omega$ (Figure 1) and for amplitude (Figure 2). These calibration charts are preliminary, in that there is an amplitude dependency which needs to be incorporated into Figure 1, and more experimental points are needed on both.

The correlation between amplitude on the spectrum chart and peak value of the time response of a damped sine wave component of a sensor response would be given by the formula

$$\rho = \frac{BSK_s}{GRA}$$

where, for an accelerometer, ρ is the peak value of a damped sine wave in g's,

B is the spectrum peak value in volts,

R is the calibration factor from Figure 2,

G is the gain in the system between tape and spectrum analyzer,

S is the full scale rms voltage calibration of the spectrum analyzer (since Figure 2 is based on $S = 1$),

A is the attenuation used at Rosman looking into the tape recorder,

K_s is the accelerometer calibration factor in g's per volt.

TRANSFER FUNCTION

If the frequency spectrum and/or the time response of a multi-degree-of-freedom system can be simulated by the addition of several single-degree-of-freedom systems, then the transfer function for the multi-degree of-freedom-system can be obtained from the addition of several elementary transfer functions, each representing a single-degree-of-freedom system. In order to check this type of simulation and develop a general procedure, first a three- and then a four-degree-of-freedom system was set up on the analog computer

Figures 3 and 4 are spectrum charts for two different points in the three-degree-of-freedom system. The resonant frequencies, damping factors, and peak amplitudes were read from the charts, and the corresponding parameters for three single-degree-of-freedom systems were computed, using the calibration charts, Figures 1 and 2. Spectra of the three single-degree-of-freedom systems used to simulate Figure 3 are shown in Figures 5, 6, and 7. Two single-degree-of-freedom systems can be added either in phase or out of phase, and the two spectra obtained are not the same. With three single-degree-of-freedom systems, there are four distinct ways of adding algebraically. The combinations for the systems of Figures 5, 6, and 7 are shown in Figure 8 through 11. From an inspection of these charts,

one may make the generalization that the amplitude of the composite spectrum is a simple algebraic addition of the individual single-degree-of-freedom spectra amplitudes (in volts, not decibels). Although this generalization appears to be consistent in the composite spectra obtained thus far, a numerical calculation of amplitude addition at several points of the frequency spectrum should be made.

Using Figure 8 as an example, for which the time responses were added in phase, the spectrum amplitudes in the designated regions would be obtained by algebraic addition according to the following table:

System	I	II	III
Time Response	+	+	+
A	+	+	+
B	-	+	+
C	-	-	+
D	-	-	-

The sign reversal shown in going from one region to another is caused by the 180-degree phase shift in passing through resonance with a lightly damped system. The spectrum analyzer presents the absolute value of the resulting addition; therefore, changing the sign (phase) of all three systems would not alter the resulting composite spectrum. Because of the subtraction involved in regions B and C, zeroes are obtained between peaks I and II and between peaks II and III, respectively.

The analogous table for Figure 10 (which is a good simulation of Figure 3) would be:

System	I	II	III
Time Response	+	-	+
A	+	-	+
B	-	-	+
C	-	+	+
D	-	+	-

There is no zero in region B because the effect of system III is small compared to that of systems I and II. Similarly, there is no zero in region C because the effect of system I is small in this region.

Based on the preceding generalization, the amplitudes of single-degree-of-freedom systems I, II, and III were reset to correspond to those of Figure 4, and the systems were added in the combination -, +, +, respectively. Figure 12 shows the result, which is a good simulation of Figure 4. The time responses of the corresponding three-degree-of-freedom systems and combined single-degree-of-freedom systems are shown in Figure 13.

On the basis of these encouraging results, a four-degree-of-freedom system was set up on the analog computer. Spectra for two points in the system are shown in Figures 14 and 15. Using the same scheme as before, four single-degree-of-freedom systems were combined, with the results shown in Figure 16. This is a good simulation of Figure 14; but upon close comparison of Figure 14A and Figure 16A, a slight discrepancy in the damping of the two high frequency peaks can be discerned.

The analogous simulation of Figure 15 is shown in Figure 17. Although Figure 17A is a satisfactory simulation of Figure 15A, there are obvious differences; the time responses are quite different. Not only does the initial waveform shape differ, but there appears to be a 90-degree phase shift between the two time responses. A possible explanation of the difference in spectra (Figure 15A and Figure 17A) may lie in the fact that the amplitudes of the three higher frequency peaks are comparable in magnitude, resulting in a more pronounced interaction of the associated single-degree-of-freedom spectra than for the previous simulations. This interaction would need to be taken into account in the calculation of the single-degree-of-freedom system amplitudes, and possibly in the corresponding damping factors. The reason for the phase difference in the time responses is not clear. Certainly a better understanding of the discrepancies between Figures 15 and 17 needs to be acquired before attempting to simulate a spectrum of one of the sensors on the antenna.

Rather than approach the simulation through the spectrum charts, one could attempt to simulate the time response directly. This was attempted for the four-degree-of-freedom system by subtracting the composite time response of four single-degree-of-freedom systems (Figure 17B) from that of the four-degree-of-freedom system (Figure 15B), using the analog computer, and trying to minimize this difference by varying the parameters in the four single-degree-of-freedom systems. The results were not encouraging. It may be possible to go back to a two- or three-degree-of-freedom system, in which there are fewer parameters to vary, and attempt to construct a systematic procedure for varying the parameters in the single-degree-of-freedom systems. However, this approach does not seem feasible because of the multiple interactions possible as one progresses to higher-degree-of-freedom systems.

CONCLUSIONS AND RECOMMENDATIONS

1. A relationship exists between amplitude peak on the spectrum analysis chart and the amplitude peak of the associated damped sine wave time response. It requires experimentally determined calibration charts, however. The preliminary charts obtained this summer need to be extended and the $\zeta\omega$ chart (Figure 1) needs to include the effect of amplitude.
2. In the simulation of multi-degree-of-freedom systems by addition of several single-degree-of-freedom systems, it does not appear feasible to work directly with the time responses.
3. It does appear feasible to obtain a simulation by operating with the frequency spectrum charts. However:
 - (a) A numerical check should be made of amplitude addition from spectrum charts.
 - (b) An investigation should be made, in adding single-degree-of-freedom spectra, of the effect of amplitude and damping factor on a "nearby" frequency peak, with the effect of the frequency difference included.
 - (c) An attempt should be made to obtain an analytical expression for the results of (b).
4. When the simulation of antenna sensor response spectra is attempted, the predominant natural frequencies should be selected from spectra peaks observed, and these should be cross-checked among all the sensors for consistency.

ACKNOWLEDGMENTS

The writer is grateful to Messrs. N. Raumann and G. Winston, GSFC, for their help and encouragement in all phases of the investigation and to Mr. J. Vinson, Lockheed Electronics Company, not only for performing most of the experiments but also for keeping the results well cataloged for easy reference.

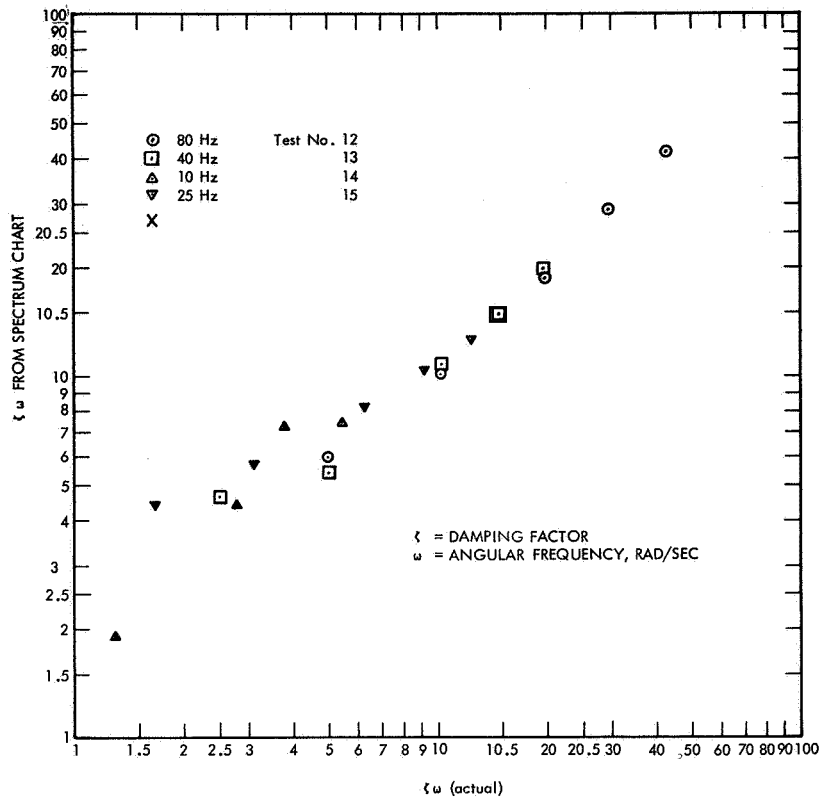


Figure 1—Spectrum analyzer calibration chart for ζ .

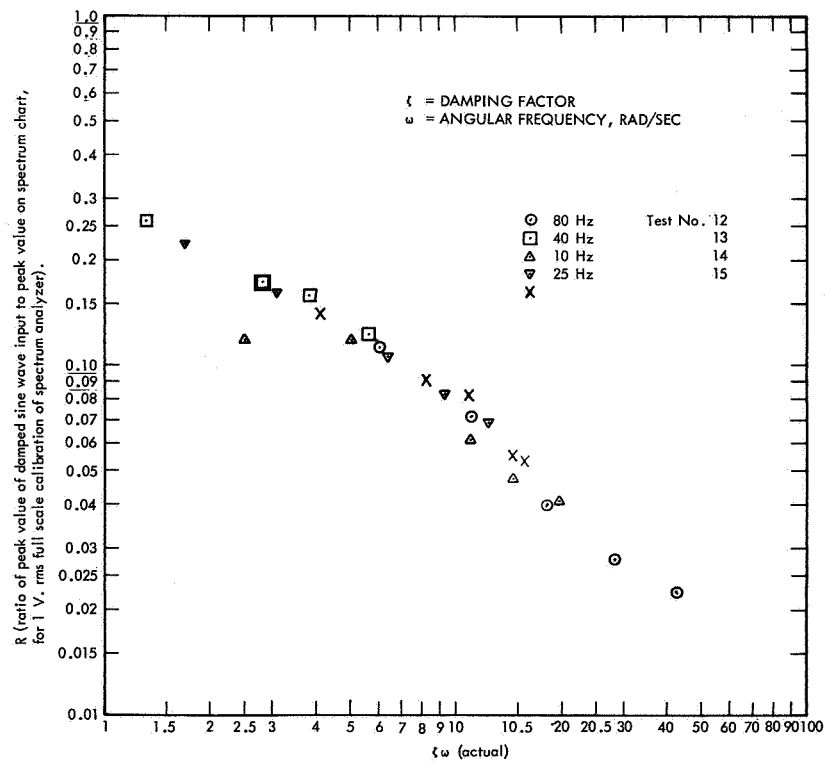


Figure 2—Spectrum analyzer calibration chart for amplitude.

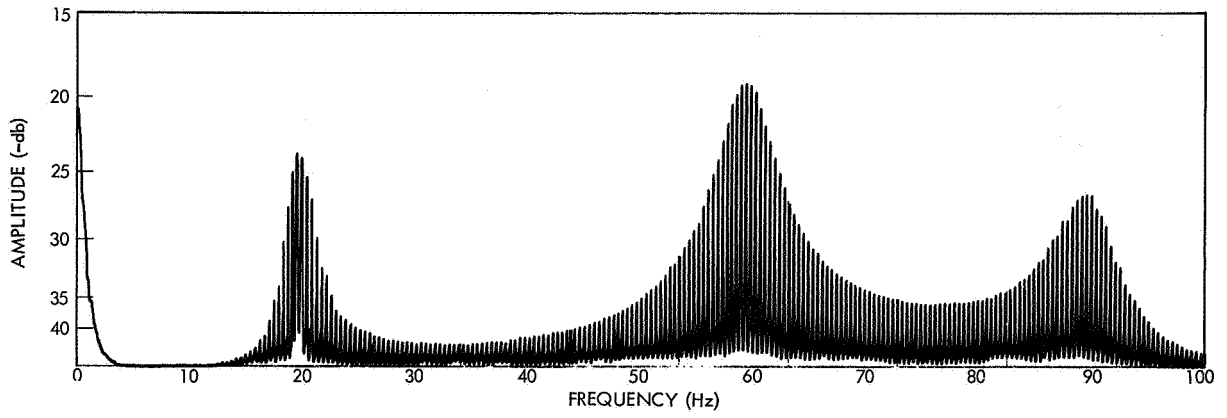


Figure 3—Spectrum chart: 3-degree-of-freedom, amp. 14.

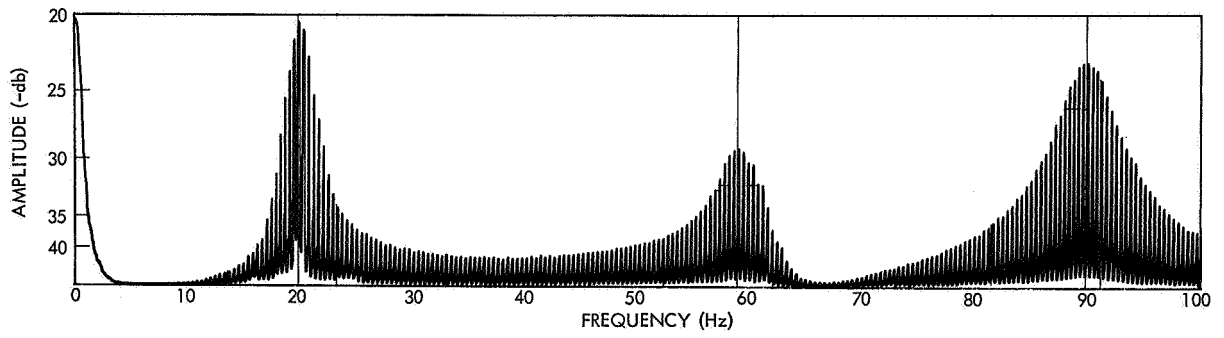


Figure 4—Spectrum chart: 3-degree-of-freedom, amp. 24.

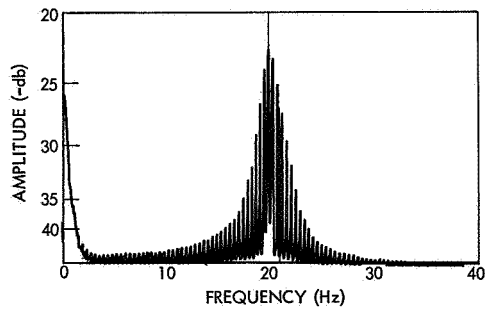


Figure 5—Spectrum chart:
1-degree-of-freedom,
System I.

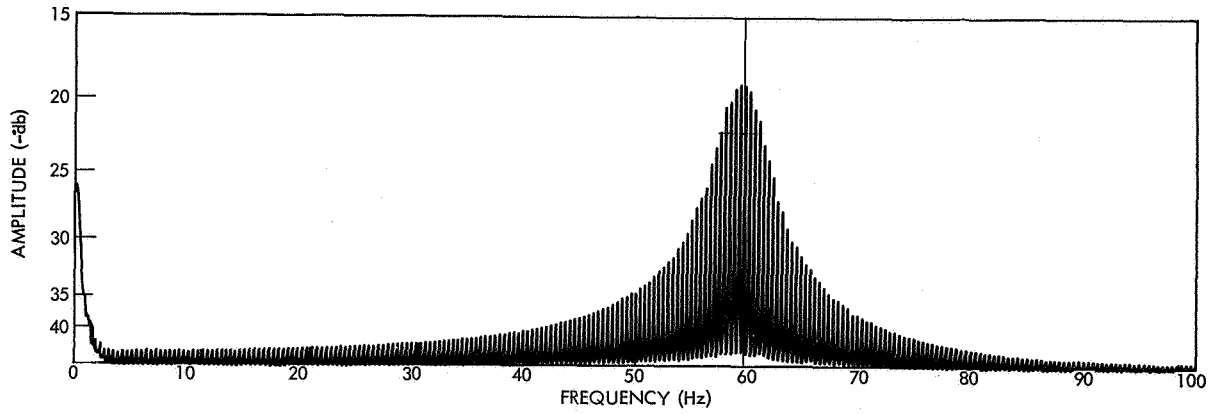


Figure 6—Spectrum chart: 1-degree-of-freedom, System II.

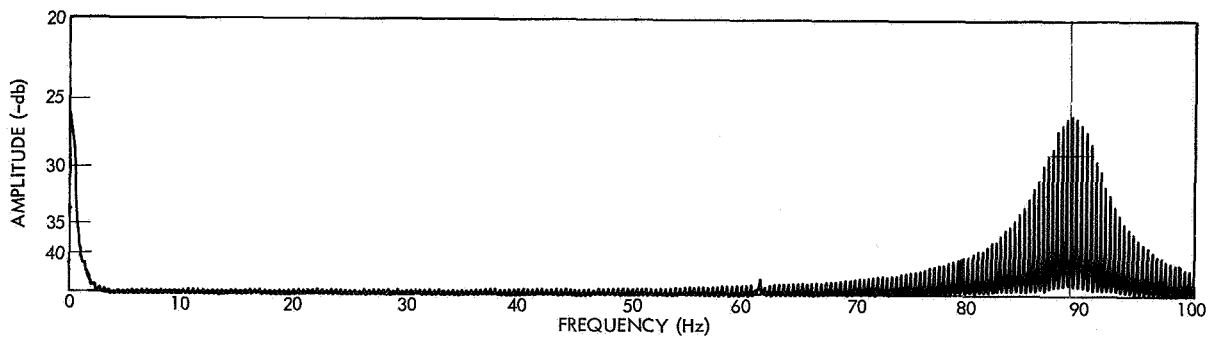


Figure 7—Spectrum chart: 1-degree-of-freedom, System III.

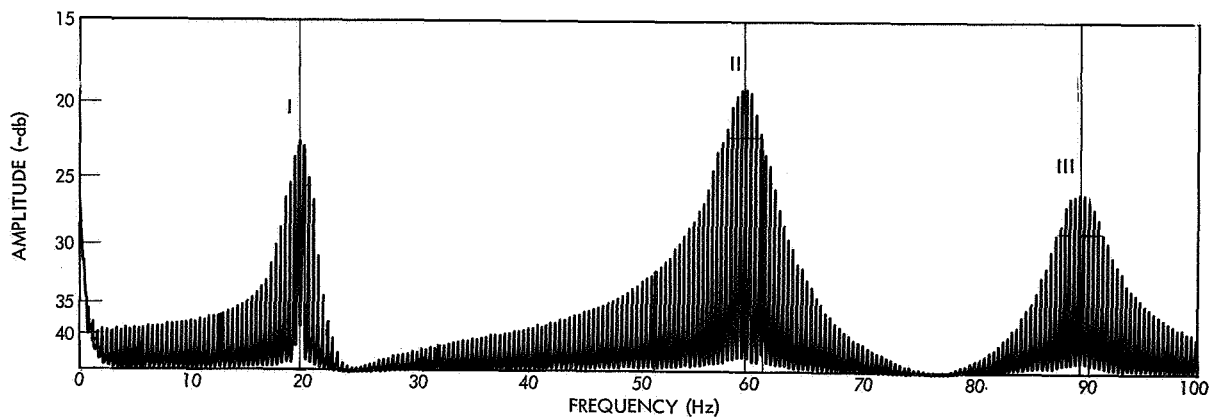


Figure 8—Spectrum chart: composite of 1-degree-of-freedom, Systems I, II, III;
time response: +, +, +, respectively.

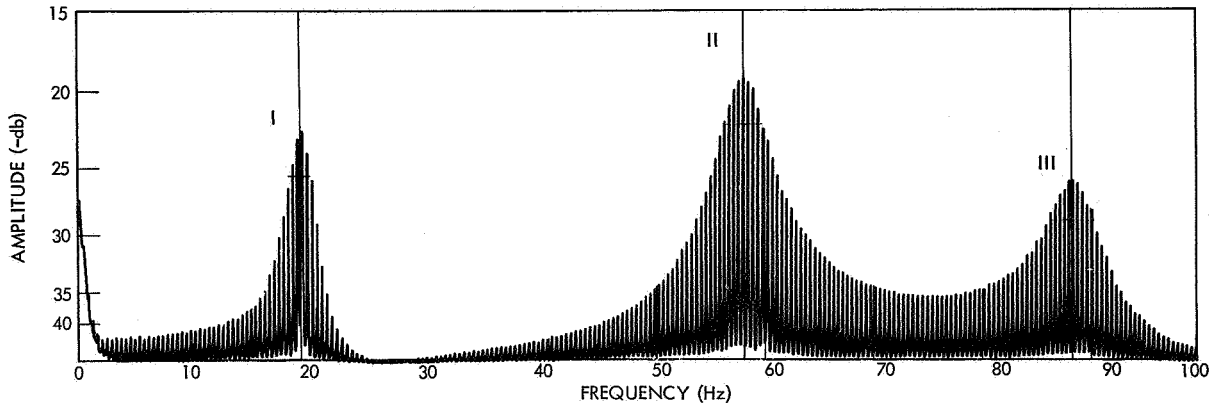


Figure 9—Spectrum chart: composite of 1-degree-of-freedom, Systems I, II, III;
time response: +, +, -, respectively.

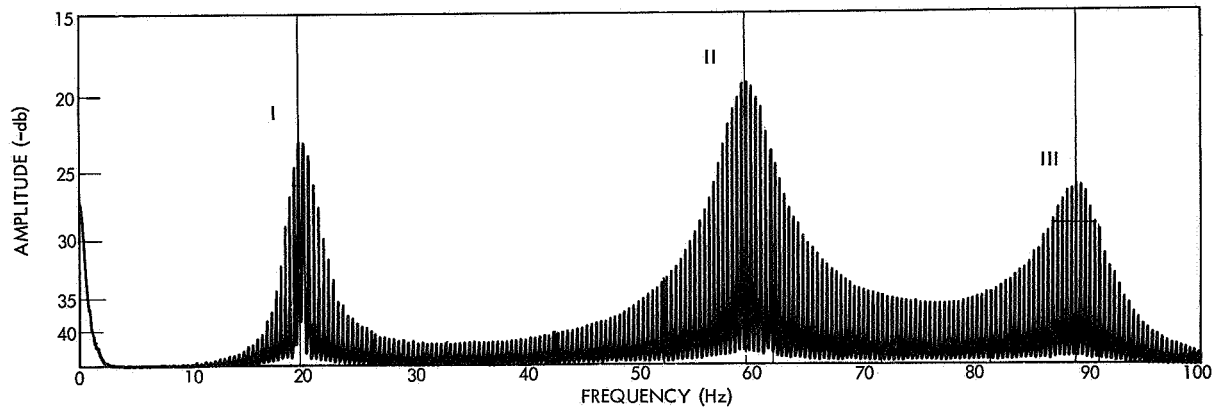


Figure 10—Spectrum chart: composite of 1-degree-of-freedom, Systems I, II, III;
time response: +, -, +, respectively.

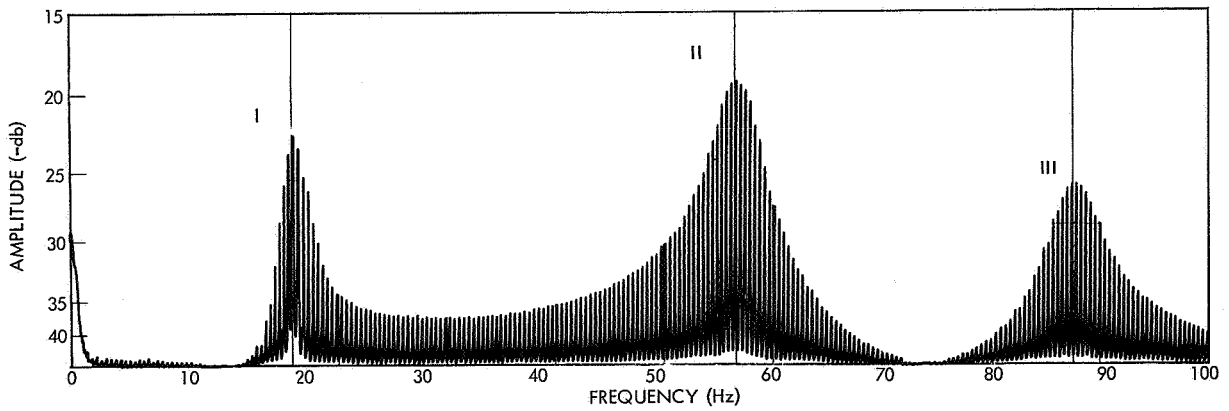


Figure 11—Spectrum chart: composite of 1-degree-of-freedom, Systems I, II, III;
time response: +, -, -, respectively.

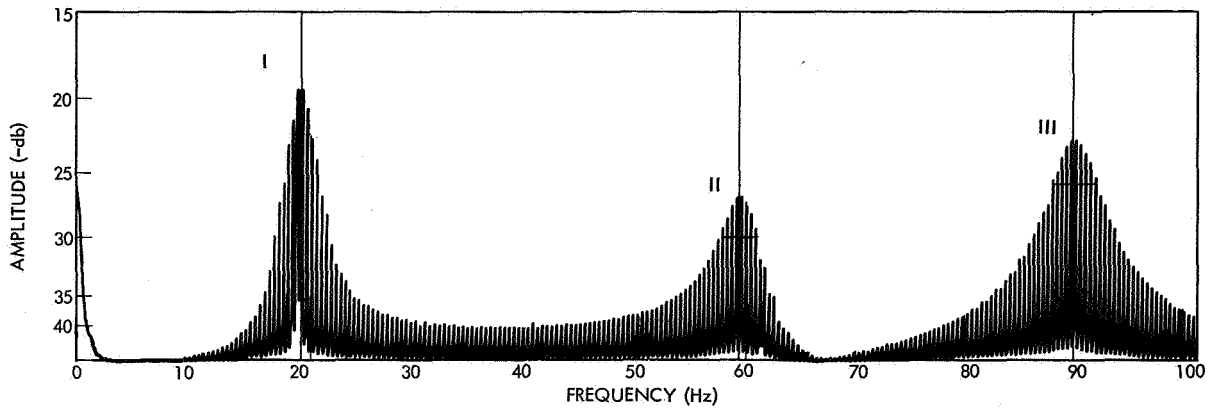


Figure 12—Spectrum chart: composite of 1-degree-of-freedom, Systems I, II, III; time response: -, +, +, respectively.

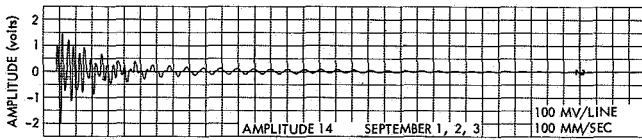


Figure 13a—Time response corresponding to Figure 3 (3-degree-of-freedom, amp. 14).

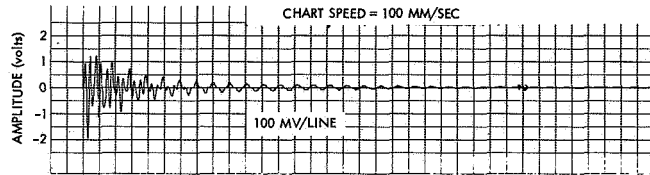


Figure 13b—Time response corresponding to Figure 10 (composite of 1-degree-of-freedom).

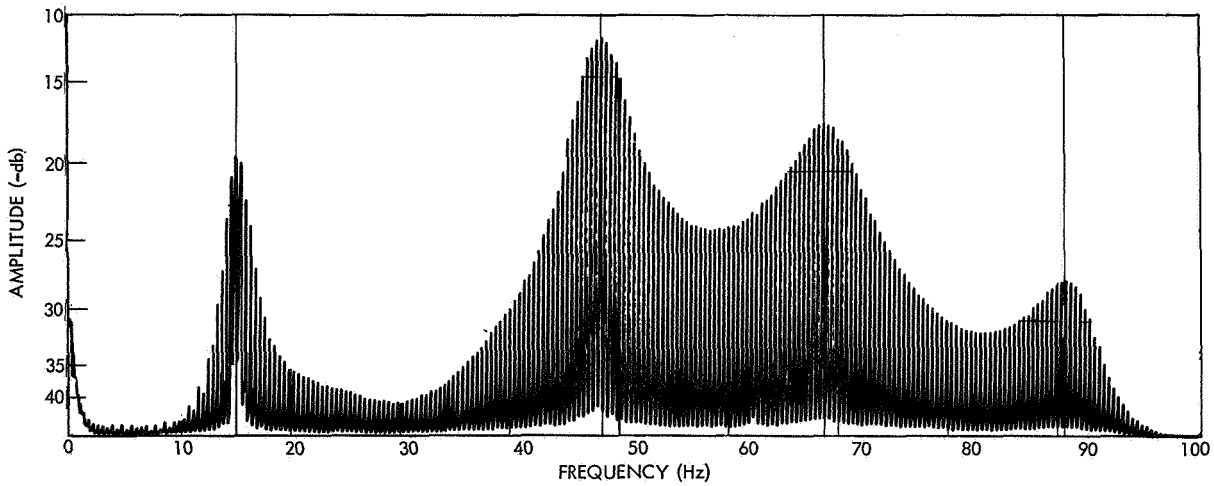


Figure 14a—Spectrum chart: 4-degree-of-freedom, amp. 12.

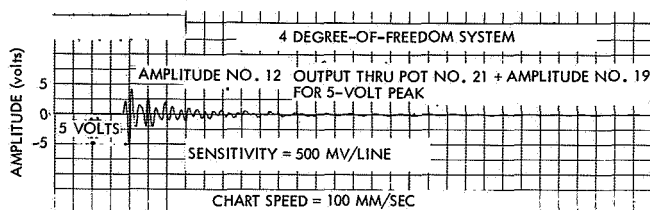


Figure 14b—Time response corresponding to Figure 14a.

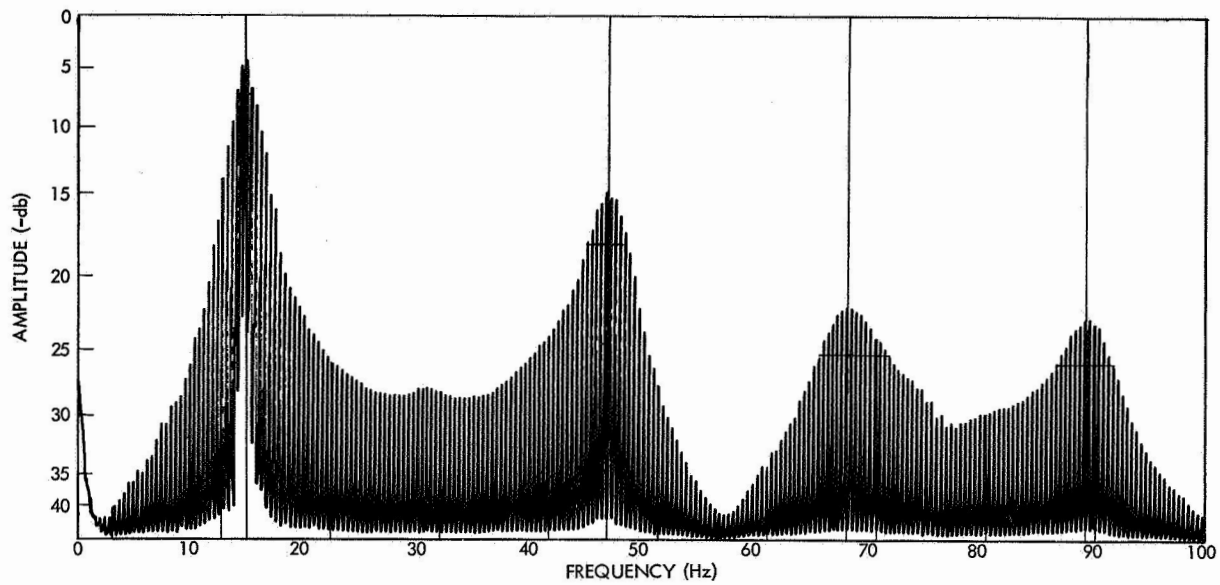


Figure 15a—Spectrum chart: 4-degree-of-freedom, amp. 15.

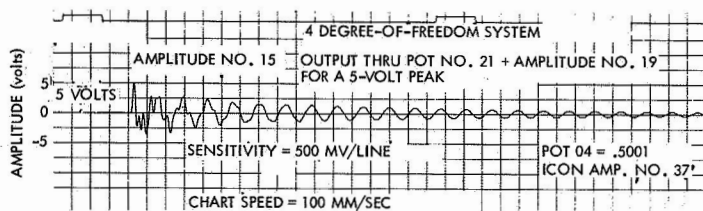


Figure 15b—Time response corresponding to Figure 15a.

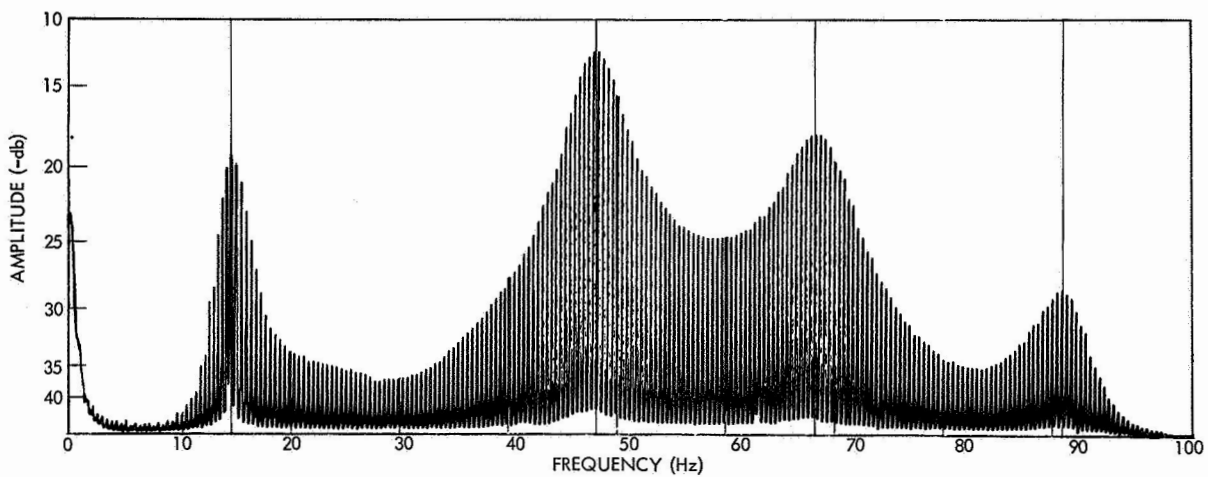


Figure 16a—Spectrum Chart: Composite of 1-Degree-of-Freedom to Simulate Figure 14a.

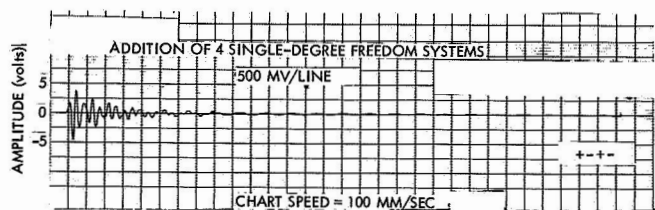


Figure 16b—Time response corresponding to Figure 16a.

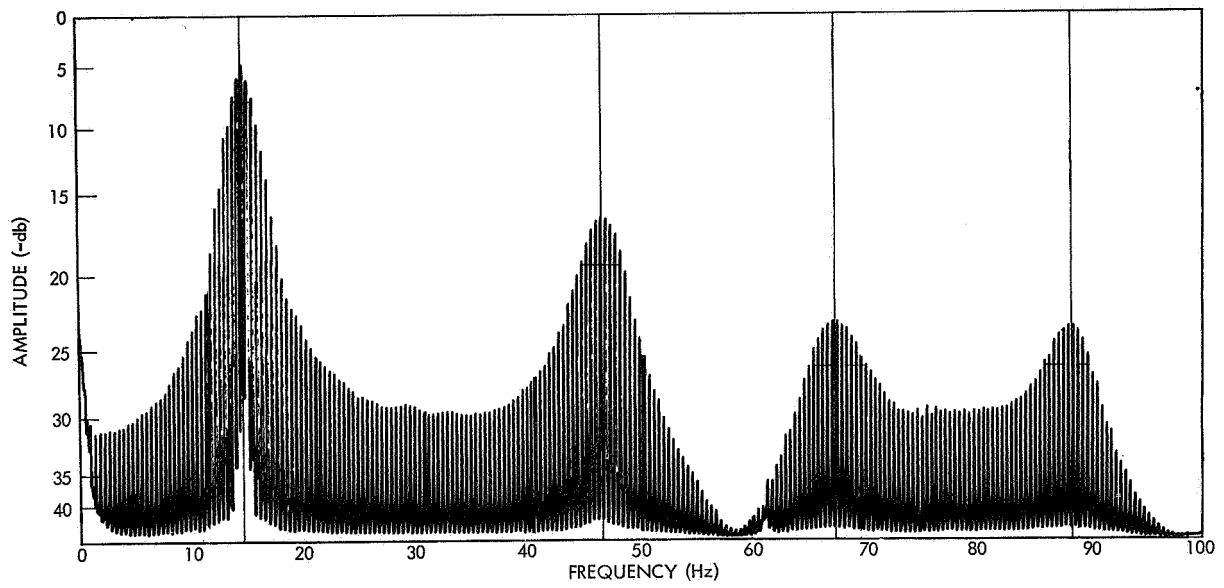


Figure 17a—Spectrum chart: composite of 1-degree-of-freedom to simulate Figure 15a.

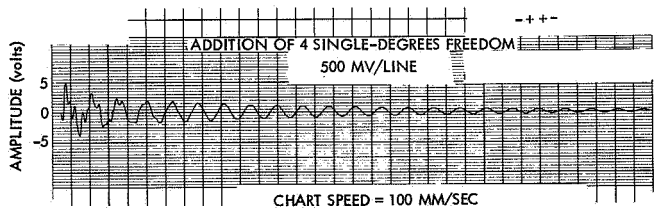


Figure 17b—Time response corresponding to Figure 17a.

GROUP D

ELECTROPHYSICS

Academic Personnel

Prin. Investigator: Dr. Theodore Leinhardt (V. P. I.)

Faculty: Dr. John Kinnier (Boston College)

Dr. Paul Berrett (Brigham Young)

Dr. Edward R. Sanford (Ohio U.)

Dr. S. Jaskolski (Marquette)

Graduate Students: Mr. Martin Sokoloski (Catholic U.)

Mr. T. D. Hargreaves (Ohio State)

Goddard Personnel

Staff Advisors: Mr. John New

Dr. Robert Coates

Mr. George Winston

DIRECT AND INDIRECT TRANSITIONS IN GALLIUM ARSENIDE

T. E. Leinhardt*

ABSTRACT

The first and second order transition probability rate equations which determine electronic transitions in a solid are discussed. These equations are specifically applied to interband transitions in gallium arsenide. Direct, photon-induced transitions are allowed between the lower minimum in the conduction band and the top of the valence band or an impurity level. The normal selection rules of a solid permit only indirect transitions from the top of the valence band or an impurity level to an upper minimum of the conduction band. Indirect, spontaneous transitions from the upper minima are more favored to terminate in a nearly discrete impurity level than in the valence band because of the impurity level's higher density.

INTRODUCTION

The ionic semiconductor gallium arsenide (GaAs) has a zinc-blend crystal structure and a band structure similar to that of indium antimonide (InSb) or germanium (Ge) (References 1 and 2). There is a minimum in the conduction band at the zone center, $\vec{k} = (000)$. The maximum of the valence band is also at $\vec{k} = (000)$. Additional minima in the conduction band are to be found close to the zone boundaries in the $\vec{k} = (100)$, (110) , and (111) directions. The latter are all at energies greater than the minimum at the center of the zone. Experimentally measured values of the effective masses at the $\vec{k} = (000)$ and $\vec{k} = (100)$ minima are $0.072 m_0$ and $\sim 1.2 m_0$, respectively (Reference 2). The effective masses of the three valence electrons near the band maximum at $\vec{k} = (000)$ are estimated to be $m_{v_1} = 0.68 m_0$, $m_{v_2} = 0.20 m_0$, and $m_{v_3} = 0.12 m_0$. Optical absorption measurements (Reference 3) indicate that the band gap between the top of the valence band and the lowest minimum of the conduction band at 300°K is 1.51 eV. The energy difference between this minimum and the one in the (100) direction is 0.36 eV. Figure 1 is a graph of the electronic energy bands determined by \vec{k} in the $\vec{k} = (100)$ direction.

Gallium arsenide is used in many solid state electronic devices, e.g., Gunn oscillators (Reference 4), optical emission p-n junctions (Reference 5), and photoconductors (Reference 6). A 0.82 micron (1.5 eV) laser was recently developed (Reference 7). It may be possible to extend the utility of this material by a method which depends upon the photon-excitation of electrons to the upper minima of the conduction band. If the process is reasonably efficient, it could lead to the development of devices capable of frequency conversion, amplification, detection, and modulation of electromagnetic radiation in the 1- to 10-micron range. To help evaluate the feasibility of this method, a discussion follows of transition theory and an analysis of interband and intraband transitions in GaAs.

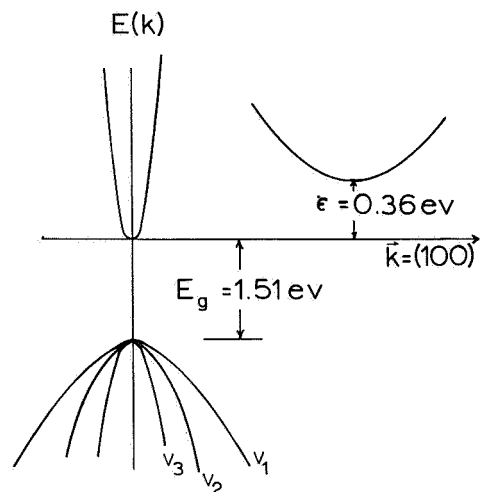


Figure 1-The energy bands of GaAs in the $\vec{k} = (100)$ direction.

*Virginia Polytechnic Institute, Blacksburg, Virginia.

THEORY

The interaction of an electromagnetic field and a system of electrons in a crystalline solid can result in electron transitions to various unoccupied energy states of the system. Approximate transition probability rates are determined by applying the time-dependent perturbation methods of quantum mechanics (References 8-10). Several applications of the quantum theory to direct and indirect transitions in solids can be found in the literature (References 11-18).

According to the one electron model, the probability per unit time that a transition will occur between the $|\vec{k}\rangle$ and $|\vec{k}'\rangle$ states is given in first order by

$$W_{\vec{k}'\vec{k}} = \frac{2\pi}{\hbar} N(\vec{k}') \left| H'_{\vec{k}'\vec{k}} \right|^2, \quad (1)$$

where $N(\vec{k}')$ is the density of states in the region of the final state, $|\vec{k}'\rangle$, and the matrix element, $H'_{\vec{k}'\vec{k}}$ is

$$H'_{\vec{k}'\vec{k}} = \int \psi_{\vec{k}'}^* H' \psi_{\vec{k}} d\tau, \quad (2)$$

where H' is the perturbation acting on the system. Here it will represent an electron-photon or an electron-phonon interaction. The $\psi_{\vec{k}}$ are eigenfunctions of the unperturbed system.

Along with the photon interaction, the electron can be inelastically scattered by the lattice. The transition probability rate must then be calculated with the second order formula,

$$W_{\vec{k}'\vec{k}} = \frac{2\pi}{\hbar} N(\vec{k}') \left| \sum_{\vec{k}'} \frac{H'_{\vec{k}'\vec{k}'} H'_{\vec{k}'\vec{k}}}{E(\vec{k}) - E(\vec{k}')} \right|^2, \quad (3)$$

where $|\vec{k}'\rangle$ are intermediate states in the bands.

A first order calculation of the transition probability per unit time induced in a system of electrons by a field of monochromatic photons yields

$$W_{\vec{k}'\vec{k}} = N(\vec{k}') \frac{4\pi^2 e^2}{m^2 c \omega_{\vec{k}'\vec{k}}^2} I(\omega_{\vec{k}'\vec{k}}) \left| \int \psi_{\vec{k}'}^* e^{i\vec{\eta} \cdot \vec{r}} \nabla_A \psi_{\vec{k}} d\tau \right|^2, \quad (4)$$

where $|\vec{\eta}| = \omega_{\vec{k}'\vec{k}}/c$, $I(\omega_{\vec{k}'\vec{k}})$ is the radiation intensity of angular frequency $\omega_{\vec{k}'\vec{k}}$ and ∇_A refers to the gradient operator component in the direction of the radiation vector potential. The same equation is used for both induced absorption and induced emission of photons.

In the dipole approximation Equation 4 may be written as

$$W_{\vec{k}'\vec{k}} = N(\vec{k}') \frac{4\pi^2 e^2}{3\hbar^2 c} I(\omega_{\vec{k}'\vec{k}}) \left| (\vec{r})_{\vec{k}'\vec{k}} \right|^2, \quad (5)$$

where

$$(\vec{r})_{\vec{k}'\vec{k}} = \int \psi_{\vec{k}'}^* \vec{r} \psi_{\vec{k}} d\tau.$$

There is also a spontaneous component of the emitted radiation that is independent of the intensity of the incident photon field. In dipole notation the transition probability rate of the spontaneous emission is

$$W_{\vec{k}' \vec{k}} = \frac{4e^2 \omega_{\vec{k}' \vec{k}}^3}{3\hbar c^3} \left| \langle \vec{r} \rangle_{\vec{k}' \vec{k}} \right|^2 N(\vec{k}') \quad (6)$$

Certain selection rules must be obeyed when these equations are applied to electron transitions in a crystal lattice. The rules are determined by the symmetry properties of the lattice and the laws of conservation of energy and conservation of momentum. Electrons interacting with a photon field undergo direct transitions only when $E(\vec{k}) - E(\vec{k}') \pm \hbar\omega = 0$ and $\vec{k} - \vec{k}' \pm \vec{\eta} - \vec{K} = 0$. The energies of the initial and final states are $E(\vec{k})$ and $E(\vec{k}')$ respectively, and $\hbar\omega$ is the incident photon energy. The (+) holds for absorption and the (-) for emission. The momenta of the electron in the initial and final states are \vec{k} and \vec{k}' respectively, and $\vec{\eta}$ is the propagation vector of the photon. Normally $|\vec{\eta}| \ll |\vec{k}|$ and, therefore, $\vec{\eta}$ can be disregarded in most calculations. \vec{K} is a vector in the reciprocal lattice space.

First order or direct transitions resulting from the interaction of electrons with a phonon field obey a similar set of selection rules. Namely, $E(\vec{k}) - E(\vec{k}') \pm \hbar\Omega = 0$ and $\vec{k} - \vec{k}' \pm \vec{q} - \vec{K} = 0$. The phonon energy ($\hbar\Omega \sim 0.01\text{eV}$) is small enough to be disregarded in many calculations. However, the propagation vector or the momentum, \vec{q} , of the phonon is usually large and must be considered. The transition probability rate for the electron-phonon interaction is directly proportional to the phonon distribution function and inversely proportional to the phonon energy (References 15, 17, and 19).

Because of the conservation of energy and conservation of momentum rules, Equations 1 and 3 are sometimes written

$$W_{\vec{k}' \vec{k}} = \frac{2\pi}{\hbar} N(\vec{k}') \left| H_{\vec{k}' \vec{k}}^s \delta_{\vec{k} - \vec{k}', \vec{k}' \mp \vec{\eta}} \right|^2 \delta_{E(\vec{k}), E(\vec{k}') \mp \hbar\omega} \quad (7)$$

and

$$W_{\vec{k}' \vec{k}} = \frac{2\pi}{\hbar} N(\vec{k}') \left| \sum_{\vec{k}'} \frac{H_{\vec{k}' \vec{k}'}^s H_{\vec{k}' \vec{k}}^s}{E(\vec{k}) - E(\vec{k}')} \delta_{\vec{k} - \vec{k}', \vec{k}' \mp \vec{\eta}} \right|^2 \delta_{E(\vec{k}), E(\vec{k}') \mp \hbar\omega \mp E^s} \quad (8)$$

where $H_{\vec{k}' \vec{k}'}^s$ is the matrix element of the electron-lattice interaction and E^s is the change in electron energy caused by this interaction. The Kronecker delta functions are defined as

$$\delta_{E(\vec{k}), E(\vec{k}') \mp \hbar\omega} = \begin{cases} 1 & \text{if } E(\vec{k}) = E(\vec{k}') \mp \hbar\omega \\ 0 & \text{if } E(\vec{k}) \neq E(\vec{k}') \mp \hbar\omega \end{cases} \quad (9)$$

and

$$\delta_{\vec{k} - \vec{k}', \vec{k}' \mp \vec{\eta}} = \begin{cases} 1 & \text{if } \vec{k} - \vec{K} = \vec{k}' \mp \vec{\eta} \\ 0 & \text{if } \vec{k} - \vec{K} \neq \vec{k}' \mp \vec{\eta} \end{cases} \quad (10)$$

All possible excitation modes must be considered when applying Equation 8. For example, in a transition involving a photon, a phonon, and an electron, the electron may be scattered in two ways: a) it may be excited from state $|\vec{k}\rangle$ to $|\vec{k}'\rangle$ by interacting with a photon, and then from state $|\vec{k}'\rangle$ to $|\vec{k}''\rangle$ by phonon scattering; or b) it may be scattered from $|\vec{k}\rangle$ to $|\vec{k}'_1\rangle$ by a phonon, and then from $|\vec{k}'_1\rangle$ to $|\vec{k}''\rangle$ by the photon. Both sequences must be counted, and the intermediate states must be among those allowed for the electron; otherwise, the value of the matrix elements $H'_{\vec{k}'\vec{k}}$ is zero.

INTERBAND AND INTRABAND TRANSITIONS IN GALLIUM ARSENIDE

Photon-induced electronic transitions (Figure 2, (a)) from the top of the valence band to the $\vec{k} = (000)$ minimum of the conduction band are permitted as first order or direct transitions in GaAs, if $\hbar\omega \gg E_g$ is the minimum energy difference, E_g , between the two

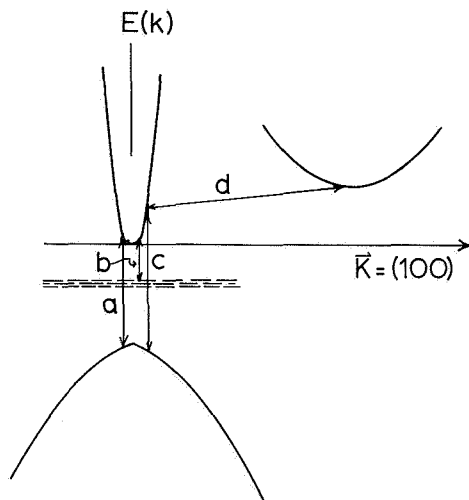


Fig. 2. Types of allowed interband transitions in GaAs: (a) is a direct transition from the top of the valence band to the $\vec{k} = (000)$ minimum of the conduction band; (b) is a similar transition between the lower minimum of the conduction band and an impurity band; (c) is the photon-excited part of a second order transition to an upper minimum of the conduction band; (d) is that part of the second-order transition caused by the lattice interaction.

bands. Similar transitions between impurity levels and the conduction band (Figure 2, (b)) can occur at smaller energies. The optical absorption data of Sturge (Reference 3) confirm this first order transition and place E_g at 1.51 eV. Sturge also observed the absorption of 1.9-eV photons, which corresponds to a second order transition from the valence band to one of the upper minima of the conduction band. The absorption indicates that $E_g + \epsilon = 1.9$ eV. Lines (c) and (d) in Figure 2 represent an allowed transition to the upper minimum.

A second order transition of the type described above requires a momentum change of the order of 10^8 cm^{-1} . This cannot be obtained from photons with less than 2-eV energies. It is necessary, therefore, to acquire the momentum from some other scattering process, e.g., the electron-phonon interaction. The following scattering processes occur to some extent in the ionic crystals (Reference 2): polar scattering, electron-hole scattering, electron-phonon scattering, electron-electron scattering, deformation potential scattering, piezoelectric scattering, and inelastic scattering from excited impurity states.

Ehrenreich (Reference 2) points out that, above room temperature, the polar interaction is responsible for most electron scattering in the transport processes. Below room temperature, on the other hand, electron-hole scattering is important. In high mobility samples of GaAs, charged impurity scattering seems to be important. Electron-electron scattering is involved to some extent, but it is not so important as lattice scattering. Deformation potential scattering is not of considerable significance here. Piezoelectric scattering can be considered above 100° K , but it is unimportant below that temperature. For the transition processes discussed in this paper, the electron-phonon scattering interaction probably plays the most important role (References 15 and 17). It is also the best understood (Reference 19).

Transitions from the bottom of the $\vec{k} = (000)$ minimum to an upper minimum in the conduction band are ruled out by the requirements of Equation 8. This is simply due to the fact that there are no intermediate energy states available for the transitions. First order phonon scattering of the electrons can take place between the minima, however. Also, it is possible to accelerate electrons to the upper minima by high electric fields.

As an application of Equation 8, consider a spontaneous electron transition from an upper minimum in the conduction band to a lower band. This type of transition will be important to the development of the devices mentioned earlier. Assume that there is an occupied state $|\vec{k}\rangle$ in the upper minimum and unoccupied states near $|\vec{k}'\rangle$ in one of the lower bands. The density of the states near $|\vec{k}'\rangle$ is $N(\vec{k}')$. Because of the GaAs band structure and the conditions imposed by Equations 9 and 10 (References 12 and 15), Equation 8 becomes,

$$W_{\vec{k}'\vec{k}} = \frac{2\pi}{\hbar} N(\vec{k}') \left| \frac{H'_{\vec{k}\vec{k}'} H'_{\vec{k}'\vec{k}}}{\hbar\omega_{\vec{k}'\vec{k}}} \right|^2 \quad (11)$$

The matrix element, $H'_{\vec{k}\vec{k}'}$, represents the contribution of lattice scattering to the transition probability, line (d) in Figure 2. $H'_{\vec{k}'\vec{k}}$ is due to the spontaneous emission of a photon with energy $E = \hbar\omega_{\vec{k}'\vec{k}}$. Line (c) represents this part of the transition.

In dipole notation Equation 11 becomes,

$$W_{\vec{k}'\vec{k}} = \frac{4e^2\omega_{\vec{k}'\vec{k}}^3}{3\hbar c^3} \frac{|(\vec{r})_{\vec{k}'\vec{k}}|^2}{\hbar^2\omega_{\vec{k}'\vec{k}}^2} |H_{\vec{k}\vec{k}'}|^2 N(\vec{k}') \quad (12)$$

If transition probability rates to an impurity level are designated W_{du} and to the valence band, W_{vu} , the ratio of these rates is

$$\frac{W_{du}}{W_{vu}} = \frac{\omega_{du}}{\omega_{vu}} \frac{|(\vec{r})_{du}|^2 N(\vec{k}_d)}{|(\vec{r})_{vu}|^2 N(\vec{k}_v)} \quad (13)$$

Here it is assumed that the lattice-scattering matrix element is the same for both transition types. It is impossible to calculate this ratio without knowing the wave functions. However, if the crystal is not overly doped, transitions from the upper minimum will occur more frequently to unoccupied impurity level states than to unoccupied states in the valence band. This happens because the near discreteness of the level makes $N(\vec{k}_d) \gg N(\vec{k}_v)$. Knowledge of the densities of states, then, would permit an estimation of Equation 13. More accurate evaluations of Equation 13 could be obtained from optical absorption and fluorescence measurements in the 1.9-ev (0.66-micron) to 0.36-ev (3.5-micron) range.

REFERENCES

1. Callaway, Joseph, "Energy Bands in Gallium Arsenide," Journal of Electronics 2(4):330-340, January 1957.
2. Ehrenreich, H., "Band Structure and Electron Transport of GaAs," Physical Review 120(6):1951-1963, December 15, 1960.
3. Sturge, M. D., "Optical Absorption of Gallium Arsenide between 0.6 and 2.75 ev," Physical Review 127(3):768-773, August 1, 1962.
4. Hilsum, C., "Transferred Electron Amplifiers and Oscillators," Proceedings of the IRE 50(2):185-189, February 1962.
5. Pankove, J. I., and Massoulié, M., "Injection Luminescence from Gallium Arsenide," Bulletin of the American Physical Society 7(1):88, January 1962.
6. Bube, R. H., "Photoelectronic Analysis of High Resistivity Crystals: (a) GaAs, (b) Sb_2S_3 ," Journal of Applied Physics 31(2):315-322, February 1960.
7. Basov, N. G., Grasyuk, A. Z., Efimkov, V. F., and Katulin, V. A., "GaAs Semiconductor Laser Optically Excited by Radiation Having Energy Close to the Band Width," Soviet Physics - Solid State 9(1):65-74, July 1967.
8. Dirac, P. A. M., The Principles of Quantum Mechanics, Fourth Edition, London: Oxford University Press, 1958, pp. 167-206.
9. Heitler, W., The Quantum Theory of Radiation, Second Edition, London: Oxford University Press, 1944, pp. 136-145.
10. Schiff, L. I., Quantum Mechanics, New York: McGraw-Hill Book Company, Inc., 1949, pp. 189-215, 382-388.
11. Dexter, D. E., "Absorption Near the Edge in Insulators," in Photoconductivity Conference, New York: John Wiley & Sons, Inc., 1956, pp. 155-183.
12. Bardeen, J., Blatt, F. J., and Hall, L. H., "Indirect Transitions from the Valence to the Conduction Bands," in Photoconductivity Conference, New York: John Wiley & Sons, Inc., 1956, pp. 146-154.
13. Fan, H. Y., Spitzer, W., and Collins, R. J., "Infrared Absorption in n-Type Germanium," Physical Review 101(2):566-572, January 15, 1956.
14. Dumke, William P., "Indirect Transitions at the Center of the Brillouin Zone with Application to InSb, and a Possible New Effect," Physical Review 108(6):1419-1425, December 15, 1957.
15. Rosenberg, R. and Lax, M., "Free-Carrier Absorption in n-Type Ge," Physical Review 122(3):843-852, November 1, 1958.
16. Dumke, W., "Quantum Theory of Free Carrier Absorption," Physical Review 124(6):1813-1817, December 15, 1961.

17. Demidenko, Z. A., and Mashkevich, V. S., "Indirect Optical Transitions at the Centre of the Brillouin Zone," Physica Status Solidi 21(1):K59, May 1967.
18. Bowers, H. C., and Wolga, G. J., "Volume Intraband Photoelectric Effect," Physical Review 157(3):518-523, May 15, 1967.
19. Ziman, J. M., Electrons and Phonons, London: Oxford University Press, 1962, pp. 175-219.



AN ARC SOURCE OF LOW-ENERGY IONS

John H. Kinnier*

ABSTRACT

An ion source for ionospheric simulation requires the production of a large quantity of low-energy ions without the disturbing effects of high-energy electrons or strong magnetic fields. A comparison of ion production by photon excitation, electron or proton bombardment, and gas discharges indicates that a low-energy arc source is suitable. A refractory metal hollow cathode source operating at 200 volts and 0.5 ampere is described. The plasma produced outside the arc column was found to have an energy from 2 to 5 ev.

INTRODUCTION

An increasing interest in and realization of the importance of plasma phenomena in the laboratory and in outer space have motivated the need for a simple, efficient source of low-energy ions. Many sources for ion energies of 100 ev or above are readily available in the form of RF or dc gas discharges and electron bombardment type sources.

The degree of complexity of these sources is directly related to the ion energy control desired and their adaptation for the production of ions of one-tenth to one-hundredth of their nominal energy is not easily accomplished. A certain simplification arises in low-energy plasma studies if the source does not require the use of strong magnetic fields which may penetrate into the test area.

A particular and important application of a low-energy ion source lies in its use for the design, testing, and calibration of spacecraft destined to measure or be operated in a charged particle region (cf. Appendix A).

IMPACT IONIZATION

A plasma may be generated whenever a beam of energetic photons or particles penetrates a region containing a gas, as, for example, the generation of the ionosphere by ultraviolet radiation from the Sun. Usually the ionization process itself does not result in the newly formed ions having any appreciable kinetic energy, though the released electrons may easily acquire significant energies in many circumstances.

The relative efficiency of photons and particles in producing a laboratory plasma may be evaluated from the cross sections presented in Figure 1, where values applying to argon gas for photons, electrons, and protons are chosen as representative. Of the three processes, photoionization is the least efficient, since it requires radiation in the far ultraviolet or soft X-ray region. The cross section for photoionization has its maximum value at the threshold frequency ν and wavelength λ for the ejection of the least tightly bound electron from an atom or molecule with a first ionization potential V_1 :

*Boston College, Chestnut Hill, Massachusetts.

$$h \nu_i = h \frac{c}{\lambda_i} = e V_i, \quad (1)$$

where h is Planck's constant, c is the velocity of light, and e is the electron charge.

It is also possible for ionization to occur at wavelengths greater than the threshold value when an excited atom or molecule takes part in a two-step process. The ionization potential in volts and the threshold wavelength in Angstroms are related by evaluating the constants of Equation 1 to produce the compact formula

$$\lambda_i = \frac{12,398}{V_i}. \quad (2)$$

The small peaks that appear in the photoionization cross section are the X-ray absorption edges. When the incident photon has sufficient energy to eject an electron from an inner shell, it is very probable that the ejected electron will be from that shell, and only a single electron is ejected by a given photon. For each photoionizing event a photon is removed, and its excess energy normally is given to the liberated electron which, in turn, may cause additional ionization of the gas by ionizing collisions.

Ionization by particle impact differs from photoionization not only in the larger value of its cross section but also in that outer electrons are preferentially ejected irrespective of the incident particle energy. The ionization cross section for protons and electrons rises steadily from its threshold value, reaches a broad maximum, and subsequently decreases. A general analysis of the process indicates that the maximum occurs when the relative speed of the colliding particles approximates the orbital speed of the electrons. In an ionizing collision a fast particle is seldom deflected appreciably from its original path and loses, on the average, two or three times the ionization energy in each ionizing encounter.

This behavior has been adapted to the production of a long column of weakly ionized gas. Although this process is not notable for its efficiency and there is the ever-present danger of oscillations from the streaming ions, the liberated electrons serve to neutralize the space charge of the fast ions and the use of a separate electron source is avoided.

Many ion sources used in the study of atomic collisions for plasma production, or even for the propulsion of space vehicles, depend upon the acceleration to 100 volts or more of thermionically emitted electrons which are directed through a gas to form ions by collisions. Electron impact ionization is essential to the operation of radio frequency, glow, and arc-discharge sources. The behavior of electrons in inelastic collisions has been studied extensively for many years (References 1 to 7).

It is most useful in the design of a plasma source, which depends upon electron impact ionization as its fundamental mode of operation, to be able to estimate the rate of ion production. The equation generally employed for small currents is

$$i^+ = i_e N q_i x, \quad (3)$$

where i^+ is the positive ion current produced, i_e is the incident electron beam current, N is the number density of the gas, and q_i is the apparent ionization cross section. The term $N q_i x$ may be considered as the probability that a particular electron will make an

ionizing collision as it travels a distance x . In many experimental circumstance conditions are such as to render the equation unreliable.

The most important considerations are:

1. Should either N or x be very large, many electrons will be able to make several ionizing collisions, losing some energy in each event. As is evident from Figure 1 (See also References 7 to 14), the value of q_i is no longer a constant and the effective q_i is in reality the sum of all cross sections involving the ejection of electrons from the target gas.
2. Should i^+ be large, the effective gas density in the electron beam region will be less than that in the region outside the beam because a high value of i_e will rapidly ionize any molecule or atom entering the beam region and consequently the rate of ion production becomes more dependent on the rate at which molecules enter the beam than on the collision cross section.

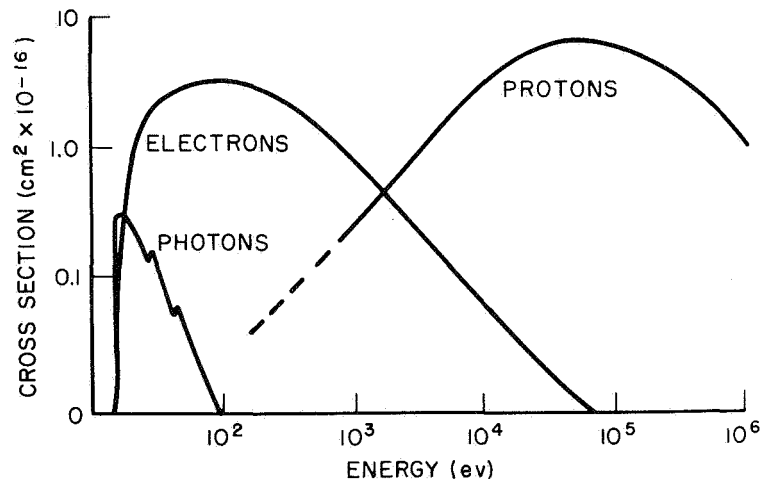


Figure 1—Ionization cross sections for photons, electrons, and protons on argon

An electron beam produced by a source and allowed to enter field free space will be attenuated by ionization and scattering processes taking place as it traverses a gas of low density. The plasma column formed will necessarily lack uniformity throughout its length. The application of an electric field parallel to the beam will enable the initial and newly formed electrons to regain sufficient energy to again become ionizing agents.

In a gas discharge plasma any distinction as to the origin of the charged particles becomes impossible and a quantitative theoretical analysis of the discharge is rendered exceedingly complicated because it must deal with rate processes for ionization, recombination, diffusion, and lifetimes in general. In those experimental situations where electrons acquire little energy between collisions, their velocity distribution reaches a state where it can be approximated by a Maxwellian distribution. These conditions prevail in high-pressure arcs and in the low-intensity electric field of a microwave discharge.

GAS DISCHARGES

Electric discharges have been studied extensively and have been classified in many ways, such as being electrode or electrodeless discharges, transient or steady-state, and high-pressure or low-pressure. Additional variations arise depending upon the geometry of the electrodes, the applied potential, or the presence or absence of a magnetic field. In discharges employing internal electrodes the discharge current is carried by both ions and electrons. At the cathode, ions are collected and electrons emitted. Because the electrons possess a much larger mobility than the ions, the ion current and the electron current at the cathode are seldom equal and their ratio determines in large part the character of the discharge.

The lack of charge neutrality near the cathode due to a positive ion space charge implies the existence of a distinctive potential difference between the cathode and the rest of the discharge. The value of the cathode potential drop v_c and the thickness of the region over which it appears are determined by the discharge plasma, but the values of ion and electron currents at the cathode are established by the emissive properties of the cathode. The behavior of a steady-state gas discharge for a given set of parameters involving the gas pressure, electrode configuration, and other similar factors will depend upon the intersection of the resistance line with the volt-ampere characteristic (Figure 2).

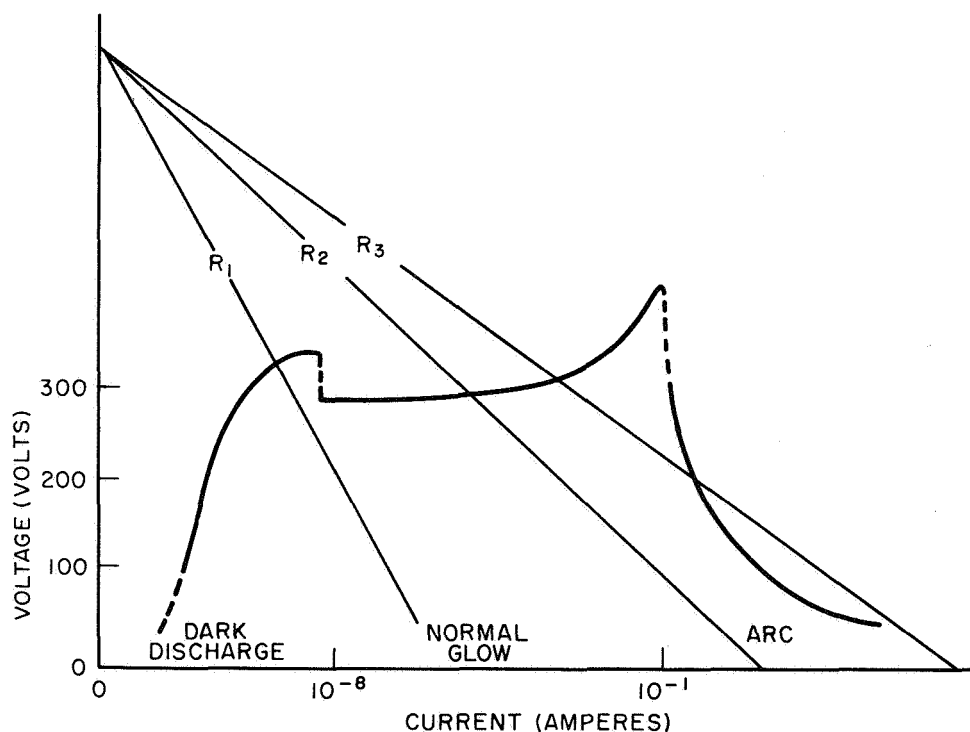


Figure 2—Characteristics of dc discharges

When neither the plasma nor the cathode is a copious source of electrons the ion density in the vicinity of the cathode tends to exceed the electron density and current continuity in the region can be achieved only by greatly increased ionization by electrons that gain energy as they cross the cathode potential difference and produce a bright

plasma region called the negative glow. The negative-glow region is a source of photons and ions. The ions traverse the cathode potential difference in a direction opposite to that of the electrons and in turn affect the cathode electron emission.

Since the electron current in the cathode region is less than the ion current, glow discharges have a high effective impedance and are limited to low current densities at the cathode as a result of the electron emission process. Ion bombardment can cause sputtering and heating of the cathode surface, which, under heavy current loading, may develop regions of high electron emissivity called cathode spots with their consequent unstabilizing effects.

Should the external circuit not limit the total current, the electron current will tend to become greater than the ion current, a characteristic feature of an arc. Current-limited glow discharges perform well at low pressures, typically having a relative ionization of one ion per thousand neutral particles.

Electron temperatures are high and recombination takes place principally on the discharge walls. The electric field applied to the discharge so increases the electron energy that the average electron temperature far exceeds the ion temperature, which is certainly not greater than the gas temperature. Wall-dominated recombination effects and low gas pressures enable the glow discharge to fill a large volume. This property is enhanced when the anode and cathode are widely separated.

Varying geometric configurations of the electrodes are accommodated by the discharge by adjusting the length of the positive column. Very long column discharges have complicated ionization processes and tend to show time and density fluctuations (References 15 to 17). It is, of course, possible to use a thermionically emitting cathode surface in a glow discharge to provide some control over the electron current with respect to the ion current. In this case the cathode potential drop decreases and the positive column lengthens.

Occasionally one observes a glow discharge that is intermittent. The interval between flashes frequently is as long as several seconds. The effect, which is sometimes called the obstructed glow discharge, is dependent on the electrode spacing if this is approximately the same as the cathode dark space. The period of the flashes is also a function of this distance.

Two causes are designated for this behavior; wall effects and changes in the cathode surface. While the discharge is operative charges accumulate on nearby surfaces and opposing electric fields are generated which finally serve to quench the discharge. Gradually the accumulated charges dissipate and the discharge renews itself. The intermittent character of the discharge can also be caused by changes in absorbed gas layers or impurities on the cathode surface which are released by positive ion bombardment and change the ion electron current ratio.

ARC DISCHARGES

An arc discharge (References 18 to 21) has a cathode fall voltage an order or magnitude less than that of a glow discharge, and a new mechanism for electron emission at the cathode surface comes into operation (References 22 and 23). With an increase in current in the abnormal glow region, the thickness of the cathode fall region decreases, the number of collisions made by outgoing electrons decreases, and the energy of the incoming positive ions increases. The increase in positive ion energy will raise the temperature of a refractory metal cathode to the point where thermionic emission is possible.

The thermal electrons emitted by the cathode are accelerated across the cathode potential difference; thus the number of ions is increased and these ions, in turn, raise the temperature of the cathode even higher. Under these circumstances a lower voltage will sustain a given current and a falling or negative volt-ampere characteristic is established.

The cathode temperature continues to rise until the saturated thermionic emission current is equal to the full discharge current and the cathode fall voltage is approximately equal to the first ionization potential of the gas used in the discharge. A constricted high-density plasma forms at the cathode end of the arc. Its kinetic and transport properties are similar to those of a glow discharge at low pressure and relatively low arc currents.

At point A in Figure 3, the arc mode is established with the thermionic electrons making enough ionizing collisions to provide the necessary positive ion current. An arc discharge can operate over a wide variety of pressures. In the high-pressure range, particle transport is reduced, recombination rates are dominated by exchange within the gas rather than at the walls, and the arc column is constricted. High degrees of ionization result and the various constituent particles of the discharge come to thermal equilibrium. Consequently, the electrons have a much lower temperature than is present in low-pressure discharges. The rapid energy exchange and high degree of ionization heat the residual neutral gas until it has nearly the same energy as that of the electrons. A reduction in gas pressure leads to a higher electron temperature and a lower gas temperature.

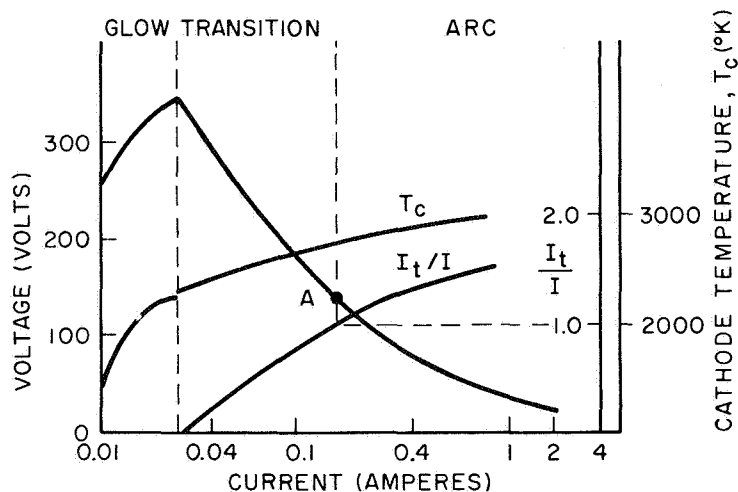


Figure 3—Transition of glow to arc discharge

Electron temperatures of a few electron volts might be expected for a discharge in the micron pressure range. The low-pressure arc column is similar to the positive column of a glow discharge. An increase in arc current at constant pressure results in an increase in positive ion density and a decrease in electron temperature. The gradient of the positive column adjusts itself so as to maintain positive and negative charge equality; as many new electrons and ions are produced as are lost to the walls.

Ions and electrons diffuse rapidly from a low-pressure, low-current, arc column. An increase in arc current will cause an increase in gas temperature along the arc axis and a constriction of the arc column. The density along the arc will be less than that at the walls. Under proper conditions the reduced density along the axis results in a longer mean free path and more efficient ionization (see Figure 4).

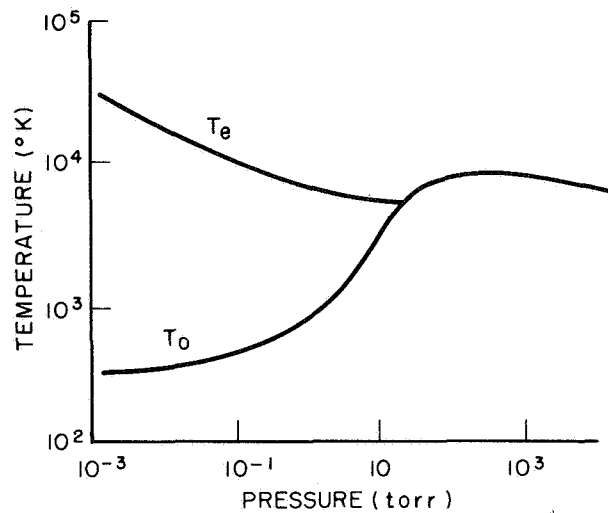


Figure 4—Electron and neutral gas temperature in arc discharge

HOLLOW CATHODE DISCHARGE

When electrons leave a cathode surface they travel through the cathode potential difference in a direction normal to the cathode surface and directed toward the anode. If two plane cathodes are arranged parallel to each other, the negative glow regions are forced to merge. This type of geometrical structure was found to have an unexpectedly high level of ionization when direct current potentials were applied. A simple form of hollow cathode discharge uses a ring anode and two plane parallel cathodes (Figure 5).

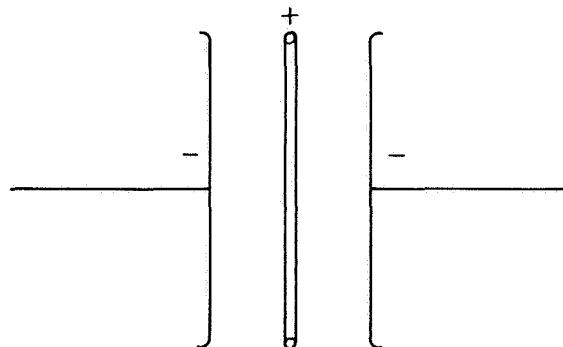


Figure 5—Ring-anode hollow cathode structure

Other cathode shapes having like proportions are a rectangular box having one side open, a sphere or cylinder with a small opening, various forms of mesh containers, or the wave guide plasma cell. (See, e.g., References 24 and 25).

A very useful shape is a hollow cylinder open at one end. In Figure 6 the electric field lines are sketched for a common form of hollow cathode source. Electrons emerging from the interior form a well collimated beam provided the cavity aperture is several times smaller than its depth. Too narrow an aperture will often prohibit the discharge from entering the cavity, and a very large aperture approaches the behavior of a plane electrode. A long narrow cavity allows a very intense discharge to build up to a high level inside the cavity; this causes the cathode fall distance to shrink with the entire potential drop taking place within the cavity, and a transition is easily made to an arc mode of operation.

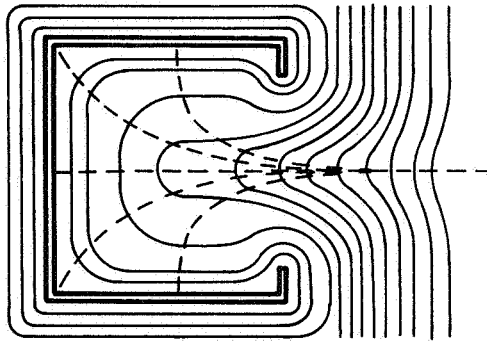


Figure 6—Electric field of a hollow cathode

Hollow cathode discharges, or Schuler discharges, have been used as spectroscopic sources for many years. Their properties may be briefly summarized as follows:

1. Given the same cathode fall potential, the discharge current is very much larger than in a conventional discharge.
2. The low cathode fall potential produces a highly ionized low-energy plasma.
3. The region within the hollow cathode emits an intense light from the confined negative glow (Reference 26).
4. Ionization products which ordinarily would diffuse to the external walls of the discharge now strike the cathode itself where secondary emission products contribute to the discharge current.
5. Unionized gas inside the cavity is heated by the high current density; a decrease in gas density results. The power dissipated at the cathode is equal to the product of the discharge current and the cathode potential fall (References 25 and 26).

EFFECT OF MAGNETIC FIELD

In this discussion it is assumed that the magnetic and electric fields are oriented along the same direction and on the discharge axis. A charged particle moving in combined electric and magnetic field is subject to a Lorentz force where the effect of the magnetic field is to cause particles not already moving parallel to it to describe helical paths about the magnetic force lines. The radius of the helix in terms of the velocity component perpendicular to the field is

$$a = \frac{qB}{m}, \quad \text{and} \quad r = \frac{mV}{qB} \quad (4)$$

where a is the particle's angular velocity. The pitch of the helix is dependent on the axial component of velocity.

Since the radius of the helix is directly proportional to the mass of the particle, only the paths of electrons will be significantly affected in moderate fields. An electron traveling a given distance forward now has a greatly increased path length and a greater chance of making an ionizing collision.

The effect of a magnetic field may also be viewed as an apparent increase in gas pressure along the direction of the field. When applied to a gas discharge, a longitudinal magnetic field changes its volt-ampere characteristic and decreases its starting potential (Reference 27). Radial diffusion from the positive column is reduced and the column can be sustained by a smaller gradient. The electron confinement properties of the field serve to lengthen the negative glow region but have little effect on the cathode dark space where electrons are moving with high velocity. The most significant effect is control over the radial motions of electrons; this allows the discharge to be maintained by a lower ionization rate.

EXPERIMENTAL ION SOURCE

Interest in thermonuclear processes and the associated high-density plasma problems motivated Luce (References 28 and 29) and others at the Oak Ridge National Laboratory in the development of energetic arcs for the disassociation of deuterium gas. One form of arc discharge consisted of a hollow cylindrical tungsten cathode having an internal gas feed at one end. The anode was located several feet away. The discharge was operated in a vacuum at a potential of a few hundred volts and carried a current of a hundred amperes or more. An axial magnetic field was used to collimate and stabilize the arc.

A requirement for a large-volume plasma of low energy and low background pressure is more closely approached by an arc discharge source than by an RF or glow discharge. Toward this end an experimental source was constructed as sketched in Figure 7. On the right a tantalum tube with a diameter of 0.200 inch and a wall thickness of 0.010 inch was mounted on the end of a stainless-steel fitting. The fitting also provided a means to introduce gas into the interior of the cathode.

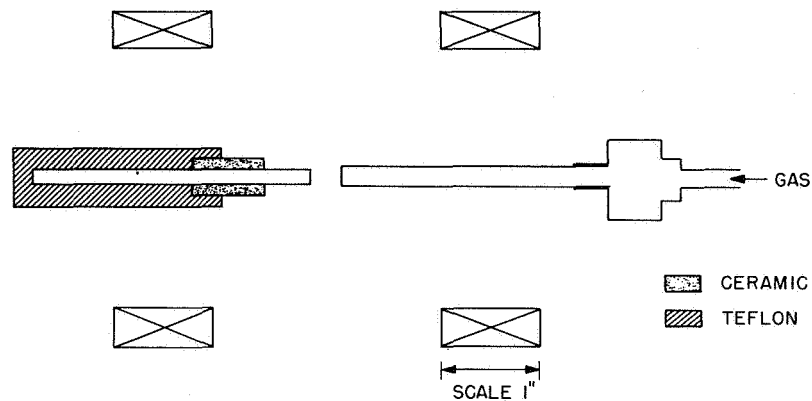


Figure 7—Hollow tantalum cathode source

The anode was a 1/8-inch-diameter copper rod protected by a ceramic sleeve and teflon insulation. Two coils designed to produce a field in the range of 500 gauss were located coaxially with the electrodes. All components were rigidly attached 2.5 inches from a teflon base plate. The system was designed to be operated in a vacuum bell jar. Gas for the discharge was passed through a precision needle valve, through the vacuum wall, and along a tube to the cathode.

SOURCE OPERATION

Source operation was limited to currents of 0.5 ampere or less because of instrumentation capabilities. The voltage drop across the source was approximately 200 volts. Frequently, the discharge started between the anode and the exterior surface of the cathode. A hollow cathode form of discharge required an ambient pressure of 10^{-3} mm Hg, an electrode voltage of 200 or more, a magnetic field of about 500 gauss, and a burst of gas from the feed line to initiate the discharge.

After startup, the tantalum cathode gradually acquired a visible bright glow under positive ion bombardment. Once the discharge has reached stable operation, the magnetic field may be reduced to a low value or even turned off, the gas flow rate can be adjusted, and the current can be varied over a wide range.

The operation of the discharge was better with a small-diameter copper rod as the anode than with a half-inch aluminum or steel anode electrode. The aluminum rapidly acquired a white oxide coating and its surface was straited with small arcs. Only a small portion of the anode rod was left exposed since the presence of a large amount of conductive anode surface along the axis of the discharge caused it to spread in an uncontrolled manner and, at low discharge currents, induced the discharge to shift to the exterior of the cathode.

Further initial difficulties in establishing the discharge were traced to the existence of an extensive ground plane beneath the electrodes caused by the metal base plate of the bell jar. It is believed that this ground plane distorted the electric field between anode and cathode. Satisfactory operation of the discharge was obtained once the electrodes, supported on an insulating plate, were raised 10 inches from the base of the bell jar. The discharge operated well at currents of 0.5 ampere and with a background pressure of 5×10^{-4} mm Hg.

During 20 hours of operation the cathode showed no visible deterioration or sputtering. Some sputtering was observed from the anode. At currents of more than 0.5 ampere it will certainly be necessary to provide for cooling of the cathode support structure.

The discharge can be operated with the cathode at ground and the anode positive or with the cathode negative and the anode grounded. This latter mode of operation was found to be more compatible with the operation of a Langmuir probe. Gas flow rates to the source were estimated to be in the range of 0.05 atm cm³/sec.

Both argon and nitrogen gas were found to operate the source satisfactorily. Argon gas was used for test purposes to avoid the possibility of negative ion formation. Gas flowing through the automatically heated cathode produces a pressure gradient along the tube which is essentially zero at the orifice. The gas flow can, therefore, be adjusted so as to achieve the optimum pressure condition for a high-density discharge at some point along the tube.

The existence of this effect is seen in a visible change in temperature along the tube. Within the hollow cathode a strongly ionized plasma is formed. This plasma becomes the source of a larger less dense external plasma as ions are swept out of the cathode by the pressure gradient. The external plasma may also be assisted by external ionization. Electrons generated by collisions and by emission from the heated tantalum ionize the gas within the cathode as they are accelerated across the cathode potential drop within the tube. Only a small potential difference is effective between the end of the cathode and anode.

MEASUREMENTS

Measurements on the external plasma were performed with Langmuir probes in a cylindrical or wire form. During these measurements the magnetic field was turned entirely off or reduced to a low value. The principal effect of a magnetic field is to retard the motions of electrons and, to a much smaller extent, that of ions across the field. Their motion along the field is not retarded. The influence of this effect was evaluated by placing the probe parallel to and then perpendicular to the field. The probe was located 15 cm from the discharge axis and no significant change was observed.

The Langmuir probe measurements were evaluated by the relations

$$\lg j_e = \text{Const} - \frac{e v}{K T_e} \quad (5)$$

and

$$j_e = e N_e \sqrt{\frac{K T_e}{2 m}} \quad (6)$$

The logarithm of the current density plotted against the probe voltage ideally gives a straight line whose slope is the electron temperature (see Figure 8 for nonlogarithm plot). The effective probe area must be known if the current density is to be calculated. At the point where the probe potential is the same as the space potential determined from the intersection of the linear parts (Figure 9), $v = 0$ and the electron density can be found from equation (6) since T_e is now known. It was found necessary to clean the probe carefully between measurements.

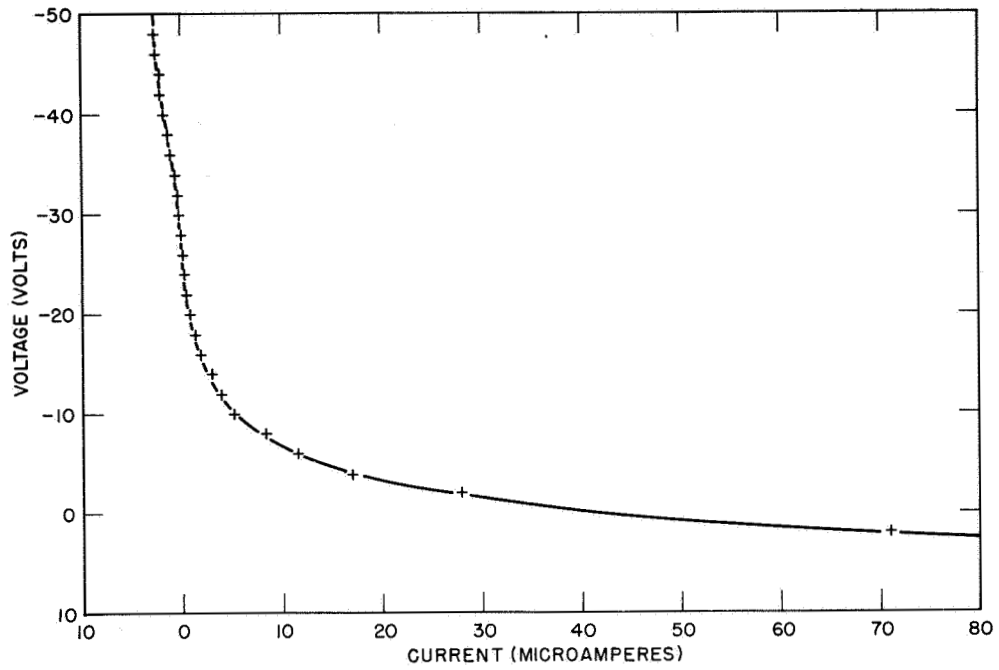


Figure 8—Typical Langmuir probe for curve $I = 0.3$ ampere

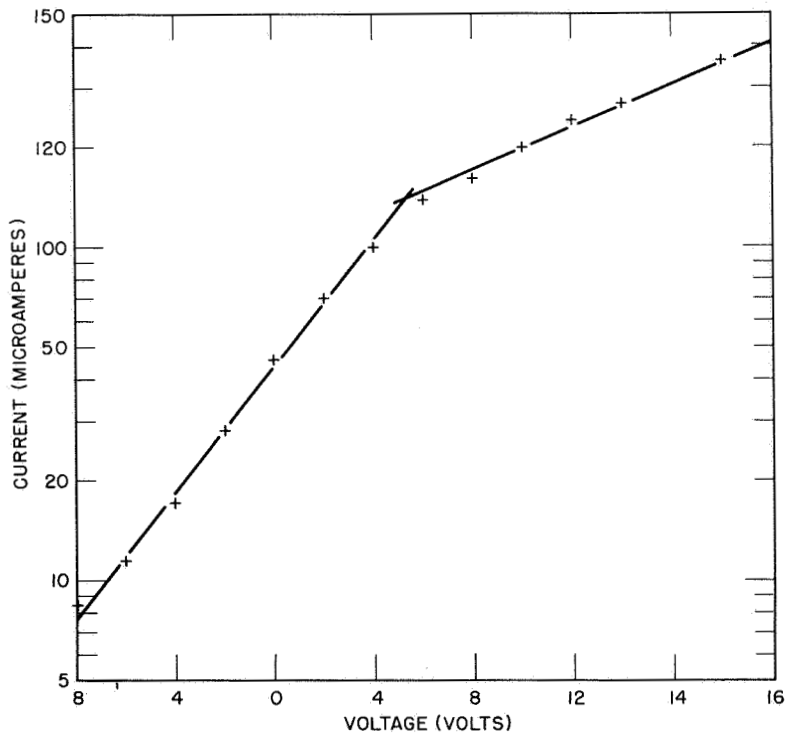


Figure 9—Probe volts with respect to ground

The electron temperature derived from probe measurement was 4.4 eV and the electron density at the probe location was 2.54×10^7 electrons/cm³. When the probe bias was set to receive ion current, the relationship of ion current to discharge current indicated a linear relationship over the range investigated (Figure 10).

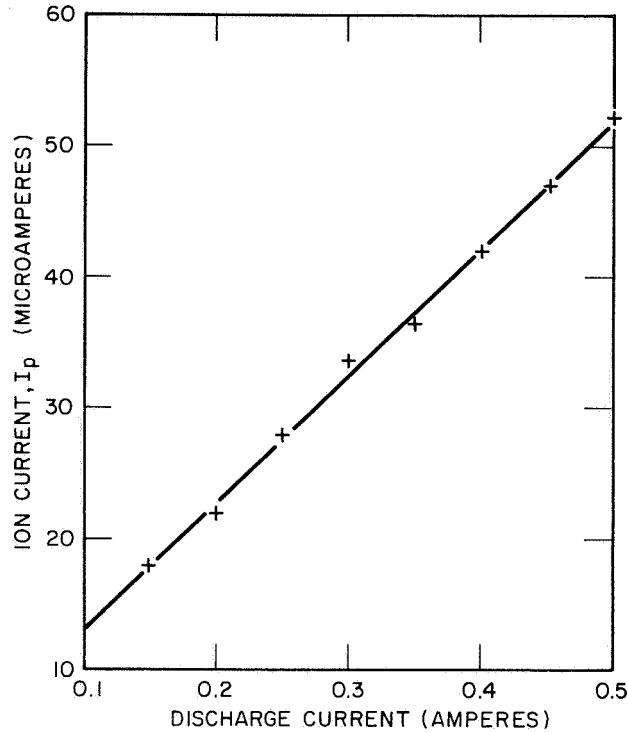


Figure 10—Discharge current versus ion current

In a highly ionized plasma (Reference 30), ions acquire energy from the electric fields of the plasma of approximately half the electron temperature and certainly not in excess of the electron temperature. Thus the ion energy is very probably approximately 2 eV and the ion density is very close to the electron density because a failure in space charge neutrality gives rise to very large potential differences to enforce this neutrality. Measurements made of the electron density as a function of distance from the source indicated an approximately exponential decrease.

CONCLUSIONS

The hollow cathode arc source proved to be a stable and durable source of low-energy ions. Its tantalum cathode is able to withstand high temperatures and ion bombardment for long periods of time without any visible or mechanical change. The wall thickness of the cathode must provide sufficient mechanical strength at operating temperatures. A thin-walled tantalum tube (0.002-inch thick) originally used in the discharge sagged under high-temperature conditions and moved a distance of 1 centimeter off axis. Even under this handicap, the discharge continued to operate. Ease of operation is assisted by accurate axial alignment.

The self-heating feature of the cathode and its gas utilization efficiency are attractive features when the source is to be used with another vacuum facility. The low values of current used in the present experiments have hardly allowed the source to produce any ions in quantity. A cooled cathode mounting would allow currents of tens of amperes to be used.

When it is used as a source for ionsphere simulation, the source could be mounted within a large chamber or mounted on a vacuum port plate (Figure 11). Mounting in this manner has these advantages: gas feeding is simplified, the electrode spacing is variable, the field coils are adjustable, differential pumping can be used, and an accelerating grid structure can be inserted if higher ion energies are required.

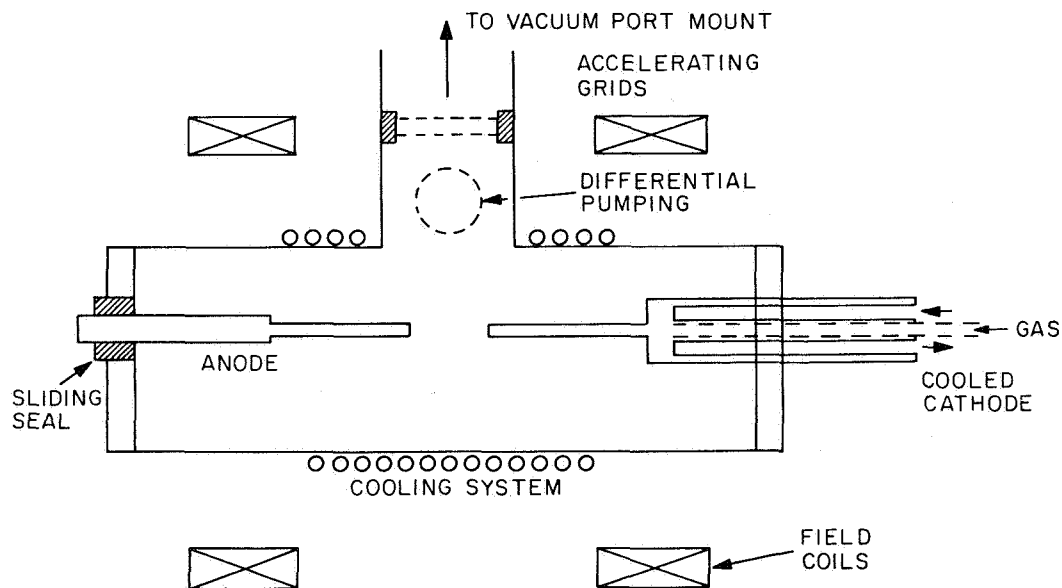


Figure 11—Adaptation of source for ionsphere simulation

REFERENCES

1. Massey, H. S. W., "Excitation and Ionization of Atoms by Electron Impact," Handbuch der Physik XXXVI, Berlin: Spinger-Verlag, 1956.
2. Craggs, J. D., and Massey, H. S. W., "The Collisions of Electrons with Molecules," Handbuch der Physik XXXVII, Berlin: Spinger-Verlag, 1959.
3. Fite, W. L., "The Measurement of Collisional Excitation and Ionization Cross Sections," Atomic and Molecular Processes, D. R. Bates, ed., New York: Academic Press, 1962.
4. Field, F. H., and Franklin, J. L., Electron Impact Phenomena and the Properties of Gaseous Ions, New York: Academic Press, 1957.
5. Mott, N. F., and Massey, H. S. W., The Theory of Atomic Collisions, Oxford: Oxford University Press, 1952.
6. Burke, P. G., and Smith, K., "The Low-Energy Scattering of Electrons and Positrons by Hydrogen Atoms," Rev. Mod. Phys. 34:458-502, 1962.
7. Burke, P. G., Schey, H. M., and Smith, K., "Collisions of Slow Electrons and Positrons with Atomic Hydrogen," Phys. Rev. 129:1258, 1963.
8. Ditchburn, D. W., Proc. Phys. Soc. (London) 75:461, 1960.
9. Baker, D. J., Bedo, D. E., and Tomboulion, D. H., "Continuous Photoelectric Absorption Cross Section of Helium," Phys. Rev. 124:1471, 1961.
10. Wainfan, N., Walker, W. C., and Weissler, G. L., "Photoionization Efficiencies and Cross Sections in O₂, N₂, CO₂, A, H₂O, H₂, and CH₄," Phys. Rev. 99:542, 1955.
11. Hooper, J. W., Harmer, D. S., Martin, D. W., and McDaniel, E. W., "Comparison of Electron and Proton Ionization Data with the Born Approximation Predictions," Phys. Rev. 125:2000, 1962.
12. McDaniel, E. W., Hooper, J. W., and Martin, D. W., "Proc. Fifth Int. Conf. on Ionization Phenomena in Gases," Amsterdam: North-Holland, I:60, 1962.
13. Smith, P. T., "The Ionization of Helium, Neon, and Argon by Electron Impact," Phys. Rev. 36:1293, 1930.
14. Tozer, B. A., and Craggs, J. D., J. Elect. and Control 8:103, 1960.
15. Robertson, H. S., "Moving Striations in Direct Current Glow Discharges," Phys. Rev. 105:368, 1957.
16. Cooper, A. W., "Experiments on the Origin of Moving Striations," J. Appl. Phys. 35:2878, 1964.
17. Lee, D. A., Beltzinger, P., and Garscadden, A., "Wave Nature of Moving Striations" J. Appl. Phys. 37:377, 1966.
18. Cabine, J. D., Gaseous Conductors, New York: McGraw-Hill Book Co., Inc., 1941.

19. Kesaev, I. G., Cathode Processes in the Mercury Arc, New York: Consultants Bureau, 1964.
20. Samerville, J. M., The Electric Arc, New York: John Wiley & Sons, Inc., 1959.
21. Boyle, W. S., Kisliuk, P., and Germer, L. H., "Electrical Breakdown in High Vacuum," J. Appl. Phys. 26:720, 1955.
22. Lander, J. J., and Germer, L. H., "The Bridge Erosion of Electrical Contacts," J. Appl. Phys. 19:910, 1948.
23. Boyle, W. S., and Kisliuk, P., "Departure from Paschen's Law of Breakdown in Gases," Phys. Rev. 97:255, 1955.
24. White, A. D., "New Hollow Cathode Glow Discharge," J. Appl. Phys. 30:711, 1959.
25. Sturges, D. G., and Oskam, H. J., "Studies of the Properties of the Hollow Cathode Glow Discharge in Helium and Neon," J. Appl. Phys. 35:2887, 1964.
26. von Engel, A., "Internal Radiation and Nature of Discharges," Appl. Sci. Res. 5:34, 1955.
27. Valle, G., Nuovo Cim. 7:174, 1950.
28. Barnett, C. F., Bell, P. A., Luce, J. S., Shipley, E. D., and Simon, A., "Proc. Second United Nations Conf. on Peaceful Uses of Atomic Energy," Geneva: United Nations, 31:298, 1958.
29. Luce, J. S., "Proc. Second United Nations Conf. on Peaceful Uses of Atomic Energy," Geneva: United Nations, 31:305, 1958.
30. Bohm, D., The Characteristics of Electrical Discharges in Magnetic Fields, A. Gurthrie and R. K. Waherling, eds., New York: McGraw-Hill Book Co., Inc., 1949.

APPENDIX A
GENERAL INFORMATION

In an effort to increase the reliability of satellites and satellite subsystems and to assess the expected performance of an experiment or to uncover an unexpected response of equipment to an ionized environment it is desirable to be able to simulate the lower and outer portions of the ionosphere in space environmental test chambers. The charged particle environment encountered by a spacecraft moving within the magnetosphere may be roughly divided into two groups: high-energy particles in the thousand- or million-electron-volt range, and low-energy particles of 10 electron volts or less. The latter group is of primary interest in this study. The data reproduced in Figures A1 and A2 give general information on charged particle and electron concentration profiles derived from a number of experimenters.

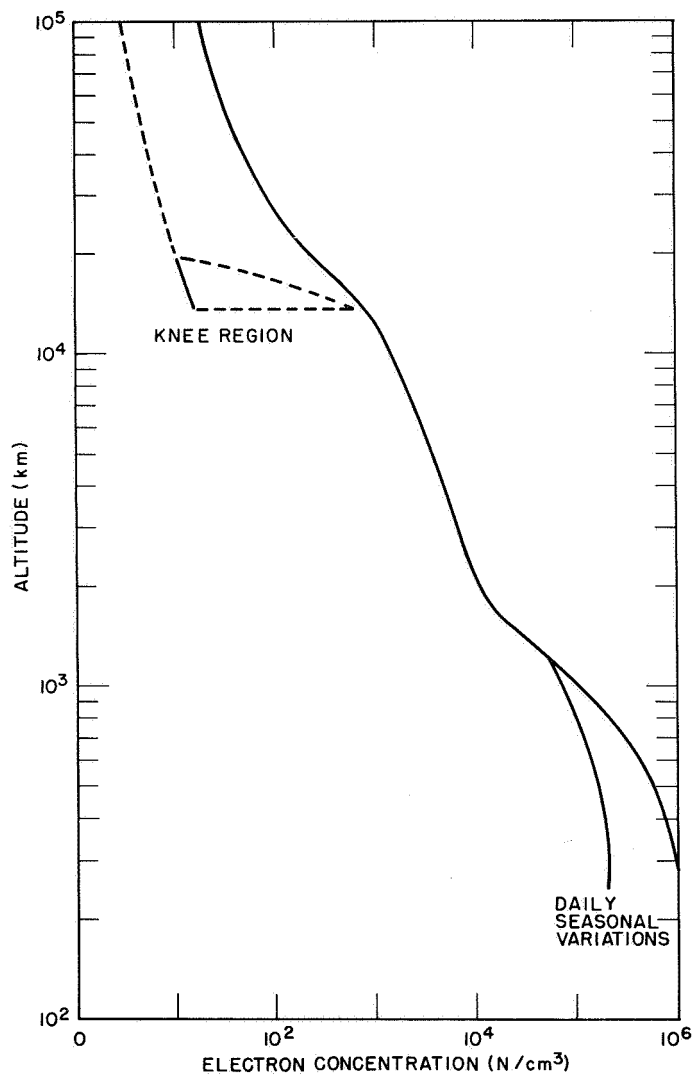


Figure A-1—Electron concentration profile
for the ionosphere

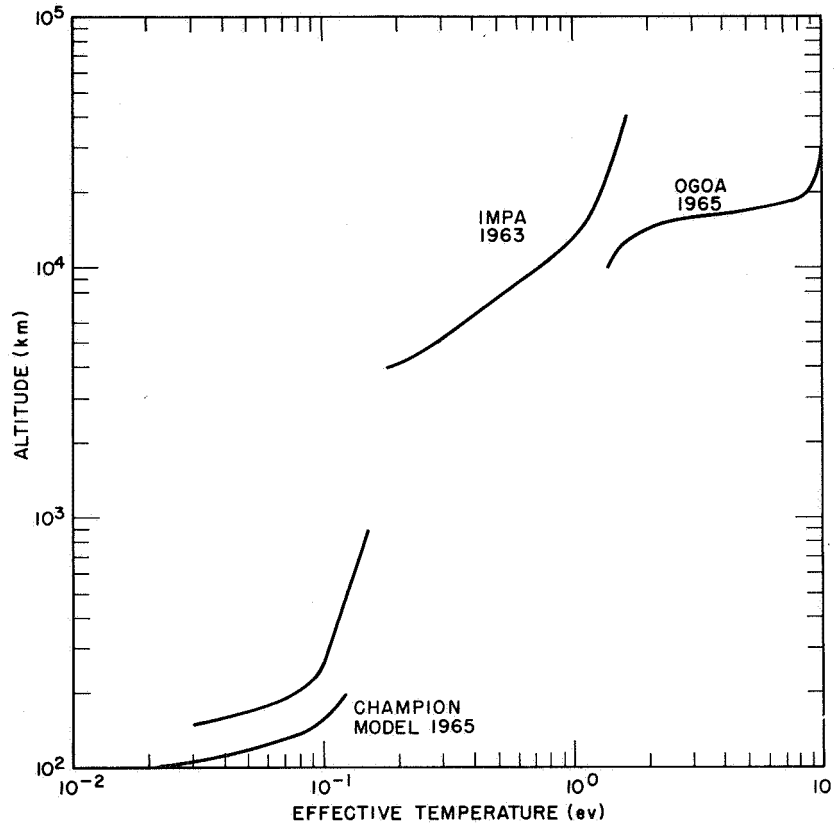


Figure A-2—Temperature of the ionosphere

INVESTIGATION AND DEVELOPMENT OF A FIELD EMISSION SOURCE FOR A QUADRUPOLE MASS SPECTROMETER

Paul O. Berrett* and T. D. Hargreaves**

ABSTRACT

The advantages of a non-fragmenting ion source for a mass spectrometer used for residual gas analysis in vacuum systems are discussed. Theory and applications of field ionization are reviewed and the particular requirements for a field ionization source for a quadrupole mass spectrometer determined. A source is designed which incorporates very fine Wollaston wire and a moderately high voltage supply to produce the high field intensities necessary for field ionization. Equations for the electric field in a grating-above-plane geometry are developed, and numerical solutions are obtained by computer and presented in graphical form. Techniques for handling and etching the very fine Wollaston wire are presented. A field-ion source built at Goddard is described and a test thereon is reported.

A BASIC NEED IN MASS SPECTROMETRY— A NON-FRAGMENTING IONIZATION SOURCE

The mass spectrometer is used as a basic analysis tool in determining the composition of the residual gas in high-vacuum systems. Ideally it is desired, as always, that the act of measuring shall not appreciably disturb the quantity to be measured. In gas analysis with a mass spectrometer, conventional ionization sources often produce an ion molecular beam having molecular species not found in the ambient gas. A conventional ion source produces ions by electron impact. Even at the nominally used electron-gun voltages of 70 to 100 volts, many of the electron-molecule impacts break up the molecule into fragment parts. This is especially true of complex hydrocarbon gas molecules. The result is a spectrum cluttered with spectral peaks not belonging to the unmolested gas. It is current practice to use a complicated numerical analysis to erase the unwanted fragment contributions from the spectrum and arrive at an approximate ambient gas composition. The procedure is made tenable only by the digital computer.

An obviously desirable step toward directly obtaining the spectrum of the ambient gas alone is to ionize the gas in a way which will not cause fragmentation. Fortunately such ionization mechanisms do exist in nature. One such phenomenon is an electric-field ionization enhanced by a surface effect. Because the process resembles electron emission in reverse, it is commonly referred to as "field emission," although strictly speaking "field ionization" is more correct.***

Field emission-type ionization sources have been designed for ion microscopes (References 2 and 3) and for mass spectrometers of the magnetic-deflection type (Reference 4). Several mass-spectrometer manufacturers allude to field emission sources as alternative sources of electron impact, but they have no developed source of this type ready for delivery. Only Beckey's work (Reference 4) describes the actual operation of a line-type field ionization source. In a different type of mass spectrometer -- a quadrupole mass spectrometer -- a pencil beam of molecules is desired. No successful source of the field

*Brigham Young University, Provo, Utah;

**Ohio State University, Columbus, Ohio.

***A second kind of ionization mechanism not conducive to fragmentation is photoionization. See Reference 1.

emission variety built for a quadrupole mass spectrometer seems to be commercially available though Stanford Research Institute has built an experimental source of this kind (Reference 5).

QUADRUPOLE MASS SPECTROMETRY

A rudimentary review of the theory and operation of a quadrupole mass spectrometer will allow a better perspective of the placement of the ionization source in the apparatus. Also, a review will provide reasons for the particular design criteria for a field-emission ionization source for this kind of mass spectrometer.

As opposed to a magnetic-deflection-type mass spectrometer which distinguishes between ions of different charge-to-mass ratios by the different radii of curvature of their flight paths in a magnetic field, the quadrupole mass spectrometer is an electric-field filter with a charge-to-mass "bandpass" determined by the geometry and the voltages applied to the electrodes. Geometrically it consists of four parallel rods. The original theory of the quadrupole operation is based on the rods being hyperbolic in cross section (Figure 1), although most quadrupole spectrometers have circular rods. The electric fields in the region of interest are essentially the same as if the rods were of hyperbolic cross section. When the rods are at potentials as shown in Figure 1, the potential in the x-y plane is

$$\Phi(x, y) = \frac{(U + v_0 \cos \omega t)(x^2 - y^2)}{r_0^2} \quad (1)$$

where U is a dc voltage and v_0 the peak value of a superimposed ac voltage at frequency ω .

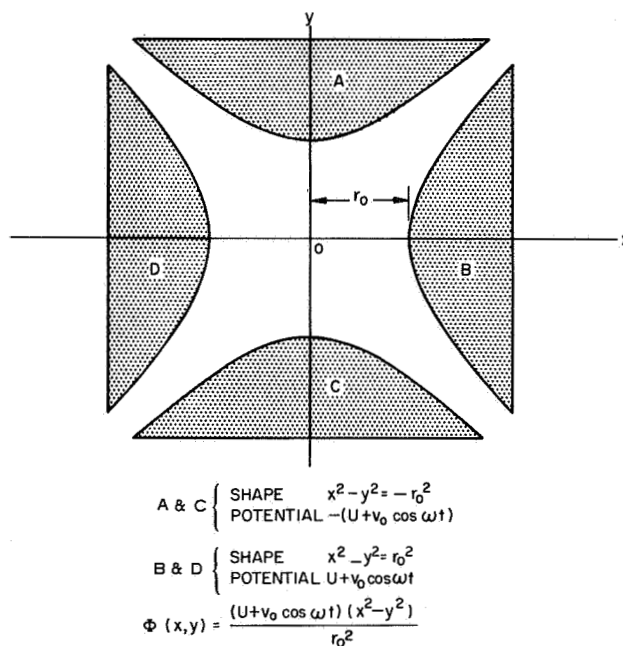


Figure 1—Cross section of quadrupole mass spectrometer rods.

An ion source at one end of the rods introduces ions into the region between the rods. At the opposite end is a detector, usually composed of an electron multiplier tube and an electrometer circuit.

The equations of motion for a singly ionized ion of mass m and charge e are found by writing the force equations for the ions in the x , y , and z directions:

$$m\ddot{x} + eE_x = 0 \quad (2)$$

$$m\ddot{y} + eE_y = 0 \quad (3)$$

$$m\ddot{z} + eE_z = 0 \quad (4)$$

where $\vec{E} = E_x \hat{x} + E_y \hat{y} + E_z \hat{z} = -\nabla\Phi$ (5)

Because $\Phi \neq \Phi(z)$, $E_z = 0$ and \dot{z} is a constant. The ions retain any z velocity they have at entrance throughout their travel between the rods.

Equations 2 and 3, for the functional forms E_x and E_y are found to have, are Mathieu equations. Classical solutions are difficult to interpret, but numerical solutions on a digital computer have yielded the necessary combinations of m , U , and v_0 for stable oscillations in the transverse (x and y) directions. In reality, ions whose masses are not unsuited for stable transverse motion may pass through the rods provided that entrance conditions are right. Hence a finite resolution results. Passage occurs only for masses near a value that gives both x and y stability.

The stability criteria are conveniently displayed in Figure 2, having coordinate variables of

$$A = \frac{8eU}{mr_0^2 \omega^2} \quad (6)$$

and

$$Q = \frac{4ev_0}{mr_0^2 \omega^2} \quad (7)$$

The A and Q quantities arise from the particular arrangements of parameters in Equations 2 and 3.

The loci of constant A/Q ratio are straight lines through the origin, as in the example line in Figure 2. It is easily seen that constant A/Q is equivalent to constant U/v_0 . This is the cue to the usual technique of sweeping the spectrum analyzer. The mass "bandwidth," $m_1 - m_2$, is determined by the value of A/Q (or equivalently U/v_0) chosen. As the dc and ac voltages are linearly swept together in an arrangement that keeps U/v_0 constant, ion passage is allowed whenever operation is in the stable region and entrance conditions are right. Resolution theoretically becomes infinite as A/Q is adjusted to the value $0.237/0.706 = 0.336$. Sweeping can be effected by varying ω , or (more usually) scale ranges are determined by specific ω values. In each range sweeping is effected by changing U and v_0 together in a fixed ratio.

As is inferred above, the stability diagram assumes ideal entrance conditions. The resolution predicted by the diagram is worsened by entry conditions that allow ions to

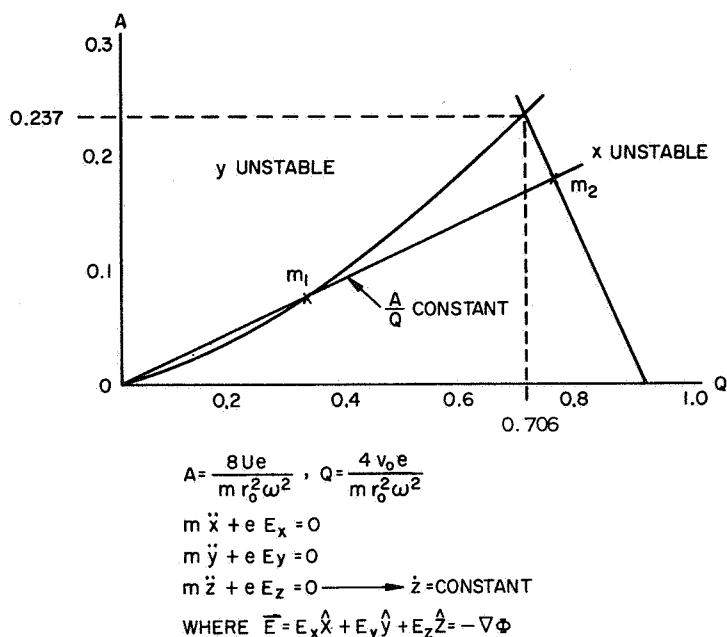


Figure 2—Stability diagram for quadrupole analyzer.

traverse the rod length which would not do so if they had no initial x or y velocity and/or off-center initial displacement. To realize as nearly as possible the ultimate resolution that the stability diagram would allow, the source should ideally supply an ion beam which is

1. of thin pencil shape and axially directed and centered in the quadrupole region,
2. "monochromatic" in ion velocity,
3. free of any magnetic fields or non-axial electric fields that may penetrate the quadrupole region.

THEORY OF FIELD IONIZATION

Field emission of electrons from metallic surfaces is a well-known process that has been used in a number of engineering applications. By definition, the direction of an electric field is that in which a positive charge is forced. When an electric field of the order of 0.3 to 0.6 volts/Angstrom is directed at a metallic surface, electrons are pulled out of the metal and accelerated away in the electric field. The threshold level of electric field and the rate of electron extraction as a function of field strength are primarily set by the work function of the metal at low temperatures, with temperature effects also playing a dominant role at elevated temperatures.

Reversing the electric field creates a situation favorable to drawing any available electrons from outside the metal into the metal. With gas molecules close to the metal surface, electrons in the potential wells of the gas atoms can be made to tunnel through the potential wall between the potential well of the atom and the Fermi sea of electrons in the metal. Fields on the order of 2 to 5 volts/Angstrom are required. Except at high temperatures, there is little temperature dependence. The mechanism can be explained with the aid of Figure 3.

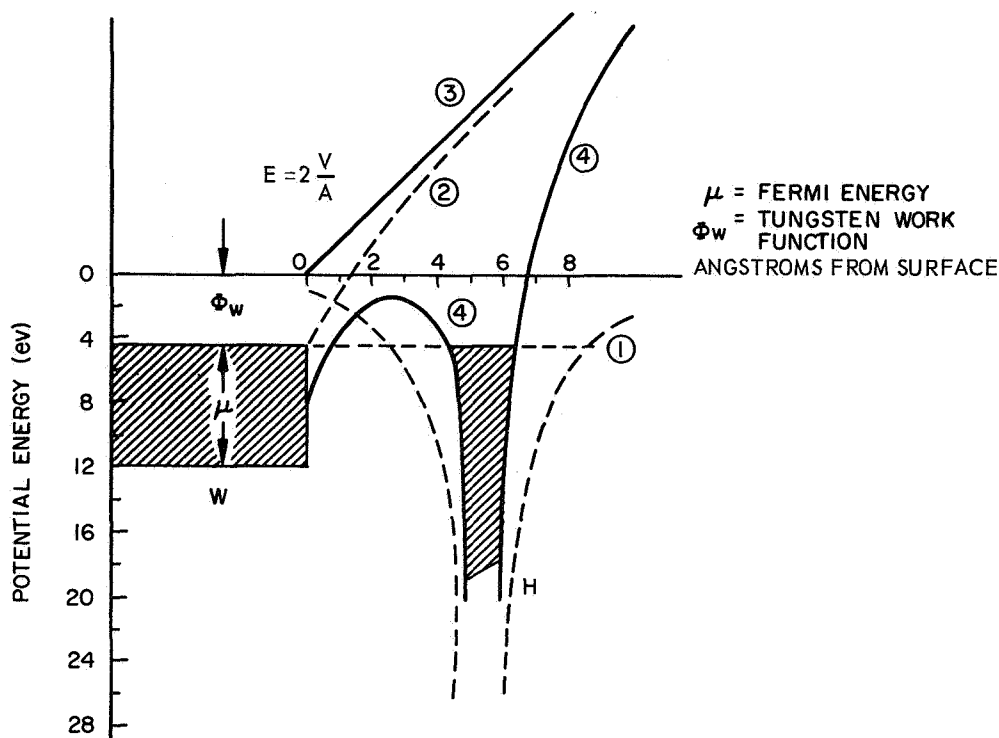


Figure 3—Potential-energy diagram for a Hydrogen Atom 5.5 \AA from a tungsten surface.

From the standpoint of quantum mechanical wavelets, it is probable that the 1S electrons of the hydrogen atom may penetrate the potential barrier into the Fermi sea of electrons. It is remotely probable that a 2S electron will tunnel into the metal. Essentially all ions formed by this process are singly ionized.

In Figure 3, curve 1 represents the unperturbed potential well of the atom. Curve 2 represents the superposition of the potential due to the image of the electron tunneling in the metal and the applied field (curve 3). Curve 4 represents the resultant potential field experienced by the electron.

Field ionization near the metal surface is a less violent process than its counterpart, electron-impact ionization. Electron impact may be likened to hitting an object, already under internal stress, with a projectile which imparts a certain range of energy to the object. Dependent on the initial stresses and the amount of energy transfer, the objects may remain intact, split in two, or split into several fragments. On the other hand, field ionization is analogous to a leakage (externally caused) from a pressure vessel that leaves the inside conditions in the vessel undisturbed.

METHODS OF ACCOMPLISHING FIELD IONIZATION

The necessity of realizing the high field intensities (10^7 to 10^8 volts/cm) required to field-ionize a gas with a reasonably low voltage source is the chief engineering challenge in designing a field ionization source. Apart from brute-force expedients like close spacing or voltage increase, the only way to obtain high voltage gradients is to select an optimum shape for the electrodes. Melmed and Muller (Reference 6) originated the use of a sharp needle point as such an ionization source for an ion microscope. This technique is a means to direct study of the atomic structure on the needle tip and has given much

insight into the atomic structure of various metals. The gas ions are not formed uniformly over the surface of the needle tip; rather, the rate is determined by the arrangements of the atoms at the tip. This atomic profile is projected onto the cathode surface along spherical radials (Figure 4). Magnifications of the order of a million have been achieved. Originally the gas used was helium, but recently neon has been found to have particular advantages (Reference 7).

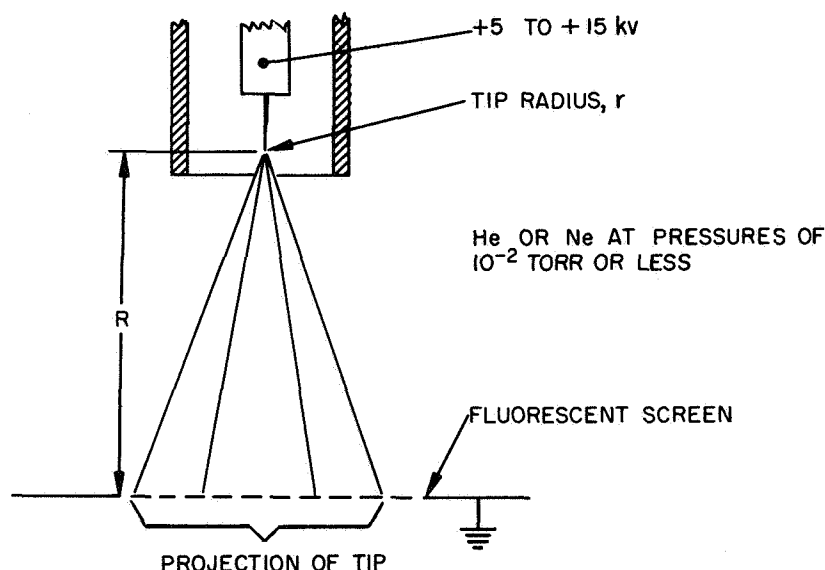


Figure 4—Field ion microscope.

As an ion source for a mass spectrometer the needle tip has the follow drawbacks:

1. The total ion current from a tip of say 1000 \AA radius is only of the order of 10^{-8} amps at 10^{-3} Torr. Only a small fraction of this current can be directed and focused into the spectrometer. Thus, especially at lower pressures, a very sensitive and/or high-gain detection system is required.
2. Drastic surface changes occur at the tip causing erratic amplitude changes of ion current and producing a "noisy" spectrum.
3. Raising the potential of the tip to increase the emission moves the ionization mechanism into a realm of operation where fragmentation occurs.

Beckey has shown that very thin wires may be used as source regions for field ionization and may overcome some of the restraints of the tip emitter. Most ionization occurs in a very thin range of radius, ΔR , and the relation of wire to tip emission is essentially one of effective area ratios. In theory, a 5-mm-long wire of 2.5μ diameter should produce about 100 times the ionization of a needle tip of radius 1000 \AA operating with the same field intensity at the surface. This 100 times enhancement is not actually realized because of wire surface irregularities. Ionization is concentrated at the protrusions; the effective area is hence reduced below what it would be if the wire were smooth. The average ratio of protrusion radius to nominal wire radius, usually denoted as β in the literature, may vary from a few score to under 10, depending on the wire-forming processes. Nevertheless, wires have an advantage over tips, because of their relatively copious ionization

capability and the fact that small-scale time fluctuations are integrated out over the larger surface.

Geometrically the best source configuration for maximum total ionization is cylindrical; however, this arrangement is not compatible with the need for a pencil ion beam for the quadrupole mass spectrometer. A wire-grating-above-sheet geometry is chosen but with the total wire-grating dimensions small so as to appear as a "button" source of ions. Figure 5 shows the design. The wire is made by the Wollaston process, which yields wires of extremely small diameter. A wire of precious metal is inserted into a heavy-wall small-bore cylinder of an appropriate ductile metal. The composite wire may be drawn out so as to produce a central core as thin as 2×10^{-6} inches (500 Å, approx.) in diameter. The ion source design uses 2.0μ platinum core Wollaston wires. The outer sheath is silver with a diameter near 100μ . In the fabrication of the grating the silver is dissolved, leaving the thin platinum wire.

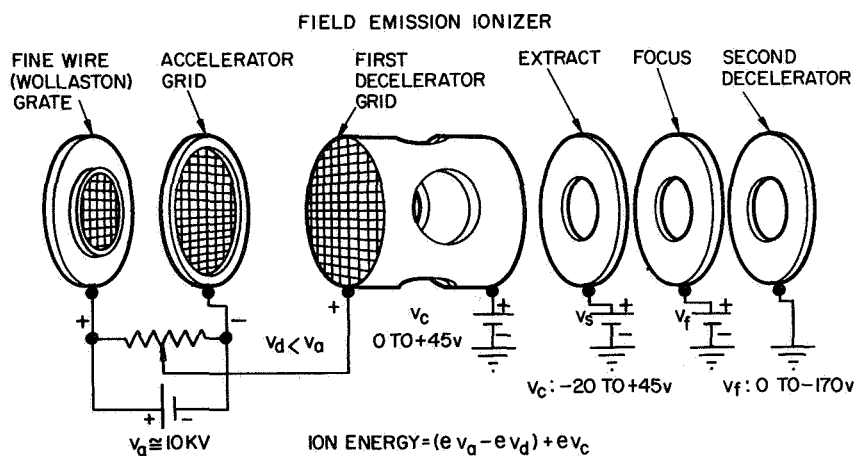


Figure 5—Schematic of field ionization source.

When trying to obtain the right conditions for a given event, the investigator inspects the role of all the physical parameters over which he has control. Incidentally, the possible advantage of materials with low work function has not been overlooked. From the argument below, it seems that the field ionizing rate is not significantly affected by the wire-material work function.

Visualize with the aid of Figure 3 a 1S electron within the potential well of the hydrogen atom. Unperturbed, it would be at energy ϕ_i (ionization potential) below the zero energy level representing an electron infinitely removed from the atom. Now suppose that the atom is near the metallic surface as pictured, and that an applied uniform field of E volts/Angstrom outward (to the right) is present. Relative to an electron at the surface, the electron in the atom has a potential energy component of $E \times$ electron volts added to it by virtue of its displacement by x Angstroms in the electric field. Because there are no empty states from 0 to ϕ electron volts, there results a minimum distance of approach for which tunneling can occur. Expressed as an inequality,

$$\phi_i = E X \leq \phi$$

for tunneling to occur. The critical distance, or distance of minimum approach, is

$$X_c = \frac{\phi_i - \phi^*}{E}$$

Work function thus sets a minimum distance for ionization to occur. Since even a 2μ - diameter wire is 20,000 Angstroms in diameter, the planar model upon which the above derivation is based is still accurately approximated. There is no significant difference in effective areas of ionization when the radius changes by at most a few Angstroms in 10,000. Finally, the resultant potential profile is in no way affected by the work function. Rate of ionization being determined by the potential barrier height and shape and by the area, the work function plays no significant role.

CALCULATION OF FIELDS IN A GRATING-SCREEN GEOMETRY

Consider first a line charge parallel to a conducting plane, as in Figure 6.

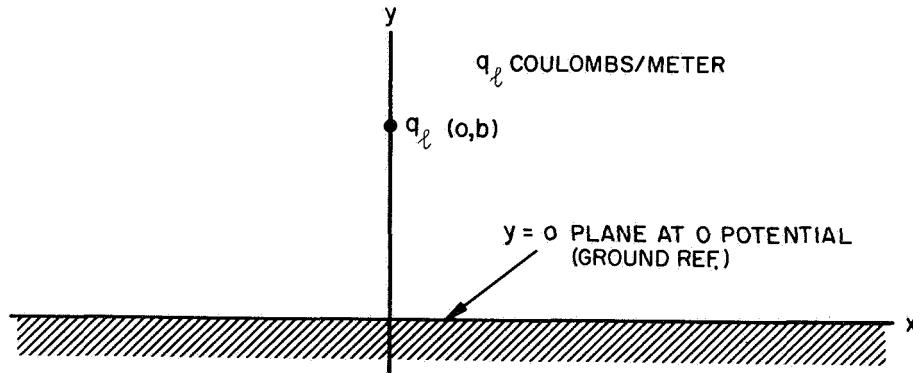


Figure 6—Line charge parallel to a conducting plane.

The potential above the ground plane is readily found as a superposition of the potential due to the line charge, q_l , and its image.

$$\Phi(x, y) = \frac{q_l}{4\pi\epsilon_0} \ln \left[\frac{x^2 + (y+b)^2}{x^2 + (y-b)^2} \right] \quad (8)$$

The locus of constant potential Φ_0 is the curve given by

$$\frac{x^2 + (y+b)^2}{x^2 - (y-b)^2} = \exp \left(\frac{4\pi\epsilon_0\Phi_0}{q_l} \right) = K. \quad (9)$$

Rearranging this gives

$$x^2 + \left(y - b \frac{K+1}{K-1} \right)^2 = b^2 \left[\left(\frac{K+1}{K-1} \right)^2 - 1 \right]. \quad (10)$$

*Gomer, (Reference 8) has another term in the equation for x_c which is due to the potential energy of the resulting ion's attraction to its image. However, this term is quite negligible when compared with nominal values of ϕ_i and ϕ .

The locus is a circle with center at $(0, (K + 1/K - 1) b)$ and radius

$$b \sqrt{\left(\frac{K+1}{K-1}\right)^2 - 1}.$$

For convenience define

$$d = \frac{K+1}{K-1} b \quad (11)$$

and

$$a = b \sqrt{\left(\frac{K+1}{K-1}\right)^2 - 1}, \quad (12)$$

which is compatible with Figure 7 where a is interpreted as the radius of a wire at potential ϕ_0 , distance d above a zero potential plane.

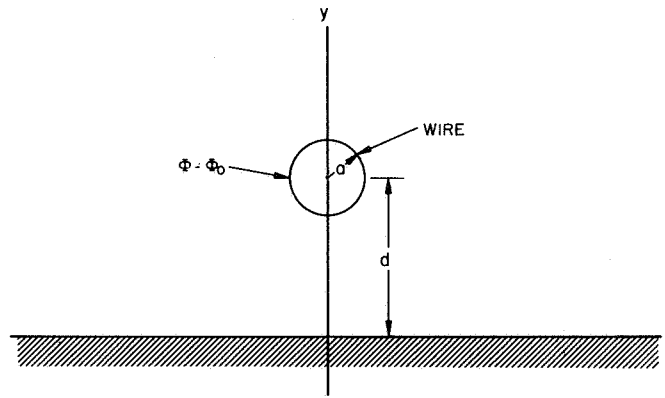


Figure 7—Wire above a conducting plane.

If ϕ_0 , a , and d are specified,

$$q_l = \frac{4\pi\epsilon_0\phi_0}{\ln K} \quad (13)$$

$$b = \frac{K-1}{K+1} d = \frac{a}{\sqrt{\left(\frac{K-1}{K+1}\right)^2 - 1}} \quad (14)$$

Note that K is determined by the ratio a/d .

(15)

The electric field intensity is now found in terms of the potential of the wire, ϕ_0 , relative to the plane, the wire radius, a , and its distance d above the plane.

$$\vec{E}(x, y) = \frac{4Ab}{[x^2 + (y+b)^2][x^2 + (y-b)^2]} \{2xy\hat{x} - (x^2 - y^2 + b^2)\hat{y}\}, \quad (16)$$

where

$$A = \frac{\Phi_0}{\ln K} ,$$

$$K = \frac{1 + \sqrt{1 - (a/d)^2}}{1 - \sqrt{1 - (a/d)^2}} ,$$

$$b = \frac{K - 1}{K + 1} d .$$

Maximum electric-field intensity occurs at $(0, d-a)$. If an enhancement factor is defined as the ratio of E_{max} to the electric field that would exist between parallel planes separated d meters in space and Φ_0 volts in potential - i.e. $\vec{E}_{||} = -\frac{\Phi_0}{d} \hat{y}$ then

$$\frac{E_{max}}{E_{||}} = \frac{4 \frac{K - 1}{K + 1} d^2}{(\ln K) \left[\left(\frac{K - 1}{K + 1} d \right)^2 - (d - a)^2 \right]} \quad (17)$$

In Figure 8 the enhancement factor is plotted as a function of a/d .

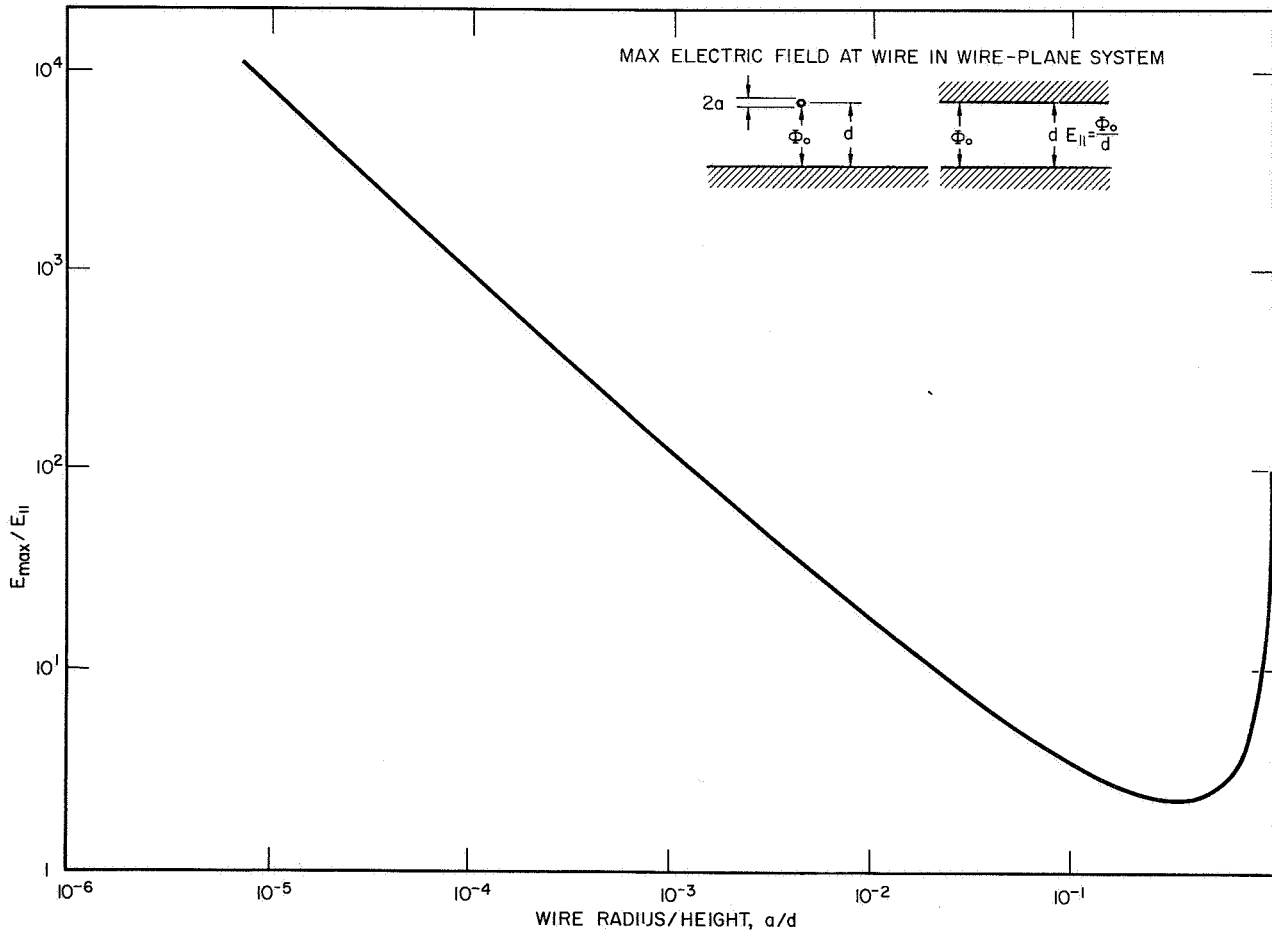


Figure 8—Enhancement factor for wire over plane.

When a wire grating is placed above an equipotential plane, the field near each wire is modified by the presence of the other wires. A sufficiently accurate calculation is made possible by conformal transformation. The solution for the case of a planar triode tube can be modified and adapted to the problem at hand. A z -plane configuration of two line charges of q_c at $(0, 0)$ and q_g at $(1, 0)$ transforms by the equation

$$w = \mu + j v = \frac{a}{2\pi} \ln z \quad (18)$$

to the planar triode configuration in the w plane of Figure 9.

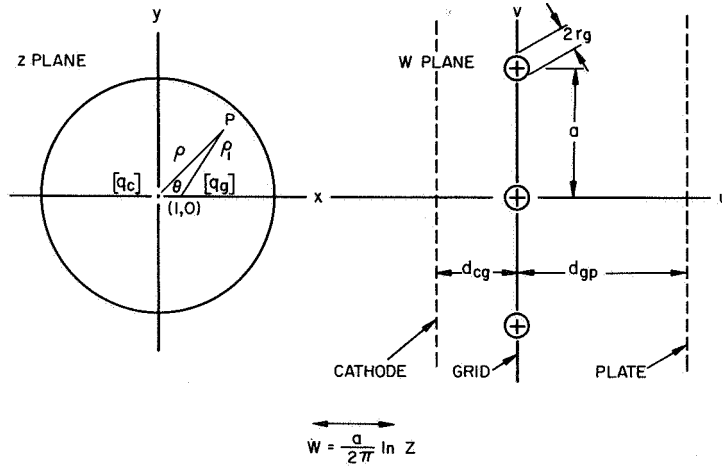


Figure 9—Schematic defining parameters in conformal transformation to grating-plane structure.

Potential in the w plane is found (subject to the conditions $d_{gp} \geq a$, $d_{cg} \geq a$, $r_g \leq \frac{a}{20}$, and cathode at zero reference potential) to be

$$v_w = -\frac{q_g}{4\pi\epsilon_0} \ln \left(e^{\frac{4\pi\mu}{a}} + 1 - 2e^{\frac{2\pi\mu}{a}} \cos \frac{2\pi v}{a} \right) - \frac{q_c \mu}{\epsilon_0 a} + c \quad (19)$$

where

$$q_c = -\frac{\epsilon_0 a (v_p + \mu v_g)}{(d_{gp} + d_{cg} + \mu d_{cg})} \quad (20)$$

$$q_g = \frac{\epsilon_0 a \mu [(d_{gp} + d_{cg}) v_g - d_{cg} v_p]}{d_{gp} (d_{gp} + d_{cg} + \mu d_{cg})} \quad (21)$$

$$\mu = \frac{-2\pi d_{gp}}{a \ln \left(2 \sin \frac{\pi r_g}{a} \right)} \quad (22)$$

$$c = -\frac{d_{cg} q_c}{a \epsilon_0} \quad (23)$$

If

$$-\frac{q_g}{4\pi \epsilon_0} = A,$$

$$\frac{2\pi}{a} = b,$$

$$-\frac{q_c}{\epsilon_0 a} = f,$$

$$\vec{E}_w = -\nabla v_w = -\left[\frac{\partial v_w}{\partial u} \hat{u} + \frac{\partial v_w}{\partial v} \hat{v} \right], \quad (24)$$

where

$$\frac{\partial v_w}{\partial u} = A \left\{ \frac{1}{e^{2bu} + 1 - 2e^{bu} \cos bv} \cdot (2be^{2bu} - 2be^{bu} \cos bv) \right\} + f \quad (25)$$

and

$$\frac{\partial v_w}{\partial v} = A \left\{ \frac{1}{e^{2bu} + 1 - 2e^{bu} \cos bv} \cdot (2be^{bu} \sin bv) \right\}. \quad (26)$$

The situation of a grating and plane will be duplicated by letting $v_c = 0$ (ref.), $v_g = v_0$, $d_{gp} \gg a$, $v_p = 0$. A computer solution (see Appendix) has provided the data plotted in Figures 10 and 11 showing the effects of the several geometric parameters. Figure 12 gives the field at the surface of the inner conductor of a coaxial conductor system. By comparison it is seen that the cylindrical geometry is much better for producing strong fields; however, a cylindrical configuration is not conducive to obtaining a strong ion beam in a single (quadrupole axis) direction, as the field is radially directed.

The computer program can evaluate the electric field anywhere in the w plane. It is interesting and significant that the field at the surface of a small diameter wire, $r_g \ll a$ and $r_g \ll d_{cg}$, varies very little around the wire circumference. As the supply voltage is increased, all parts of the wire surface reach the ionizing condition at once since ionization takes place within a few Angstroms of the surface, i.e., essentially "at" the surface. This is fortunate in terms of total ionization but does not necessarily mean better sensitivity. The ions, once formed, are accelerated radially from the wire and only a small fraction can be focused into the quadrupole region.

Figure 13 schematically shows the salient electrical design features of a field ionization source. The distances between the thin wire grating and the acceleration grid and between the accelerating and decelerating grids are adjustable by changing spacers. To bring the ions within an energy range where they are easily focused requires a

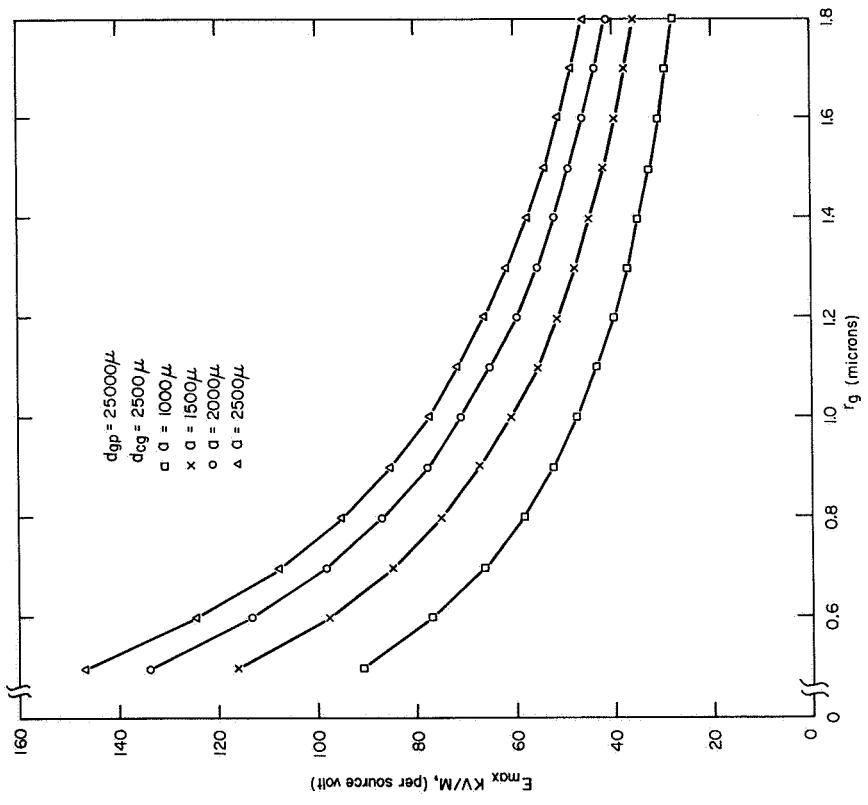


Figure 10—Field-enhancement curves — grating above equipotential plane.

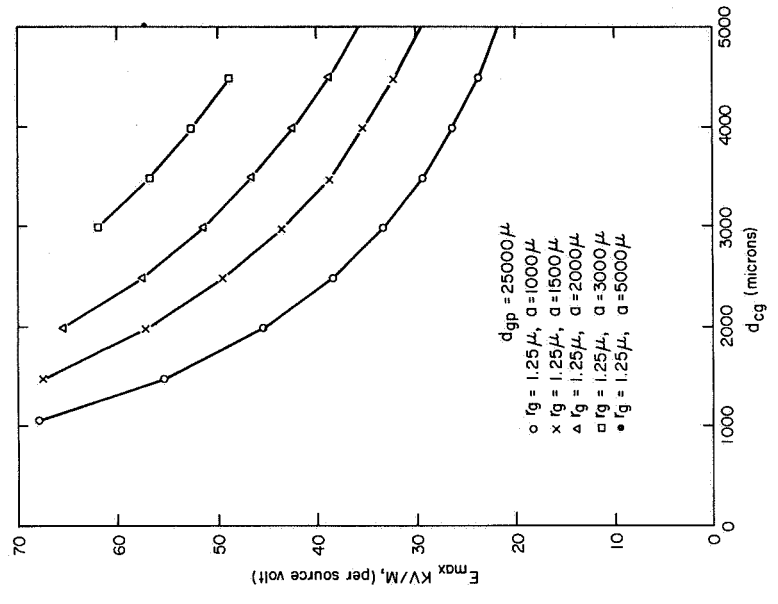


Figure 11—Field-enhancement curves — grating above equipotential plane.

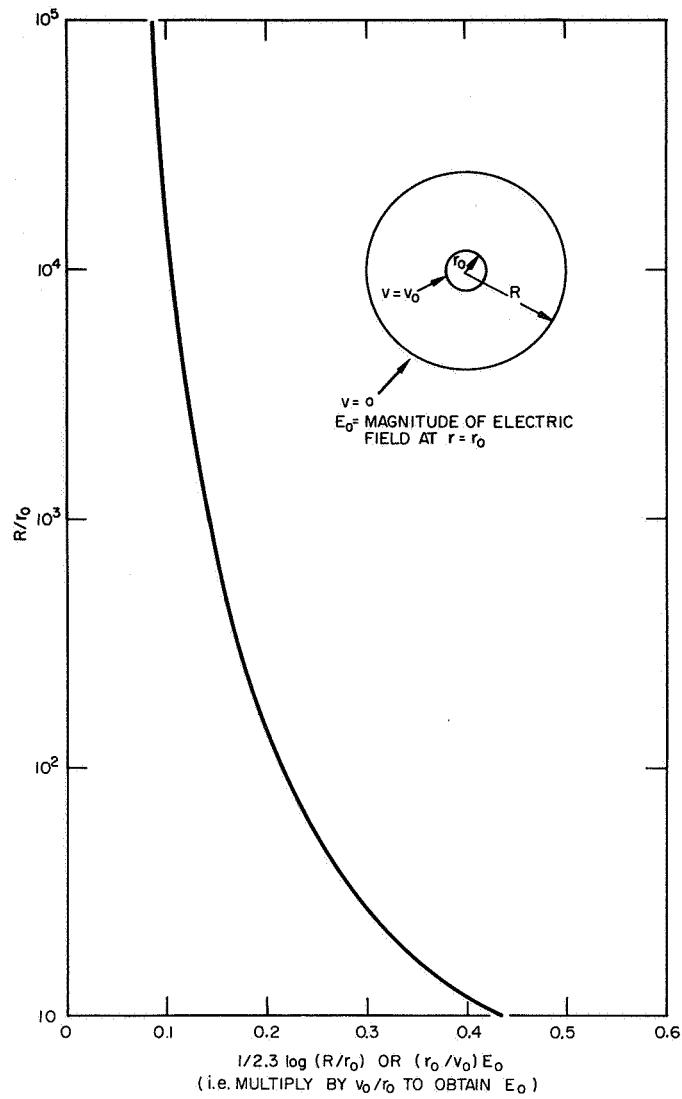


Figure 12—Electric field at inner conductor of a coaxial system.

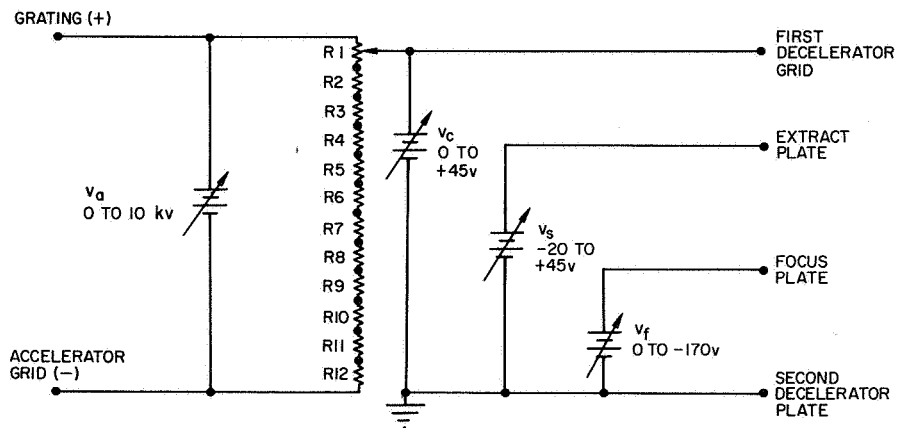


Figure 13—Electrical connections to ion source.

decelerating field between the accelerating and decelerating grids. Ions formed near the Wollaston wires are accelerated through the accelerator grid, at which plane they have an energy near v_0 electron volts. By the time they arrive at the focusing discs they are decelerated to about 50 to 70 volts; from here they exit at about the same energy range and enter the quadrupole. According to the analysis and computer results, a 10-kv supply should yield fields near 8×10^6 v/cm at the Wollaston wires. If the enhancement factor is near 10 there should be ionization; otherwise a higher voltage supply will be required. Needless to say, the supply should be stable and very free of ripple.

DESIGN AND CONSTRUCTION OF THE FIELD IONIZER

Two guiding principles were followed in designing a field ionization source to test the theory set forth above. First, the instrument must be able to achieve the required field intensities of $10^7 - 10^8$ v/cm and produce an ion beam compatible with the entrance conditions of the quadrupole mass spectrometer. Second, the usable parts of the existing electron-bombardment-type source (basically the ion-optical section) should be changed as little as possible; thus introducing fewer variables to analyze should problems occur. The short time available for the project dictated this second principle and its corollary: use readily available materials and processes.

Two basic designs were selected for the tests; each used the thin-wire, high-potential systems to achieve the necessary field intensities; and each used a deceleration system to slow down the high-energy ions before they entered the focusing regions. The differences occurred in the methods of mounting and etching the Wollaston wires—one being somewhat simpler and faster than the other. The most promising design consisted of a platinum ring of 1/4-inch inside diameter with a smooth, flat top surface. The unetched Wollaston wires were ultrasonically welded to the top of the ring, parallel to each other and spaced to produce optimum conditions around each wire. Computer calculations indicated that a spacing of about 1.5 mm. (0.059 in.) should produce the best field intensities compatible with the other design features. The ring was of platinum to compensate for thermal expansion of the fine wire during vacuum bakeout. It was loosely fitted into a Pyrex support base, 1-inch outside diameter by 3/16-inch thick. This also served to insulate the other electrical inputs from each other. The ring was held in place by two stainless-steel clips, which also served as electrical contacts. The cathode, or acceleration grid, was thick stainless steel, 1-inch outer diameter, 1/2-inch inner diameter, 1/16-inch thick supporting seven 10-mil parallel wires on the bottom. Four glass spacers supported the acceleration grid so that it was 0.1 inch above the Wollaston wires and parallel to the plane in which they lay. It was intended that this distance be large enough to prevent arcing but small enough to permit the use of reasonable potentials. This whole assembly fitted in the position of and replaced the thermal-emission portion of an existing electron-bombardment source from an Electronic Associates, Inc. (E.A.I.) Quadrupole Mass Spectrometer (see Figures 14 and 15). The existing source used a fine-mesh screen to accelerate electrons from the filament, and a cylindrical Faraday Cup as an ionizing chamber (see Figure 16). This structure was retained and used as the deceleration grid (anode) to slow the high-energy ions produced in the ionizer and acceleration subsystems (compare Figures 5 and 16). The remainder of the original source was retained, except for lengthening the electrical connection-and-support studs.

When it became apparent that the welding and etching of the Wollaston wires on the platinum ring might take too much time, a simpler design was initiated. This consisted of a stainless steel ring, 1/16-inch thick, to fit on top of the glass base. Around a 1/4-inch-diameter hole in the center, four 1/32-inch wide gold ribbons were welded on coplanar perpendicular axes, such that about 1/16 inch of each protruded past the inside lip. These

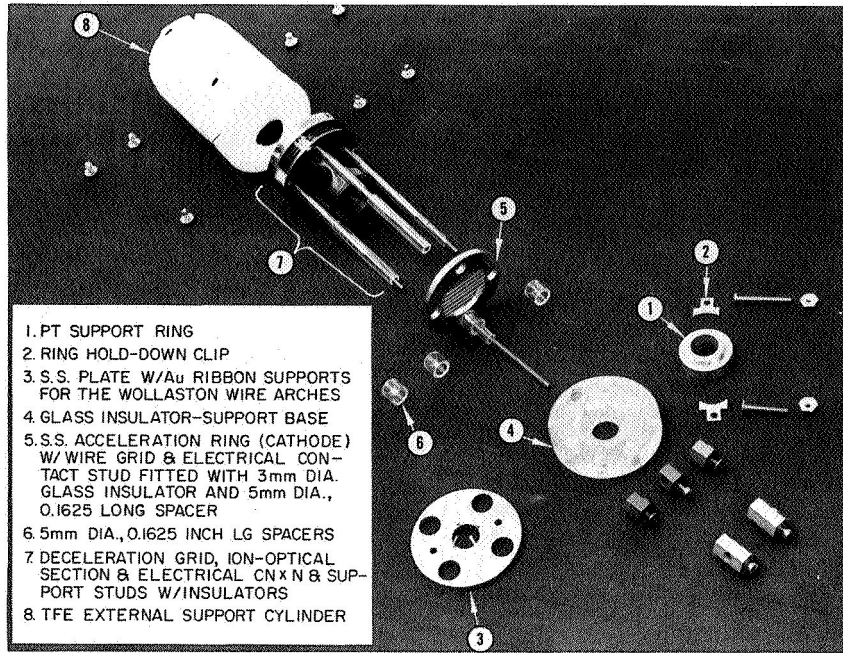


Figure 14—Working parts of field ionization source. 1. Pt. support ring; 2. Ring hold-down clip; 3. S. S. plate w/Au ribbon supports for the Wollaston wire arches; 4. Glass insulator-support base; 5. S. S. acceleration ring (cathode) w/wire grid electrical contact stud fitted with 3mm dia. glass insulator and 5mm dia., 0.1625" long spacer; 6. 5mm dia., 0.1625" long spacers; 7. Deceleration grid, ion-optical section and electrical connection and support studs w/insulators; 8. TFE external support cylinder.

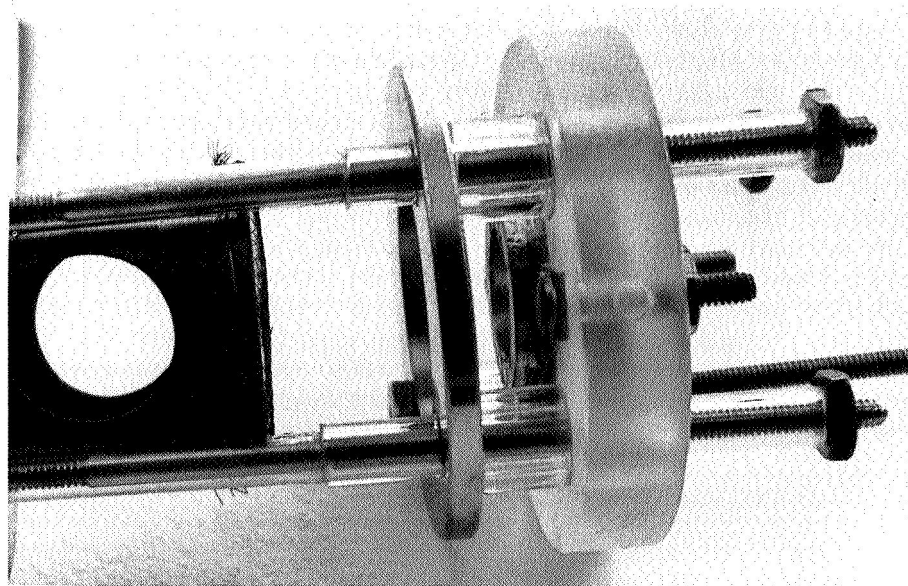


Figure 15—Field ionization source, ionization and acceleration section, platinum-ring support system.

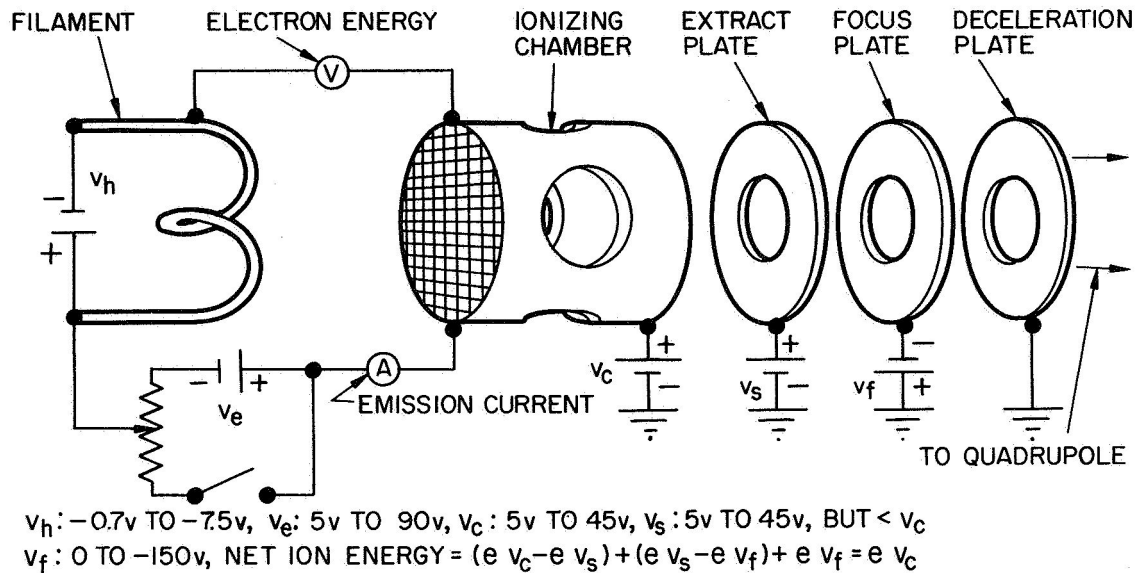


Figure 16—Electron bombardment ionizer.

free ends were bent upwards; short pieces of unetched Wollaston wire were welded to these to form two crossed arches, one slightly below the other so that they did not quite touch in the center. This was to permit just a small section of each wire at the center of each arch to be etched by careful dipping into nitric acid solution, removing the silver. Placed in the ionizer and with the ionizing potential applied, the thin wires would be pulled to a sharp "V" and produce field ionization. Additional spacers had to be added to raise the acceleration grid to the proper distance above the wires in the ionizer, but no other changes were necessary. (See Figure 17.)

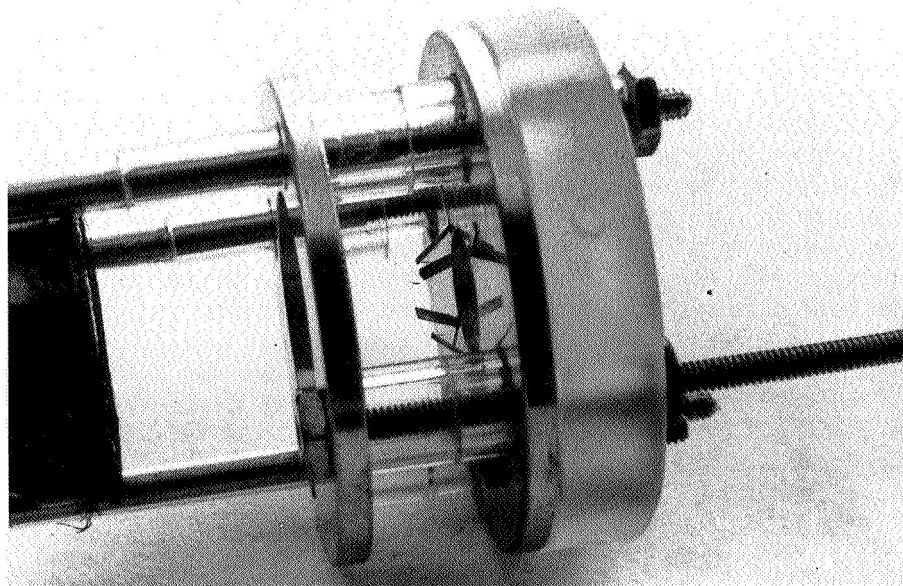


Figure 17—Field ionization source, ionization and acceleration section, gold-ribbon support system.

The most difficult part of fabricating the ion source was etching the silver off the Wollaston wire so as to leave the platinum core without dissolving the welds that held them to the support structure. Finally, a 1-molar KCN solution with a 3-volt potential proved to work best on the ring-wire combination. The wires formed the anode and, with the welds protected by Glyptol, the silver was removed quite readily. The cyanide did attack the Glyptol, but so slowly that the etching was finished long before the welds were exposed. The ring was then placed in alcohol to rinse off the cyanide solution, and the operation was complete. Alcohol was used instead of water because the surface tension of water was sufficient to break the wire as the assembly was dipped in and pulled out. Rough calculations show that the etched wires cannot withstand a tensile force greater than 10^{-3} pound. The ribbon-support system was far easier to etch than the ring. The mounted wires were carefully dipped into a 40-percent solution of nitric acid wetting just the apices of the arches. When the silver was etched away, the assembly was rinsed in water. Apparently the unetched portion of the wire could support the force exerted by the surface tension sufficiently to prevent the thin sections from breaking.

TEST AND RESULTS

The ion source was tested in a bell-jar vacuum chamber pumped out with a two-stage mechanical pump and two 6-inch, liquid-nitrogen-baffled, oil-diffusion pumps. The vacuum capability of the chamber was between 10^{-7} and 10^{-8} Torr, but for the most part the testing was carried out between 5×10^{-6} and 5×10^{-7} Torr. The required voltages were supplied by a 10-kv source with an accuracy of ± 1 percent. A resistor voltage-divider network (Figure 13) enabled changing the deceleration-grid potential. The whole power supply had to be floated above ground, to avoid shorting out the supply voltage, V_c ; this, in turn, led to a charge buildup on the chassis (causing some mild shocks) but gave little trouble at twice that voltage until one of the connectors apparently accumulated some dirt and shorted out. Replacement of the connector and cleaning all the others with alcohol and freon eliminated the problem.

With the quadrupole in place, the source was approximately in the center of the cylindrical chamber, with insulated wire running to it through appropriately protected feed-throughs. The ribbon support for the wires was used first. With all circuits checked for shorts, the potential was brought up slowly to keep from breaking the fine wires. At 7 kv, an arc occurred within the ionizer which shorted out the supply and blew the circuit breaker. The oscilloscope connected to the output from the quadrupole had been showing only a base line; at the moment the arc occurred, a very large peak appeared and then disappeared. This procedure was tried several times more, always with the same result. Observation indicated that the arcs occurred along one or another of the four spacer legs between the acceleration grid and the base. When removed from the chamber, close inspection showed this to be true, also that the thin wires were completely burned away. The whole system was cleaned with alcohol and freon, the glass insulators were replaced, and the source was put back into the chamber without replacing the Wollaston wire. After the entire system had been carefully cleaned and checked, the potential was again brought up, this time all the way to 10 kv. Apparently the power supply was not as stable as claimed because the voltage drifted slowly at this point until the circuit breaker opened, showing an "over-voltage" condition. Repeated tests showed the arcing was infrequent and that the supply would consistently hold at 9700 volts. Unfortunately, there was no longer time to have the Wollaston wire replaced for this source, and the stainless-steel support base was replaced with the now finished platinum ring.

To replace the ribbon support system with the ring system, it was necessary to halve the total distance between the glass base and the acceleration grid and this caused trouble. With the platinum ring and wires in place and the whole system cleaned out again, the potential could only be brought to 5500 volts before arcing occurred. After the first arcover, the source was inspected--the fine wires were completely burned away. Without the wires

and after another thorough cleaning, the potential still could not be increased over 5500 volts. The electrical fireworks in the source were no longer confined to the inside, but were also observed to be playing around the electrical connectors at the base. The internal parts of the system could no longer be seen clearly, because of the closer spacing, but later investigation showed the glass insulators on the supports, as before, to be the arc path. At this point there was no longer time to check other methods of making the electrical connections and testing had to be discontinued.

CONCLUSION AND RECOMMENDATIONS

Problems in the secondary structure of the field ionization source have made it impossible to obtain experimental results on the theory set forth in the first part of this paper. It is therefore necessary to dwell on the secondary problems rather than the primary.

The Stanford Research Institute studies have shown that the thin wires can withstand greater forces than our design could produce--12 kv at 1 mm spacing, as opposed to our 10 kv at 2.5 mm so that the wires were probably not forming an arc path by breaking but breaking because of the arc. Secondly, the S.R.I. studies were made with the above potentials and spacing at about 10^{-5} Torr--a full decade greater than our pressures--so that the breakdown probably did not occur in the free spaces. The glass insulator was thick enough to withstand 200 times the voltage used on this source (the dielectric strength of Pyrex is about 4800 kv/cm and the glass insulator wall was 0.05-cm thick) and the spacers were certainly long enough to prevent breakdown. This evidence suggests several conclusions. First, the arcs did not occur directly between the thin platinum wires and the acceleration grid. The wires were strong enough to keep from breaking and the overall pressure was too low to permit electrical breakdown. No arcing occurred through the glass insulators because the dielectric strength of the glass was enough to withstand the voltages. What may have been happening was that a surface breakdown on the spacers or the insulators formed a conduction path between the acceleration grid and the base. Absorbed moisture on the surface of a piece of glass can drastically reduce the surface resistivity. Glyptol was used to insulate the external contacts, and it is conceivable that this was outgassing sufficiently to produce a breakdown path between the high- and low-voltage connections. The thin wire itself was probably burned away by the first arc. If these arcs could be prevented, the ionization abilities of the source could be properly evaluated.

It is recommended that two changes be made to the present source to eliminate the arcing. First, completely separate the high- and low-voltage sections electrically. This would eliminate the metal conductors that run through holes in the acceleration grid. Second, use a different material--such as mica or Teflon--for the spacers supporting the acceleration grid, and for other parts that are now glass; if glass must be used, thoroughly clean the surface and coat it with a non-porous, insulating substance that will prevent contamination buildup and subsequent arcing.

Once the arcing problem is overcome, this source should show promise as an ionizer. With the spacings and voltages used, computer calculations based on the equations in the first section of this paper give a field intensity of 6×10^6 volts/cm. With an enhancement factor of about 10, this should be sufficient for ionization. With closer spacing, even this could be improved.

Some problems have been foreseen with this source. The objective is not only to ionize the molecules but also to channel the ions into a pencil beam with velocities suitable for the spectrometer. The S.R.I. studies resulted in lower ion currents than expected, apparently because the dispersion of the ions away from the single wire they used was great enough

to prevent all but a very small portion of the total from reaching the spectrometer entrance. It was hoped that our multiple-wire system would prevent some of this dispersion; but it may also be necessary to change the configuration of the acceleration grid and the optical system to achieve optimum results.

Should tests on this field ionization source not provide good results, there are other ways of producing the high field intensities necessary to field ionization, and some have already been suggested. Perhaps there are yet other more practical ways of achieving gentle ionization, but at this time the most promising way seems to be the use of very small diameter wires to produce very high field intensities, allowing electrons to tunnel from the molecules to the metal surface.

REFERENCES

1. Vilesov, F. I., and Akopyan, M. E., "Photoionization and Its Application in Analytical Mass Spectroscopy," Instrum. Exper. Tech., 1009, trans. from Pribory i Tekhnika Eksperimenta 5:145-148, Sept. - Oct. 1962.
2. Muller, E. W., Ergeb. exact. Naturwiss 27:290, 1953.
3. Good, R. H., and Muller, E. W., "Handbuch der Physik" 21:176, Berlin: Springer, 1956.
4. Beckey, H. D., Knoppel, H., Metzinger, G., and Schulze, P., "Advances in Experimental Techniques, Applications, and Theory of Field Ion Mass Spectrometry," in: Proc. Institute of Petroleum/ASTM Mass Spectrometry Symp., Bungay, England: Richard Clay and Co., Ltd., 1965.
5. Fies, W. J., Spokes, G. N., and Heynick, L. N., "Development of a Cold Ionizer for a Quadrupole Mass Spectrometer," Final Technical Report, Contract DA-44-009-AMC-895(T), Dept. of the Army, U.S. Army Engineer Res. and Dev. Labs., Ft. Belvoir, Va., Jan. 9, 1965-Dec. 31, 1965.
6. Melmed, A. J., and Muller, E. W., "Study of Molecular Patterns in the Field Emission Microscope," J. Chem Phys. 29:1037, 1958.
7. Brandon, D. G., "The Resolution of Atomic Structure; Recent Advances in the Theory and Development of the Field Ion Microscope," Brit. J. Appl. Phys. 14:474, 1963.
8. Gomer, R., "Field Emission and Field Ionization," Harvard Monographs in Applied Science No. 9, Cambridge, Mass.: Harvard University Press, 1961.

BIBLIOGRAPHY

Beckey, H. D., "Field Ionization Mass Spectroscopy," in: Advances in Mass Spectrometry, Proc. of a Conf. Held in Oxford, England, by R. M. Elliott, Sept. 1961.

Inghram, M. G., and Gomer, R., "Mass Spectrometric Analysis of Ions from the Field Microscope," J. Chem. Phys. 22:1279, 1954. Also J. Amer. V. Soc. 77:500, 1955.

Llewellyn-Jones, F., Ionization and Breakdown in Gases, New York: John Wiley and Sons, 1966.

McDowell, Charles A., Mass Spectrometry, New York: McGraw-Hill Book Co., 1963.

Pierce, J. R., Theory and Design of Electron Beams, Princeton, N. J.: D. Van Nostrand Co., 1954.

Spangenberg, K. R., Vacuum Tubes, New York: McGraw-Hill Book Co., Inc., 1948, pp. 125-128.

APPENDIX
PROGRAM FOR CALCULATING FIELD IN GRATING - PLANE GEOMETRY

3200 FORTRAN (2.2)

```

PROGRAM MAIN
WRITE (61,2)
2 FORMAT(112H1CALCULATION OF ELECTRIC FIELD AT GRATING WIRES IN A PA
1RALLEL GRATING-PLANE DESIGN OF A FIELD IONIZATION SOURCE.)
WRITE (61,3)
3 FORMAT(135H0CODE---RG=RADIUS OF GRID WIRE,A=SPACING BETWEEN GRID W
1IRES,DCG=DISTANCE PLANE TO GRATING,DGP=DISTANCE GRATING TO FIRST L
2ENS ELECTRODE.)
WRITE (61,4)
4 FORMAT(127H U=AXIS VARIABLE PERPENDICULAR TO PLANE, V=AXIS VARIABLE
1E ALONG GRATING CENTERS,MODE---0 CALCULATES ONLY INPUT U AND V VAR
2IABLES)
WRITE (61,5)
5 FORMAT( 50H ,1 CALCULATES AT 10 DEGREE INTERVALS AROUND WIRE.)
WRITE(61,9)
9 FORMAT(104H0KAD IS ANGLE INCREMENT INDEX -IE KAD=180 GIVES INCRME
1NT OF 1 DEGREE, KAD=18 GIVES 10 DEGREE INCREMENT.)
WRITE(61,14)
14 FORMAT( 53H 1B AND 1E ARE BEGINING AND ENDING DO LOOP INDEX NO:5)
E0=8.854E-12
PI=3.1415926536
N=0
READ (60,13)NO
13 FORMAT(15)
8 READ (60,1)RG,A,DCG,DGP,U,V,VG,VP,MODE
1 FORMAT(6E10.3,2F5.2,15)
READ(60,7)KAD,1B,1E
7 FORMAT(315)
WRITE (61,6)
6 FORMAT(131H0 WIRE RADIUS WIRE SPACING DCG VP DGP
1 U V VG VP
2 MODE )
WRITE (61,10)RG,A,DCG,DGP,U,V,VG,VP,MODE
10 FORMAT(E13.3,E 17.3,6E15.3,18)
FMU=(2.*PI*DGP)/(A*ALOG(2.*SIN(PI*RG/A)))
DF=DGP+DCG+FMU*DCG
QC=(E0*A*(VP+FMU*VG))/DF
QG=(E0*A*FMU*((DGP+DCG)*VG-DCG*VP))/(DGP*DF)
C=-(DCG*QC)/(A*E0)
AA=-QG/(4.*PI*E0)
B=2.*PI/A
F=-QC/(E0*A)
ANG=0.0
WRITE(61,11)
11 FORMAT(132H0 ANG U V
1 POT EU EV
2 EMAG )
COM=EXP(2.*B*U)+1.-2.*EXP(B*U)*COS(B*V)
VW=AA*ALOG(COM)+F*U+C
EU=-AA*(2.*B*EXP(2.*B*U)-2.*B*EXP(B*U)*COS(B*V))/COM-F
EV=AA*(2.*B*EXP(B*U)*SIN(B*V))/COM
EUM=-AA*(2.*B*EXP(-B*RG))/(EXP(-R*RG)-1.)-F
IF(MODE)77,77.55
77 WRITE(61,12)ANG,U,V,VW,EU,EV,EUM
12 FORMAT(F13.3,6E20.3)
N=N+1

```

```

IF(N-NO)44,33,33
55 DO 89K=18,1E,1
AN=KAD
FK=K
ANG=(FK-1)*PI/AD
DANG=ANG*180./PI
U=-RG*COS(ANG)
V=RG*SIN(ANG)
COM=EXP(2.*B*U)+1.-2.*EXP(B*U)*COS(B*V)
VW=AA*ALOG(COM)+F*U+C
EU=-AA*(2.*B*EXP(2.*B*U)-2.*B*EXP(B*U)*COS(B*V))/COM-F
EV=-AA*(2.*B*EXP(B*U)*SIN(B*V))/COM
EMAG=SQRT(EU**2+EV**2)
89 WRITE(61,12)DANG,U,V,VW,EU,EV,EMAG
N=N+1
IF(N-NO)44,33,33
44 GO TO 8
33 WRITE(61,22)
22 FORMAT(30H0 ALL DATA HAS BEEN PROCESSED.)
STOP
END

```

3200 FORTRAN DIAGNOSTIC RESULTS - FOR MAIN



PRECEDING PAGE BLANK NOT FILMED.

SECONDARY TORQUES ON SPACECRAFT

E. R. Sanford*

INTRODUCTION

A study was made to identify all torque-producing mechanisms which might operate on spacecraft and to study the nature and magnitude of those which, considering the expected magnitudes of spacecraft dimensions and environmental parameters, could conceivably be significant in certain missions. In this context, "secondary" torques are those due neither to mass ejection nor to internal mass redistribution. The study also considered the feasibility of simulating the various torque-producing mechanisms in the laboratory.

Since considerable work has been done on spacecraft dynamics and on torque mechanisms, this report will be largely a literature review, and partly a guide to the literature - with an attempt to reference only papers that clearly summarize or that are essential for an understanding of certain points. Therefore, most detail is omitted, since the reader can quickly understand the physics involved or determine the qualitative (and, to the extent possible without numerical work, the quantitative) nature of the mechanisms by consulting the references.

When possible, the torques are classified according to the major environmental factor producing them.

TORQUES ON SPACECRAFT DUE TO NEUTRAL ATMOSPHERIC INTERACTIONS

At altitudes where there are significant percentage constitutions of neutral atoms and molecules, the surface of a spacecraft can undergo momentum interchange with these particles. With relative motion, these interactions can result in torques, if the interactions lead to forces that are asymmetrically acting about the center of mass.

Since the trajectories of the neutrals are unaffected by the presence of a spacecraft until a surface encounter occurs, the problem of calculating the interactions basically depends upon the mathematical complexity of the geometry. However, the major uncertainty involves the nature of the surface interactions - the processes of sorption, accommodation and re-emission. The amount of momentum re-emitted is not well known at present.

Although the aerodynamics for the spacecraft case should be simpler than for ordinary cases (the mean free path in satellite environments is probably always much greater than satellite dimensions so that collisions between neutrals can be neglected), little or no experimental evidence is available to determine the drag coefficients. Furthermore, even for the earth, densities at typical satellite altitudes are both poorly known and variable.

There are three torque mechanisms to consider. A fourth, due to density gradients in the atmosphere, is probably of no importance for even very large satellites.

*Ohio University, Athens, Ohio.

The first torque mechanisms might be termed aerodynamic drag torque; it is due simply to the normal drag forces acting on projected areas removed from the center of mass. If the center of aerodynamic drag forces does not coincide with the center of mass, a torque will result. Estimates of the magnitude of drag forces can be made by assuming no compression on the front of the satellite due to collisions among neutrals, and assuming diffuse reflection, from*

$$F = \frac{1}{2} C (\text{Area}) (\text{density}) (\text{velocity})^2,$$

with the drag coefficient $C = 2$. Reference 1 gives a good review of work in the field. Also see References 2, 3, and 4.

Two additional mechanisms depend upon the spin of the satellite. The first is the Magnus torque, familiar in the exterior ballistics of shells (see Reference 5). Since it is small even for rapidly rotating shells in dense atmosphere near the earth, and since it is proportional to density, slip coefficient, and spin rate (all of which are very small for satellites), this mechanism is negligible.

The second spin-dependent mechanism might be called aerodynamic torque (References 6 and 7). The same difficulties encountered in the drag forces beset its evaluation. This mechanism arises from the differing relative velocities of the peripheral parts of the spacecraft due to rotation about an axis perpendicular to the flight path. Hohl (Reference 6) calculates its value for the ECHO case, where it is found to be quite small. From the functional dependence of its value in that (spherical) case, it can be inferred that this torque component is small in all practical cases.

TORQUES ON SPACECRAFT DUE TO MAGNETIC FIELDS AND/OR IONIZED MEDIA

Plasma-Spacecraft Interaction

By far the most difficult torque-producing mechanisms to evaluate quantitatively are those involving the interactions of spacecraft with ionized media, such as characterize satellite environments. The problem of the interaction of conducting bodies with ionized gases is a very old and still active one; and it has not been solved precisely for even simple geometries, nor in the absence of magnetic fields. The literature is quite extensive, but an adequate review and evaluation of those aspects important to spacecraft can be found in Reference 8. This reference is a clear, cogent discussion of the mechanisms involved in the problem and a physical evaluation of the approximations made in the various attempts to attack the problem theoretically. Therefore, we will not detail the mechanisms here.

Our concern here is the situation where the free molecular flow regime applies (mean free paths much larger than spacecraft dimensions or ion-sheath thicknesses), where cyclotron radii are such that the electrons are effectively confined to magnetic field lines, and where satellite potentials are likely to be negative – the only cases thus far considered. As discussed in References 8 and 9, these conditions apply between about 300 km and about 3,000 km above the earth. Below 300 km satellites normally do not operate for long periods, and above 3,000 km the ion densities are so low and magnetic fields so small that the torques discussed are probably negligible.

*Provided spacecraft velocity \gg neutral thermal velocity (always true at altitudes where neutral effects exceed ion effects).

All previous analyses have assumed that steady-state conditions apply and that the electromagnetic effects have negligible relaxation times. Certainly with respect to both response times important to satellite attitude change and time intervals during which satellite environmental changes of significance take place, the latter assumption is valid. As for the former, only low-frequency oscillations of the plasma can take place, and they should contain sufficiently small amounts of energy so that their effect on the torque problem is negligible.

As the only realistic cases, reference will be made to those papers in which finite bodies are considered and in which the non-linear Boltzmann and Poisson equations are used.* Moreover, there are only three papers that treat the effect of the magnetic field in the region of the satellite surface (References 6, 12, and 13). It has been shown that if the cyclotron radius is much greater than the satellite radius (usually true), the effect of the magnetic field on ion behavior is small. However, the presence of an induction potential along the satellite greatly modifies the current pattern in the satellite skin, a result which should alter the torques significantly. Another serious problem, although its severity is difficult to evaluate in the absence of calculations and of a thorough study of the mechanisms involved, is the neglect of the effects of secondary and photoelectric emission, which can even drive the potential positive** below about 200 km and above about 1,000 km (Reference 9). Not only would the satellite equilibrium potential be modified by these effects, but their nonuniformity would also be expected to modify the surface charge density and, hence, the torques.

A good discussion of possible particle trajectories in the field of a charged body in a plasma and of the conditions of thermodynamic equilibrium can be found in Reference 10. See Reference 11 for a review of prior work and a presentation of a numerical method for finding particle trajectories, densities, and potentials. This study contains a method of doubtful validity and one applying only to satellities which have equipotential surfaces (not true in the presence of a magnetic field).

The work of (Reference 14) Al'pert et al. contains the most complete discussion of the physics and mathematics of the problem, but considers the effect of a magnetic field only for the linear case and in the wake of the satellite. Medved (Reference 9) discusses the effect of secondary and photoelectric emission on the formation of the plasma sheath, but only approximately and in the absence of a magnetic field. Sawchuk (Reference 15) considers prolate spheroids, but not the effect of a magnetic field. Hohl and Wood (Reference 13) allow for the effect of the field, but consider only the case of axial symmetry about the vector product of the relative velocity and the magnetic field. Further, they take the ion density as constant and the electrons as arriving strictly along field lines – an approximation which may be good, but how good is not known. The same comments apply to the work of Hohl (Reference 6), where, additionally, the effect of photoemission is crudely considered. The work of Hohl and of Hohl and Wood in fact ignores the sheath effects entirely. Although this neglect might not change the total surface currents or potential greatly, it might alter the surface potential gradients enough to have a marked effect on torques, which are quite sensitive to changes in surface current distribution changes.

Torques

There is but one paper (Hohl, Reference 6) on the torques that might be present due to plasma-spacecraft interaction. There are three torque mechanisms. The first is called Coulomb torque, which is caused by the asymmetrical momentum exchange of ions with

*Maxwellian distributions far from the body are assumed (see Appendix A).

**See Appendix A.

the spacecraft. Hohl considers only the symmetric ECHO case, where asymmetric ion impact is due solely to the presence of the induction potential. It is a quite small effect, as might be surmised from the quite small Coulomb drag effect (Reference 16).

The second torque, surface charge torque, is due to the presence of a nonrotating surface charge density resulting from the asymmetric surface potential gradient. If the satellite is rotating, the relative movement of the surface charge and the skin of the satellite leads to joule heating and a despin torque. This is also a quite small effect; but, like all of the torques considered here, very difficult to calculate reliably.

The third torque, the induction torque, results from the interaction of the magnetic field with the surface currents flowing as a result of the induced potential gradient along the surface of the satellite. While subject to all the difficult numerical calculation problems of the torques of this paper, and while beset with all the uncertainties of the physical mechanisms affecting its magnitude, this torque should be investigated further, since Hohl found it to have a magnitude (in the case of ECHO) equal to the eddy-current torque - which is not negligible.

Simulation of the Torques

Since the plasma-interaction torques are the most obscure and difficult to predict, experimental verification of their presence and determination of their magnitude may be important in those (fortunately few) cases in which it might be suspected that they are important to the mission of the spacecraft. The primary problem in the laboratory testing of actual or model spacecraft for these effects lies in the simulation of the ambient field. While considerable progress has been made in the difficult problem of simulating the plasma environment for both stationary and moving spacecraft (References 17 and 18), it has been impossible so far to simulate the relative motion of the spacecraft and the ambient magnetic field. Since the field is crucial to the torques considered here, this is a fatal flaw.

TORQUE EXERTED ON RADIATING ELEMENTS

Introduction

It is well known that any interpretation of both classical and quantum physics which contains conservation of momentum must necessarily conclude that electromagnetic radiation carries both linear and angular momentum. In the case of angular momentum, the predictions are most transparent when a multipole expansion of the radiation field is made, since the angular expansion functions can be shown to be the eigenfunctions of angular momentum. Since the radiated flux of angular momentum must be the negative of the time rate at which the radiating system loses angular momentum, a torque equal to this loss rate must be exerted on the radiating elements. With reference to space vehicles, this torque can result in an attitude change which could be significant under proper conditions. Although it requires significant radiated power of a polarized nature to yield a torque that is other than negligible, radiation torques may become significant in the future when spacecraft carry high-power transmitters,* since in that case not only may the

*It should be remembered that the character of the pattern radiated from a system does not depend only upon the pattern of the antenna proper. Interaction with the skin of the spacecraft can, for example, cause elliptically-polarized radiation to be emitted in certain directions even when the antenna is linearly polarized. A further practical consideration, of value in estimating the importance of higher modes for a given radiating system, follows from the work of Harrington (Reference 23) and of Chu (Reference 24). They show that, for a system in which the radiators are confined to a sphere of radius a , modes of order $l > 2\pi a/\lambda$ are supported with difficulty, that is, require excessive driving currents. This is because they have large reactive impedances, so either the source cannot supply the requisite currents or resistance losses damp these modes.

power be large, but for long-range communication in ionized media the choice of polarized radiation may be essential. Moreover, suggestions have already been made for controlling the attitude of spacecraft by radiation torque (References 19, 20). Although the expressions for angular momentum density of a radiation field are available in the literature, either these expressions are quantum mechanical (References 21, 22) or they apply to simple radiation patterns only. Moreover, the author has found no classical expression for other than the z -component of the angular momentum. Therefore, it is the primary purpose of this paper to develop the general expression for the vector components of radiation torque, considering an arbitrary current and charge distribution in the radiating elements.

In what follows, gaussian units will be used and the development carried out in the terminology of the book by Morse and Feshbach (Reference 25), since this is a readily available reference containing much detail which affords a starting point well on the way toward the final result. The use of this reference will save much labor. The only other reference to come to the author's attention that carries out a sufficient classical development for our purposes is in the book by Papas (Reference 26).

Multipole Expansions

For purposes of computing angular momentum, the expansion of the radiation field in multipole field components is the most convenient method. Of course, any complete set of functions could be used, including plane waves, but the mathematics would be prohibitively difficult and the results hard to interpret. The expansion is done for monochromatic sinusoidal exciting currents,* and complex notation is used. The final results, naturally, will be obtained from the real parts only. It should be noted that the expansion of the field is arbitrary, in the sense that the orthogonal axes can be chosen at will. Therefore, in practice it is well to choose the axes with care, otherwise the radiation field contains more components than are necessary. For example, if the radiation were pure dipole and the z -axis were not chosen to be the z -axis of the dipole moment, the resulting field would contain more than a simple dipole component – a condition which would not change the physical results, but which would result in awkward expressions. Anticipating the results below, it might be noted at this point that, if there is only one multipole component, the torque has z component only (provided the "natural" z -axis was selected) and that its value is m/ω (total radiated power), where m is the axial index in the spherical harmonic Y_{1m} and ω is the angular frequency. For example, for circularly polarized dipole radiation, where the Y_{11} component only is present, the torque on a 1-kw, 100-mc antenna would be $(1)(1,000)/2\pi(10^8) = 10^{-5}/2\pi$ newton-meters. Although in general the radiation pattern and the torque contain interference terms, the radiated power (total integrated over solid angle) is given by the sum of the powers radiated by each multipole.

In any spherical shell, the angular momentum flux is the same, since its density decreases as r^2 ; however the volume of the shell varies as r^2 also. So, we will evaluate the last integral as $r \rightarrow \infty$.

Notation

We shall follow the notation of Morse and Feshbach (Reference 25). Some of the relevant definitions are given below. Spherical harmonics:

$$Y_{\ell m}^e = \cos m\phi P_{\ell}^m(\cos \theta)$$

$$Y_{\ell m}^o = \sin m\phi P_{\ell}^m(\cos \theta)$$

$$X_{\ell}^m = e^{im\phi} P_{\ell}^m = Y_{\ell m}^e + i Y_{\ell m}^o$$

*This could be one Fourier component of a general excitation.

$$\int Y_{\ell' m'} Y_{\ell m} d\Omega = \frac{4\pi}{\epsilon_m (2\ell + 1)} \frac{(\ell + m)!}{(\ell - m)!} \delta_{\ell\ell'} \delta_{mm'}$$

$$\epsilon_0 = 1 ; \epsilon_m = 2 , m > 0.$$

Electromagnetic quantities:

$$\text{Poynting vector (power flux)} = \mathbf{S} = \frac{c}{4\pi} (\mathbf{E} \times \mathbf{H})$$

$$\text{Linear momentum density} = \mathbf{S}/c^2$$

$$\text{Angular momentum density} = \mathbf{R} \times \mathbf{S}/c^2$$

$$\text{Angular momentum flux} = c\mathbf{R} \times \mathbf{S}/c^2 = \frac{1}{4\pi} \mathbf{R} \times (\mathbf{E} \times \mathbf{H})$$

$$\text{Torque} = \mathbf{T} = \int \frac{1}{4\pi} \mathbf{R} \times (\mathbf{E} \times \mathbf{H}) d\Omega$$

$$= \frac{|\mathbf{R}|^2}{4\pi} \int_{\text{sphere}} \mathbf{R} \times (\mathbf{E} \times \mathbf{H}) \sin \theta d\theta d\phi$$

Since we shall be using complex vectors, the results will be given by, for example, one-half the real part of $(\mathbf{E}^* \times \mathbf{H})$.

Spherical Bessel functions:

$$j_\ell(kr) = \sqrt{\frac{\pi}{2kr}} J_{\ell + \frac{1}{2}}(kr)$$

$$n_\ell(kr) = \sqrt{\frac{\pi}{2kr}} N_{\ell + \frac{1}{2}}(kr)$$

$$h_\ell = j_\ell + in_\ell \xrightarrow{kr \rightarrow \infty} \frac{1}{kr} i^{-\ell-1} e^{ikr} \text{ (outgoing wave).}$$

These functions will not be normalized.

Computation of Torque

We will begin with the expressions in Morse and Feshbach (Reference 25) for the electric and magnetic field intensities (their equation 13.3.86). These expressions are in terms of the M and N vectors of their equations 13.3.68 and 13.3.69, which, in turn, are expressed in terms of the vector functions P, B, and C of the tables on pages 1898-1900. From these we find that

$$\mathbf{E}^* \times \mathbf{H} = k^4 \sum_{\substack{\ell \ell' \\ m m' \\ \sigma \sigma'}} \frac{2^\ell 2^{\ell'} k^\ell k^{\ell'} (\ell-1)! (\ell'-1)!}{(2\ell)! (2\ell')!} \epsilon_m \epsilon_{m'} \frac{(\ell-m)! (\ell'-m')!}{(\ell+m)! (\ell'+m')!} \\ \times \left[\frac{-i}{c^2} \frac{\ell \ell'}{(\ell+1)(\ell'+1)} h_{m\ell}^{\sigma*} h_{m'\ell'}^{\sigma'} M_{\sigma m \ell}^{3*} \times N_{\sigma' m' \ell'}^3 - \right. \\ \left. i P_{m\ell}^{\sigma*} P_{m'\ell'}^{\sigma'} N_{\sigma m \ell}^{3*} \times M_{\sigma' m' \ell'}^3 \right]$$

Here

$$h_{m\ell}^\sigma = \frac{(2\ell+1)!}{2^\ell \ell! \ell! k^\ell} m_{m\ell}^\sigma$$

and

$$p_{m\ell}^\sigma = \frac{i(2\ell+1)!}{2^\ell (\ell+1)!} n_{m\ell}^\sigma,$$

where $\sigma = \text{odd or even}$, and $m_{m\ell}^\sigma$ and $n_{m\ell}^\sigma$ are the multipole parameters in the expansion of the vector potential; i.e. for an excitation current density $\mathbf{J}(\mathbf{R}_0)$,

$$m_{m\ell}^\sigma = \int \mathbf{J}(\mathbf{R}_0) \cdot \mathbf{M}_{\sigma m \ell}^1(\mathbf{R}_0) dV_0$$

and

$$n_{m\ell}^\sigma = \int \mathbf{J}(\mathbf{R}_0) \cdot \mathbf{N}_{\sigma m \ell}^1(\mathbf{R}_0) dV_0,$$

where

$$A(\mathbf{R}) = \frac{ik}{c} \sum_{\ell=1}^{\infty} \frac{(2\ell+1)}{\ell(\ell+1)} \sum_{m, \sigma} \epsilon_m \frac{(\ell-m)!}{(\ell+m)!} \left[m_{m\ell}^\sigma M_{\sigma m \ell}^3(\mathbf{R}) + n_{m\ell}^\sigma N_{\sigma m \ell}^3(\mathbf{R}) \right] e^{-i\omega t};$$

ℓ is summed from 1 to ∞ ;

m runs from 0 to ℓ .

Two terms in the summation have been omitted. These involve terms in $M^* \times M$ and $N^* \times N$. It is easily seen that the sum of these terms is zero.

We now express the M^3 and N^3 vectors in terms of the P, B, and C vector functions in the spherical coordinate system. Since the torque expression contains $R \times E^* \times H$, we need use only the θ and ϕ components of M^3 and N^3 . Moreover, it is easily seen that the terms in $p_{m\ell}^\sigma p_{m'\ell'}^{\sigma'}$ will yield $n_{m\ell} n_{m'\ell'}$, as the terms in $h_{m\ell}^\sigma h_{m'\ell'}^{\sigma'}$ yield $m_{m\ell} m_{m'\ell'}$, provided the sums give $\delta_{\ell\ell'}$, as they will be shown to do. So, we will consider in detail only the term in the brackets

$$-\frac{i}{c^2} \frac{\ell \ell'}{(\ell+1)(\ell'+1)} h_{m\ell}^{\sigma*} h_{m'\ell'}^{\sigma'} M_{\sigma m \ell}^3 \times N_{\sigma' m' \ell'}^3.$$

Writing this out in vector components, we obtain

$$\frac{-i(\ell \ell')^2}{c^2(2\ell+1) \sin \theta} h_{m\ell}^{\sigma*} h_{m'\ell'}^{\sigma'} \frac{h_\ell^* h_{\ell'}}{kr} \left[\frac{i m(2\ell+1)}{\ell(\ell+1)} X_{\ell m}^* X_{\ell' m'} \hat{e}_\phi - \right. \\ \left. \frac{\ell-m+1}{\ell+1} X_{\ell+1, m}^* X_{\ell' m'} \hat{e}_\theta + \frac{\ell+m}{\ell} X_{\ell-1, m}^* X_{\ell' m'} \hat{e}_\theta \right]$$

Taking the cross-product of $r \hat{e}_r$ with this, we get

$$\frac{i(\ell \ell')^2}{c^2(2\ell+1) \sin \theta} h_{m\ell}^{\sigma*} h_{m'\ell'}^{\sigma'} \frac{h_\ell^{*(kr)} h_{\ell'}^{(kr)}}{k} \left[\frac{i m(2\ell+1)}{\ell(\ell+1)} X_{\ell m}^* X_{\ell' m'} (-\hat{e}_\theta) - \right. \\ \left. \frac{\ell-m+1}{\ell+1} X_{\ell+1, m}^* X_{\ell' m'} \hat{e}_\phi + \frac{\ell+m}{\ell} X_{\ell-1, m}^* X_{\ell' m'} \hat{e}_\phi \right]$$

Transforming to Cartesian coordinates from

$$\hat{e}_\theta = \cos \theta \cos \phi \hat{e}_x + \cos \theta \sin \phi \hat{e}_y - \sin \theta \hat{e}_z$$

$$\hat{e}_\phi = -\sin \phi \hat{e}_x + \cos \phi \hat{e}_y,$$

and further transforming to spherical basis vectors

$$\hat{e}_\pm = \mp \frac{1}{\sqrt{2}} (\hat{e}_x \pm i \hat{e}_y)$$

$$\hat{e}_0 = \hat{e}_z,$$

we obtain

$$\begin{aligned}
& \frac{(\ell\ell')^2 h_\ell^{*(kr)} h_{\ell'}^{(kr)} h_m^{\sigma*} h_{m'}^{\sigma'}}{\sqrt{2} kc^2 (2\ell+1) \sin \theta} \left\{ \hat{e}_+ \left[-\cos \theta \cos \phi \frac{m(2\ell+1)}{\ell(\ell+1)} X_{m\ell}^* X_{m'\ell'} + \right. \right. \\
& \quad i \sin \phi \frac{\ell+m}{\ell} X_{\ell-1,m}^* X_{\ell'm'} - i \sin \phi \frac{\ell-m+1}{\ell+1} X_{\ell+1,m}^* X_{\ell'm'} + \\
& \quad i \cos \theta \sin \phi \frac{m(2\ell+1)}{\ell(\ell+1)} X_{m\ell}^* X_{m'\ell'} - \cos \phi \frac{\ell+m}{\ell} X_{\ell-1,m}^* X_{\ell'm'} + \\
& \quad \left. \left. \cos \phi \frac{\ell-m+1}{\ell+1} X_{\ell+1,m}^* X_{\ell'm'} \right] + \hat{e}_- \left[-\cos \theta \cos \phi \frac{m(2\ell+1)}{\ell(\ell+1)} X_{m\ell}^* X_{m'\ell'} - \right. \right. \\
& \quad i \sin \phi \frac{\ell+m}{\ell} X_{\ell-1,m}^* X_{\ell'm'} + i \sin \phi \frac{\ell-m+1}{\ell+1} X_{\ell+1,m}^* X_{\ell'm'} + \\
& \quad i \cos \theta \sin \phi \frac{m(2\ell+1)}{\ell(\ell+1)} X_{m\ell}^* X_{m'\ell'} - \cos \phi \frac{\ell+m}{\ell} X_{\ell-1,m}^* X_{\ell'm'} + \\
& \quad \left. \left. \cos \phi \frac{\ell-m+1}{\ell+1} X_{\ell+1,m}^* X_{\ell'm'} \right] + \hat{e}_0 \left[-\sin \theta \frac{m(2\ell+1)}{\ell(\ell+1)} \sqrt{2} X_{\ell,m}^* X_{\ell',m'} \right] \right\}
\end{aligned}$$

This can be written

$$\begin{aligned}
& \frac{(\ell\ell')^2 h_\ell^{*(kr)} h_{\ell'}^{(kr)} h_m^{\sigma*} h_{m'}^{\sigma'}}{\sqrt{2} kc^2 (2\ell+1) \sin \theta} \left\{ \hat{e}_+ \left[\cos \phi - i \sin \phi \right] \left[-\cos \theta \frac{m(2\ell+1)}{\ell(\ell+1)} X_{\ell m}^* X_{\ell' m'} - \right. \right. \\
& \quad \left. \left. \frac{\ell+m}{\ell} X_{\ell-1,m}^* X_{\ell' m'} + \frac{\ell-m+1}{\ell+1} X_{\ell+1,m}^* X_{\ell' m'} \right] + \hat{e}_- \left[\cos \phi + i \sin \phi \right] \right. \\
& \quad \left[\cos \theta \frac{m(2\ell+1)}{\ell(\ell+1)} X_{\ell m}^* X_{\ell' m'} - \frac{\ell+m}{\ell} X_{\ell-1,m}^* X_{\ell' m'} + \frac{\ell-m+1}{\ell+1} X_{\ell+1,m}^* X_{\ell' m'} \right] + \\
& \quad \left. \left. \hat{e}_0 \left[-\sin \theta \frac{\sqrt{2}m(2\ell+1)}{\ell(\ell+1)} X_{\ell n}^* X_{\ell' m'} \right] \right\}.
\end{aligned}$$

Consider the following recursion relation (Reference 25, p. 152) for associated Legendre polynomials:

$$\begin{aligned} (2\ell + 1) \sin \theta P_{\ell}^{m+1} &= (\ell + m + 1)(\ell + m) P_{\ell-1}^m - (\ell - m)(\ell - m + 1) P_{\ell+1}^m \\ &= (\ell + 1)(\ell + m) P_{\ell-1}^m - (\ell - m + 1)\ell P_{\ell+1}^m + m \left[(\ell + m) P_{\ell-1}^m + (\ell - m + 1) P_{\ell+1}^m \right]; \\ \frac{2\ell + 1}{\ell(\ell + 1)} \sin \theta P_{\ell}^{m+1} &= \frac{(\ell + 1)(\ell + m) P_{\ell-1}^m - \ell(\ell - m + 1) P_{\ell+1}^m}{\ell(\ell + 1)} + \frac{m}{\ell(\ell + 1)} (2\ell + 1) \cos \theta P_{\ell}^m \end{aligned}$$

We have used another recursion relation to replace the last square bracket. From this, the \hat{e}_+ term in the several earlier equations becomes

$$\begin{aligned} \hat{e}_+ e^{-i\phi} \left[-\cos \theta \frac{m(2\ell + 1)}{\ell(\ell + 1)} X_{\ell m}^* X_{\ell' m'} + \cos \theta \frac{m(2\ell + 1)}{\ell(\ell + 1)} X_{\ell m}^* X_{\ell' m'} - \right. \\ \left. \frac{2\ell + 1}{\ell(\ell + 1)} \sin \theta P_{\ell}^{m+1} e^{-im\phi} X_{\ell' m'} \right] = \hat{e}_+ \left[-\frac{2\ell + 1}{\ell(\ell + 1)} \sin \theta X_{\ell, m+1}^* X_{\ell' m'} \right] \end{aligned}$$

Now consider the recursion relations

$$\begin{aligned} P_{\ell+1}^m &= (\ell + m) \sin \theta P_{\ell}^{m-1} + \cos \theta P_{\ell}^m \\ P_{\ell-1}^m &= -(\ell - m + 1) \sin \theta P_{\ell}^{m-1} + \cos \theta P_{\ell}^m \end{aligned}$$

Multiply the first by $\ell - m + 1/\ell + m$, the second by $\ell + m/\ell$, and subtract the first from the second. We get

$$\frac{\ell + m}{\ell} P_{\ell-1}^m - \frac{\ell - m + 1}{\ell + 1} P_{\ell+1}^m = \frac{m(2\ell + 1)}{\ell(\ell + 1)} \cos \theta P_{\ell}^m - \frac{(\ell - m + 1)(\ell + m)(2\ell + 1)}{\ell(\ell + 1)} \sin \theta P_{\ell}^{m-2}$$

So, the \hat{e}_- term becomes

$$\hat{e}_- \left[\cos \theta \frac{m(2\ell + 1)}{\ell(\ell + 1)} X_{\ell m}^* X_{\ell' m'} - \cos \theta \frac{m(2\ell + 1)}{\ell(\ell + 1)} P_{\ell}^m e^{-i(m-1)\phi} X_{\ell' m'} + \right.$$

$$\left. \frac{(\ell - m + 1)(\ell + m)(2\ell + 1)}{\ell(\ell + 1)} \sin \theta P_{\ell}^{m-1} e^{-i(m+1)\phi} X_{\ell', m'} \right] e^{i\phi}$$

$$= \hat{e}_- \left[\frac{(\ell - m + 1)(\ell + m)(2\ell + 1)}{\ell(\ell + 1)} \sin \theta X_{\ell, m-1}^* X_{\ell', m'} \right]$$

Hence, the integrals involved are of the form

$$\int_0^{2\pi} d\phi \int_0^{\pi} \sin \theta d\theta \left[-\frac{2\ell + 1}{\ell(\ell + 1)} X_{\ell, m+1}^* X_{\ell', m'} \hat{e}_+ + \right.$$

$$\left. \frac{(\ell - m + 1)(\ell + m)(2\ell + 1)}{\ell(\ell + 1)} X_{\ell, m-1}^* X_{\ell', m'} \hat{e}_- - \frac{m(2\ell + 1)}{\ell(\ell + 1)} X_{\ell m}^* X_{\ell', m'} \right].$$

From the orthogonality relations, we get for

$$\hat{e}_+ : \frac{-(2\ell' + 1)}{\ell'(\ell' + 1)} 2 \frac{4\pi}{\epsilon_m (2\ell' + 1)} \frac{(\ell' + m')!}{(\ell' - m')!} \delta_{\ell\ell'} \delta_{m, m'-1},$$

for

$$\hat{e}_- : \frac{(\ell' - m')(\ell' + m' + 1)(2\ell' + 1)}{\ell'(\ell' + 1)} 2 \frac{4\pi}{\epsilon_m (2\ell' + 1)} \frac{(\ell' + m')!}{(\ell' - m')!} \delta_{\ell\ell'} \delta_{m, m'+1},$$

and for

$$\hat{e}_0 : -\frac{(2\ell' + 1)m'}{\ell'(\ell' + 1)} 2 \frac{4\pi}{\epsilon_m (2\ell' + 1)} \frac{(\ell' + m')!}{(\ell' - m')!} \delta_{\ell\ell'} \delta_{mm'}$$

The entire expressions then become, for

$$\hat{e}_+ : -\frac{(\ell')^4 h_{\ell'}^{2(kr)}}{\sqrt{2} k c^2 (2\ell' + 1)} h_{m', -1, \ell'}^* h_{m', \ell'} \frac{2}{\epsilon_m} \frac{4\pi}{\ell'(\ell' + 1)} \frac{(\ell' + m')!}{(\ell' - m')!} \delta_{\ell\ell'} \delta_{m, m'-1},$$

for

$$\hat{e}_- : \frac{(\ell')^4 h_{\ell'}^2(kr)}{\sqrt{2} kc^2 (2\ell'+1)} h_{m'+1, \ell'}^* h_{m, \ell'} \frac{2}{\epsilon_m} \frac{4\pi}{\ell'(\ell'+1)} \frac{(\ell'+m')!(\ell'-m')(\ell'+m'+1)}{(\ell'-m')!} \delta_{\ell \ell'} \delta_{m, m'+1},$$

and for

$$\hat{e}_0 : -\frac{(\ell')^4 h_{\ell'}^2(kr)}{kc^2 (2\ell'+1)} h_{m, \ell'}^2 \frac{2}{\epsilon_m} \frac{4\pi}{\ell'(\ell'+1)} \frac{(\ell'+m')!}{(\ell'-m')!} \delta_{\ell \ell'} \delta_{mm'},$$

Now, we multiply by $r^2/4\pi$ and take the limit as $r \rightarrow \infty$.

$$\lim_{r \rightarrow \infty} r^2 h_{\ell'}^* h_{\ell'} = \frac{r^2}{k^2 r^2} (i^{-\ell'-1})(-i^{-\ell'-1}) e^{-ikr} e^{ikr} = \frac{1}{k^2}.$$

So 4π cancels in the above expressions, and there is k^3 in the denominators.

Referring to the expression for $E^* \times H$ near the beginning of this subsection, we get the final results for the torque components:

$$\begin{aligned} & \frac{1}{2} \sum_{\ell, m} \left[\frac{k^4 2^{2\ell} k^{2\ell} (\ell-1)! (\ell-1)!}{(2\ell)! (2\ell)!} \epsilon_m^2 \frac{\ell^4}{k^3 c^2 (2\ell+1)} \frac{2}{\epsilon_m} \frac{1}{\ell(\ell+1)} \right] \\ & \left[- \frac{(\ell-m+1)! (\ell-m)!}{(\ell+m-1)! (\ell+m)!} \frac{(\ell+m)!}{(\ell-m)!} h_{m+1, \ell}^* h_{m, \ell} \frac{\hat{e}_+}{\sqrt{2}} + \right. \\ & \left. \frac{(\ell-m-1)! (\ell-m)! (\ell+m)!}{(\ell+m+1)! (\ell+m)! (\ell-m)!} (\ell-m)(\ell+m+1) h_{m-1, \ell}^* h_{m, \ell} \frac{\hat{e}_-}{\sqrt{2}} - \right. \\ & \left. m \frac{(\ell-m)! (\ell-m)!}{(\ell+m)! (\ell+m)!} \frac{(\ell+m)!}{(\ell-m)!} h_{m, \ell}^2 \hat{e}_0 + \text{identical terms in } p_{m\ell} \right] \end{aligned}$$

Using the definitions of the h and p coefficients, we get

$$T = k \sum_{\ell, m} \frac{(2\ell + 1) \epsilon_m}{c^2 \ell(\ell + 1)} \frac{(\ell - m)!}{(\ell + m)!} \left[(\ell - m + 1)(\ell + m) (m_{m+1, \ell}^* m_{m\ell} + n_{m+1, \ell}^* n_{m\ell}) \frac{\hat{e}_+}{\sqrt{2}} + \right. \\ \left. (m_{m-1, \ell}^* m_{m\ell} + n_{m-1, \ell}^* n_{m\ell}) \frac{\hat{e}_-}{\sqrt{2}} - m(m_{m\ell}^2 + n_{m\ell}^2) \hat{e}_0 \right]$$

So,

$$T_z = \frac{k}{c^2} \sum_{\ell, m} \frac{m(2\ell + 1) \epsilon_m}{\ell(\ell + 1)} \frac{(\ell - m)!}{(\ell + m)!} (m_{m\ell}^2 + n_{m\ell}^2) \hat{e}_z,$$

which is m/ω times the radiated power expression (13.3.87) of Morse and Feshbach.

To find the x and y components of torque, the transformation equation for a vector expressed in spherical basis vectors should be used; that is

$$T = - \frac{T_x + i T_y}{\sqrt{2}} \hat{e}_+ + \frac{T_x - i T_y}{\sqrt{2}} \hat{e}_- + T_z \hat{e}_0$$

One then takes the real part of this, the factor $1/2$ having been included above already.

TORQUES ON SPACECRAFT DUE TO PLANETARY MAGNETIC FIELDS

Several torque-producing mechanisms result from the interaction of the conducting materials of or the magnetic moments aboard satellites within external magnetic fields, such as the earth's. Here we consider only uniform external fields, since the effects of any field gradient over the dimensions of satellites will be small compared with the primary effects due to the average field.

If the ambient magnetic field is known and the satellite is spinning or tumbling, energy will be taken from the spin kinetic energy by what might be called ferromagnetic hysteresis torque. If any ferromagnetic or strongly paramagnetic substances are aboard, the changing magnetic field in them caused by rotation will lead to hysteresis loss, hence, a despin effect. The ability to compute the magnitude of the effect is strongly dependent upon knowledge of the magnetic history and magnetization curves of the materials. In the very low fields encountered in space, this knowledge is scanty. In addition, theories for hysteresis loss are not well developed. A good exposition of this "torque" can be found in Reference 4. If a conducting medium rotates with a component of its angular velocity perpendicular to a magnetic field, eddy currents can be set up. These currents interact with the field to produce the eddy-current torque. In general, this torque has a despin component and precessing components, the latter

tending to average out over an orbital period. The computation of eddy currents and their resulting torques is quite complex, except for simple geometries, such as uniformly-conducting spheres (References 27, 28-31). Applications to more complex geometries can be done with numerical methods (References 28, 31, 32). In general, this torque should be proportional to the angular velocity and the square of the field, as well as to some high power of the size of the satellite.

A possible torque-producing mechanism would be the interaction of RF-generated currents in spacecraft surfaces and the ambient magnetic field. For radiated power levels currently envisaged, this effect may be small, and, in any event, would be expected to average to zero because of the cyclic nature of the currents. However, this aspect has not been investigated in detail.

If the spacecraft has permanent magnetic dipoles aboard, there will be torques produced given by the cross product of the dipole moment and the magnetic induction. Permanent dipole moments can be those of current loops or those of ferromagnets. Moreover, the field can induce dipole moments in strongly paramagnetic materials. These moments have been shown to be significant in certain spacecraft (References 2, 30, 33, 34, 35) and can be used for orientation and spin control (References 30, 32, 35). With magnetic test facilities in which the fields can be rotated, it should be possible to simulate these torques.

VARIOUS TORQUE MECHANISMS IN SPACECRAFT

This section discusses several secondary torque mechanisms which form no class. In addition, it concerns the satellite dynamics which must be understood to evaluate the effect, and sometimes the importance, of various torques on the orientation of a satellite relative to its center of mass.

Satellite Dynamics

The classical mechanics of the behavior of rigid bodies is so well known as to require no elaboration here. The best sources of the theoretical development with emphasis on the spacecraft case are found in References 4, 36, and 37. These are but two comments required concerning the torque problem. First, since all the torques we have considered are "feeble" relative to onboard reactions torques, and in view of the magnitude of asymmetric-satellite moments of inertia, the time intervals required for significant changes in spacecraft attitude are quite long as compared with the relaxation times of the many mechanisms leading to the torques. Therefore, in solving the dynamical equations of motion, instantaneous torque values can be used. Second, since the general dynamical equations for a rigid body involve six degrees of freedom, three of which can be written in terms of the the center-of-mass coordinates and three in terms of the orientation coordinates relative to the center of mass, the coupling of these equations must be considered. To a good approximation, the torque-dependent, center-of-mass equations are independent of the orientation equations (for small bodies), except insofar as the changes in orientation affect the forces leading to changes in orbital elements. However, the center-of-mass motion affects the torque equations strongly, since most torque-producing mechanisms are strong functions of the environment, which changes rapidly for orbital motion about most celestial bodies.

There are times when the fact that a satellite is not truly a rigid body is important. As is shown in References 4, 36, 37, and 38, a satellite subject to no external torque will lose energy of rotation such that it changes its orientation, because its stable spin axis is along the axis having the largest moment of inertia. This effect could be called a vibration-damping "torque."* It has, in fact, been used for attitude control.

*See Appendix B.

Radiation Pressure

Obviously if a satellite is not area-symmetric with respect to the center-of-mass on a projection plane perpendicular to sources of radiation, a torque due to radiation pressure can exist. In the solar system, probably only the sun has a density of radiation sufficient to make this pressure a significant torque mechanism. The problem of computing the magnitude of this effect is quite straightforward (References 3, 4) and only complicated by complex geometry and the uncertain knowledge of the reflection properties of surfaces. The first complication is a purely mathematical one; but the latter is quite serious, and leads to large uncertainties.

Solid-Body Impact

Space is permeated with a large flux of more-or-less solid bodies of large velocities. If they strike a spacecraft, impact angular momentum will, of course, be imparted to it. The magnitude and frequency of such momentum transfers are quite uncertain, not only because of the relatively unknown nature of the mass and speed distributions of the impacting bodies, but also because of the somewhat uncertain resistance properties of the satellite materials.

Electric Torque

If an electric dipole moment is aboard and if the satellite enters an electric field, a torque will result. No known electric fields of any significant magnitude exist in space, and the charge separation on board is small, being due primarily to the surface charge accumulation caused by induction.

Gravity-Gradient Torque

This well-known torque (References 4, 39-43) is significant in many cases of interest, and is being utilized for attitude control. Without damping, in an orbit, it leads to oscillations of spacecraft attitude, but no constant rotation. Provided the moments of inertia and the gravity field are known, it is readily calculable.

General

It would appear that, to a high order of precision, all of the torque-producing mechanisms are (instantaneously) independent of each other. Only if a torque were to produce a distortion of the structure (impossible for the feeble effects considered), or if the field produced by one mechanism interacted with those of another, need interaction be considered. The latter does, of course, occur, but must be very small. Even in the case of the eddy-current torque, where quite large (relative to those of other mechanisms) body currents are generated, the field produced by these currents, for the low satellite spin velocities extant, is orders of magnitude smaller than the ambient field causing the currents.

Many of the torque mechanisms considered in this paper, as well as some of the vector components of many, while momentarily large, average to zero or a small value over finite times* (commonly, an orbital period). This fact should always be kept in mind when evaluating the importance of a torque, since satellite rotation velocities resulting from these feeble torques are low.

*But see Reference 44.

REFERENCES

1. Beck, J.W., "Aerodynamic Coefficients of Wings and Fuselages in Rarefied Gas Flow," in: The Fluid Dynamic Aspects of Space Flight, Gordon and Breach, 1966.
2. Naumann, R.J., "Observed Torque-Producing Forces Acting on Satellites," in: Dynamics of Earth Satellites, New York: Academic Press, 1963. See also Reference 33.
3. Evans, . . ., "Aerodynamic and Radiation Disturbance Torques on Satellites Having Complex Geometry," in: Torques and Attitude Sensing in Earth Satellites, New York: Academic Press, 1964.
4. "Orbiting Solar Observatory Satellite," NASA SP-57, 1965.
5. Davis, L.J., et al., Exterior Ballistics of Rockets, New York: Van Nostrand, 1958.
6. Hohl, F., "The Electromagnetic Torques on Spherical Earth Satellites in a Rarefied Partially Ionized Atmosphere," NASA TR R-231, 1966.
7. Davis, R.J., Whipple, F.L., and Zirker, J.B., Scientific Uses of Earth Satellites, University of Michigan, 1956.
8. De Leeuw, J.H., "A Brief Introduction to Ionospheric Aerodynamics," in: Rarefied Gas Dynamics, Vol. 2, Suppl. 4, Advances in Applied Mechanics, New York: Academic Press, 1967.
9. Medved, D.B. "On the Formation of Satellite Electron Sheaths Resulting from Secondary Emission and Photoemission," in: Interactions of Space Vehicles with an Ionized Atmosphere, New York: Pergamon Press, 1965.
10. Opik, E.J. "Particle Distribution and Motion in a Field of Force," in: Interactions of Space Vehicles with an Ionized Atmosphere, New York: Pergamon Press, 1965.
11. Walker, E.H., "Plasma Sheath and Screening around a Stationary Charged Sphere and a Rapidly Moving Charged Body," in: Interactions of Space Vehicles with an Ionized Atmosphere, New York: Pergamon Press, 1965.
12. Shea, J.J., "Collisionless Plasma Flow Around a Conducting Sphere," in: Rarefied Gas Dynamics, Vol. 2, Suppl. 4, Advances in Applied Mechanics, New York: Academic Press, 1967.
13. Hohl, F., and Wood, G.P., "The Electrostatic and Electrodynamic Drag Forces on a Spherical Satellite in a Rarefied Partially Ionized Atmosphere," in: Rarefied Gas Dynamics, Vol. 2, Suppl. 2, 1963.
14. Al'pert, I.L., et al., Space Physics With Artificial Satellites, Consultants Bureau, 1965.
15. Sawchuk, W., "Wake of a Charged Prolate Spheroid at Angle of Attack in a Rarefied Plasma," in: Rarefied Gas Dynamics, Vol. 2, Suppl. 2, 1963.
16. Brundin, "Effects of Charged Particles on the Motion of an Earth Satellite," AIAA Jour. 1:2529, 1963.

17. Pitts, W.C., and Knechtel, E.D., "Electric Drag on Satellites—Theory and Experiment," in: The Fluid Dynamic Aspects of Space Flight, Vol. 1, Gordon and Breach, 1966.
18. Clayden, W.A., "Facilities to Simulate the Aerodynamics of Charged Particles in the Ionosphere," in: The Fluid Dynamic Aspects of Space Flight, Gordon and Breach, 1966.
19. Chute, F.S., and Walker, G.B., Canadian Aeronautics and Space Jour. 11:219, 1965.
20. Bruscaiglioni, A., et al., Alta Frequenza, 32:768, 1963.
21. Rose, M.E., Multipole Fields, New York: John Wiley, 1955.
22. Dewitt, C.M. and Jensen, H.D., Z. Naturforsch. 8a:267, 1953.
23. Harrington, R.F., Time-Harmonic Electromagnetic Fields, New York: McGraw-Hill, 1961.
24. Chu, L.J., "Physical Limitations of Omni-Directional Antennas," Appl. Phys. 19(12): 1163-1175, 1948.
25. Morse, P.M., and Feshbach, H., Methods of Theoretical Physics, New York: McGraw-Hill, 1953.
26. Papas, C.H., "Theory of Electromagnetic Wave Propagation," New York: McGraw-Hill, 1965.
27. Smythe, W.R., Static and Dynamic Electricity, New York: McGraw-Hill, 1950.
28. Hohl, F. "The Electromagnetic Torques on Spherical Earth Satellites in a Rarefied Partially Ionized Atmosphere," NASA TR R-231, 1966.
29. Halverson, R.P., IEEE Trans. Aerospace and Navigational Elec. 11:118, 1964.
30. Wilson, R.H., Jr., Rotational Magnetodynamics and Steering of Space Vehicles, NASA Technical Note D-566, 1961. See also Reference 34.
31. Smith, G.L., A Theoretical Study of the Torques Induced by a Magnetic Field on Rotating Cylinders and Spinning Thin-Wall Cones, Cone Frustums and General Body of Revolution, NASA TR R-129, 1962.
32. McElvain, . . ., "Satellite Angular Momentum Removal Utilizing the Earth's Magnetic Field," in: Torques and Attitude Sensing in Earth Satellites," New York: Academic Press, 1964.
33. Colombo, "On the Motion of Explorer XI Around Its Center of Mass," in: Torques and Attitude Sensing in Earth Satellites, New York: Academic Press, 1964.
34. Naumann, "An Investigation of the Observed Torques Acting on Explorer XI," in: Torques and Attitude Sensing in Earth Satellites, New York: Academic Press, 1964.
35. Wilson, . . ., "Exploitation of Magnetic Torques on Satellites," in: Torques and Attitude Sensing in Earth Satellites, New York: Academic Press, 1964.
36. Thomson, W.T., Introduction to Space Dynamics, Wiley, 1961.
37. Halfman, R.L., Dynamics, Vol. 1, Addison-Wesley, 1962.

38. Reiter, . ., and Thomson, . ., "Rotational Motion of Passive Space Vehicles," in: Torques and Attitude Sensing in Earth Satellites, Academic Press, 1964.
39. "Passive Gravity-Gradient Stabilization," NASA SP-107, 1966.
40. Fischell, . ., "Passive Gravity-Gradient Stabilization for Earth Satellites," in: Torques and Attitude Sensing in Earth Satellites, New York: Academic Press, 1964.
41. Roberson, . ., "Generalized Gravity-Gradient Torques," in: Torques and Attitude Sensing in Earth Satellites, New York: Academic Press, 1964.
42. Nidey, R.A., "Gravitational Torque on a Satellite of Arbitrary Shape," ARS Jour. 30:203, 1960.
43. Roberson, R.E., "Alternate Form of a Result by Nidey," ARS Jour. 31:1292, 1961.
44. Beletsky, V.V., "Some Problems of Motion of Artificial Satellites About the Center of Mass," in: Dynamics of Satellites, Academic Press, 1963.
45. Etkin, . ., Spin Decay of a Flexible Satellite by Structural Dissipation of Energy, UTIAS (University of Toronto Institute of Aerophysics) Report 105, 1965.
46. Etkin, . ., and Hughes, . ., Spin Decay of a Class of Satellites Caused by Solar Radiation, UTIAS Report 107, 1965. See also NASA SP-107, 1966.

APPENDIX A

Are the electrons and ions in the ionosphere in thermal equilibrium, even in the absence of a spacecraft? Certainly not during the day in, say, the peak of the F region. There must be a high-energy tail to the distribution. This tail could cause a satellite to acquire a quite large negative potential. The same lack of equilibrium must exist in radiation belts, which are characterized by long relaxation times.

An upper limit to the positive potential that a satellite can acquire due to photo-emission can be estimated to be about 6 volts, since the emitted electrons are of low energy. However, for secondary emission caused by ions or, more importantly, by neutrals, the potential can be much greater, in principle, perhaps even hundreds of volts, for the high densities present at low altitudes. (See Beard and Johnson, "Ionospheric Limitations of Attainable Satellite Potentials," J. Geophys. Res. 66:12, 1961).

APPENDIX B

An interesting mechanism for structural hysteresis effects on spin rate, one which is of current interest, concerns long, flexible booms on spacecraft. Bending of the booms can result from two causes: gravity-gradient forces (Reference 45) and thermal bending (Reference 46). For a satellite rotating with respect to the gravity vector, a periodic storage and release of strain energy results, which can lead to spin decay. For orbital motion, there is also the possibility of resonance effects between the frequency of strain release and the natural frequency of the boom.

Although thermal bending in itself cannot cause spin decay, since the energy originates in the thermal source (solar radiation) – not in the spin kinetic energy –, because of thermal delay times, a resonant transfer of rotational momentum can occur for a spinning satellite. For a non-spinning satellite, if the bending is such that the boom enters a non-elastic range, there is the possibility of shock-excitation of boom oscillation when the boom enters or leaves the shadow of the radiation source.

MICROWAVE AMPLIFICATION AND GENERATION EMPLOYING SOLID STATE BULK EFFECT DEVICES

S. V. Jaskolski*

ABSTRACT

The immediate goal of this project was the in-house construction of a solid state microwave source, generating 100 mw, of continuous power, at 55 GHz. Because the state of the art lacks the degree of sophistication in device construction required to accomplish this feat, this goal was not attained. It is our opinion that this goal will not be achieved employing the pure Gunn mode, but will be achieved employing the LSA mode of operation of a Gunn effect device. In the process of attempting to attain this goal, we have successfully developed an extremely reliable contacting technique which will be of particular use for epitaxial material. Also, reproducible pulse-operated devices have been constructed which function as either oscillators or amplifiers. In addition, the existence of a heretofore unrecognized difficulty in device construction has been established, namely, the importance of trapping levels in the forbidden gap of GaAs. Finally, an anomalous photo-effect has been observed in bulk GaAs, in which, as the wavelength is increased, the induced photovoltage reverses polarity, in a symmetrical fashion, at energies corresponding approximately to the fundamental band gap energy.

INTRODUCTION

The immediate goal of this project was the in-house construction of a solid state microwave source, generating 100 mw, of continuous power, at 55 GHz. With this goal in mind, all single solid state devices are totally eliminated from application with the unique exception of bulk effect or, somewhat synonymously, "Gunn" effect devices (References 1, 2). The "Gunn" effect is a quantum mechanical phenomenon, initially observed by J. B. Gunn in 1963, although previously theoretically postulated by Ridley and Watkins (Reference 3) and Hilsum (Reference 4). The phenomenon occurs in bulk and polycrystalline material which possesses a particular band structure in k (momentum) space. The bulk samples do not contain any junctions, other than the low resistance, ohmic, non-rectifying, non-injecting metal to semiconductor contacts.

The generation of RF energy always requires the existence, somewhere within the circuit, of negative resistance. The mechanism by which the Gunn effect negative resistance is attained can be simply understood when one recalls that the carrier effective mass in a semiconductor is inversely proportional to the curvature of the energy band diagram in k (momentum) space. The conduction band structure of GaAs in the reduced Brillouin zone is illustrated in Figure 1, along with the effective mass and the corresponding mobility values for each valley. Note that the secondary or subsidiary or satellite minima (which are sixfold degenerate) possess far less curvature than the lowest minima. Hence, if a carrier can be transferred from the lowest minima to the subsidiary minima, its effective mass is drastically increased and, correspondingly, its mobility is drastically reduced. If the appropriate scattering mechanism is available to supply the momentum change required in the valley transfer process, a carrier can be made to transfer from the lowest minima to the subsidiary minima by simply supplying to the sample a sufficient amount of energy.

*Marquette University, Milwaukee, Wisconsin.

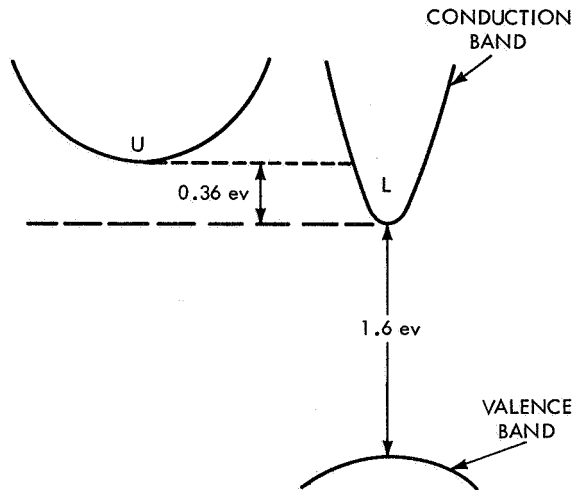


Figure 1—The conduction and valence band structure of GaAs. The carrier effective mass and mobility for the lower valley, L, and the upper valley, U, are as follows:

	Lower Valley	Upper Valley
Effective Mass	$0.72 m_0$	$1.2 m_0$
Mobility (cm^2/vsec)	5×10^3	100

m_0 = rest mass of an electron

In practice, the predominant scattering mechanism in polar semiconducting GaAs is optical phonon scattering (assuming doping concentrations less than 10^{17} /cc) (Reference 5), which can account for the required momentum (mutation of the k vector) change in the valley transfer process. Hence, when an increasing dc voltage is placed across an n-type GaAs sample, the carrier - or, rather, carriers - "move up" in energy in the lowest valley ($k = 0$). However, when a sufficiently large dc voltage is applied, the carrier energy in the lowest valley can exceed 0.36 eV and, at this time, the carriers will scatter into the subsidiary minima and, from a quantum mechanical viewpoint, will take on the characteristics of that valley. The critical or threshold field for the valley transfer process in GaAs is on the order of 3,000 v/cm (References 6, 7, 8).

Physically, one places a dc voltage across the sample of n-type GaAs, and increases the voltage. Correspondingly, the current increases, at first linearly, but eventually non-linearly, reflecting the dependence of the carrier mobility on the electric field (References 9, 10, 11). When the threshold field is reached, a sufficient number of carriers are transferring to the subsidiary minima so that the mobility term in the conduction current density takes on the value of the subsidiary minima mobility. Hence, the current decreases with an increase in voltage, and a bulk negative resistance effect is obtained, as illustrated in Figure 2.

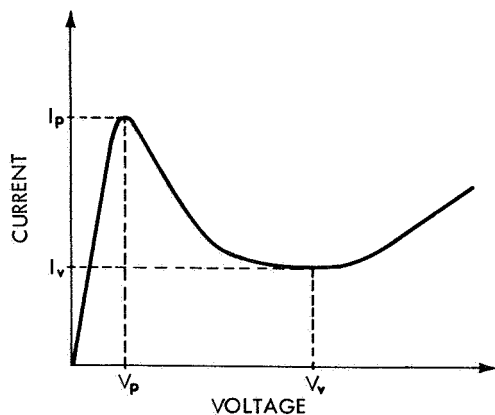


Figure 2—The volt-ampere (or velocity-field) characteristic for a GaAs Gunn type bulk effect device.

Shockley has shown that this is an unstable situation, and that when the critical field is exceeded, the field within the sample becomes highly non-uniform (Reference 12). A typical non-uniform field is illustrated in Figure 3(a), where the total area under the field versus distance plot must satisfy the boundary condition. Furthermore, as experimentally verified (References 1, 2), Shockley has shown that the sample field non-uniformity convectively propagates, as illustrated in Figures 3(b) to 3(d). During the convective propagation process, the high field region, or domain, grows in amplitude and decreases in width. Correspondingly, in general, the field throughout the remainder of the sample (termed the sample low field) decreases, so as always to satisfy the boundary condition. The peak field within the convectively propagating domain has been shown experimentally (References

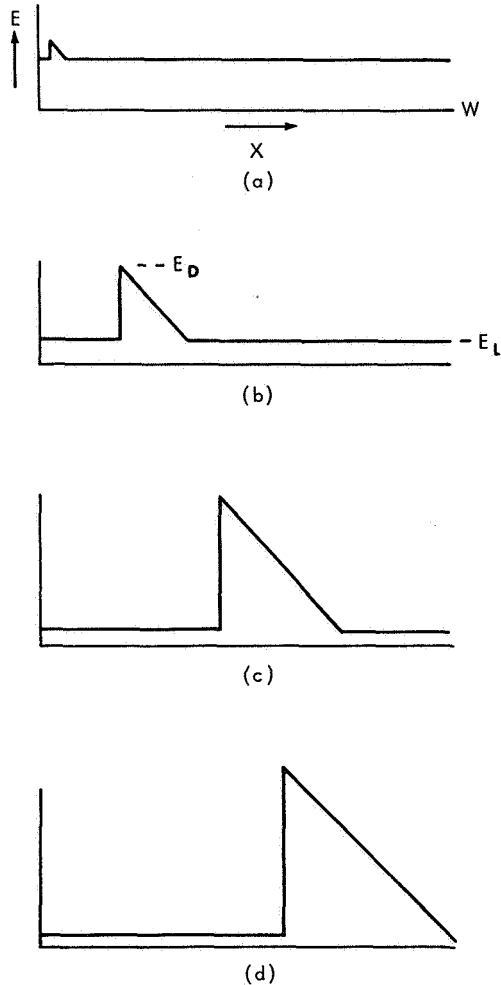


Figure 3—This sequence illustrates the formation and convective propagation of a high field domain within a Gunn type bulk effect device biased into the negative resistance region, as a function of position. The sample length is W . The domain forms, convectively propagates, and exits from the bulk sample at microwave frequencies, thereby producing microwave current oscillations. As the domain propagates, the peak domain field, E_D , as in (b), increases in magnitude, and the sample low field, E_L , as in (b), decreases in magnitude, as shown in the sequence of figures. For simplicity, the ordinate and abscissa are labeled only in Figure 3(a).

13, 14) and theoretically (References 15, 16) to exceed 80kv/cm, and the sample low field approaches 1,300 v/cm (References 15, 16, 17). Each time the propagating domain exits from the sample, a burst of current is observed. In a homogeneous sample, due to polarization effects, the domain originates at the cathode and exits at the anode. Hence the oscillation frequency is inversely proportional to the sample length and directly proportional to the carrier drift velocity. Thus, assuming a carrier drift velocity of 1×10^7 cm/sec, a sample 100 microns thick will oscillate at 1 gHz. The frequency of oscillation is commonly termed the Gunn transit time frequency, f_T .

Hence, the Gunn effect is basically a transit time effect, a fact of vast importance to those interested in solid state microwave generation. Since there is no junction present, capacitance plays a negligible role in terms of frequency determination. To increase the oscillation frequency, one simply decreases the sample length. Since the sample cross-sectional area is irrelevant, arbitrarily large cross-sectional area samples can be constructed, and hence phenomenal power handling capabilities can be foreseen. It should be mentioned that the phenomenon has also been observed in InP and CdTe (Reference 18), both compound semiconductors possessing band structures similar to that of GaAs.

The qualitative discussion presented thus far is simplicity in itself, but adequate to provide a basis for mutual discussion. In practice, many subtle difficulties have arisen in the construction and implementation of bulk effect or Gunn effect devices. Although the phenomenon was observed in 1963, reliable commercial devices have yet to be marketed.

In terms of construction, the difficulties are: (a) obtaining homogeneous material of accurately known carrier concentration and carrier mobility, (b) construction of low resistance, ohmic, non-rectifying, non-injecting contacts, (c) determination of the electrically active length as well as the physical sample length, (d) construction of reliable, long-lifetime contacts, (e) obtaining adequate heat dissipation so as to promote the continuous operation of the devices, (f) obtaining CW operation. In addition, since GaAs is an extremely brittle material, extreme difficulties in sample handling are incurred.

Experimentally, the major difficulty concerns inconsistency relative to the theoretically expected results. In general, Gunn effect type devices have been observed to generate frequencies much greater than the Gunn transit time frequency, f_T (References 13, 15, 19), equal to the Gunn transit time frequency (References 15, 20, 21), and much less than the Gunn transit time frequency (References 15, 21, 22 23). Hakki and Knight have observed drastically different experimental microwave results from devices made from the same ingot, but subjected to different contact alloy temperature cycles (Reference 21). In addition, Copeland (Reference 20) and Shaw and Shuskus (Reference 23) have observed a new mode of oscillation in Gunn effect type devices which is definitely not a transit time effect. Copeland has termed this mode of operation, which results in greater frequency and power capabilities than the normal Gunn transit time effect, the Limited Space-charge Accumulation, or LSA, mode.

Thus, because of the difficulties with device construction and circuit implementation encountered in bulk effect semiconductors, a large amount of research is being actively pursued. Although the primary goal of this project was to develop bulk effect Gunn type oscillators and amplifiers, the above-mentioned difficulties were so prevalent that the following sub-categories were deemed advisable as "steps along the way":

1. Develop a theoretical analysis of domain dynamics, with the goal being to explain the large number of seemingly anomalous experimental results (References 15, 19, 21, 22).
2. Experiment with device construction techniques, that is, sample handling, preparation, contacting, and heat dissipation techniques.
3. Employ the constructed devices as oscillators and/or amplifiers. Determine the effect, on the microwave performance of these devices, of sample resistivity, sample preparation, and contact alloying techniques.

THEORETICAL ANALYSIS

A great amount of theoretical effort has been devoted towards developing an understanding of Gunn effect domain dynamics (References 6, 7, 24). Unfortunately, the results contain such a large degree of mathematical sophistication that their usefulness is all but totally lost. In addition, the theoretical results verify nothing other than the Gunn transit time mode, and hence are of no use in explaining the large amount of anomalous data reported.

To obtain a more heuristic knowledge of domain dynamics, the author has recently developed, prior to his joining the Goddard Summer Workshop, a graphical analytical technique of analysis of domain motion, which is being published elsewhere (Reference 16). The results of the graphical analytical technique do explain all of the anomalous modes which have been experimentally observed (References 13, 15, 16, 19-22). The salient points of the results of this analysis will now be qualitatively presented so as to serve as a basis for further discussion.

Five distinct bias-voltage-dependent modes of oscillation can be obtained from a given Gunn effect device in a given microwave circuit. These are listed alphabetically, in an order which corresponds to the increasing voltage ranges over which they are observed.

Mode A. This is a pulsed microwave mode of operation. It is observed at bias voltages over a narrow range just about the threshold voltage. The total sample voltage across the GaAs bulk effect device consists of the dc bias and a superimposed RF due to the voltage developed across the resonant circuit. If the period of the RF is much greater than 2γ , where γ is the normal Gunn transit time, and if the RF amplitude is such that over some portion of the RF cycle the total sample voltage drops below the dynamic (References 15, 16, 25, 26) threshold (the dynamic threshold voltage is less than the static threshold voltage and is of significance only when a domain exists within the sample), then the sample will be observed to oscillate in the normal Gunn transit time mode or at the normal Gunn transit time frequency while the total sample voltage exceeds the threshold voltage. However, when the total sample voltage is below the threshold, the device cannot oscillate and the sample current is determined by the low field current. Hence a pulsed microwave mode occurs, with the microwave oscillations being generated for approximately one-half the RF period. Employing a low-frequency scope, one sees a low-frequency relaxation oscillation (Reference 22), which corresponds to the RF period. This mode of operation has been observed in some of the samples constructed during the Summer Workshop. The RF period is determined by the external bias circuit and hence is extremely circuit-dependent. It occurs only near threshold because here the possibility is greatest that the initial oscillation is such that the microwave RF by-pass circuit is not functioning properly.

Mode B. When the bias is increased above threshold, the RF period is less than γ , and it is possible for the RF amplitude to be so large (particularly in a high Q circuit) that the total sample voltage drops below the dynamic threshold before the convectively propagating domain reaches the anode. Hence, the domain effectively travels a distance much less than the sample length, simply because the total sample voltage is not large enough to sustain it. The oscillation frequency is much greater than the Gunn transit time frequency; but the microwave power is much less, since the domain has not been allowed to grow to its full extent. Assuming an RF amplitude of essentially constant magnitude, as the dc bias is increased, the oscillation frequency will decrease because the total sample voltage lies below the dynamic threshold for successively shorter amounts of time. Correspondingly, the microwave power will increase because the domain is allowed to grow to a fuller extent. This mode is still a transit time mode, but the effective transit distance is rigidly controlled by the dc bias. For Gunn oscillators with a transit time frequency of 18 GHz, Mode B operation has been obtained which produced oscillation frequencies which varied from 35 to 28 GHz over a one-volt bias range (References 15, 16).

Mode C. Again assuming a constant RF amplitude, as the dc bias is increased, Mode B will eventually cease when the total sample voltage is such that it always exceeds the dynamic threshold. However, over a small voltage range exceeding the Mode B range, it is possible for the total sample voltage to lie, at some time during the RF period, between the dynamic and static threshold voltage. In this mode of operation, multi-frequency oscillation is usually observed, due to the multiple points of operation on the static-dynamic volt-ampere characteristic of the device.

Mode D. If the dc bias is further increased, and the RF amplitude is assumed to remain constant in magnitude, a bias point is reached where the total sample voltage never drops below the static threshold. In this case, the pure Gunn transit time mode is observed. The frequency of oscillation is essentially voltage-independent, and will be observed over a large bias voltage range up to essentially the valley voltage, V_v (see Figure 2).

Mode E. When the bias voltage exceeds the valley voltage, a new multi-frequency mode is observed, due to the possibility of more than one domain forming or existing within the sample. This mode has been experimentally observed by Gunn (Reference 13), and theoretically verified (References 15, 16).

The theoretical analysis then indicates the possibility of at least five unique voltage-dependent transit time modes in a given Gunn effect device. All of these modes have been experimentally observed and reported in the literature, and the theoretical correlation with the experimental results is quite satisfying (References 15, 16). In addition, of course, there is the sixth possible mode of operation of a Gunn effect device, not a transit time effect, namely, the LSA mode.

DEVICE CONSTRUCTION

Difficulties

In general, we have attempted to construct Gunn type bulk effect devices from n-type GaAs. The GaAs was purchased from the Monsanto Co. and was bulk material of the boat grown, oxygen doped variety. We have also employed epitaxial GaAs obtained from Monsanto. The use of epitaxial material was attempted because bulk GaAs cannot be lapped to thicknesses less than about 2 mils. Since the Gunn effect is a transit time effect, thinner material was desired in order to obtain higher oscillation frequencies. The epitaxial material was purchased in thicknesses ranging from 1 to 19 microns.

To construct a high-frequency, continuous-operation Gunn effect device, ohmic, non-rectifying, non-injecting contacts are required. Also, to obtain continuous operation, some adequate means of heat dissipation must be developed. To remove the heat, or rather to reduce the effects of electrical heating, several approaches, or a combination of these approaches, were taken. Most obviously, good heat sinking of the material is required. This fact in itself presented a problem, because of the limited variety of microwave packages available. Second, the thinner the sample, the smaller is the distance for the heat to travel through the material before it is removed. As pointed out, because of the brittle character of GaAs, bulk GaAs can practically be lapped down to a minimum thickness of 2 mils. Thus, to lessen the heating effects, thinner material is advisable, which is another reason why the use of epitaxial material was explored. Also, it has recently been pointed out that epitaxial GaAs has a positive temperature coefficient of resistance, as opposed to a negative temperature coefficient for bulk GaAs (Reference 27). Thus epitaxial GaAs has a built-in protection against thermal runaway. From this standpoint also, then, the use of epitaxial material seems advisable.

Because of the heating difficulties, that is, thermal runaway, we have not yet obtained continuous operation of any bulk effect devices. We have thus far always operated in the pulsed mode, and have reached a maximum duty cycle of about 65 percent. The primary difficulties we have encountered, other than heating, or rather thermal runaway, are the construction of contacts, annealing effects due to the contact alloying cycle, and packaging of the devices. Each of these difficulties will now be treated separately.

Contacts

Since the original observations by Gunn, it has become evident that the role of the electrical contact is not always negligible in what is primarily a bulk effect in GaAs (References 1, 2, 21, 28). It is desirable that the contact have a low, linear series resistance, be non-injecting in the presence of high applied fields, and be uniform and reproducible. It is also desirable that the contacted device be bidirectional, that is, function identically

in either direction. Tin has been largely employed as an alloyed contact for GaAs (References 2, 19, 28, 29), and was the initial contacting process attempted in this project. The GaAs samples were lapped and cleaned employing standard techniques. The GaAs die dimensions were on the order of $30 \times 30 \times 10$ mils. Two-, 5-, and 10-mil diameter tin spheres were alloyed onto both sides of the GaAs sample, the sample being held in a carbon jig. The alloying cycle lasted approximately four minutes, reaching a maximum of 450°C for about 20 seconds. Many samples appeared shorted after the alloying process, and those that were not shorted did electrically short out under the application of fields far below threshold for the Gunn effect. Occasionally, however, some functioning devices were constructed employing this technique. With the devices that did function, the microwave results usually consisted of multi-frequency fundamental oscillations, the fundamental frequencies being on the order of 2 to 3 GHz. These microwave results indicated that the tin contacts were not very uniform, so that there were several domains forming and existing, simultaneously, within the samples. Also, the oscillation frequencies for these samples were unusually high for the given sample thicknesses. This result indicated that the tin was diffusing, during the alloying process, a considerable distance into the bulk of the GaAs sample, thus effectively reducing the electrically active sample length.

Detailed examination of the shorted samples indicated that the tin tended to form islands on the GaAs surface and also to channel or "finger" deep into the bulk of the GaAs samples. On the basis of the microwave results of the functioning samples, this observation seemed to be verified. On the samples that were found to be shorted after the contact alloying process, it was found that the tin had channeled through the entire sample. In those that were not initially shorted, channeling still occurred, to such an extent that a low field actually produced a breakdown in the bulk of the material.

Low melting temperature indium alloys and pure indium were also investigated for their contact properties. The pure indium alloy contact process seemed to yield the best results in terms of the number of successfully contacted samples. The alloy cycle which proved most fruitful lasted over 20 minutes, with the maximum temperature of $350\text{-}400^\circ\text{C}$ being reached after approximately three minutes. This maximum temperature was maintained for at least two minutes, and was followed by an extremely slow cooling process so as to eliminate thermally induced stress and strain at the contacts.

Eventually, the indium alloy contact process evolved into a single cycle, in which an In-GaAs-In sandwich was placed into the microwave mount and the mount placed into the carbon jig. The sample was then alloy contacted within the microwave mount, employing an RF furnace.

The RF furnace was produced by Lepal High Frequency Laboratories, Inc., Model T-1-WH-MC2-A-B. The furnace itself proved to be a source of considerable irritation. Although the RF coil diameter was on the order of 1.5 inches, both radial and vertical temperature gradients existed. The radial gradient was of such a magnitude that samples placed simultaneously on opposite ends of a line drawn diametrically within the RF coil alloyed, in the temperature cycle, several minutes apart. Obviously, then, two samples being alloyed simultaneously encountered indeed distinctly different alloy cycles. This difficulty, as will be seen in the next section, is of significant importance in bulk effect device construction.

Further investigation of the contacting problem yielded still another and even more satisfactory contacting technique, particularly for the epitaxial layers. (With some of the very thin epitaxial layers, 1-10 microns, the alloying process always resulted in "punch-through," that is, shorting through the active epitaxial layer.) It was found that the eutectic alloy of Au and Ge, melting at 330°C , could be used to form excellent n+ contacts on GaAs and could be deposited by vacuum evaporation. However, the simultaneous occurrence of evaporation and alloying proved to be a difficult task; the film still tending to form

islands, and a two-cycle process, required to apply contacts to both sides of the GaAs, doubling the chances of contamination of the GaAs.

These difficulties were overcome by separating the evaporation and the alloying process. This separation was accomplished by adding a small amount of Ni (2-11 percent by weight) to the Au-Ge eutectic before evaporation. The presence of Ni tends to hold the Au-Ge melt in intimate contact with the GaAs, the resulting contact being uniform over the surface of the semiconductor. The order of the deposition of the contact constituents during evaporation depends on the temperature required to attain a specified vapor pressure: the Ge evaporates first (i.e. at 1,250°C at 10^{-2} torr) followed by Au (1,460°C) and then Ni (1,500°C). When the GaAs evaporated sample is alloyed, the Au and Ge recombine at the eutectic temperature, and owing to the low solubility of Ni in Au-Ge at the alloying temperature, the Ni layer remains intact and covers the liquid Au-Ge on the GaAs surface.

This evaporation-alloy technique proved to be the best contacting technique for both bulk and epitaxial material. Initially, the epitaxial material was alloyed on both sides and then diced to the desired cross-sectional area. The dicing of these samples pulled the alloy down the side of the epitaxial layers and shorted the 1-to-10-micron-thick active epitaxial layers. A mask is presently being prepared which will eliminate this difficulty. With the mask, the substrate side of the epitaxial layer will be totally covered. The epitaxial layer will have 3-mil dots evaporated onto its surface, separated by 30 mils, to allow for sample cutting with the wire saw.

At this time I would like to acknowledge the assistance of Mr. Thomas P. Sciacca, without whose consistently diligent efforts the construction and development of the evaporation-alloy technique would not have been accomplished.

Annealing Effects in GaAs

In attempting to construct Gunn effect devices, a number of bulk GaAs samples, boat grown and oxygen compensated, were purchased from Monsanto. These samples are listed below, along with parameter information supplied by Monsanto.

Ingot No.	Resistivity (ohm-cm)	Carrier Concentration (per cc)	Mobility cm^2/vsec
G-1237	2.4	2×10^{15}	5,400
G 108-130/134	270	2.8×10^{13}	860
G-1222	2,700	4.55×10^{11}	5,250

A standard criterion which must be satisfied for the observance of Gunn effect oscillations is that the nL product exceed $2 \times 10^{11}/\text{cm}^2$ (References 6, 7, 21), where n is the carrier concentration and L is the sample length. If the nL product magnitude is less than the above number, there simply are not enough carriers present to cause convective domain propagation and hence microwave oscillation.

On this basis, ingot number G-1222, the high-resistivity sample, should not produce Gunn oscillations unless extremely thick samples are employed. Typically, all of our samples were less than 10 mils thick, which, for the 2,700 ohm-cm sample, results in an nL product of less than $1 \times 10^{10}/\text{cm}^2$, apparently ruling out all possibilities of observing Gunn effect type oscillations in this sample.

However, it is known that oxygen-compensated GaAs possesses many trapping levels (which contain or have trapped electrons) in the forbidden gap. These trapping levels have been investigated solely by photoelectronic analysis. In particular, the role of oxygen in controlling the electrical properties of GaAs has been investigated by Woods and Ainslie (Reference 30). Photoelectronic analysis of GaAs crystals has been performed by Bube (Reference 31), Michel et al. (Reference 32), and Turner et al. (Reference 33). In general, the results obtained by the above-mentioned authors suggest the existence of multiple donor levels in the forbidden gap of GaAs, from which carriers can be excited to the free state.

With this background, it was decided to attempt to "anneal" the oxygen-compensated 2,700 ohm-cm GaAs in a hydrogen-forming gas flow, at a high temperature, during the alloying process. The concept was to reduce the amount of oxygen compensation via the "annealing" process, and hence to increase the carrier concentration and reduce the sample resistivity, such that the required nL product would be obtained. There has been some evidence that different alloy cycles applied to the same sample host material result in drastically different microwave results (Reference 21), indicating that perhaps bulk heating, that is, heating of the bulk material, does in some way alter the host material characteristics.

Experimentally, the 2,700 ohm-cm oxygen-compensated GaAs was indium contacted in an alloying RF furnace, in the presence of hydrogen-forming gas flow. The samples were mounted in a varactor package. The sample lengths were on the order of 50 microns, with the resulting nL product on the order of $2.2 \times 10^9/\text{cm}^2$, far too low for Gunn oscillations to occur.

The initial alloy cycle reached 350°C for a maximum of two minutes. The varactor-mounted samples were placed in an X-band mount and pulsed with an HP 214A pulse generator. With sample voltages on the order of 150v and with pulse widths less than 3 microsec, no oscillations were detected. However, with the pulse amplitude constant, when the pulse width was increased above 3 microsec, microwave oscillations were generated. Figure 4 illustrates the result, where the 3-microsec time delay before the onset of Gunn oscillations is easily seen. The vertical scale for the square-shaped applied pulse signal is 50 v/cm, and the vertical scale for the detected microwave signal is 1 mv/cm. The repetition rate was 50 cps. Note that when the oscillation commences, the signal input amplitude decreases by about 10 volts, indicating the reduction in total sample resistance due to the presence of the oscillating Gunn high field domain. With this result, it was surmised that the alloying cycle had indeed reduced the oxygen compensation considerably, and that with the application of a voltage pulse of sufficient width, electrical heating produced thermal ionization of the remaining oxygen-compensated donors to such an extent that the required nL product for Gunn oscillations was eventually satisfied. In this particular instance, the fundamental oscillation frequency was 2.1 GHz, with harmonics of 8.4 and 10.5 GHz observed in the X-band. When the pulse amplitude was increased, the original time delay, which was 3 microsec before the onset of Gunn oscillations, could be decreased down to zero.

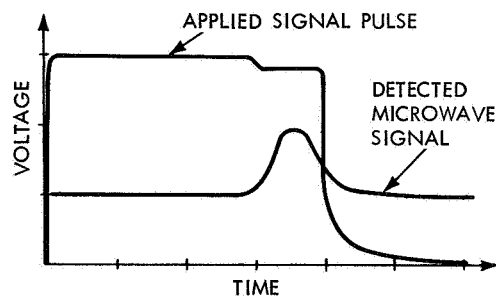


Figure 4—The applied square wave pulse ($V = 50 \text{ v/cm}$) and the detected microwave signal pulse ($V = 1 \text{ mv/cm}$). The horizontal time scale is one microsec per division. The alloy temperature for this device was 350°C.

Additional samples were constructed in an identical fashion, except that the maximum alloy temperature now was 250°C for two minutes. The experimental results are shown in

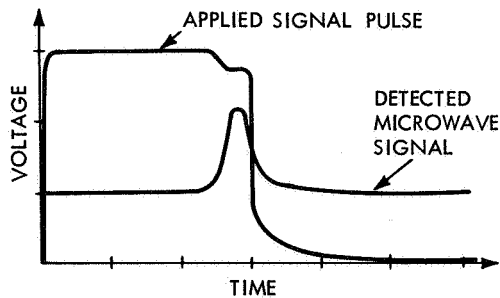


Figure 5—The applied square wave signal pulse ($V = 50$ v/cm) and the detected microwave signal pulse ($V = 1$ mv/cm). The horizontal scale is five microsec per division. The alloy temperature for this device was 250°C .

Figure 5. In this case Gunn oscillations were not observed until the repetition rate was increased to 800 cps and the pulse width to approximately 14 microsec. Thus, employing a lower alloy temperature cycle, the time delay before the onset of Gunn oscillations was increased to 14 microsec. The maximum time delay observed thus far has been on the order of 30 microsec.

Finally, several other 2,700 ohm-cm samples were prepared using an alloy cycle where the maximum temperature reached 400°C for two minutes. In this case, no time delay was observed, that is, the Gunn oscillations occurred essentially simultaneously with the occurrence of the input signal.

The following conclusions can be drawn. First, high resistivity GaAs, which is desirable for Gunn device construction in order to obviate low device impedance and to minimize thermal runaway effects, can be made to oscillate employing an electrical heating process. The oxygen levels play a key role in this mechanism, as they supply the required carriers so as to satisfy the nL product required for Gunn oscillations. Second, bulk heating of the sample in the RF furnace is quite different phenomenologically than electrical heating during device use. Apparently, bulk heating in a hydrogen atmosphere, employing the RF furnace, produces bulk, irreversible, "total annealing" type effects, in that it changes the amount of oxygen compensation, and hence the free carrier concentration. Electrical heating during device use appears to produce reversible heating effects, which also thermally produce the required free carrier concentration for Gunn effect oscillations. Physically, the two heating mechanisms are obviously significantly different; bulk heating producing irreversible effects, electrical heating producing reversible effects. Third, and certainly most important, the contact alloy cycle in oxygen-compensated GaAs is extremely critical in terms of device performance. It appears that a perturbation of several degrees is sufficient to considerably change the host material and hence the microwave properties of the device under construction. This fact undoubtedly plays a major role in explaining the anomaly that no two devices, even though both employing the same host material, perform the same as microwave devices. In the past, this trait has been generally attributed to changes in the contact or the contact mechanism. Although this idea certainly is valid to some extent, we advance that a more predominant factor is that the basic properties of the host oxygen-compensated material can be and actually are changed during the alloying cycle, and that this feature accounts for the reproducibility difficulties encountered.

A considerable amount of investigation remains to be performed. Although work is constantly being reported concerning trap concentrations and energies in GaAs, the complex distribution of deep levels in GaAs is still not established. At this point, however, it is clear that contacts are not by any means the only difficulty in producing repeatable Gunn effect devices, and that a more salient difficulty is the reorientation of trap concentrations and energies in oxygen-compensated GaAs, during the alloying cycle.*

* S. V. Jaskolski and W. E. Hughes, "Modes of Oscillation in a Gunn-type Transitime Oscillator," submitted to Appl. Phys. Lett.

Microwave Mounting

To reduce the effects of electrical heating, as has been already indicated, adequate heat sinking is required. To promote this end, the largest microwave packages produced were desired; but they were not available. This type of package is essentially that of a 1N23 X-band detector package, which no vendor was able to supply us.

To obviate this problem, many 1N23 packages were disassembled, the pn junction removed, and the entire package adequately cleaned. The 1N23 package has a gold whisker which contacts the semiconducting material. In turn, a bulk GaAs sample was mounted on the cleaned 1N23 stud, and the gold whisker turned into the ceramic package in such a way that electrical contact was made. Unfortunately, none of these experimental samples generated Gunn oscillations for more than two minutes. While the device was functioning, the oscillations were very noisy and intermittent. Eventually, the device either opened or shorted. Inspection of the device after failure indicated that proper gold whisker-semiconductor contact was not being achieved and that arcing, eventually causing either a short or an open, was very prevalent.

It is felt that if, after a pressure contact has been established, a forming pulse is applied to the device, coherent operation can eventually be obtained. This technique, however, was not investigated.

Several surface contact devices were successfully contacted and employed as microwave devices and in optical experiments (which are reported on under the heading "Photo-Effects" in this report). The surface devices consisted of two contacts placed on the same surface or side of a given GaAs sample. The contacts employed were indium contacts, utilizing the 20-minute-long alloy process previously described. The surface devices were mounted directly into waveguide structures, usually modified capacitive waveguide to coaxial coupling mounts. Depending upon the contact separation, frequencies between 0.1 and 5 GHz were obtained.

Most of the samples constructed were placed, employing the In-GaAs-In sandwich structure, into a pill-type varactor package whose total height was less than 0.15 inches. The contact alloying process was performed with the GaAs-contact sandwich in the microwave mount. Thus the contacting process and the mounting of the device into a microwave mount were designed to be just one process. Because multi-cycle heating processes were avoided, more consistent device performance was attained.

All of the pill-type varactor mounted samples were placed in specially designed, laboratory constructed, waveguide mounts. The waveguide mounts were constructed in the C, X, K, and M bands. The waveguide mounts for the packaged devices bear striking resemblance to slide screw tuners. A non-movable post sticks up from the bottom of the guide. Onto the top of the post, at approximately the vertical center of the waveguide, is placed the pill-type varactor packaged Gunn effect device. The top of the device is contacted by a spring loaded conducting post which is physically insulated from the waveguide. The post leads out of the top of the waveguide mount to a coaxial BNC connector. To this connector, then, the sample bias voltage is applied. The mount was the culmination of a design effort initiated by Mr. W. E. Hughes, who originally proposed this entire project.

DEVICE IMPLEMENTATION

Many operating devices were constructed from the 2.4, the 270 and the 2,700 ohm-cm samples. The most successful devices, to date, have all been indium alloy contacted at a temperature of 320°C, and mounted in the pill-type varactor package. All of the devices have operated only in the pulsed mode, yielding microwave fundamental frequencies,

harmonic rich, on the order of 1-5 GHz. It appears that all of these devices were functioning in the Gunn mode of oscillation. As explained in an earlier section, even the high resistivity samples, under appropriate conditions, were made to oscillate.

Most of the devices exhibited higher frequency modes of oscillation when the pulse width was increased sufficiently, the pulse amplitude remaining constant. In general, as the pulse width was increased, microwave signals of much greater power were detected. In addition, with several samples, the much higher oscillation frequency could be greatly pulled with microwave circuit tuning. These two facts, that is, a sudden increase in detected microwave power and wide circuit tuning effects, are strong, but not conclusive, indications that we were operating in the LSA mode (References 34, 35). These observations should definitely be pursued further, because of the observed improved performance as opposed to that when the device was performing in the purely Gunn mode. However, thermal runaway difficulties made these results difficult to reproduce. It is certain, however, that as the construction technique advances, this mode of operation will be more consistently reproduced, thus allowing further study.

Several researchers have obtained microwave amplification employing Gunn effect devices (References 21, 36). As pointed out by Thim and Barber (Reference 36), Gunn effect type devices where the nL product does not exceed $5 \times 10^{11}/\text{cm}^2$ will not oscillate, but will possess negative conductance over limited frequency ranges about multiples of the Gunn transit time frequency. Gains of 10-20db have been reported (Reference 36). Realizing that with the high resistivity GaAs we could control when the Gunn oscillations commence (see Figure 4), the notion was advanced that we might also be able to control the carriers in such a way that the nL product would be appropriate for amplification. Several attempts at amplification were made employing a standard reflection type waveguide amplifier circuit, in the C-band. To date, however, no conclusive results have been obtained.

PHOTO-EFFECTS

Prior to the author's joining the Goddard Summer Workshop, Mr. W. E. Hughes had performed some optical experiments on surface contacted GaAs samples. In general, he observed the induced photovoltage as a function of the wavelength of the incident radiation. His observations indicated that as the wavelength is increased, a reversal in the polarity of the induced photovoltage occurred at approximately the band gap energy. With the cooperation of Mr. W. Viehmann, we have investigated this phenomenon in great detail, employing a large number of samples of all available resistivities. In addition, we have performed the experiment employing samples contacted in a variety of manners and configurations.

In general, this effect is consistently observed in all of the samples employed, regardless of the contacting material, contacting mechanism, or contacting configuration. The results of our efforts are being published elsewhere.*

CONCLUSIONS

Because of the wide scope of our research efforts, many pages of conclusions could be presented. Very briefly, however, we have not yet reached the level of sophistication in device construction to yield the ultimate goal of this project, that is, the continuous generation of 55 GHz at 100 mw. Because of our efforts, it is our opinion that this goal

* W. Viehmann, S. V. Jaskolski, and W. E. Hughes, "Anomalous Optical Effect in Bulk Gallium Arsenide," submitted to Appl. Phys. Lett.

will not be achieved employing the pure Gunn mode, but will indeed be achieved employing the LSA mode of operation of a Gunn effect type of device. In the process of attempting to attain this goal, we have successfully developed an extremely reliable contacting technique (the evaporation-alloying technique) which will be of particular use for epitaxial and extremely thin bulk material. We have also constructed reasonably reproducible pulse-operated devices, which function as either oscillators or amplifiers. In addition, we have established the existence of the heretofore unrecognized difficulty in device construction, namely, the importance of trapping levels in the forbidden gap of the host GaAs. This result is being reported in the literature.** Finally, the observation of the anomalous photo-effect in bulk GaAs is unique,* and deserves much more attention.

ACKNOWLEDGMENTS

It is with great pleasure and sincerity that the author acknowledges and thanks Mr. W. E. Hughes, the initiator of this project. His consistent interest, concern, and assistance have made this an extremely fruitful experience from many points of view. Also, the diligent efforts of Mr. A. Guerra in the construction of the desired devices are gratefully acknowledged. The cooperation of Mr. T. Sciacca and Mr. W. Viehmann in many phases of this project is also gratefully acknowledged. The author would also like to express his gratitude to Dr. T. Leinhardt, of Virginia Polytechnic Institute, for many stimulating and informative discussions.

* W. Viehmann, S. V. Jaskolski, and W. E. Hughes, "Anomalous Optical Effect in Bulk Gallium Arsenide," submitted to Appl. Phys. Lett.

** S. V. Jaskolski and W. E. Hughes, "Modes of Oscillation in a Gunn-type Transit-time Oscillator," submitted to Appl. Phys. Lett.

REFERENCES

1. Gunn, J. B., "Microwave Oscillations of Current in III-V Semiconductors," Solid State Comm. 1:88-91, 1963.
2. Gunn, J. B., "Instabilities of Current in III-V Semiconductors," IBM J. Res. Dev. 9:141-159, 1964.
3. Ridley, B. K., and Watkins, T. B., "The Possibility of Negative Resistance Effects in Semiconductors," Proc. Phys. Soc. London 78:293-304, 1961.
4. Hilsum, C., "Transferred Electron Amplifiers and Oscillators," Proc. IRE 50:185-190, Feb. 1962.
5. Conwell, E. M., and Vassell, M. O., "High-Field Distribution Function in GaAs," IEEE Trans. ED-13:22-27, 1966.
6. McCumber, D. E., and Chynoweth, A. G., "Theory of Negative-Conductance Amplification and of Gunn Instabilities in 'Two-Valley' Semiconductors," IEEE Trans. ED-13:4-21, 1966.
7. Kroemer, H., "Nonlinear Space-Charge Domain Dynamics in a Semiconductor with Negative Differential Mobility," IEEE Trans. ED-13:27-40, 1966.
8. Shyam, M., Allen, J. W., and Pearson, G. L., "Effect of Variation of Energy Minima Separation on Gunn Oscillations," IEEE Trans. ED-13:63-67, 1966.
9. Conwell, E. M., and Brown, A. L., "Scattering of Hot Carriers in Germanium," J. Phys. Chem. Sol. 15:208-217, 1960.
10. Stratton, "The Influence of Interelectronic Collisions on Conduction and Breakdown in Covalent Semi-conductors," Proc. Roy. Soc. A. 242:355-373, 1957.
11. Yamashita, J., and Watanabe, M., "On the Conductivity of Non-polar Crystals in the Strong Electric Field, I," Progr. Theor. Phys. 12:443-453, 1954.
12. Shockley, W., "Negative Resistance Arising from Transit Time in Semiconductor Diodes," Bell Syst. Tech. J. 33:799-826, 1954.
13. Gunn, J. B., "Effect of Domain and Circuit Properties on Oscillations in GaAs," IBM J. Res. Dev. 10:310-321, 1966.
14. Heeks, J. S., "Some Properties of the Moving High-Field Domain in Gunn Effect Devices," IEEE Trans. ED-13, 68-79, 1966.
15. Jaskolski, S. V., Ph. D. dissertation, Marquette University, 1967.
16. Jaskolski, S. V., "Effect of Oxygen Compound on Gunn-effect Oscillators," IEEE Proc., to be published.
17. Copeland, J. A., "Electrostatic Domains in Two-Valley Semiconductors," IEEE Trans. ED-13:189-191, 1966.
18. Foyt, A. G., and McWhorter, A. L., "The Gunn Effect in Polar Semiconductors," IEEE Trans. ED-13:79-87, 1966.

19. Hasty, T. E., Cunningham, P. A., and Wisseman, W. R., "Microwave Oscillations in Epitaxial Layers of GaAs," IEEE Trans. ED-13:114-117, 1966.
20. Copeland, J. A., "Theoretical Study of a Gunn Diode in a Resonant Circuit," IEEE Trans. ED-14, 55-59, 1967.
21. Hakki, B. W., and Knight, S., "Microwave Phenomena in Bulk GaAs," IEEE Trans. ED-13:94-105, 1966.
22. Jaskolski, S. V., and Ishii, T. K., "Simultaneous Low-Frequency Relaxation and High Frequency Microwave Oscillation of a Bulk GaAs C. W. Oscillator," Elect. Lett. 3:12-13, 1967.
23. Shaw, M. P., and Shuskus, A. J., "Current Instability Above the Gunn Threshold," IEEE Proc. 54:1580-1581, 1966.
24. Allen, J. W., Shockley, W., and Pearson, G. L., "Gunn Domain Dynamics," J. Appl. Phys. 37:3191-3194, 1966.
25. Heeks, J. S., Woode, A., and Sandbank, C., "The Mechanism and Device Applications of High Field Instabilities in Gallium Arsenide," Radio Elect. Eng. 30:377-387, 1965.
26. Heinle, W., "Determination of Current Waveform and Efficiency of Gunn Diodes," Elect. Lett. 3:52-54, 1967.
27. Berson, B. E., and Yegna Narayan, S., "L-Band Epitaxial Gunn Oscillators," IEEE Proc. 55:1078, 1967.
28. Hasty, T. E., Marquette University Dept. of Elect. Eng., Colloquium, April 25, 1967.
29. Day, G. F., "Microwave Oscillations in High-Resistivity GaAs," IEEE Trans. ED-13: 88-94, 1966.
30. Woods, J. F., and Ainslie, N. G., "Role of Oxygen in Reducing Silicon Contamination of GaAs during Crystal Growth," J. Appl. Phys. 34:1469-1475, 1963.
31. Bube, R. H., "Photoelectronic Analysis of High Resistivity Crystals: (a) GaAs, (b) Sb_2S_3 ," J. Appl. Phys. 31:315-322, 1960.
32. Michel, A. E., Turner, W. J., and Reese, W. E., "Photoconductivity and Optical Absorption Measurements on n-type GaAs," Bull. Am. Phys. Soc. 8:215, 1963.
33. Turner, W. J., Pettit, G. D., and Ainslie, N. G., "Luminescence of GaAs Grown in Oxygen," J. Appl. Phys. 34:3274-3276, 1963.
34. Copeland, J. A., "CW Operation of LSA Oscillator Diode - 44 to 88 GHz," Bell Syst. Tech. J. 46:284-287, 1967.
35. Copeland, J. A., "GaAs Bulk Oscillators Stir Millimeter Waves," Electronics 40(12):96, 1967.
36. Thim, H. W., and Barber, M. R., "Microwave Amplification in GaAs Bulk Semiconductors," IEEE Trans. ED-13:110-114, 1966.



PSEUDOPOTENTIAL METHOD IN THE THEORY OF DEFECTS
IN CRYSTALS - THE DIAMOND STRUCTURE

M. M. Sokoloski

ABSTRACT

A pseudopotential method is employed to calculate the electronic energy up to second order in time-independent perturbation theory and an Ewald-Fuchs potential to calculate the electrostatic energy for a static imperfect crystal with D defects. The static energy consists of geometry-dependent terms called the structure factors. These factors, in turn, are readily evaluated for the case of a dynamic crystal to obtain the dynamic energy. The difference in dynamic and static energy is quadratic in displacements from the equilibrium positions. As a result, all of the force constants can be obtained and should be dependent on the long-range interactions due to the inclusion of conduction and valence electron energy terms. Therefore, a means of obtaining long-range interactions between defects is achieved. The future program of the calculation is discussed.

INTRODUCTION

Defects play a very important role in the electrical, mechanical, and magnetic properties of crystals. In the elemental semiconductors such as Si and Ge, defects can drastically alter the electronic and vibrational modes of the crystal.* Indeed, these defects can so perturb the electronic wave functions that trapping and recombination levels are created in the band gap. The resulting traps can decrease the photoconductivity as well as other electronic parameters. As a result, the efficiency of any photovoltaic device such as solar cells is apt to suffer.

Satellites, which employ solar cells as energy conversion devices, can be severely affected in orbits that take them through the radiation belts. The energetic particles trapped in these belts can cause atomic displacements, thus creating defects. These defects can be very simple, i.e. vacancies or interstitials of either impurity or host atoms; or they can be quite complicated, such as vacancy-vacancy, vacancy-impurity, or other combinations.

Nevertheless, out of this maze of defect conglomerations, the vacancy is perhaps the most important - it can trap charge carriers. Also, since the diamond lattice is quite open, the vacancy, once created, has no trouble migrating through the lattice.** When it encounters a substitutional defect such as a dopant atom or the more common "interstitial" oxygen atom, it forms a very stable complex defect which in turn can have trapping and recombination levels in the forbidden gap. Therefore, it is of utmost importance to study this point defect in the diamond lattice.

* The literature in this field is quite exhaustive. See Reference 1.

** The maximum portion of volume that can be filled by hard spheres is only 46 percent of the packing density for closest-packed structures in which many metals crystallize (Reference 2).

So far, it has been experimentally determined that the migration energy for a positively charged vacancy in Si is about 0.33 eV and that for negatively charged vacancies somewhat lower (Reference 3), while that for Ge is about 0.9 eV and probably independent of charge state (Reference 4). Meanwhile, interstitials have yet to be experimentally identified in Si and Ge.

Earlier attempts to calculate the formation and migration energies of vacancies in covalent crystals have used a Morse, or a Morse and Born lattice potential with the harmonic approximation and a Morse potential for the interactions between atoms (References 5 and 6). However, there is no theoretical justification for using such potentials in the case of tetrahedrally bonded covalent crystals such as Si and Ge. Also since these defects interact at long ranges, it is desirable to have some mechanism, namely, conduction electrons, through which the interaction manifests itself.

A T-matrix approach formerly had been employed in such a calculation, but free-electron wave functions of zero order were employed as pointed out by Callaway and Hughes (References 7 and 8). The latter two, in turn, used a Green's function approach using Wannier functions for their basis functions. However, the fact that symmetry has been used limits the usefulness of this method to the calculations of properties of only one defect. Actually the defects are interacting with other defects, and as a result all symmetry is destroyed. It is this interaction energy which is to be calculated.

GENERAL THEORY

It has been known for some time that a pseudopotential calculation gives quite good results in the calculation of the electronic bands in covalent crystals (Reference 9). This technique was extended thoroughly by Harrison in the calculation of various atomic properties of metals (Reference 10). This technique has been extended here to an arbitrary number of defects in a crystal lattice in an attempt to calculate the formation, migration, and interaction energies for and among the defects.

The first section is essentially a review of the pseudopotential method. The value of the pseudopotential method manifests itself in the fact that a nearly free plane wave equation, where the new potential is a pseudopotential, is manipulated out of the exact one-electron Schrodinger equation. It also turns out that the pseudopotential, $W(\mathbf{r})$, is small and therefore can be treated as a perturbation as was done by Harrison in his approach in metals.* It is also shown in this section that both the pseudopotential and the pseudowave function are non-unique. The fact that this is so is exploited in the third section (Calculation of the Pseudopotential and Pseudowave Function) by finding the smoothest pseudowave function by minimizing the normalized matrix elements of the pseudopotential. This smoothest pseudopotential is next linearized, and it is shown that this new potential is a good approximation in calculating the electronic energy up to second order.

The first two sections lay the groundwork for calculations on the imperfect crystal which are begun in the third section. Here the pseudowave function and potential are calculated for a crystal with D defects. It is also shown rigorously that these pseudowave functions and potentials are also non-unique. Therefore, the smoothest pseudowave function is determined in the fourth section just as in the second. The fifth section now concerns itself with the factorization of the nondiagonal matrix elements of the D defect pseudopotential which occur in the electronic energy obtained from a second-order

* An effect pseudopotential employing only several Fourier coefficients has been used by Brust (Reference 11) in calculating the electronic spectra of Ge and Si.

perturbation calculation and the calculation of the electronic energy. The electronic energy now includes a term called the structure factor, which is strictly geometry-dependent, multiplied by an energy-wavenumber characteristic which is dependent on the crystal potential and pseudopotential.

The sixth section is a calculation of the electrostatic energy using an Ewald-Fuchs potential in place of a Coulomb potential. The calculation is done as if point ions were embedded in a sea of electrons, the whole configuration being electrically neutral. A Fourier transform of the potential is made to bring about geometry-dependent terms. The final form of the electrostatic energy looks very similar to one of the terms in the electronic energy, i.e. products of structure factor terms appear.

Finally, in the seventh section each ion is displaced from its equilibrium position and the dynamical energy of the lattice is calculated in the harmonic approximation. Then the difference between the energy of the dynamic and that of the static crystal is obtained. This term is quadratic in the displacements. As a result, the force constants can be found, which now incorporate the long-range interactions due to incorporation of the conduction and valence electron energy and also interactions due to vibrations of the atomic nuclei. No crystal symmetry has been assumed. If one or two defects are introduced into the crystal, all the force constants change. The next step in the calculation is to compute the normal modes of vibration and then the total energy, including the ground state energy, of the imperfect crystal. This will be done for arbitrary temperature and distribution of defects, by using a simple force-constant model. However, force constants between all cores should be retained, since the calculation of the force constants in the first place retains long-range interactions.

REVIEW OF THE PSEUDOPOTENTIAL METHOD

The one-electron Hamiltonian of the crystal is given by

$$H = T + V(\mathbf{r}), \quad (1.1)$$

where $V(\mathbf{r})$ is some suitable self-consistent potential, i.e. Hartree or Hartree-Fock, seen by each electron. The exact electronic wave functions of the crystal will then be eigenfunctions of the time-independent Schrödinger equation, i.e.

$$H \Psi_{\mathbf{k},n} = E_{\mathbf{k},n} \Psi_{\mathbf{k},n}, \quad (1.2)$$

where the subscript n designates the n -th eigenstate of energy $E_{\mathbf{k},n}$.

A nearly free plane wave is constructed as follows:

$$\chi_{\mathbf{k}} = e^{i\mathbf{k}\cdot\mathbf{r}} - \sum_{a,l} B_{al} \psi_a(\mathbf{r} - \mathbf{r}_l), \quad (1.3)$$

where $\psi_a(\mathbf{r} - \mathbf{r}_l)$ is the a -th core state centered at \mathbf{r}_l . The nearly free plane wave is made orthogonal to every core state, $(\psi_{al}, \chi_{\mathbf{k}}) = 0$, and this in turn fixes the coefficients $B_{al} = (\psi_{al}, e^{i\mathbf{k}\cdot\mathbf{r}})$. * These nearly plane waves are known as orthogonalized plane waves (OPW). The true wave function, $\Psi_{\mathbf{k}}$, where the eigenstate label is now dropped,

* The notation here means the scalar product of two functions defined as $(\psi, \varphi) = \int \psi^* \varphi \, d\mathbf{r}$ or the following scalar product involving an operator: $(\psi, \theta \varphi) = \int \psi^* \theta \varphi \, d\mathbf{r}$.

in order to keep the notation simple, is now expanded in a linear combination of orthogonalized plane waves since they form a complete set of functions, i.e.

$$\begin{aligned}\Psi_{\mathbf{k}} &= \sum_{\mathbf{q}} a_{\mathbf{q}}(\mathbf{k}) \chi_{\mathbf{k}+\mathbf{q}} \\ &= \sum_{\mathbf{q}} a_{\mathbf{q}}(\mathbf{k}) e^{i(\mathbf{k}+\mathbf{q}) \cdot \mathbf{r}} - \sum_{a l \mathbf{q}} a_{\mathbf{q}}(\mathbf{k}) \langle \psi_{a l}, e^{i(\mathbf{k}+\mathbf{q}) \cdot \mathbf{r}} \rangle \psi_{a l}.\end{aligned}\quad (1.4)$$

The plane wave states are next normalized to the volume of the crystal, Ω , so that $|\mathbf{k}\rangle = \Omega^{-1/2} e^{i\mathbf{k} \cdot \mathbf{r}}$, and the a -th core state is defined as $|a l\rangle = \psi_{a l}(\mathbf{r} - \mathbf{r}_l)$. Then Equation 1.4 can be rewritten in bra and ket notation as

$$\Psi_{\mathbf{k}} = \sum_{\mathbf{q}} a_{\mathbf{q}}(\mathbf{k}) \left(|\mathbf{k}+\mathbf{q}\rangle - \sum_{a l} |a l\rangle \langle a l | \mathbf{k}+\mathbf{q}\rangle \right),$$

or

$$= \sum_{\mathbf{q}} a_{\mathbf{q}}(\mathbf{k}) \left(1 - \sum_{a l} |a l\rangle \langle a l | \right) |\mathbf{k}+\mathbf{q}\rangle.\quad (1.5)$$

An operator, called the projection operator since it projects any function onto the core states, is defined as

$$\mathbf{P} = \sum_{a l} |a l\rangle \langle a l |,$$

and Equation 1.5 can finally be written in terms of \mathbf{P} as

$$\Psi_{\mathbf{k}} = \sum_{\mathbf{q}} a_{\mathbf{q}}(\mathbf{k}) (1 - \mathbf{P}) |\mathbf{k}+\mathbf{q}\rangle.*\quad (1.6)$$

This in turn is placed into Equation 1.2 and the following expression is obtained:

$$\sum_{\mathbf{q}} a_{\mathbf{q}}(\mathbf{k}) \mathbf{H} (1 - \mathbf{P}) |\mathbf{k}+\mathbf{q}\rangle = E_{\mathbf{k}} \sum_{\mathbf{q}} a_{\mathbf{q}}(\mathbf{k}) (1 - \mathbf{P}) |\mathbf{k}+\mathbf{q}\rangle.\quad (1.7)$$

This is now rearranged into a more suitable form by taking all terms involving the projection operator to the left-hand side, i.e.

$$\begin{aligned}(\mathbf{T} + \mathbf{V}(\mathbf{r})) \sum_{\mathbf{q}} a_{\mathbf{q}} |\mathbf{k}+\mathbf{q}\rangle + E_{\mathbf{k}} \mathbf{P} \sum_{\mathbf{q}} a_{\mathbf{q}} |\mathbf{k}+\mathbf{q}\rangle - \mathbf{H} \mathbf{P} \sum_{\mathbf{q}} a_{\mathbf{q}} |\mathbf{k}+\mathbf{q}\rangle = \\ E_{\mathbf{k}} \sum_{\mathbf{q}} a_{\mathbf{q}} |\mathbf{k}+\mathbf{q}\rangle.\end{aligned}\quad (1.8)$$

*The projection operator is sometimes defined as $\mathbf{P} = |a l\rangle \langle a l |$. Here the projection operator as defined is not equal to one because the sum is over an incomplete set of states.

A new function, called the pseudowave function, is defined as

$$\varphi_{\mathbf{k}} = \sum_{\mathbf{q}} a_{\mathbf{q}}(\mathbf{k}) |\mathbf{k} + \mathbf{q}\rangle, \quad (1.9)$$

and all the terms involving the projection operator and crystal potential are collected and called the pseudopotential

$$W(\mathbf{r}) = V(\mathbf{r}) + (E_{\mathbf{k}} - H) P. \quad (1.10)$$

With these simplifications Equation 1.8 becomes

$$[T + W(\mathbf{r})] \varphi_{\mathbf{k}}(\mathbf{r}) = E_{\mathbf{k}} \varphi_{\mathbf{k}}(\mathbf{r}). \quad (1.11)$$

In essence, a transformation has been found which leaves the original eigenvalue invariant. The new equation strongly resembles that of the nearly free electron (NFE) model and demonstrates why the NFE is so remarkably accurate for its simplicity. The core states are the same as those in the isolated atom, but their energies are different. Nevertheless, they are still eigenstates of the Hamiltonian, since they form narrow fully occupied bands in the crystal, i.e.

$$H |\alpha l\rangle = E_{\alpha} |\alpha l\rangle. \quad (1.12)$$

Equation 1.10 can also be rewritten as

$$W(\mathbf{r}) = V(\mathbf{r}) + \sum_{\alpha l} (E_{\mathbf{k}} - E_{\alpha}) |\alpha l\rangle \langle \alpha l|. \quad (1.13)$$

The true wave function (Equation 1.5) can also be written in terms of the pseudowave function by means of Equation 1.9 as

$$\Psi_{\mathbf{k}} = (1 - P) \varphi_{\mathbf{k}}. \quad (1.14)$$

A very important property of the pseudopotential and pseudowave function which will be fully exploited later is that they are not unique. In other words, the pseudopotential can be replaced by an arbitrary pseudopotential of the form

$$W(\mathbf{r}) \varphi_{\mathbf{k}}(\mathbf{r}) = V(\mathbf{r}) \varphi_{\mathbf{k}}(\mathbf{r}) + \sum_{\alpha l} [F(\mathbf{r}, \alpha l), \varphi_{\mathbf{k}}(\mathbf{r})] \psi_{\alpha l}, \quad (1.15)$$

where $F(\mathbf{r}, \alpha l)$ is an arbitrary function of \mathbf{r} , and labels α and l , and the original eigenvalue will remain invariant. This can be demonstrated by substituting Equation 1.15 into Equation 1.11 and by writing the eigenfunction and eigenvalue arbitrarily as χ and E' :

$$H \chi + \sum_{\alpha l} [F(\mathbf{r}, \alpha l), \chi] \psi_{\alpha l} = E' \chi. \quad (1.16)$$

The scalar product is now taken with the true wave function

$$(\Psi_{\mathbf{k}}, H \chi) + \sum_{\alpha} [F(\mathbf{r}, \alpha l), \chi] (\Psi_{\mathbf{k}}, \psi_{\alpha l}) = E' (\Psi_{\mathbf{k}}, \chi), \quad (1.17)$$

and this leads to

$$E_{\mathbf{k}}(\Psi_{\mathbf{k}}, \chi) = E'(\Psi_{\mathbf{k}}, \chi). \quad (1.18)$$

For $E' = E_{\mathbf{k}}$, χ is non-orthogonal to $\Psi_{\mathbf{k}}$ and satisfies an equation whose eigenvalue is $E_{\mathbf{k}}$; therefore, it is or contains the pseudowave function. For the pseudowave function, an arbitrary linear combination of core states can be added to it without affecting the original true wave function; to demonstrate this fact, the following function is defined:

$$\varphi'_{\mathbf{k}} = \varphi_{\mathbf{k}} + \sum_{al} b_{al} |al\rangle. \quad (1.19)$$

This is inserted into Equation 1.14 to yield

$$\begin{aligned} \Psi_{\mathbf{k}} &= \left(1 - \sum_{al} |al\rangle \langle al| \right) \left(\varphi_{\mathbf{k}} + \sum_{al} b_{al} |al\rangle \right) \\ &= \varphi_{\mathbf{k}} + \sum_{al} b_{al} |al\rangle - \sum_{al} |al\rangle \langle al| \varphi_{\mathbf{k}} - \sum_{al} b_{al} |al\rangle \\ &= (1 - \mathbf{P}) \varphi_{\mathbf{k}}, \end{aligned} \quad (1.20)$$

which, of course, is the true wave function. Thus, both assertions are proven.

OPTIMIZATION AND LINEARIZATION OF THE PSEUDOPOTENTIAL

As was seen, the pseudopotential defined in Equations 1.10 and 1.13 is not unique, in that any linear combination of core wave functions can be added to the pseudowave function, and the result will still remain a solution of Equation 1.11 with the same eigenvalue. Therefore, a particular pseudowave function can be obtained by defining a smoothest pseudowave function to be that which has a minimum value of

$$\frac{\int |\nabla^2 \varphi_{\mathbf{k}}|^2 d\mathbf{r}}{\int |\varphi_{\mathbf{k}}|^2 d\mathbf{r}}. \quad (2.1)$$

The numerator can be written, by partial integration, as

$$\int |\varphi_{\mathbf{k}}|^2 d\mathbf{r} = |\varphi_{\mathbf{k}}^* \nabla \varphi_{\mathbf{k}}|_{\text{surface}} - \int \varphi_{\mathbf{k}}^* \nabla^2 \varphi_{\mathbf{k}} d\mathbf{r},$$

or

$$= - \int \varphi_{\mathbf{k}}^* \nabla^2 \varphi_{\mathbf{k}} d\mathbf{r}.$$

For $-(\varphi_{\mathbf{k}}, \nabla^2 \varphi_{\mathbf{k}})/(\varphi_{\mathbf{k}}, \varphi_{\mathbf{k}})$ being a minimum implies that $(\varphi_{\mathbf{k}}, \mathbf{W} \varphi_{\mathbf{k}})/(\varphi_{\mathbf{k}}, \varphi_{\mathbf{k}})$ will have a maximum. A slight variation is made on $\varphi_{\mathbf{k}}$, where b_{al} 's are small quantities, i.e.

$$\varphi'_{\mathbf{k}} = \varphi_{\mathbf{k}} + \sum_{al} b_{al} \psi_{al}$$

Then the variation of the normalized expectation value of W should be zero, i.e.

$$\langle \varphi'_k, W \varphi'_k \rangle / \langle \varphi'_k, \varphi'_k \rangle - \langle \varphi_k, W \varphi_k \rangle / \langle \varphi_k, \varphi_k \rangle = 0.$$

First, the matrix elements of W with respect to φ'_k are computed as follows:

$$\langle \varphi'_k, W \varphi'_k \rangle = \left\langle \varphi_k + \sum_{al} b_{al} \psi_{al}, W \varphi_k + \sum_{al} b_{al} W \psi_{al} \right\rangle,$$

or

$$\begin{aligned} &= \langle \varphi_k, W \varphi_k \rangle + \sum_{al} b_{al} \langle \varphi_k, W \psi_{al} \rangle + \sum_{al} b_{al}^* \langle \psi_{al}, W \varphi_k \rangle \\ &+ \sum_{al} \sum_{a'l'} b_{al} b_{a'l'}^* \langle \psi_{a'l'}, W \psi_{al} \rangle. \end{aligned}$$

Then the normalization constant is computed as follows:

$$\langle \varphi'_k, \varphi'_k \rangle = \left\langle \varphi_k + \sum_{al} b_{al} \psi_{al}, \varphi_k + \sum_{al} b_{al} \psi_{al} \right\rangle,$$

or

$$\begin{aligned} &= \langle \varphi_k, \varphi_k \rangle + \sum_{al} b_{al} \langle \varphi_k, \psi_{al} \rangle + \sum_{al} b_{al}^* \langle \psi_{al}, \varphi_k \rangle \\ &+ \sum_{al} \sum_{a'l'} b_{al} b_{a'l'}^* \langle \psi_{a'l'}, \psi_{al} \rangle. \end{aligned}$$

The normalized expectation value becomes

$$\begin{aligned} \frac{\langle \varphi'_k, W \varphi'_k \rangle}{\langle \varphi'_k, \varphi'_k \rangle} &= \frac{1}{\langle \varphi_k, \varphi_k \rangle} \left[\langle \varphi_k, W \varphi_k \rangle + \sum_{al} b_{al} \langle \varphi_k, W \psi_{al} \rangle + \sum_{al} b_{al}^* \langle \psi_{al}, W \varphi_k \rangle \right. \\ &+ \left. \sum_{al} \sum_{a'l'} b_{al} b_{a'l'}^* \langle \psi_{a'l'}, W \psi_{al} \rangle \right] \times \left[1 + \langle \varphi_k, \varphi_k \rangle^{-1} \sum_{al} b_{al} \langle \varphi_k, \psi_{al} \rangle \right. \\ &+ \left. \langle \varphi_k, \varphi_k \rangle^{-1} \sum_{al} b_{al}^* \langle \psi_{al}, \varphi_k \rangle + \langle \varphi_k, \varphi_k \rangle^{-1} \sum_{al} |b_{al}|^2 \right]^{-1}. \end{aligned}$$

The second product term is expanded to first order in b_{al} as follows:

$$\begin{aligned} \frac{(\varphi'_k, W \varphi'_k)}{(\varphi'_k, \varphi'_k)} &= \frac{1}{(\varphi_k, \varphi_k)} \left[(\varphi_k, W \varphi_k) + \sum_{al} b_{al} (\varphi_k, W \psi_{al}) + \sum_{al} b_{al}^* (\psi_{al}, W \varphi_k) \right. \\ &+ \sum_{al} \sum_{a'l'} b_{al} b_{a'l'}^* (\psi_{a'l'}, W \psi_{al}) \left. \right] \times \left[1 - (\varphi_k, \varphi_k)^{-1} \sum_{al} b_{al} (\varphi_k, \psi_{al}) \right. \\ &\left. - (\varphi_k, \varphi_k)^{-1} \sum_{al} b_{al}^* (\psi_{al}, \varphi_k) + \dots \right]. \end{aligned}$$

Terms up to first order in b_{al} are retained, as follows:

$$\begin{aligned} \frac{(\varphi'_k, W \varphi'_k)}{(\varphi'_k, \varphi'_k)} - \frac{(\varphi_k, W \varphi_k)}{(\varphi_k, \varphi_k)} &= \sum_{al} \left[(\varphi_k, W \psi_{al}) - \frac{(\varphi_k, W \varphi_k)}{(\varphi_k, \varphi_k)} (\varphi_k, \psi_{al}) \right] \frac{b_{al}}{(\varphi_k, \varphi_k)} \\ &+ \sum_{al} \left[(\psi_{al}, W \varphi_k) - \frac{(\varphi_k, W \varphi_k)}{(\varphi_k, \varphi_k)} (\psi_{al}, \varphi_k) \right] \frac{b_{al}^*}{(\varphi_k, \varphi_k)}. \end{aligned}$$

For the normalized variation of the expectation value of W to be zero, the quantity in the brackets should be zero. But since the b_{al} 's are arbitrary parameters, then the coefficients of b_{al} and b_{al}^* must be zero identically. This implies that

$$(\psi_{al}, W \varphi_k) = \frac{(\varphi_k, W \varphi_k)}{(\varphi_k, \varphi_k)} (\psi_{al}, \varphi_k), \quad (2.2)$$

which defines the matrix element for the "smoothest" pseudopotential. From Equation 1.13, the pseudopotential operating on any φ_k is

$$W \varphi_k = V(\mathbf{r}) \varphi_k + \sum_{al} (E_k - E_a) (\psi_{al}, \varphi_k) \psi_{al}. \quad (2.3)$$

If the inner product is taken on the left with ψ_{al} the following expression is obtained:

$$(\psi_{al}, W \varphi_k) = [\psi_{al}, V(\mathbf{r}) \varphi_k] + \sum_{a'l'} (E_k - E_{a'}) (\psi_{a'l'}, \varphi_k) (\psi_{al}, \psi_{a'l'}),$$

or
$$= [\psi_{al}, V(\mathbf{r}) \varphi_k] + (E_k - E_a) (\psi_{al}, \varphi_k). \quad (2.4)$$

This can be readily solved for $(E_k - E_a)$ as follows:

$$(E_k - E_a) = \frac{1}{(\psi_{al}, \varphi_k)} [(\psi_{al}, W \varphi_k) - (\psi_{al}, V \varphi_k)], \quad (2.5)$$

and in turn substituted into Equation 2.3 to obtain

$$W \varphi_{\mathbf{k}} = V(\mathbf{r}) \varphi_{\mathbf{k}} - \sum_{al} (\psi_{al}, V \varphi_{\mathbf{k}}) \psi_{al} + \sum_{al} (\psi_{al}, W \varphi_{\mathbf{k}}) \psi_{al}. \quad (2.6)$$

Next the smoothest pseudopotential matrix element is substituted for $(\psi_{al}, W \varphi_{\mathbf{k}})$, so that Equation 2.6 can finally be written as

$$W \varphi_{\mathbf{k}} = V \varphi_{\mathbf{k}} - \sum_{al} (\psi_{al}, V \varphi_{\mathbf{k}}) \psi_{al} + \frac{(\varphi_{\mathbf{k}}, W \varphi_{\mathbf{k}})}{(\varphi_{\mathbf{k}}, \varphi_{\mathbf{k}})} \sum_{al} (\psi_{al}, \varphi_{\mathbf{k}}) \psi_{al}, \quad (2.7)$$

which can be rewritten in terms of the projection operator as

$$W \varphi_{\mathbf{k}} = (1 - \mathbf{P}) V \varphi_{\mathbf{k}} + \frac{(\varphi_{\mathbf{k}}, W \varphi_{\mathbf{k}})}{(\varphi_{\mathbf{k}}, \varphi_{\mathbf{k}})} \mathbf{P} \varphi_{\mathbf{k}}. \quad (2.8)$$

Then $(\varphi_{\mathbf{k}}, W \varphi_{\mathbf{k}})$ can be readily calculated by taking the inner product on the left with $\varphi_{\mathbf{k}}^*$,

$$(\varphi_{\mathbf{k}}, W \varphi_{\mathbf{k}}) = [\varphi_{\mathbf{k}}, (1 - \mathbf{P}) V \varphi_{\mathbf{k}}] + \frac{(\varphi_{\mathbf{k}}, W \varphi_{\mathbf{k}})}{(\varphi_{\mathbf{k}}, \varphi_{\mathbf{k}})} (\varphi_{\mathbf{k}}, \mathbf{P} \varphi_{\mathbf{k}}),$$

or

$$\frac{(\varphi_{\mathbf{k}}, W \varphi_{\mathbf{k}})}{(\varphi_{\mathbf{k}}, \varphi_{\mathbf{k}})} = \frac{[\varphi_{\mathbf{k}}, (1 - \mathbf{P}) V \varphi_{\mathbf{k}}]}{(\varphi_{\mathbf{k}}, \varphi_{\mathbf{k}}) - (\varphi_{\mathbf{k}}, \mathbf{P} \varphi_{\mathbf{k}})}.$$

This in turn can be placed into Equation 2.8 to obtain the final result for the pseudopotential operating on the smoothest wave function, i.e.

$$W \varphi_{\mathbf{k}} = (1 - \mathbf{P}) V \varphi_{\mathbf{k}} + \frac{(\varphi_{\mathbf{k}}, (1 - \mathbf{P}) V \varphi_{\mathbf{k}})}{(\varphi_{\mathbf{k}}, \varphi_{\mathbf{k}}) - (\varphi_{\mathbf{k}}, \mathbf{P} \varphi_{\mathbf{k}})} \mathbf{P} \varphi_{\mathbf{k}}. \quad (2.9)$$

The optimum pseudopotential is next linearized in such a way that it will yield the same results in second-order perturbation theory as Equation 2.9. First the pseudopotential is expanded in terms of plane waves as in the first section,

$$\varphi_{\mathbf{k}} = \sum_{\mathbf{q}} a_{\mathbf{q}} |\mathbf{k} + \mathbf{q}\rangle, \quad (2.10)$$

and as in the perturbation expansion in Appendix A, a_0 is taken to be of first order. This is substituted into the pseudopotential equation (1.11) where the optimum pseudopotential (Equation 2.9) is used,

$$-\frac{\hbar^2}{2m} \nabla^2 |\varphi_{\mathbf{k}}\rangle + W |\varphi_{\mathbf{k}}\rangle = E_{\mathbf{k}} |\varphi_{\mathbf{k}}\rangle. \quad (2.11)$$

This in turn is multiplied through by the zero order $\varphi_{\mathbf{k}}$, $|\mathbf{k}\rangle$, to obtain

$$a_0 \frac{\hbar^2 k^2}{2m} + \langle \mathbf{k} | W | \varphi_{\mathbf{k}} \rangle = a_0 E_{\mathbf{k}}. \quad (2.12)$$

Again Equation 2.11 is multiplied through by $|\mathbf{k} + \mathbf{q}\rangle$ to obtain

$$a_{\mathbf{q}} \left(\frac{\hbar^2}{2m} \right) |\mathbf{k} + \mathbf{q}|^2 + \langle \mathbf{k} + \mathbf{q} | W | \varphi_{\mathbf{k}} \rangle = a_{\mathbf{q}} E_{\mathbf{k}}, \quad (2.13)$$

or

$$a_{\mathbf{q}} = \frac{\langle \mathbf{k} + \mathbf{q} | W | \varphi_{\mathbf{k}} \rangle}{E_{\mathbf{k}} - \frac{\hbar^2}{2m} |\mathbf{k} + \mathbf{q}|^2}, \quad (2.14)$$

which becomes, to first order in $E_{\mathbf{k}} = \hbar^2 k^2 / 2m$,

$$a_{\mathbf{q}} = \frac{\langle \mathbf{k} + \mathbf{q} | W | \varphi_{\mathbf{k}} \rangle}{\frac{\hbar^2}{2m} (k^2 - |\mathbf{k} + \mathbf{q}|^2)}. \quad (2.15)$$

Now $W | \varphi_{\mathbf{k}} \rangle$ is replaced by the form of Equation 2.9 to first order, i.e.

$$a_{\mathbf{q}} = \frac{\langle \mathbf{k} + \mathbf{q} | (1 - \mathbf{P}) \mathbf{V} | \mathbf{k} \rangle + \frac{\langle \mathbf{k} | (1 - \mathbf{P}) \mathbf{V} | \mathbf{k} \rangle}{1 - \langle \mathbf{k} | \mathbf{P} | \mathbf{k} \rangle} \cdot \langle \mathbf{k} + \mathbf{q} | \mathbf{P} | \mathbf{k} \rangle}{\frac{\hbar^2}{2m} (k^2 - |\mathbf{k} + \mathbf{q}|^2)}. \quad (2.16)$$

A comparison with $a_{\mathbf{q}}$ in Equation 17, Appendix A, suggests that the linearized pseudopotential is given by

$$W_L = (1 - \mathbf{P}) \mathbf{V} + \frac{\langle \mathbf{k} | (1 - \mathbf{P}) \mathbf{V} | \mathbf{k} \rangle}{1 - \langle \mathbf{k} | \mathbf{P} | \mathbf{k} \rangle}. \quad (2.17)$$

Now it must be shown that Equation 2.17 yields the same energy as the optimum pseudopotential to second order. With $a_0 = 1$ in Equation 2.12 the energy becomes

$$E_{\mathbf{k}} = \frac{\hbar^2 k^2}{2m} + \langle \mathbf{k} | W | \varphi_{\mathbf{k}} \rangle. \quad (2.18)$$

The energy from the above equation is now written out to second order, using Equation 2.10, as follows:

$$E_{\mathbf{k}} = \frac{\hbar^2 k^2}{2m} + \langle \mathbf{k} | (1 - \mathbf{P}) \mathbf{V} | \varphi_{\mathbf{k}} \rangle + \frac{\langle \varphi_{\mathbf{k}} | (1 - \mathbf{P}) \mathbf{V} | \varphi_{\mathbf{k}} \rangle}{\langle \varphi_{\mathbf{k}} | \varphi_{\mathbf{k}} \rangle - \langle \varphi_{\mathbf{k}} | \mathbf{P} | \varphi_{\mathbf{k}} \rangle} \langle \mathbf{k} | \mathbf{P} | \varphi_{\mathbf{k}} \rangle. \quad (2.19)$$

The second term above can be written by using Equation 2.10 as follows:

$$\langle \mathbf{k} | (1 - \mathbf{P}) \mathbf{V} | \varphi_{\mathbf{k}} \rangle = \langle \mathbf{k} | (1 - \mathbf{P}) \mathbf{V} | \mathbf{k} \rangle + \sum_{\mathbf{q}}' a_{\mathbf{q}} \langle \mathbf{k} | (1 - \mathbf{P}) \mathbf{V} | \mathbf{k} + \mathbf{q} \rangle ,$$

which includes the $\mathbf{q} = 0$ term and higher order terms, and the prime indicates a restricted sum, $\mathbf{q} \neq 0$. In a similar manner, the numerator of the third term can be expanded as follows:

$$\begin{aligned} \langle \varphi_{\mathbf{k}} | (1 - \mathbf{P}) \mathbf{V} | \varphi_{\mathbf{k}} \rangle \langle \mathbf{k} | \mathbf{P} | \varphi_{\mathbf{k}} \rangle &= \langle \mathbf{k} | (1 - \mathbf{P}) \mathbf{V} | \mathbf{k} \rangle \langle \mathbf{k} | \mathbf{P} | \mathbf{k} \rangle \\ &+ \sum_{\mathbf{q}}' a_{\mathbf{q}} \left[\langle \mathbf{k} | (1 - \mathbf{P}) \mathbf{V} | \mathbf{k} \rangle \langle \mathbf{k} | \mathbf{P} | \mathbf{k} + \mathbf{q} \rangle \right. \\ &+ \left. \langle \mathbf{k} | (1 - \mathbf{P}) \mathbf{V} | \mathbf{k} + \mathbf{q} \rangle \langle \mathbf{k} | \mathbf{P} | \mathbf{k} \rangle \right] \\ &+ \sum_{\mathbf{q}}' a_{\mathbf{q}}^* \langle \mathbf{k} + \mathbf{q} | \mathbf{P} | \mathbf{k} \rangle \langle \mathbf{k} | \mathbf{P} | \mathbf{k} \rangle . \end{aligned}$$

The denominator of the third term can also be expanded, as follows:

$$\begin{aligned} \left(\langle \varphi_{\mathbf{k}} | \varphi_{\mathbf{k}} \rangle - \langle \varphi_{\mathbf{k}} | \mathbf{P} | \varphi_{\mathbf{k}} \rangle \right)^{-1} &= \left(1 - \langle \mathbf{k} | \mathbf{P} | \mathbf{k} \rangle - \sum_{\mathbf{q}}' a_{\mathbf{q}} \langle \mathbf{k} | \mathbf{P} | \mathbf{k} + \mathbf{q} \rangle \right. \\ &\left. - \sum_{\mathbf{q}}' a_{\mathbf{q}}^* \langle \mathbf{k} + \mathbf{q} | \mathbf{P} | \mathbf{k} \rangle \right) \end{aligned}$$

or

$$\begin{aligned} &= \left(1 - \langle \mathbf{k} | \mathbf{P} | \mathbf{k} \rangle \right)^{-1} + \frac{\sum_{\mathbf{q}}' a_{\mathbf{q}} \langle \mathbf{k} | \mathbf{P} | \mathbf{k} + \mathbf{q} \rangle}{1 - \langle \mathbf{k} | \mathbf{P} | \mathbf{k} \rangle} \\ &+ \frac{\sum_{\mathbf{q}}' a_{\mathbf{q}}^* \langle \mathbf{k} + \mathbf{q} | \mathbf{P} | \mathbf{k} \rangle}{1 - \langle \mathbf{k} | \mathbf{P} | \mathbf{k} \rangle} . \end{aligned}$$

Equation 2.19 becomes, after substituting all expanded terms,

$$\begin{aligned} E_{\mathbf{k}} &= \frac{\hbar^2 k^2}{2m} + \langle \mathbf{k} | (1 - \mathbf{P}) \mathbf{V} | \mathbf{k} \rangle + \frac{\langle \mathbf{k} | (1 - \mathbf{P}) \mathbf{V} | \mathbf{k} \rangle \langle \mathbf{k} | \mathbf{P} | \mathbf{k} \rangle}{1 - \langle \mathbf{k} | \mathbf{P} | \mathbf{k} \rangle} \\ &+ \sum_{\mathbf{q}}' a_{\mathbf{q}} \left[\langle \mathbf{k} | (1 - \mathbf{P}) \mathbf{V} | \mathbf{k} + \mathbf{q} \rangle + \frac{\langle \mathbf{k} | (1 - \mathbf{P}) \mathbf{V} | \mathbf{k} \rangle \langle \mathbf{k} | \mathbf{P} | \mathbf{k} + \mathbf{q} \rangle}{1 - \langle \mathbf{k} | \mathbf{P} | \mathbf{k} \rangle} \right. \\ &\left. + \frac{\langle \mathbf{k} | (1 - \mathbf{P}) \mathbf{V} | \mathbf{k} + \mathbf{q} \rangle \langle \mathbf{k} | \mathbf{P} | \mathbf{k} \rangle}{1 - \langle \mathbf{k} | \mathbf{P} | \mathbf{k} \rangle} + \frac{\langle \mathbf{k} | (1 - \mathbf{P}) \mathbf{V} | \mathbf{k} \rangle \langle \mathbf{k} | \mathbf{P} | \mathbf{k} \rangle \langle \mathbf{k} | \mathbf{P} | \mathbf{k} + \mathbf{q} \rangle}{(1 - \langle \mathbf{k} | \mathbf{P} | \mathbf{k} \rangle)^2} \right] \end{aligned}$$

$$\begin{aligned}
& + \sum a_q^* \left[\frac{\langle \mathbf{k} + \mathbf{q} | (1 - \mathbf{P}) \mathbf{V} | \mathbf{k} \rangle \langle \mathbf{k} | \mathbf{P} | \mathbf{k} \rangle}{1 - \langle \mathbf{k} | \mathbf{P} | \mathbf{k} \rangle} \right. \\
& \left. + \frac{\langle \mathbf{k} | (1 - \mathbf{P}) \mathbf{V} | \mathbf{k} \rangle \langle \mathbf{k} | \mathbf{P} | \mathbf{k} \rangle \langle \mathbf{k} + \mathbf{q} | \mathbf{P} | \mathbf{k} \rangle}{(1 - \langle \mathbf{k} | \mathbf{P} | \mathbf{k} \rangle)^2} \right]. \tag{2.20}
\end{aligned}$$

The second and third terms are first-order terms from the linearized pseudopotential of Equation 2.17, while the next two terms are second-order corrections to the energy. The last four terms will be shown to be of order greater than two and thus can be neglected.

First it should be noted that

$$\mathbf{P} \mathbf{V} | \mathbf{k} \rangle = \sum_{al} | al \rangle \langle al | \mathbf{H} - \mathbf{T} | \mathbf{k} \rangle,$$

or

$$= \sum_{al} | al \rangle \langle al | \mathbf{k} \rangle \left(E_a - \frac{\hbar^2 k^2}{2m} \right), \tag{2.21}$$

which follows since \mathbf{H} , \mathbf{T} , and \mathbf{V} are hermitian. In Appendix B, it is shown that

$$\langle \mathbf{k} + \mathbf{q} | \mathbf{P} | \mathbf{k} \rangle^* = \langle \mathbf{k} | \mathbf{P} | \mathbf{k} + \mathbf{q} \rangle. \tag{2.22}$$

Then the following terms are calculated by using the linear pseudopotential.

$$\langle \mathbf{k} + \mathbf{q} | \mathbf{W} | \mathbf{k} \rangle^* = \langle \mathbf{k} + \mathbf{q} | (1 - \mathbf{P}) \mathbf{V} | \mathbf{k} \rangle^* + \frac{\langle \mathbf{k} | (1 - \mathbf{P}) \mathbf{V} | \mathbf{k} \rangle^*}{1 - \langle \mathbf{k} | \mathbf{P} | \mathbf{k} \rangle^*} \langle \mathbf{k} + \mathbf{q} | \mathbf{P} | \mathbf{k} \rangle^*,$$

or

$$\begin{aligned}
& = \langle \mathbf{k} | \mathbf{V} | \mathbf{k} + \mathbf{q} \rangle - \sum_{al} \langle \mathbf{k} | al \rangle \langle al | \mathbf{k} + \mathbf{q} \rangle \left(E_a - \frac{\hbar^2 k^2}{2m} \right) \\
& + \frac{\langle \mathbf{k} | (1 - \mathbf{P}) \mathbf{V} | \mathbf{k} \rangle}{1 - \langle \mathbf{k} | \mathbf{P} | \mathbf{k} \rangle} \cdot \langle \mathbf{k} | \mathbf{P} | \mathbf{k} + \mathbf{q} \rangle,
\end{aligned}$$

and

$$\begin{aligned}
\langle \mathbf{k} | \mathbf{W} | \mathbf{k} + \mathbf{q} \rangle & = \langle \mathbf{k} | \mathbf{V} | \mathbf{k} + \mathbf{q} \rangle - \sum_{al} \langle \mathbf{k} | al \rangle \langle al | \mathbf{k} + \mathbf{q} \rangle \left(E_a - \frac{\hbar^2 |\mathbf{k} + \mathbf{q}|^2}{2m} \right) \\
& + \frac{\langle \mathbf{k} | (1 - \mathbf{P}) \mathbf{V} | \mathbf{k} \rangle}{1 - \langle \mathbf{k} | \mathbf{P} | \mathbf{k} \rangle} \cdot \langle \mathbf{k} | \mathbf{P} | \mathbf{k} + \mathbf{q} \rangle.
\end{aligned}$$

Then the difference between these two terms gives the non-hermiticity of W , i.e.

$$\langle \mathbf{k} + \mathbf{q} | W | \mathbf{k} \rangle^* - \langle \mathbf{k} | W | \mathbf{k} + \mathbf{q} \rangle = \frac{\hbar^2}{2m} (k^2 - |\mathbf{k} + \mathbf{q}|^2) \langle \mathbf{k} | P | \mathbf{k} + \mathbf{q} \rangle. \quad (2.23)$$

Since the left-hand side is of first order and

$$\frac{\hbar^2}{2m} (k^2 - |\mathbf{k} + \mathbf{q}|^2)$$

is of zero order, $\langle \mathbf{k} | P | \mathbf{k} + \mathbf{q} \rangle$ must be of first order. Therefore, the last four terms in Equation 2.20 are of order greater than two. As a result, the linear pseudopotential agrees with the optimum pseudopotential up to second order. If Equation 2.17 is now multiplied by $\langle \mathbf{k} |$, then the diagonal matrix elements of the linear pseudopotential become

$$\langle \mathbf{k} | W | \mathbf{k} \rangle = \frac{\langle \mathbf{k} | (1 - P) V | \mathbf{k} \rangle}{1 - \langle \mathbf{k} | P | \mathbf{k} \rangle}, \quad (2.24)$$

which in turn can be substituted back into Equation 2.17 to yield a self-consistent relation for W as follows:

$$W | \mathbf{k} \rangle = (1 - P) V | \mathbf{k} \rangle + \langle \mathbf{k} | W | \mathbf{k} \rangle P | \mathbf{k} \rangle. \quad (2.25)$$

This can be rewritten by using Equation 2.20 in the following manner:

$$W | \mathbf{k} \rangle = V | \mathbf{k} \rangle + \langle \mathbf{k} | W | \mathbf{k} \rangle P | \mathbf{k} \rangle + \sum_{al} \left(\frac{\hbar^2 k^2}{2m} - E_a \right) | al \rangle \langle al | \mathbf{k} \rangle. \quad (2.26)$$

This self-consistent expression can be solved by successive iteration to obtain an expression involving only W on the left. This has been done in Appendix C.

CALCULATION OF THE PSEUDOPOTENTIAL AND PSEUDOWAVE FUNCTION FOR THE CASE OF POINT DEFECTS IN THE CRYSTAL WITH NO LATTICE RELAXATION

A linear combination of atomic orbitals will now be constructed for the case of N_σ identical substitutional defects and N_γ interstitial defects in a crystal of N_λ host atoms as follows:

$$\chi_{\mathbf{k}}^{(D)} = e^{i\mathbf{k} \cdot \mathbf{r}} - \sum_{\lambda, l} B_{\lambda l} \psi_{\lambda}(\mathbf{r} - \mathbf{r}_l) - \sum_{\sigma, s} C_{\sigma s} \psi_{\sigma}(\mathbf{r} - \mathbf{r}_s) - \sum_{\gamma, g} D_{\gamma g} \psi_{\gamma}(\mathbf{r} - \mathbf{r}_g)$$

or

$$= e^{i\mathbf{k} \cdot \mathbf{r}} - \sum_{\lambda l} B_{\lambda l} \psi_{\lambda l} - \sum_{\sigma, s} C_{\sigma s} \psi_{\sigma s} - \sum_{\gamma, g} D_{\gamma g} \psi_{\gamma g}. \quad (3.1)$$

The notation is such that Greek subscripts refer to the type of ion core; i.e. λ signifies host atom core states, σ the substitutional core states, and γ the interstitial core states. The corresponding Roman lower-case script, l , s , and g , refer to the host atom core,

substitutional atom core, and interstitial atom core sites, respectively. The total number of atoms will then be $N = N_\lambda + N_\sigma + N_\gamma$, and $D = N_\sigma + N_\gamma$. It should be noted that each of the sums is restricted in that l cannot take any value of s or g , while s cannot take any value of l or g , and likewise for g . In a similar manner as in the perfect crystal, the χ_k must now be made orthogonal to all core states, defect as well as host atom core states, i.e.

$$(\psi_{\lambda l}, \chi_k^{(D)}) = (\psi_{\sigma s}, \chi_k^{(D)}) = (\psi_{\gamma g}, \chi_k^{(D)}) = 0. \quad (3.2)$$

If there is no overlap, then eigenstates with corresponding different site and energy labels will be orthogonal in the following sense:

$$(\psi_{\lambda' l'}, \psi_{\lambda l}) = \delta_{\lambda \lambda'} \delta_{l l'}. \quad (3.3)$$

The same is true for core eigenstates of the impurity atoms if there is no overlap:

$$(\psi_{\gamma' g'}, \psi_{\gamma g}) = \delta_{\gamma \gamma'} \delta_{g g'}. \quad (3.4)$$

However, care must be taken with scalar products of host and defect core states. Although these terms do not enter the final calculations of this section, they are not zero.

The first scalar product of Equation 3.2 yields

$$0 = (\psi_{\lambda' l'}, e^{i\mathbf{k} \cdot \mathbf{r}}) - \sum_{\lambda l} B_{\lambda l} (\psi_{\lambda' l'}, \psi_{\lambda l}) - \sum_{\sigma s} C_{\sigma s} (\psi_{\lambda' l'}, \psi_{\sigma s}) - \sum_{\gamma g} D_{\gamma g} (\psi_{\lambda' l'}, \psi_{\gamma g}). \quad (3.5)$$

The last two scalar products of the above expression are zero. This implies that

$$B_{\lambda l} = (\psi_{\lambda l}, e^{i\mathbf{k} \cdot \mathbf{r}}). \quad (3.6)$$

The second and third scalar products of Equation 3.2 yield in a similar manner

$$C_{\sigma s} = (\psi_{\sigma s}, e^{i\mathbf{k} \cdot \mathbf{r}}) \quad (3.7)$$

and

$$D_{\gamma g} = (\psi_{\gamma g}, e^{i\mathbf{k} \cdot \mathbf{r}}) \quad (3.8)$$

respectively. The complete orthogonalized plane wave for $D = N_\sigma + N_\gamma$ defects becomes

$$\chi_k^{(D)} = |k\rangle - \sum_{\lambda l} |\lambda l\rangle \langle \lambda l | k\rangle + \sum_{\sigma s} |\sigma s\rangle \langle \sigma s | k\rangle + \sum_{\gamma g} |\gamma g\rangle \langle \gamma g | k\rangle. \quad (3.9)$$

And the true wave function becomes

$$\Psi_k^{(D)} = \sum_{\mathbf{q}} a_{\mathbf{q}}(\mathbf{k}) \chi_{\mathbf{k}+\mathbf{q}}^{(D)}, \quad (3.10)$$

or

$$= \sum_{\mathbf{q}} a_{\mathbf{q}}(\mathbf{k}) (1 - P_D) |k + \mathbf{q}\rangle,$$

where the D defect projection operator, \mathbf{P}_D , is

$$\mathbf{P}_D = \sum_{\lambda l} |\lambda l\rangle \langle \lambda l| + \sum_{\sigma s} |\sigma s\rangle \langle \sigma s| + \sum_{\gamma g} |\gamma g\rangle \langle \gamma g|, \quad (3.11)$$

and the D defect pseudopotential is given by

$$\mathbf{W}_D(\mathbf{r}) = \mathbf{V}_D(\mathbf{r}) + (\mathbf{E}_k^{(D)} - \mathbf{H}^{(D)}) \mathbf{P}_D,$$

or

$$\begin{aligned} &= \mathbf{V}_D(\mathbf{r}) + \sum_{\lambda l} (\mathbf{E}_k^{(D)} - \mathbf{E}_{\lambda l}) |\lambda l\rangle \langle \lambda l| + \sum_{\sigma s} (\mathbf{E}_k^{(D)} - \mathbf{E}_{\sigma s}) |\sigma s\rangle \langle \sigma s| \\ &+ \sum_{\gamma g} (\mathbf{E}_k^{(D)} - \mathbf{E}_{\gamma g}) |\gamma g\rangle \langle \gamma g|. \end{aligned} \quad (3.12)$$

With the addition of many more terms, the question arises whether, as in the first section, this pseudopotential is uniquely defined. To see that the D defect pseudopotential is still not uniquely defined, the following general pseudopotential is constructed:

$$\begin{aligned} \mathbf{W}(\mathbf{r}) = \mathbf{V}^{(D)}(\mathbf{r}) + \sum_{\lambda l} |\lambda l\rangle \langle \mathbf{F}_1(\lambda l)| + \sum_{\sigma s} |\sigma s\rangle \langle \mathbf{F}_2(\sigma s)| \\ + \sum_{\gamma g} |\gamma g\rangle \langle \mathbf{F}_3(\gamma g)|, \end{aligned} \quad (3.13)$$

where $\mathbf{F}_1(\lambda l)$, $\mathbf{F}_2(\sigma s)$, and $\mathbf{F}_3(\gamma g)$ are arbitrary functions of \mathbf{r} and core labels λ , σ , and γ . As in the first section, this is placed into

$$(\mathbf{T} + \mathbf{W}^{(D)}) \varphi_k^{(D)} = \mathbf{E}_k^{(D)} \varphi_k^{(D)}, \quad (3.14)$$

and by writing the eigenfunction and eigenvalue arbitrarily as χ and \mathbf{E}' , Schrödinger's equation now becomes

$$\begin{aligned} \mathbf{H}^{(D)} |\chi\rangle + \sum_{\lambda l} |\lambda l\rangle \langle \mathbf{F}_1(\lambda l)| \chi\rangle + \sum_{\sigma s} |\sigma s\rangle \langle \mathbf{F}_2(\sigma s)| \chi\rangle \\ + \sum_{\gamma g} |\gamma g\rangle \langle \mathbf{F}_3(\gamma g)| \chi\rangle = \mathbf{E}' \chi. \end{aligned} \quad (3.15)$$

Then in a similar manner as in Section I this is multiplied by $\langle \Psi_k^{(D)} |$ to become

$$\begin{aligned} \langle \Psi_k^{(D)} | \mathbf{H}^{(D)} | \chi\rangle + \sum_{\lambda l} \langle \mathbf{F}_1(\lambda l) | \chi\rangle \langle \Psi_k^{(D)} | \lambda l\rangle + \sum_{\sigma s} \langle \mathbf{F}_2(\sigma s) | \chi\rangle \langle \Psi_k^{(D)} | \sigma s\rangle \\ + \sum_{\gamma g} \langle \mathbf{F}_3(\gamma g) | \chi\rangle \langle \Psi_k^{(D)} | \gamma g\rangle = \mathbf{E}' \langle \Psi_k^{(D)} | \chi\rangle. \end{aligned} \quad (3.16)$$

But all the core states above have been made orthogonal to the D defect wave function $\Psi_k^{(D)}$. Therefore, since $H^{(D)}$ is hermitian, the following expression is obtained:

$$E_k^{(D)} \langle \Psi_k^{(D)} | \chi \rangle = E' \langle \Psi_k^{(D)} | \chi \rangle.$$

This demonstrates that $E' = E_k^{(D)}$ for $\Psi_k^{(D)}$ not orthogonal to χ . Therefore, the defect pseudopotential is not unique. Likewise it can be shown that the D defect pseudopotential is arbitrary within a linear combination of core states. A new D defect pseudopotential is defined as

$$\varphi'_k = \varphi_k + \sum_{\lambda l} b_{\lambda l} |\lambda l\rangle + \sum_{\sigma s} c_{\sigma s} |\sigma s\rangle + \sum_{\gamma g} d_{\gamma g} |\gamma g\rangle. \quad (3.17)$$

This in turn is placed into the definition of the true D defect wave function

$$\Psi_k^{(D)} = (1 - P_D) \varphi'_k$$

to obtain

$$\Psi_k^{(D)} = \left(1 - \sum_{\lambda l} |\lambda l\rangle \langle \lambda l| - \sum_{\sigma s} |\sigma s\rangle \langle \sigma s| - \sum_{\gamma g} |\gamma g\rangle \langle \gamma g| \right) \times \left(|\varphi_k^{(D)}\rangle + \sum_{\lambda l} b_{\lambda l} |\lambda l\rangle + \sum_{\sigma s} c_{\sigma s} |\sigma s\rangle + \sum_{\gamma g} d_{\gamma g} |\gamma g\rangle \right),$$

or

$$= (1 - P_D) \varphi_k^{(D)}. \quad (3.18)$$

Therefore the D defect pseudopotential is again not unique. Equations 3.10 and 3.11 can easily be generalized to the case of $n_1, n_2, n_3, \dots, n_i$ distinct substitutional defects and $m_1, m_2, m_3, \dots, m_j$ distinct interstitial defects.

OPTIMIZATION AND LINEARIZATION OF THE D DEFECT PSEUDOPOTENTIAL

The procedure followed here is identical to that in the second section. It was shown in the third section that the D defect pseudowave function is not uniquely defined, in that linear combinations of host and defect core states can be added to the pseudowave function with the result that the true eigenfunctions and eigenvalues remain invariant. As in the second section, a variation is made on $\varphi_k^{(D)}$ where the $b_{\lambda l}$'s, $c_{\sigma s}$'s, and $d_{\gamma g}$'s are small quantities:

$$\varphi'_k = \varphi_k^{(D)} + \sum_{\lambda l} b_{\lambda l} |\lambda l\rangle + \sum_{\sigma s} c_{\sigma s} |\sigma s\rangle + \sum_{\gamma g} d_{\gamma g} |\gamma g\rangle. \quad (4.1)$$

Then the variation of the normalized expectation value of $W^{(D)}$ should be zero for the smoothest D defect pseudowave function, i.e.

$$\frac{\langle \varphi'_k | W^{(D)} | \varphi'_k \rangle}{\langle \varphi'_k | \varphi'_k \rangle} - \frac{\langle \varphi_k^{(D)} | W^{(D)} | \varphi_k^{(D)} \rangle}{\langle \varphi_k^{(D)} | \varphi_k^{(D)} \rangle} = 0. \quad (4.2)$$

First

$$\langle \varphi'_k | \mathbf{W}^{(D)} | \varphi'_k \rangle = \left(\langle \mathbf{D} | + \sum b_{\lambda l}^* \langle \lambda l | + \sum c_{\sigma s}^* \langle \sigma s | + \sum d_{\gamma g}^* \langle \gamma g |, \right. \\ \left. \mathbf{W}^{(D)} | \mathbf{D} \rangle + \sum b_{\lambda l} \mathbf{W}^{(D)} | \lambda l \rangle + \sum c_{\sigma s} \mathbf{W}^{(D)} | \sigma s \rangle + \sum d_{\gamma g} \mathbf{W}^{(D)} | \gamma g \rangle \right), \quad (4.3)$$

where

$$\varphi_k^{(D)} \equiv | \mathbf{D} \rangle .$$

This becomes, after expanding,

$$\langle \varphi'_k | \mathbf{W}^{(D)} | \varphi'_k \rangle = \langle \mathbf{D} | \mathbf{W}^{(D)} | \mathbf{D} \rangle + \sum b_{\lambda l} \langle \mathbf{D} | \mathbf{W}^{(D)} | \lambda l \rangle + \sum c_{\sigma s} \langle \mathbf{D} | \mathbf{W}^{(D)} | \sigma s \rangle \\ + \sum d_{\gamma g} \langle \mathbf{D} | \mathbf{W}^{(D)} | \gamma g \rangle + \sum b_{\lambda l}^* \langle \lambda l | \mathbf{W}^{(D)} | \mathbf{D} \rangle + \sum \sum b_{\lambda l}^* b_{\lambda' l'} \langle \lambda l | \mathbf{W}^{(D)} | \lambda' l' \rangle \\ + \sum \sum b_{\lambda l}^* c_{\sigma s} \langle \lambda l | \mathbf{W}^{(D)} | \sigma s \rangle + \sum \sum b_{\lambda l}^* d_{\gamma g} \langle \lambda l | \mathbf{W}^{(D)} | \gamma g \rangle \\ + \sum c_{\sigma s}^* \langle \sigma s | \mathbf{W}^{(D)} | \mathbf{D} \rangle + \sum \sum c_{\sigma s}^* b_{\lambda l} \langle \sigma s | \mathbf{W}^{(D)} | \lambda l \rangle + \\ + \sum \sum c_{\sigma s}^* c_{\sigma' s'} \langle \sigma s | \mathbf{W}^{(D)} | \sigma' s' \rangle + \sum \sum c_{\sigma s}^* d_{\gamma g} \langle \sigma s | \mathbf{W}^{(D)} | \gamma g \rangle \\ + \sum \sum d_{\gamma g}^* \langle \gamma g | \mathbf{W}^{(D)} | \mathbf{D} \rangle + \sum \sum d_{\gamma g}^* b_{\lambda l} \langle \gamma g | \mathbf{W}^{(D)} | \lambda l \rangle \\ + \sum \sum d_{\gamma g}^* c_{\sigma s} \langle \gamma g | \mathbf{W}^{(D)} | \sigma s \rangle \\ + \sum \sum d_{\gamma g}^* d_{\gamma' g'} \langle \gamma g | \mathbf{W}^{(D)} | \gamma' g' \rangle . \quad (4.4)$$

The normalizing factor is computed next.

$$\begin{aligned}
\langle \varphi'_k | \varphi'_k \rangle &= \langle D | D \rangle + \sum b_{\lambda l} \langle D | \lambda l \rangle + \sum c_{\sigma s} \langle D | \sigma s \rangle \\
&+ \sum d_{\gamma g} \langle D | \gamma g \rangle + \sum b_{\lambda l}^* \langle \lambda l | D \rangle \\
&+ \sum c_{\sigma s}^* \langle \sigma s | D \rangle + \sum d_{\gamma g}^* \langle \gamma g | D \rangle \\
&+ \sum |b_{\lambda l}|^2 + \sum |c_{\sigma s}|^2 + \sum |d_{\gamma g}|^2, \tag{4.5}
\end{aligned}$$

which can be written as

$$\begin{aligned}
\langle \varphi'_k | \varphi'_k \rangle &= \langle D | D \rangle \left[1 + \langle D | D \rangle^{-1} \sum b_{\lambda l} \langle D | \lambda l \rangle + \dots \right. \\
&\left. + \langle D | D \rangle^{-1} \sum b_{\lambda l}^* \langle \lambda l | D \rangle + \dots \right]. \tag{4.6}
\end{aligned}$$

Then the normalized diagonal matrix elements of $W^{(D)}$ can be written, to second order in the coefficients, as

$$\begin{aligned}
\frac{\langle \varphi'_k | W^{(D)} | \varphi'_k \rangle}{\langle \varphi'_k | \varphi'_k \rangle} &= \langle D | D \rangle^{-1} \left(\langle D | W^{(D)} | D \rangle + \sum b_{\lambda l} \langle D | W^{(D)} | \lambda l \rangle \right. \\
&+ \sum b_{\lambda l}^* \langle \lambda l | W^{(D)} | D \rangle + \dots \left. \right) \left(1 + \langle D | D \rangle^{-1} \sum b_{\lambda l} \langle D | \lambda l \rangle \right. \\
&\left. + \langle D | D \rangle^{-1} \sum b_{\lambda l}^* \langle \lambda l | D \rangle + \dots \right)^{-1}. \tag{4.7}
\end{aligned}$$

The last term in parentheses in Equation 4.7 is expanded to first order in the arbitrary coefficients as

$$\begin{aligned}
\frac{\langle \varphi'_k | W^{(D)} | \varphi'_k \rangle}{\langle \varphi'_k | \varphi'_k \rangle} &= \langle D | D \rangle^{-1} \left(\langle D | W^{(D)} | D \rangle + \sum b_{\lambda l} \langle D | W^{(D)} | \lambda l \rangle \right. \\
&+ \sum b_{\lambda l}^* \langle \lambda l | W^{(D)} | D \rangle + \dots \left. \right) \left(1 - \langle D | D \rangle^{-1} \sum b_{\lambda l} \langle D | \lambda l \rangle \right. \\
&\left. - \langle D | D \rangle^{-1} \sum b_{\lambda l}^* \langle \lambda l | D \rangle + \dots \right). \tag{4.8}
\end{aligned}$$

The product is then expanded and terms of first order in the coefficients are retained.

$$\begin{aligned}
& \frac{\langle \varphi'_k | W^{(D)} | \varphi'_k \rangle}{\langle \varphi'_k | \varphi'_k \rangle} - \frac{\langle D | W^{(D)} | D \rangle}{\langle D | D \rangle} = \\
& = \sum \left(\langle D | W^{(D)} | \lambda l \rangle - \frac{\langle D | W^{(D)} | D \rangle}{\langle D | D \rangle} \langle D | \lambda l \rangle \right) \frac{b_{\lambda l}}{\langle D | D \rangle} + \text{c.c.} \\
& + \sum \left(\langle D | W^{(D)} | \sigma s \rangle - \frac{\langle D | W^{(D)} | D \rangle}{\langle D | D \rangle} \langle D | \sigma s \rangle \right) \frac{c_{\sigma s}}{\langle D | D \rangle} + \text{c.c.} \\
& + \sum \left(\langle D | W^{(D)} | \gamma g \rangle - \frac{\langle D | W^{(D)} | D \rangle}{\langle D | D \rangle} \langle D | \gamma g \rangle \right) \frac{d_{\gamma g}}{\langle D | D \rangle} + \text{c.c.}, \tag{4.9}
\end{aligned}$$

where c.c. stands for the complex conjugate of the preceding term.

For the variation of the normalized expectation value of $W^{(D)}$ to be zero, the quantity on the right-hand side should be zero. However, since the parameters b , c , and d are all arbitrary, then the coefficients of b and b^* , etc., should be identically zero. This implies that

$$\langle \lambda l | W^{(D)} | D \rangle = \frac{\langle D | W^{(D)} | D \rangle}{\langle D | D \rangle} \langle \lambda l | D \rangle,$$

$$\langle \sigma s | W^{(D)} | D \rangle = \frac{\langle D | W^{(D)} | D \rangle}{\langle D | D \rangle} \langle \sigma s | D \rangle,$$

and

$$\langle \gamma g | W^{(D)} | D \rangle = \frac{\langle D | W^{(D)} | D \rangle}{\langle D | D \rangle} \langle \gamma g | D \rangle. \tag{4.10}$$

From Equation 3.12, the D defect pseudopotential operating on any defect pseudo-wave function is

$$\begin{aligned}
W^{(D)} | D \rangle & = V^{(D)} | D \rangle + \sum_{\lambda l} (E_k - E_{\lambda}) | \lambda l \rangle \langle \lambda l | D \rangle + \sum_{\sigma s} (E_k - E_{\sigma}) | \sigma s \rangle \langle \sigma s | D \rangle \\
& + \sum_{\gamma g} (E_k - E_{\gamma}) | \gamma g \rangle \langle \gamma g | D \rangle. \tag{4.11}
\end{aligned}$$

The inner product of Equation 4.11 is taken with $\langle \lambda l |$, $\langle \sigma s |$, and $\langle \gamma g |$, respectively, yielding

$$\langle \lambda l | \mathbf{W}^{(D)} | \mathbf{D} \rangle = \langle \lambda l | \mathbf{V}^{(D)} | \mathbf{D} \rangle + (E_{\mathbf{k}} - E_{\lambda}) \langle \lambda l | \mathbf{D} \rangle ,$$

$$\langle \sigma s | \mathbf{W}^{(D)} | \mathbf{D} \rangle = \langle \sigma s | \mathbf{V}^{(D)} | \mathbf{D} \rangle + (E_{\mathbf{k}} - E_{\sigma}) \langle \sigma s | \mathbf{D} \rangle ,$$

and

$$\langle \gamma g | \mathbf{W}^{(D)} | \mathbf{D} \rangle = \langle \gamma g | \mathbf{V}^{(D)} | \mathbf{D} \rangle + (E_{\mathbf{k}} - E_{\gamma}) \langle \gamma g | \mathbf{D} \rangle . \quad (4.12)$$

These can be solved for terms such as

$$(E_{\mathbf{k}} - E_{\alpha}) = \frac{1}{\langle \alpha \alpha | \mathbf{D} \rangle} \left(\langle \alpha \alpha | \mathbf{W}^{(D)} | \mathbf{D} \rangle - \langle \alpha \alpha | \mathbf{V}^{(D)} | \mathbf{D} \rangle \right) , \quad (4.13)$$

where

$$(\alpha \alpha) = (\lambda l), (\sigma s), \text{ or } (\gamma g).$$

From here onward, the subscript $\alpha \alpha$ or $\beta \beta$ signifies a sum over all states, λ , σ , and γ , and all sites, l , s , and g . These expressions can be substituted back into Equation 4.11 to obtain

$$\begin{aligned} \mathbf{W}^{(D)} | \mathbf{D} \rangle &= \mathbf{V}^{(D)} | \mathbf{D} \rangle - \sum_{\lambda l} |\lambda l\rangle \langle \lambda l | \mathbf{V}^{(D)} | \mathbf{D} \rangle - \sum_{\sigma s} |\sigma s\rangle \langle \sigma s | \mathbf{V}^{(D)} | \mathbf{D} \rangle \\ &\quad - \sum_{\gamma g} |\gamma g\rangle \langle \gamma g | \mathbf{V}^{(D)} | \mathbf{D} \rangle + \sum_{\lambda l} |\lambda l\rangle \langle \lambda l | \mathbf{W}^{(D)} | \mathbf{D} \rangle \\ &\quad + \sum_{\sigma s} |\sigma s\rangle \langle \sigma s | \mathbf{W}^{(D)} | \mathbf{D} \rangle + \sum_{\gamma g} |\gamma g\rangle \langle \gamma g | \mathbf{W}^{(D)} | \mathbf{D} \rangle . \end{aligned} \quad (4.14)$$

Now the conditions for the smoothest D defect pseudopotential, Equation 4.10, are placed into Equation 4.14.

$$\begin{aligned} \mathbf{W}^{(D)} | \mathbf{D} \rangle &= \left(1 - \sum_{\lambda l} |\lambda l\rangle \langle \lambda l | - \sum_{\sigma s} |\sigma s\rangle \langle \sigma s | - \sum_{\gamma g} |\gamma g\rangle \langle \gamma g | \right) \mathbf{V}^{(D)} | \mathbf{D} \rangle \\ &\quad + \frac{\langle \mathbf{D} | \mathbf{W}^{(D)} | \mathbf{D} \rangle}{\langle \mathbf{D} | \mathbf{D} \rangle} \left(\sum_{\lambda l} |\lambda l\rangle \langle \lambda l | + \sum_{\sigma s} |\sigma s\rangle \langle \sigma s | + \sum_{\gamma g} |\gamma g\rangle \langle \gamma g | \right) | \mathbf{D} \rangle , \end{aligned} \quad (4.15)$$

which can be rewritten in terms of the D defect projection operator as

$$\langle \mathbf{W}^{(D)} | \varphi_{\mathbf{k}}^{(D)} \rangle = (1 - \mathbf{P}_{\mathbf{D}}) \mathbf{V}^{(D)} | \varphi_{\mathbf{k}}^{(D)} \rangle + \frac{\langle \varphi_{\mathbf{k}}^{(D)} | \mathbf{W}^{(D)} | \varphi_{\mathbf{k}}^{(D)} \rangle}{\langle \varphi_{\mathbf{k}}^{(D)} | \varphi_{\mathbf{k}}^{(D)} \rangle} \mathbf{P}_{\mathbf{D}} | \varphi_{\mathbf{k}}^{(D)} \rangle , \quad (4.16)$$

which, in turn, is identical in form to the optimum pseudopotential for a perfect crystal obtained in the second section. As in that section, Equation 4.16 can be multiplied by $\langle \varphi_{\mathbf{k}}^{(D)} |$ and the resultant expression inserted back into 4.16 to obtain

$$W\varphi_{\mathbf{k}} = (1 - P) V\varphi_{\mathbf{k}} + \frac{\langle \varphi_{\mathbf{k}} | W | \varphi_{\mathbf{k}} \rangle}{\langle \varphi_{\mathbf{k}} | \varphi_{\mathbf{k}} \rangle - \langle \varphi_{\mathbf{k}} | P | \varphi_{\mathbf{k}} \rangle} \cdot P\varphi_{\mathbf{k}}, \quad (4.17)$$

where the D's have been dropped. The linearization of the optimum D defect pseudopotential is accomplished exactly as in the second section. Next the elements $\langle \mathbf{k} + \mathbf{q} | W_L | \mathbf{k} \rangle$ and $\langle \mathbf{k} | W_L | \mathbf{k} + \mathbf{q} \rangle$ need to be evaluated. Again all three operators $H^{(D)}$, $T^{(D)}$, and $V^{(D)}$ are hermitian. First the following operator is computed:

$$PV|\mathbf{k}\rangle = \left(\sum |\lambda l\rangle \langle \lambda l| + \sum |\sigma s\rangle \langle \sigma s| + \sum |\gamma g\rangle \langle \gamma g| \right) (H - T)|\mathbf{k}\rangle,$$

or

$$= \sum_{\alpha m} |\alpha m\rangle \langle \alpha m | \mathbf{k} \rangle \left(E_{\alpha} - \frac{\hbar^2 k^2}{2m} \right). \quad (4.18)$$

And as before

$$\langle \mathbf{k} + \mathbf{q} | P | \mathbf{k} \rangle^* = \langle \mathbf{k} | P | \mathbf{k} + \mathbf{q} \rangle. \quad (4.19)$$

Now the following term is evaluated:

$$\langle \mathbf{k} + \mathbf{q} | W_L | \mathbf{k} \rangle^* = \langle \mathbf{k} + \mathbf{q} | (1 - P) V | \mathbf{k} \rangle^* + \frac{\langle \mathbf{k} | (1 - P) V | \mathbf{k} \rangle^*}{1 - \langle \mathbf{k} | P | \mathbf{k} \rangle} \langle \mathbf{k} + \mathbf{q} | P | \mathbf{k} \rangle. \quad (4.20)$$

The first term above becomes

$$\begin{aligned} \langle \mathbf{k} + \mathbf{q} | (1 - P) V | \mathbf{k} \rangle^* &= \langle \mathbf{k} + \mathbf{q} | V | \mathbf{k} \rangle^* \\ &\quad - \sum \langle \mathbf{k} + \mathbf{q} | \lambda l \rangle^* \langle \lambda l | \mathbf{k} \rangle^* \left(E_{\lambda} - \frac{\hbar^2 k^2}{2m} \right) \\ &\quad - \sum \langle \mathbf{k} + \mathbf{q} | \sigma s \rangle^* \langle \sigma s | \mathbf{k} \rangle^* \left(E_{\sigma} - \frac{\hbar^2 k^2}{2m} \right) \\ &\quad - \sum \langle \mathbf{k} + \mathbf{q} | \gamma g \rangle^* \langle \gamma g | \mathbf{k} \rangle^* \left(E_{\gamma} - \frac{\hbar^2 k^2}{2m} \right). \end{aligned} \quad (4.21)$$

As a result, Equation 4.20 becomes

$$\begin{aligned} \langle \mathbf{k} + \mathbf{q} | W_L | \mathbf{k} \rangle^* &= \langle \mathbf{k} | V | \mathbf{k} + \mathbf{q} \rangle - \sum \langle \mathbf{k} | \lambda l \rangle \langle \lambda l | \mathbf{k} + \mathbf{q} \rangle \left(E_{\lambda} - \frac{\hbar^2 k^2}{2m} \right) \\ &\quad - \sum \langle \mathbf{k} | \sigma s \rangle \langle \sigma s | \mathbf{k} + \mathbf{q} \rangle \left(E_{\sigma} - \frac{\hbar^2 k^2}{2m} \right) - \sum \langle \mathbf{k} | \gamma g \rangle \langle \gamma g | \mathbf{k} + \mathbf{q} \rangle \left(E_{\gamma} - \frac{\hbar^2 k^2}{2m} \right). \end{aligned} \quad (4.22)$$

However,

$$\begin{aligned} \langle \mathbf{k} | W_L | \mathbf{k} + \mathbf{q} \rangle &= \langle \mathbf{k} | V | \mathbf{k} + \mathbf{q} \rangle - \sum \langle \mathbf{k} | \lambda l \rangle \langle \lambda l | \mathbf{k} + \mathbf{q} \rangle \left(E_\lambda - \frac{\hbar^2}{2m} |\mathbf{k} + \mathbf{q}|^2 \right) \\ &\quad - \sum \langle \mathbf{k} | \sigma s \rangle \langle \sigma s | \mathbf{k} + \mathbf{q} \rangle \left(E_\gamma - \frac{\hbar^2}{2m} |\mathbf{k} + \mathbf{q}|^2 \right) - \sum \langle \mathbf{k} | \gamma g \rangle \langle \gamma g | \mathbf{k} + \mathbf{q} \rangle \left(E_\gamma - \frac{\hbar^2}{2m} |\mathbf{k} + \mathbf{q}|^2 \right). \end{aligned} \quad (4.23)$$

As a result the non-hermiticity of W_L is

$$\langle \mathbf{k} + \mathbf{q} | W_L | \mathbf{k} \rangle^* - \langle \mathbf{k} | W_L | \mathbf{k} + \mathbf{q} \rangle = \frac{\hbar^2}{2m} (k^2 - |\mathbf{k} + \mathbf{q}|^2) \langle \mathbf{k} | P | \mathbf{k} + \mathbf{q} \rangle. \quad (4.24)$$

The next goal is to write the matrix elements of $\langle \mathbf{k} | W_L | \mathbf{k} \rangle$, by using Equation 2.17 with P replaced by P_D , as follows:

$$\langle \mathbf{k} | W_L | \mathbf{k} \rangle = \frac{\langle \mathbf{k} | (1 - P) V | \mathbf{k} \rangle}{1 - \langle \mathbf{k} | P | \mathbf{k} \rangle}. \quad (4.25)$$

Then this expression is substituted back into Equation 2.17 to obtain

$$W | \mathbf{k} \rangle = (1 - P) V | \mathbf{k} \rangle + \langle \mathbf{k} | W_L | \mathbf{k} \rangle P | \mathbf{k} \rangle. \quad (4.26)$$

This can be rewritten by using Equation 4.18 as (dropping the subscript L)

$$\begin{aligned} W | \mathbf{k} \rangle &= V | \mathbf{k} \rangle \\ &\quad + \sum_{\alpha a} | \alpha a \rangle \langle \alpha a | \mathbf{k} \rangle \left(\frac{\hbar^2 k^2}{2m} - E_\alpha \right), \end{aligned}$$

where again $(\alpha a) = (\lambda l)$, (σs) , and (γg) . (4.27)

By successive iterations, as is done in Appendix C, the diagonal matrix elements of W can be written as

$$\begin{aligned} \langle \mathbf{k} | W | \mathbf{k} \rangle &= \langle \mathbf{k} | V | \mathbf{k} \rangle \\ &\quad + \left(1 - \langle \mathbf{k} | P | \mathbf{k} \rangle \right)^{-1} \left[\sum_{\alpha a} \left(\frac{\hbar^2 k^2}{2m} + \langle \mathbf{k} | V | \mathbf{k} \rangle - E_\alpha \right) \langle \mathbf{k} | \alpha a \rangle \langle \alpha a | \mathbf{k} \rangle \right], \end{aligned} \quad (4.28)$$

and the off diagonal elements written as

$$\begin{aligned} \langle \mathbf{k} + \mathbf{q} | W | \mathbf{k} \rangle &= \langle \mathbf{k} + \mathbf{q} | V | \mathbf{k} \rangle + \sum_{\alpha a} \left(\frac{\hbar^2 k^2}{2m} + \langle \mathbf{k} | V | \mathbf{k} \rangle - E_\alpha \right) \langle \mathbf{k} + \mathbf{q} | \alpha a \rangle \langle \alpha a | \mathbf{k} \rangle \\ &\quad + \frac{\langle \mathbf{k} + \mathbf{q} | P | \mathbf{k} \rangle}{1 - \langle \mathbf{k} | P | \mathbf{k} \rangle} \left[\sum_{\alpha a} \left(\frac{\hbar^2 k^2}{2m} + \langle \mathbf{k} | V | \mathbf{k} \rangle - E_\alpha \right) \langle \mathbf{k} | \alpha a \rangle \langle \alpha a | \mathbf{k} \rangle \right]. \end{aligned} \quad (4.30)$$

FACTORIZATION OF THE NON-DIAGONAL MATRIX ELEMENTS
OF THE D DEFECT LINEAR PSEUDOPOTENTIAL AND CALCULATION OF THE ELECTRONIC ENERGY

The crystal potential, $V(\mathbf{r})$, which is included in the pseudopotential can be decomposed into "local" crystal potentials associated with each site in the crystal. Even if the potential includes a Hartree or Hartree-Fock self-consistent potential, this in turn can also be decomposed by just integrating over Wigner Seitz cells. As a result, the crystal potential for the D defects will be

$$V^{(D)}(\mathbf{r}) = \sum_{l=0}^{N_\lambda-1} v_\lambda(\mathbf{r} - \mathbf{r}_l) + \sum_{s=0}^{N_\sigma-1} v_\sigma(\mathbf{r} - \mathbf{r}_s) + \sum_{g=0}^{N_\gamma-1} v_\gamma(\mathbf{r} - \mathbf{r}_g). \quad (5.1)$$

The overlap integrals defined in the first section can be written for a general core state, $|\alpha a\rangle$, as

$$\langle \alpha a | \mathbf{k} \rangle = \Omega^{-1/2} \int \psi_\alpha^*(\mathbf{r} - \mathbf{r}_a) e^{i\mathbf{k} \cdot \mathbf{r}} d\mathbf{r},$$

or

$$= N^{-1/2} e^{i\mathbf{k} \cdot \mathbf{r}_a} \langle \alpha | \mathbf{k} \rangle,$$

where

$$\langle \alpha | \mathbf{k} \rangle = \Omega_0^{-1/2} \int \psi_\alpha^*(\mathbf{R}) e^{i\mathbf{k} \cdot \mathbf{R}} d\mathbf{R}, \quad \alpha = \lambda, \sigma, \text{ or } \gamma, \text{ and } \Omega_0 = \frac{\Omega}{N}.$$

The off diagonal matrix elements of Equation 5.1 can now be calculated as

$$\langle \mathbf{k} + \mathbf{q} | V^{(D)} | \mathbf{k} \rangle = \frac{1}{N} \sum_{l=0}^{N_\lambda-1} e^{-i\mathbf{q} \cdot \mathbf{r}_l} \cdot \frac{1}{\Omega_0} \int e^{-i(\mathbf{k} + \mathbf{q}) \cdot \mathbf{R}} v_\lambda(\mathbf{R}) e^{i\mathbf{k} \cdot \mathbf{R}} d\mathbf{R} \quad (5.2)$$

+ similar terms for σ and γ core sites. This can be written in terms of the host, substitutional defect, and interstitial defect structure factors, $S_\lambda(\mathbf{q})$, $S_\sigma(\mathbf{q})$, and $S_\gamma(\mathbf{q})$, respectively, as

$$\langle \mathbf{k} + \mathbf{q} | V^{(D)} | \mathbf{k} \rangle = \sum_{\alpha}^{\lambda, \sigma, \gamma} S_\alpha(\mathbf{q}) \langle \mathbf{k} + \mathbf{q} | v_\alpha | \mathbf{k} \rangle, \quad \text{where } S_\alpha(0) = \frac{N_\alpha}{N}. \quad (5.3)$$

Scalar products such as $\langle \mathbf{k} + \mathbf{q} | \alpha a \rangle \langle \alpha a | \mathbf{k} \rangle$ can also be factored as follows:

$$\langle \mathbf{k} + \mathbf{q} | \alpha a \rangle \langle \alpha a | \mathbf{k} \rangle = \left(N^{-1/2} e^{-i(\mathbf{k} + \mathbf{q}) \cdot \mathbf{r}_a} \langle \mathbf{k} + \mathbf{q} | \alpha \rangle \right) \left(N^{-1/2} e^{-i\mathbf{k} \cdot \mathbf{r}_a} \langle \alpha | \mathbf{k} \rangle \right),$$

or

$$= \frac{1}{N} e^{-i\mathbf{q} \cdot \mathbf{r}_a} \langle \mathbf{k} + \mathbf{q} | \alpha \rangle \langle \alpha | \mathbf{k} \rangle. \quad (5.4)$$

Thus the off diagonal elements of the D defect pseudopotential can also be factored as

$$\langle \mathbf{k} + \mathbf{q} | P_D | \mathbf{k} \rangle = \sum_{\alpha} S_\alpha(\mathbf{q}) \langle \mathbf{k} + \mathbf{q} | P_\alpha | \mathbf{k} \rangle, \quad (5.5)$$

where the P_α 's can be viewed as "local" projection operators on arbitrary core states $|\alpha\rangle$ and are defined as

$$P_\alpha = |\alpha\rangle \langle \alpha|. \quad (5.6)$$

To simplify the notation, the following operator, which is just a modified "local" projection operator, is defined as

$$T_\alpha = \sum'_{\text{core}} \left(\frac{\hbar^2 k^2}{2m} + \langle \mathbf{k} | \mathbf{V}^{(N)} | \mathbf{k} \rangle - E_\alpha \right) |\alpha\rangle \langle \alpha|, \quad (5.7)$$

where this sum is not over $\lambda, \sigma,$ and γ ; but over all core states of $\alpha = \lambda, \sigma,$ or γ . By using this operator and Equation 5.3, the off diagonal elements of the D defect pseudopotential can be written as

$$\langle \mathbf{k} + \mathbf{q} | \mathbf{W}^{(D)} | \mathbf{k} \rangle = \sum_\alpha \langle \mathbf{k} + \mathbf{q} | w_\alpha | \mathbf{k} \rangle S_\alpha(\mathbf{q}), \quad (5.8)$$

where

$$\begin{aligned} \langle \mathbf{k} + \mathbf{q} | w_\alpha | \mathbf{k} \rangle &= \langle \mathbf{k} + \mathbf{q} | v_\alpha | \mathbf{k} \rangle + \langle \mathbf{k} + \mathbf{q} | T_\alpha | \mathbf{k} \rangle \\ &+ \frac{\langle \mathbf{k} + \mathbf{q} | P_\alpha | \mathbf{k} \rangle}{1 - \langle \mathbf{k} | P_D | \mathbf{k} \rangle} \sum_\beta \langle \mathbf{k} | T_\beta | \mathbf{k} \rangle, \text{ where } \beta = \lambda, \sigma, \gamma. \end{aligned} \quad (5.9)$$

It should be noted that since $N_0 = N - N_1$

$$S_\lambda(\mathbf{q}) = \frac{1}{N} \sum_{j=0}^{N-1} e^{-i\mathbf{q} \cdot \mathbf{r}_j} - \frac{1}{N} \sum_{s=0}^{N_1-1} e^{-i\mathbf{q} \cdot \mathbf{r}_s},$$

or

$$= S(\mathbf{q}) - S_\sigma(\mathbf{q}), \quad (5.10)$$

where the index j now runs over all the sites of the perfect crystal. Equation 5.8 can subsequently be written as

$$\begin{aligned} \langle \mathbf{k} + \mathbf{q} | \mathbf{W}^{(D)} | \mathbf{k} \rangle &= S(\mathbf{q}) \langle \mathbf{k} + \mathbf{q} | w_\lambda | \mathbf{k} \rangle + S_\sigma(\mathbf{q}) \langle \mathbf{k} + \mathbf{q} | w_\sigma - w_\lambda | \mathbf{k} \rangle \\ &+ S_\gamma(\mathbf{q}) \langle \mathbf{k} + \mathbf{q} | w_\gamma | \mathbf{k} \rangle, \end{aligned} \quad (5.11)$$

where $S(\mathbf{q})$, without a subscript, is the structure factor for the perfect crystal. The electronic energy from second perturbation theory can now be written as

$$\begin{aligned} E(\mathbf{k}) &= \frac{\hbar^2 k^2}{2m} + \frac{1}{N} \sum_\alpha \langle \mathbf{k} | w_\alpha | \mathbf{k} \rangle \\ &+ \sum_{\alpha\beta\mathbf{q}} \frac{S_\alpha(\mathbf{q}) S_\beta^*(\mathbf{q}) \langle \mathbf{k} + \mathbf{q} | w_\alpha | \mathbf{k} \rangle \langle \mathbf{k} | w_\beta | \mathbf{k} + \mathbf{q} \rangle}{\frac{\hbar^2}{2m} (k^2 - |\mathbf{k} + \mathbf{q}|^2)}. \end{aligned} \quad (5.12)$$

The second term is not the same as setting $S_\alpha(\mathbf{q}) = S_\alpha(0)$. The total electronic energy of the defect crystal will now be equal to the sum of Equation 5.12 over all \mathbf{k} -space:

$$E_{\text{electronic}} = \sum_{\mathbf{k}} \frac{\hbar^2 k^2}{2m} + \frac{1}{N} \sum_{\mathbf{k}} \sum_{\alpha} \langle \mathbf{k} | w_{\alpha} | \mathbf{k} \rangle + \sum_{\alpha\beta\mathbf{q}} S_{\alpha}(\mathbf{q}) S_{\beta}^*(\mathbf{q}) F_{\alpha\beta}(\mathbf{q}), \quad (5.13)$$

where

$$F_{\alpha\beta}(\mathbf{q}) = \sum_{\mathbf{k}} \frac{\langle \mathbf{k} + \mathbf{q} | w_{\alpha} | \mathbf{k} \rangle \langle \mathbf{k} | w_{\beta} | \mathbf{k} + \mathbf{q} \rangle}{\frac{\hbar^2}{2m} (k^2 - |\mathbf{k} + \mathbf{q}|^2)}. \quad (5.14)$$

In order to keep the terminology consistent with that of the perfect crystal, Equation 5.14 will be called the energy-wavenumber characteristic, and the last term in Equation 5.13 will be called the band-structure energy, $E_{b.s.}$. Products such as $S_{\alpha}(\mathbf{q}) S_{\beta}^*(\mathbf{q})$ are very important, since they occur not only in the evaluation of the electronic energy, but also in that of the electrostatic energy. These factors subsequently lead to interactions among the various defects, as will be seen in the seventh section.

CALCULATION OF THE ELECTROSTATIC ENERGY FOR THE DEFECT LATTICE

The potential at a host atom core site due to all other sites is given by

$$V_{\lambda}(|\mathbf{r}_l|) = \sum_{l'}' V(|\mathbf{r}_l - \mathbf{r}_{l'}|) + \sum_s V(|\mathbf{r}_l - \mathbf{r}_s|) + \sum_g V(|\mathbf{r}_l - \mathbf{r}_g|), \quad (6.1)$$

at a substitutional ion core site by

$$V_{\sigma}(|\mathbf{r}_s|) = \sum_l V(|\mathbf{r}_s - \mathbf{r}_l|) + \sum_{s'}' V(|\mathbf{r}_s - \mathbf{r}_{s'}|) + \sum_g V(|\mathbf{r}_s - \mathbf{r}_g|), \quad (6.2)$$

and at an interstitial ion core site by

$$V_{\gamma}(|\mathbf{r}_g|) = \sum_l V(|\mathbf{r}_g - \mathbf{r}_l|) + \sum_s V(|\mathbf{r}_g - \mathbf{r}_s|) + \sum_{g'}' V(|\mathbf{r}_g - \mathbf{r}_{g'}|). \quad (6.3)$$

The primes on the summations above indicate that each ion self-energy term has been excluded. The total static electrostatic energy can then be written as

$$\begin{aligned} E_{l.s.} &= \frac{1}{2} \left[\sum_l V_{\lambda}(|\mathbf{r}_l|) + \sum_s V_{\sigma}(|\mathbf{r}_s|) + \sum_g V_{\gamma}(|\mathbf{r}_g|) \right], \text{ or} \\ &= \frac{1}{2} \left[\sum_{ll'}' V(|\mathbf{r}_l - \mathbf{r}_{l'}|) + \sum_{ss'}' V(|\mathbf{r}_s - \mathbf{r}_{s'}|) + \sum_{gg'}' V(|\mathbf{r}_g - \mathbf{r}_{g'}|) \right] \\ &\quad + \sum_{ls} V(|\mathbf{r}_l - \mathbf{r}_s|) + \sum_{lg} V(|\mathbf{r}_l - \mathbf{r}_g|) + \sum_{sg} V(|\mathbf{r}_s - \mathbf{r}_g|), \end{aligned} \quad (6.4)$$

where the factor 1/2 is included to account for summing over pairs, and $V(|\mathbf{r}_a - \mathbf{r}_b|) = V(|\mathbf{r}_b - \mathbf{r}_a|)$. The most common potential employed in such calculations is the Ewald-Fuchs potential,

$$V(|\mathbf{r}_a - \mathbf{r}_b|) = \frac{Z_\alpha^* Z_\beta^* e^2}{|\mathbf{r}_a - \mathbf{r}_b|} \left(\frac{2}{\pi}\right) \int_0^{\sqrt{\eta}|\mathbf{r}_a - \mathbf{r}_b|} e^{-x^2} dx, \quad (6.5)$$

where η is a parameter such that for $|\mathbf{r}_a - \mathbf{r}_b| \gg \eta^{-1/2}$

$$V \rightarrow \frac{Z_\alpha^* Z_\beta^* e^2}{|\mathbf{r}_a - \mathbf{r}_b|}, \quad (6.6)$$

and

$$\lim_{|\mathbf{r}_a - \mathbf{r}_b| \rightarrow 0} V(|\mathbf{r}_a - \mathbf{r}_b|) = 2 Z_\alpha^* Z_\beta^* e^2 \left(\frac{\eta}{\pi}\right)^{1/2}. \quad (6.7)$$

This is the potential to be used in the calculation. The Fourier transform of the potential is made in such a way that structure factor terms appear in the energy just as in the electronic energy case:

$$V(|\mathbf{r}_a - \mathbf{r}_b|) = \left(\frac{1}{2\pi}\right)^3 \int F[V(|\mathbf{r}_a - \mathbf{r}_b|)] e^{i\mathbf{q} \cdot (\mathbf{r}_a - \mathbf{r}_b)} d\mathbf{q}, \quad (6.8)$$

where

$$F[V(\mathbf{R})] = \int V(\mathbf{R}) e^{-i\mathbf{q} \cdot \mathbf{R}} d\mathbf{R}, \quad (6.9)$$

$$\mathbf{R} = \mathbf{r}_a - \mathbf{r}_b,$$

and

$$R = |\mathbf{R}|.$$

It is shown in Appendix D that the Fourier transform of the Ewald-Fuchs potential is

$$F[V(\mathbf{R})] = \frac{4\pi Z_\alpha^* Z_\beta^* e^2}{q^2} e^{-q^2/4\eta}. \quad (6.10)$$

If the integral over \mathbf{q} is now changed into a summation, i.e.

$$\int d\mathbf{q} \rightarrow \frac{(2\pi)^3}{\Omega} \sum'_{\mathbf{q} \neq 0},$$

and Equation 6.10 placed into Equation 6.8,

$$V(|\mathbf{r}_a - \mathbf{r}_b|) = \frac{4\pi Z_\alpha^* Z_\beta^* e^2}{\Omega} \sum'_{\mathbf{q}} e^{i\mathbf{q} \cdot (\mathbf{r}_a - \mathbf{r}_b)} \frac{e^{-q^2/4\eta}}{q^2}. \quad (6.11)$$

Next a summation over all indices and a limit as $\eta \rightarrow \infty$ is performed:

$$\sum'_{\mathbf{a} \neq \mathbf{b}} V(|\mathbf{r}_a - \mathbf{r}_b|) = \frac{4\pi Z_\alpha^* Z_\beta^* e^2}{\Omega_0} \lim_{\eta \rightarrow \infty} \sum'_{\mathbf{q}} S_\beta(\mathbf{q}) S_\alpha^*(\mathbf{q}) \frac{e^{-q^2/4\eta}}{q^2}, \quad (6.12)$$

which can be written in a more symmetric manner by noticing that \mathbf{q} is summed over negative reciprocal vectors as well as positive:

$$\sum_{a \neq b}' V(|\mathbf{r}_a - \mathbf{r}_b|) = \frac{4\pi N Z_\alpha^* Z_\beta^* e^2}{\Omega_0} \lim_{\eta \rightarrow \infty} \frac{1}{2} \sum_{\mathbf{q}}' [S_\beta(\mathbf{q}) S_\alpha^*(\mathbf{q}) + S_\alpha(\mathbf{q}) S_\beta^*(\mathbf{q})] \frac{e^{-q^2/4\eta}}{q^2}. \quad (6.13)$$

The case for summation over identical ion cores can be written as

$$\sum_{aa'}' V(|\mathbf{r}_a - \mathbf{r}_{a'}|) = \sum_{aa'} V(|\mathbf{r}_a - \mathbf{r}_{a'}|) - 2 Z_\alpha^{*2} e^2 \left(\frac{\eta}{\pi}\right)^{1/2}$$

or

$$= \frac{4\pi N Z_\alpha^{*2} e^2}{\Omega_0} \lim_{\eta \rightarrow \infty} \sum_{\mathbf{q}}' S_\alpha(\mathbf{q}) S_\alpha^*(\mathbf{q}) \frac{e^{-q^2/4\eta}}{q^2} - 2e^2 N S_\alpha(0) Z_\alpha^{*2} \lim_{\eta \rightarrow \infty} \left(\frac{\eta}{\pi}\right)^{1/2}. \quad (6.14)$$

Then the total electrostatic energy can be written as

$$E_{l.s.} = \frac{2\pi N e^2}{\Omega_0} \sum_{\alpha\beta} Z_\alpha^* Z_\beta^* \lim_{\eta \rightarrow \infty} \sum_{\mathbf{q}}' S_\beta(\mathbf{q}) S_\alpha^*(\mathbf{q}) \frac{e^{-q^2/4\eta}}{q^2} - N e^2 \sum_{\alpha} S_\alpha(0) Z_\alpha^{*2} \lim_{\eta \rightarrow \infty} \left(\frac{\eta}{\pi}\right)^{1/2} \quad (6.15)$$

which can be rewritten in a fashion similar to that of the 3rd term in the electronic energy, i.e.

$$E_{l.s.} = \lim_{\eta \rightarrow \infty} \sum_{\alpha\beta\mathbf{q}}' S_\beta(\mathbf{q}) S_\alpha(\mathbf{q}) G_{\alpha\beta}(\mathbf{q}) + \text{const. term in } \mathbf{q}, \quad (6.17)$$

where

$$G_{\alpha\beta}(\mathbf{q}) = \frac{2\pi N e^2}{\Omega_0} Z_\alpha^* Z_\beta^* \frac{e^{-q^2/4\eta}}{q^2}. \quad (6.18)$$

The limit here is to be taken after summation over \mathbf{q} . The first term in Equation 6.17 will be called the "admixture" energy.

LATTICE VIBRATIONAL ENERGY FOR THE CASE OF THE IMPERFECT CRYSTAL

In the two immediately preceding sections, the total static energy, consisting of the electronic and electrostatic energy, was calculated for the imperfect crystal. The calculations were done in such a manner that structure-dependent terms, i.e. quadratic terms in the structure factors, were isolated. Hence, to evaluate the dynamic crystal, it is necessary only to evaluate the dynamic nature of the structure-dependent terms, namely, $S_\alpha(\mathbf{q}) S_\beta^*(\mathbf{q})$. Before this is done, it will be assumed a priori that the equilibrium positions of all the ions, given by \mathbf{r}_a , are known. These can be calculated by minimizing the total static energy with respect to the \mathbf{r}_a 's. This means that

$$\sum_{\alpha\beta} \frac{\partial}{\partial (\delta \mathbf{r}_\alpha)} \left[\sum_{\mathbf{q}} S_\alpha(\mathbf{q}) S_\beta^*(\mathbf{q}) \right] = 0,$$

which is just the harmonic approximation. Then the dynamic structure factor for the α -th ions can be calculated in terms of the deviations from the equilibrium positions, namely,

$$S_\alpha^{(v)}(\mathbf{q}) = \frac{1}{N} \sum_{\mathbf{q}} e^{-i\mathbf{q} \cdot (\mathbf{r}_\alpha + \delta \mathbf{r}_\alpha)}$$

Since the deviations from the equilibrium positions are assumed to be very small, the exponential can be expanded in terms of the $\delta \mathbf{r}_\alpha$'s,

$$S_\alpha^{(v)}(\mathbf{q}) = \frac{1}{N} \sum_{\mathbf{q}} e^{-i\mathbf{q} \cdot \mathbf{r}_\alpha} \left[1 - i\mathbf{q} \cdot \delta \mathbf{r}_\alpha - \frac{1}{2}(\mathbf{q} \cdot \delta \mathbf{r}_\alpha)^2 + \dots \right].$$

Then the following product, which occurs in the electronic and electrostatic energies, is evaluated up to quadratic terms in the displacements:

$$S_\alpha^{(v)}(\mathbf{q}) S_\beta^{(v)*}(\mathbf{q}) = \frac{1}{N^2} \sum_{a,b} e^{-i\mathbf{q} \cdot (\mathbf{r}_a - \mathbf{r}_b)} \left\{ 1 + (\mathbf{q} \cdot \delta \mathbf{r}_a)(\mathbf{q} \cdot \delta \mathbf{r}_b) - \frac{1}{2}[(\mathbf{q} \cdot \delta \mathbf{r}_a)^2 + (\mathbf{q} \cdot \delta \mathbf{r}_b)^2] \right\}.$$

Now it is obvious that in calculating the energy difference between the dynamic and the static crystal, the only important terms are the band structure energy in the electronic energy and the admixture energy in the electrostatic energy, the other terms being independent of \mathbf{r}_α . Therefore the energy difference is

$$\begin{aligned} \delta E &= \sum_{\alpha\beta\mathbf{q}}' [S_\alpha^{(v)}(\mathbf{q}) S_\beta^{(v)*}(\mathbf{q}) - S_\alpha(\mathbf{q}) S_\beta^*(\mathbf{q})] F_{\alpha\beta}(\mathbf{q}) \\ &+ \lim_{\eta \rightarrow \infty} \sum_{\alpha\beta\mathbf{q}} [S_\alpha^{(v)}(\mathbf{q}) S_\beta^{(v)*}(\mathbf{q}) - S_\alpha(\mathbf{q}) S_\beta^*(\mathbf{q})] G_{\alpha\beta}(\mathbf{q}), \text{ or} \\ &= \frac{1}{N^2} \left[\sum_{\alpha\beta\mathbf{q}}' \sum_{ab} e^{-i\mathbf{q} \cdot (\mathbf{r}_a - \mathbf{r}_b)} F_{\alpha\beta}(\mathbf{q}) + \lim_{\eta \rightarrow \infty} \sum_{\alpha\beta\mathbf{q}}' \sum_{ab} e^{-i\mathbf{q} \cdot (\mathbf{r}_a - \mathbf{r}_b)} G_{\alpha\beta}(\mathbf{q}) \right] \times \\ &\times \left\{ (\mathbf{q} \cdot \delta \mathbf{r}_a)(\mathbf{q} \cdot \delta \mathbf{r}_b) - \frac{1}{2}[(\mathbf{q} \cdot \delta \mathbf{r}_a)^2 + (\mathbf{q} \cdot \delta \mathbf{r}_b)^2] \right\}, \end{aligned}$$

which is quadratic in the displacements and now can be written in matrix form as

$$\delta E = \sum_{ij} \mathbf{D}_{ij} \delta \mathbf{r}_i \delta \mathbf{r}_j$$

where the sum i & j is over all sites, host as well as defect.

Actually, time-dependent perturbation theory should be used to calculate the dynamic energy of the imperfect crystal. Nevertheless, the contribution to the total energy of the normal modes, i.e. D_{ij} , can be neglected as compared to the electronic energy. In other words, phonon modes can be easily excited at rather low temperatures, but electronic modes need a much larger temperature or energy to be excited. However, a self-consistent calculation can be done by first using time-independent perturbation, calculating D_{ij} , then finding the normal modes, ω_0 . The ω_0 's can be used as the first-order approximation in the time-dependent expression for the dynamic energy to calculate new ω_1 's. The new ω_1 's are in turn placed back into the time-dependent expression for the dynamic energy and the third round of ω_2 's is obtained. This iterative calculation should be continued until convergence is obtained.

CONCLUSION

The force constants D_{ij} have now been obtained rather rigorously. The next step is to calculate the normal modes of vibration. Since the force constants have been calculated by introducing the long range interactions due to the conduction and valence electrons through the electronic energy, it would be inconsistent to calculate the normal modes using equations of motion with the same force constants or to consider just the force constants associated with the defect to differ only out to a certain number of nearest neighbors. Therefore, the equations of motion should be written down in which all the force constants between all ions are capable of being different. Indeed, if only one defect is introduced in the crystal, it is not difficult to see from the change in the pseudopotential and electronic and electrostatic energies that all force constants will be changed. Also, the introduction of two or more defects makes the force constants dependent on the relative distance between defects. Therefore, the normal modes of the imperfect crystal and its total energy, including the ground state energy, will be dependent on the relative distance between defects.

The virtues of the theory lie in the fact that all calculations are self-contained. Nevertheless, just as a chain is no stronger than its weakest link, the drawbacks of the theory, even if minute, should be exposed.

First, some scheme must be invented to handle the relaxation of the lattice due to the introduction of defects.

Second, overlap of core states will definitely complicate the calculation. The OPW's on different crystal sites will no longer be orthogonal. As a result, a new set of basic functions should be employed, i.e. Wannier functions.

Third, because of the inclusion of one or more defects, all translational symmetry is destroyed.* This means that the linear momentum is no longer a generator of the translational symmetry group which happens to be abelian, and no longer commutes with the Hamiltonian. Therefore, \mathbf{k} cannot be a good eigenstate label.

Fourth and last, some defects have several equivalent configurations. Therefore, they are degenerate in energy, the degeneracy manifesting itself in the local symmetry of the defect and its surroundings. To jump into another equivalent position, the defect

*In the case of one defect, the rotation group of the crystal about the defect may be a subgroup of the perfect crystal point group.

has to surmount a potential barrier which in some cases is very small.* In these cases, the harmonic approximation is no longer valid. This is probably the case of the interstitial Li, which is interesting in itself since it interacts in some unknown way with vacancies. To treat such examples an anharmonic calculation is undoubtedly needed. Nevertheless, a calculation in which the present theoretical treatment is employed should prove to be exceedingly useful.

ACKNOWLEDGMENTS

I would like to acknowledge the prior work of Dr. P. H. Fang, who originally proposed the problem, particularly the unexplained drastic effect of interstitial Li on the trapping and recombination levels due to vacancies and vacancy-impurity defects. I would also like to thank Dr. T. Tanaka, whose advice and consultation made the calculation herein possible.

REFERENCES

1. Sokoloski, M. M., "Structure and Kinetics of Defects in Silicon," which has a comprehensive bibliography (to be published as a GSFC Technical Note on the subject).
2. Kittel, C., Introduction to Solid State Physics, New York: John Wiley & Sons, p. 27.
3. Watkins, G. D., J. Phys. Soc. Japan 18 (Suppl. II, 22), 1963. Also see Reference 1 for more information.
4. Logan, R. A., Phys. Rev. 101:1455, 1956.
5. Swalin, R. A., J. Phys. Chem. Solids 18:290, 1960.
6. Scholz, A., Phys. Status Solidi 3:43, 1963.
7. Benneman, K. H., Phys. Rev. 137:A1497, 1965.
8. Callaway, J., and Hughes, A. J., Phys. Rev. 156:860, 1967.
9. Kleinman, J., and Phillips, J. C., Phys. Rev. 118:1153, 1960.
10. Harrison, W. A., Pseudopotential in the Theory of Metals, Frontiers in Physics Series, New York: W. A. Benjamin Pub., 1966.
11. Brust, D., Phys. Rev. 134:A1337, 1964.

*The "interstitial" oxygen atom in Si has six equivalent positions. However, it has been pointed out (Hrowstowski and Adler, J. Phys. Chem. Solids 25:873, 1964) that the barrier for reorientation from one equivalent position to another is so small that at room temperature the oxygen in the Si-O-Si bond is essentially a free rotator. It has also been pointed out (K. Weiser, Phys. Rev. 126:1427, 1962) that the interstitial atom (host or impurity) can occupy either of two saddlepoint positions whose potential barrier for reorientation may be quite small.

APPENDIX A
CALCULATION OF E_k FOR A STATIC CRYSTAL BY USING
TIME-INDEPENDENT PERTURBATION THEORY

The wave equation for the crystal is given by Equation 1.11 as

$$(\mathbf{T} + \mathbf{W}) \varphi_k = E_k \varphi_k \quad (\text{A-1})$$

The pseudopotential is treated as a small perturbation on the exact free electron equation, i.e. $\mathbf{T}|k\rangle = E_0|k\rangle$, where

$$E_0 = \frac{\hbar^2 k^2}{2m}$$

Then Equation 1.12 is written as

$$(\mathbf{T} + \lambda \mathbf{W}) \varphi_k = E_k \varphi_k, \quad (\text{A-2})$$

and the perturbed function φ_k and energy E_k are expanded in a power series in λ . The subscript k is dropped for the time being:

$$\begin{aligned} \varphi_k &= \varphi_0 + \lambda \varphi_1 + \lambda^2 \varphi_2 + \dots, \text{ and} \\ E_k &= E_0 + \lambda E_1 + \lambda^2 E_2 + \dots \end{aligned} \quad (\text{A-3})$$

This in turn is placed into Equation A-1 to yield

$$(\mathbf{T} + \lambda \mathbf{W}) (\varphi_0 + \lambda \varphi_1 + \lambda^2 \varphi_2 + \dots) = (E_0 + \lambda E_1 + \lambda^2 E_2 + \dots) (\varphi_0 + \lambda \varphi_1 + \lambda^2 \varphi_2 + \dots). \quad (\text{A-4})$$

Since λ is an arbitrary parameter ($0 \leq \lambda \leq 1$), which will subsequently be set equal to 1, the coefficients of like powers of λ are equal. Then

$$\mathbf{T} \varphi_0 = E_0 \varphi_0, \text{ to zero order in } \lambda, \quad (\text{A-5})$$

$$\mathbf{T} \varphi_1 + \mathbf{W} \varphi_0 = E_0 \varphi_1 + E_1 \varphi_0, \text{ to first order in } \lambda, \quad (\text{A-6})$$

and finally

$$\mathbf{T} \varphi_2 + \mathbf{W} \varphi_1 = E_0 \varphi_2 + E_1 \varphi_1 + E_2 \varphi_0, \text{ to second order in } \lambda. \quad (\text{A-7})$$

Now the zero order state φ_0 is just

$$\varphi_0 = \Omega^{-1/2} |k\rangle, \quad (\text{A-8})$$

and the zero order energy is

$$E_0 = \frac{\hbar^2 k^2}{2m}. \quad (\text{A-9})$$

From the first section, it is already known that plane waves form a basis for the $\varphi_{\mathbf{k}}$'s. Therefore

$$\varphi_1 = \sum_{\mathbf{q}} a_{\mathbf{q}}^{(1)}(\mathbf{k}) |\mathbf{k} + \mathbf{q}\rangle, \quad (\text{A-10})$$

where $\mathbf{q} = 0$ yields the zero order state (Equation A-8). This in turn is placed into the first-order expression in Equation A-6:

$$\sum_{\mathbf{q}} a_{\mathbf{q}}^{(1)} T |\mathbf{k} + \mathbf{q}\rangle + W |\mathbf{k}\rangle = E_0 \sum_{\mathbf{q}} a_{\mathbf{q}}^{(1)} |\mathbf{k} + \mathbf{q}\rangle + E_1 |\mathbf{k}\rangle. \quad (\text{A-11})$$

Then Equation A-11 is multiplied through by $\langle \mathbf{k}' |$, and the orthogonality of the plane wave functions is used,

$$\sum_{\mathbf{q}} a_{\mathbf{q}}^{(1)} \langle \mathbf{k}' | T |\mathbf{k} + \mathbf{q}\rangle + \langle \mathbf{k}' | W |\mathbf{k}\rangle = E_0 \sum_{\mathbf{q}} a_{\mathbf{q}}^{(1)} \langle \mathbf{k}' | \mathbf{k} + \mathbf{q}\rangle + E_1 \langle \mathbf{k}' | \mathbf{k}\rangle. \quad (\text{A-12})$$

Now

$$T |\mathbf{k} + \mathbf{q}\rangle = \left(\frac{\hbar^2}{2m} |\mathbf{k} + \mathbf{q}|^2 \right) |\mathbf{k} + \mathbf{q}\rangle, \quad (\text{A-13})$$

and

$$\langle \mathbf{k}' | \mathbf{k}\rangle = \delta_{\mathbf{k}', \mathbf{k}}. \quad (\text{A-14})$$

Then Equation A-12 becomes, by using Equations A-13 and A-14,

$$\sum_{\mathbf{q}} a_{\mathbf{q}}^{(1)} \left(\frac{\hbar^2}{2m} |\mathbf{k} + \mathbf{q}|^2 \right) \delta_{\mathbf{k}', \mathbf{k} + \mathbf{q}} + \langle \mathbf{k}' | W |\mathbf{k}\rangle = E_0 \sum_{\mathbf{q}} a_{\mathbf{q}}^{(1)} \delta_{\mathbf{k}', \mathbf{k} + \mathbf{q}} + E_1 \delta_{\mathbf{k}', \mathbf{k}}, \quad (\text{A-15})$$

and for $\mathbf{k}' = \mathbf{k}$

$$E_1 = \langle \mathbf{k} | W |\mathbf{k}\rangle, \quad (\text{A-16})$$

and for $\mathbf{k}' = \mathbf{k} + \mathbf{q}$

$$a_{\mathbf{q}}^{(1)} = \frac{\langle \mathbf{k} + \mathbf{q} | W |\mathbf{k}\rangle}{\frac{\hbar^2}{2m} (k^2 - |\mathbf{k} + \mathbf{q}|^2)}, \quad (\text{A-17})$$

which are the first-order correction terms to $\varphi_{\mathbf{k}}$ and $E_{\mathbf{k}}$. To find the second-order correction in energy, the function is again expanded as in Equation A-10,

$$\varphi_2 = \sum_{\mathbf{q}} a_{\mathbf{q}}^{(2)}(\mathbf{k}) |\mathbf{k} + \mathbf{q}\rangle. \quad (\text{A-18})$$

This is placed into Equation A-7 to obtain

$$\sum_{\mathbf{q}} a_{\mathbf{q}}^{(2)} T |\mathbf{k} + \mathbf{q}\rangle + \sum_{\mathbf{q}} a_{\mathbf{q}}^{(1)} W |\mathbf{k} + \mathbf{q}\rangle = E_0 \sum_{\mathbf{q}} a_{\mathbf{q}}^{(2)} |\mathbf{k} + \mathbf{q}\rangle + E_1 \sum_{\mathbf{q}} a_{\mathbf{q}}^{(1)} |\mathbf{k} + \mathbf{q}\rangle + E_2 |\mathbf{k}\rangle. \quad (\text{A-19})$$

Again Equation A-19 is multiplied through by $\langle k' |$ and use is made of Equation A-14 to obtain

$$\begin{aligned} & \sum a_q^{(2)} \left(\frac{\hbar^2}{2m} |k + q|^2 \right) \delta_{k', k+q} + \sum a_q^{(1)} \langle k' | W | k + q \rangle \\ & = E_0 \sum a_q^{(2)} \delta_{k', k+q} + E_1 \sum a_q^{(1)} \delta_{k', k+q} + E_2 \delta_{k', k}. \end{aligned} \quad (\text{A-20})$$

Now for $k' = k$,

$$\begin{aligned} E_2 & = \sum_q' a_q^{(1)} \langle k | W | k + q \rangle, \text{ or} \\ & = \sum_q' \frac{\langle k + q | W | k \rangle \langle k | W | k + q \rangle}{\frac{\hbar^2}{2m} (k^2 - |k + q|^2)}. \end{aligned} \quad (\text{A-21})$$

where the prime signifies $q = 0$ term is missing. Then $E_k = E_0 + \lambda E_1 + \lambda^2 E_2$, to second order. Setting $\lambda = 1$, and substituting Equations A-21 and A-16 into the above expression,

$$E_k = \frac{\hbar^2 k^2}{2m} + \langle k | W | k \rangle + \sum_q' \frac{\langle k + q | W | k \rangle \langle k | W | k + q \rangle}{\frac{\hbar^2}{2m} (k^2 - |k + q|^2)}, \quad (\text{A-22})$$

which is the energy as a function of k correct to second order in the perturbation.

APPENDIX B
CALCULATION OF THE HERMITICITY OF P AND THE ENERGY
TO SECOND ORDER BY USING W_L

The non-diagonal matrix elements of P are given by

$$\langle \mathbf{k} + \mathbf{q} | P | \mathbf{k} \rangle^* = \sum_{\alpha a} \langle \mathbf{k} + \mathbf{q} | \alpha a \rangle^* \langle \alpha a | \mathbf{k} \rangle^* ,$$

or

$$= \frac{1}{\Omega} \sum_{\alpha a} \int e^{i(\mathbf{k} + \mathbf{q}) \cdot \mathbf{r}} \psi_{\alpha}^* (\mathbf{r} - \mathbf{r}_a) d\mathbf{r} \int e^{-i\mathbf{k} \cdot \mathbf{r}'} \psi_{\alpha} (\mathbf{r}' - \mathbf{r}_a) d\mathbf{r}' ,$$

or

$$= \frac{1}{\Omega} \sum_{\alpha a} \int e^{-i\mathbf{k} \cdot \mathbf{r}'} \psi_{\alpha} (\mathbf{r}' - \mathbf{r}_a) d\mathbf{r}' \int e^{i(\mathbf{k} + \mathbf{q}) \cdot \mathbf{r}} \psi_{\alpha}^* (\mathbf{r} - \mathbf{r}_a) d\mathbf{r} ,$$

or

$$= \sum_{\alpha a} \langle \mathbf{k} | \alpha a \rangle \langle \alpha a | \mathbf{k} + \mathbf{q} \rangle ,$$

or finally

$$= \langle \mathbf{k} | P | \mathbf{k} + \mathbf{q} \rangle . \tag{B-1}$$

From Equation 2.23, the difference between the off diagonal matrix elements of the D defect pseudopotential and its complex conjugate is given by

$$\langle \mathbf{k} + \mathbf{q} | W_L | \mathbf{k} \rangle^* - \langle \mathbf{k} | W_L | \mathbf{k} + \mathbf{q} \rangle = \frac{\hbar^2}{2m} (k^2 - |\mathbf{k} + \mathbf{q}|^2) \langle \mathbf{k} | P | \mathbf{k} + \mathbf{q} \rangle . \tag{B-2}$$

The second-order contribution to the energy from Appendix A is given by

$$E_{\mathbf{k}}^{(2)} = \sum_{\mathbf{q}}' \frac{\langle \mathbf{k} + \mathbf{q} | W_L | \mathbf{k} \rangle \langle \mathbf{k} | W_L | \mathbf{k} + \mathbf{q} \rangle}{\frac{\hbar^2}{2m} (k^2 - |\mathbf{k} + \mathbf{q}|^2)} , \tag{B-3}$$

which can be rewritten by substituting Equation B-2 for $\langle \mathbf{k} | W_L | \mathbf{k} + \mathbf{q} \rangle$ as

$$E_{\mathbf{k}}^{(2)} = \sum_{\mathbf{q}}' \frac{|\langle \mathbf{k} + \mathbf{q} | W_L | \mathbf{k} \rangle|^2}{\frac{\hbar^2}{2m} (k^2 - |\mathbf{k} + \mathbf{q}|^2)} - \sum_{\mathbf{q}}' \langle \mathbf{k} | P | \mathbf{k} + \mathbf{q} \rangle \langle \mathbf{k} + \mathbf{q} | W | \mathbf{k} \rangle . \tag{B-4}$$

The last term can be rewritten as

$$\sum_{\mathbf{q}} \langle \mathbf{k} | P | \mathbf{k} + \mathbf{q} \rangle \langle \mathbf{k} + \mathbf{q} | P | \mathbf{k} \rangle - \langle \mathbf{k} | P | \mathbf{k} \rangle \langle \mathbf{k} | W | \mathbf{k} \rangle , \tag{B-5}$$

where the first term is now an unrestricted sum and the second term is the $q = 0$ term. If the following closure relation is used:

$$\sum_{\mathbf{q}} |\mathbf{k} + \mathbf{q}\rangle \langle \mathbf{k} + \mathbf{q}| = 1,$$

then B-5 becomes

$$\langle \mathbf{k} | \mathbf{P} \mathbf{W} | \mathbf{k} \rangle - \langle \mathbf{k} | \mathbf{P} | \mathbf{k} \rangle \langle \mathbf{k} | \mathbf{W} | \mathbf{k} \rangle. \quad (\text{B-6})$$

The first term again can be written by using Equation 2.21 and the fact that $\mathbf{P} \cdot \mathbf{P} = \mathbf{P}$, as

$$\langle \mathbf{k} | \mathbf{P} \mathbf{W} | \mathbf{k} \rangle = \langle \mathbf{k} | \mathbf{P} (1 - \mathbf{P}) \mathbf{V} | \mathbf{k} \rangle + \frac{\langle \mathbf{k} | (1 - \mathbf{P}) \mathbf{V} | \mathbf{k} \rangle}{1 - \langle \mathbf{k} | \mathbf{P} | \mathbf{k} \rangle} \langle \mathbf{k} | \mathbf{P} | \mathbf{k} \rangle,$$

or

$$= \frac{\langle \mathbf{k} | (1 - \mathbf{P}) \mathbf{V} | \mathbf{k} \rangle}{1 - \langle \mathbf{k} | \mathbf{P} | \mathbf{k} \rangle} \cdot \langle \mathbf{k} | \mathbf{P} | \mathbf{k} \rangle,$$

which becomes, by using Equation 2.24,

$$\langle \mathbf{k} | \mathbf{P} \mathbf{W} | \mathbf{k} \rangle = \langle \mathbf{k} | \mathbf{W} | \mathbf{k} \rangle \langle \mathbf{k} | \mathbf{P} | \mathbf{k} \rangle$$

Therefore B-5 is zero to second order, and the second-order term in the energy can simply be written as

$$E_{\mathbf{k}}^{(2)} = \sum_{\mathbf{q}}' \frac{|\langle \mathbf{k} + \mathbf{q} | \mathbf{W}_L | \mathbf{k} \rangle|^2}{\frac{\hbar^2}{2m} (k^2 - |\mathbf{k} + \mathbf{q}|^2)}.$$

APPENDIX C

THE SELF-CONSISTENT DETERMINATION OF $W|k\rangle$ AND $W^{(D)}|k\rangle$ BY SUCCESSIVE ITERATIONS

The linear operator on eigenstate $|k\rangle$ is given by Equation 2.25 as

$$W|k\rangle = V|k\rangle + \sum_{\alpha a} \left(\frac{\hbar^2 k^2}{2m} - E_\alpha \right) |\alpha a\rangle \langle \alpha a|k\rangle + \langle k|W|k\rangle P|k\rangle$$

The first iteration yields

$$\begin{aligned} W|k\rangle = & V|k\rangle + \sum_{\alpha a} \left(\frac{\hbar^2 k^2}{2m} - E_\alpha \right) |\alpha a\rangle \langle \alpha a|k\rangle + \langle k|V|k\rangle P|k\rangle \\ & + \sum_{\alpha a} \left(\frac{\hbar^2 k^2}{2m} - E_\alpha \right) \langle k|\alpha a\rangle \langle \alpha a|k\rangle P|k\rangle + \langle k|W|k\rangle \langle k|P|k\rangle P|k\rangle \end{aligned} \quad (C-1)$$

The second iteration yields

$$\begin{aligned} W|k\rangle = & V|k\rangle + \sum_{\alpha a} \left(\frac{\hbar^2 k^2}{2m} - E_\alpha \right) |\alpha a\rangle \langle \alpha a|k\rangle + \langle k|V|k\rangle P|k\rangle \\ & + \sum_{\alpha a} \left(\frac{\hbar^2 k^2}{2m} - E_\alpha \right) \langle k|\alpha a\rangle \langle \alpha a|k\rangle P|k\rangle + \langle k|V|k\rangle \langle k|P|k\rangle P|k\rangle \\ & + \sum_{\alpha a} \left(\frac{\hbar^2 k^2}{2m} - E_\alpha \right) \langle k|\alpha a\rangle \langle \alpha a|k\rangle \langle k|P|k\rangle P|k\rangle \\ & + \langle k|W|k\rangle \left(\langle k|P|k\rangle \right)^2 P|k\rangle . \end{aligned} \quad (C-2)$$

Each iteration adds the same two factors, $\langle k|V|k\rangle$ and

$$\sum_{\alpha a} \left(\frac{\hbar^2 k^2}{2m} - E_\alpha \right) \langle k|\alpha a\rangle \langle \alpha a|k\rangle P|k\rangle ,$$

multiplied by a power of $\langle k|P|k\rangle$. The $N + 1$ iteration yields

$$\begin{aligned} W|k\rangle = & V|k\rangle + \sum_{\alpha a} \left(\frac{\hbar^2 k^2}{2m} + \langle k|V|k\rangle - E_\alpha \right) |\alpha a\rangle \langle \alpha a|k\rangle \\ & + \left[1 + \langle k|P|k\rangle + \left(\langle k|P|k\rangle \right)^2 + \left(\langle k|P|k\rangle \right)^3 + \dots \right. \\ & \left. \dots + \left(\langle k|P|k\rangle \right)^N \right] \sum_{\alpha a} \left(\frac{\hbar^2 k^2}{2m} + \langle k|V|k\rangle - E_\alpha \right) \langle k|\alpha a\rangle \langle \alpha a|k\rangle P|k\rangle . \end{aligned} \quad (C-3)$$

By mathematical induction it follows that after infinite number of iterations

$$\begin{aligned}
 W|\mathbf{k}\rangle = & V|\mathbf{k}\rangle + \sum_{\alpha a} \left(\frac{\hbar^2 k^2}{2m} + \langle \mathbf{k}|V|\mathbf{k}\rangle - E_a \right) |\alpha a\rangle \langle \alpha a|\mathbf{k}\rangle \\
 & + \left(1 - \langle \mathbf{k}|P|\mathbf{k}\rangle \right)^{-1} \sum_{\alpha a} \left(\frac{\hbar^2 k^2}{2m} + \langle \mathbf{k}|V|\mathbf{k}\rangle - E_a \right) \langle \mathbf{k}|\alpha a\rangle \langle \alpha a|\mathbf{k}\rangle P|\mathbf{k}\rangle
 \end{aligned} \tag{C-4}$$

The diagonal elements can be obtained by multiplying Equation C-4 through by $\langle \mathbf{k}|$:

$$\langle \mathbf{k}|W|\mathbf{k}\rangle = \langle \mathbf{k}|V|\mathbf{k}\rangle + \frac{\sum_{\alpha a} \left(\frac{\hbar^2 k^2}{2m} + \langle \mathbf{k}|V|\mathbf{k}\rangle - E_a \right) \langle \mathbf{k}|\alpha a\rangle \langle \alpha a|\mathbf{k}\rangle}{1 - \langle \mathbf{k}|P|\mathbf{k}\rangle}, \tag{C-5}$$

and the off diagonal elements by $\langle \mathbf{k} + \mathbf{q}|$:

$$\begin{aligned}
 \langle \mathbf{k} + \mathbf{q}|W|\mathbf{k}\rangle = & \langle \mathbf{k} + \mathbf{q}|V|\mathbf{k}\rangle + \sum_{\alpha a} \left(\frac{\hbar^2 k^2}{2m} + \langle \mathbf{k}|V|\mathbf{k}\rangle - E_a \right) \times \\
 & \times \langle \mathbf{k} + \mathbf{q}|\alpha a\rangle \langle \alpha a|\mathbf{k}\rangle \\
 & + \sum_{\alpha a} \left(\frac{\hbar^2 k^2}{2m} + \langle \mathbf{k}|V|\mathbf{k}\rangle - E_a \right) \langle \mathbf{k}|\alpha a\rangle \langle \alpha a|\mathbf{k}\rangle \frac{\langle \mathbf{k} + \mathbf{q}|P|\mathbf{k}\rangle}{1 - \langle \mathbf{k}|P|\mathbf{k}\rangle}.
 \end{aligned} \tag{C-6}$$

The diagonal and non-diagonal matrix elements of the D defect pseudopotential can be obtained from Equations C-5 and C-6 by merely replacing $V(\mathbf{r})$ by the D defect crystal potential $V^{(D)}(\mathbf{r})$ and requiring the indices $\alpha a = \lambda l, \sigma s$, and γg . Otherwise the equations are identical, since the indices αa are arbitrary.

APPENDIX D
CALCULATION OF THE FOURIER TRANSFORM OF
THE EWALD-FUCHS POTENTIAL

The Ewald-Fuchs potential between two arbitrary lattice sites a and b is given by

$$V(|\mathbf{r}_a - \mathbf{r}_b|) = \frac{Z_a^* Z_\beta^* e^2}{|\mathbf{r}_a - \mathbf{r}_b|} \left(\frac{2}{\pi}\right) \int_0^{\sqrt{\eta} |\mathbf{r}_a - \mathbf{r}_b|} e^{-x^2} dx. \quad (\text{D-1})$$

The Fourier transform of this potential will then be

$$F[V(\mathbf{R})] = \int V(\mathbf{R}) e^{-i\mathbf{q} \cdot \mathbf{R}} d\mathbf{R}, \quad (\text{D-2})$$

where $\mathbf{R} = \mathbf{r}_a - \mathbf{r}_b$ and $R = |\mathbf{R}|$. If $\angle(\mathbf{q}, \mathbf{R}) = \theta$, then this can be written as

$$F[V(\mathbf{R})] = 2\pi \int_0^\infty \int_0^\pi V(R) e^{-i q R \cos \theta} \sin \theta d\theta R^2 dR, \quad (\text{D-3})$$

which can immediately be integrated to yield

$$F[V(\mathbf{R})] = \frac{4\pi}{q} \int_0^\infty V(R) \sin qR R dR. \quad (\text{D-4})$$

Upon substituting $V(R)$ into the above expression, the following form is obtained:

$$F[V(\mathbf{R})] = \frac{8\pi Z_a^* Z_\beta^* e^2}{q \sqrt{\pi}} \int_0^\infty \sin qR G(R) dR, \quad (\text{D-5})$$

where

$$G(R) = \int_0^{\sqrt{\eta} R} e^{-x^2} dx. \quad (\text{D-6})$$

A partial integration is done on the R dependent part:

$$F[V(\mathbf{R})] = \left(\frac{\cos qR \cdot G(R)}{q} \Big|_0^\infty - \frac{\sqrt{\eta}}{q} \int_0^\infty \cos qR e^{-\eta R^2} dR \right) \frac{8\pi Z_a^* Z_\beta^* e^2}{q \sqrt{\eta}}. \quad (\text{D-7})$$

The first term, the surface term, is zero at the lower limit and at the upper limit oscillates rapidly enough to give zero contribution. Therefore, the total contribution comes from the second term, which can be rewritten as

$$F[V(\mathbf{R})] = \left(\frac{\sqrt{\eta}}{q} R \int_0^\infty e^{-i q R - \eta R^2} dR \right) \frac{8\pi Z_a^* Z_\beta^* e^2}{q \sqrt{\eta}}. \quad (\text{D-8})$$

This can be recognized as just the Fourier transform of a gaussian distribution, which is readily integrated by completing the square in the exponent,

$$F [V(R)] = \frac{4\pi Z_\alpha^* Z_\beta^* e^2}{q^2} e^{-q^2/4\eta} \quad (D-9)$$

GROUP E

INTERDISCIPLINARY INFORMATION TRANSFER

(BIOMEDICAL)

Academic Personnel

Principal Investigator:	Dr. Sun (Drexel)
Faculty:	Dr. Fromm (Drexel)
Graduate Students:	Mr. Zeskind (George Wash. U.)

Goddard Personnel

Staff Advisor:	Mr. New
-----------------------	----------------

PROCESS OF INFORMATION TRANSFER AND TECHNOLOGY UTILIZATION

H. H. Sun,* E. Fromm,** J. C. New†

INTRODUCTION

There exists at the present time a growing interest in developing new knowledge through information transfer between disciplines and an awareness of the important process of technology transfer within various sectors of our society. These two closely related processes are derived from the same motivation; i.e., to effectively use knowledge by encouraging communications between disciplines and different sections of society in an effort to solve problems of common needs or objectives.

Adapting space technology to biomedicine for civilian use provides an excellent example of information transfer (References 1 and 2). The research must be conducted by an interdisciplinary team of medical and physical scientists capable of recognizing the potential application and adapting the technology to solution of biomedical problems. The interdisciplinary team must be able to communicate with each other and to disseminate information from government agencies or government-sponsored industries for effective use in biomedical problems.

The paper will present a brief study of the information transfer process among various sectors of society and also of information transfer among persons in an interdisciplinary team. A case study of information transfer and technology utilization from the space effort to biomedicine will be presented. From this result, a system model of the technology transfer will be presented, which will cover the major elements and processes involved in this transfer.

INFORMATION TRANSFER PROCESS BETWEEN SECTORS OF SOCIETY

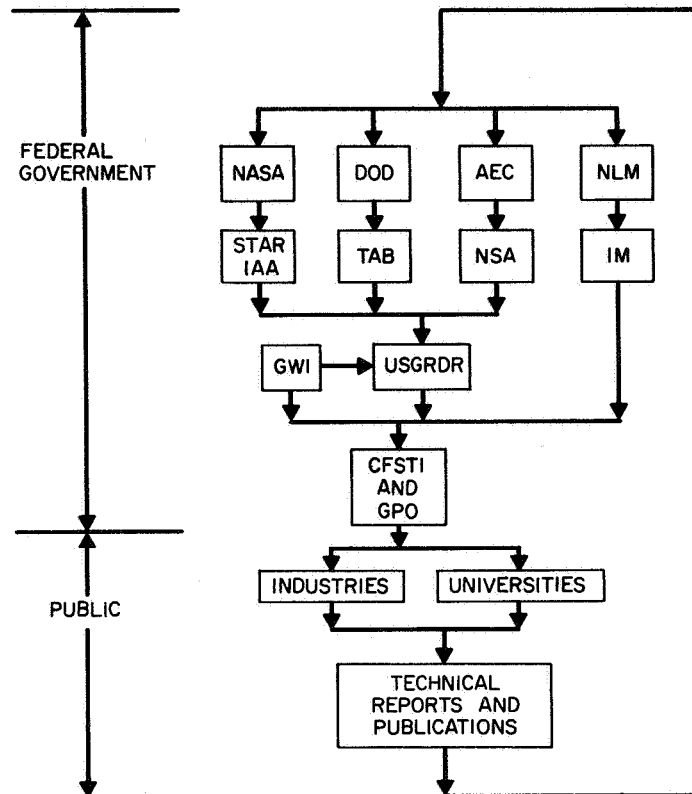
There are three sectors of our society that are concerned with the problem of technology transfer (References 3 and 4): federal government, industries, and universities. The federal government is currently supporting research and development programs at an annual rate of more than \$23 billion. The process of information transfer is made within these three sections, with the federal government providing the major sources of information and new technology.

Three agencies, Department of Defense (DOD), NASA, and Atomic Energy Commission (AEC), account for nearly 90 percent of the federal research and development (R & D) spending (Reference 5). From 1962 to 1966 the number of abstracts in NASA's listing of Scientific and Technical Aerospace Reports (STAR) in the Biomedicine area (Bioscience and Biotechnology) increased about twenty fold. Because of the large number of governmental agencies and their involvement in different technical areas, the problem of communication with the government agencies themselves becomes formidable. Communication between government and industries and universities, therefore, becomes a very difficult task (Reference 6).

*Director, Biomedical Engineering Program, Drexel Institute of Technology, Philadelphia, Pa.

**Assistant Professor, Biomedical Engineering Program, Drexel Institute of Technology, Philadelphia, Pa.

†Chief, Test and Evaluation Division, Goddard Space Flight Center, Greenbelt, Md.



STAR—Scientific and Technical Aerospace Reports, IAA—International Aerospace Abstracts, TAB—Technical Abstracts Bulletin, (As of September 1, 1967, all DOD publications will go directly into USGRDR and TAB will only list the classified documents.) NSA—Nuclear Science Abstracts IM—Index Medicus.

Figure 1—Major channels of information transfer.

A detailed study was conducted to identify the major channels of communication for technical and scientific information transfer. The result is presented in a flow chart in Figure 1. DOD, NASA, and AEC, together with the National Library of Medicine (NLM), comprise the major source of technical information, with each publishing an abstract and index. The federal government is now publishing the Government Wide Index (GWI) and United States Government Research and Development Reports (USGRDR) to consolidate output of the three agencies. The Clearinghouse for Federal Scientific and Technical Information (CFSTI) and the Government Printing Office (GPO) act as the outlet for providing documents to the public. Industries and universities that are under contract from one government agency normally can obtain these documents without cost. The R & D results are published in technical reports, symposium proceedings, or scientific and technical journals, which are then returned to the government agencies for indexing and abstracting. This completes the closed loop of the information transfer system. It is obvious that major information transfer can be established only if the loop is closed, and the cycle time within the closed loop must be kept as small as possible.

The major problems in the information transfer process can be summarized as follows:

1. Identification for the source of information – The information source from various government-sponsored research and development efforts, as shown in Figure 1, is a very complicated process to identify. The various agencies, each with its own publication and line of communication, are not clearly specified in any library or reference desk.

2. Time lag on the information flow – The flow of the information from government agencies to research, and from research to the document centers, generally takes considerable time. Most publications take from 8 months to 1 year from the time the paper is submitted to the time when the published paper is available for abstracting (Reference 2).
3. Dissemination process – The dissemination of information requires that a researcher must have the documents readily available. Government agencies must make all the information available to the general public without restriction and cost.

INFORMATION TRANSFER BETWEEN VARIOUS DISCIPLINES OF TECHNOLOGY

Recent technological advances have developed a new concept of the nature and behavior of matter and energy. The boundaries among different scientific disciplines gradually have disappeared, and a unification of science has evolved. The tools and techniques of physics and engineering have reached a level of sophistication that can be applied equally to biomedicine and the social sciences. The development of space technology provides an excellent example in the information exchange among disciplines (Reference 1).

Scientists and engineers have become aware of the importance of transfer of knowledge from the study of inanimate systems to the living and social systems. Universities have recognized this problem and have established many interdisciplinary programs to conduct research and training (Reference 4). NASA has been actively involved in this type of information transfer and has exerted a major influence in helping to form these new disciplines (Reference 7).

Figure 2 illustrates the process of transferring information from space technology to the civilian population and the gradual evolvement of new disciplines in universities. The advances made by various areas in space research and development can be easily

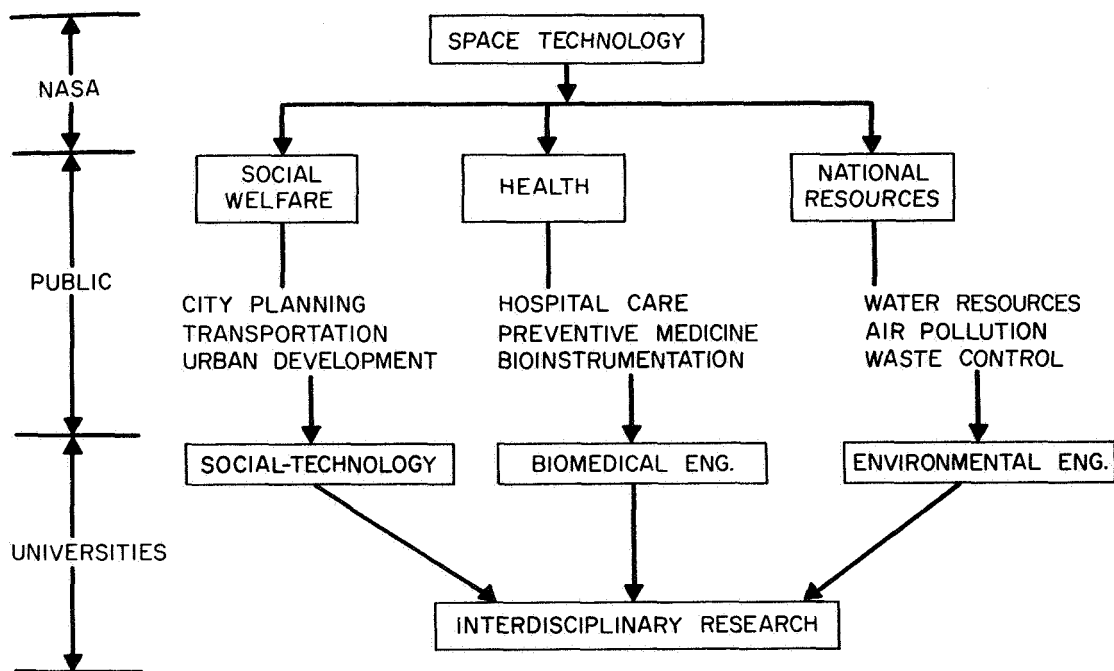


Figure 2—Information transfer from space technology to various disciplines.

applied to problems in social welfare, health, and national resources (Reference 8). The complexity and urgency of these problems have become a great national concern. A valuable process for information transfer has been developed by incorporating scientific and engineering knowledge gained through space technology into social, health, and environmental problems.

The teamwork of sociologists and engineers has been successfully utilized by many space-oriented industries to solve social-based problems. A new discipline of social-technology has been established by social scientists and physical scientists to bridge the gap (Reference 9). Biomedical engineering was first established about 10 years ago by a group of physical scientists and life scientists (Reference 10). Since then, many important discoveries in basic and applied physiologic research have been made that will greatly improve the health of the nation. The problem of national resources is now being attacked by chemists, engineers, and medical researchers. This group is organized into the new discipline of environmental engineering and has concentrated its efforts in this major problem (Reference 9).

PROCESS OF TECHNOLOGY TRANSFER AS DEVELOPED THROUGH A SPECIFIC R AND D PROBLEM

To identify the information transfer process from space technology to other sectors of the society through interdisciplinary approach, study of a specific R & D problem has been undertaken. The result of this study can be easily applied to the general problem of information transfer for technology utilization of space work.

The specific problem is how to develop a miniaturized personal-borne physiological monitoring system for continuously monitoring body functions while the subject is performing his normal activities in his native environment. This problem will greatly affect the study of information transfer and technology utilization. NASA has developed a complete monitoring system for astronauts in the Mercury Gemini projects. The prime consideration of NASA, however, is reliability under high-impact, gravitational, and vibration environments. The system was developed at a cost not suitable for civilian purposes. Furthermore, most of the information is scattered through a large variety of sources, such as contractor's reports, technical documents, and scientific journals in various government agencies, industries, and universities.

An interdisciplinary team, consisting of engineers and physiologists from universities, was organized, and the project was launched at the Goddard Space Flight Center (GSFC) as a part of the Summer Workshop. The process of this R & D effort is shown in a block design in Figure 3. Preliminary concepts were developed through personal contacts and library search of NASA-published literature and abstracts. A tentative model was then developed from these concepts through additional information transfer from NASA contractors and other NASA centers. Conferences were held with clinical medical personnel to obtain their opinions on the types of parameters required and size and weight problems. Preliminary designs were made using materials from information and data banks, and testing and evaluation of the system blocks were conducted using GSFC's testing facilities. This completed the first phase of the work. Further work on interface and system refinement, system test, and final model, development can be carried out within a short period of time.

The results of this study can be applied to other problems of information transfer and technology utilization from space effort to social welfare, health, and natural resources as mentioned earlier. NASA, with its great potential of technical development and scientific knowledge, provides the three major requirements of the technology

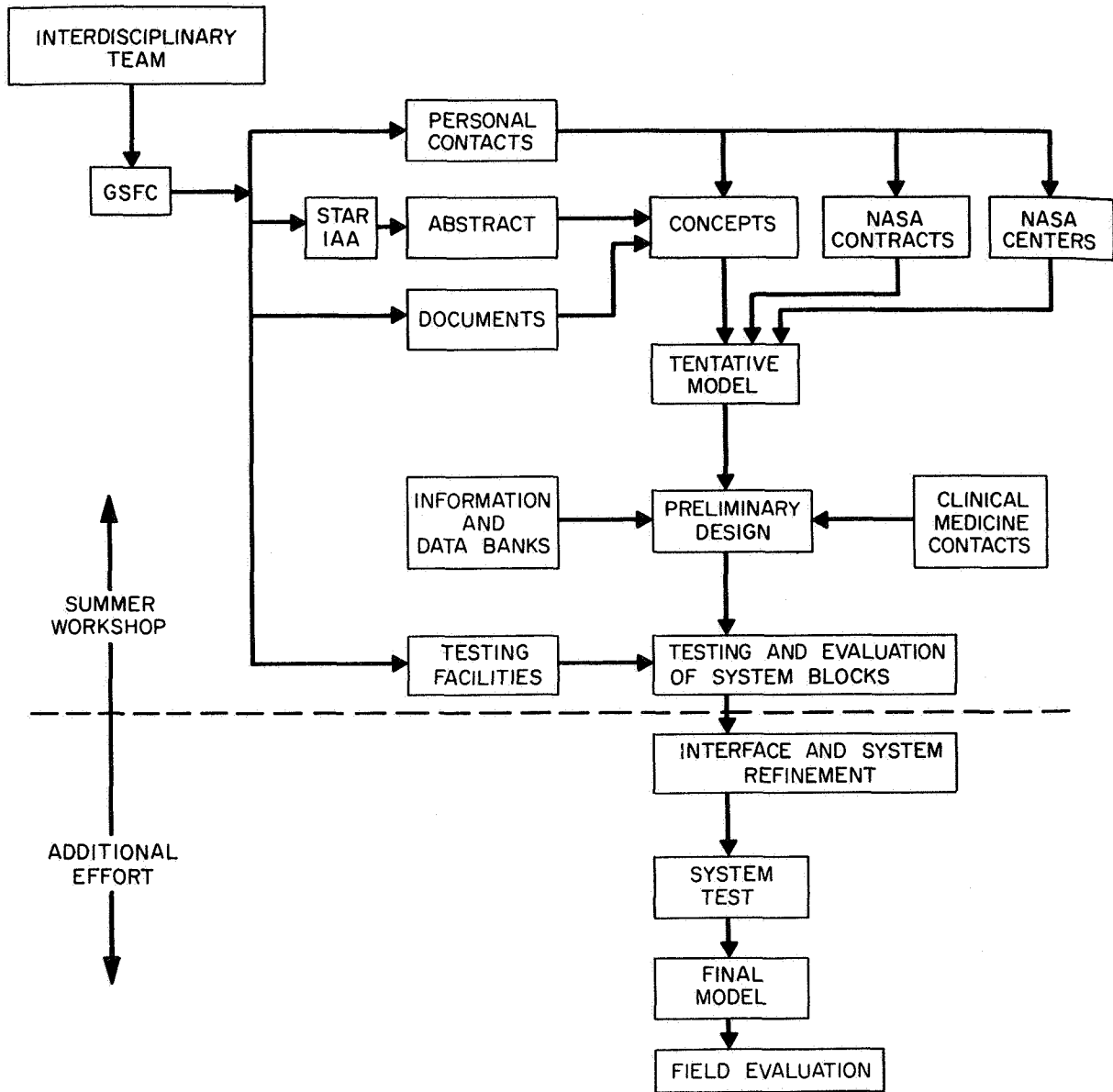


Figure 3—Process of information transfer for an R & D problem.

transfer, i.e., technical documents, scientific environment, and research and engineering facilities. Technology transfer and utilization can be easily accomplished through dissemination of the documents, personal contact, and work in the NASA's scientific environment, using its facilities for laboratory and experimental study. The interdisciplinary team of scientists can be considered as the input function and the final result or product as the output function of this technology transfer system. The final model of the technology transfer is shown in Figure 4.

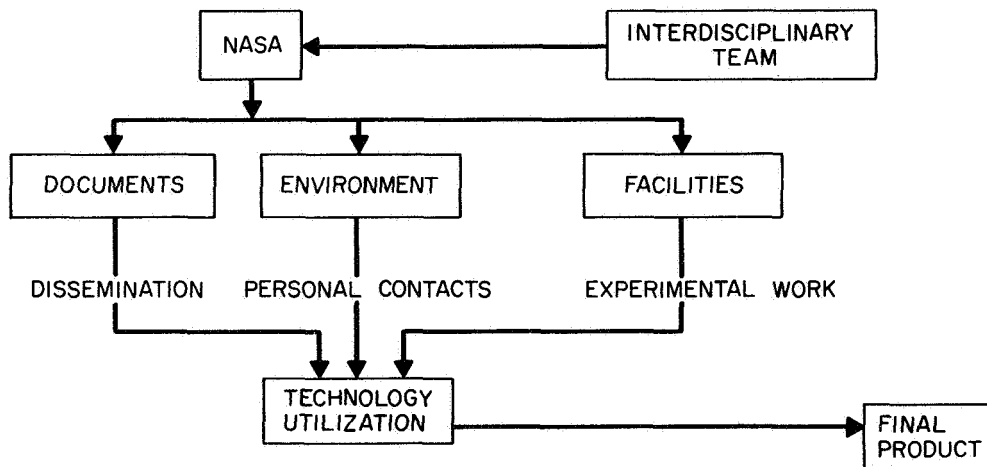


Figure 4--Technology transfer system.

CONCLUSION

The process of information transfer and technology utilization is very complicated. This paper has presented the results of a study identifying most of the processes and their major difficulties through a specific R & D problem. Actual work in a NASA center, with the close cooperation of the NASA personnel in the technical divisions and library and technology utilization group, has resulted in the process identification and system modeling of the technology transfer, in addition to the successful completion of the design of the specific R & D project. It is hoped that these results will benefit the other efforts of technology utilization and information transfer and will generate interest in effective civilian use of space technology.

REFERENCES

1. "Medical Applications of NASA-Developed Science and Technology," Midwest Research Institute, NASA N65-33128, July 1965.
2. "Study of the Transferral of Space Technology to Biomedicine," Bio-Dynamics Inc., NASA N65-16932, Feb. 1964.
3. Gilmore, J. S. et al., "The Channels of Technology Acquisition in Commerical Firms and the NASA Dissemination Program," NASA CR-790, 1967.
4. NASA University Program Review Conference, Kansas City, Missouri, NASA SP-85, 1965.
5. Leshner, R. L. and Howick, G. J., "Assessing Technology Transfer," NASA SP-5067, 1966.
6. "Transforming and Using Space-Research Knowledge (Ten Diversified Views)," Los Angeles, Calif., NASA SP-5018, 1964.
7. Howick, G. J. and Mahoney, J. E., "Technology: a Resource," Research and Development, Sept. 1966, pp. 18-22.
8. Fifth National Conference on the Peaceful Uses of Space, St. Louis, Missouri, NASA SP-82, 1965.
9. Hummel, B., "Technology in Turmoil," Machine Design, March 30, 1967, pp. F1-F16.
10. Sun, H. H., "A Survey of the Graduates from an Existing Biomedical Engineering Program," Proc. of the Sym. on Biomedical Eng., Milwaukee, Wis., June 1966, pp. 240-241.



100%

PHYSIOLOGIC SIGNALS FOR A PERSONAL-BORNE MONITORING SYSTEM

E. Fromm* and H. H. Sun**

INTRODUCTION

This paper briefly discusses the basic human physiology of the parameters pertinent to the present personal monitoring system development and attempts to set the broad engineering specifications of these parameters for appropriate equipment interfacing. The parameters discussed are those that were considered reasonable to transduce within the framework of the system objectives. Details of cellular-level neural and control mechanisms have been omitted, since these are not pertinent to the transduction and recording phenomenon considered in this project.

CARDIAC ACTIVITY

The heart undergoes both electrical and mechanical changes. Monitoring the electrical changes provides information on the integrity of the electrical conducting system, its delay times, and rhythms. Monitoring the mechanical changes provides information on the integrity and coordination of the mechanical parts, (e.g., valves, septum, and chambers). The mechanical activity follows, and is a direct result of, the electrical impulse and propagation.

Electrical

The electrocardiogram (ECG) is a graphic trace of fluctuations in electrical potential. These fluctuations represent the algebraic sum of the action potentials of the myocardial fibers as recorded from the surface of the body. Depolarization of the normal heart follows the path shown in Figure 1. It begins in the sino-atrial node, which is considered the pacemaker, and spreads evenly through the atrial musculature to the atrio-ventricular node. After a slight delay, the wave of depolarization (action potentials) spreads rapidly through special nerve paths (perkinje fibers) throughout the ventricular musculature. As can be seen from the figure, however, the entire ventricle is not depolarized simultaneously; the right side slightly precedes the left side. The left chamber walls are thicker than the right, having more perkinje fibers and action potentials. This condition combined with the phase shift results in an algebraic sum which varies when different positions of the heart are viewed. The body, because of its good conducting fluid, acts as a volume conductor; these potentials, therefore, may be perceived at the skin surface.

An idealized ECG wave from lead II (right arm and left leg) is seen in Figure 2. The P-wave represents atrial depolarization, the QRS complex represents ventricular depolarization, and the T-wave represents ventricular repolarization. From these representations and from the short description previously given of the sequence and conduction paths, it can be seen how delay time, magnitude, and slope variations may be interpreted as changes in the integrity of the cardiac electrical cycle.

*Assistant Professor, Biomedical Engineering Program, Drexel Institute of Technology, Philadelphia, Pa.

**Director, Biomedical Engineering Program, Drexel Institute of Technology, Philadelphia, Pa.

This paper will not describe the numerous clinical lead configurations for taking the ECG since a physiology text may be consulted for discussion of the standard limb leads, the unipolar leads, and the augmented unipolar leads. When monitoring relatively active subjects, leads placed at the extremities become too restricted. Furthermore, when placed over large muscle masses, leads on the torso may pick up significant electromyographic interferences. Under such conditions axillary and sternal lead systems have been used to make the leads less mobile and to place them over cartilagenous or bone structures. To have effective interpretation with respect to established clinical norms, care must be taken to place leads as close as possible to standard positions.

As measured from the surface of the body, cardiac potentials have peak amplitudes of 1 to 2 mv, a dynamic range of 50 db, and a frequency spectrum of 0.1 to 100 Hz between the half-power points (3 db down). Electrode impedances vary with the particular electrode, conducting media, and form of attachment. Impedance ranges from 1000 to 5000 ohms are a satisfactory approximation for good wet electrolyte-type electrodes and as high as 100 000 ohms for dry-type electrodes. These conditions vary according to skin preparation techniques.

Mechanical

The mechanical energy of the heart is converted to acoustic energy. Among the sources of the sounds accompanying the cardiac cycle are the hydraulic pressure transients associated with sudden blood flow acceleration or deceleration; valve closure; vibration of the heart chamber walls and valves; and blood flow turbulence.

There are four heart sounds associated with different parts of the cardiac cycle. The first is associated with the onset of ventricular contraction and the closing of the mitral and tricuspid valves. The second sound is caused by closure of the aortic and pulmonic valves and opening snap of the mitral and tricuspid valves at the end of the ventricular systole. The third sound, probably caused by vibrations set up by the inrush of blood, coincides with rapid ventricular filling. The fourth sound is rare but coincides with atrial contraction and final blood movement from atrium to ventricle. With high-pressure gradients, fluid flow, valvular actions, and chamber wall vibrations recorded in this manner, it may be readily appreciated how modifications of valvular structure, opening, closing, and chamber configuration would be detected.

In addition to the stethoscope, microphone pickup is used for phonocardiography procedures. A 15- to 2000-Hz bandwidth at the 3-db points is usually considered for sophisticated work; however, a 500- or 1000-Hz cutoff is sometimes employed to minimize noise and movement artifact. An 80-db dynamic range is sufficient to handle the high intensity low frequencies and the lower intensity high frequencies.

Transducer placement is obviously a critical factor. Microphone placement on various parts of the chest will enhance the pickup from one area of the heart as compared to another. For monitoring active subjects, transducer placement and attachment are also important. Movements at the point of attachment are difficult to overcome; therefore, many studies on the active subject exclude phonocardiography because of poor signal-to-noise conditions.

ELECTROENCEPHALOGRAPH

The electroencephalograph (EEG) records electrical activity of the neurons in the brain, detected by electrodes placed on the surface of the head. The resultant data have been used to study organic disorders such as brain lesions and tumors and to study the biochemical and electrical activity of the central nervous system with the relation of EEG potentials to psychophysiological responses.

The EEG is a complex, nonperiodic waveform containing many frequencies with shifting phase relations and varying amplitudes. Inspection of the EEG tracings indicates the distinct frequency bands shown in Table 1.

Table 1
Frequency Bands Established By
Inspection of EEG Tracings

Tracings	Frequency (Hz)
Delta rhythms	0.5 to 3.5
Theta rhythms	4 to 7
Alpha rhythms	8 to 13
Intermediate frequencies	14 to 17
Beta rhythms	18 to 30
Fast frequencies	Above 30

Certain of these rhythms are associated with specific psychophysiological states, e.g., alpha with the relaxed awake state and variations with sleep, excitement, and eye blinking. Since some of these low intensity waves appear to correspond to definite activity states of the brain, certain waves are more prominent over specific areas of the cortex.

The average potential difference between electrodes in an EEG is $50 \mu\text{v}$, but ranges of 2 to $200 \mu\text{v}$ may be encountered with a frequency spectrum of 0.1 to 80 Hz between half-power points. Unipolar and bipolar electrode configurations are employed with standard wet electrode impedances of 3000 ohms or less.

RESPIRATION

The respiratory system provides the body with oxygen to carry out some of the many oxidation reduction reactions of the metabolic processes. The system returns to the atmosphere carbon dioxide and water that are formed by the chemical reactions in the cells. The physical chemistry and biochemistry aspects of the cellular-level gas transport, exchange, and metabolic processes are not considered within the framework of the miniature monitoring system with which this program is concerned. The mechanics of respiration are discussed to offer a background for rate and volume measurements.

The normal pressures within the lung (intrapulmonic) and the thoracic cavity (intrapleural) during the inspiratory and expiratory processes are diagrammed in Figure 3. The lungs and chest wall are elastic structures, with the space between the lungs and chest wall containing only a very thin fluid layer. Inspiration is an active process with inspiratory muscles contracting to raise the lower ribs, which pivot as if hinged at the

back. The diaphragm has an even more important role and accounts for 75 percent of the intrathoracic volume change. It is attached around the bottom of the thoracic cage and, when stimulated, moves downward like a piston. The increased volume of the intrathoracic space during inspiration creates a greater negative pressure in this space than exists in the relaxed state. The lungs respond and expand to fill the void now created, thus establishing a negative intrapulmonic pressure. The situation has been created for an inrush of atmospheric air into the lung through the open air passages until the intrapulmonic and atmospheric pressures equalize. The inspiratory process has increased the thoracic volume both internally and externally, altered the quantity of gas within this volume, and caused a rapid inrush of atmospheric air.

The normal expiratory process is a passive one. The thoracic cage returns to its initial condition when stimuli to the respiratory muscles and diaphragm are withdrawn, forcing the lungs, aided by their own elastic recoil to contract. In this manner the passive processes force the intrathoracic pressure to increase with the lungs responding and acutally forcing the air out of the passages. The entire process normally takes about 4 seconds, with slightly less than half that time for inspiration. The forced air flow, as well as thoracic dimension and content changes, may be monitored to determine respiration rates and volumes.

This study is not concerned with constituent gases at inspiration and expiration, but these may be investigated with instream instrumentation. The frequency of such information is very low. If only rate information is desired, then a response range of 0.1 to 1 Hz is sufficient. If true waveshape is desired, as from volume curves, then a frequency spectrum of 0 to 10 Hz is encountered. Signal magnitudes depend, of course, on transducing mechanism and sensitivity. Average tidal volume is approximately 500 ml of room air. Forced inspirations and expirations will increase this total flow to approximately 5 liters for an adult male. These figures depend on the subject's physical size, age, and lung compliance. When monitoring from a mobile subject, it should be noted that lung volumes change with position change. Tidal volume remains relatively constant, but a shift of the volume on which this is superimposed is noted.

TEMPERATURE

Body heat is produced by muscular exercise, assimilation of food, and the vital processes that contribute to the basal metabolic rate. Heat is lost by radiation, conduction, vaporization in the respiratory passages, vaporization on the skin, and waste matter elimination. The balance between heat-production and heat-loss mechanisms

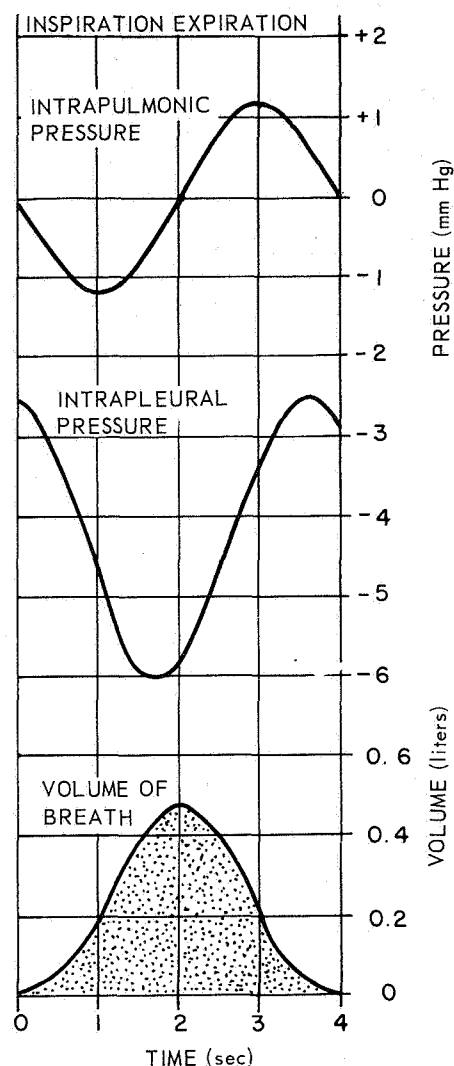


Figure 3—Changes in intrapleural and intrapulmonary pressure during respiration.

determines the body temperature. Man is hemeothermic; i.e., he has a group of reflex responses integrated in the hypothalamus to maintain the body temperature within a narrow range. These reflexes may control body temperature by increasing or decreasing heat production through shivering, mild muscle exercise, sweating, and panting.

Temperature can be recorded in the mouth, axilla, groin, ear, or rectum. With all of these methods the goal is to determine indirectly the temperature of the blood and, thus, of the deeper body tissues. Rectal and middle ear temperatures are representative of this "core" temperature, while oral temperature is usually about 1°F lower. Maximum temperature in the axilla is 1°F lower than that in the mouth and that in the groin closely approximates that in the mouth. Skin temperatures are, of course, related to environmental conditions and, to be meaningful, must be well insulated from such influences.

Normal deep-body temperature in an adult at rest is 97° to 99.5°F (36° to 37.5°C) and remains fairly constant in health. The average adult oral temperature of 98.6°F (37.0°C) is relatively stable for an individual but may vary among individuals. Diurnal fluctuations of as much as 3°F may occur normally, with the minimum occurring in early morning hours of deep sleep and the maximum during late afternoon and evening.

GALVANIC SKIN RESPONSE

Galvanic skin response (GSR) is used as an indication of autonomic nervous system activity due to psychophysiologic effects. Changes in skin resistance result from autonomic reflexes to internal and external stimuli, changing the vascular bed tone by constricting near-surface capillaries, and controlling the activity of the sweat glands. Skin resistance measurements should be made, however, at areas having significant sweat glands but which do not participate significantly in the temperature control mechanism. Such areas would increase and decrease sweat gland activity with reference to environmental conditions. Body surface areas useful for such purposes are soles of the feet and palms of the hands.

Human skin resistance may vary from a few thousand ohms to several megohms depending upon area and composition of electrodes and electrolyte, current density, condition of subject, temperature, humidity, and air pressure. This resistance is a very slow varying dc phenomenon called base resistance. Physiological or psychological stimuli cause variations of the order of a few percent of this resistance and are referred to as the specific response. It is this ac phenomenon, superimposed over the slowly varying dc, that is of interest. The resistance can be measured by passing ac or dc between two electrodes placed close together on the skin. Measurement of skin potentials has also been used for this purpose, although the constant current method is more prevalent. Frequency response range of 0.01 to 1 Hz is sufficient for GSR signal conditioning equipment.

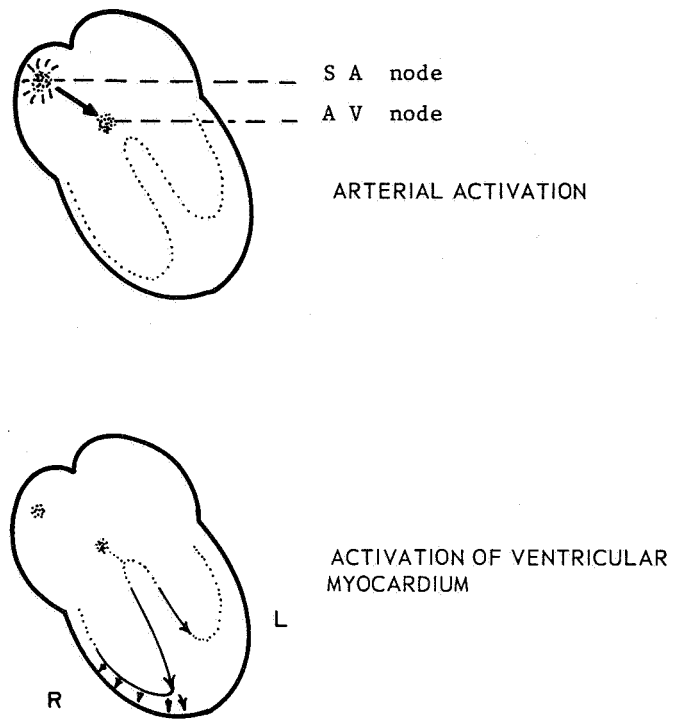


Figure 1—Normal spread of electrical activity in the heart.

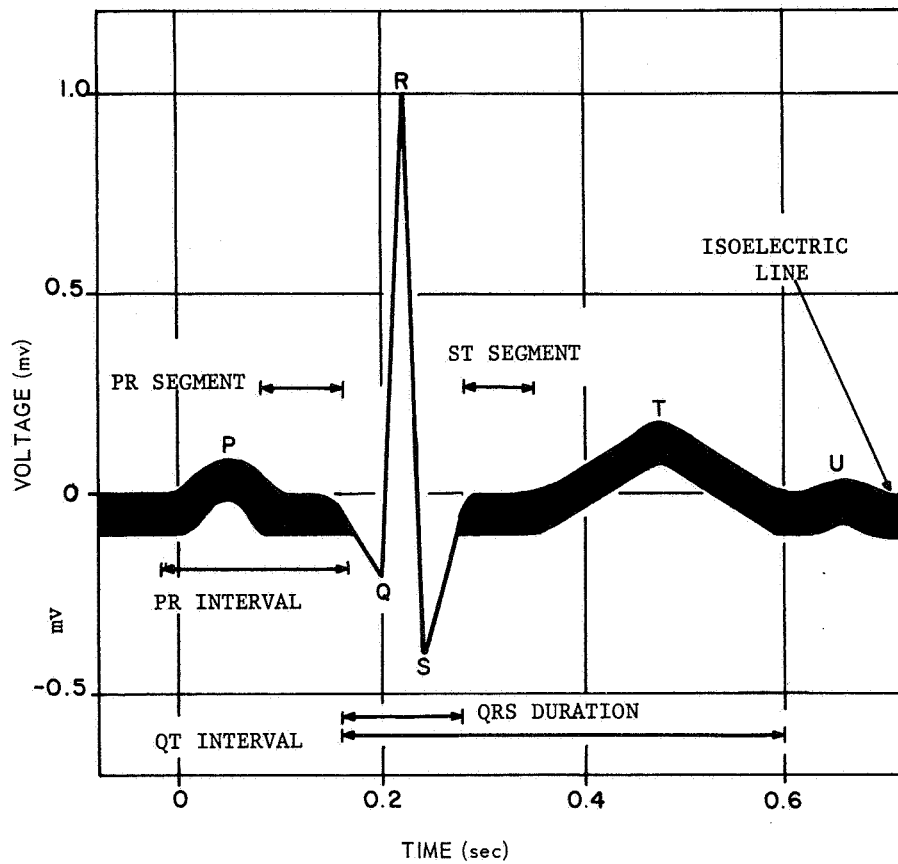


Figure 2—An ECG wave.

REFERENCES

1. Barbieri, R. E. et al, Techniques of Physiological Monitoring, Vol. 1: "Fundamentals," AMRL-TDR-62-98(1), 6570th Aerospace Med. Resch. Lab., Wright-Patterson AFB, Ohio, AD-288905, 1962.
2. Barbieri, R. E., ed. Techniques of Physiological Monitoring, Vol. III: "Systems," AMRL-TDR-69-98(111), 6570th Aerospace Med. Resch. Lab., Wright-Patterson AFB, Ohio, AD-609481, 1964.
3. Ganong, W. F., Review of Medical Physiology, Los Altos, Calif. Lange Medical Publications, 1963.
4. Keele, C. A. and Neil, E., Samson Wright's Applied Physiology, London: Oxford University Press, 1965.



A SURVEY OF RECENT DEVELOPMENTS IN PHYSIOLOGICAL MONITORING SYSTEMS

H. H. Sun,* E. Fromm,** and R. Zeskind†

INTRODUCTION

The term "homeostasis" describes functions of the human organism that automatically regulate parameters so as to maintain the internal environment at a constant level. Any degenerative process will change the system into maladaptive behavior, and the only way to reduce its occurrence is to detect symptoms in the early phases. This requires a continuous measurement of the parameters that regulate the equilibrium condition of the human system (e.g., body temperature (BT) heart rate, and mechanical and electrical signals generated by the body itself).

Recent space efforts have developed elaborate and sophisticated physiological monitoring systems related to astronauts in space. These systems have generated great interest in the information exchange between the space and biomedical scientists. The transferring of knowledge represents a major step in the development of civilian-based physiological monitoring systems and has contributed greatly toward the study of preventive and industrial medicine.

A detailed study of the physiological monitoring systems developed through the space effort is important for the following reasons:

1. It brings to the attention of biomedical engineers and medical researchers the vast amount of knowledge that is presently available and can be easily adapted to immediate application.
2. The study will provide a good example of the technological utilization of space knowledge and will generate wide interest in the information transfer to other scientific disciplines, such as social technology and environmental engineering.

This paper presents a detailed study of the physiological sensors that have been successfully tested and proved useful for this purpose. The studies of the signal conditioners and recorders are briefly discussed, but specific details and comparisons are beyond the scope of the paper. References 1 through 12 are general studies covering the overall monitoring system. References on sensors are described and compared in the remainder of this paper followed by the detailed references investigated that may be consulted for specific details of signal conditioning equipment.

SIGNAL SENSORS (TRANSDUCERS)

The signal sensors or transducers are devices that measure physiological parameters and transmit or convert them to electrical energy for signal conditioning equipment. The amount of energy for measurement purposes is usually small and, therefore, necessitates extremely sensitive electrodes or a contacting device not affected by body

*Director, Biomedical Engineering Program, Drexel Institute of Technology, Philadelphia, Pa.

**Assistant Professor, Biomedical Engineering Program, Drexel Institute of Technology, Philadelphia, Pa.

†Graduate student, Electrical Engineering, George Washington University, Washington, D. C.

movements or noise degradation. The signal sensors discussed in the following sections are for electrocardiograms (ECG), electroencephalograms (EEG), galvanic skin response (GSR), BT, blood pressure (BP), and respiration.

Electrocardiogram

The ECG electrodes used on the first Mercury flights were made of stainless steel mesh. These electrodes, however, were the cause of skin irritation after long usage and caused motion artifact in the ECG tracing (Reference 13). A wet electrode system was developed by NASA using silver or silver-chloride electrodes with an electrode paste that was tested for up to 96 hours with satisfactory results (Reference 14). The skin-electrode impedance for these electrodes was found to be almost constant at 10K ohms for 4 days.

NASA at Edwards has developed a spray-on electrode (Reference 15) using a conductive spray over a wire placed on the skin. This electrode has a high impedance and requires a specially designed signal-conditioning circuit that has also been developed for this purpose. NASA-Edwards has found this electrode to be very satisfactory and, through its technology utilization program, has generated interest to the point that it is now commercially available through the Hauser Research and Engineering Co.

Other electrodes suitable for monitoring systems are the ones used by the Navy (Reference 16) and the wire-mesh type developed by a number of commercial firms, including Cordis Corp. and Telemedics, Inc.

Electroencephalogram

NASA has not been extremely active in EEG-electrode development. Cup electrodes are generally used, and some attempts with spray-on electrodes have been made. The Navy has used 5/8-inch diameter silver wire mesh electrodes attached with Bentonite paste to the unshaven scalp. This paste, however, begins to dry up in approximately 2 hours.

Cup electrodes, used in aerospace study, are attached to the skin with adhesive cement with the hollow portion filled with electrode jelly. A good liquid contact is achieved that can be maintained for extended measurements of up to 24 hours. With careful preparation of the skin, electrode lead impedances under 2000 ohms can be obtained.

Galvanic Skin Resistors

NASA has not monitored the GSR from its space flights; however, studies have found that zinc and lead are good electrodes for GSR measurement and that polarizing electrodes would be the best for this purpose (References 17 and 18). Many electrodes that make excellent electrical skin contact are not, however, suitable for long-term studies.

Body Temperature

On all but the last of the Mercury flights, a rectal deep-body temperature probe was used. It consists of a 2-inch probe, with a thermistor at the tip imbedded in a coating of late rubber. On the last Mercury flight, the rectal probe was modified for oral use and mounted in the pilot's helmet so that he could take his own temperature upon request

(Reference 19). NASA has also developed a device to measure integrated skin temperature by using sensor wires affixed on flexible strips of cotton knit cloth inside the space suit (Reference 20). The wire temperature follows the body surface temperature and the signal is monitored by a differential voltmeter. A constant current source supplies the current to the wire, and a selector switch is used so that the integrated surface temperature of the body, forearms, chest, back, lower trunk, thighs, or legs can be monitored.

Blood Pressure

NASA developed a blood pressure measuring device for the Mercury program. It is an automatic auscultatory method using an inflatable cuff that is automatically blown up to a pressure greater than the diastolic and slowly leaked off. A microphone picks up the Korotkoff sounds and superimposes them on the output of a cuff pressure transducer (Reference 18). Unfortunately, a high-pressure air supply and sequencing valve are needed for successful operation.

The U.S.A.F. School of Aerospace Medicine has developed a similar system with an automatic cut-off pressure at 1 mm of mercury above diastolic so that the subject will be more comfortable (Reference 21). It sequences automatically every minute.

An earpiece device for blood pressure measurement was developed under NASA support (Reference 22). This device has a light source and photocell to pick up light intensity change due to blood flow through the ear. A bellow occludes blood flow through the ear so that diastolic and systolic pressure measurements can be obtained. This system, however, is difficult to calibrate, and the reading is temperature-sensitive.

Another method is the device to measure the temporal artery pressure (Reference 23). It uses a diaphragm-suspension, differential-transformer-type, direct-force measuring transducer for the skin deflection caused by the temporal artery. This device gives blood pressure measurement and pulse-wave shape. Calibration of the readings again presents difficulty.

A wireless earpiece oximeter developed under NASA support (Reference 24), uses infrared light to give pressure readings and red light to give oxygen-content readings. The oximeter is the size of a cigarette package and contains a computing network to transform the photocell readings to oxygen content. It uses heat dilation of the ear and a mechanical clamp to constrict the ear. This system, also has, calibration and reliability problems.

Respiration

NASA has monitored astronaut respiration rate and depth. It has developed and used several methods including, the belt and potentiometer system, the mouth and nostrils system, and - in the last two Mercury flights - the impedance pneumographic technique (Reference 19). The electrodes used are the same as mentioned under the ECG (Reference 14).

The Navy has developed an impedance pneumographic technique of measuring respiration rate and depth (Reference 25). This technique uses two rectangular electrodes constructed of woven monofilament silver-coated nylon with leads attached to the cloth from two edges. By insulating the silver-fabric electrodes from the skin with polyethylene bags, the electrode-skin resistance is kept constant. Baseline shift and movement artifacts are also eliminated by capacitive coupling.

Signal Conditioners

NASA, as well as the Air Force and Navy, has done considerable work in the development of a variety of signal conditioners designed to meet specific flight objectives. EEG and ECG amplifiers have been developed, some of which are single-ended and some differential input, high gain with varying input impedances to suit the particular purpose. Constant current GSR and ZPN systems have also been described. The details of these circuits, some of which have been miniaturized, are too involved for inclusion in this report. References 26 through 49 indicate those units investigated and considered within the objectives of this project.

CONCLUSION

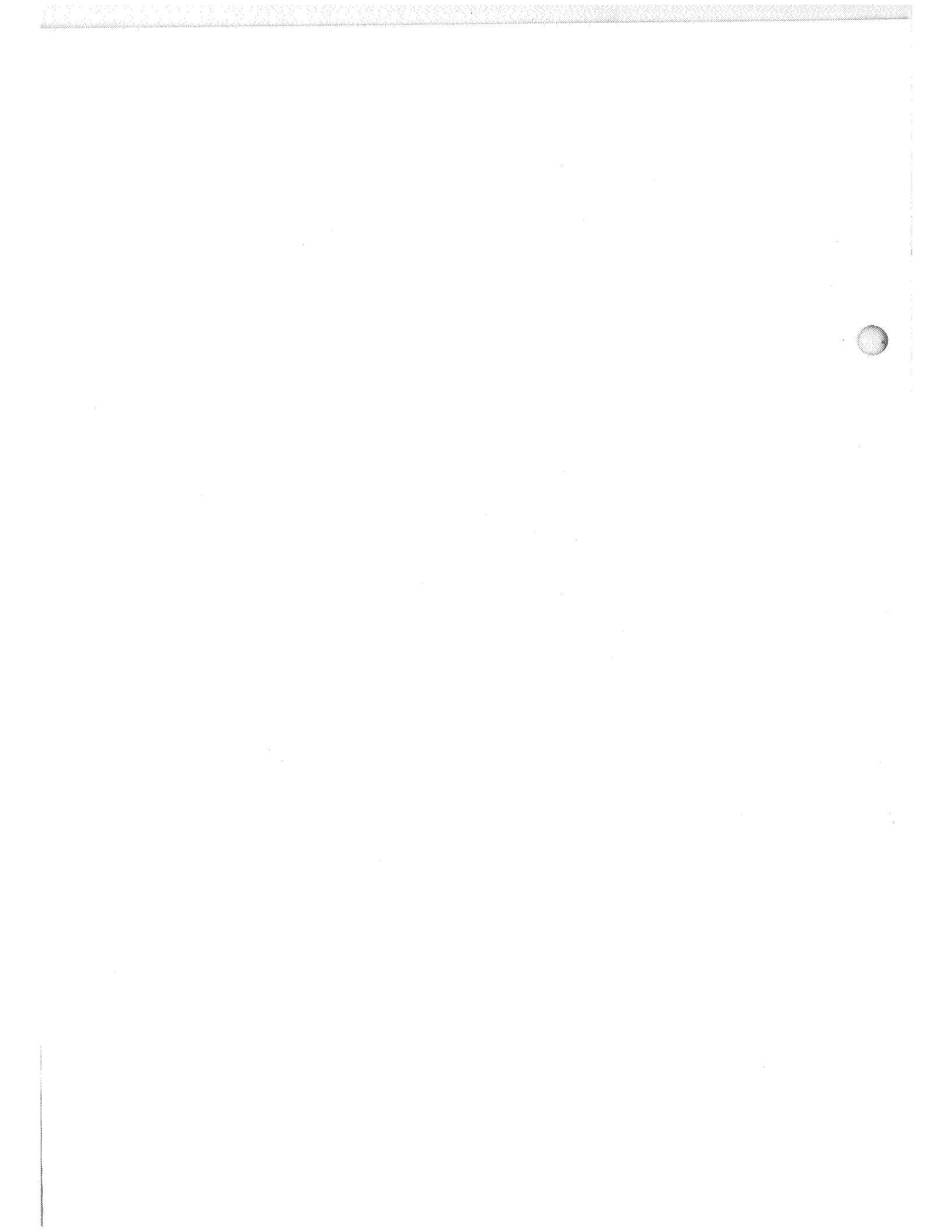
Additional work is still needed in the development of monitoring systems and sensors. Because most of the research has been performed by engineers under government contact, supplemental contributions from physiologists and clinical researchers would help achieve the ultimate objective of hospital or personal-borne usage. Biomedical engineers trained in such interdisciplinary research work appear to be the appropriate choice of personnel to channel their efforts in this area.

REFERENCES

1. Biomedical Telemetry, Caceres, C. A., ed., New York: Academic Press, 1965.
2. "Medical and Biological Applications of Space Telemetry," NASA SP-5023, July 1965.
3. Barbieri, R. E. et al., Techniques of Physiological Monitoring, Vols. I, II, and III, AMRL TDR-62-98(1, 2,3), 6570th Aerospace Medical Research Laboratories, Wright-Patterson AFB, Ohio, 1962-64.
4. Advances in Bioengineering and Instrumentation, Alt, F., ed., New York: Plenum Press, 1966.
5. Medical Physics, Glasser, O., ed., Chicago: Year Book Publishers, Inc., Vol. I, 1944, Vol. II, 1950, Vol. III, 1960.
6. Jones, W. J., and Simpson, W. C., "NASA Contributions to Cardiovascular Monitoring," NASA SP-5041, 1966.
7. Smith, C. R., and Bickley, W. H., "The Measurement of Blood Pressure in the Human Body," NASA SP-5006, April 1964.
8. "Significant Achievements in Space Bioscience, 1958-1964," NASA SP-92, 1966.
9. Stiffer, J. J., "Space Technology," Vol. V, Telecommunications, NASA SP-69, 1966.
10. Aerospace Telemetry, Stiltz, H. L. ed., Prentice-Hall, Inc., Englewood Cliffs, N. J., 1961, 1966.
11. Healer, J., "Bibliography on Biosensors: A Sampling of the World Literature, 1960-1964," NASA N65-25270, April 1965.
12. "Telemetry Systems for the Life Sciences: A Survey," NASA N63-32047, 1963.
13. Smedal, H. H., Holden, G. R., and Smith, J. R., Jr., "A Flight Evaluation of an Airborne Physiological Instrumentation System, Including Preliminary Results under Conditions of Varying Accelerations," NASA Technical Note D-351, Dec. 1960.
14. Day, J. L., and Lippitt, M. W., "A Long-term Electrode System Suitable for ECG and Impedance Pneumography," NASA N65-35216, 1962.
15. Patten, C. W., Ramme, F. B., and Roman, J., "Dry Electrodes for Physiological Monitoring," NASA Technical Note D-3414, May 1966.
16. Bergey, G. E., Sipple, W. C., Hamilton, W. A., and Squires, R. D., "A Personal FM/FM Biotelemetry System," 38th Annual Scientific Meeting, Aerospace Medical Assn., Washington, D. C., April 1967.
17. Bolie, V. W., and Bishop, L. G., "Theoretical Aspects of Metal Electrolyte Interfaces," Final Report, Autonetics, NASA CR-57211, NASA N66-31164, Sept. 14, 1964.
18. Wheelwright, C. D., "Physiological Sensors for Use in Project Mercury," NASA Technical Note D-1082, Aug. 1962.

19. "Mercury Project Summary, Including Results of the Fourth Manned Orbital Flight, May 15-16, 1963," NASA SP-45, May 1963.
20. Prudden, T. M. et al., "Development and Fabrication of an Instrument to Measure Integrated Skin Temperature," Final Report, Aerojet-General Corp., NASA N66-30536, June 1966.
21. Allred, J. E., and Johnson, J. B., "Design and Development of an Automatic Indirect Blood Pressure Monitoring Device," U.S.A.F. School of Aerospace Medicine, Aerospace Medical Division, Brooks AFB, Texas, SAM TR-66-80, NASA AD-641017, Sept. 1966.
22. Corbin, T., "Study Program for the Development of a Blood Pressure Measuring and Monitoring System for Remote Use on Man in Flight," Final Report, Corbin-Farnsworth Inc., Palo Alto, Calif., NASA N62-10687, March 1962.
23. Pressman, C. L., and Newgard, P. M., "Development of a Blood Pressure Transducer for the Temporal Artery," Stamford Research Institute, Menlo Park, Calif., NASA N65-32277, Sept. 1965.
24. Pintar, R. R., "Wearable, Wireless Oximeter," Final Report Beckman Instrument Inc., Fullerton, Calif., NASA N65-30480, Dec. 16, 1964.
25. Bergey, G. E., Sipple, W. C., Hamilton, W. A., and Squires, R. D., "A Quantitative Impedance Pneumograph," Aerospace Medical Research Department, NADC MR-6622, Nov. 10, 1966.
26. Simons, D. G., Prather, W., and Coombs, F. K., "The Personalized Telemetry Medical Monitoring and Performance Data-Gathering System for the 1962 SAM-MATS Fatigue Study," SAM TR-65-17, U.S.A.F. School of Aerospace Medicine, Brooks AFB, Texas, 1965.
27. Marko, Adolf R., McLennin, M. A., Correll, E. G., Potor, G., and Gibson, S. M., "Research and Development on Pulse-Modulated Personal-Telemetry Systems," AMRL TDR-63-96, Wright-Patterson AFB, Ohio, 1963.
28. Barker, P. R., and Wright, L. N., "Internal Four-Channel Physiological Telemetry System Prototype Development," SSD TDR-63-153, Air Force Systems Command, Los Angeles, California, 1963.
29. Sensory Systems Laboratory, "Nerve Coding Studies Phase II, Instrumentation," AD-612908, Army Research Office, Washington, D. C., 1965.
30. Hixson, W. C., Paludan, C. T., and Downs, S. W., Jr., "Primate Bio-Instrumentation for Two Jupiter Ballistic Flights," IRE Transactions on Medical Electronics, Oct. 1960, pp. 318-325.
31. "Microelectronics in Space Research," NASA SP-5031, August 1965.
32. "Selected Electronic Circuitry," NASA SP-5046, 1966.
33. Fryer, T. B., and Deboo, G. J., "Tiny Biomedical Amplifier Combines High Performance, Low Power Drain," NASA Tech. Brief 65-10203, July 1965.

34. Fryer, T. B. and Deboo, G. J., "A High Performance Miniaturized Preamplifier for Biological Applications," Medical Electronics and Biological Engineering, Vol. 3, New York: Pergamon Press, 1965, pp. 203-204.
35. Wenzel, G. E., "The Development of a Micro-miniature dc Signal Conditioning Amplifier," NASA Technical Note D-4091, July 1967.
36. Moede, L. W., "Simple Circuit Provides Adjustable Voltage with Linear Temperature Variation," NASA Tech. Brief 63-10537, March 1964.
37. "Temperature Transducer Has High Output, Is Time Stable," NASA Tech. Brief 65-10362, Nov. 1965.
38. Fryer, T. B., "Miniature Bioelectronic Device Accurately Measures and Telemeters Temperature," NASA Tech. Brief 66-10057, Feb. 1966.
39. Fryer, T. B., Deboo, G. J., and Winget, C. M., "Miniature Long-Life Temperature Telemetry System," Journal of Applied Physiology 21(1):295-298, Jan. 1966.
40. "Space Physiology," NASA N66-22247, 1964.
41. Marko, A. R., McLennan, M. A., and Correll, E. G., "A Solid-State Measuring Device for Galvanic Skin Response," AMRL TDR-62-117, Biomedical Lab., Wright-Patterson AFB, Ohio, Oct. 1962.
42. Sydnor, R. L., "Voltage Controlled Oscillator Is Easily Aligned, Has Low Phase Noise," NASA Tech. Brief 65-10223, 1965.
43. Hearn, C. P., "Voltage Variable Oscillator Has High Phase Stability," NASA Tech. Brief 65-10204, 1965.
44. "Circuit Converts AM Signals to FM for Magnetic Recording," NASA Tech. Brief 65-10001, 1965.
45. "Improved Chopper Circuit Uses Parallel Transistors," NASA Tech. Brief 66-10113, 1966.
46. Sun, Hun H., Synthesis of RC Networks, New York: Hayden Book Co., Inc., 1967.
47. Geffe, Philip R., Simplified Modern Filter Design, New York: John F. Rider, Publisher, Inc., 1963.
48. "A Handbook On Electrical Filters," White Electromagnetics, Inc., Rockville, Md., 1963.
49. "High Performance RC Bandpass Filters are Adapted to Miniaturized Construction," NASA Tech. Brief 66-10309, 1966.



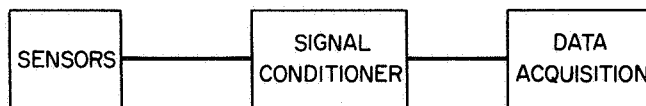
A MONITORING SYSTEM FOR PATIENT STUDIES

H. H. Sun,* E. Fromm,** R. Zeskind†

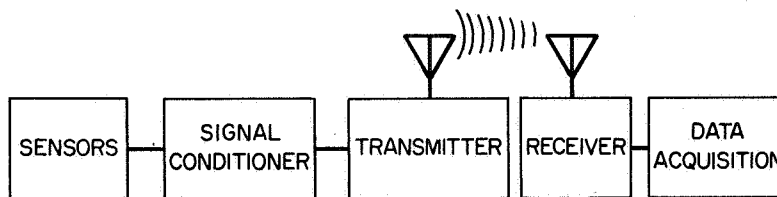
INTRODUCTION

The objective of this project has been to develop a small, personal-borne physiologic monitoring system. Earliest concepts envisioned a small lightweight system that could be worn inconspicuously by the patient and that could gather information of several parameters simultaneously and continuously for 8 hours or more.

The information monitored by such a system may be gathered and stored through a direct wire-linked system or a telemetry system (Figure 1). Each system has specific advantages and disadvantages that were initially considered to narrow the conceptional phase to more specific design.



(a) DIRECT WIRE SYSTEM



(b) TELEMETRY SYSTEM

Figure 1-Block diagram of wire vs telemetry system.

The telemetry system may have the data acquisition section at a remote location. Assuming the volume and weight of a transmitter to be less than that of a typical data acquisition system, the telemetry scheme would have a lighter size and weight burden on the subject. Although one immediately surmises a situation of complete freedom of subject movement without wire restraints, this is not always the case with telemetry links. Typical short-range telemetry commercially available in physiologic systems have a range of approximately 200 feet (suppliers include Gulon Industries, Vector Manufacturing Co., and Signatron.) Thus, for the subject to be completely free in his normal working environment (capable of going between locations and buildings), he must carry receiver and recorder similar to an attaché case. Federal Communication Commission requirements for long-range telemetry licensing would prohibit this since the objective has been

*Director, Biomedical Engineering Program, Drexel Institute of Technology, Philadelphia, Pa.

**Assistant Professor, Biomedical Engineering Program, Drexel Institute of Technology, Philadelphia, Pa.

†Graduate Student, Electrical Engineering, George Washington University, Washington, D. C.

a simply operated system, having wide clinical and research acceptance, without sizeable stumbling blocks and licensing procedures.

A direct wire-link system requires that the subject be restrained by wiring to a data acquisition console or that the entire system be carried by him. The advantage of an entirely personal-borne system is that movement is completely unrestricted. Not only is inter-office and interbuilding movement possible but intercity as well, if the subject is so inclined. It appeared, therefore, that the personal-borne system would be the more desirable, provided the data acquisition section could be designed so as not to burden the subject. The decision to orient the project to this objective was made early and has been pursued with reasonable success.

RECORDER

From the brief discussion above, it may be noted that the authors anticipated the largest problem to be in the development of a small data acquisition system. A number of signal conditioner and electrode systems have been developed, and it was felt that modification and redesign of these would be sufficient for the problem at hand, but no recorder with the desired characteristics was available.

The physiologic parameters considered for the present were the electrocardiogram (ECG) as an indication of the integrity of the cardiac electrical system, conduction, and delay times; galvanic skin response (GSR) as an indication of psychological stress and function of the autonomic nervous system; body temperature for an indication of gross changes of metabolic activity; and respiration rate and volume. The information content of these parameters is within a dc to 100-Hz bandwidth (Reference 1) to which the recording media must be adaptable. Design goals for the data acquisition system were small size (less than 30 cm³), light weight (approximately 1 lb), continuous recording for a minimum of 8 hours, data of dc to 100-Hz frequency range, and production cost of no more than \$1000.

A number of recording media were investigated with respect to the design goals. In addition, the limited time of the Summer Workshop made it necessary to consider recorders that could be reasonably modified to meet project specifications. Existing optical- and galvanometric-type systems are too large and not oriented toward the project objectives. Paper tape, wire recorders, and electrochemical processes recording media are incapable of giving the necessary resolution, recording time, and small size in the framework of limited modifications. A magnetic tape recorder using 1/4 in. tape on 3-in. diameter reels at a speed of approximately 0.2 ips, fulfilled the requirements for this conceptual phase.

It has been indicated that pulse code modulation (PCM) is a more efficient means of information transmission than frequency modulation (FM) and is the technique to which space communication has been oriented. The authors investigated the possibility of using PCM vs FM and direct recording by examining the requirements for only one channel of physiologic information (ECG). Considering the PCM first, the 100-Hz bandwidth of the ECG would require a minimum rate of 200 samples per second. A 5-bit work resolution (i.e., 32-level discrimination) would cause an inherent 3 percent error that is the maximum tolerable. A digital tape with packing density of 2000 bits per inch is reasonable and implies, therefore, a minimum tape speed of 0.5 ips and a maximum recording time of 4 hours on a 3-in., 600 ft reel. Thus, considering only the one parameter, PCM use would not meet the recording time requirements unless multiple-track parallel recording techniques were used, thereby ruling out ready expansion to multiple physiologic parameters. In contrast to this, with FM and direct recording, a 100-Hz bandwidth and 2000 cycles per inch packing density would allow a minimum speed of 0.05 ips, or 40 hours on a 3-in.,

600-ft tape. In actual experimentation, it has been found that the 2000 cycles per inch of direct recording packing density is very conservative and may be multiplied by a factor of three, thereby requiring even less of the tape capacity for this one data channel. The foregoing analysis, therefore, indicated direct and FM recording to be the appropriate approach.

A number of commercially available recorders, developed through governmental funding, were investigated. The Leach Corp. LEM Recorder and Cook Electric Bio-medical Recorder have been developed specifically for Apollo project personal-borne information retrieval (Reference 2). Although a significant advance of the state-of-the-art, these units were considered unsuitable for this project because of their size, power requirements, and most importantly high cost. The Garrett Airesearch unit developed for NASA Flight Research Center (FRC) approaches the desired characteristics but is still somewhat large. Small scientific satellite recorders are larger than desired and not readily adaptable to the project specifications. The commercial unit presently available from Avionics Research Corp. and used for such physiologic monitoring is four to five times as large and heavy as desired, while having only single data-channel capability.

A recently released announcement by Edwards Engineering describes a small audio unit developed for law enforcement and intelligence service. The unit has a volume of less than 15 cm³, weighs 12 ounces, operates from a single 1.35 v mercury cell at a current drain of 30 ma, permitting 24-hour operation. It is sold with a drive speed of 1.875 ips, allowing approximately 45 minutes of recording with standard Scotch 290 tape. This commercial unit in binaural form has been selected as the most suitable for appropriate modification to system specifications. Such a unit, modified to operate at a drive speed of 0.1875 ips, uses a standard Nortronics C204K record/reproduce head and has enabled recording and playback of up to 1200-Hz signals. The modified unit is pictured in Figure 2. The 1200-Hz bandwidth will allow several signals to be multiplexed on a single tape channel and thus four parameters with the binaural recording head. Future expansion to a BQQ4K Nortronics head will allow four tape channels, i.e., eight parameters. The unit will record and reproduce in real time but, to increase low-frequency response and decrease reproduce time, the tapes may be played back on any standard 1/4-inch tape stereo recorder. Playback at standard 7.5 ips would mean a 40:1 increase, and recorded frequencies of 0.5 to 1000 Hz would look like 20 to 40 KHz in the playback mode.

SIGNAL CONDITIONERS AND ELECTRODES

Choice of specific signal conditioners must be related to input parameters and, thus, to electrodes, transducers, and impedances. The authors had not anticipated that specific circuits and configurations were available for inclusion in the final design without modification and certain interface changes. From the comprehensive survey of signal conditioners developed and presented in the literature, those deemed appropriate for modification and interfacing into the monitoring system were selected. Coincident with this selection, of course, was choice of desirable electrode systems.

Extensive research was undertaken to find specific documentation developed through various major space projects. The problem of information transfer is a formidable one since most of the information is not readily available to the regular researcher. Results developed by engineers from major NASA contractors, subcontractors, or both are not available until their final publications. Efforts were made to obtain materials, such as specific circuit diagrams, applicable to this project through an intensive search on the appropriate contract numbers and drawing numbers. The authors obtained several pertinent documents, including an advanced manuscript on bioinstrumentation from Spacelabs,

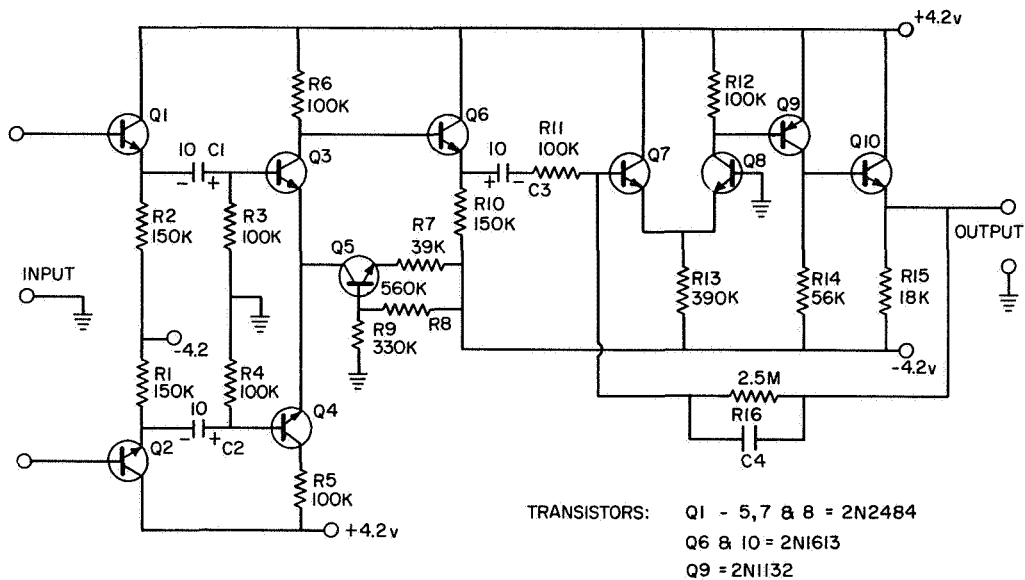


Figure 3-ECG amplifier.

ZPN

The impedance pneumograph technique has been selected to measure respiration rate and volume. The choice of electrodes at this point has been confined to three systems, two of which have performed satisfactorily. The authors would like the third to be investigated. This third category is the use of the dry spray-on electrode, previously described for ECG, as an impedance pneumograph electrode. Experimentation has not yet begun but, should it prove successful, this electrode would again be the most desirable because of its unobtrusiveness, ease of application, and low cost throw-away design. The other two selected electrodes are the Lippitt Ag-Ag Cl ECG electrode (References 7 and 8) and a capacitive plate electrode described by Bergey et al. (References 9 and 10), which uses silver-coated nylon in plastic bags. The signal conditioners for ZPN consist of a battery-operated oscillator whose output is loaded by the varying transthoracic impedance. Bergey offers a good miniaturized unit considered suitable for the basis of modification and incorporation into this system (Figure 4). The 300-Hz oscillator signal is rectified and may then control a low frequency voltage controlled oscillator (VCO) whose output will be mixed with another data channel. Intended for use is a unijunction VCO, shown in Figure 5, with appropriate bandpass filtering for the fundamental oscillator frequency.

Body Temperature

Temperature may be readily transduced with a thermistor probe, as has been done in most of the manned space flights. This system uses a Yellow Springs Thermistor energized by a dc bridge. The output of the system may then control another unijunction VCO, appropriately filtered. The unijunction VCO has been selected for its simplicity, small size, low power, and low cost. Although not generally considered with the flyable VCO's it is sufficiently stable and responsive to the project's requirements (Reference 11).

Galvanic Skin Response

NASA has not used GSR in its manned space program and, consequently, has not contributed as much to this parameter as others. Work sponsored by NASA (Reference 12) indicates that commercially available small, lead-plate electrodes (E & M Instrument Co.,) are ideal for GSR. Marko describes a GSR signal conditioner, with decreased voltage supply and miniaturization, considered appropriate for modification (Reference 13). It is essentially a constant transformer-coupled direct current supply to the plate electrodes with measurement of the voltage between the plates (Figure 6). This could again be fed into a third unijunction VCO and multiplexed with another data channel.

CONCLUSION

Specific blocks of the personal-borne physiological monitoring system have been described. Each block has been developed to a significant extent but must be further modified to allow appropriate system interfacing. The 1967 Summer Workshop has resulted in the definition of the information transfer process, modification and fabrication of an appropriate recording system, selection of signal conditioners to form the basis of system design and fabrication with some breadboarding completed, and the selection of appropriate electrode systems. An overall system block diagram may be seen in Figure 7.

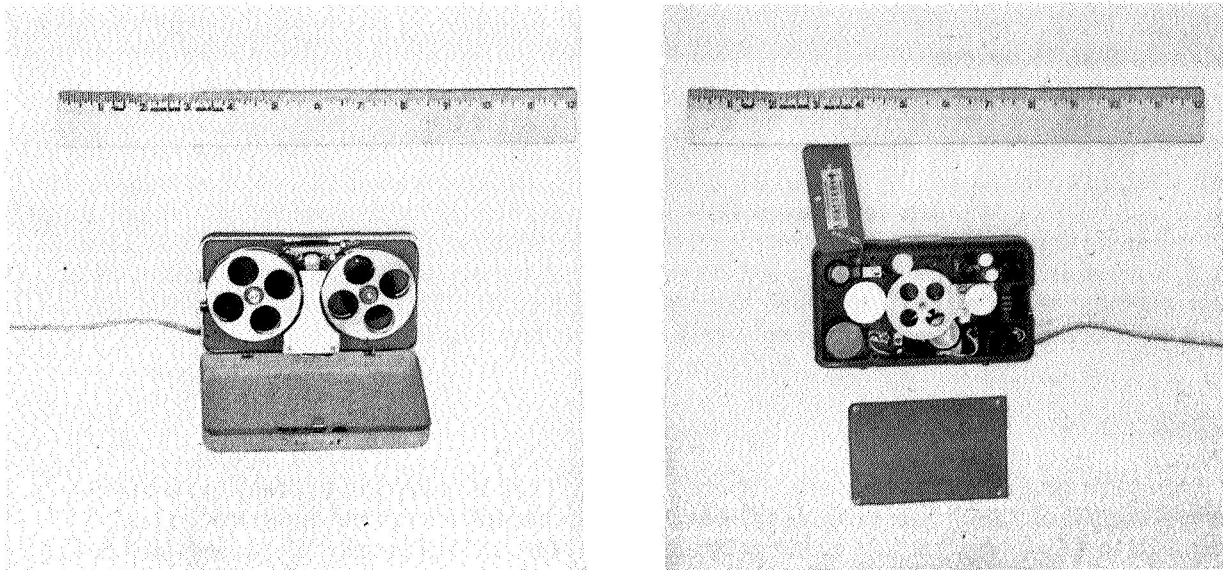


Figure 2—Miniature recorder.

Inc. Several of these are presented below as preliminary design, and others will be delivered and tested as soon as they can be disseminated.

Electrocardiogram

Selection of ECG amplifier characteristics depends, to a large extent, on input electrode impedances. Electrodes for this project must be unobtrusive, long-lived (approximately 1 day), nonirritating, noise free, easy to apply, and low in cost. A disposable system was considered most desirable to meet the low cost requirement. To satisfy these conditions, two electrode systems were selected. Dry spray-on electrodes, developed by NASA-FRC and now available commercially through Hauser Research and Engineering Co., were selected as most suitable for the monitoring system. The system, described in a number of publications (References 3 and 4), is basically an extremely thin layer of conductive adhesive spray over a fine wire fixed to the skin surface. This is then oversprayed with a thin mechanical protection layer. Rapid application with good attachment and minimal skin reaction has been confirmed.* The impedance of these units are necessarily high and require high input impedance amplifiers. A circuit described by Fryer (References 5 and 6) is considered as an ideal basis for a slightly modified ECG signal conditioner (Figure 3). It has a high impedance differential input, high gain, low power requirements, with low impedance single-ended output. A breadboard of this unit is under evaluation. As second choice, the authors have selected the wet electrolyte and electrode system described by Lippitt et al. of NASA Manned Spaceflight Center (References 7 and 8). The lower impedance and longer useful life of this system offers distinct advantages over the spray-on system. The former, however, is a bulkier unit and less desirable in studies of normal working day activities of the subject unless considered for several days of continuous data collection. The same signal conditioner will be useful for the lower impedance source, as for the spray-on electrodes, thus not necessitating dual selection of electronics.

*Private communication with R. Carpenter, NASA-FRC, Edwards, Calif.

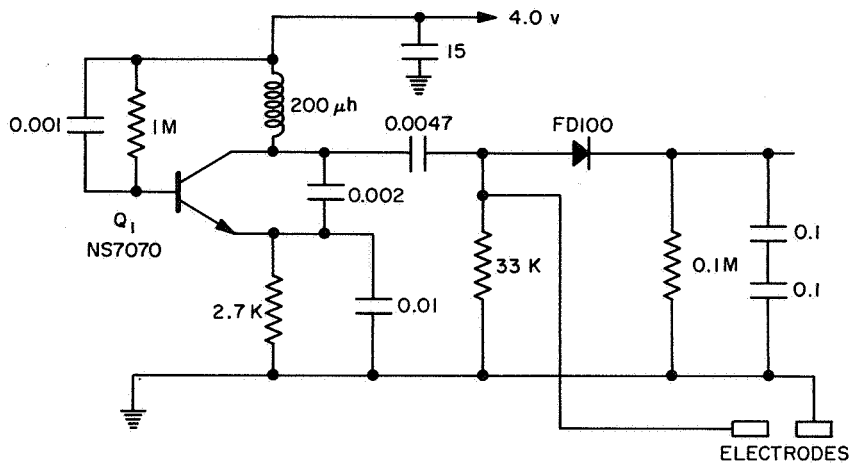


Figure 4—Impedance pneumograph circuit.

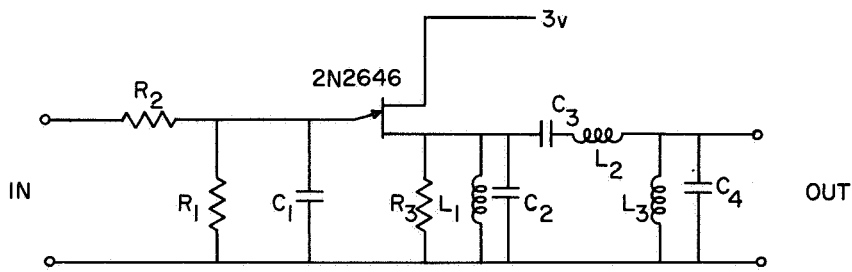


Figure 5—Unijunction VCO and filter.

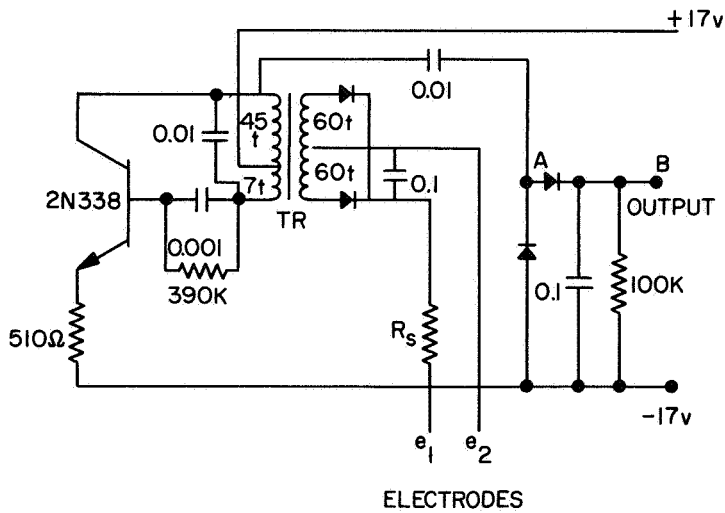


Figure 6—GSR signal conditioner.

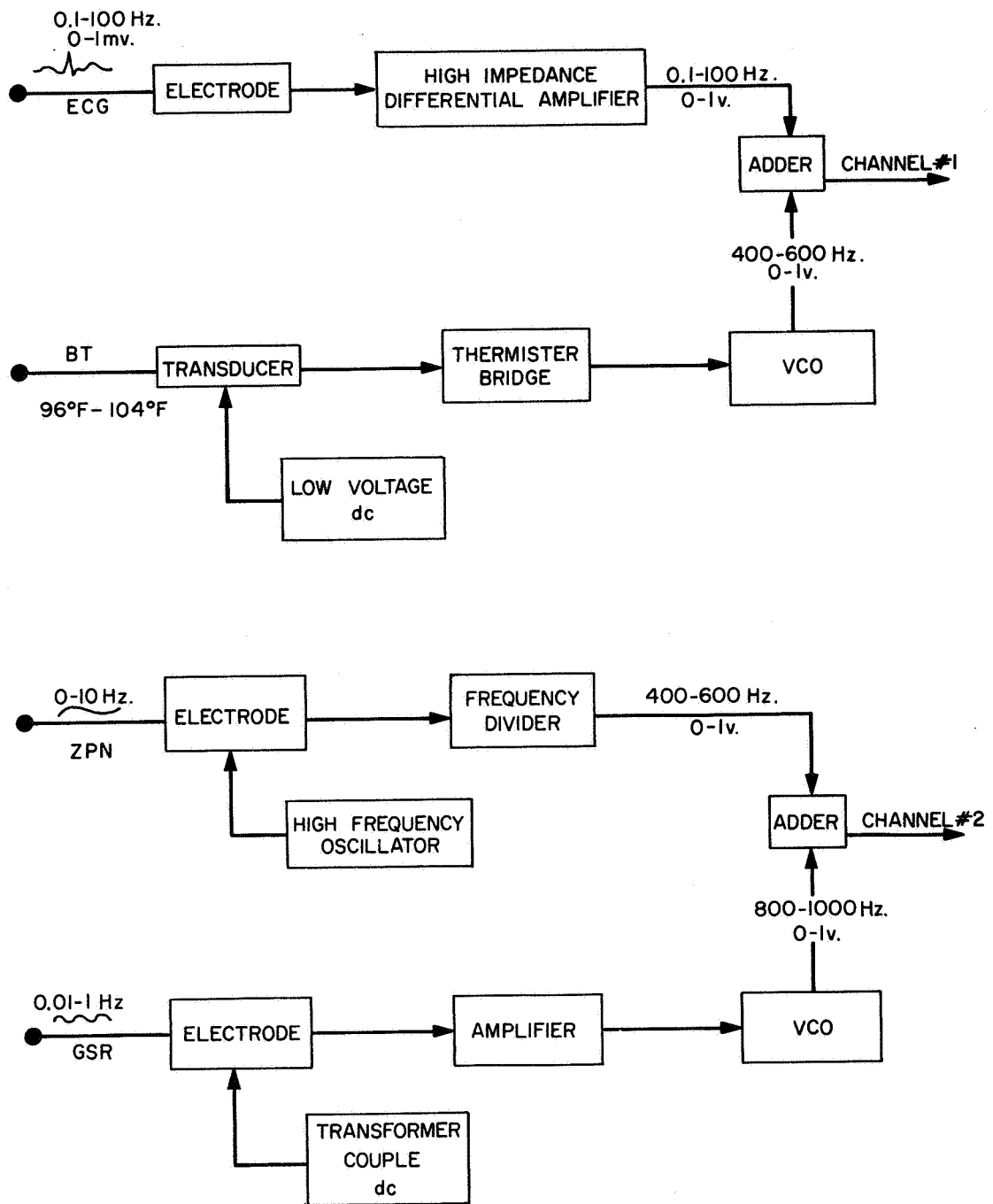


Figure 7—Monitoring system block diagram.

REFERENCES

1. Alnut, R. W. et al., Techniques of Physiological Monitoring, Vol. 3, DDC Document No. AD609481, Oct. 1964.
2. Skipwith, W. A., "Magnetic Tape Recording," NASA SP-5038, Jan. 1966.
3. Roman, J., "High Impedance Electrode Techniques," Aerospace Medicine, 37(8), 1966.
4. Pattern, F. W., Ramme, F. B., and Roman, J., "Dry Electrodes for Physiological Monitoring," NASA Technical Note D-3414, May 1966.
5. Fryer, T. B., and Deboo, G. J., "Tiny Biomedical Amplifier Combines High Performance, Low Power Drain," NASA Tech. Brief 65-10203, July 1965.
6. Fryer, T. B., and Deboo, G. J., "A High-Performance Miniaturized Preamplifier for Biological Applications," Medical Electronics and Biological Engineering, Vo. 3, New York: Pergamon Press, 1965, pp. 203-204.
7. Day, J. L., and Lippitt, M. W., "A Long-Term Electrode System Suitable for ECG and Impedance Pneumography," NASA N65-35216, 1962.
8. Lippitt, M. W., and Day, J. L., "Improved Electrode Gives High-Quality Biological Recordings," NASA Tech. Brief 64-10025, May 1964.
9. Bergey, G. E., Sipple, W. C., Hamilton, W. A., and Squires, R. D., "A Personal FM/FM Biotelemetry System," 38th Annual Scientific Meeting, Aerospace Medical Assn., Washington, D. C., April 1967.
10. Bergey, G. W., Sipple, W. C., Hamilton, W. A., and Squires, R. D., "A Quantitative Impedance Pneumograph," Aerospace Medical Research Department, NADC MR-6222, Nov. 10, 1966.
11. Simons, D. G., Prather, W., and Coombs, F. K., "The Personalized Telemetry Medical Monitoring Performance Data-Gathering System for the 1962 SAM-MATS Fatigue Study," SAM TR-65-17, U.S.A.F. School of Aerospace Medicine, Brooks AFB, Texas, 1965.
12. "Electrical Resistance of the Skin," NASA STAR Document N66-31162, Nov. 1964.
13. Marko, A. R., McLennan, M. A., and Correll, E. G., "A Solid-State Measuring Device for Galvanic Skin Response," AMRL TDR-62-117, Biomedical Lab., Wright-Patterson AFB, Ohio, Oct. 1962.

GROUP H

ATMOSPHERIC STUDIES

Academic Personnel



Prin. Investigator: Dr. William Callahan (Weston College)

Faculty: Dr. Eugene Mohr (Columbia College)

Dr. James McElaney (Fairfield)

Prof. Edgar Franz (Illinois College)

Mr. Randy Ross (Wis.)

Goddard Personnel

Staff Advisor: Mr. Nelson Spenser

EQUIVALENT BLACKBODY TEMPERATURES OVER THE MOHAVE DESERT FROM 8.5 TO 16 MICRONS

William R. Callahan*

ABSTRACT

In May and June of this year, three filter-wedge spectrometers scanning the intervals from 0.7 to 1.2, from 1.2 to 6.4, and from 8.5 to 16 microns were flown on the NASA Convair 990 jet flying laboratory. Initial results have been obtained for the flights over the Bristol Dry Lake region of the southern Mohave Desert. These results give the equivalent blackbody temperatures as a function of wavelength for the 8.5 to 16 micron wavelength interval. These observations have been correlated with laboratory emissivity measurements made on surface samples which the author obtained from this region.

INTRODUCTION

For the past three years, Dr. Warren A. Hovis, Jr., of the Goddard Space Flight Center has been engaged in a remote sensing program directed toward a study of the earth's surface and, eventually, that of other planetary bodies (References 1-4). In this work the infrared emission and reflection spectra of various minerals are employed to detect and map surface materials.

EXPERIMENTAL

Beginning in April of this year, three filter-wedge spectrometers scanning the regions from 0.7 to 1.2, from 1.2 to 6.4, and from 8.5 to 16 microns were installed and flown on the NASA Convair 990 jet flying laboratory. These flights, in which the author took part, covered large areas of this country, especially the Southwest, as well as the Pacific Ocean off the West Coast, Alaska, the Gulf of Mexico, the Yucatan Peninsula and the east coast of Mexico. Observations were taken at altitudes ranging from 400 ft to 37,000 ft.

The construction and operation of the filter-wedge spectrometer developed by Dr. Hovis have been discussed in the literature (Reference 5). On these flights the signal from the filter-wedge spectrometers was fed into a Brush recorder and also into a 14-channel Ampex CP-100 magnetic tape recorder. The output of the detector channel was then fed back from the tape recorder into a persistence oscilloscope. This display gave a redundancy check that quickly showed up operating irregularities in either the spectrometers or the tape recorder. This arrangement proved its value on several occasions.

Of particular interest for the work this summer have been the data taken on flights over the Bristol, Cadiz, and Danby Dry Lakes of the southern Mohave desert. This hot, dry area is located in a rather flat valley with very little vegetation obscuring the surface. The aircraft flew several passes over this region, including the Amboy lava bed, at altitudes between 3,000 ft and 33,000 ft.

*Fairfield University, Fairfield, Connecticut.

In order to obtain close correlation between these airborne observations and the actual surface materials, the author, in late July of this year, drove into that region and obtained surface samples along the 60-mile flight path. The emissivity of these samples has been measured in the laboratory, and results are plotted along with the airborne data.

DISCUSSION

Figure 1 shows the general flight path followed in the successive passes over this region. Two additional passes at 4,200 ft and at 5,000 ft were made over the lava bed at the northwest end of the flight path.

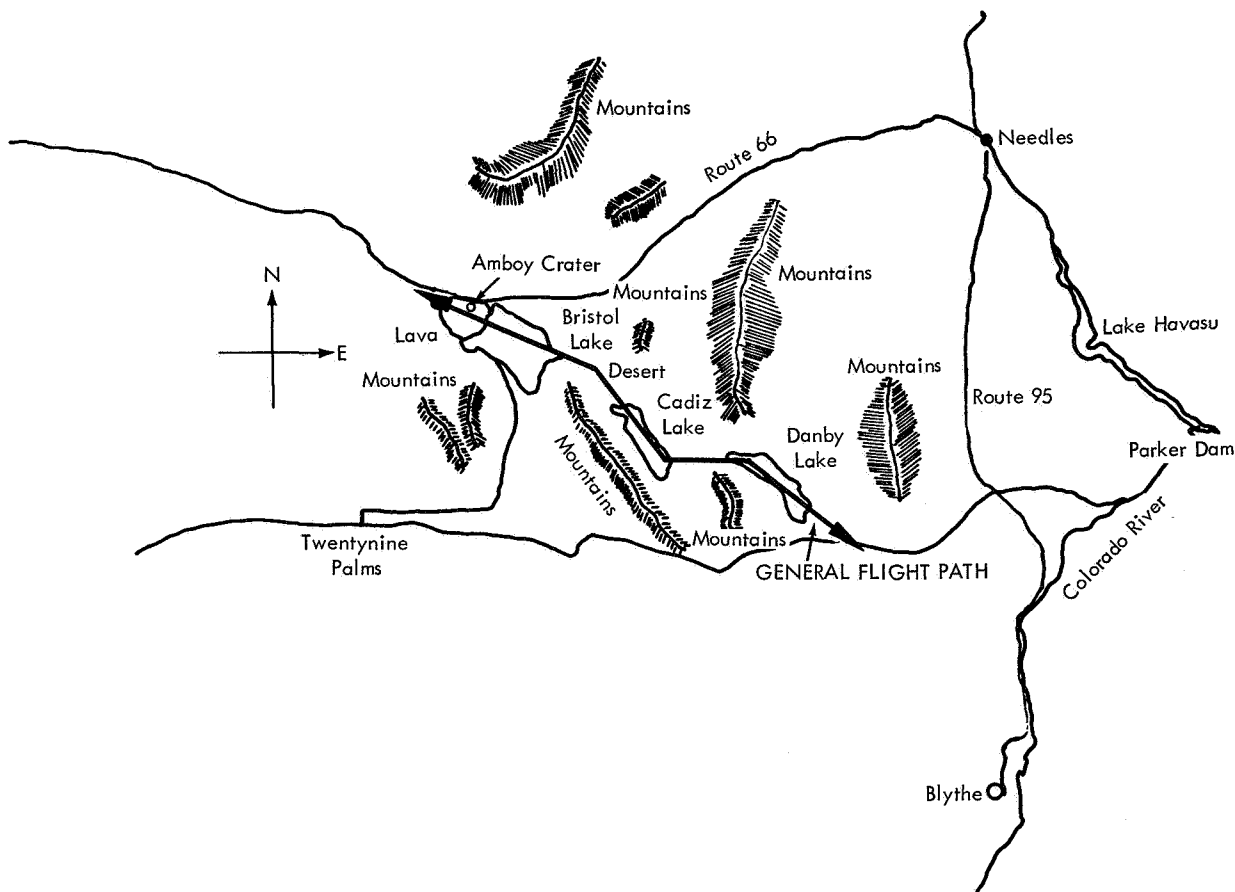


Figure 1—General flight path

Figures 2-6 plot equivalent blackbody temperature vs wavelength, for the scans made at the times indicated. Times are listed in Universal Time from Greenwich, giving the day, hour, and minute of the observation.

The equivalent blackbody temperature for a particular wavelength is obtained by measuring the voltage output of the detector with respect to a reference blackbody whose temperature is known. Using tables compiled by Mr. Fred Blaine in the post-flight calibration, the voltage was converted to an energy output and added to the energy output of the reference blackbody. Using tables prepared by Mr. Michael Forman, this energy was converted to an equivalent blackbody temperature on the Kelvin scale and then converted to centigrade values. These temperatures were calculated at half-micron intervals between 8.5 and 16 microns.

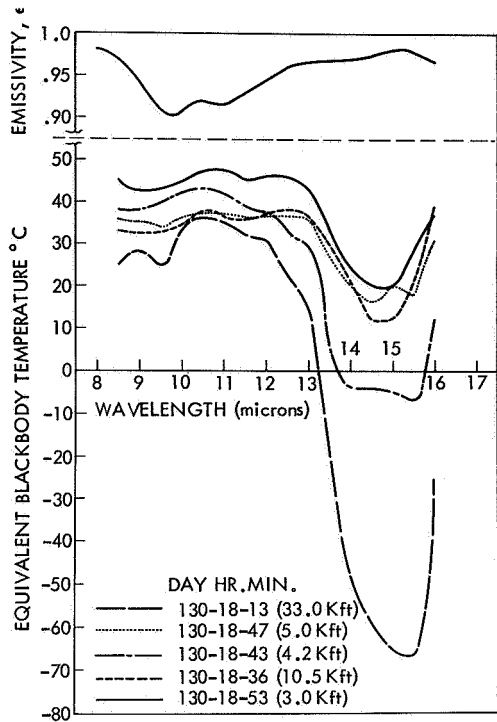
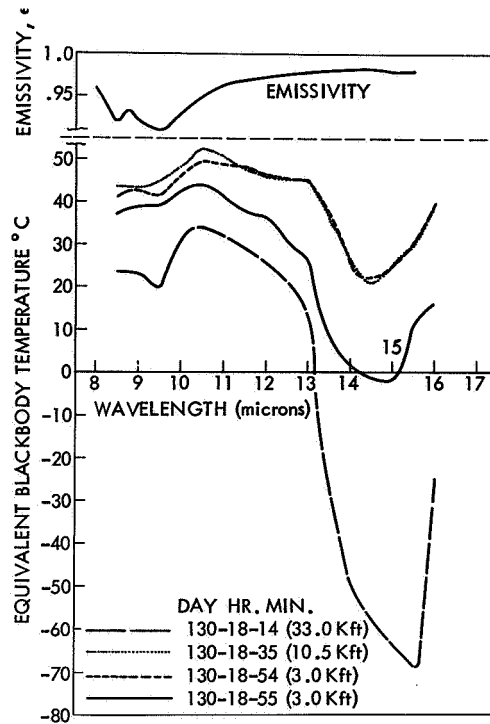


Figure 2—Equivalent blackbody temperatures for lava fields near Amboy Crater

Figure 3—Equivalent blackbody temperatures for Bristol Dry Lake



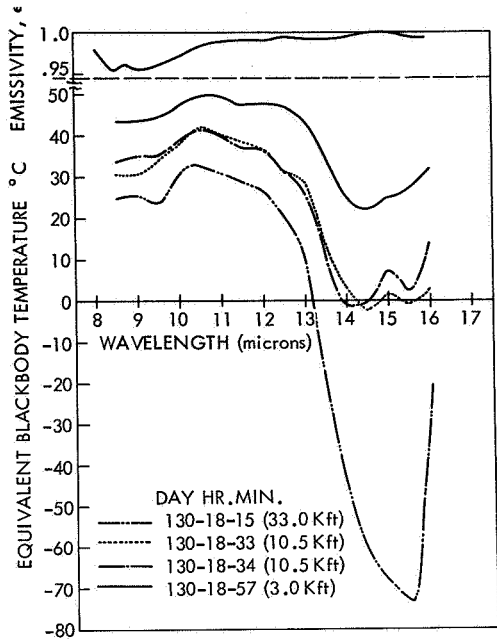


Figure 4—Equivalent blackbody temperatures for desert east of Bristol Dry Lake

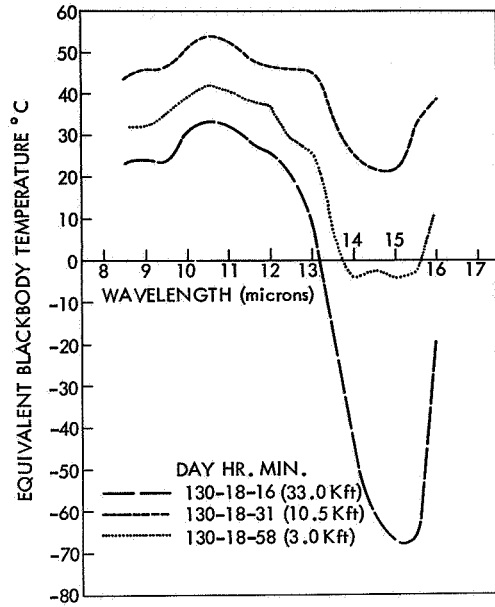


Figure 5—Equivalent blackbody temperatures for Cadiz Dry Lake

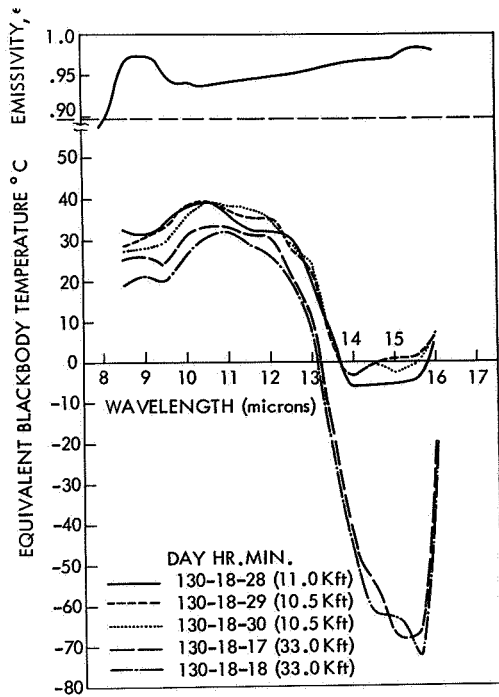


Figure 6—Equivalent blackbody temperatures for Danby Dry Lake

Figures 2-6 show the results obtained for the various segments of this flight. Two general regions may be distinguished. The 8.5 to 13 micron region is a good atmospheric window in which lie the characteristic reststrahlen features produced by the vibration of the SiO_2 molecule in various surface materials. The shifting of frequency of this vibration depends on the concentration of SiO_2 in the mineral. SiO_2 is taken as the "acidic" oxide in minerals. High concentrations of the molecule, as in quartz and granite (greater than 65 percent), shift the vibration to the neighborhood of 9 microns; while low concentrations in the so-called "basic" materials such as dunite (less than 50 percent) shift the vibration toward 11 microns. The shifting of this vibration may be used to separate out basic from acidic surface regions, and its use as a mapping technique is a goal of this program.

The region from 13 to 16 microns is the region of the CO_2 atmospheric absorption which completely bars observations from space of the earth's surface in this wavelength region. At the present writing, the 15.5 and 16 micron readings are tentative, awaiting a more refined calibration of the instrument for these two wavelengths. In general, however, a distinct warming trend was noted as the plane flew at lower altitudes, and the results at each altitude are quite consistent. Changes of a few degrees would be expected because of the high speed of the Convair 990, which resulted in sampling large distances in a short time.

With the exception of Cadiz Dry Lake, each figure contains a plot of emissivity vs wavelength for surface samples taken from that area. The actual effect of these changing emissivities is presently being computed but not yet available. The curves are included to indicate, what preliminary computations confirm, that accurate temperature measurements of surfaces will have to take into account the changing emissivities of surface materials in the reststrahlen region.

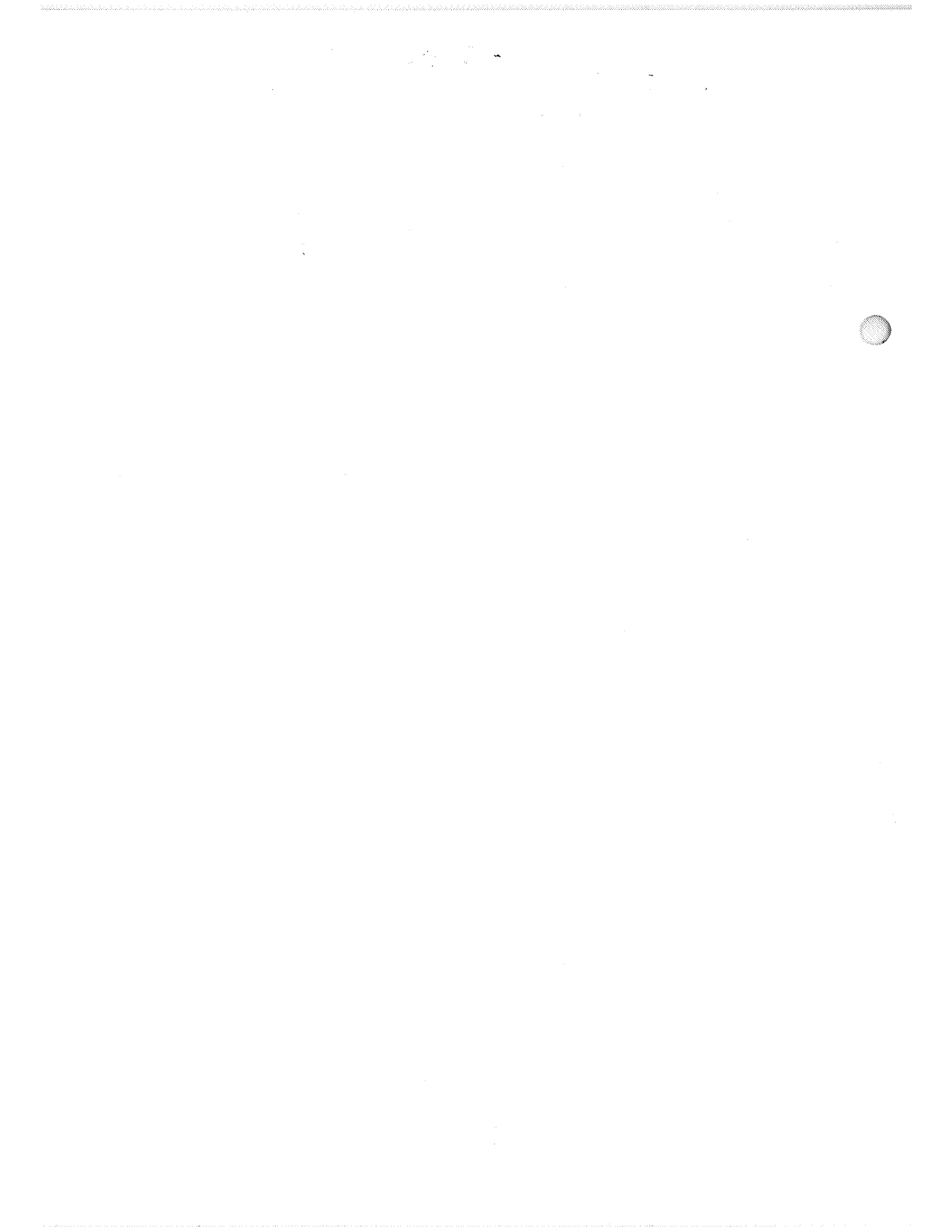
It will also be noted that each curve measured at 33,000 ft shows an apparent temperature drop at 9.5 microns. This effect is due to absorption by atmospheric ozone and vanishes at lower altitudes.

CONCLUSION

Equivalent blackbody temperatures vs wavelength curves have been obtained for several exposed mineral surfaces in the Bristol Dry Lake region of the Mohave Desert. These results have been calculated for the various altitudes at which the plane flew. Surface emissivity measurements made in the laboratory have also been included. Effects of these varying emissivities are now being calculated. These measurements will both yield a measurement of the apparent temperature drop introduced when emissivities below 1 are viewed by the instrument, and also permit measurement of the atmospheric transmission over that wavelength region, 8.5 to 13 microns.

REFERENCES

1. Hovis, W. A., Jr., Applied Optics 5:245, 1966.
2. Hovis, W. A., Jr., Applied Optics 5:815, 1966.
3. Hovis, W. A., Jr., and Callahan, W. R., Journal of the Optical Society of America 56: 639, 1966.
4. Hovis, W. A., Jr., and Tobin, M., Applied Optics 6:1399, 1967.
5. Hovis, W. A., Jr., Kley, W. A., and Strange, M. G., Applied Optics 6:1057, 1967.



THE QUARTZ-IODINE LAMP AS A SECONDARY STANDARD FOR TOTAL RADIANT FLUX

E. I. Mohr*

ABSTRACT

A method is described for using 1000-watt quartz-iodine lamps, calibrated as secondary standards of spectral irradiance, and reevaluating them as secondary standards of total irradiance. Three quartz-iodine lamps were reevaluated by this method. The total irradiance values were compared with the value of a 1000-watt lamp calibrated as a standard of total irradiance by the Eppley Laboratories, Inc. The results indicated an irradiance difference of less than 2 percent.

INTRODUCTION

The National Bureau of Standards (NBS) has issued several types of standards of spectral radiance and irradiance. Work has been reported on the applicability of these lamps as secondary standards of total radiance. Reference 1 describes a method for obtaining the total radiant flux of a standard quartz-iodine lamp of given spectral radiance by finding the area under the curve of spectral radiant power versus wavelength in the 0.25- to 2.5-micron range. In addition, a method is described for evaluating the energy radiated by the tungsten coil and the quartz envelope in the 2.5- to 20-micron range. This extrapolated value is then added to the area under the curve to obtain total lamp radiance.

These total radiance standards have been used to calibrate a thermopile, which has also been calibrated by means of a blackbody. It has been found that the calibration curves of the thermopile vary with blackbody temperature, and all of these are different from the curve obtained by using these secondary standards of total radiance. Moreover a secondary standard of total radiance, developed recently by the NBS and available through the Eppley Laboratories, gives a calibration curve intermediate between those for the blackbody calibration and that of the quartz-iodine lamp used as a standard of total radiance. Therefore, it has seemed desirable to reexamine the method used to determine the total flux emitted by a quartz-iodine lamp.

REEVALUATION OF THE METHOD

The energy emitted by the quartz envelope of the quartz-iodine lamp was evaluated by obtaining the product of the blackbody spectral radiance and fused quartz emissivity. This emissivity was based on the work reported by Pirani (Reference 2), however, more recent data (References 3 and 4) indicate that the emissivity is not as high as the values given by Pirani. Table 1 gives the values obtained from these references. These new values for the emissivity of fused quartz, as well as a different value of the temperature (described below) were used to recalculate the total quartz envelope radiance of the 1000w quartz-iodine lamp.

*Chairman, Physics Department, Columbia Union College

Table 1
Spectral Emissivity of Fused Quartz

λ	ε	λ	ε	λ	ε
3.0	.02	--	--	--	--
3.2	.07	5.5	.96	11	.83
3.4	.11	6.0	.95	12	.84
3.6	.16	6.5	.94	13	.80
3.8	.24	7.0	.93	14	.99
4.0	.44	7.5	.84	15	.99
4.2	.70	8.0	.75	16	.99
4.4	.83	8.5	.66	17	.99
4.6	.92	9.0	.45	18	.95
4.8	.97	9.5	.64	19	.98
5.0	.96	10.0	.76	20	.85

The method used to estimate quartz envelope temperature is described in Reference 1. Because this method may be prone to error, an attempt has been made to measure the temperatures of the lamp support and envelope. For this purpose a thermocouple of platinum-platinum plus 13 percent rhodium was used. A spring clamp held the hot junction firmly against the surface to be measured. The temperatures measured on different parts of the lamp support varied between 360 and 390°K. In order to determine the temperature of the quartz envelope, the spring clamp pressed a Teflon strip against the hot junction of the thermocouple to ensure good envelope-thermocouple contact. The temperature was found to be 660°K at the lower end of the lamp (mounted vertically) and 705°K at the upper end. These values may be excessive, since the Teflon minimizes the loss by radiation and convection.

It was impossible to use the thermocouple to measure the temperature at the mid-point of the envelope. Industrial laboratory investigations of quartz-iodine lamp temperatures suggest a rather high temperature gradient from the center to the end of the lamp. The length of the lamp should be divided into short sections each at a known temperature, to determine the summation of $N_{\lambda} E_{q\lambda} \Delta A$, over the 3.0- to 20-micron range for each section. The total envelope radiance would be obtained by adding section outputs. An alternate method to evaluate the output for "average" temperature would assume 700°K as a reasonable average value. The total radiance of the envelope was obtained by evaluating the sum

$$\sum_{3.0}^{20} N_{\lambda} E_{q\lambda} A \Delta \lambda$$

where N_{λ} is the blackbody spectral radiance at 700°K, $E_{q\lambda}$ the quartz emissivity, A the longitudinal section area, and $\Delta \lambda$ the wavelength increment. The resulting value for the total envelope radiance is only 41 percent of the value reported in Reference 1.

The investigations reported in Reference 1 used the ratio $P_{\lambda} / N_{\lambda} E_{\omega} T_q$ to evaluate the tungsten coil temperature and obtain coil radiance for wavelengths greater than 2.5 microns. P_{λ} is the spectral radiance of the standard lamp, N_{λ} the spectral radiance of the blackbody at a given temperature, E_{ω} the tungsten emissivity, and T_q the quartz transmission. This ratio shows a sharp increase from approximately 2 to 3 in the

2.1- to 2.5-micron range. This slope (Reference 1), was used to obtain the coil radiance for the 2.6 to 4.8 micron range at which point the quartz becomes opaque. Theoretically, it would seem that this ratio should remain constant if tungsten emissivity were known accurately. Thus, a constant ratio was assumed to be the value at 2.0 microns. The total coil radiance in the 2.6- to 4.8-micron range was obtained by the summation $\sum R N_{\lambda} E_{\omega} T_q \Delta \lambda$, where R is the above-mentioned ratio. The result was a decrease in the tungsten radiance to 84.5 percent of its previous value for lamp QM-B, and a decrease of 81.9 percent for lamp QM-95.

The decrease in the flux due to coil radiance in the 2.6- to 4.8-micron range and the quartz envelope radiance caused the radiant flux (in watts per steradian) to decrease to 92.6 percent of the value obtained by the former method for lamp QM-B, and to 92.2 percent for lamp QM-95.

ANGULAR DISTRIBUTION OF FLUX AROUND THE LAMP

Lamp QM-B, mounted with its axis vertical, was rotated about the vertical axis through 360 degrees. The water-cooled thermopile 4928A, mounted on the same optical bench at a distance of 70 cm, was used to measure the intensity of the flux emitted normal to the lamp. This was measured for every 15 degrees of rotation. The flux remained approximately constant.

The lamp was then mounted with its axis horizontal and rotated about a vertical axis through its center while the thermopile remained at 70 cm. While the lamp was rotated through 180 degrees, the flux intensity was measured for every 10 degrees. (From the position in which one end of the lamp was toward the detector until the opposite end pointed toward the thermopile.) This data was plotted on polar-coordinate paper, and a Rousseau diagram was constructed by use of this graph. The average height of the Rousseau diagram was multiplied by 4π to obtain the total power radiated by the lamp in all directions.

INPUT POWER VERSUS TOTAL FLUX EMITTED BY THE LAMP

The quartz-iodine standard lamp operates at 8.30 amperes. This current was monitored by the standard Weston ammeter Model 326, No. 3112. The voltage across the lamp was measured by the standard Weston voltmeter Model 326, No. 3113. The product of the two values gave the input into the lamp in watts. Table 2 gives the power input into three standard lamps and the corresponding power output of the same lamps as determined by the angular distribution and the Rousseau diagram, assuming that the three standard lamps have the same angular distribution as that of lamp QM-B.

Table 2
Comparison of Input Power and Radiant Flux

Lamp	Input power	Output power	Difference	Difference (%)
QM-95	889.3	876.0	-13.3	-1.50
EPI-1154	879.4	865.4	-14.4	-1.64
EPI-1155	904.3	891.3	-13.0	-1.44

From the dimensions of the leads and the ceramic ring around the leads and the measured and estimated temperature differences, the estimated loss by conduction is approximately 0.3 watt. No estimate has been made of energy loss from the lamp due to air convection.

DISCUSSION OF THE RESULTS

The average output of the three standard lamps is 1.53 percent, or 13.6 watts less than the power input. As stated above, conduction losses represent only about 2.5 percent of this difference. A portion of this difference may be due to energy radiated by the lamps at wavelengths greater than 20 microns, although it most likely represents only a fraction of this difference. It is probable that the greater portion of this difference may be caused by a loss of lamp energy due to convection currents. However, no evaluation of these convection losses is possible at this time.

Total irradiance standards of higher accuracy and greater intensity than formerly have recently become available (Reference 5). Two standard lamps of total irradiance, 500 and 1000 watts respectively, were purchased during the summer. These lamps made it possible to compare the total irradiance determined for the quartz-iodine lamps with that of these total irradiance standards. This comparison was made by determining the responsivity of the Eppley water-cooled thermopile 4928A to the three quartz-iodine lamps and to the two total irradiance standards. The resulting data is given in Table 3 and plotted in Figure 1.

Table 3
Responsivity of Thermopile 4928A

Distance (cm)	Responsivity of Quartz- Iodine Lamps (volts·watt·cm ²)			Responsivity of Total Irradiance Standards (volts·watt·cm ²)	
	QM-95	EPI-1154	EPI-1155	ETK-6711	ET5-6708
40	.1323	.1315	.1320	.1354	.1459
50	.1321	.1313	.1321	.1342	.1430
60	.1320	.1313	.1322	.1335	.1412
75	.1314	.1307	.1317	.1326	.1401
100	.1306	.1303	.1310	.1320	.1388
125	.1298	.1296	.1304	.1310	.1381
150	.1297	.1288	.1300	.1304	.1372
175	.1294	.1287	.1295	.1303	.1353
190	.1291	.1289	.1296	.1297	.1380

It will be observed that the responsivity of the thermopile to lamps QM-95, EPI-1154, and EPI-1155 varies less than 1 percent among the three. In addition, the average responsivity to these three lamps differs from the responsivity to the 1000-watt total irradiance standard by amounts ranging from 1 to 2 percent, depending on the distance between the lamps and the thermopile. On the other hand, the average responsivity to the three lamps differs from the responsivity to the 500-watt standard of total irradiance by varying amounts between 4.5 and 9.5 percent.

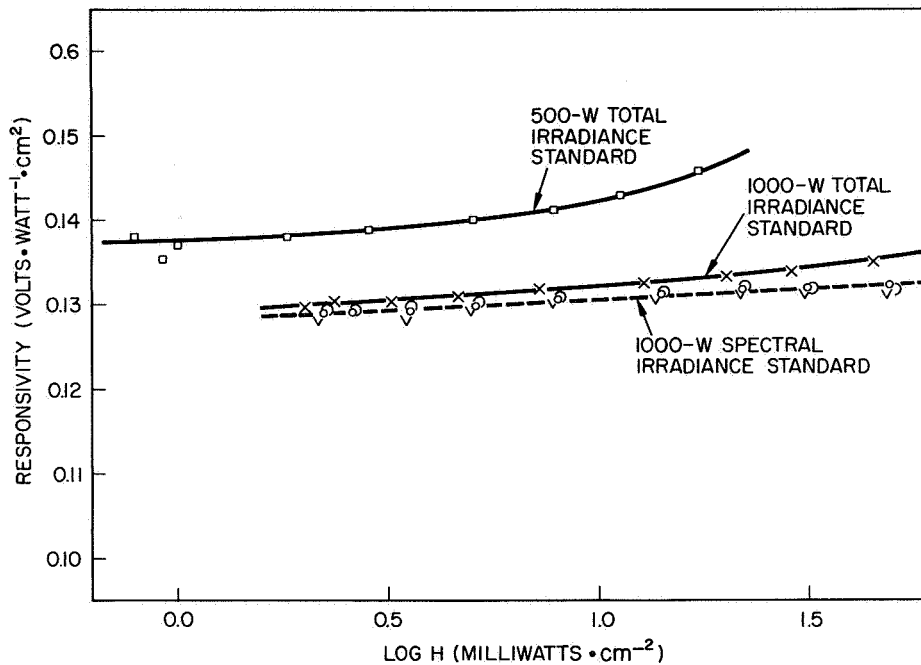


Figure 1—Responsivity of thermopile 4928A.

Responsivity to the 500-watt standard of total irradiance differs from the responsivity to the 1000-watt standard of total irradiance by varying amounts from 3.8 to 7.7 percent. This difference is much greater than those between the responsivity of the thermopile to the quartz-iodine lamps and the 1000-watt standard of total irradiance. This higher responsivity of the thermopile to the 500-watt standard of total irradiance agrees with previously reported responsivities of the thermopile to tungsten ribbon lamps and blackbodies operating at lower temperatures (References 6 and 7). The reason for this difference has not been determined.

CONCLUSIONS

The values for the total irradiance, determined for the three quartz-iodine lamps, agree with each other and with the irradiance of the 1000-watt standard of total irradiance No. ETK-6711 as shown by the responsivity of thermopile 4928A. Hence, the revised method for evaluating the 1000-watt quartz-iodine lamp as a standard of total irradiance seems valid.

REFERENCES

1. Final Report of the Goddard Summer Workshop Program, NASA Goddard Space Flight Center Document X-100-65-407, 1965, pp. B-39.
2. Pirani, M., "Radiation Properties of Different Substances Within the Temperature Range 250°C to 800°C," J. of Sci. Instruments 16:372-78, 1939.
3. Lyon, R. J. P., "Rough and Powdered Surfaces," Evaluation of Infrared Spectrometry for Compositional Analysis of Lunar and Planetary Soils, NASA CR-100, Nov. 1964.

4. McMahon, H. O., "Thermal Radiation Characteristics of Some Glasses," J. of the American Ceramic Soc. 34:91-96, 1951.
5. Stair, R., Schneider, W. E., and Fussell, W. B., "The New Tungsten-Filament Lamp Standards of Total Irradiance," Appl. Optics 6:101-105, 1967.
6. Final Report of the Goddard Summer Workshop Program, NASA Goddard Space Flight Center Document X-100-65-407, 1965, pp. B-23.
7. Final Report of the Goddard Summer Workshop Program, NASA Goddard Space Flight Center Document X-700-67-94, 1966, p. 393.

CALIBRATION OF THE SIX-FOOT SPHERICAL INTEGRATOR

E. I. Mohr*

ABSTRACT

Preliminary calibrations of this integrator were reported in the Final Report of the 1966 Workshop Program. In examining this calibration, it was found advisable to reposition the exit port and sources in the sphere, to design an improved power supply and monitoring equipment, and to repaint the integrator. While these changes were being made, the spectral reflectance of the sphere paint was determined again by means of Cary 14 and Cary 90 spectrophotometers. These instruments had not been available previously.

The relative spectral emittance of the integrator was determined by comparing the spectral emittance of the sphere with that of three standard lamps every tenth of a micron, or less, from 0.32 to 2.7 microns. The absolute spectral emittance was obtained by comparing the emittances of a 16-inch integrating sphere while alternately receiving flux from the 6-foot integrator and one of the standard lamps. These absolute values were determined at a few points and then used to normalize the relative values to these absolute values. The mean of the values obtained independently by means of the three standard lamps was accepted as the spectral radiant emittance of the 6-foot integrator.

INTRODUCTION

Several years ago, a 6-foot spherical integrator was purchased at GSFC for possible use as a wide-angle source for the calibration of radiometers in the visible and near-infrared regions. Team A of the 1964 Summer Workshop calibrated this integrator (Reference 1) by using the Eppley 4928A water-cooled thermopile. Subsequent investigations have shown decided differences in the response of the thermopile to a standard quartz-iodine lamp and to a blackbody operated at various temperatures (References 2 and 3). The cause of these differences is still under investigation. Meanwhile, a new approach in the integrator calibration procedure has been proposed, since the calibration based on the thermopile is presently in doubt. Some preliminary investigations using the new procedure were made toward the end of the 1966 Summer Workshop (Reference 3) and during the winter of 1966-67. As a result of this preliminary work, it was seen that it would be desirable to change the position and size of the exit port, and the position of the quartz-iodine lamps. In addition, a greatly improved power supply was designed and built to operate the lamps in the sphere.

THEORY

The principle of spherical integration was proposed by Sumpner (Reference 4) in 1892. He showed that if a source of light is placed inside a hollow sphere coated internally with a perfectly diffusing coat, the luminance of any portion of the surface, because of the light reflected from the rest of the sphere, is everywhere the same and directly proportional to the total flux emitted by the source.

* Columbia Union College, Takoma Park, Maryland.

The theoretical expression for this relation (Reference 5) in terms of the reflectance ρ of the perfectly diffusing coat of the sphere wall due to an infinite number of reflections is given by

$$\Phi = \frac{F}{4\pi r^2} \frac{\rho}{1-\rho}, \quad (1)$$

where Φ is the total radiant flux reaching unit area of the spherical surface by reflection, F the total flux emitted by the source, and r the radius of the sphere. In the derivation of Equation 1 it is assumed that ρ is constant, that the surface is a perfect diffuser, that the sphere is empty, and that it has no ports. As a matter of fact, the reflectance ρ of the coating varies with wavelength. Moreover, there is no perfect diffuser, so Lambert's cosine law does not hold accurately. In addition, the sphere has sources, shields, and ports, all of which affect the total radiant flux.

It has been shown that the error introduced by the finite size of holes and samples may be as much as 25 percent (Reference 6). Moreover, the spectral dependence of the reflection can modify considerably the spectral distribution of the flux streaming from the port of the sphere (Reference 1). Thus the intensity is increased for wavelengths for which the reflectance is high, and decreased for wavelengths for which the reflectance is low. In spite of the above mentioned uncertainties, it is possible to obtain relative values of flux from two sources. If one of these is a standard source and reasonable precautions are taken, one may obtain satisfactory data for the spectral radiant emittance of the spherical integrator.

THE SPHERICAL INTEGRATOR

The spherical integrator has a diameter of 6-feet (182.5 cm inside diameter). It consists of two hollow fiberglass hemispheres, one of which is mounted on a rigid but movable framework. The second hemisphere is hinged to the first and held shut by a latch, permitting easy access to the interior. (See Figure 1.)

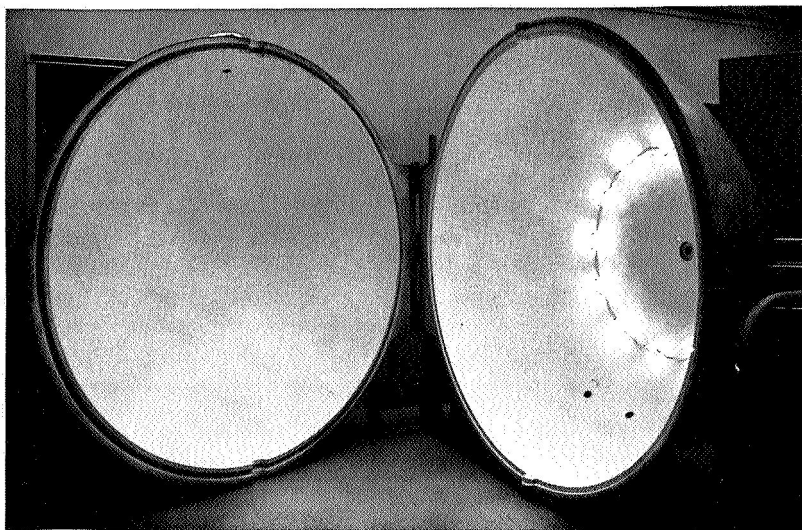


Figure 1-Stationary and movable hemispheres of the 6-foot integrator (inside view).

An exit port with a diameter of 6.0 cm is located at the midpoint of the surface of the stationary hemisphere. This port allows ready access for the calibration of radiometers in the visible and near-infrared regions and provides a sufficiently large field of view. The inside of the sphere is covered with several coats of a white paint with a magnesium carbonate base, manufactured by the Burch Co. This coating provides a satisfactory diffusing surface.

To hold to a minimum the size of the objects introduced into the sphere and also to have some means of varying the intensity of the source, 12 quartz-iodine lamps, rated at 200 watts each, are mounted inside the sphere. These lamps are evenly spaced around the exit port on a circle with a radius of 18 inches. Small Teflon shields, mounted in front of the lamps, prevent the flux from these lamps from reaching the port directly. Figure 2 is a view of the inside of the stationary hemisphere showing the position of the exit port surrounded by the 12 lamps.

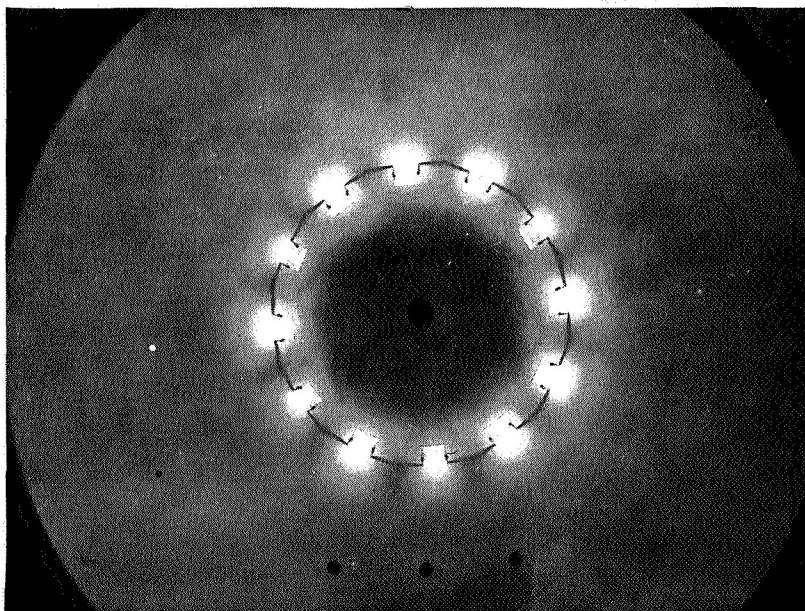


Figure 2-Inside view of the stationary hemisphere showing the position of the exit port and of the 12 quartz-iodine lamps.

A 3.8-cm diameter hole on top of the sphere, with a fan mounted over it, together with three holes of the same size in the bottom of the sphere, provides a continuous flow of air through the sphere. For a more complete description of the sphere in terms of the original position of ports and lamps, see Reference 1.

POWER SUPPLY FOR THE INTEGRATOR LAMPS

The 200-watt quartz-iodine lamps require a 6.5-amperes at approximately 30.3 volts. The lamps are operated in three banks of four lamps each. The four lamps in a given bank are in series. Each bank of four lamps is operated by one of three power supplies. These power supplies are Model 590-11 power supplies manufactured by Edgerton, Germeshausen & Grier, Inc. They have been specifically designed for use with various types of standard lamps. They are solid-state supplies designed to furnish programmed voltage and rms regulated current in preset combinations at power levels

ranging from 2 to 1000 watts (1 to 50 amperes and 2 to 160 volts). The chopper-stabilized square wave current is feedback-regulated within 0.25 percent rms of the selected digital value for control of light output within 1 percent. In the present application, the power supplies were preset to provide a constant current of 6.5 amperes with a maximum available potential of 152 volts.

A switching arrangement allows any one or all of the lamps in a given bank to be turned off. Since such a turn-off would result in a considerable decrease in the load in the given bank, when one of the lamps is turned off it is replaced at once by an equivalent load outside of the sphere. This load consists of a parallel combination of two 10-ampere, 200-watt Ohmite Dividohn power resistors, located in the control rack so that the dissipated power does not contribute to the total flux in the sphere.

The circuit arrangement provides for constant monitoring of the voltage drop across each lamp separately, by means of a Hewlett-Packard Model 3400A True RMS Meter. The dc output of this meter is fed into a Non-Linear Systems Model M25 Digital Volt-Ohmmeter, which may be read to four significant digits. This voltage may also be recorded by means of a Hewlett-Packard Model 561B Digital Recorder. This continuous monitoring of the voltage permits the operator to note if and when the resistance of a given lamp begins to change. Since such a change is accompanied by a change in the lamp output, and hence its intensity, the investigator knows that the particular lamp must be replaced by an equivalent lamp in order to keep the emittance of the sphere constant.

Figure 3 shows the 6-foot integrator with the lamp power supply and the voltage monitoring equipment mounted in the rack to the left of the sphere. A Perkin-Elmer Double-Pass Monochromator, Model 99, with a 16-inch integrator attached to it in front of the slit, is shown positioned in front of the exit port of the 6-foot integrator. The power supply and recording equipment for the monochromator are mounted in the rack to the right of the sphere.

SPECTRAL REFLECTANCE OF THE BURCH SPHERE PAINT

The spectral reflectance of the sphere paint used in the preliminary calibration of the sphere was obtained by means of a Beckman DK-2A spectrophotometer and a Beckman IR-7 spectrophotometer (Reference 1). The measurements were made by comparing the reflectance of the paint with that of freshly smoked magnesium. The values obtained for the paint seemed rather high in comparison with those for magnesium oxide.

With the recent availability of a Cary 14 double-beam spectrophotometer and a Cary 90 double-beam instrument, both designed for reflectance measurements, the reflectance of the sphere paint was measured again. The reflectance of the paint was compared with that of freshly smoked magnesium oxide in the range from 0.2 to 2.5 microns by means of the Cary 14. For the range from 2.5 to 20 microns, the reflectance of the paint was compared with that of a calibrated aluminum mirror as standard by means of the Cary 90. The corresponding data are given in Table 1 and plotted in Figure 4. (Values above 3.0, being insignificant, are not shown.)

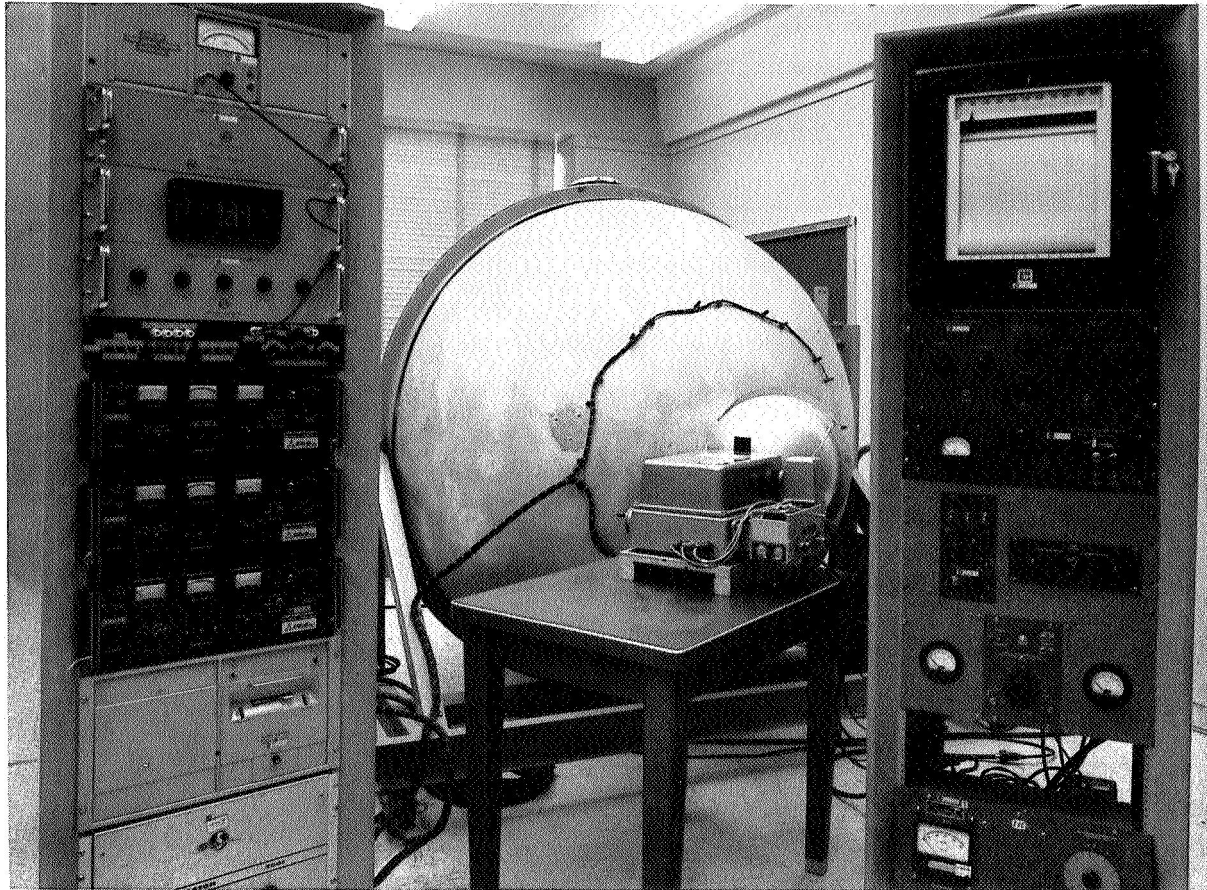


Figure 3—Outside view of the 6-foot integrator. The rack to the left of the sphere contains the power supply and monitoring equipment for the lamps. The monochromator, with the 16-inch sphere attached, is located at the exit port of the integrator. The rack to the right contains the amplifier and recorder for the monochromator.

Table 1
Spectral Reflectance of Burch Sphere Paint
(λ in microns)

λ	ρ_{λ}	λ	ρ_{λ}	λ	ρ_{λ}
0.20	0.141	0.45	0.844	1.6	0.803
0.21	0.145	0.50	0.874	1.7	0.756
0.22	0.225	0.55	0.891	1.8	0.740
0.23	0.336	0.60	0.903	1.9	0.698
0.24	0.342	0.65	0.912	2.0	0.645
0.25	0.426	0.70	0.914	2.1	0.644
0.26	0.620	0.75	0.913	2.2	0.654
0.27	0.735	0.80	0.913	2.3	0.548
0.28	0.820	0.90	0.910	2.4	0.490
0.29	0.769	1.00	0.904	2.5	0.460
0.30	0.626	1.1	0.895	2.6	0.443
0.32	0.627	1.2	0.877	2.7	0.291
0.35	0.705	1.3	0.870	2.8	0.059
0.37	0.755	1.4	0.825	2.9	0.025
0.40	0.802	1.5	0.806	3.0	0.048

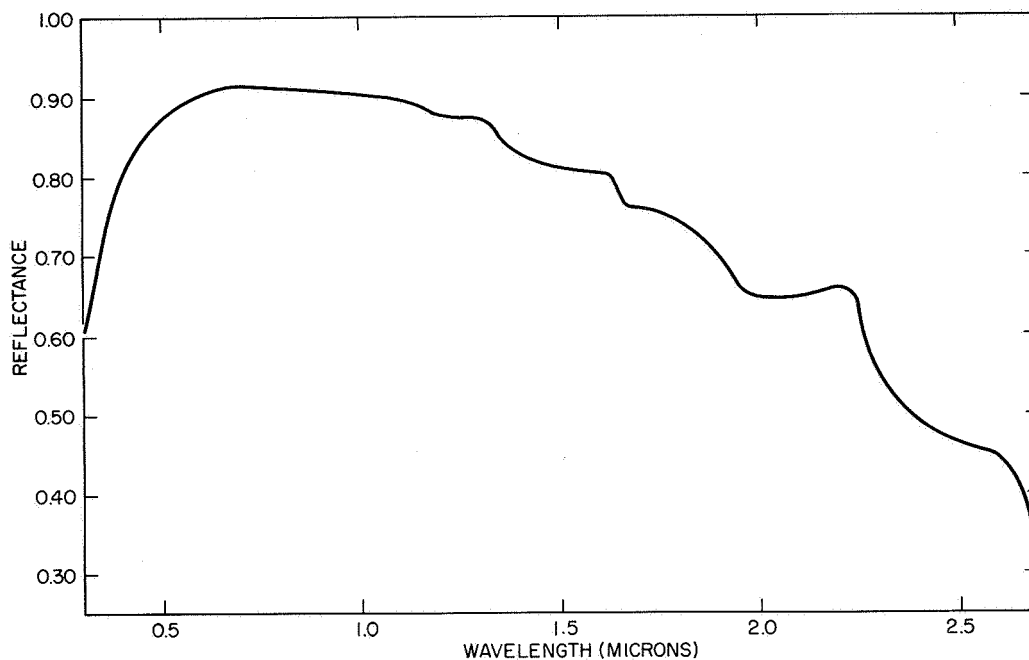


Figure 4-Spectral reflectance of sphere paint.

OPERATING PROCEDURE

Before any measurements were made on or with the sphere, the fan and all 12 lamps were turned on. One hour was allowed for the sphere to attain equilibrium. This wait ensured repeatable steady-state conditions.

When a radiometer is to be calibrated, from one to N lamps will be required, where $N + 1$ lamps would saturate the detector. In this case, lamps Nos. 12, 11, . . . $N + 1$ are turned off after steady-state conditions have been reached. Thus the operator will start with N lamps. This number is decreased one lamp at a time till only lamp No. 1 is in use. This procedure gives the available range of intensities. It is important to decrease the current through a given lamp slowly when turning it off in order to assure its maximum useful lifetime.

RELATIVE SPECTRAL DISTRIBUTION

Since the integrating effect of the sphere is influenced by the spectral dependence of the reflectance, it is necessary to compare the spectral distribution of the output with that from a standard of spectral radiance. Tests have shown that the number of lamps used in the sphere has no effect on the spectral distribution of the output within the limits of experimental accuracy (Reference 1); hence 12 lamps were used to calibrate the sphere in order to get a satisfactory flux intensity.

The measurements of the spectral distribution of the sphere were made with a Perkin-Elmer Double-Pass Monochromator, Model 99. The slit of the monochromator was positioned as close to the port of the spherical integrator as possible. The slit width and gain were held at the smallest values possible in order to have the best resolution possible as well as a minimum amount of noise. For the wavelength range from 0.45 to 2.7 microns, a Reeder thermocouple detector with quartz window was used. A

1P28 photomultiplier detector was used in the range from 0.32 to 0.7 micron. The spectral distribution for both ranges was automatically recorded by means of a Leeds and Northrup Speedomax G. Whenever it was necessary to change the slit width of the monochromator or the gain of the amplifier, a portion of the previously recorded spectral range was scanned again to normalize all parts of the recorded range to the peak value of the deflection. This procedure was repeated several times to obtain the average value of the distribution.

In order to get the spectral distribution of the standard of radiance, the NBS-calibrated QM-95 1,000-watt quartz-iodine lamp and the Eppley Laboratories EPI-1154 and EPI-1155 lamps were used. For a given trial, one of these lamps was positioned about 2.4 meters in front of the slit of the monochromator and on a line with its axis. The spectral distribution of each lamp was obtained under the same conditions of slit width and amplifier gain as those which were used to obtain the spectral distribution of the output of the sphere, and the results normalized as before.

The normalized recorder deflections $D_{sr\lambda}$ obtained for the output of the sphere were divided by the corresponding normalized recorder deflections $D_{lr\lambda}$ obtained for each of the standard lamps. This division was done at intervals of 0.1 micron or less over the entire spectral range which was scanned, and gave the relative values for the ratio of the spectral distribution of the sphere to that of a specific lamp. These ratio values, $k_{r\lambda} = D_{sr\lambda} / D_{lr\lambda}$, were determined separately for each of the standard lamps used.

ABSOLUTE SPECTRAL DISTRIBUTION

The spherical integrator as a source of radiant flux has a spectral configuration different from that of an approximate point source such as the standard quartz-iodine lamp. To obtain an absolute calibration by comparing the spectral distribution of the sphere with that of the standard lamp, it is necessary to eliminate the effects of this difference. Since "the role of a diffusely reflecting surface is to obliterate the past history of the incident radiation" (Reference 7), a 16-inch spherical integrator was mounted on the front of the Perkin-Elmer Monochromator. This small sphere consists of two plastic hemispherical shells painted with Burch sphere paint on the inside and aluminum paint on the outside. The two hemispheres are held together by means of clamps. One of the hemispheres was rigidly fastened to the monochromator so that a 1.8-cm diameter exit port was centered in front of the monochromator slit. The second hemisphere was a 3.7-cm diameter entrance port designed to be rotated alternately into a position (a) that it may be positioned at the exit port of the 6-foot integrator so that it is on the inside curvature of the 6-foot integrator and thus receive flux from all parts of the large sphere, or (b) so as to be in line with the standard quartz-iodine lamp located 20 cm from this port and thus receive the flux from the standard lamp. Using the small sphere in this way, the monochromator alternately saw the flux emitted by the 6-foot integrator and the flux from the standard lamp at 20 cm - both of them after the flux had been integrated by the small sphere.

Using a given slit width of the monochromator and gain of the recorder, a direct comparison was made between the total flux the small sphere received from the 6-foot integrator and the flux from the standard lamps used to get the relative ratios as described above. This comparison was made using the 1P28 photomultiplier detector at the following wavelengths: 0.45, 0.50, 0.53, 0.55, and 0.60 micron. The procedure was repeated using the Reeder thermocouple detector at the following wavelengths: 0.6, 0.9, 1.0, 1.1, 1.2, and 1.3 microns.

Let $D_{sa\lambda}$ be the recorder deflection of the monochromator at one of the above-mentioned wavelengths when the small sphere receives flux from the 6-foot integrator, and $D_{la\lambda}$ the deflection at the same wavelength when it receives flux from one of the

standard lamps placed 20 cm from the entrance port. Then $k_{a\lambda} = D_{sa\lambda}/D_{la\lambda}$ is the absolute ratio of the flux from the 6-foot integrator to that of the standard lamp at this wavelength. The absolute ratios for all wavelengths measured may be obtained by normalizing the relative ratios $k_{r\lambda}$ to these absolute ratios $k_{a\lambda}$.

CALIBRATION OF THE SPHERICAL INTEGRATOR

When the small sphere, mounted on the monochromator, has its entrance port located at the exit port of the 6-foot integrator, the flux incident on the entrance port is obviously the same flux incident on the corresponding portion of the exit port of the 6-foot integrator. Since this flux comes from all parts of the inside surface of the integrator by diffuse reflection, each elemental area of the inside surface of the small sphere receives flux from an equivalent fractional portion of the inside surface of the integrator that is on the line of sight through the port with that of the small sphere. This means that the small sphere receives completely diffuse radiation from the 6-foot integrator.

To determine the total flux received by the small sphere, one must evaluate it in terms of the flux incident at the exit port of the integrator which has come from all parts of the diffusing surface of the integrator. Let $F_{s\lambda}$ watts $\text{cm}^{-2} \mu^{-1}$ be diffusely reflected into the solid angle 2π . Then the diffuse spectral radiation in the normal direction is $F_{s\lambda}/\pi$. The spectral radiant flux from the diffusely reflecting surface of the spherical segment of area dA_s incident at the effective area of the exit port, and hence of the area A of the entrance port of the small sphere, is equal to

$$A dW_s = \frac{F_{s\lambda}}{\pi} \frac{\left(dA_s \cos \frac{1}{2} \theta\right) \left(A \cos \frac{1}{2} \theta\right)}{d^2}, \quad (2)$$

where d is the distance between the element of area dA_s and the port, and $1/2 \theta$ is the angle between the line-of-sight propagation from this area and the inner normal to the sphere at the same point on dA_s , as is shown in Figure 5. Since $d = 2r \cos 1/2 \theta$, and $dA_s = 2\pi r^2 \sin \theta d\theta$, the element of spectral radiant power at the entrance port of the small sphere is

$$dP_{s\lambda} = A dW_s = \frac{F_{s\lambda}}{\pi} \frac{2\pi r^2 \sin \theta d\theta \cos^2 \frac{1}{2} \theta A}{4r^2 \cos^2 \frac{1}{2} \theta}. \quad (3)$$

Upon simplification, this becomes $dP_{s\lambda} = 1/2 F_{s\lambda} A \sin \theta d\theta$. Thus the spectral radiant power at the port of the 6-foot integrator and hence at the entrance port of the small sphere is

$$P_{s\lambda} = \frac{1}{2} F_{s\lambda} A \int_0^\theta \sin \theta d\theta = \frac{1}{2} F_{s\lambda} A (1 - \cos \theta). \quad (4)$$

Since θ varies essentially from 0 to 180 degrees because of the size of the port, and the relative positions of the ports of the two spheres, Equation 4 becomes

$$P_{s\lambda} = W_{s\lambda} A = F_{s\lambda} A \text{ watts/micron}. \quad (5)$$

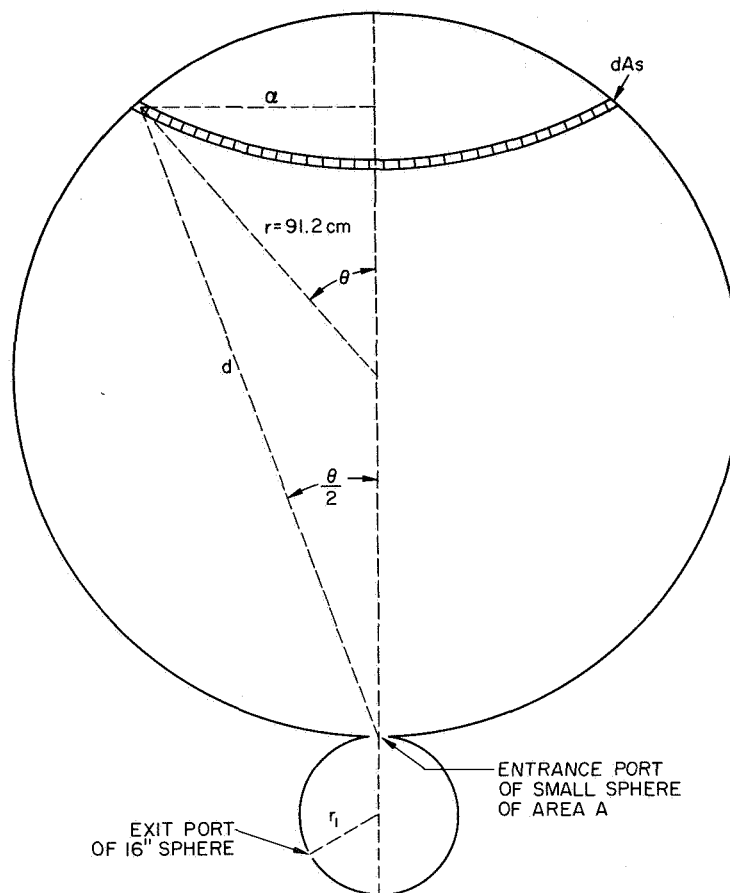


Figure 5-Cross-section of large and small spheres showing data used to derive Equations 4 and 5.

This diffuse flux from the 6-foot integrator was integrated by the small sphere so that the radiant emittance at the exit port of the small sphere is given by Equation (1) as

$$W'_{s\lambda} = \frac{W_{s\lambda} A}{4\pi r_1^2} \frac{\rho_\lambda}{1 - \rho_\lambda}, \quad (6)$$

where r_1 is the radius of the small sphere and ρ_λ is the spectral reflectance of the sphere paint. This flux was viewed by the monochromator. The resulting recorder deflection $D_{sa\lambda}$ was proportional to the integrated flux $W'_{s\lambda}$ and hence to the spectral radiant emittance $W_{s\lambda}$ of the 6-foot integrator.

On the other hand, when the small sphere, mounted on the monochromator, receives flux from the standard lamp, it comes from approximately a point source. Let $J_{\ell\lambda}$ watts/steradian/micron be the spectral radiant intensity of the standard quartz-iodine lamp. Then the spectral irradiance per unit area at the port of the small sphere due to the standard lamp at 20 cm is given by

$$H_{\ell\lambda} = CJ_{\ell\lambda}/r^2 \text{ watts/cm}^2/\text{micron}, \quad (7)$$

where $r = 20$ cm is the distance from the lamp to the entrance port and C is a correction factor to correct for inverse square failure (Reference 2). The spectral radiant power received by the small sphere from the standard lamp is given by

$$P_{\ell\lambda} = H_{\ell\lambda} A \text{ watts/micron,} \quad (8)$$

where A is the area of the entrance port of the small sphere.

As mentioned previously, the flux received by the small sphere from the 6-foot integrator is diffuse radiation. The flux from the standard lamp, however, comes from approximately a point source and falls on a relatively small area of the inside of the small sphere, after which event it is diffusely reflected. Thus the flux from the standard lamp becomes comparable to the diffuse radiation received from the 6-foot integrator only after undergoing a single diffuse reflection. Hence the effective radiant power from the standard lamp which will be integrated by the small sphere is obtained by multiplying Equation 8 by the spectral reflectance of the sphere paint ρ_{λ} so that

$$P'_{\ell\lambda} = \rho_{\lambda} H_{\ell\lambda} A \text{ watts/micron.} \quad (9)$$

This correction was not made in the preliminary results reported previously (Reference 4). This effective flux was integrated by the small sphere. Hence the spectral radiant emittance at the exit port of the small sphere viewed by the monochromator is found by Equation 1 to be

$$W_{\ell\lambda} = \frac{\rho_{\lambda} H_{\ell\lambda} A}{4\pi r_1^2} \frac{\rho_{\lambda}}{1 - \rho_{\lambda}} \text{ watts/cm}^2/\text{micron,} \quad (10)$$

where r_1 is the radius of the small sphere. The corresponding recorder deflection $D_{\ell a\lambda}$ was proportional to the emittance $W_{\ell\lambda}$ and thus to the effective flux $\rho_{\lambda} H_{\ell\lambda}$ received from the lamp after a single diffuse reflection.

It is therefore possible to compare the spectral radiant emittance which the small sphere received from the 6-foot integrator with the spectral intensity from the standard lamp after a single diffuse reflection in terms of the corresponding deflections of the recorder as seen by dividing Equation 6 by Equation 10, or

$$\frac{W'_{s\lambda}}{W_{L\lambda}} = \frac{\frac{W_{s\lambda} A}{4\pi r_1^2} \frac{\rho_{\lambda}}{1 - \rho_{\lambda}}}{\frac{\rho_{\lambda} H_{L\lambda} A}{4\pi r_1^2} \frac{\rho_{\lambda}}{1 - \rho_{\lambda}}} = \frac{W_{s\lambda}}{\rho_{\lambda} H_{L\lambda}} \quad (11)$$

As stated before, the monochromator deflections are proportional to the intensity of the flux seen by the monochromator if the gain and the slit width are held constant. Hence the absolute ratio of the recorder deflections is equal to the ratio given by Equation 11, or

$$k_{a\lambda} = D_{sa\lambda}/D_{\ell a\lambda} = W'_{s\lambda}/W_{\ell\lambda} = W_{s\lambda}/\rho_{\lambda} H_{L\lambda} \quad (12)$$

Thus one obtains

$$W_{s\lambda} = \rho_{\lambda} H_{\ell\lambda} D_{sa\lambda} / D_{\ell a\lambda} \text{ watts/cm}^2/\text{micron.} \quad (13)$$

for the spectral radiant emittance of the 6-foot integrator.

Using Equation 13, the diffuse spectral emittance of the 6-foot integrator was calculated every tenth of a micron or less from 0.32 to 2.7 microns for each standard lamp separately. The resulting data for standard lamp QM-95 is given in Table 2. The wavelength is in microns. The second column gives the spectral irradiance of the standard lamp QM-95 at 20 cm (in milliwatts/cm²/micron). The third column gives the spectral radiance after a single reflection by the small sphere. The fourth column gives the absolute ratios of the recorder deflections. The fifth column gives the diffuse spectral radiant emittance of the 6-foot integrator when 12 lamps are operating. Table 3 gives the mean spectral radiant emittance of the integrator as determined by means of the standard lamps QM-95, EPI-1154, and EPI-1155. Figure 6 shows the spectral distribution of the 6-foot integrator as determined by the use of lamp QM-95, and also shows the spectral distribution of lamp QM-95.

Table 2
Spectral Radiant Emittance of Spherical Integrator by Use of Lamp QM-95

λ (microns)	H_{λ}	$\rho_{\lambda} H_{\lambda}$	$D_{sa\lambda} / D_{\ell a\lambda}$	$W_{s\lambda}$
0.32	2.202	1.381	0.0967	0.1335
0.35	5.058	3.566	0.2059	0.7343
0.37	7.831	5.915	0.3352	1.983
0.40	13.63	10.93	0.5713	6.246
0.45	27.19	22.95	0.9023	20.71
0.50	45.45	39.72	1.203	47.79
0.55	66.01	58.81	1.457	85.68
0.60	87.60	79.10	1.748	138.2
0.65	108.0	98.45	1.781	175.3
0.70	124.6	113.9	1.810	206.1
0.75	136.9	125.0	1.883	235.5
0.80	144.3	131.8	1.965	259.0
0.90	149.9	136.4	1.777	242.4
1.00	146.8	132.7	1.562	207.4
1.1	138.2	123.7	1.378	170.4
1.2	126.4	110.9	1.197	132.8
1.3	114.1	99.29	1.082	107.4
1.4	101.8	83.97	0.5685	47.74
1.5	90.06	72.59	0.5604	40.68
1.6	78.96	63.40	0.5701	36.15
1.7	69.09	52.23	0.3925	20.50
1.8	60.01	44.41	0.2988	13.27
1.9	51.94	36.25	0.1877	6.806
2.0	44.91	28.96	0.1851	5.362
2.1	39.23	25.27	0.1921	4.853
2.2	34.67	22.67	0.1792	4.064
2.3	30.89	19.93	0.1062	1.798
2.4	27.88	13.66	0.07856	1.073
2.5	25.54	11.75	0.05798	0.6811
2.6	19.84	8.790	0.03022	0.2656
2.7	17.41	5.067	0.03016	0.1528

Table 3
Spectral Radiant Emittance of 6-foot
Spherical Integrator

λ (microns)	W_λ (milliwatts/cm ² - μ) ⁻¹	λ (microns)	W_λ (milliwatts/cm ² - μ)
0.32	0.136	1.1	170
0.35	0.745	1.2	132
0.37	1.99	1.3	106
0.40	6.24	1.4	48.0
0.45	20.3	1.5	40.7
0.50	47.3	1.6	36.5
0.55	84.8	1.7	20.6
0.60	139	1.8	13.1
0.65	176	1.9	6.82
0.70	204	2.0	5.32
0.75	237	2.1	4.77
0.80	263	2.2	3.92
0.90	249	2.3	1.73
1.00	209	2.4	1.05
		2.5	0.665
		2.6	0.252
		2.7	0.140

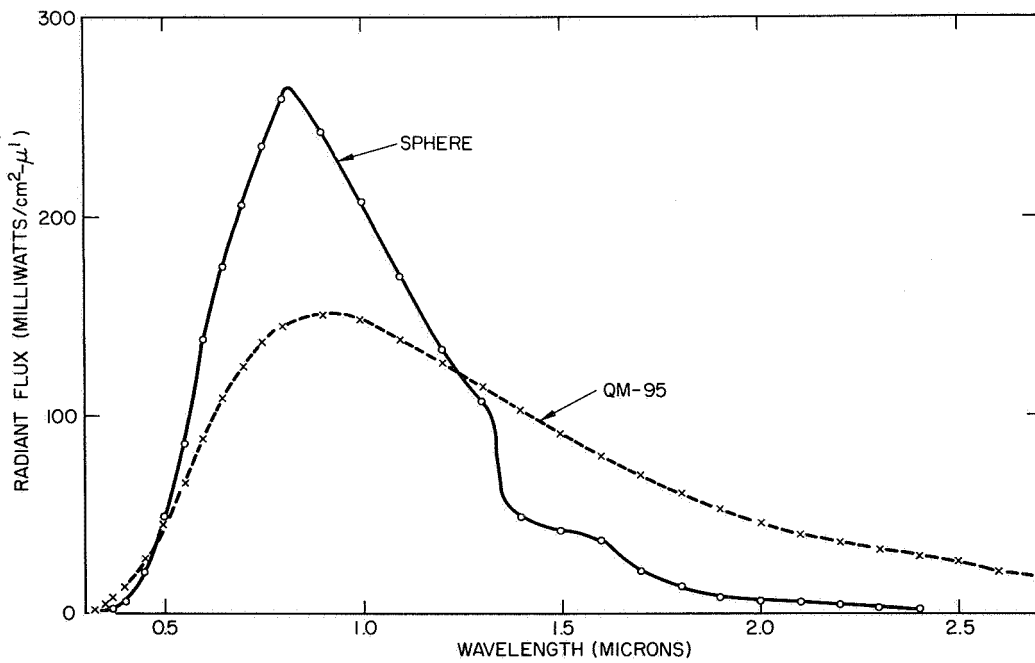


Figure 6-Spectral curves of sphere and lamp QM-95.

INTEGRATOR EMITTANCE VS NUMBER OF LAMPS

To use the spherical integrator for calibrating radiometers, it is necessary to vary the magnitude of the spectral radiant emittance. To permit such a change in intensity, the "source" consists of 12 200-watt quartz-iodine lamps operating at 6.5 amperes. As stated above, the circuit design permits turning on or off any one of the lamps independently. Thus any number of lamps from 1 to 12 may be used as the source in the integrator.

To determine the emittance vs number of lamps, the slit of the monochromator was positioned as close to the port of the spherical integrator as possible. The monochromator was set for the fixed wavelength 0.55 micron, the wavelength at which the 1P28 photomultiplier gives the greatest recorder deflection when the flux comes from a quartz-iodine lamp. The slit width and the amplifier gain were the smallest possible in order to have good resolution and low noise and still obtain approximately full-scale deflection when 12 lamps were operating in the sphere. This deflection was recorded. Then the lamps were turned off one at a time in order from No. 12, 11, 10, etc., until only lamp No. 1 was operating. The recorder deflection was recorded in each case. This procedure was repeated three times. Similarly, the same measurements were made twice at 1.09 microns by means of the thermocouple detector.

The ratio of the intensity of the integrator emittance vs number of lamps was obtained by dividing the deflection for N lamps by the deflection for 12 lamps. The mean of the ratios for the five trials is given in Table 4. The spectral radiant emittance for 10 lamps may be obtained by multiplying the spectral radiant emittance for 12 lamps by the ratio of the intensity of 10 lamps to that of 12 lamps, and similarly for any number of lamps from 1 to 11.

Table 4
Ratio of Intensity of N Lamps to 12 Lamps
in Spherical Integrator

No. of Lamps	$W_{\lambda_n} / W_{\lambda_{12}}$
12	1.0000
11	0.9154
10	0.8310
9	0.7468
8	0.6627
7	0.5782
6	0.4962
5	0.4115
4	0.3286
3	0.2471
2	0.1640
1	0.08215

ANALYSIS OF RESULTS

An examination of the spectral curves in Figure 6 reveals several significant facts. First, it will be observed that the peak value of the integrator emittance is 1.73 times the peak value of the irradiance of the standard lamp at 20 cm. Second, the maximum intensity of the integrator emittance is located at approximately 0.82 micron,

while the maximum value of the irradiance of the standard lamp is located at approximately 0.92 micron. Third, for those wavelengths for which the reflectance of the sphere paint is high, the sphere amplifies the emitted power; while for the wavelengths for which the reflectance is low, the emitted power of the sphere is less than that of the source.

A comparison of the spectral distribution of the integrator emittance as determined by the three standard lamps shows that the results are reasonable consistent. The greatest difference at a given wavelength between the three sets of data is usually less than 3 percent. At a few points, the difference is as large as 6 percent. The National Bureau of Standards reports that the calibration of the standard lamps has an uncertainty of 8 percent in the ultraviolet and one of 3 percent in the visible and the infrared (Reference 8). The data for the calibration of the sphere which were obtained by the use of the three standard lamps differ by the same order of magnitude.

There are a number of possible sources of error. First, there is some uncertainty in the reflectance of the sphere paint. The recording on the chart may be read to within 0.5 percent. In reversing the two samples of freshly smoked MgO in the Cary 14 spectrophotometer while determining the reflectance of the Burch sphere paint, the difference in reflectance was found to be less than 0.5 percent at most points. The data for the reflectance of MgO which have been reported by various observers differ somewhat. It seems to depend on the nature of the surface, the thickness of the layer, and the age. Thus the uncertainty in the reflectance of the MgO standard is probably less than 1 percent in the spectral range where the quartz-iodine lamp is most intense, while in the near-infrared this uncertainty may be as high as 5 percent.

Second, there is a variation in the voltage across the 200-watt lamps in the integrator. This variation has been found to be 1 percent or less in the case of the eight lamps operated by two of the power supplies, and has been as high as 2 percent in the lamps operated by the third power supply. This would represent a variation in the flux of the lamps and hence of the sphere of about 2 percent in the case of lamps 1 through 8, and one of up to 4 percent in the case of lamps 9 through 12.

Among other sources of error may be mentioned the monochromator slit, which may be set within 0.2 percent. The chart which records the magnitude of the flux at various wavelengths can be read within 0.5 percent. It has been observed that there is a decrease in the 0.1 microvolt test signal as shown by the corresponding recorder deflections at the beginning and the end of a run. This change at times was as high as 5 to 6 percent. If this change is due to non-constancy of the amplifier, the data obtained for the spectral distribution of the sphere and of the standard lamps may vary by a similar amount. Since the three lamps were used independently and since the differences in the resulting data show a random variation, some of these errors may compensate for each other. Thus the over-all uncertainty of the data may be of the order of 5 percent or less. This is more or less the same as the difference between the values of the integrator emittance as obtained by means of the three standard lamps.

In comparing the calibration reported here with the calibration reported in 1964 (Reference 1), it is observed that the present values of the spectral emittance of the sphere are about 30 percent greater. This change is supported by the response of a thermopile to the energy emitted by the sphere. In comparing the response of thermopile 4928A to the present flux with its response in 1964, it is found that the present flux gives an output voltage which is 39.6 percent greater. This increase may be due in part to the fact that the sphere was repainted, and also to the fact that the lamps were previously at 29.8 volts while at present they are operated at 6.5 amperes (or about 30.3 volts). It would seem that these factors might contribute to this increase by at most several percent. More important as a factor in this increase may be the relocation of the lamps in the sphere.

CONCLUSIONS

It would seem that the present arrangement of the 6-foot spherical integrator provides a satisfactory extended source for the calibration of detectors in the visible and near-infrared. The uncertainty of the calibration is estimated to be at most 5 percent. Work is under way to test this estimate by comparing the calibration of radiometers obtained with the present set-up with that obtained previously.

ACKNOWLEDGMENTS

The investigator wishes to acknowledge the help of William B. Boyer and Bernard S. Prichnick in setting up the power supply and monitoring system, and the suggestions and cooperation of Andrew McCulloch and James McLean in carrying on the investigations.

REFERENCES

1. "Final Report of the Goddard Summer Workshop Program, 1964," Goddard Space Flight Center Document X-320-64-341, p. A-17.
2. "Final Report of the Goddard Summer Workshop Program, 1965," Goddard Space Flight Center Document X-100-65-407, p. B-23.
3. "Final Report of the Goddard Summer Workshop Program, 1966," Goddard Space Flight Center Document X-700-67-94, pp. 393-399.
4. Sumpner, W. E., Physics Society Proceedings 12:10, 1892.
5. Walsh, J. W. T., Photometry, London: Constable and Co., 1958.
6. Hardy, A. C., and Pineo, O. W., "The Errors Due to the Finite Size of Holes and Sample in Integrating Spheres," J. of the Optical Soc. of America 21:502, 1931.
7. Sparrow, E. M., and Cess, R. D., Radiation Heat Transfer, Belmont, Calif.: Brooks Cole Pub. Co., 1966.
8. Stair, Ralph, Schneider, W. E., and Jackson, J. K., "A New Standard of Spectral Irradiance," Appl. Optics 2:1151, 1963.



PRECEDING PAGE BLANK NOT FILMED.

EFFECTS OF A HIGH-ENERGY PARTICLE ENVIRONMENT ON THE QUANTUM EFFICIENCY OF SPECTRALLY SELECTIVE PHOTOCATHODES FOR THE MIDDLE AND VACUUM ULTRAVIOLET

James H. McElaney* and Donald F. Heath**

ABSTRACT

The quantum efficiencies of spectrally selective photocathodes for the middle and vacuum ultraviolet were measured. The photocathode materials investigated were semitransparent depositions of CsI, CuI, and CsTe, deposited on Al_2O_3 windows and a solid tungsten photocathode located behind a MgF_2 window. The quantum efficiencies were measured before and after use as detectors in an Aerobee 150 rocket experiment. Measurements were made later after a dose of 5×10^{13} electrons/cm² at 1.0 Mev, and 5×10^{13} electrons/cm² at 2.0 Mev, each for a period of 35 minutes. The electron energy and dose represent what might be expected in the artificial radiation belt after 1 year in a circular, near-polar orbit at 1400 km. In addition, one photodiode was irradiated with gamma rays. From these measurements it is apparent that the quantum efficiencies of the photodiodes are quite stable, although an increase in the quantum efficiency of one of the CsI photodiodes was noted.

INTRODUCTION

During the past 10 years, considerable time and effort have been expended in the development of photodetectors possessing high quantum efficiencies in the far and extreme ultraviolet (Reference 1). These detectors are described as being "solar blind" because they are generally insensitive to light of wavelengths greater than 3000 Å (the short wavelength transmission limit of the terrestrial atmosphere). The detectors were at first subjected to a space environment only during the few minutes when sounding rockets are operational. Since the development of earth satellites, these detectors have been used in experimental payloads that are expected to remain operational for a year or more. Generally, the satellites spend a considerable portion of their lifetimes in the Van Allen radiation belts where they are subjected to the bombardment of high-energy electrons and protons, and the resultant Bremsstrahlung produced by the particles colliding with the satellite.

This paper considers the effects of a high-energy electron environment (1 to 2 Mev) on the quantum efficiency of some representative photocathode materials commonly used in space research. Previous research dealing with the effect of high-energy electrons (Reference 2) and protons (Reference 3) on the ultraviolet transmission of materials has shown that the effects caused by radiation on the window materials Al_2O_3 and MgF_2 should be negligible in this investigation. Observable effects may therefore be attributed to the irradiation of the photocathode materials.

*Goddard Space Flight Center, Greenbelt, Md.
**Fairfield University, Fairfield, Conn.

It is well known that the alkali halides are highly susceptible to the formation of F- or color-centers (the trapping of an electron at the site of a crystal lattice vacancy) when subjected to high-energy radiation. This radiation may be electromagnetic or caused by high-energy particles. These trapped electrons may then indicate a wavelength-dependent increase in quantum efficiency. Presumably the wavelength dependence would be characteristic of the crystal structure.

The photocathode materials that were investigated are semitransparent depositions of CsI, CuI, and CsTe deposited on 0.5-min Al_2O_3 windows, and a solid tungsten photocathode located behind an MgF_2 window. The tungsten photocathode served only as a control of the total electron irradiation. These are sensors scheduled to be flown on a Nimbus spacecraft in an experiment designed to monitor the ultraviolet flux from 1100 to 3000Å. The long wavelength response of the sensors is used in conjunction with the short wavelength transmission limit of various optical materials to separate the solar spectrum into broad intervals.

EXPERIMENTAL PROCEDURE

Five vacuum photodiodes (produced by the Princeton Division of Electro-Mechanical Research Inc.) were irradiated together at 1.0 Mev for a dose of 5×10^{13} electrons/cm² over 35 minutes, and at 2.0 Mev for a dose of 5×10^{13} electrons/cm² for the same length of time. This irradiation is an approximation of the estimated flux experienced in a circular polar orbit at 1400 kilometers in January 1966. The initial set of diodes investigated included four semitransparent photocathodes (two CuI, one CsI, and one CsTe), deposited on sapphire, and one opaque tungsten photocathode behind an MgF_2 window. On August 29, 1966, these sensors were flown from White Sands, New Mexico, in the Aerobee 150 rocket version of the Nimbus experiment. They were subsequently recovered intact and fully operational.

The quantum efficiencies of the five sensors were calibrated before the June 1966 flight. One year later they were recalibrated and subsequently irradiated. The four sensors with semitransparent photocathodes were recalibrated within 4 days and the opaque cathode within 11 days after the irradiation. The absolute calibration used the standard technique of calibrating a freshly deposited film of sodium salicylate in front of a photomultiplier at H-Lyman α against a calibrated nitric oxide ionization cell, and at 2537Å against a calibrated thermopile. It was assumed that the response of sodium salicylate was uniform between 1216 and 2537Å. The calibrations obtained with the ionization cell and the thermopile agreed to within better than 15 percent. The freshly prepared film of sodium salicylate was then used to calibrate a tungsten diode and a CsTe diode, which were subsequently used as standard detectors. All calibrations used in this work were obtained by comparison measurements with these two standard detectors.

RESULTS

The results showing the two calibrations made before irradiation and the calibration made after irradiation are plotted in Figures 1 through 4. No significant changes were observed, except in the case of the CsI photodiode (Figure 3), which showed a definite increase in quantum efficiency. Recalibration of this diode 10 days after irradiation indicated no observable reduction of the previously noted increase.

To investigate this effect further, two additional CsI diodes, constructed from two separate processings, were irradiated. One of these diodes, with a design similar to the diode described in Figure 3 but processed to it, was subjected to irradiation by gamma rays

from a Co^{60} source with a dosage of 10^5 rad. (One radian represents an absorbed dose of 100 ergs/gram of material.) The results showing quantum efficiency before and after the gamma irradiation are plotted in Figure 5. There was not observable change in the quantum efficiency. The second CsI diode, a newer and more rugged model, was irradiated with electrons, using the same electron flux and energies as in the previous experiments. There was no apparent change in the quantum efficiency of this photodiode (Figure 6). There is no doubt, however, that the induced radiation effect indicated in Figure 3 is a real increase in the quantum efficiency. Sets of measurements preceding and following the irradiation, clearly support this conclusion.

DISCUSSION

While the increase in the quantum efficiency of one of the irradiated CsI diodes is a genuine increase, it is surprising that such an increase is not reproducible in other irradiated CsI diodes. Perhaps the reason is that the processing of these photocathodes still contains certain uncertainties as far as reproducibility is concerned. The crystal structure (i.e., the number of crystal defects and lattice-site vacancies) may be different in those diodes which change under irradiation and those which do not.

Figure 7 shows the ratio of the quantum efficiencies measured before and after irradiation for the diode with the changed quantum efficiency. The three peaks at 1600, 1825, and 2260 Å should be noted. Each of these points represents the average of quantum efficiency measurements after irradiation to measurements after irradiation.

The CsTe cathode is prepared by evaporating Cs and Te separately, whereas CuI and CsI are evaporated as molecules from ultra-high purity single crystals.* Only CsI is an alkali halide; thus, of the photocathodes considered in this work, only CsI would be expected to show a radiation induced change in quantum efficiency. This change would be related to the formation of F- or color-centers at the sites of crystal lattice vacancies. The number of vacancies may be related to the deposition process and could vary considerably in different processings. The increased quantum efficiency could be caused by the ejection of the trapped electrons. A pending test of this hypothesis, will determine if the quantum efficiency may be reduced to its pre-irradiation value by annealing the diode for several hours at elevated temperatures (not high enough to decompose the crystal structure of the photocathode). This method of annealing the alkali halides to remove color centers is an established technique. (A recent attempt to bleach the CsI photodiode showing an increase in quantum efficiency after irradiation was not successful because of a diode failure after baking. This method of bleaching the photodiodes will be retested in the near future.)

REFERENCES

1. Hennes, J., and Dunkelman, L., The Middle Ultraviolet, ed. A Green, New York: John Wiley and Sons, 1966, p. 304.
2. Heath, D. F., and Sacher, P. A., "Effects of a Simulated High-Energy Space Environment on the Ultraviolet Transmittance of Optical Materials between 1050 Å and 3000 Å," Appl. Optics 5:937, 1966.
3. Sacher, P. A., "The Effects of a Simulated Proton Space Environment on the Ultraviolet Transmittance of Optical Materials between 3000 Å and 1050 Å," unpublished manuscript.

* Private communication with M. Rome.

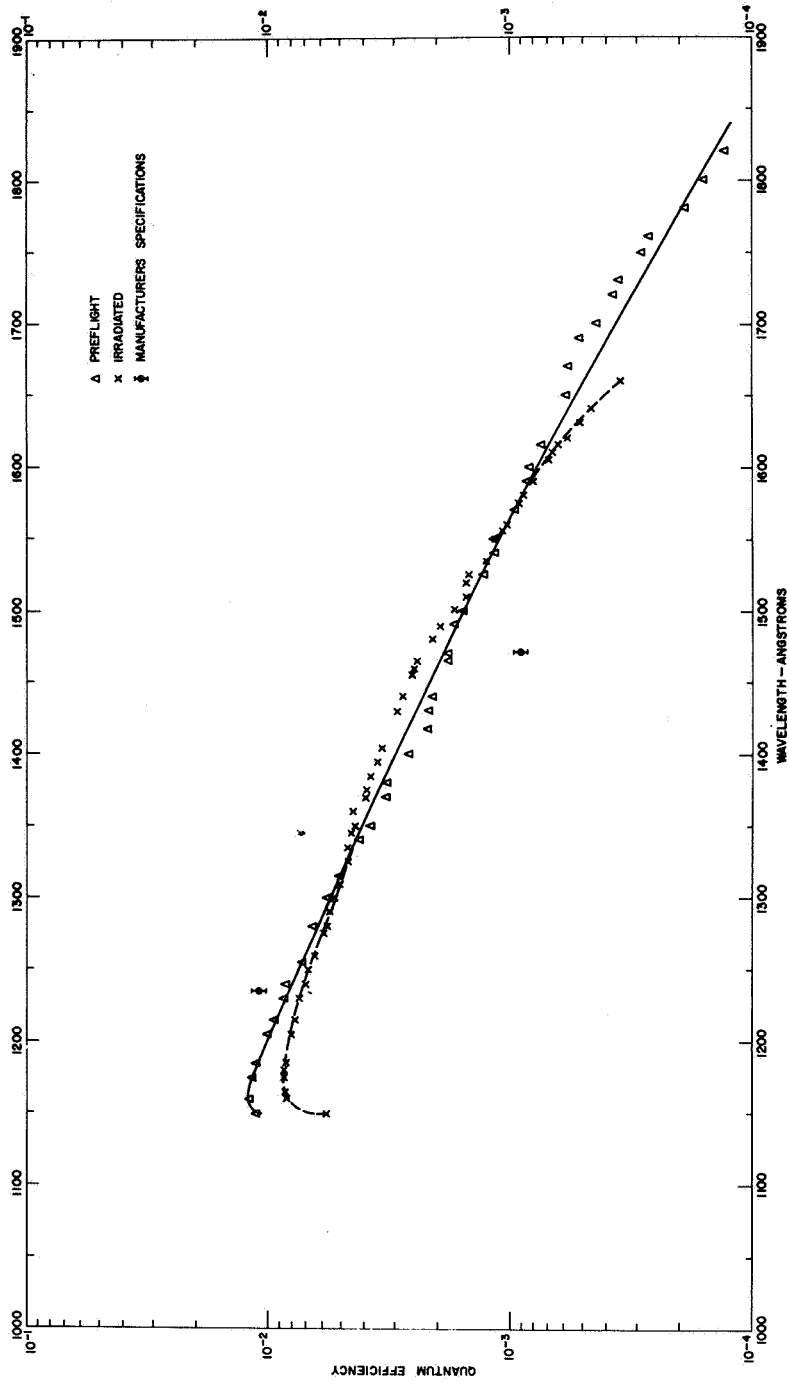


Figure 1—Quantum efficiency of tungsten photodiode before and after irradiation by 5×10^{13} electrons/cm² at 1.0 and 2.0 Mev.

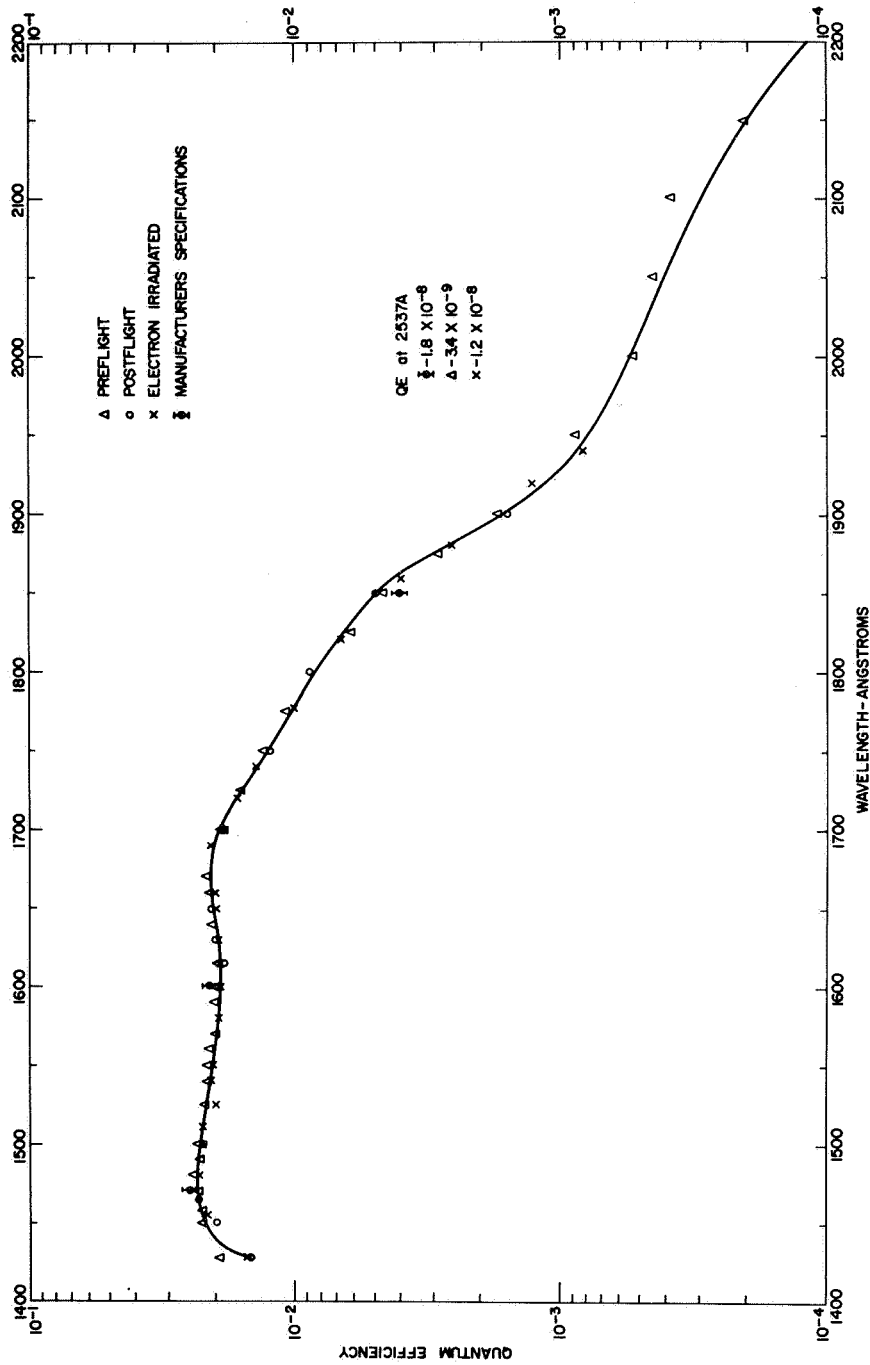


Figure 2—Quantum efficiency of CuI photodiode before and after irradiation by 5×10^{13} electrons/cm² at 1.0 and 2.0 Mev.

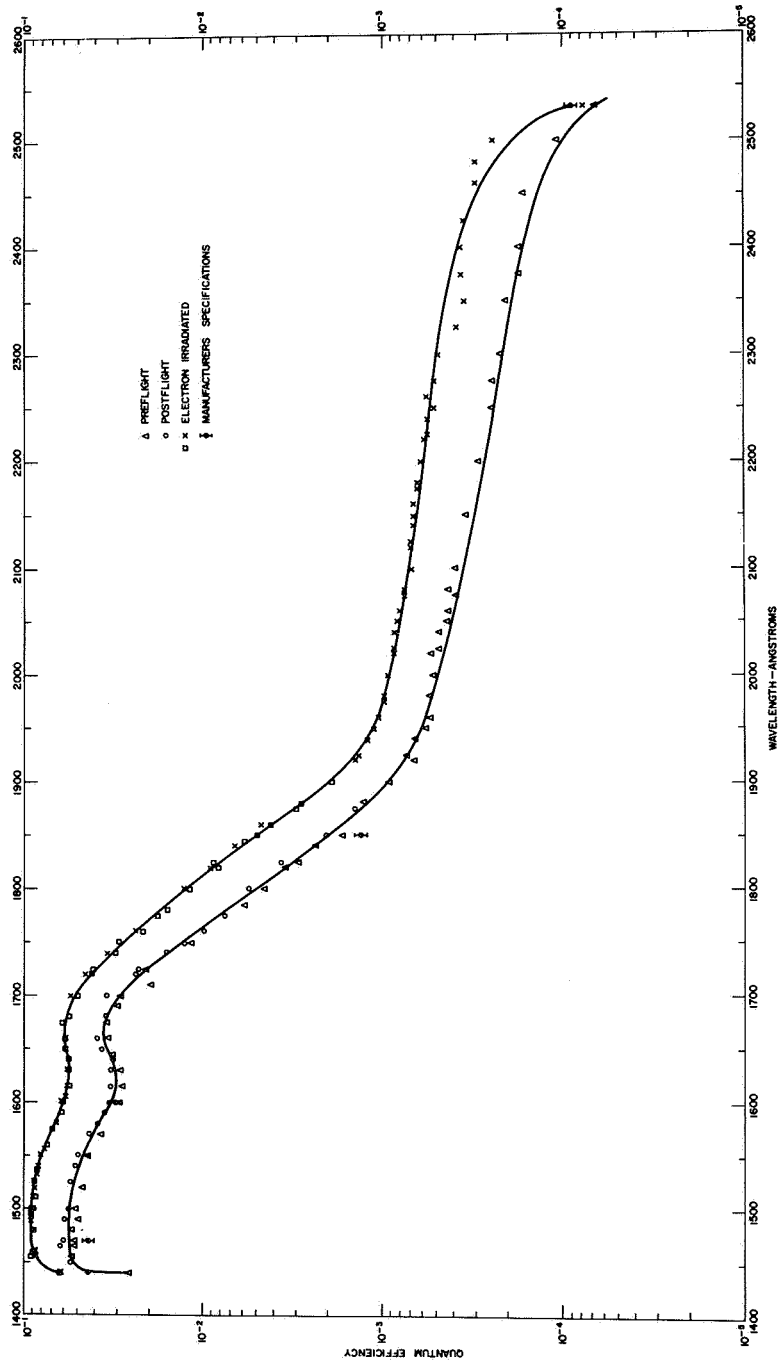


Figure 3—Quantum efficiency of one CsI photodiode before and after irradiation by 5×10^{13} electrons/cm² at 1.0 and 2.0 Mev.

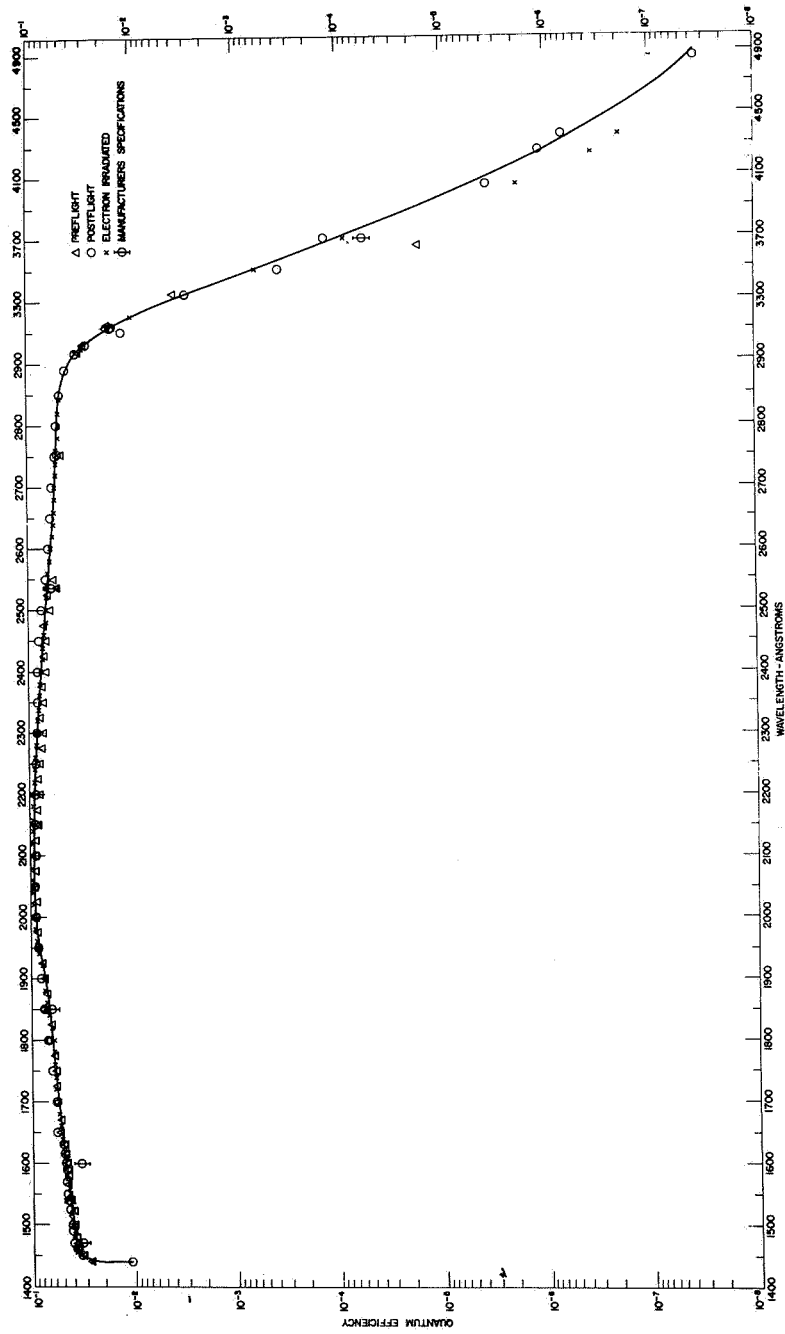


Figure 4—Quantum efficiency of CsTe photodiode before and after irradiation by 5×10^{13} electrons/cm² at 1.0 and 2.0 Mev.

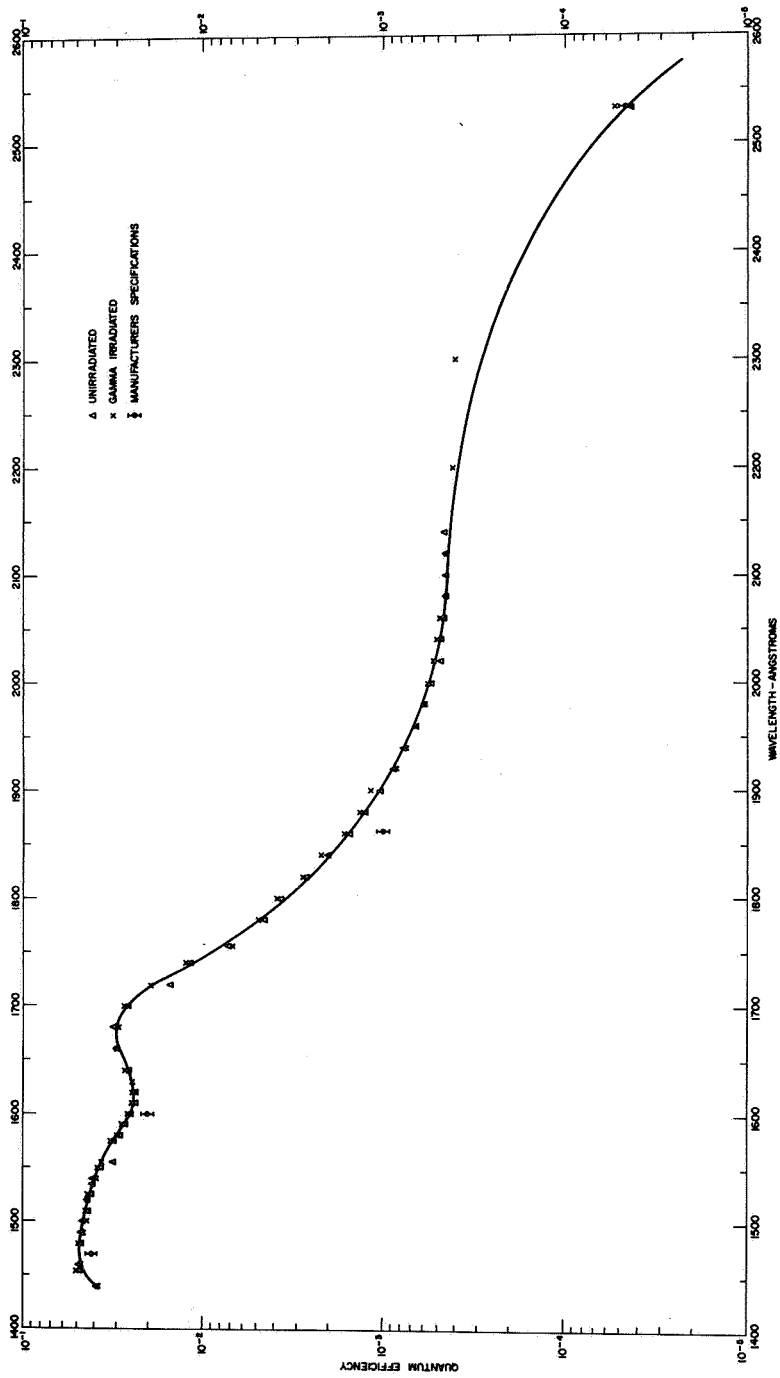


Figure 5—Quantum efficiency of one CsI photodiode before and after gamma irradiation with a dosage of 10^5 rads.

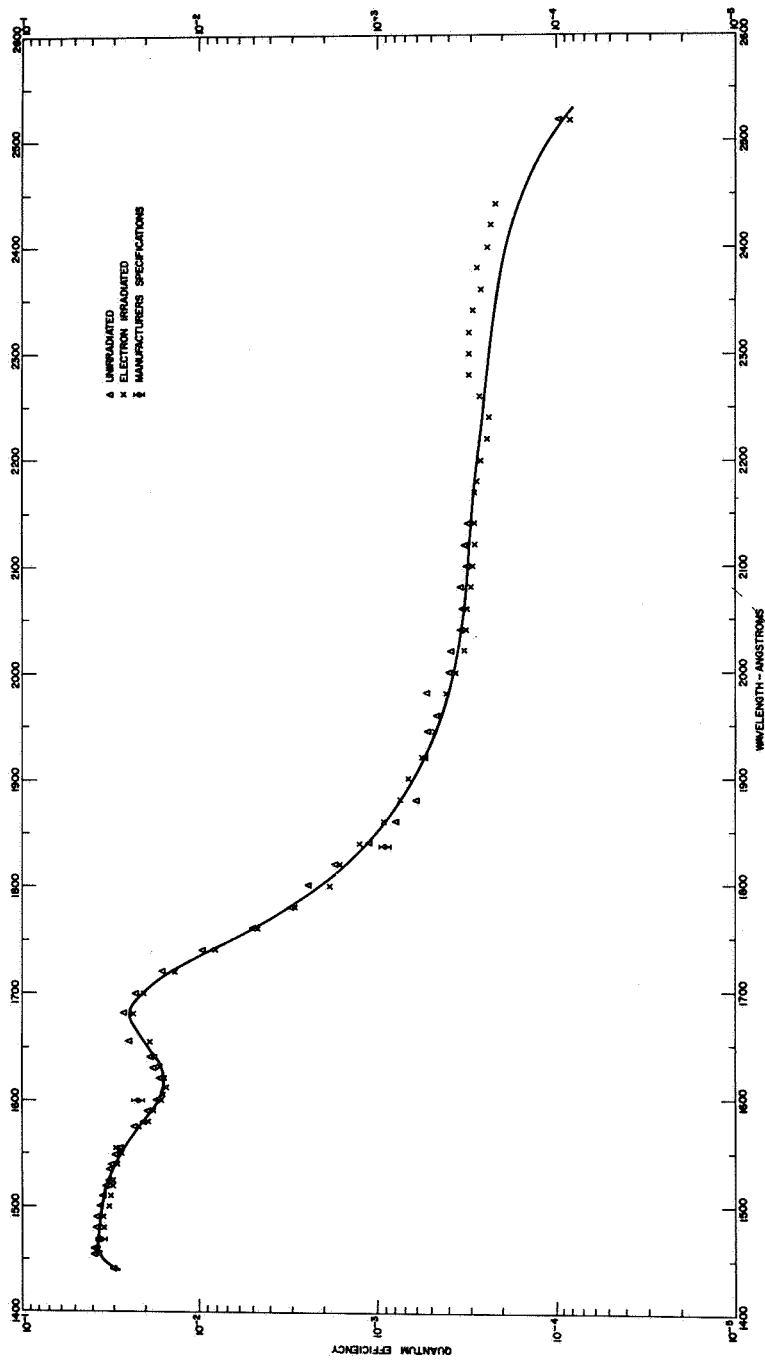


Figure 6—Quantum efficiency of one CsI photodiode before and after irradiation by 5×10^{13} electrons/cm² at 1.0 and 2.0 Mev.

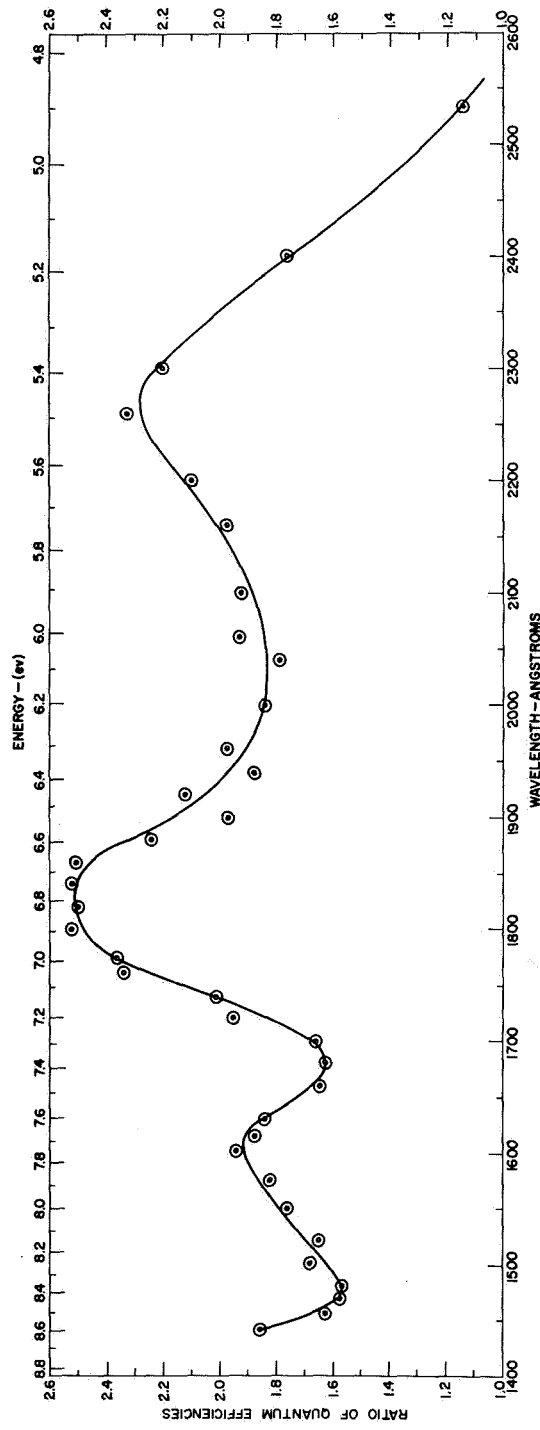


Figure 7.—Ratio of the quantum efficiencies, before and after irradiation by 5×10^{13} electrons/ cm^2 at 1.0 and 2.0 Mev, of the CsI photodiode illustrated in Figure 3.

SOME MATHEMATICAL ASPECTS OF THE PROBLEM OF OBTAINING VERTICAL TEMPERATURE PROFILES FROM RADIOMETRIC DATA

E. A. Franz*

ABSTRACT

A review is made of mathematical problems involved in solving the equation of radiative transfer when the outgoing intensity of radiation at the top of the atmosphere is known, and the temperature at various levels in the atmosphere is desired. This paper discusses a widely-used "smoothing" technique to approximate the solution of the equation in the presence of data errors, which are greatly amplified in the solution by the nature of the integral and matrix operator. It also discusses the maximum and minimum errors in the solution when the rms error of the input data can be estimated.

INTRODUCTION

In recent years, much interest has been shown in the possibility of inferring vertical temperature profiles from a small set of spectral intensities of vertically outgoing thermal radiation at several frequencies in the 15μ CO_2 absorption band. The set of spectral intensities would be obtained by a radiometer located in a satellite or balloon near the effective top of the atmosphere. Actual experiments and reduction of data have shown that, in principle, the inference can be made. However, it is questionable whether the results can be obtained with an accuracy (approximately 2°K) suitable for meteorological purposes. The problem – not entirely one of refining the experimental techniques or increasing the number of observations to obtain the desired accuracy – is to solve the equation obtained in the mathematical formulation of the problem in the presence of errors in the input data without magnifying these errors to such an extent that the real solution is covered up.

The mathematical formulation of this problem, after simplifying, is given by

$$g(\nu) = \int_a^b f(x) K(\nu, x) dx, \quad (1)$$

where $g(\nu)$ is a known simple linear function of the observed intensity at wave number ν , x is any single-valued function of atmospheric pressure (usually taken as $\log p$), $f(x)$ is Planck's function for any x and for some wave number central to the wave numbers of the data, a and b are the values of x at the top of the atmosphere and the earth's surface respectively, and $K(\nu, x) = \partial T(\nu, x) / \partial x$, where $T(\nu, x)$ is the known transmissivity function for the atmosphere.

* Illinois College, Jacksonville, Illinois.

Thus, with $g(\nu)$ known from the data and $K(\nu, x)$ having been calculated from the known gaseous structure of the atmosphere, we have a linear Fredholm integral equation of the first kind with unknown $f(x)$. Since there is a known functional relationship between Planck's function, $f(x)$, and the temperature, $T(x)$, in the spectral region being used, finding $f(x)$ will allow us to infer $T(x)$.

Of course, we do not have an analytic expression for $g(\nu)$; we only know $g(x)$ for a set of (say, N) discrete values of ν . Thus, for an analytic solution of the integral equation (which would allow us to find $f(x)$ for more than N values of x), we would have to specify some interpolation scheme for $g(\nu)$. The problem of using function sets (viz., trigonometric functions, line segments, empirical orthogonal functions, etc.) to expand $f(x)$ and provide an implicit interpolation scheme for $g(\nu)$ is not considered in this paper.

However, even if $g(\nu)$ were given as an analytic expression, there would still be problems in the solution of the integral equation; the number of solutions (none, finite, or infinite) to the equation for a particular $g(\nu)$ and $K(\nu, x)$ will depend on the form of $g(\nu)$ and $K(\nu, x)$. In this paper, it is assumed that there is a unique solution for the given $g(\nu)$ and $K(\nu, x)$.

However, the little work that has been done on this type of Fredholm equation shows that there is a type of instability associated with it for most "smooth" forms of the kernel; i.e., a small change in the form of $g(\nu)$ can produce a large change in the solution, $f(x)$. Of course, the $g(\nu)$ is an observed quantity and will thus have errors associated with it. These errors can be magnified in the solution (usually in an oscillatory way) to such an extent that the resulting solution has no resemblance to the desired solution.

NUMERICAL SOLUTION OF THE INTEGRAL EQUATION

The most direct way to attack the problem of solving this equation is to use a numerical quadrature scheme to replace Equation 1 by a system of linear equations. Thus, given data $g(\nu_1), g(\nu_2), \dots, g(\nu_N)$ and kernel functions $K(\nu_1, x), K(\nu_2, x), \dots, K(\nu_N, x)$ corresponding to the same wave numbers associated with the data, we divide the X -axis from a to b into M ($M \leq N$) parts and locate points x_1, x_2, \dots, x_M in those parts according to some quadrature scheme. Then we can approximate Equation 1 by the system

$$g(\nu_i) = \sum_{k=1}^M f(x_k) K(\nu_i, x_k) w(x_k), \quad i = 1, 2, \dots, N, \quad (2)$$

where $w(x_k)$ is the weighting factor appropriate to the quadrature scheme employed. If we let

$$A_{ik} = K(\nu_i, x_k) w(x_k),$$

then we can conveniently represent this system in matrix notation by

$$g = A f, \quad (3)$$

where g and f are column matrices. We can formally solve this equation for f by pre-multiplying by A^* and then by $(A^*A)^{-1}$. Thus,

$$f = (A^*A)^{-1}A^*g. \tag{4}$$

The result with a matrix A obtained from the usual kernel functions encountered in this work (see Figure 1, courtesy V. Kunde, GSFC) leads to a wildly oscillating solution, although soundings have shown that the solution should be rather smooth. The reason for this situation is that the observed g has random errors that are magnified by the "ill-conditioned" matrix A . The ill-conditioning is a result of the fact that the rows of A are not very independent; i.e., we can find a linear combination of the rows, or vectors, of A that will approximately equal the zero vector. Figure 1 shows that this non-independence is caused by the excessive overlapping of the kernel functions. Also, taking more observations will create more kernel functions in the same spectral range, and thus greater overlapping; the ill-conditioning then will become worse.

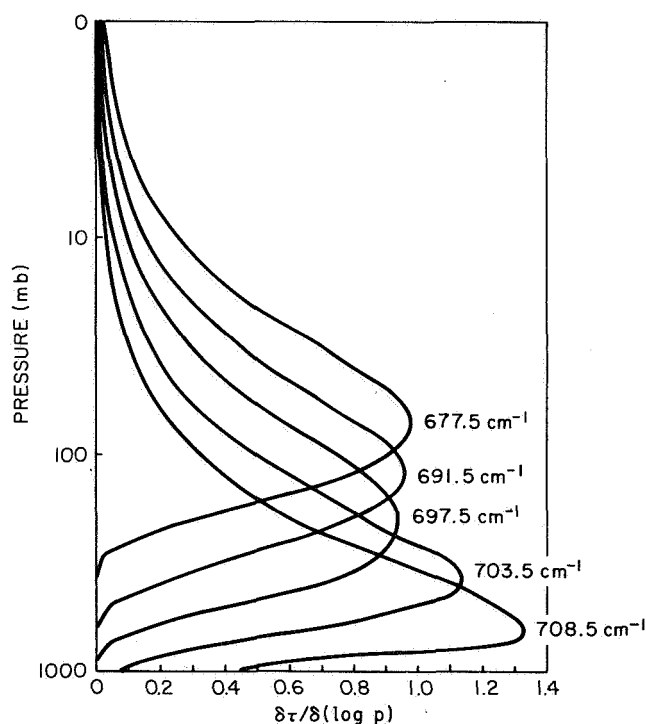


Figure 1-An example of the kernel functions for five different wavenumbers in the 15μ CO_2 band.

In symbols, we are solving not the desired Equation 3, but the equation

$$g' = A f',$$

where $g' = g + \Delta g$, and $f' = f + \Delta f$, and where Δg and Δf are the error matrices for g and f respectively. Subtracting Equation 3 from Equation 5 gives

$$\Delta g = A \Delta f \tag{6}$$

or

$$\Delta f = (A^* A)^{-1} A^* \Delta g. \quad (7)$$

To gain an understanding of the possible magnitude of the Δf_i for a given A, we will determine the maximum and the minimum values of

$$\sum_i (\Delta f_i)^2,$$

assuming that the only information on the Δg error matrix is that

$$\sum_i (\Delta g_i)^2 = e^2 = \text{a constant}. \quad (8)$$

Equation 6 implies

$$\frac{\partial \Delta g_i}{\partial \Delta f_k} = A_{ik}. \quad (9)$$

Then, a necessary condition for a maximum or minimum value of

$$\sum_i (\Delta f_i)^2$$

is, using the Lagrange multiplier technique, that

$$\frac{\partial V}{\partial \Delta f_k} = 0, \quad k = 1, 2, \dots, N, \quad (10)$$

where

$$V = \sum_i (\Delta f_i)^2 + \gamma \left(\sum_i (\Delta g_i)^2 - e^2 \right), \quad (11)$$

and γ is the Lagrange multiplier. Performing the differentiation and substituting into Equation 10 leads to

$$\Delta f_k + \gamma \sum_i A_{ki}^* \Delta g_i = 0, \quad k = 1, 2, \dots, N, \quad (12)$$

where A_{ki}^* is an element of A transpose = A^* . This can be expressed in matrix notation as

$$\Delta f + \gamma A^* A \Delta f = \bar{0},$$

or

$$(A^* A - \gamma' I) \Delta f = \bar{0}, \quad (13)$$

where $\gamma' = -\gamma$.

Thus, a necessary condition for

$$\sum_i (\Delta f_i)^2$$

to be a maximum or minimum is that Δf be an eigenvector of the matrix $A^* A$. The arbitrary k that appears in each component of Δf can be evaluated by substituting into

$$\Delta f^* A^* A \Delta f = e^2, \quad (14)$$

which comes from Equation 3 and

$$\sum_i (\Delta g_i)^2 = \Delta g^* \Delta g = e^2.$$

To illustrate, using a 2×2 matrix, let

$$A = \begin{pmatrix} \frac{1}{2} & \frac{1}{2} \\ \frac{1}{4} & \frac{3}{4} \end{pmatrix}$$

The eigenvalues of $A^* A$ are 1.064 and 0.0587, and the associated eigenvectors are $(\pm 0.487e, \pm 0.839e)$ and $(\pm 7.25e, \mp 4.22e)$. Thus, for the first eigenvalue,

$$\sum_i (\Delta f_i)^2$$

= 0.940 e², and for the second,

$$\sum_i (\Delta f_i)^2 = 70.6 e^2.$$

The worst case is associated with the smallest eigenvalue.

Figure 2 is a geometrical interpretation of this procedure. It also uses a 2 × 2 example, although analogous results follow for the higher dimensional case. The condition

$$\left(\sum_i (\Delta g_i)^2 = e^2 = \text{a constant} \right)$$

means location on a circle of radius e in the $\Delta g_1 - \Delta g_2$ plane. Each point in this plane is mapped into a point in the $\Delta f_1 - \Delta f_2$ plane by the matrix A^{-1} (if A is square). Since $A \Delta f = \Delta g$, and $\Delta f^* A^* = \Delta g^*$, then $\Delta f^* A^* A \Delta f = e^2$. But this is the matrix representation of a quadratic form with symmetric matrix $A^* A$ in the variables Δf_1 and Δf_2 , and thus represents an ellipse symmetrical about the origin, but whose principal axes are rotated with respect to the coordinate axes.

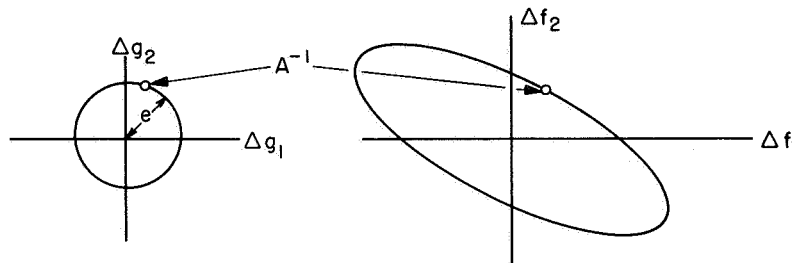


Figure 2-Geometric representation of the 2x2 matrix.

Since

$$\sum_i (\Delta f_i)^2$$

can be interpreted as the square of the distance from a point on the ellipse to the origin, the points of maximum and minimum distance are sought. These will be the semimajor and semiminor axes, respectively, of the ellipse.

The three-dimensional case involves a sphere of radius e in the $\Delta g_1 - \Delta g_3$ coordinate system and an ellipsoid in the $\Delta f_1 - \Delta f_3$ system.

Figure 3 shows that with most error matrices, Δg , the solution will oscillate because of sign changes from component to component in Δf .

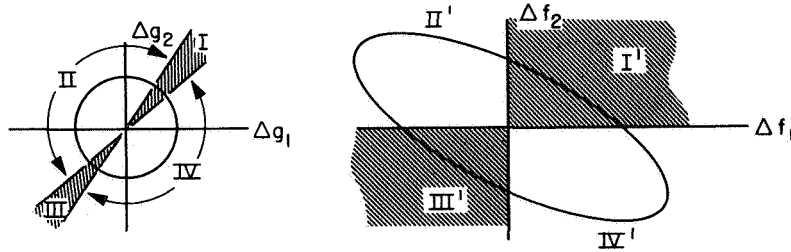


Figure 3-Geometric representation of the 2x2 matrix showing oscillation of solution to equation.

It can easily be shown that points in shaded regions I and III are mapped into points in shaded regions I' and III', and points in regions II and IV into II' and IV'. If the matrix is very ill-conditioned, the two lines enclosing the shaded region in the $\Delta g_1 - \Delta g_2$ plane almost coincide. Thus, most points in the $\Delta g_1 - \Delta g_2$ plane are mapped into points in the $\Delta f_1 - \Delta f_2$ plane whose coordinates have opposite signs.

A SMOOTHING TECHNIQUE

Since the nature of Δg will be unknown (except possibly for the information that

$$\sum_i (\Delta g_i)^2 = e^2 = 'a$$

constant), there will be an infinite number of solutions, f , to the equation

$$A(f + \Delta f) = g + \Delta g,$$

and most of these solutions will be wildly oscillating. An objective smoothing technique then will constrain the problem so that, out of this family of solutions, a single smooth solution will be selected.

Phillips (Reference 4) and Twomey (Reference 5) have developed such a smoothing technique. It imposes the additional constraint that some quadratic function,

$$Q = \sum_j \sum_i H_{ij} f_i f_j$$

will be a minimum. For instance, the selection of the minimization of the norm,

$$\sum_i (f_i - 2 f_{i+1} + f_{i+2})^2,$$

of the second differences produces a solution whose mean curvature will be a minimum. The H_{ij} in this case are elements of the matrix

$$H = \begin{bmatrix} 1 & -2 & 1 & 0 & 0 & \cdot & \cdot & \cdot \\ -2 & 5 & -4 & 1 & 0 & \cdot & \cdot & \cdot \\ 0 & 1 & -4 & 6 & -4 & 1 & \cdot & \cdot \\ 0 & 0 & 1 & -4 & 6 & -4 & 1 & \cdot \\ \cdot & \cdot \end{bmatrix}$$

The desired solution in this case is given by

$$f = (A^*A + \gamma H)^{-1} A^* g'$$

where γ is a Lagrange multiplier and g' is the actual observation matrix.

The γ is definitely determined by this procedure, but only by an implicit expression which is difficult to solve. Therefore, in practice, γ is not actually calculated; instead, the solutions and corresponding values of e^2 are calculated for several values of γ , and that solution used for which the corresponding e^2 is equal to, or just greater than, the estimated e^2 for the observations. Values of γ greater than this will cause the matrix H to dominate A^*A in the solution.

Figure 4 shows how e^2 varies with γ for exact data provided by B. Conrath (GSFC) into which simulated errors, Δg_i , were inserted. The region of best smoothing determined by visual inspection of the resulting solutions (for various γ) corresponds in this case to a plateau region in the e^2 vs γ graph. It is also interesting to note that the set of values of Δg_i which is actually being used in the solution of the problem when one of these successful γ is used corresponds in no way to the actual Δg_i inserted into the problem (except that both sets have the property

$$\sum_i (\Delta g_i)^2 = e^2.$$

CONCLUSIONS

This investigator thoroughly reviewed recent literature and results pertaining to linear methods of solution of the temperature inversion problem. This effort included (although not discussed in this report) a study of the use of empirical orthogonal functions as an expansion set, in order to provide interpolation of results to a number of atmospheric levels greater than the number of observations. Even though these functions seem the best to use, it is questionable whether a set of such functions derived from sample observations made over a given period of time can be reliably used in the determination of temperature profiles at another time. There is also the problem of the objectivity of current smoothing techniques; the selection of the smoothing matrix, H ; the selection of the best smoothing factor, γ , etc.

ACKNOWLEDGMENTS

The author gratefully acknowledges the assistance of Dr. Barney J. Conrath in providing the data given in Figure 4.

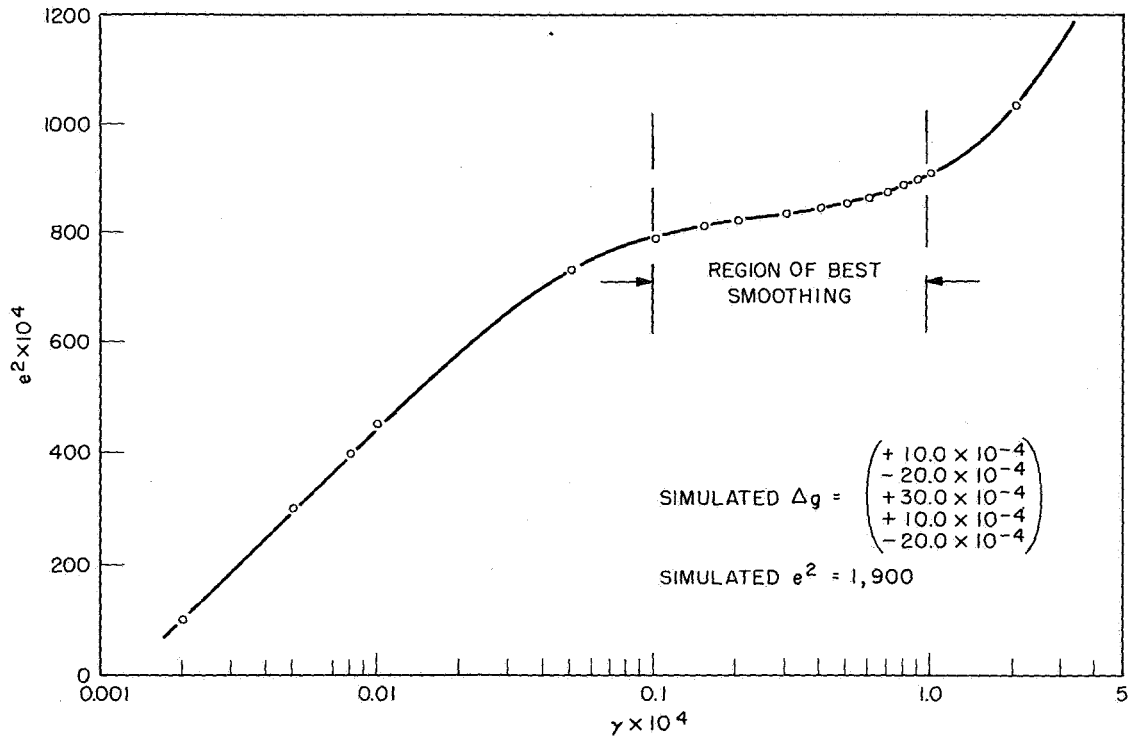


Figure 4-Variation of error function (e^2) with a smoothing factor (γ).

REFERENCES

1. Baker, C. T. H., Fox, L., Mayers, D. F., and Wright, K., "Numerical Solution of Fredholm Integral Equations of First Kind," The Computer Journal, 7(2): 141-148, July 1964.
2. Conrath, B. J., "Inverse Problems in Radiative Transfer: A Review," GSFC Document X-622-67-57, February 1967.
3. Drayson, S. R., "Errors in Atmospheric Temperature Structure Solutions from Remote Radiometric Measurements," Technical Report, University of Michigan, December 1963.
4. Phillips, D. L., "A Technique for the Numerical Solution of Certain Integral Equations of the First Kind," J. Assoc. For Computing Mach., 9: 84-97, 1962.
5. Twomey, S., "On The Numerical Solution of Fredholm Integral Equations of the First Kind by the Inversion of the Linear System Produced by Quadrature," J. Assoc. for Computing Mach., 10: 97-101, 1963.
6. Twomey, S., "The Application of Numerical Filtering to the Solution of Integral Equations Encountered in Indirect Sensing Measurements," J. Franklin Institute, 279(2): 95-109, 1965.
7. Twomey, S., "Indirect Measurements of Atmospheric Temperature Profiles from Satellites: II. Mathematical Aspects of the Inversion Problem," Monthly Weather Review, 94: 351-361, 1966.

PRECEDING PAGE BLANK NOT FILMED.

THE INFRARED EMISSIVITY AND REFLECTANCE OF LAVA

Randy R. Ross*

ABSTRACT

It would be desirable to know the spectral emissivity of basaltic lava as a function of temperature. Serious experimental difficulties stand in the way of laboratory measurements. In anticipation of this eventual goal, the reflectance spectra ($2.5-22\mu$) of four solid lava samples were measured over the temperature range 60° to 280°C . The four lava samples were an obsidian, a pumice, a tuff, and a welded tuff. Natural surfaces exhibited slightly sharper features than sliced surfaces. No appreciable variation was observed over the temperature range studied.

INTRODUCTION

The emission properties of molten lava in the middle and far infrared regions have apparently never been accurately determined. Knowledge of these properties is essential, however, in the study of volcanic heat dissipation. The work done this summer has laid the foundation for the determination of the spectral emissivity of basaltic lava as a function of temperature.

This information will be useful in an attempt to perform an in-flight calibration of the High Resolution Infrared Radiometer (HRIR) on the Nimbus II satellite. This radiometer takes radiance maps of the earth in the 3.5 to 4.1μ region. On August 13, 1966, a flank eruption occurred at the new volcano "Surtsey" in the ocean just south of Iceland. It remained active for about 1-1/2 months. During that time it appeared as a very small, hot spot in the Nimbus HRIR photographs. This occurrence offers an excellent opportunity to calibrate the HRIR, since it provides a fairly small area of high temperature surrounded by an ocean of approximately uniform low temperature. Careful radiance maps of the Surtsey lava and atmospheric conditions were made. Thus, if the emissivity of lava as a function of temperature and frequency were known, the total radiance measured by the HRIR could be determined by

$$W = \int_{\nu_1}^{\nu_2} A(\nu) f(\nu) \epsilon(\nu, T) J(\nu) d\nu. \quad (1)$$

where

$A(\nu)$ = atmospheric transmission factor

$f(\nu)$ = sensitivity of HRIR

$\epsilon(\nu, T)$ = emissivity of lava

$J(\nu)$ = Planck radiation formula.

(The actual calculation would be complicated by the temperature distribution over the lava area.) This calculated radiance could then be compared to that actually recorded by the HRIR.

*University of Wisconsin, Madison, Wisconsin.

EXPERIMENTAL PROCEDURE

Direct emissivity measurements have good spectral resolution only at very high temperatures. An entire range of temperatures is desired, so the emissivity is obtained instead through the reflectance of the sample, which can be measured with much greater resolution. Assuming no transmission by the sample,

$$\rho + \alpha = 1, \quad (2)$$

where ρ is the reflectance and α the absorption constant. Kirchhoff's Law then states that the absorption equals the emissivity,

$$\epsilon = \alpha,$$

so from Equation 2 we obtain

$$\epsilon = 1 - \rho, \quad (3)$$

where ρ is the experimentally measured quantity.

The reflectance is measured using a Cary-White Model 90 dual-beam spectrophotometer with a special hemispherical reflectance attachment as described by White (Reference 1). The infrared source and the sample are located at conjugate foci in a hemispherical mirror. Radiation is thus incident on the sample over an entire 2π steradians. Reflected radiation from the sample is viewed through a hole in the top of the mirror and is compared to the radiation from the source. This ratio is then compared to that of a standard aged aluminum mirror, and the absolute reflectance is computed. Examples of infrared reflectance spectra of common minerals and igneous rocks determined in this manner can be found in the literature (References 2, 3).

The tungsten source has a manually variable power output; this allows variation of the sample surface temperature (due to radiative heating) up to about 300°C . A special furnace sample holder will have to be constructed to provide higher temperatures (basaltic lava is completely liquid at about $1,200^{\circ}\text{C}$). This furnace must have the features of small size, high temperature, and a completely open, flat sample surface. Any indentation would produce an undesirable blackbody absorption effect.

Several suggestions concerning future experimental technique may be made. If the sample has a natural (uneven) surface, the exact position of the observed sample area must be checked to be reasonably flat. The surface height is also critical; a uniform method for measuring the height of the observed surface area, such as a caliper on a table mount, would be desirable. Furthermore, some trouble with a shifting of the zero position of the spectrophotometer was encountered. It is suggested that the zero reflectance curve be made at the end of a set of measurements as well as at the beginning to check for such a shift.

RESULTS AND CONCLUSIONS

Natural and sliced surfaces of four random lava samples – an obsidian, a pumice, a tuff, and a welded tuff – were studied. Reflectance measurements were made with the infrared source at its low setting (75 watts) and with the source output at 200 watts. The low setting gave sample surface temperatures near 60°C . A thermocouple was used to determine the surface temperature of each sample in the 200-watt trials. These "high" surface temperatures varied from 170° to 280°C depending on the specific heat and heat conductivity of the sample.

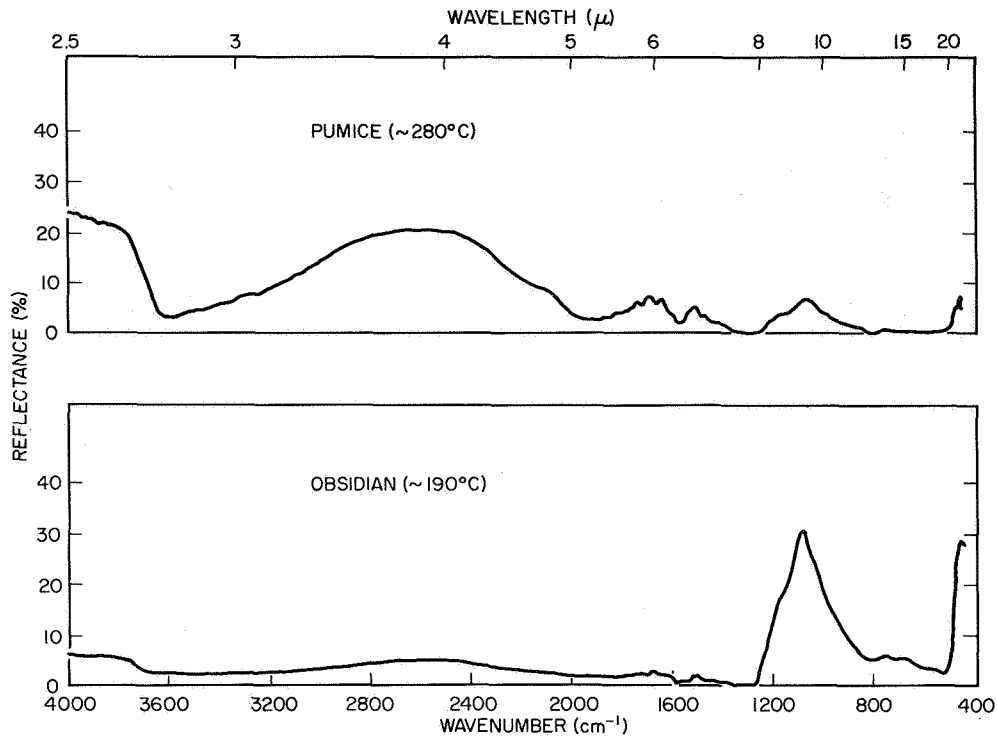


Figure 1—Reflectance spectra of natural surfaces.

Figure 1 shows the reflectance spectra obtained for natural obsidian and pumice surfaces at high temperatures. These data have not yet been reduced and are included for heuristic purposes only. Restrahlen peaks occur at about $1,080$ and 460 cm^{-1} (9.3 and 22μ). The position of the primary restrahlen peak between 935 and $1,110\text{ cm}^{-1}$ (9 to 10.7μ) indicates the degree of acidity (SiO_2 content) of the lava (Reference 3). All four samples exhibited restrahlen peaks at about $1,080\text{ cm}^{-1}$ (9.3μ), indicating over 65 percent SiO_2 composition (acidic lava). The lava from Surtsey should be basaltic (basic) and thus should exhibit the restrahlen peak at a lower wavenumber (higher wavelength). The reflection minima near $3,620$ and $1,570\text{ cm}^{-1}$ (2.7 and 6.35μ) are due to high absorption by water of hydration.

Natural surfaces were found to possess slightly sharper reflectance spectra than the corresponding sliced surfaces. No shifts in any of the reflectance features were observed, however. No appreciable difference was observed between the lower and higher temperature reflectivities of the samples tested. It is too early to form any conclusions concerning the emissivity of molten lava. However, no variation with temperature appears in the 60° - 280°C range, and this work should lay the foundation for the final measurement of the emissivity of molten basaltic lava.

REFERENCES

1. White, J. U., "New Method for Measuring Diffuse Reflectance in the Infrared," Journal of the Optical Society of America 54:1332-1337, 1964.
2. Hovis, W. A., Jr., "Infrared Reflectivity of Some Common Minerals," Applied Optics 5:245-248, 1966.
3. Hovis, W. A., Jr., and Callahan, W. R., "Infrared Reflectance Spectra of Igneous Rocks, Tuffs, and Red Sandstone from 0.5 to 22 Microns," Journal of the Optical Society of America 56:639-643, 1966.

GROUP I

COMPUTERIZED GUIDANCE COUNSELING

Academic Personnel

Prin. Investigator:

Dr. Richard Royall (Johns Hopkins)

Faculty:

Graduate Students:

Goddard Personnel

Staff Advisor:

Dr. Fred B. Haynes

ON PREDICTION AND DISCRIMINATION IN HIGH SCHOOL GUIDANCE COUNSELING

Richard M. Royall*

ABSTRACT

A study was made of some statistical prediction techniques potentially useful to high school counselors engaged in educational and vocational guidance. Widespread availability of electronic computer could enable most counselors to apply rather sophisticated techniques routinely in daily practice. From a sample of published study reports it is inferred that certain widely-used predictive discrimination techniques might be substantially improved, and possible means of effecting such improvements are sketched. It is suggested, however, that there are at present severe limitations on the accuracy and hence the usefulness of statistical predictors of criteria of interest to high school counselors.

INTRODUCTION

Many activities are grouped under the label "selection and guidance." The Air Force must decide who is to attend flight school. An insurance company screens applicants for positions in sales. A university counselor advises a junior who is dissatisfied with his course of study. The National Science Foundation selects recipients for graduate fellowships. Each of these activities presents a different set of difficult problems. A bewildering combination of these problems confronts the high school guidance counselor who is attempting to pick out those vocational and educational pursuits that a particular student is most likely to find satisfying and rewarding.

The general objective of this study was to seek means of improving the effectiveness of educational and vocational guidance counseling in the high school, with particular reference to the guidance of students into engineering. One emphasized aspect of the study was an investigation of some of the opportunities that would be highlighted as a result of the availability of electronic computers to high school guidance counselors.

This report contains a -necessarily somewhat cursory- critical analysis of some phases of high school guidance counseling, with some suggestions for improving statistical techniques. It is not intended to be comprehensive, and such topics as the "quality of the counselor-client relationship" and psychological theories of development are disregarded altogether.

One important aspect of the high school counselor's job is prediction—he must try to foretell the immediate and long-run consequences of each decision that the student might make. For example, whether a student should be encouraged to study engineering depends on the answers to many questions: Can he gain admission to college? Can he do satisfactory work in an engineering curriculum? Will he be satisfied with his choice of engineering as a vocation when he has had a few years' job experience? Will he be happier 10 years from now if he chooses to try to become a physician instead? The value of counseling to the student strongly depends on the accuracy with which such questions can be answered.

*Johns Hopkins University, Baltimore, Maryland.

Most attempts to answer such questions as those just mentioned rest on the assumptions that: (a) most individuals do find their ways into vocations for which they are well suited; (b) individuals having similar characteristics (interests, aptitudes, etc.) tend to be happy and successful in similar occupations; and (c) these characteristics are measurable and are sufficiently stable over time that they can be used as the basis for rational vocational choice. Thus the goal of vocational guidance counseling has been described as the fitting of square pegs into square holes, with the "shape" of an individual being determined by his interests, aptitudes, etc., and the "shape" of a vocation being inferred from studies of the characteristics of individuals who have chosen that vocation.

RELEVANT CHARACTERISTICS

One of the first problems of the guidance counselor is to ascertain what characteristics of his clients determine the "appropriateness" of various vocational decisions. The variables with which counselors have been primarily concerned can be divided into five categories:

- (1) Aptitudes,
- (2) Interests,
- (3) Skills,
- (4) Biographical data,
- (5) Other psychological characteristics.

These categories are, unavoidably, somewhat ambiguous and highly interdependent. The first three are relatively self-explanatory. Category (4) includes academic records as well as such characteristics as "father's educational level." Measures of motivation and whether or not an individual is "compulsive" according to some particular definition are characteristics from the fifth category.

Having somehow decided what characteristics to work with, the counselor must then learn how to measure them and how they relate, individually and jointly, to vocational success. For the measurement of aptitudes, the Differential Aptitude Tests are popular. The Strong Vocational Interest Blank (SVIB) and the Kuder Preference Record are widely used to measure interests, and there are many achievement tests available for determining the present skills of high school students. The relationship of measurable characteristics of students to their later vocational success is strongly dependent upon how such "success" is defined.

CRITERIA

One of the most pervasive problems encountered in attempts to study high school guidance counseling is that of specifying the criteria for evaluating a guidance program. A. S. Thompson (Reference 1) states, "The objective of vocational guidance is to help the individual develop and carry out a vocational plan which will be personally satisfying and socially useful. The vocational goal of the individual is to have a satisfying career, i.e. a sequence of positions which provides an outlet for his developing needs and an opportunity to implement his self-concept." Studies of the relationships between measurable characteristics of young people and later "vocational success" have necessarily been restricted to simple criterion variables which are hopefully indicative of personal

satisfaction, social usefulness, and implementation of self-concept. College grade-point average, college field of concentration, occupation entered upon graduation, and score on a test designed to measure "job satisfaction" are some criterion variables used.

Each of the criterion variable studied has severe shortcomings. For example, grade-point average is used as a measure of success in college, but such an average is probably more indicative of a student's skill at preparing for and taking written examinations than of his depth of knowledge or his personal and professional maturity. There is also the troublesome fact that, if two students are in different curricula or in different colleges, a direct comparison of their grade-point averages is meaningless. At present, however, the grade-point average is probably the best available single index of college success.

RESULTS OF SOME INVESTIGATIONS

Relationships of simple criteria to some variables that can be observed by high school counselors have received attention from researchers. Even more effort has been devoted to similar studies conducted at the college level. Many of these studies have been attempts to use statistical techniques to predict the value of the criterion variable, e.g. freshman grade-point average, on the basis of such observed characteristics as rank in high school graduating class and scores on college entrance examinations.

Since college students are presumably more mature and stable, with respect to most of the characteristics studied by counselors, than high school students, it might be expected that high school counselors can never achieve the accuracy of prediction attainable at the college level.

In most studies, the predictors have all been from within one of the five categories of characteristics (examples of exceptions are the investigations reported by Ghiselli (Reference 2) and by Frederiksen and Melville (Reference 3)); despite widespread recognition of the fact that, to make the "best" prediction, a counselor should consider all bits of available data simultaneously, considering such interactions as exist between, say, interests and skills.

Of course it is not expected that any approach will ever, in a free society, yield perfect prediction of any educational or vocational criterion. On the other hand, a test whose scores show no predictive validity with reference to some criterion of interest is of no value to the counselor. No study of which the author is aware has indicated that any presently available predictor or statistical prediction scheme can properly be described as highly accurate. However, most studies have used sufficiently large samples and powerful techniques to demonstrate statistically significant relationships between the predictors studied and the criteria that they would be expected to predict.

A brief look at the published reports of three studies will give some indication of the degree of accuracy attainable in predictions made at the high school level. Berdie (Reference 4) investigated the relationship between the Strong Vocational Interest Blank (SVIB) scores of high school seniors and their later occupational entry. The SVIB records of individuals who were tested in high school and who later received degrees in journalism (28 cases), dentistry (40), mechanical engineering (48), or architecture (14) were studied. Each individual's SVIB grade (A being the highest and C the lowest of six possible grades) on each of 13 occupational interest scales was determined. While 67 percent of the engineers received an A on the engineering interest scale, 79 percent received A on the aviator scale. Among student who became dentists, 45 percent had A on the farmer scale, while 28 percent had A and 18 percent had C on the dentist scale.

Only 36 percent of the architects had A on the architect scale; an equal percentage had A on the engineer scale, and 43 percent had A on the aviator scale. However, architects had more high (A or B+) grades than any of the other groups on the architect scale; engineers had more high grades on the engineer scale, etc. Berdie concluded that the results justify careful use of the SVIB in counseling high school seniors.

Bennett, Seashore, and Wesman (Reference 5), authors of the Differential Aptitude Tests (DAT), reported on an early study of their tests in an article entitled "Aptitude Testing: Does It 'Prove Out' in Counseling Practice?" Juniors and seniors in six public school systems took the DAT. Two years later 1,700 of these students returned a questionnaire which called for a report of activities since high school graduation. For each of 15 groups (e.g. engineering students, salesmen, clerks) the authors calculated the percentile equivalent of their average score on each of eight aptitude tests (e.g. Verbal Reasoning, Clerical Speed and Accuracy). Without mentioning within-group variation, the authors proceed to point out certain gross characteristics of the data - e.g. the average Mechanical Reasoning score for engineering students occurred at the 82nd percentile, while the corresponding average for liberal arts students was at the 64th percentile. In the final section of the paper they state that one conclusion justified by their data is that ". . . within any career group there exists a wide variety of talent. In the case of academic groups there is positive selection, yet even the most select groups contain some individuals who fall at or below the mean of their high school class on those tests which are commonly thought to have the greatest validity for predicting academic success."

Reid and others (Reference 6) studied the entire freshmen class at Newark College of Engineering and found that average scores on various aptitude tests were higher for the 147 students who were to graduate in 4 years than for the other 263 members of the freshman class. The successful students also had a lower average score on the Literary scale of the Kuder Preference Record. None of the differences between group averages was sufficiently large, relative to the variation of scores within the two groups, to indicate that any of the tests is of much practical value in predicting the success or failure of individual students. No attempt at analyzing a number of aptitude and preference scores simultaneously seems to have been made.

These and many other studies indicate that attempts to produce formulas for predicting simple criteria from scores on a single test or test battery available for used in high schools today have not yielded results of much proven practical value to high school guidance counselors. This finding does not mean that they are not of great practical value - perhaps the SVIB, for instance, is the perfect guide to vocational choice in that a student will be happiest and most successful in that vocation for which his score on the corresponding test scale is highest. The problem is that there is no other perfect means of selecting the best vocation with which the SVIB can be compared. If the vocations eventually chosen by individuals are usually the right ones, then the SVIB quite often makes the wrong choice. The criterion problem is inescapable and unsolved.

STATISTICAL TECHNIQUES

Two classes of statistical techniques, regression and discrimination, have played prominent roles in criterion-prediction studies. Regression techniques are frequently used in college admissions offices to predict such criteria as a student's freshman year grade-point average from various pre-admission variables. In counseling a freshman who has an interest in engineering and who wants to know whether he can be expected to perform reasonably well if he chooses to enroll in engineering, it might be appropriate for the counselor to apply regression techniques to predict grade-point average

in engineering from the student's scores on various tests. The usefulness of such techniques in vocational counseling at the high school level has not been clearly demonstrated.

A class of techniques which seem more promising for use in high school counseling, and which are widely used, are those of discrimination (classification). These are techniques directed towards (Geisser, Reference 7) ". . . the problem of rationally assigning individuals . . . to categories based on one or more observational characteristics." A familiar example is the use of various vocational scales of the SVIB to determine, on the basis of his answers to certain questions, whether a student is more "like" architects, journalists, or physicians.

Actually both regression and discrimination techniques are useful in attempting to answer the question "How well will the student perform?" For example, a medical school applicant's grade in anatomy might be predicted by discrimination techniques if the question is asked, "On the basis of his records and test scores, is this student most similar to students who have gotten A's, to those who have gotten B's, or to those who have gotten C's?"

In the simplest probabilistic formulation of the discrimination problem, an observation x is available on a random variable which has one of two known probability distributions. Say these distributions are determined by f_1 and f_2 respectively, where f_1 and f_2 are two probability density functions or two probability mass functions. The problem is to decide, on the basis of the observation x , whether the true distribution of the random variable is that determined by f_1 (call this the f_1 distribution) or by f_2 . With respect to many criteria for evaluating classification procedures, the best rule is "Decide that the f_1 distribution is correct if

$$f_1(x) > c f_2(x) . \quad (1)$$

Otherwise choose the f_2 distribution." The positive constant c is determined by f_1 and f_2 , certain prior knowledge, and the relative seriousness of the two possible misclassifications. This same rule applies also in the more general case in which the random variable of interest is vector-valued, so the observation is a vector, \vec{x} , and f_1 and f_2 are multivariate densities or probability mass functions.

A version of the discrimination problem which is sufficiently flexible to be useful in approximating many practical situations does not require complete knowledge of the two probability distributions: \vec{x} is a vector of observations on a random vector with one of two multivariate normal distributions. The distributions have different unknown mean vectors and a common unknown covariance matrix. For each distribution there is available a sample of (vector) observations from which the mean vectors and covariance matrix can be estimated. The well-known linear discriminant function of R. A. Fisher is frequently used in this situation. This linear discriminant function, while suggested by the multivariate normal distribution, has desirable geometrical properties which make it appealing in the still more general problems in which the two possible distributions of the random variable in question are not assumed to be normal.

Generalizations of the linear discrimination technique are available for more general cases in which there are many possible probability distributions for the random vector (see Rao, Reference 8), and a few moderately successful attempts (References 9 and 10), have been made to use these techniques in classifying students into occupational or performance groups.

On the other hand, the discrimination approach used by Strong in constructing the various vocational scales of his Vocational Interest Blank is not suggested by a probabilistic model, but is basically empirical. The SVIB consists of a series of statements to which the subject is to indicate a response of "like," "dislike," or "indifferent." If a student's reaction to a particular statement is "indifferent," he is given a score which is determined by the quantity $\hat{p}_E - \hat{p}_G$, where \hat{p}_E is the proportion of members of a group of engineers whose reaction to the statement was "indifferent" and \hat{p}_G is the corresponding proportion of a group of "men-in-general." The student's total score on all statements on the SVIB is taken as an index of how similar his interests are to the interests of engineers as opposed to interests of "men-in-general." Such scores can be calculated for each of many occupations.

Kuder (Reference 11) suggested that the ability of interest tests to discriminate between various occupational groups might be enhanced by a new scoring system. As before, an "engineering score" would be obtained from a subject's response vector $x = (x_1, x_2, \dots, x_n)$, where x_j , $j = 1, 2, \dots, n$, is the response to the j^{th} item on the test. But under Kuder's system this score is

$$S_E = \sum_{j=1}^n \hat{p}_E(x_j, j)$$

where $\hat{p}_E(x_j, j)$ is, for a large sample of engineers, the proportion whose response to the j^{th} item was x_j . If S_A is his "architecture score," and if S_E is greater than S_A , then the subject might be said to be more likely to be (or to become) an engineer than an architect.

Kuder applied this system in an attempt to classify individuals from six occupational groups (journalist, architect, pediatrician, etc.) according to their responses to items on the Kuder Preference Record, and obtained a degree of differentiation "... seldom if ever reached before in the field on interests."

The approach of Kuder represents a step towards the scoring system suggested most strongly by statistical theory. If the subject's response vector is considered to be such that the probability of a particular observed value, \vec{x} , is $p_E(\vec{x})$ if the subject is an engineer and $p_A(\vec{x})$ if the subject is an architect, then the suggestion is "Classify a subject with response vector \vec{x} as an engineer if and only if $p_E(\vec{x}) > c p_A(\vec{x})$ "; i.e. subjects for whom $\log p_E(\vec{x}) - \log p_A(\vec{x})$ is large are classified as engineers. If engineers' responses to the various test items are independent, then

$$p_E(\vec{x}) = \prod_{j=1}^n p_E(x_j, j) \quad (2)$$

$$\text{and } \log p_E(\vec{x}) = \sum_{j=1}^n \log p_E(x_j, j)$$

where $p_E(x_j, j)$ is the probability that an engineer will make response x_j to item j .

Even if item responses are not independent, Equation 2 may still provide a useful approximation to $p_E(\vec{x})$ (see Bahadur, Reference 12, and Solomon, Reference 13). The subject is then said to be more likely to be an engineer than an architect (or more "similar" to engineers than to architects) if

$$\sum_{j=1}^n \log p_E(x_j, j) - \sum_{j=1}^n \log p_A(x_j, j) \quad (3)$$

is large, and more likely to be an architect if the difference is small. Note that this is essentially Kuder's procedure with the score $p_E(x_{ij})$ replaced by $\log p_E(x_{ij})$. The score assigned to response i to item j for differentiating between architects and engineers is $\log [p_E(i,j)/p_A(i,j)]$ instead of Kuder's score $p_E(i,j) - p_A(i,j)$.

In applications of either scoring system, the probabilities $p_E(i,j)$ can be estimated from a sample of responses of engineers to the j^{th} item. If there are N_E engineers in this sample, and $N_E(i,j)$ of them make response i to the j^{th} item, then the proportion $\hat{p}_E(i,j) = N_E(i,j)/N_E$ is the estimate used by Kuder. Since the score $\log p_E(i,j)$ is extremely sensitive to slight variations in $p_E(i,j)$ when this probability is nearly zero, a better estimate for use in the log score might be

$$p_E(i,j) = \frac{N_E(i,j) + k}{N_E + Jk} \quad (4)$$

where k is a small positive integer and J is the number of possible responses to the j^{th} item. (In the case of the SVIB $J = 3$ for every item, since there are three possible responses - like, indifferent, and dislike.) For discussion of the estimate in Equation 4 see Good (Reference 14).

In case $p_E(\vec{x})$ is not well-approximated by

$$\prod_{j=1}^n p_E(x_j, j),$$

the probability of \vec{x} can be estimated directly as the fraction of individuals in the known engineer group whose response vector was \vec{x} , if this group is large and the random vector takes on only few possible values. For example, if the components of the vector are dichotomous variables, then there are 2^n possible values for the observed vector. If $n = 4$ and $N_E = 500$, then the approximation represented by the independence assumption may not be necessary.

Many quite complicated discrimination problems can be put into a form in which useful results can be derived from Equation 1. In the example of discriminating between engineers and architects, suppose, as before, that for each subject to be classified, a data vector \vec{x} is observed, and that data vectors are also available for two large groups - individuals known to be architects and individuals known to be engineers. Assume that \vec{x} has many components, say, results of various interest, aptitude, and achievement tests, and biographical information. First the data might be reduced to a "summary" vector, \vec{y} , with only a few (say five) components. If the first 400 components of \vec{x} are the subject's responses to items on the SVIB, these might be reduced to one number, y_1 , say the engineer-vs-architect discrimination score Equation 3. The next two components, y_2 , and y_3 , might be some functions, suggested by factor analysis, of the subject's aptitude test scores. Suppose y_4 is 0 or 1 to indicate the absence or presence of some biographical characteristic and y_5 is a percentile score on a mathematics achievement test. Hopefully \vec{y} contains most of the pertinent information in \vec{x} .

Next \vec{y} is transformed into $\vec{z} = (z_1, z_2, \dots, z_5)$, where z_1 is -1, 0, or 1 depending on whether y_1 is "low," "moderate," or "high," z_2 is 0 or 1 indicating that y_2 is "low" or "high," etc. If $\hat{p}_E(\vec{z})$ is the relative frequency of the vector \vec{z} in the engineer group and $\hat{p}_A(\vec{z})$ is the relative frequency in the architect group, a classification rule can be based on the ratio $\hat{p}_E(\vec{z})/\hat{p}_A(\vec{z})$.

Such a procedure represents a multivariate approach to the problem which has the advantages of requiring neither (a) that all variable in question be continuous, nor (b) such assumptions as equality of covariance matrices. Although there is at present no comprehensive theory for determining what components should comprise the vector \vec{y} and in what way they should be "discretized" to form the vector \vec{z} , factor analysis, experimental design, and information theory have contributions to make, and an approach based on "educated intuition" might produce interesting results.

Similar techniques are applicable in attempts to discriminate between students who will pass and those who will fail some future test. These techniques can also be generalized to apply to discrimination problems involving more than two categories.

CONCLUSION

The ability to make good predictions by using probabilistic statistical techniques is not required of a good counselor. The ability to make good predictions somehow is what is important. Some investigators (Meehle, Reference 15; Lewis and MacKinney, Reference 16; and Bartlett and Green, Reference 17) have asked whether experienced counselors or mathematical formulas can make better predictions. Efforts are being made at computer simulation of the decision-making process of an expert counselor (Cogswell, Reference 18; after Kleinmuntz, Reference 19). If such attempts are successful and if the counselor's predictions are quite accurate, efforts at prediction based on probabilistic statistical theory can be left to the theorist and researcher. However, studies to date have indicated that counselor predictions are likely to be inferior to statistical ones.

Such studies as Berdie's (Reference 4) indicate that records of interest tests administered in high school are of some value in discriminating between individuals who have wound up in different professions. The practical value, to high school counselors, of making such tests slightly better discriminators or predictors by refinement of statistical techniques is not obvious. In fact, it is not clear what a high school counselor would do with a formula for predicting, say, a student's occupation 10 years after high school graduation, if such a formula existed.

The counselor's real questions seem to be of the form, "If this student goes into engineering, what are his chances of success?" Attempts to produce techniques for constructing profiles, based on tests and other data, showing the student's probability of success in each of several educational or vocational fields have been made. (Note that the criterion problem lingers.) Dyer (Reference 20) describes the results of such attempts as "discouraging" and goes on to state:

"They provide reasonably good over-all prediction, but so far they do not provide much differential prediction. That is, the probability that a given student will succeed in any one field is not so greatly different from the probability that he will succeed in most other fields . . . it is a moot question, it seems to me, whether any tests can ever be found that will separate very far in advance the student more likely to succeed in biology from the one more likely to succeed in history . . . I think it is possible that human abilities are sufficiently fluid over time so that, if circumstances are right, the person who today looks like a good biologist and a poor historian may undergo experiences which will convert him into a good historian and a poor biologist. You see, the trouble with the well-known square-peg-in-a-round-hole analogy is that neither the peg nor the hole can ever change shape,

when we know perfectly well that the patterns of people's abilities change as they adapt to circumstances, and circumstances change as people adapt to them. In other words, I suspect that there are dynamic elements in the relation of an individual to his changing environment which are not being taken into account in the differential prediction studies and which may, indeed, prevent them from even arriving at any very fruitful results."

One point which has received very little attention is that of the long-run effects of a guidance system that directs a student towards engineering if he has characteristics similar to those of the "average" engineer. One effect would almost surely be a reduction in the degree of variation of interests and abilities between individuals within each vocation. An individual with outstanding administrative abilities or potential might not be counseled to study engineering, and one who is a "natural" engineer might be advised to study engineering in preference to medicine. If such individuals enter the professions into which they "fit" most naturally, according to the counselor's formula for assigning pegs to holes, who will head the engineering schools and who will perfect the mechanical heart? Most occupations, however defined, encompass a tremendous variety of activities, and any career group requires not stereotypes but persons with a wide range of abilities and interests. Frequently it is not those abilities which he has in common with most of his colleagues, but those which are unusual, which make an individual valuable to his profession.

Prediction is but one of the activities of high school vocational guidance counselors. Another is education, and here there seem to be opportunities for immediate, meaningful improvements. In a study of how more students might be attracted to engineering, Renner (Reference 21) asserts that students generally do not gain any understanding of the engineering profession while in senior high school. There is some evidence (Renner, Reference 22) that most high school students do not understand the differences between the duties of scientists, engineers, and technicians, and it is likely that high school students' attitudes towards most professions are dominated by romantic false impressions - an architect is a brilliant, unorthodox "fountainhead" of creativity, a musician is a soloist who holds audiences spellbound with his virtuosity, a scientist is either Thomas Edison or Albert Einstein. Such misconceptions constitute real but, at least partially, removable obstacles to rational vocational choice.

REFERENCES

1. Thompson, A. S., "The Criterion Problem in Selection and Guidance," Occupational Psych. 39:83-88, 1965.
2. Ghiselli, E. E., "Differentiation of Tests in Terms of the Accuracy with which They Predict for a Given Individual," Educational and Psychological Measurement 20:675-684, 1960.
3. Frederiksen, N., and Melville, D. S., "Differential Predictability in the Use of Test Scores," Educational and Psychological Measurement 14:647-656, 1954.
4. Berdie, R. F., "Strong Vocational Interest Blank Scores of High School Seniors and Their Later Occupational Entry II," J. of Appl. Psych. 49:188-193, 1965.
5. Bennett, G. K., Seashore, H. G., and Wesman, A. G., "Aptitude Testing: Does It 'Prove Out' in Counseling Practice?" Occupations 30:584-593, 1952.
6. Reid, J. W., Johnson, A. P., Entiwisle, F. N., and Angers, W. P., "A Four-Year Study of the Characteristics of Engineering Students," Personnel and Guidance Journal 41:38-43, 1962.
7. Geisser, S., "Predictive Discrimination," in: Multivariate Analysis, Af 33(615)-3016, New York: Academic Press, 1966.
8. Rao, C. R., Linear Statistical Inference and Its Applications, New York: Wiley, 1965.
9. Hall, R. C., "Occupational Group Contrasts in Terms of the Differential Aptitude Tests: An Application of Multiple Discriminant Analysis," Educational and Psychological Measurement 17:556-567, 1957.
10. Calia, V. F., "The Use of Discriminant Analysis in the Prediction of Scholastic Performance," Personnel and Guidance Journal 39:184-190, 1960.
11. Kuder, G. F., "A Rationale for Evaluating Interests," Educational and Psychological Measurement 23:3-12, 1963.
12. Bahadur, R. R., "A Representation of the Joint Distribution of Responses to n -Dichotomous Items," in: Studies in Item Analysis and Prediction, ed. by H. Solomon, Stanford Univ. Press, 1961, pp. 158-168.
13. Solomon, H., "Classification Procedures Based on Dichotomous Response Vectors," in: Studies in Item Analysis and Prediction, ed. by H. Solomon, Stanford Univ. Press, 1961, pp. 177-186.
14. Good, I. J., The Estimation of Probabilities, Research Monograph No. 30, Cambridge, Mass.: The M. I. T. Press, 1965.
15. Meehle, P. E., Clinical versus Statistical Prediction, Minneapolis: University of Minnesota Press, 1954.

16. Lewis, E. C., and MacKinney, A. C., "Counselor vs Statistical Predictions of Job Satisfaction in Engineering," Journal of Counseling Psychology 8:224-230, 1961.
17. Bartlett, C. J., and Green, C. G., "Clinical Prediction: Does One Sometimes Know Too Much?" J. of Counseling Psych. 13:267-270, 1966.
18. Cogswell, J. F., "A Study of Psycho-Educational Appraisal by Digital Computer" (unpublished report, April 1963), System Development Corporation, Santa Monica, Calif.
19. Kelinmuntz, B., "Profile Analysis Revisited: A Heuristic Approach," J. of Counseling Psych. 10:315-324, 1963.
20. Dyer, H. S., "A Psychometrician Views Human Ability," Teachers College Record 61:394-403, 1960.
21. Renner, J. W., "Engineering and the High School," Clearing House 39:137-140, 1964.
22. Renner, J. W., "Senior High School Students and the Scientist, Engineer and Technician," School Science and Mathematics 64:513-517, 1964.